CITY UNIVERSITY LONDON

School of Engineering & Mathematical Sciences

OPTICAL CHARACTERISATION OF CAVITATING FLOWS IN DIESEL FUEL INJECTION EQUIPMENT

Mahesh Jeshani (MEng)

A thesis submitted for the fulfilment of the requirements of City University London

for the degree of Doctor of Philosophy

September 2013

શ્રીજીબાપા સ્વામીબાપા

ૐ શ્રી સ્વામિનારાયણબાપા સ્વામીબાપા ભગવતે નમ:

દિવ્ય જીવનની જ્યોત જગાવો, આપ કર્તા થઈ કાર્યો દિપાવો, મંગલમય સુખ નિત્ય દેનારા, જય ઘનશ્યામ જય જય કરનારા

Blank Page

Table of Contents

Table of Figures

List of Tables

Blank Page

Acknowledgements

To Lord Swaminarayanbapa Swamibapa without whose divine blessings and constant encouragement education for me was impossible.

I would like offer my deepest gratitude towards my supervisor Dr Russel Lockett who provided me with the opportunity to complete a PhD through constant financial and moral support and more over ample patience and advice when things were not going perfectly well. I am glad I had him as my supervisor due to his large knowledge database and critical analysis techniques; I have grown to count him more as a friend than a supervisor over number the years I have worked under his supervision. Without his advice and guidance I would not have been able to complete this work and I offer my deepest appreciation for all that he has done for me. I would also like to express gratitude towards Shell Global Solutions, in particular Mr Richard Price and Mr Trevor Davies for funding my research for a number of years. They have given me ample advice and training over the numerous presentations to them. The periodic meetings with them have been inspiring towards taking new approaches in my studies and I have learnt a lot from them.

I would like to thank my maternal grandparents Mr Jadva Bhimji Sanghani and Mrs Viruben Jadva Sanghani for all their support towards my education. They have supported me both financially and morally throughout my studies from my O' level education throughout my University undergraduate studies and I would like to dedicate all my achievements to them as they are the sole reason I stand up on my own two feet today. My parents did not have the financial capability to send me through further studies however, they showed faith in me and have morally supported me throughout my education without any financial restraints. I am lucky to have them as my grandparents and I hope I have made them proud. I will never be able to repay their kindness, however I would like to dedicate this work to them. I would also like to thank my paternal grandparents Mr Dhanji Kurji and Mrs Kunverbai Kurji for their constant support throughout my childhood and then once again throughout my life in the UK. A big thank you to my parents for their support and my upbringing

I must express my gratitude to the staff at City University, London especially the technical staff namely, Mr Grant Clow, Mr Jim Ford, Mr Mike Smith, Mr Jim Hooker and Mr Robert Cherry. They have great abilities in manufacturing and have advised me on numerous occasions on designs for manufacture for my experimental work. Mr Mike Smith has this unique ability of manufacturing the 6 hole real size acrylic injector nozzle tips. I am sorry for all the numerous nozzle tips he had to manufacture due to my scrutiny; however he was always happy and willing to help. Mr Grant Clow has manufactured numerous parts for the setup of both experimental rigs used in this work and I am highly thankful of him. He also has given me very good design advice and I am thankful for this. A big thank you also goes to Mr Jim Ford, whose skills cover all fields. His skills in solving complex electronic challenges are exceptional and he solved and designed all the electric controls of both the experiment rigs I have used. It has been great working with them of which I do not regret a moment. I hope I have not caused any grievances during my stay. Thanks to Dr Nic Mitrologou, for all his advice and help throughout my studies and Dr Liverani for providing a kick start during the initial phase of my studies.

Finally I would like to thank my life long companion Mrs Jagruti Jeshani for putting up with me during up my PhD. She has been of tremendous support and encouragement during this period of my life and has given me a wonderful gift of a new life in the form of Mukti Jeshani.

Mahesh Jeshani

Blank Page

Abstract

The recent advances in Fuel Injection Equipment (FIE) have led to the identification of deposits found in the fuel filters and injector equipment. The work carried out here identifies the effects of cavitating flows on the physical and chemical properties of diesel fuel in order to try to evaluate the mechanism for deposit formation in FIE equipment using optical techniques to characterise the cavitating flows.

Two sets of experiments have been carried out in order to understand the impact of cavitating flow on diesel fuels. The first experiment investigated the effects of sustained cavitating flow using a fuel recirculation rig. Samples of commercial diesel were subjected to forty hours of intense cavitating flow across a diesel injector in a specially designed high-pressure recirculation flow rig. Changes to the optical absorption and scattering properties of the diesel over time were identified by the continuous measurement of spectral attenuation coefficients at 405 nm by means of a simple optical arrangement. Identical diesel samples were maintained at 70 ^{o}C for forty hours in a heated water bath, in order to distinguish the effects of hydrodynamic cavitation and the regulated temperature on the cavitated diesel samples. The commercial diesel samples subjected to high pressure cavitating flow and heat tests revealed a response to the flow and temperature history that was identified by an increase in the optical attenuation coefficients of the cavitated and heated samples. The contribution of cavitating flow and temperature to the variation in spectral attenuation coefficient was identified. It was hypothesised that the increases observed in the spectral attenuation coefficients of the cavitated commercial diesels were caused by the cavitation affecting the aromatics in the commercial diesel samples. The fuels were sent for a GC x GC and particle count analysis and results show significant increase in particle number count in the fuels as a result of cavitating flow. An increase in particle count to such high magnitudes was not observed for the heat test samples. Qualitative chemical modelling results of the pyrolysis of fuel vapour cavities during collapse at high pressures and temperatures have shown possible pathways leading to the formation of particulates. The presence of aromatics in diesel fuel was considered to be key species to the formulation of soot particles, however at extreme pressures and temperature paraffins may also have the propensity to breakdown into aromatics and further on to the formation of soot particles as observed by the pathway analysis in the modelling in the appendix.

The second study undertaken involved the analysis of the near nozzle external spray dropsizing and atomisation characteristics of fuels with different distillation profiles using LIF-MIE image ratios. The LIF-Mie image ratios were simultaneously captured synchronously with the internal nozzle hole cavitating flow. Internal nozzle flow and sac observations after needle return have led to the conclusions that flow angular momentum is sustained in the sac flow after needle return. This flow was observed to have a high angular momentum which reduced over time. During the end of needle return, bubbles were observed in the sac hole forming as a result of needle cavitation. These bubbles retained the angular momentum of the flow post injection (after needle seal). The vortical motion in the sac lead to regions of high and low pressures in the sac volume and thus resulted in suction and discharge of bubble in the nozzle holes. The bubbles may have a high propensity of containing a mixture of fuel and air vapour whereas the suction and discharge offers a pathway to external gases entering the nozzle holes and sac volume. For operating engine conditions this would be post-combustion exhaust gases re-entering the nozzle holes. The combination of the bubble formation, its vortical motion due to the angular momentum of the liquid flow, its composition and high temperature, may form ideal conditions for pyrolysis like reactions which may lead to the formation of soot particles and deposits in the nozzle hole, sac and needle. Fuels with different distillation profiles were investigated to observe their external dropsizing distributions at 350 bar injection pressure. Results showed that fuels with lighter fractional compositions which also had lower viscosity produced lower Sauter Mean Diameter (SMD) distributions than fuels with higher distillation fractions and higher viscosity. Whether this is as a consequence of the distillation profile alone and is not influenced by the viscosity differences has not been investigated yet and would form the basis of further investigations and publications.

Blank Page

Nomenclature

Symbols

p_v	Vapour Pressure
p_{cr}	Critical Pressure
p	Pressure
P_{up}	Upstream Pressure
P_{down}	Downstream Pressure
R	Universal Gas Constant
T	Temperature
t	Time
V	Volume
Re	Reynolds Number
We	Weber Number
Oh	Ohnesorge Number
CN	Cavitation Number
U	Liquid Velocity
D	Diameter
U_l	Nozzle Flow Rate
l	Characteristic Length Scale
L_c	Length of Liquid Core
L_p	Distance of Penetration
θ	Spray Angle
μ	Viscosity
χ	Dimensionless size parameter
D_{inlet}	Inlet Diameter
D_{exit}	Exit Diameter
D_{32}	Sauter Mean diameter
σ	Surface Tension
C_d	Discharge Coefficient
ρ	Density
v_B	Bernoulli Velocity
K- factor	Conical Shape Factor

λ	Wavelength
m	Refractive Index
I	Intensity
h	Planck's Constant
c	Speed of Light
φ_F	Fluorescence Quantum Yield
S_{LIF}	LIF signal
S_{MIE}	Mie Signal
$\dot{V}$	Volume Flow Rate
A	Cross Sectional Area
I_t	Transmission Intensity
I_o	Incident Intensity
$\propto$	Absorption Coefficient
t_f	Transmission Factor
r_f	Reflectivity
I_T	Total intensity emitted by laser
I_R	Part of Intensity I_T reflected to by beam splitter
I_{T2}	Part of intensity I_T transmitted through filter/splitter
t_{fs1}	Intensity I_{T2} absorbed by window 1
t_{fs2}	Intensity absorbed by window 2
$I_{T3\,(M)}$	Final intensity into detector 2 (mirrored)
$I_{T3\,(A)}$	Final intensity onto detector 2 (un-mirrored)
I_{T1}	Laser intensity past First beam splitter
μ_{sig}	Mean of the background-subtracted intensity
STD_{signal}	Standard Deviation of signal
SNR	Signal to Noise

Acronyms

AGO	Atmospheric Gas Oil
CCD	Charge Coupled Device
CFD	Computational Fluid Dynamics
CI	Cetane Index
CR	Common Rail

EGR	Exhaust Gas Recirculation
FAME	Fatty Acid Methyl Esther
FCC	Fluid Catalytic Cracking
FDD	Fluorophore - Decanol Mixture in Diesel
FDP	Fluorophore - Decanol mixture in Paraffinic Fuel
FID	Flame Ionisation Detector
FIE	Fuel Injection Equipment
FOLD	Fluorophore - Octanol Mixture in Diesel
FTIR	Fourier Transform Infrared
GC	Gas Chromatography
GHG	Green House Gases
GTL	Gas to Liquid
HCO	Heavy Cycle Oil
INF	Internal Nozzle Flow
LDV	Laser Doppler Velocimetry
LIF	Laser Induced Fluorescence
LPG	Liquefied Petroleum Gas
LSD	Laser Sheet Dropsizing
MC	Mass Spectrometry
NI	National Instruments
OD	Optical Depth
PAH	PolyAromatic Hydrocarbon
PDA	Phase Doppler Anemometry
PDPA	Phase Doppler Particle Analyser
PIV	Particle Image Velocimetry
PLIF	Planar Laser Induced Fluorescence
PM	Particulate matter
RhB	Rhodamine B
RME	Rapeoilmethylesther
SLIPI	Structured Laser Illumination Planar Imaging
SMD	Sauter Mean Diameter
TTL	Transistor Transistor Logic
VCO	Valve Covered Orifice
VGO	Vacuum Gas Oil

Blank Page

Chapter 1 Introduction

In recent years, significant progress has been achieved in the development of diesel fuel injection technology. Its biggest advance is a result of the development of efficient high-pressure common-rail technology which provides flexibility during engine management and control over the entire range of engine speeds and fuelling requirements. In direct injection diesel engines equipped with a common rail system high injection pressures (up to 2000 bar) are used to enhance the spray atomisation and air-fuel formation in the combustion chamber. Air-fuel mixtures with high homogeneity result in; shorter ignition delays, low local temperatures and low CO and soot emissions, due to the improved energy delivery to the piston. As a result, the performance efficiency is significantly affected by the quality of the fuel atomization, evaporation and mixing [1].

Recent developments in common rail diesel engine technology still leave space for further improvements in its ecological and economical features. One of the possible improvements here is to control atomization and mixing of the fuel spray. The characteristics of a fuel spray depend on the fuel properties, geometry of the injector and the flow conditions upstream (inside) and downstream of the injection nozzle. Two main types of diesel injectors that are used in direct injection systems are: valve covered orifice (VCO) injectors and sac-type injectors as seen in Figure 1.1. The number and arrangement of nozzle holes, as well as their geometries may vary depending on the desirable conditions of operation of diesel engine. Computational fluid dynamics provides a useful tool for the prediction of the flow in a diesel injector and, thus, design and optimisation of the injection process. Although numerical simulations have become more efficient, the experimental method of study is considered more

reliable for use in the design of diesel injectors due to the uncertainties in specification of many parameters, such as geometry imperfections of real injectors, and also difficulties in the numerical modelling of the cavitation phenomena, which always accompanies the flow in diesel injectors [2,3].

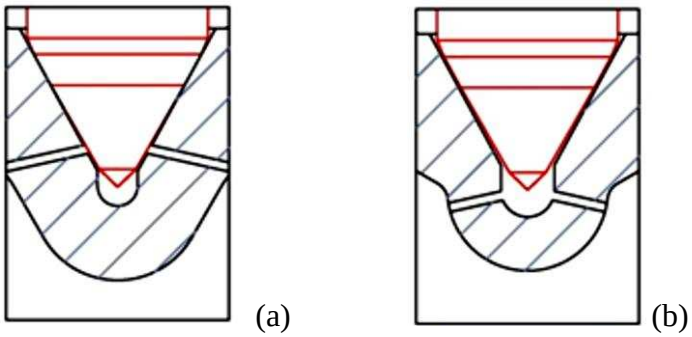

Figure 1.1 Two Types of diesel Injector Nozzles: (a) Valve-Covered Orifice (VCO) and; (b) the Sac Type

Recent developments in diesel engines and fuel injection equipment combined with the change to ultra-low sulphur diesel and bio blends have resulted in increased reports regarding deposits in injectors and filters [4]. These deposits appear to be more carbon like and more granular than deposits seen previously [5]. The deposition of materials within diesel fuel injection equipment and the blockage of fuel filters by material phase separating from diesel fuels are far from new phenomena. Previously identified causes include [5]:

- Fuel Adulteration with lubricant oil
- Additive miss-or over treatment
- Or bio-fouling.

The observed change in frequency of such occurrences suggests strongly that one or more recent changes must be responsible. Possibilities of the candidates responsible are:

- Higher injection pressure to meet tighter emission requirements and

- Shear and/or resulting temperature generated within the injectors.

It should also be noted that in a high pressure common rail engine, fuel is released from the high pressure common rail to the low pressure fuel return line through inlet and outlet restrictors on the valve control chamber [6]. Dependent upon the pressure drop and orifice size involved, there arises the possibility of jetting high pressure liquids into liquids with lower pressure, thus generating shear, friction and consequently heat. So far the extent and possibility of these effects are not clear. It has been suggested that engineering improvements involving increased fuel injection pressure and the resultant high pressures and concomitant high temperatures contribute to the observed fouling problem by accelerating fuel aging [5].

Power Setting	Supply Flow (GPH)	Return Flow (GPH)	Burn Rate (GPH)	Return %
idle - 5%	900	870	30	96.67
20%		808	92	89.78
40%		716	184	79.56
60%		624	276	69.33
80%		532	368	59.11
100%		440	460	48.89

Table 1.1 Table showing the fuel consumption and return rate in gallons per hour of a marine boat engine [7]

In diesel engines, fuel is pumped in a re-circulating loop at a higher volume than actually required by the engine. This serves to cool the injectors as well as powering the engine. Fuel unused is circulated back into the tank for re-use. Data from a large scale Caterpillar engine model 3612 of rated power 4640 bhp and rated speed 900 rpm [8] shows that when the engine is running at a full load the diesel fuel burn rate was 3.55 gallons per minute however its supply was 19 gallons per minute thus close to 81% of fuel supply was returned back to the tank. Data from a marine workboat diesel engine shows the supply return and burn rates from idle to full power as seen in Table 1.1. Modern common rail direct injection diesel engines

operate through the injection of high pressure liquid diesel fuel through magnetic solenoid actuated injectors directly into the engine cylinders. The diesel fuel is supplied to the injectors at high pressure from the common rail. When the fuel is supplied to the injectors, a proportion is injected into the engine, and the balance is returned to the fuel tank. If the engine is operated at low/part load, the rail pressure may be as low as 600 bar, and up to 40% of the high pressure diesel supplied to the common rail and the injectors may be returned to the fuel tank via the fuel return pipes in the pump, common rail, and injectors. However, when the engine is operated at high load, and depending on the engine, pump and common rail selected, the rail pressure may attain pressures of 1,400 to 2,000 bar. At these high load operating conditions, approximately 70% to 80% of the diesel supplied to the common rail and the injectors is injected into the engine, with the remainder being returned to the fuel tank [9]. Valves on the high pressure pumps, common rail and injectors regulate fuel through small orifices to release the high fuel pressure. Fuel flowing through an orifice, from a very high pressure environment to a lower pressure environment, results in it undergoing cavitation.

The consequences of returning a significant fraction of the fuel supplied to the injectors back to the tank is that the proportion of diesel fuel subjected to repeated high pressure pumping is a substantial fraction of the original volume. This implies that a significant proportion of the diesel fuel has been re-circulated through the high pressure pump and rail and returned to the fuel tank, prior to admission to the engine.

In connection to this, fuel-derived deposits and sediments have been observed to develop at the entrance to, and inside the nozzle holes in modern multi-hole diesel injectors [10–14]. Indeed, deposits along the needle and on the needle seat have also been discovered [13–15]. These deposits are likely to have an impact on the internal flow and the external atomisation

of the fuel jets emanating from the nozzle holes [16,17]. Engine performance is significantly impacted by the formation of deposits which may lead to increased fuel consumption, loss in power, poor driveability and failure to start [12].

Deposits at the exit of the injector nozzle holes may be formed through the partial oxidation and/or pyrolysis of liquid diesel fuel located on the outer surface of the injector body, coming into contact with hot combustion gases originating in the cylinder [18–20]. The mechanisms for deposit formation inside the nozzle holes, on the needle seat and along the needle are presently unknown.

The introduction of ultra-low sulphur diesel fuel, bio fuel blending components and modern diesel technology, has led to a rise in the incidence of fuel filter and injector fouling. This fouling takes the form of black, granular deposits in the injector and filter systems of modern engines. These deposits are carbon in nature with C16-C18 acids/esters present [5,21]. Filter deposits are a complex mixture of graphitic carbon, polyaromatics, cycloalkanes, aromatics, straight chain and substituted alkanes, acids, and inorganics. The cause is independent of whether a bio diesel blend or a straight run diesel is being used and thus they may be as a result of the higher thermal and pressure loads that the fuel is subjected to as a result of fuel injection equipment.

Cavitating flow is believed to occur in high pressure diesel nozzles during diesel fuel injection, to significantly affect the structure and atomisation of the fuel jets emanating from the nozzles and entering the engine cylinders [2,22]. Cavitation occurs when the diesel passes through or over a restriction, causing a large local pressure gradient and/or shear stress in the fluid. If the pressure gradient or shear stress in the fluid causes the local pressure to drop to

less than the saturated vapour pressure at the local temperature, then the liquid may begin to boil locally, forming local pockets of diesel fuel vapour [23]. Cavitation is also thought to be capable of altering injector surfaces though local hydro-erosion and hydro grinding [24]. In extreme circumstances, cavitation may cause injector failure [25]. It has been observed directly in a number of diesel fuel injection experiments [26–28]. There is anecdotal evidence that cavitating flow occurs inside automotive diesel common rail pumps during high pressure pumping [29]. Hydrodynamic cavitation is likely to occur near the high pressure cylinder valves in the pump, and in the fuel return valves located in the pump, common rail, and the injectors. In addition, there is a trend within the diesel fuel injection equipment (FIE) industry towards increasing common rail pressures. Indeed, Bosch has developed a 2,500 bar common rail fuel injection system [30], while both Denso and Delphi diesel Systems have reported the development of 3,000 bar common rail diesel fuel injection systems [31]. The industry trend towards larger common rail pressures may begin to affect the diesel fuel subjected to such extreme conditions, during pumping, storage and in-flow. This may occur through pyrolysis and/or intense cavitating flow, causing chemical re-arrangement and decomposition. This may, in turn, lead to deposit formation (sedimentation) and ultimately, to equipment failure.

The effect of cavitation on alkanes was first investigated by Suslick et al. [32]. They employed high intensity ultrasound on alkane solutions, and discovered primary products of hydrogen, methane, acetylene, and smaller 1-alkenes. They suggested that the reactions in the system bore strong similarities to high temperature pyrolysis, and concluded that the principal sono-chemical process responsible was C-C bond cleavage with secondary abstractions and re-arrangements. This was considered to be the consequence of high temperature regions developing in the multi-phase solution as a result of cavitation bubble collapse. Bubbles arise

due to the nucleation of small voids or cavities in the liquid. The process of nucleation will be discussed later on in Chapter 2.

The corresponding effects of ultrasound cavitation in diesel has been investigated by Price et al. [33,34]. They employed high intensity ultrasound to irradiate a diesel fuel sample, and observed the decomposition of saturated alkanes, and identified sonically promoted polymerization reactions that led to aromatics forming insoluble sediments (gums), similar to those reported by Pedley et al. [35] and Kalitchin et al. [36] as a result of the long term storage of diesel.

These investigatory reports [32–34] are about ultrasonic sono-chemistry in liquids. This is a recently developing field of chemistry, which involves theoretical, modelling and experimental research into the acceleration of reaction rates involving chemical reactions in liquid suspensions, solutions and/or pure liquids through the use of intense ultrasound. It is believed that intense ultrasonic excitation of a suspension, solution or pure liquid induces the formation and collapse of many micro-bubbles within the liquid, which are thought to develop very large internal vapour temperatures and pressures during bubble collapse. This process is known as ultrasonic cavitation, or ultrasound induced cavitation. Indeed, Suslick et al. have reported internal bubble temperature measurements of up to 5,000 K occurring during ultrasonic cavitation bubble collapse [37,38]. These observations in ultra-sound cavitation of diesel raise the question of whether similar effects occur, and are observable in hydrodynamic cavitation of diesel. Furthermore, it is necessary to discover whether high pressure diesel common rail fuel injection equipment produce hydrodynamic cavitation internally, and whether any such cavitation induces sonochemistry effects on the diesel fuel, resulting in deposit formation (sedimentation), similar to that reported earlier. It was therefore considered necessary to investigate the conditions that exist in high pressure pumping systems, and their

effect on the physical and chemical stability of the diesel fuel (through an analysis of the variation of the physical and chemical properties and composition of the fuel).

The aim of this work was to establish whether hydrodynamic cavitation introduced alterations to diesel fuel that could be identified using a simple measurement technique. This led to the design and manufacture of a high pressure, continuous re-circulation, cavitating flow rig that produced intense hydrodynamic cavitating flow continuously, involving a moderate volume of re-circulating diesel. A simple measurement technique for the identification and determination of change in composition and rate of change of composition of the diesel sample was required to be developed.

In this regard, the measurements and observations reported in Suslick et al. [32] and Price et al. [33,34] suggest that ultrasonic cavitation in diesel produces pyrolysis and the formation of insoluble sediments. Pyrolysis reactions in diesel necessarily result in the formation of primary soot particles (1 nm - 10 nm diameter), which are then able to aggregate to form larger soot particles (100 nm - 10 Gm), or bind to other particulates to form other sediments [39]. Both of these sets of findings and observations suggest the formation and development of soot-like particle suspensions in the diesel fuel samples. These lead to two significant hypotheses: (1) hydrodynamic cavitation of diesel will produce similar observable effects to those produced by ultrasonic cavitation (suggesting that the mechanisms for inducing the pyrolysis sono-chemistry in the diesel samples are similar), and (2) the formation of a particulate suspension in the diesel will be detectable using a simple optical extinction measurement system.

The second hypothesis required the development of a simple optical extinction measurement system, intended to identify and determine variations in the spectral extinction coefficients of

the diesel samples as a result of changes in the composition of the samples, and/or the formation and development of particle suspensions in the samples, arising out of cavitation induced diesel fuel pyrolysis.

The optical extinction measurement system developed and employed in these experiments was a simplification of the spectral extinction and scattering method [40,41]. This method is used widely in the determination of particle properties in suspensions, colloids and aerosols [42,43]. It is also employed in the determination of real and imaginary refractive indices in absorptive media [42].

A number of commercial and non-commercial diesel samples were subjected to continuous cavitating flow and exposure to a hot water bath in the course of the experimental work reported here. The results obtained from the diesel samples and model diesel samples are reported and will be discussed herewith. The commercial diesel samples discussed here consisted of newly bought samples, and samples that had been stored separately in diesel storage tanks for a year. The model diesel samples tested comprised of a paraffin blend (> 98 % paraffins), containing zero aromatics and a mixture of the Paraffin blend with biofuel.

A hot water bath was employed in order to separate out the combined effects of cavitation and the release of internal compression energy during the diesel flow through the diesel nozzle into the receiver. This was in order to identify and separate out the effects of temperature and cavitation on the diesel samples.

The second set of experiments were initially conducted for the analyses of diesel fuels of different distillation profiles and viscosity, to observe the effect of these variations on the

internal nozzle cavitation and its link to the external spray drop sizing distribution and thus atomisation characteristics. The prospect of this project was large, however only a few aspects have been discussed in the work here. Further analysis from the results obtained will form part of future publications. The work carried out here does not distinguish whether the effects are as a result of a combination of distillation profile variation and viscosity variation. In the fuels analysed, the lighter fuels, had lower viscosity than the heavier fuels and thus in order to determine whether the changes in Sauter mean diameter distributions were occurring due to the varying distillation profile or varying viscosity profiles, it is important to analyse the internal flow images, which is out of the prospect of the work reported here. The study here does not distinguish the effects solely to be occurring due to changes in distillation profile of the fuels.

During the initial testing some phenomena were observed occurring in the nozzle sac and holes that led to a link to the base of this thesis and thus the experimental apparatus, methodology and characterisation techniques are presented in this work here. The basis of this work from the experiments conducted will concentrate on the phenomena observed inside the nozzle sac and holes. Some spray sizing distributions will also be presented for completion. The degree of atomisation in the spray is related to its combustion characteristics and thus formation of particulates and emissions. The degree of atomisation can be controlled by an increase in injection pressure, change in nozzle characteristics and changes in fuel volatility and distillation characteristics. Thus the drop sizing distribution of fuels with different distillation profiles is also important due to the relationship of the degree of atomisation of the fuel to its combustion characteristics and thus particulate formation and emissions.

A vortex flow phenomenon was observed at the end of the injection in the sac volume. The vortex flow occurred as a result of needle cavitation and continued after the needle had returned to seal. Circular bubble movement in the nozzle holes due to the sac vortex flow was observed and their effects on the potential of deposit formation inside the nozzle holes, sac and needle tip analysed. Deposits have been observed to form in these locations in high pressure fuel injection equipment by various authors [12–16,19,21,44–46], however the phenomena observed here has not been reported in publications thus far.

The importance of the understanding of deposit formation in diesel high pressure injection equipment is of grave importance especially because the recent trend to obtain higher pressures results in injectors with smaller nozzle hole diameters and thus the formation of deposits in these could be catastrophic due to blockages.

This work is divided into eight chapters. **Chapter 2** gives a review on the fuels, cavitation, atomisation and measurement techniques. The chapter highlights research carried out by various authors in the field, combined with information available from theoretical books. Initially the chapter develops an understanding of fuel refinement, and fuel composition and its performance parameters before moving on to a review on cavitation and atomisation and finally experimental measurement techniques used to characterise cavitating flows.

In **Chapter 3** a description of the experimental apparatus, experimental procedures and calibration work carried out for the analysis of the effects of prolonged periods of cavitating flow on diesel fuel. The results obtained here are described in **Chapter 4** with a combination of the fuel GC x GC analysis results. In addition to this two merged chemical kinetics models have been used to obtain effects of high pressure bubble collapse on the fuel chemical

composition and the possible pathways leading to the formation of soot, which are presented in Appendix B. The results of the analysis will identify a pathway to the formation of soot particles from a derived chemical composition of diesel fuel. Due to the model having no validation, as it was compiled by merging two separate models, the results are qualitative and are only used to observe possible pathways to the formation of soot.

In **Chapters 5** and **6** the experimental setup, apparatus, high speed acquisition setup and timing, laser sheet dropsizing setup, experimental methodology and calibration are described of the second investigation. The design of an acrylic nozzle used in these studies is described here. Chapter 6 also includes the results from the injected mass calibration, manufacturing calibration, imaging error analysis and laser profile measurement. These two chapters provide an overview of the experimental setup and run procedures with calibration analysis for the results to follow.

The results from experiment described in Chapters 5 and 6 are discussed in **Chapter 7** giving importance to the vortex flow occurring in the sac volume and the resulting rotational bubble movement in the sac and linear motion in the nozzle holes. This chapter also describes the effects of various fuels of different distillation profiles on their Sauter mean diameter intensity distributions and thus atomisation characteristics.

Finally **Chapter 8** provides an overall conclusion of the results obtained thus far concluding with some ideas of further work in the field.

Chapter 2 Literature Review

2.1 Diesel Fuel Background

Diesel fuel keeps the world economy moving. When burnt it produces chemical energy and this energy is used in many applications and industries for example in electric power generation, road transport, farming, marine shipping, military transportation, rail transportation and off-road uses such as mining and construction. Most of these applications however use the chemical energy produced and convert it to mechanical power. This section will discuss the production, composition, performance parameters of diesel fuel and diesel fuelled cars. The review on this section on diesel Fuels has mainly been compiled from [47] and other fuel regulatory data and reviews found online. A single reference has been stated as work found various sources provided similar accounts through various documents from fuel manufacturers and webpages found on the internet. The work describes fuel refinement processes from which the reader can gain a brief understanding of the processes involved in fuel manufacture and thus its composition. The fuel composition will relate to work found in later chapters which include fuels analysis. Fuel performance parameters define how a fuel will act in a combustive environment. The work here describes the effects of this performance parameters on the fuel properties and how they will affect the propensity of the fuels to cavitate, atomise and thus combust. Finally a few alternative fuels are discussed before concluding with a section on fuel additives used in the commercial fuels today and how they affect the fuel performance.

2.1.1 Refinement from crude oil

Diesel fuel is made from petroleum crude oil which is primarily composed of hydrocarbons of the paraffinic, naphthenic, and aromatic classes. The petroleum crude oil is refined to produce various fuels including diesel, and other oils and waxes. The refining process consists of the separation, upgrading and conversion processes. During the initial two stages the feedstock crude oil remains otherwise unchanged however the final refining stage changes its molecular structure.

The most common separation process is distillation. In the separation process, the feed crude oil is separated into two or more components based on a physical property. This physical property when distilling is the boiling point. Distillation is a process used to separate wide boiling range mixtures into products with narrower boiling point ranges. Initially hydrocarbons with low boiling points like propane and butane rise to the top and are removed. Gasoline has a slightly higher boiling point and does not rise to the top of the distillation chamber. It is drawn off from the side of the column. Kerosene and diesel which have even higher boiling points are drawn off successively lower from the column. Refining by distillation alone yields too much of the high boiling point hydrocarbons and not enough low boiling point ones. In addition to this the quality is often poor.

The upgrading processes improve the quality of the distillates obtained earlier by using a chemical reaction to remove compounds present in trace amounts that give them an undesirable quality. During the upgrading process undesired components in the hydrocarbons past the refining process are removed by a hydrogen treating process. The processes run the gamut from mild conditions that remove compounds like olefins, some sulphur and oxygen

compounds, to more severe conditions that saturate aromatic rings and remove almost all sulphur and nitrogen compounds.

The conversion process fundamentally changes the molecular structure by catalytic cracking and hydrocracking. In the cracking process heavy hydrocarbons are broken down into simpler molecules such as light hydrocarbons, by the breaking of carbon-carbon bonds in the precursors. Hydrocarbons with higher boiling points are broken down into lower boiling point hydrocarbons by subjecting them to a very high temperature.

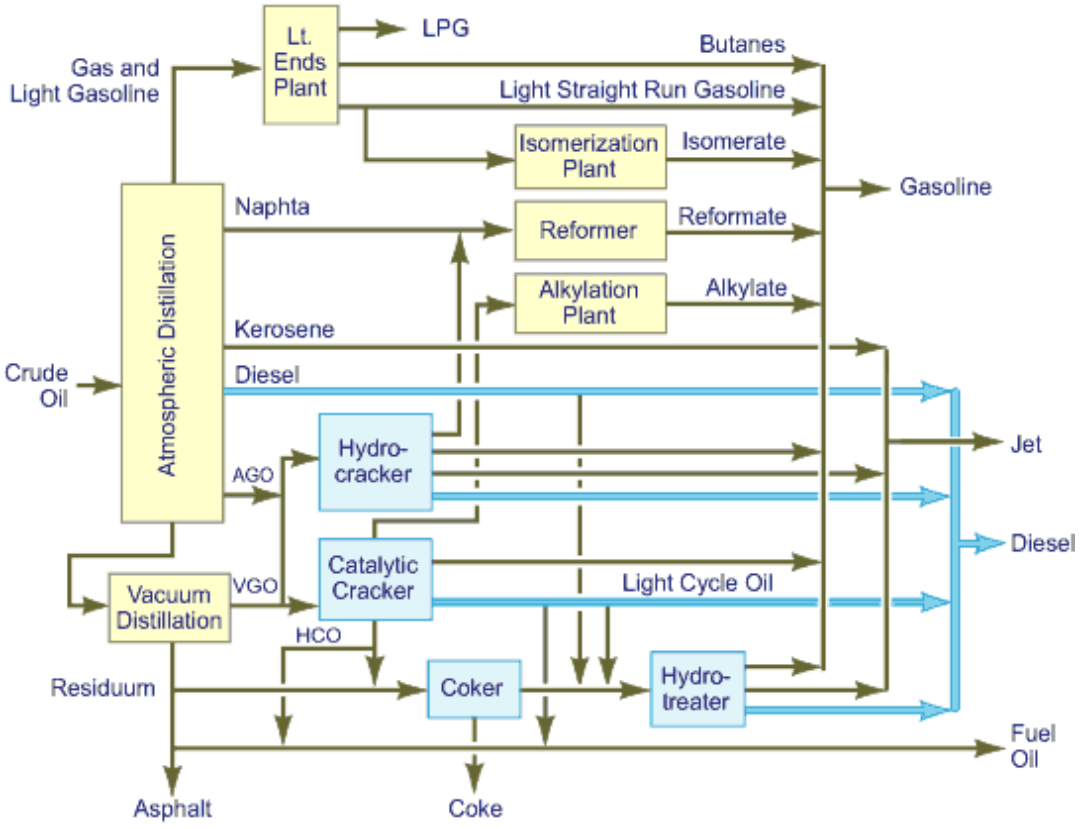

Figure 2.1 The crude oil refining process [48]

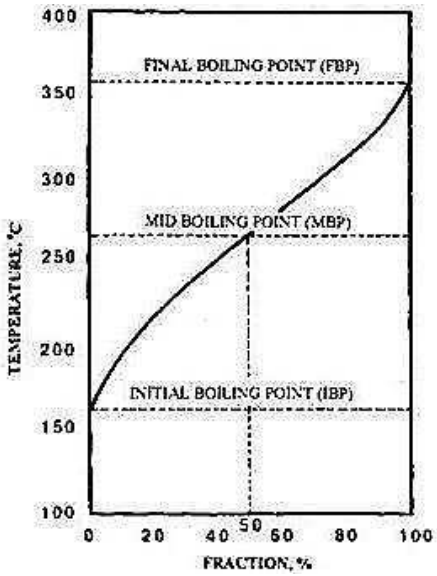

Figure 2.2 The distillation curves for diesel fuels over a range of fractions from about 150- 360 °C [47]

In a modern refinery crude oil is fed to the distillation column where the straight run naphtha, light and heavy boiling point gasoline, chemical naphtha, kerosene, and diesel are separated at atmospheric pressure. The vacuum gas oil (VGO) obtained from the vacuum distillation of the atmospheric bottoms are fed to either the fluid catalytic cracking (FCC) unit or the hydrocracker. The vacuum distillation resid may be used as a low value, high sulphur fuel oil for onshore power generation or marine fuel. The diesel fuel produced by a refinery is a blend of all the appropriate available streams: straight run product, FCC light cycle oil and hydrocracked gas oil. Figure 2.1 gives an overview of the crude oil refining process. The straight run diesel may be acceptable as is, or may need minor upgrading for diesel used in off road use. The diesel blends formed have to meet all performance, regulatory and economic requirements. Although crude oil can continue up to about 370 ºC, or slightly higher, before thermal cracking is liable to occur, diesel fuel mostly comprises of fractions boiling off from approximately 250 ºC to 355 ºC as compared to 15 ºC to 210 ºC for gasoline [47]. The final diesel blend detailed composition will highly depend on the primary crude oil feed and the refiner has limited control over it. Figure 2.2 shows the typical distillation curve of commercial diesel fuel.

2.1.2 Composition of diesel fuel

Diesel fuel is a very complex mixture of thousands of individual compounds, most with carbon numbers between 10 and 22. Diesel fuels are commonly mixtures of hydrocarbons of class; paraffins, olefins, napthenes and aromatics. Each class of hydrocarbon has different physical and chemical properties and thus each blend of diesel fuels is different from another relative to each having different proportions of these classes. Important fuel properties like boiling point, freezing point, density, heating value, Cetane number and viscosity vary depending on their relative proportions of classes of hydrocarbons.

Paraffins have the general formula C_nH_{2n+2}, where "n" is the number of carbon atoms (carbon number) in the molecule. There are two subclasses of paraffins: normal paraffins and iso-paraffins. Normal paraffins have carbon atoms linked to form chain-like molecules, with each carbon– except those at the ends – bonded to two others, one on either side. Iso-paraffins have a similar carbon backbone, but they also have one or more carbons branching off from the backbone. Normally decane and 2, 4-dimethyloctane have the same chemical formula, $C_{10}H_{22}$, but different chemical and physical properties as seen in Figure 2.3. Compounds like this, with the same chemical formula but a different arrangement of atoms, are called structural isomers.

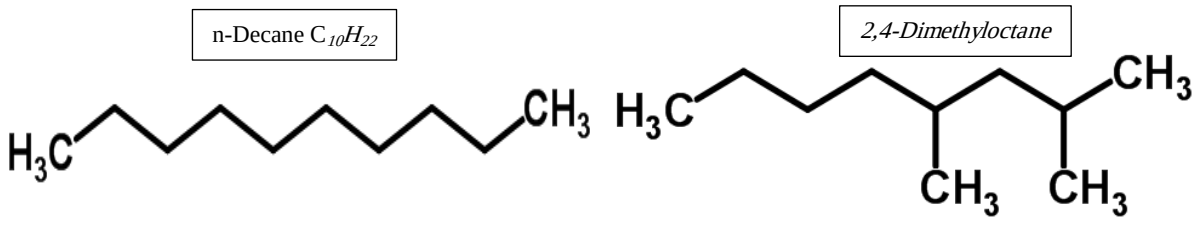

Figure 2.3 Paraffins: n-Decane $C_{10}H_{22}$ and 2, 4-Dimethyloctane $C_{10}H_{22}$

Naphthene is the term used in the petroleum industry to describe saturated cyclic or ring hydrocarbons. The same compounds are also known as cycloalkanes and cycloparaffins. They have some of their carbon atoms arranged in a ring as can be observed in Figure 2.4. The napthenes in diesel fuel have rings of five or six carbons. Sometimes two or more rings are fused together, with some carbons shared by adjacent rings. Napthenes with one ring have the general formula C_nH_{2n}.

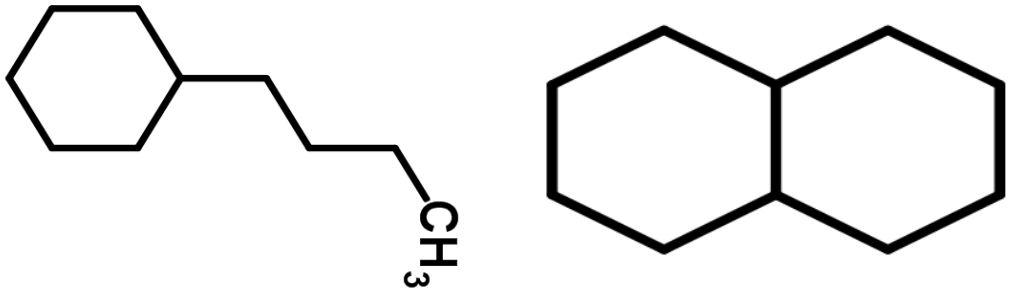

Figure 2.4 Napthenes: Butylcyclohexane $C_{10}H_{20}$ and Decalin $C_{10}H_{18}$

Olefins are similar to paraffins but have fewer hydrogen atoms and contain at least one double bond between a pair of carbon atoms. Olefins rarely occur in crude oil; they are formed by certain refinery processes. Like paraffins, olefins with four or more carbons can exist as structural isomers. Olefins with one double bond have the general formula C_nH_{2n}, the same as napthenes as observed in Figure 2.5.

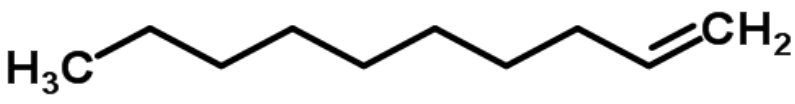

Figure 2.5 Olefin: 1-Decene

As with napthenes, some of the carbon atoms in aromatics are arranged in a ring, but they are joined by aromatic bonds, not the single bonds found in napthenes. Aromatic hydrocarbon

rings contain six carbon atoms. Benzene is the simplest aromatic compound. The benzene structure was originally conceptualized as two equivalent structures with alternating single and double bonds. Each structure continually transformed itself into the other as the double bonds flipped back and forth between different pairs of carbon atoms. Now, we know that all the carbon to carbon bonds in benzene are equivalent. The shorthand representation of benzene is a hexagon with a circle inside representing the aromatic bonds as in Figure 2.6. One-ring aromatics have the general formula $C_nH_{2n-6.}$ Polycyclic aromatics are compounds with two or more aromatic rings. These rings are fused together, with some carbons being shared by adjacent rings.

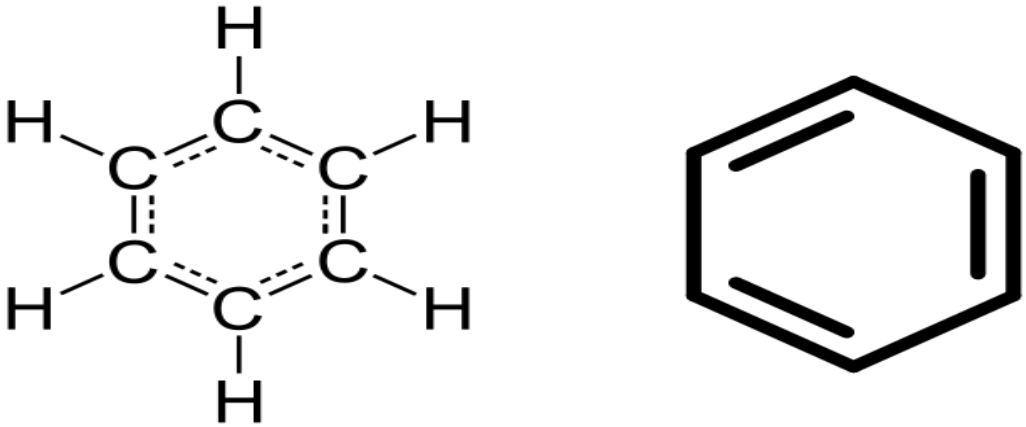

Figure 2.6 Aromatics: Benzene

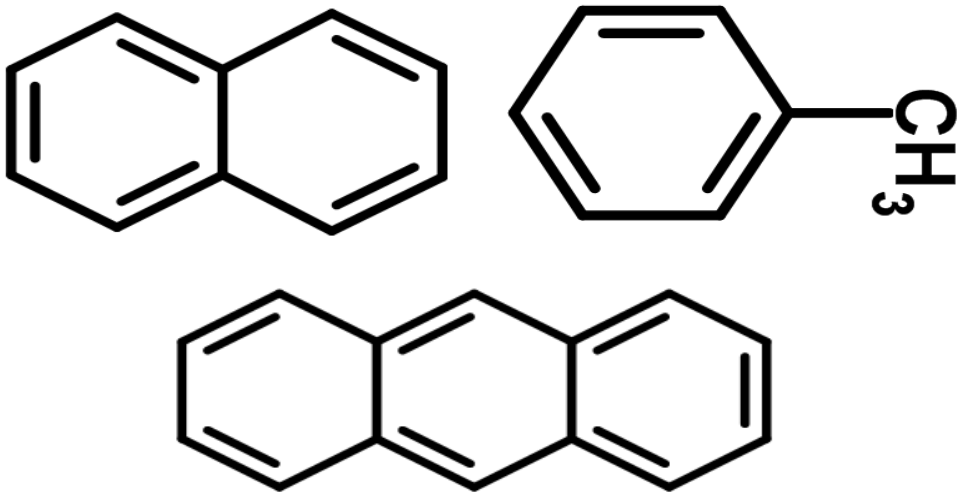

Figure 2.7 Aromatics: Naphthalene $C_{10}H_8$, Toluene $C_6H_5.CH_3$, Anthracene $C_{14}H_{10}$

Paraffins and napthenes are classified as saturated hydrocarbons because no more hydrogen can be added to them without breaking the carbon backbone. Aromatics and olefins are classified as unsaturated hydrocarbons. They contain carbon to carbon double bonds or aromatic bonds that can be converted to single bonds by adding hydrogen atoms to the adjacent carbons. When straight-chain olefins are saturated with hydrogen, they become paraffins by a process called hydrogenation. When aromatics are completely saturated with hydrogen, they become napthenes; when they are partially saturated, they become cyclic olefins. Some molecules contain structural features characteristic of two or more hydrocarbon classes. For example, a molecule could contain an aromatic ring, a naphthenic ring, and a paraffinic chain. Chemists have established a hierarchy of hydrocarbon structural features, with aromatics at the top, followed by olefins, napthenes, and paraffins. A compound with features of more than one class is placed in the class highest in the hierarchy. So, in our example, the molecule is classified as an aromatic.

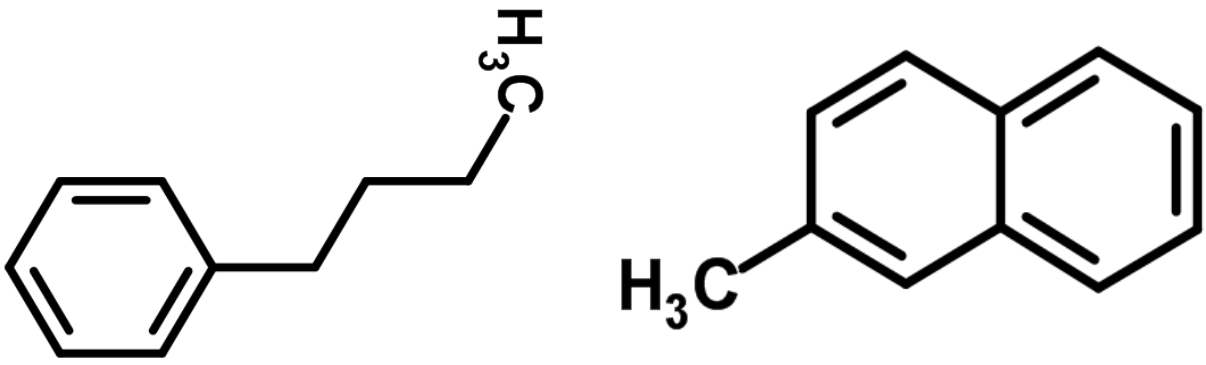

Figure 2.8 Other Aromatics: Butyl benzene $C_{10}H_{14}$ and 2-Methylnaphthalene $C_{11}H_{10}$

While carbon and hydrogen are the predominant elements in crude oil, small amounts of sulphur, nitrogen, and oxygen are also present. These elements are called heteroatoms ("other" atoms). Molecules containing heteroatoms are not classified as hydrocarbons. Typical examples found in diesel fuel include dibenzothiophene and carbazole.

The effects on emissions of fuel aromatic content were examined by Cuvelier et al [49]. Tests were conducted on three cars and two heavy-duty engines, representing a range of typical Euro 3/III technologies. One of the cars was equipped with common-rail injection, one with unit injectors, and one with an advanced rotary pump. The cars reflected the most advanced engine technologies available at the time. One of the heavy-duty engines had a capacity of 7.3 litres and was equipped with an in-line pump but not exhaust gas recirculation (EGR). The other engine had a capacity of 10.6 litres, and was equipped with unit injectors and cooled EGR. The Euro 3 Motor Vehicle Emission Group (MVEG) test cycle was used to test the cars, and the European Stationary (steady-state) Cycle (ESC) test was used for the heavy-duty engines. Fuel effects were generally found to be small compared with engine technology effects and between-test variability, and significant fuel effects were difficult to identify. For the cars, the effects of changing the fuel aromatic content varied between vehicles. Only one vehicle showed significant effects on particulate matter (PM) and NOx; in this case NOx emissions decreased and PM emissions increased as aromatics were reduced, however the effects were very small. There were no consistent trends in hydrocarbon (HC) emissions, but carbon monoxide (CO) emissions tended to decrease with lower aromatic content. As the total aromatics effects were small, it was not possible to quantify separately the relative contributions from mono-aromatics versus poly-aromatics. The variation in total aromatic content of the fuels was very small and thus no significant effects were observed in the emissions. In the case of the heavy-duty engines, reducing the aromatic content of the fuel reduced HC emissions but had no significant effect on PM, NOx or CO. The researchers here did not vary the total aromatics content in the fuels, an increase in one subset of aromatics was compensated by a reduction in another and thus no significant effects due to aromatics were observed.

A study by Emissions, Fuels and Engine Technologies (EPEFE) [50], tested 19 diesel Light duty vehicles. They found that reducing poly-aromatics decreased NOx, PM, formaldehyde and acetaldehyde emissions, but increased hydrocarbon, benzene and CO emissions. For heavy-duty vehicles, reducing poly-aromatics decreased NOx, PM and hydrocarbon emissions [51,52].

Doel et al. [53] examined the relationships between fuel composition and exhaust emissions of PAHs from a range of diesel and gasoline vehicles and fuels. The testing was separated into two phases. Phase 1 of the experiment consisted of tests on Euro 1 and 2 diesel cars, and a Euro II heavy-duty diesel engine. A 1994 heavy-duty engine was also tested during Phase 1. This engine had an emissions performance close to the Euro II standard, and was considered to be typical of the bulk of the European Euro II heavy-duty diesel fleet. Phase 2 consisted of tests on Euro 3 and Euro 4 cars. The cars and heavy-duty engines were tested over the NEDC and ECE49 cycles respectively. Five diesel fuels were used in Phase 1. These had a PAH concentration of between <1% and 12% by mass. Five more diesel fuels were also used for the Phase 2 tests, with a PAH concentration of between <1% and 9% by mass. For the gasoline engine vehicle tests, two petrol fuels were used in Phase 1, with benzene content of 0.17% and 1.59% respectively. These were produced by blending fuels to produce a range of aromatic and sulphur content, but were both within the specification limits of EN228. In Phase 2 a single gasoline fuel with a benzene content of 0.09% was used. This was considered to be representative of the 50 ppm sulphur EN228 grade required from 2005. They found older diesel vehicles produced higher PAH emissions and were also more sensitive to fuel composition than newer or more advanced vehicle. They concluded that the inclusion of mono-aromatics increased the emissions of PAHs having two plus rings, but the poly aromatics were found to have a greater effect. Reducing the polyaromatic content to zero, did

not eliminate the PAH emissions. A significant proportion of these PAHs being formed were combustion-derived. All the gasoline cars tested with three-way catalysts gave lower emissions of 2+ rings PAH than the older technology light duty diesel vehicles. A variable valve timing (VVT) equipped gasoline vehicle was the lowest emitting of all the gasoline vehicles tested.

2.1.3 Diesel fuel performance parameters and effects on engine performance

This section will discuss the performance parameters of fuels and their effect on engine performance. The performance critical properties to be controlled when fuel is blended are: Cetane number, Volatility, Density, Viscosity, Flash point, Sulphur and Waxing tendancy [47]. Each of these properties influences engine performance.

Cetane number is a measure of how readily the fuel starts to burn (autoignites) under diesel engine conditions. It is a measure of the percentage of Cetane in a mixture of cetane and heptamethyl nonane that has the same ignition delay as the fuel under test. Cetane is a straight chain normal hexadecane ($C_{16}H_{34}$) whereas heptamethyl nonane is a multiple branched alkane. The cetane number is precisely defined as the percentage n-cetane + 0.15 times the percentage of heptamethyl nonane contents of the blend of reference fuel having the same ignition quality as the fuel under test. A fuel with high cetane number starts to burn shortly after it is injected into the cylinder. Therefore it has a short ignition delay period. A fuel with low cetane number resists autoignition and has a longer ignition delay period. Ignition delay is important because, if it is too long, the bulk of the charge in the cylinder tends to fire simultaneously, causing violent combustion. Although too high a cetane number can cause ignition before adequate mixing and thus increase emissions. The actual delay represented by

the cetane number is only valid in the engine it was measured and the fuel performance may differ in other engines.

Carrying out laboratory engine tests, however is not a convenient method of assessing the quality of fuel, so two other criteria are widely used. One is the diesel index and the other cetane index. The diesel index computed mathematically is computed by multiplying the aniline point of the fuel by (lowest temperature in ºF at which a fuel is completely miscible with an equal volume of phenylamine aminobenzene) its API (American Petroleum Institution) gravity divided by 100. The Cetane index CI is calculated from API gravity and its mid-volatility (mid-boiling point T_{50} (50% recovery temperature). According to ASTM D 4737 1988, the cetane index is given by:

$$CI = 45.2 + 0.0892(T_{10} - 215) + 0.131(T_{50} - 260) + 0.0523(T_{90} - 310) + 0.901B(T_{50} - 260) - 0.420B(T_{90} - 310) + 0.0049(T_{10} - 215)^2 - 0.0049(T_{90} - 310)^2 + 107B + 60B^2$$

Equation 2.1

Where $B=e^{[-3.5(D-0.85)]}$, D is the specific gravity at 15ºC and T_x represents x% distillation temperatures in ºC.

The cetane and diesel indices vary with the hydrocarbon structure and thus the blends need to be controlled to be able to set a reasonable cetane number within regulations. In general alkanes have high, aromatics, low and napthenes intermediate cetane and diesel indices. A value of 50 or above for either diesel or cetane index is an indication that the combustion and ignition characteristics of the fuel are good. Very low indices indicate cold starting will be

difficult and result in high engine noise. The higher the cetane number, the more complete the combustions and the cleaner the exhaust.

Cuvelier et al. [49] examined the effect of cetane number on emissions from the different vehicles and engines. Increasing the Cetane Number (from 53 to 58) had no significant effect on NOx or PM emissions from either the cars or the heavy-duty engines tested, but it did reduce CO and HC emissions (although the reductions were not always significant). No differences in emissions were observed between natural cetane fuels and those in which the cetane number was boosted using ignition-improving additives.

Volatility in chemistry and physics refers to the tendancy of a substance to vaporize and is directly related to its vapour pressure. High volatility could cause fuel to change from liquid to vapour while in the fuel delivery system (vapour lock) and lower the flash point. The flash point of a volatile material is the lowest temperature at which it can vaporize to form an ignitable mixture in air. A low flash point can have an adverse effect on safety in handling and storage. The higher the volatility the more easily complete vaporisation of fuel takes place, whereas low volatility components may not burn completely and therefore leave deposits and increase smoke. In practice it is the mix of components with different volatilities that is important; high volatility components improve cold starting and warm up, while low volatility increase deposits, smoke and wear.

Density is significantly important as it is related to the energy content. Injection equipment meters fuel on volume basis and any variations in density will affect the power output. Density will vary with blends and the proportions of aromatics, napthenes and alkanes in the

fuel. Fuels with higher density have a little higher mass flow rate for the same injection conditions and thus the mass quantity in the chamber is higher [54,55].

Viscosity of the fuels affects its spray formation as will be discussed later in the chapter. Defined simply, viscosity means resistance to flow or movement. In metric system, centistoke is the unit for its measurement. It is function of time taken in seconds for a given volume of oil to flow through a calibrated viscometer under specified conditions. Viscosity depends on temperature and decreases as the temperature increases, so no numerical value has any meaning unless the temperature is specified. In the case of diesel fuels, low viscosity may give rise to: -

(i) Leakage of fuel from pumps and injectors.

(ii) Abnormal rate of wear of the moving parts of pumps and injectors owing to lack of lubricity.

(iii) Too fine a degree of atomisation with the result that the fuel will not penetrate sufficiently far into the compressed air in the cylinder to give the good mixing essential for efficient combustion.

(iv) Overheating of the injector owing to the concentration of the fuel spray and hence the flame in a relatively small area around the injector nozzle.

If the viscosity of the fuel is too high, it will impede the flow of fuel to the pump, giving rise to poor atomisation and excessive penetration with inefficient combustion of fuel. Suitable lower and upper limits are therefore specified for viscosity of diesel fuels. An increase in viscosity results in lower velocities inside the sac and orifice in a nozzle, which in turn decreases the velocity gradients and lowers cavitation patterns [56].

Waxing tendancy – wax precipitation can render cold starting difficult and subsequently stop the engine. In cold conditions small wax content can crystallise out and partially gel a fuel. These crystals can block fuel filters interposed between the tank and the injection equipment on the engine, and ultimately cause it to stall. The most likely constituents to form wax deposits are paraffins.

2.1.4 Alternative fuels

The need to reduce greenhouse gas emissions (GHG) has accelerated efforts to increase the use of non- fossil fuels in road transport. Potential substitutes for diesel fuel include: bio diesels; Gas To Liquid (GTL) and; Natural Gas. The importance of alternative fuels to the work here is due to their mixture in different blends especially GTL and biodiesel.

2.1.4.1 Biodiesel

In general the term biodiesel covers a variety of materials in fuels made from vegetable oils, recycled cooking greases or oils or animal fats; (rape seed methyl ester-RME; sunflower, safflower, babacu, corn, cotton, peanut, soya and castor oils). The definition of biodiesel is a fuel comprised of mono-alkyl ester of long chain fatty acids derived from vegetable or animal fats. Biodiesel is defined by ASTM (American Society for Testing and Materials) as “a fuel comprised of mono-alkyl esters of long-chain fatty acids derived from vegetable oils or animal fats, designated B100”. The percentage volume of biodiesel in fuel is represented by Bx, where x is the percentage volume (100-x = percentage volume of diesel fuel). E.g. a 100% pure biodiesel is B100. For a B20 fuel, the composition is 20% biodiesel fuel and 80% diesel fuel.

Vegetable oils and animal fats consist of three fatty acids (hydrocarbon chains of varying lengths bonded to glycerol molecule) commonly known as a triglyceride molecule. In a process known as transesterification, these triglycerides react with an alcohol, in the presence of a base chemical to form fatty acid methyl esters (FAME). Although biodiesel fuel produced from transesterification of triglycerides contains numerous individual FAME species, a particular fuel is generally dominated by only a few species. Five species typically dominate the composition of FAME derived from vegetable oils and animal fats: palmitic acid, stearic acid, oleic acid, linoleic acid and linolenic acid [57].

Biodiesels have zero sulphur content and relatively high cetane numbers. Due to their renewable character, GHG emission reduction potential, and a generally favourable life-cycle analysis, they are an attractive alternative to petroleum diesel fuel. The production of biodiesel can also result in substantially less pollutant emissions and waste by-products. However, as production methods and sources of biodiesel vary greatly, there is a large range in the CO2 emissions per amount of fuel produced [58].

There is a general agreement in the literature that biodiesel and its blends decrease exhaust emissions of CO and HC [59,60]. This effect is attributed to the oxygen content in biodiesel, which enables more complete oxidation in the engine cylinder. The magnitude of the reduction varies. Studies have shown that the use of biodiesel tends to result in reduced PM emissions [61]. The effect of biodiesel on PM depends on the composition of diesel particulates, and it is specific to the engine and the test cycle.

There are however concerns with the use of biofuels, i.e. materials compatibility; potential of increased water content and microbial contamination; increase in NOx emissions; impact on

low temperature operability if not properly additized; thermal and oxidative stability and; filter plugging [62]. The oxidative stability of biodiesel is also worse than the oxidative stability of diesel. This is a critical issue in industry because it affects the quality of the fuel and the materials in contact with it. The greater the degree of unsaturation in a biodiesel, the greater is its susceptibility to oxidation. This is because the hydrogens of the allylic and double allylic positions of unsaturated and polyunsaturated alkyl chains are easily oxidized [63]. Westbrook [64] has examined the storage stability of the B100. The author reported wide variations if insolubles formation, acid number and viscosity increase. The least stable samples of biodiesel exhibited unacceptable levels of insolubles and acidity as early as 4-8 weeks into a 12 weeks storage test. McCormick et al. [65] examined the stability characteristics of biodiesel samples that were commercially available at distributors in 2004 and showed that the stability range results primarily from the differences in fatty acid makeup and natural antioxidant content. The presence of higher levels of oxidation products in the biodiesel can lead to the formation of insoluble gums and sediment deposits in the fuel systems that can influence vehicle operability. This is one of the main concerns for engine and fuel injector manufactures. Terry et al. [66] showed that at very high levels of oxidation, biodiesel blends can separate into two phases to cause fuel pump and injector operational problems or lacquer deposits on fuel system components. Antioxidants improve biodiesel oxidation stability and assure its long tern storage stability [64].

Biodiesel have shown the propensity to cavitate less than diesel fuels [56,67] due to the biofuels having higher viscosity than conventional diesel. The higher viscosity results in decrease velocity gradient in the nozzle and thus lowering the cavitation patterns. The vapour pressure of biodiesel is lower than that of diesel fuel [56]. Cavitation occurs when the local pressure is lower than the vapour pressure of the fuel. Hence, reduction in vapour formation

can be expected for fuels with lower vapour pressures. Although recent advances in FIE equipment result in injection pressures that are very high, the differences in vapour pressure values are important for cavitation inception.

2.1.4.2 Gas to Liquid (GTL)

GTL is synthetic diesel fuel produced from natural gas using the Fischer-Tropsch process. GTL processes can yield high quality fuels with exceptional properties. It is comprised entirely of paraffins, with no aromatic content and in addition to that it is free of sulphur and nitrogen. GTL has a significantly higher cetane number than conventional diesel typically 70-75 depending on the paraffin content. It is compatible with existing fuel technology however a lubricant additive must be added due to its poor Lubricity properties. GTL has however not seen commercial use because of its high production costs.

2.1.4.3 Natural gas

Natural gas alternatives to fuel include liquefied natural gas (LNG) and compressed and adsorbed natural gas (CNG and ANG). Literature for these can be found from various sources however they will not be discussed in great detail here due to their relevance to this work.

2.1.5 Fuel additives

Over the next 10 to 20 years, the efforts to improve efficiency, fuel economy and reduce emissions will be the dominant factors driving change in engine and fuel technology. Over time, the most effective means of meeting the efficiency and emission goals will become clear, however, the direction for change is apparent and some of the first steps required for engines and fuel technology are well known. A key factor that is enabling the evolution in

both the engine and the fuel is the development of effective fuel additive technology that allows for the production and safe distribution of quality transportation fuel and ensures optimal engine performance and low fuel consumption. There are a number of commercial diesel fuel additives that the petroleum industry may use to meet and maintain diesel fuel properties. Additives are not the same as fuel components. Fuel components add volume to the fuel and fall into hydrocarbon classes whereas additives are added at very low levels usually in parts per million (ppm) and do not add any significant volume to the fuels. Table 2.1 shows additive types with their functions.

The most important and widely used additives are cetane enhancing additives, lubrication additives, pour depressant and cloud point depressant additives.

Type of additive	**Function/ Improvement**	**Examples of additives**
Cetane number improver	Improves ignition quality by raising cetane number. Reduces white smoke during start up and produces better start-ups	2-Ethylhexyl nitrate or other alkyl nitrates are used as the compounds are thermally instable and decompose rapidly at high temperatures and the products of decomposition help initiate fuel combustion and shorten ignition delay
Lubricity improver	Improve fuel lubricity to produce better injections and pump lubrication	Mono acids, amides and esters that contain a polar group that is attracted to metal surfaces to form a thin surface film of lubrication
Detergents/ Dispersants	Clean injectors and improve spray patterns Control deposit formation	Ash-less polymeric detergent additives composed of polar groups that bond to deposits and deposit precursors and a non-polar group that would enable dissolution in the fuel
Antioxidants	Extend storage life Inhibit oxidation Reduce gum and precipitate formation	Phenols and amines such as 2, 6 Di-t-butyl-4-methyl phenol and phenylenediamine, are the most commonly used antioxidants. Antioxidants work by interrupting the chain reaction that are set of when oxygen in the fuel reacts with other reactive compounds in the fuel
Fuel stabilisers	Inhibit oxidation Extend storage life	Basic amines such as Dimethylcylohexyl amine are used as stabilizers as they react with weakly acidic compounds in the fuel to form products that remain dissolved in the fuels, but not react any further

Type of additive	Function/ Improvement	Examples of additives
Metal deactivators	Deactivate copper compounds in fuel, thereby promoting longer storage life	Metals like iron and copper already dissolved in the fuels accelerate reactions involved in fuel instability and metal deactivators such as Disalicylidene-1,2-propanediamine (DMD) are used to neutralize this catalytic effect
Biocides	Inhibit bacterial and fungi growth Help prevent fuel filter plugging	Biocides attack bacteria and fungi in the fuels formed as a presence of air and water
Pour point depressants	Improve low temperature operability Improve cold flow properties	Polymers are used that can interact with the wax crystals that form in diesel fuel when it is cooled. They are usually blended before wax has formed in the fuel. The polymers mitigate the effect of wax crystals on fuel flow by modifying their size, shape, and/or degree of agglomeration
Cloud point depressant/suppressants	Reduce temperature at which paraffins form wax	Similar to pour point depressants
De-icers	Prevent fuel lines from freezing	Low molecular weight alcohols or glycols are used to prevent free water in diesel fuels freezing at low temperatures
Anti-foam agents	Reduce foaming when filling tanks	Organosilicone compounds used in low concentration to suppress foam formation
Smoke suppressants	Promote complete combustions Reduce exhaust smoke	Organo-metallic compounds (based on iron, cerium or platinum) to act as combustion catalysts
Rust preventers	Reduce the formation of rust in the fuel systems and storage tanks	Compounds such as sarcosines that attach to metal surfaces and from a protective barrier that prevents attack by corrosive agents are used
Demulsifiers/ dehazers	Used to increase the rate if water separation from the fuel	They are surfactants such as resin alkoxylates, modified polyols and polyimine alkoxylates that break up emulsions formed by the polar compounds in fuel, and water, and allow them to separate
Dyes	Identification of diesel for regulatory compliance	Red dye or other dyes to mark certain diesel fuels for certain specific uses

Table 2.1 Table showing the different types of diesel fuel quality and performance improvement additives and their functions [52,62,68]

2.1.6 Summary

Properties	Units	Limits	
		Min	Max
Cetane number		51	
Cetane index		48	
Density @ 15ºC	kg/m^3	820	850
Viscosity @ 40 ºC	mm^2/s	2	4
Sulphur	mg/kg		50
Total Aromatics	% m/m		25
PAH (di and tri)	% m/m		5
T_{90}	ºC		340
T_{95}	ºC		355
Final boiling point	ºC		365
Flash point	ºC	55	
Carbon residue	% m/m		0.3
Water	mg/kg		200
Fame	% v/v		5
Ash	% m/m		0.01
Particulate contamination, total	mg/kg		10
Lubricity	µm		460

Table 2.2 Diesel fuel properties for markets with requirements for emission controls or other market demands from Worldwide Fuel Charter 2012. [52]

The quality of all the diesel fuels is not the same; they depend largely on the source of the crude oil. Refiners have to meet fuel specifications and also be at the top of their market. The refiner can use various ways to meet the desired specifications i.e. choice of crude oil, refinery process, refinery bleeding, or the use of additives. The balance between refining actions and additive use is driven by economics. Some refiners may use no additives at all apart from regulatory dyes and still provide high quality fuels. Information is not available on what types of additives refiners use specifically obviously due to the reasons known to all. Table 2.2 shows a table of regulatory specifications to meet emission controls.

A summary of diesel fuel parameters, refining, components and additives has been provided in here with the effects of these properties to fuel performance or engine performance. The sections to follow will discuss literature on cavitation and atomisation in liquids.

2.2 Cavitation, Atomisation and Spray Break Up

Modern common rail direct injection diesel engines operate through the injection of high pressure liquid diesel fuel into the engine combustion chamber. The fuel is normally injected through a number of nozzle holes located at the base of an injector. The liquid fuel is subjected to large pressure gradients inside the injector and the nozzle passages, which often causes local boiling of the fuel to create local pockets of fuel vapour. This type of flow is called cavitating flow, and is associated with unstable, unsteady vapour cavities forming inside the flowing fuel. This subsection will discuss the cavitation phenomena with links to relative literature. It begins with a brief overview of the definition and formation of cavitation and concludes with its links to the external spray atomisation.

When a liquid is heated at constant pressure, or when the liquid's pressure is reduced under constant temperature conditions by static or dynamic means, a fluid state is reached ultimately at which vapour and gas filled voids become visible and grow due to diffusion and vaporisation effects. In the case of heating at constant pressure we call the void formation boiling while in the case of reduced pressure at constant temperature it is named cavitation. Cavitation can also be described as the formation of vapour or gas cavities within a given liquid due to pressure drop. Cavitation is commonly known as the process of formation of voids in a liquid due to sudden pressure drop, when the local tension $p_v - p$ exceeds the tensile

strength of the liquid $p_v - p_{cr}$ [69]. The tensile strength of a liquid depends on the presence of weak spots in the liquid, which provide the nuclei for the phase transition process.

Cavitation in a more general sense is a process of formation and also consequent collapse of bubbles in a liquid under a local decrease in pressure [70]. Due to the inertia of the liquid and compressibility of the gas-vapour bubble content, the pressures and temperatures can become extremely high inside a bubble under collapse. Depending on the topology of the vapour structures in the flow, cavitation can run in a form of travelling bubbles, or vapour pockets, extending over the partial length of the nozzle body (cloud and sheet cavitation), or the full range of the nozzle body (supercavitation).

Cavitation can occur at millions of locations in a reactor simultaneously and generate conditions of very high temperatures and pressures (few thousand atmospheres pressure and a few thousand Kelvin temperature) locally, with the overall environment being that of ambient conditions [71]. Gogate et. al [71] states four principle types of cavitation namely:

(i) Acoustic cavitation - using sound waves usually ultrasound (16 kHz-100 MHz) to create pressure variations in the liquid.

(ii) Hydrodynamic cavitation - pressure variations obtained by using the geometry of the system to create velocity variations.

(iii) Optic cavitation - produced by photons of high intensity light (laser) rupturing the liquid continuum

(iv) Particle cavitation - produced by a beam of elementary particles, e.g. a neutron beam rupturing a liquid.

The study here will cover mainly hydrodynamic cavitation, will touch up briefly on acoustic cavitation and try and link up the effects of acoustic cavitation to the effects of hydrodynamic cavitation on fuel properties and parameters.

2.2.1 Cavitation bubble dynamics, nucleation, growth and implosion

Many observations have proved that the hydrodynamic cavitation occurs in the bulk liquid [69] where the vapour-gas bubbles provide the main contribution to the nucleation process. Nucleation is the process of the formation of small voids in the liquid. These voids are then convected into a region of low pressure within cavitating flows where they grow explosively to macroscopic size and collapse when convected back into a region of higher pressure. Two types of nucleation can be defined depending on the nature of the weaknesses, which initiate the bubble growth, namely homogeneous and heterogeneous.

Homogeneous nucleation is the process of macroscopic bubble development from small voids, which appear in the liquid due to the thermal molecular motion. In classical kinetic theory of liquids the thermal motion of molecules is considered as the only mechanism of homogeneous nucleation. In pure liquids contained in ideal environments, the nuclei that can initiate phase change are microscopic voids caused by thermal motion within the liquid. This kind of nucleation is termed homogeneous. In real systems micro-bubbles filled with a gas can also initiate homogeneous nucleation. These gas micro bubbles can be present in crevices at solid boundaries or small suspended particles.

Contrary to this, in most engineering systems phase transition occurs due to contamination associated with the presence of other types of nuclei which are unrelated to the thermal

motion of the liquid but occur as a result of the existence of a weakness between the liquid and a solid interface. This solid interface can be either the wall of the container or small impurities suspended in the liquid. For this reason this kind of nucleation is termed heterogeneous. When a liquid is undergoing a constant temperature depressurization, under certain conditions, the local pressure can drop below its vapour pressure without any phase change occurring. In this case the liquid is in a metastable state and is said to undergo "tension" or to be under "tension", which is essentially the level of pressure drop below its saturated vapour pressure it can withstand without phase change. Tension in a liquid prior to the occurrence of cavitation is similar to superheat prior to boiling. The conditions that influence the outcome of the depressurization are directly related to the existence of nucleation sites in the liquid. When there are not sufficient nucleation sites the liquid can endure relatively high levels of tension until, due to homogeneous nucleation, the liquid ruptures and cavitation takes place. When sufficient nuclei are present, prior to depressurization, phase change will take place as soon as the pressure reaches vapour pressure.

Cavity nucleation is a complex function of a number of variables including solvent vapour pressure, hydrostatic pressure, solution contamination (gas, solid, liquid), surface characteristics of solid contaminants (smooth, cratered, etc.), the ratio of heat capacities (C_p/C_v) of the dissolved gas, and the ambient solution temperature [72]

Inertial, thermal and gas diffusion effects can drive bubble growth. It is widely accepted that bubble growth and collapse in cavitating flows is mainly governed by inertial effects, due to the small timescales and bubble sizes. It is in this field of bubble inertial effects that Lord Rayleigh [73] pioneered theoretical bubble dynamics by deriving equations for the bubble

wall velocity and time of collapse of an empty cavity through energy considerations assuming bubble sphericity and constant pressure surrounding the bubble. His analysis despite being simplistic set the tone for further research on the behaviour of symmetrical cavities. Plesset [74], then formulated the equation of motion for the wall velocity of a spherical bubble by dropping the constant surrounding pressure assumption and this equations came to be known as the Rayleigh-Plesset equation.

Plesset and Prosperetti [75] carried out a review on the most important works on bubble dynamics. They accumulated the vast majority of the most significant research up to then and discussed many uncertainties regarding bubble dynamics and its relevance to cavitation. The review is in three sections and discusses: behaviour of bubbles which contain contaminant gas and can also contain vapour; analysis of features of bubbles that are composed predominantly of vapour and; non spherical effects and analysis. Pertinent to the behaviour of gas bubbles are many phenomena, some of which are especially critical in acoustic cavitation; these include gas diffusion, damping effects which can be sub-divided into viscous, thermal and acoustic, and the thermodynamic behaviour of the gas itself inside the bubble during violent growth and collapse. For vapour bubbles condensation and evaporation phenomena can affect their behaviour, especially when they are collapsing. Finally, non-spherical effects affect their collapsing behaviour. Theoretical investigations on these effects are discussed, and the method of non-viscous mirror bubble, by which assumes potential flow, is examined as a tool to study bubble collapse near a solid wall. The behaviour of pure vapour bubbles is expected to be quite distinct from the behaviour of gas or gas and vapour bubbles in cavitation, due to above issues. A potential flow describes the velocity field as the gradient of a scalar function: the velocity potential. Potential flow is frictionless, irrotational flow. Even though all real fluids are viscous, if the effects of viscosity are sufficiently small then the accompanying

frictional effects may be negligible. Viscous effects become negligible, for example, for flows at high Reynolds number that are dominated by convective transport of momentum. Thus potential flow is often useful for analysing external flows over solid surfaces or objects at high Reynolds number, provided the flows still remain laminar. Moreover, when the flow over a surface has a high Reynolds number, the viscous boundary layer region that forms next to the solid body is very thin. Then, to a very good approximation, the presence of the boundary layer can be neglected when analysing the potential flow region. That is, the potential flow can be assumed to follow the contours of the solid surface, as if the boundary layer was not present. In the case of an incompressible flow the velocity potential satisfies Laplace's equation. However, potential flows also have been used to describe compressible flows.

The collapsing stages of cavitation bubbles appear to be very complex, with many physical processes becoming important only during this part of their life-cycle. During a bubble collapse the initial hydrodynamic bubble energy is redistributed in at least five different channels [76]: a new, subsequent bubble caused by a partial elastic rebound; shockwaves; liquid jets; electromagnetic radiation if visible; thermal motions and cold nuclear fusion. The rebound bubble distributes its energy in the same channels, when collapsing. The relative amount of energy released in each of these energy channels strongly depends on the sphericity of the collapsing bubble at its very last stage. This sphericity is in turn determined by the presence of boundaries and inertial forces, such as centrifugal forces and gravity. However observations in real flows have demonstrated that even single cavitating bubbles are far from spherical. This is due the interaction of the bubble with pressure gradients and shear forces in the flow or interactions with a solid surface [77].

The frequency of cavitation events increase in space or time such that they begin to interact with each other a whole new set of phenomena manifest [69] such as the formation of large scale cavitation structures either because of coalescence of individual bubbles or because a large region of flow vaporises. Typical large scale structures include vortex cavitation, sheet and cloud cavitation which will be discussed later in this section

In order to investigate the chemical consequences of hydrodynamic cavitation (the formation, growth and implosive collapse), Suslick et. al [78] carried out an investigation where they introduced a solution of Potassium iodide in purified water saturated by calcium tetrachloride at a constant rate into a microfluidizer with a liquid pressure of 1.24 kbar. They varied the upstream pressure between 100 and 1500 bar. They had previously conducted tests using acoustic cavitation and found out that the sonochemical rates were affected by both the polytropic ratio of the dissolved gas and the thermal conductivity of the dissolved gas. The former parameter determined the temperature achieved during bubble collapse whereas the later was responsible for heat dissipation from the collapsing bubble to the surrounding solution. While conducting the hydrodynamic study they fixed the polytropic ratio and varied the thermal conductivity. They observed that the rate of formation of reactive species tri-iodide increased with increase in liquid pressure, whereas it exponentially decreases with increase in both thermal conductivity of the dissolved gas. They demonstrated that the chemical effects of hydrodynamic cavitation and acoustic cavitation respond identically to experimental parameters. However these two are different modes of introducing cavitation into a liquid (acoustically or hydrodynamically) and the result they obtained shows that the chemical effects from both these processes are similar. This opens up investigations whether this is the case for multicomponent chemicals such as diesel fuel. It is important at this point

to introduce the two different methods of inducing cavitation and thus sections 2.2.2 and 2.2.3 will discuss the literature available from these fields.

2.2.2 Hydrodynamic induced cavitating flow in injector nozzles

Hydrodynamic cavitation as previously mentioned relates to cavitation produced by pressure variations obtained by using the geometry of the system to create velocity variations. Cavitating flow intensity and structure depend strongly on the Cavitation Number [79]. The Cavitation number is defined by the equation (Equation 2.2):

$$CN = \frac{P_{up} - P_{down}}{P_{down} - P_v}$$

Equation 2.2

Where CN represents the Cavitation number, P_{up} is the pressure upstream of the injection hole (usually approximated to the injection pressure), P_{down} the downstream pressure (usually the hole exit pressure) and P_{vapour} is the vapour pressure of the liquid. Cavitation number is directly related to the cavitation intensity- the higher the CN the higher the cavitation intensity.

When increasing the cavitation number, cavitating flow assumes different forms:

(i) Incipient-cavitation: when small bubbles are generated and are present only at the hole inlet. The cavitating area appears as a glossy cloud of indistinguishable micro-bubbles that collapse much before the hole exit. Incipient cavitation identifies flow conditions when hydrodynamic cavitation just appears in the flow, in order to establish the boundary between a cavitating and non cavitating flow.

(ii) Transient/Developed cavitation is induced by a slightly higher Cavitation Number. The cavitation glossy cloud diffuses along the hole but doesn't reach the hole exit.

(iii) Super-cavitation: the cloud-like cavitation pattern in the hole occupies all its length and it's a typical phenomenon present in injection systems.

Forms (i), (ii) and (iii) are accompanied by certain levels of turbulence in the flow; liquid tends to fill the cavitating voids, breaking larger void areas in several tiny micro-bubbles. The typical glossiness is given by the mixture of liquid and micro-bubbles into a foam-like state.

(iv) Hydraulic-flip happens when very high Cavitation Numbers are applied, Reynolds numbers are compatible with laminar fluid motion, and when the flow is perfectly axially-symmetric with respect to the hole axis. This pattern requires particular geometric configurations (single hole nozzles).

The Cavitation and Reynolds numbers, and discharge coefficient are defined by Equation 2.2, Equation 2.3 and Equation 2.4 respectively. Cavitation numbers describes the nature of the flow. It relates the pressure drop (or dynamic head) to the local static pressures. An increase in cavitation number signifies an increase in cavitation intensity. Studies of cavitating flows in nozzles have revealed that the cavitation number determines an extent of the region inside the nozzle filled with the vapour. The discharge coefficient characterises the amount of losses in a real flow with respect to the theoretical limit. Decreasing discharge coefficient means that losses are increasing in the flow.

$$\mathrm{Re} = \frac{\mathrm{U} \cdot \mathrm{D}}{\nu}$$

Equation 2.3

$$C_d = \frac{U}{v_B} = \frac{U}{\sqrt{\frac{2(P_{up} - P_{down})}{\rho}}}$$

Equation 2.4

Re represents the Reynolds number, where U is the liquid velocity of the flow through the injection hole, D is the diameter of the injection hole and v is the kinematic viscosity of the fluid. Re is a dimensionless number that gives a measure of the ratio of inertial forces to viscous forces. C_d represents the discharge coefficient, where ρ is the density of the liquid and v_B is the Bernoulli velocity of the liquid due to pressure differences.

Another important parameter is the conical shape factor (K- factor) defined as a ratio of the outlet diameter subtracted from the inlet diameter to the inlet diameter as:

$$K = \frac{D_{inlet} - D_{exit}}{10}(\mu m)$$

Equation 2.5 [80]

Where D_{inlet} is the hole inlet diameter and D_{exit} is the hole exit diameter all given in μm. A negative K factor represents increasing diameter towards the exit (diverging hole) whereas a decrease in K factor represents a hole with decreasing diameter (converging hole).

Recent research in large scale injector studies, for cavitation, has identified two clearly distinguishable types of cavitating flow; Geometric cavitation as seen in Figure 2.9 and string/vortex cavitation observe in Figure 2.10. Geometric cavitation forms at orifice inlets and it is due to the abrupt acceleration of the fuel flow as it enters the nozzle holes. It appears to be initiated as dense foam of micro bubbles developing in the liquid phase, which evolve into a connected volume of fuels vapour running from the hole inlet to the hole exit.

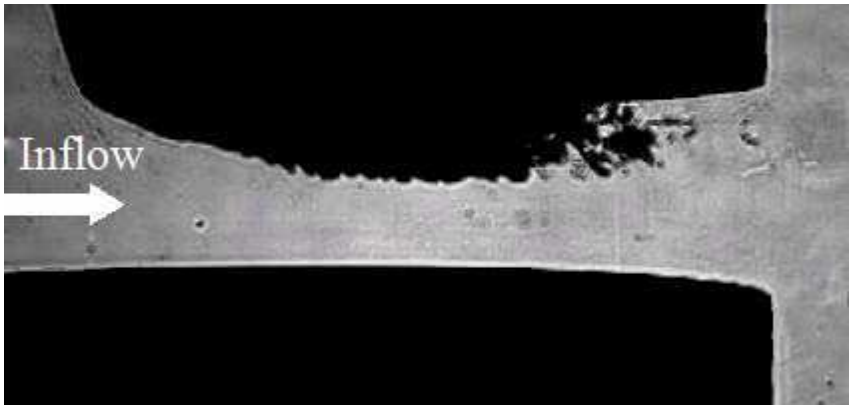

Figure 2.9 Geometry-induced cavitation in a nozzle [81]

In multi-hole injectors cavitation in one nozzle hole can affect the flow in the other. In a sac volume of injectors, string or vortex cavitation is observed. String cavitation is a highly transient phenomenon which occurs inside the nozzle sac. String formation was attributed to the interaction between the high momentum annulus flow and the cross flow, which occurs due to the intermittent throttling of individual holes by already existing recirculation zones or cavitation at their entry. As a result, the flow conditions at the vortex core lead to the formation of a low pressure region and, subsequently, of cavitation bubbles, which coalesce immediately into a continuous vapour string [26].

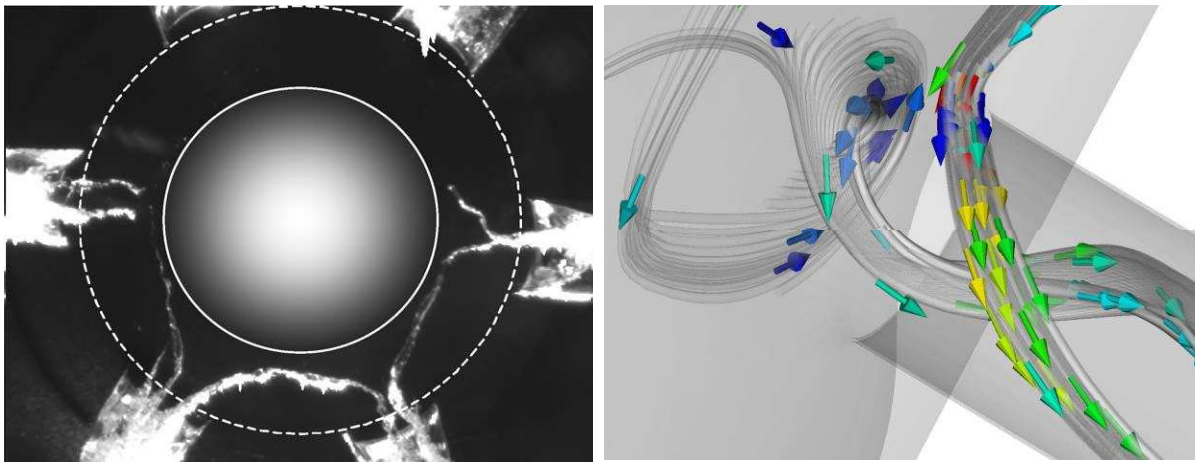

Figure 2.10 String-type cavitation in the sac volume of the sac type nozzle [82]; predicted flow structure inside the injection hole of a VCO nozzle [83]

In fuel injectors huge pressure drops are encountered within very short distances in the nozzle, while the life time of the formed vortical structures is usually only a fraction of the injection period (approximately 1 ms for typical engine operating conditions). This is the reason the formation and development of such vortical structures has only be studied in enlarged nozzle models operating under steady-state conditions as observed by [23,27,84–86].

At present, a number of experimental works have been published in the literature to determine the behaviour of cavitating flows in nozzles and orifices in both real-size and enlarged models. These experiments help to identify the structure of cavitating flow, i.e. the pattern of two-phase flow and the hydraulic resistance of nozzle, which determine impacts of cavitation on the flow and the nozzle performance.

2.2.2.1 Investigations of cavitating flow in enlarged model nozzles.

To determine the structure of a cavitating flow in a nozzle, hydraulic measurements are accompanied by visual observations of the flow inside the nozzle. A difficulty in determining the structure of cavitating flow in nozzles appears due to the problem of visualizing the flow in real-scale transparent nozzles, due to their small size. This requires the application of special methods and equipment. To overcome this difficulty, a scaling theory is applied, so that larger models can be used. Arcoumanis, Gavaises and others have identified the likelihood of cavitation occurring in the internal fuel flow inside these large scale injectors [2,87,88].

One of the most frequently used methods of nozzle investigation is to manufacture transparent large scale nozzles (10x-20x) from transparent material in order to allow visualization of the internal nozzle flow and the cavitation structures. Moreover, if the liquid medium that is used

has the same refractive index as the transparent material of the nozzle then it is possible by using LDV to determine the velocity distribution inside the injection holes and the nozzle. An early investigation that utilized this technique was that of Arcoumanis et al. [89]. In this study a Steady-state flow test rig with enlarged model injector (transparent single-hole nozzle) was used along with refractive index matching and LDV. Among the major findings, simulating diesel fuel with a mixture of hydrocarbons having the same refractive index as the acrylic model nozzle was proven to be a useful tool in characterising the internal nozzle flow in diesel injectors. Through a series of parametric studies, the measured flow field provided insight into the dependence of the injector flow on nozzle geometry, needle lift and injection pressure. These results were concluded to be useful for validating multi-dimensional CFD models.

Later on in 1999 Arcoumanis et.al [90] used a steady flow test rig with a 20 times enlarged mini-sac nozzle in a closed loop common rail injection test rig with optical access, using a working fluid that exhibited similar refractive index to acrylic nozzles. A high-resolution CCD camera with high-magnification lenses attached was used for flow visualization purposes. A spark-light was used as source of back-illumination; the latter was quite important for obtaining fine-detail images of the flow. Needle lift and eccentricity were varied as part of a parametric study. The authors found that needle eccentricity caused cavitation inception to move from the upper part of the holes' entrance to the lower part. The eccentric needle created off centred low-pressure regions in the holes that were at an angle to the direction of the needle movement. The most interesting find was the strings seen in the sac volume which seemed to develop transiently and periodically between adjacent holes. The strings interacted with existing cavitation films as they convected into the injection holes giving rise to significant flow disturbances and hole to hole variations. The authors also

identified different flow types with increase in cavitation numbers namely bubbly flow (incipient), pre-film stage (plug-type cavitation) and film stage (separated flow).

Focusing now on cavitation effects in nozzle flow, Soteriou et al. [2] were among the first to use large-scale transparent diesel injector nozzles to visualize and understand cavitation phenomena in such geometries. A steady-state flow rig was used to investigate the flow in real-size simple orifices, in sac-type single hole and in VCO/sac-type multi-hole nozzles; additionally it was used to visualize the flow in twenty times enlarged transparent models of the above nozzles. A transient injection rig was employed with the real-size multi-hole nozzles, in order to investigate unsteady phenomena. Injection into liquid and into gas was considered, in order to identify different cavitation patterns. Still imaging was used for visualization of the cavitating flow inside the large-scale models and for studying the spray behaviour in both real-size and large-scale nozzles. Pressure and flow rate measurements were carried out in order to calculate the discharge coefficients of each nozzle. From the authors' experiments it became clear that once the Reynolds and the cavitation number were matched simultaneously, between real-size flow conditions and large-scale ones, the same transition flow regimes and the same dependence of the discharge coefficient on cavitation number were observed. This finding was important since it established a macroscopic link between large-scale and real-size nozzle cavitation.

Another interesting finding was that in the case of a simple submerged orifice with increase of cavitation number choking would occur, whereas for the case of injection into gas transition, hydraulic flip would take place; the latter transition in the case of the real-size orifice was not so clear due to the unavoidable geometrical asymmetries. The effect of turbulence and geometrical asymmetries was identified in the experiments which were carried out with a

multi-hole nozzle; even with such a nozzle when the needle was absent and with increasing cavitation number there would be transition into a hydraulic flipped state; however no flipping was observed even with the needle present. Nevertheless, partial hydraulic flip could be present in multi-hole VCO nozzles, which were found to produce asymmetric sprays. Finally, it is important to report the authors' finding that with the presence of cavitation sprays were observed to atomize right at the hole exit, which means that cavitation enhanced the atomization process.

In order to gain more insight in fundamental cavitating flow characteristics, Soteriou et al. 1998 [91] using the well-known techniques of Refractive index matching, LDV, pressure measurements and Laser light sheet illumination along with still imaging of cavitation; investigated scaled up plain orifice nozzle; injection with an un-submerged and submerged outlet, attached on a steady-state flow test rig. Due to the enhanced clarity of the flow visualization technique, cavitation inception was found to take place in three distinct locations; in the separated boundary layer, which is located at the hole entrance, in the mainstream flow, close to locations of peak velocity, and within the attached boundary layer, which is located downstream of the separated one.

Furthermore it was seen that formation of hole cavitation structures depended on Reynolds number of flow upstream of orifice; Laminar flow allowed large voids to form while Turbulent flow encouraged formation of small bubbles. On the spray characteristics it was found that cavitation within attached boundary layer caused the emerging spray to become slightly bushy and increased the spray angle. Increase of cavitation number led to the formation of plug-cavitation, which appeared much more dense and turbulent, when compared to the structures that had been identified up to that transition. As the cavitation

number was increased the plug was seen to extend towards the hole exit; prior to reaching it there was a significant increase in the spray angle, and the spray appeared bushy and atomized directly at the hole exit. Moreover, when plug cavitation extended to orifice outlet the angle and bushiness of spray increased significantly and flow in cavitating plug was more turbulent than non-cavitating flow which was believed to be a reason for the improved spray development.

Kim et al.[88] tested minisac, VCO and hybrid type large scale-transparent nozzles using water as the working fluid, capturing images of the internal flow and spray. The authors' concluded that there was unstable cavitation in the sac volume when the upstream conditions were steady, which in turn caused fluctuations in the spray shape and axis. They also observed that an increase in sac turbulence occurred as a result of low needle lifts which in turn resulted in larger spray cone angles.

Roth et. al [27] in 2002 used a 6-hole large scale transparent minisac and VCO type nozzle in both steady state and quasi transient flows. The authors used the test rig described in Arcoumanis et. al above, to obtain quantitative information about the flow field inside the nozzles using a fixed needle. Using the refractive index matching test rig, LDV measurements of the flow in both the VCO and minisac nozzles were captured using high temporal resolution imaging cameras. Interesting findings were made due to the fact that cavitation strings were found to induce hole cavitation, as they were seen to transport bubble nuclei from one hole, where cavitation would have already started, to an adjacent one which wouldn't be cavitating up to that time. They also observed vortex/string flow between the needle, needle seat and two adjacent holes in both VCO and minisac nozzles. Needle strings were observed for both high and low needle lifts in the minisac nozzle however, they were only observed at

high needle lifts in a VCO nozzle. The LDV measurements showed that there was an increase in turbulence levels in the lower part of the injection hole away from recirculation zones which occurred at the hole entry, as the cavitation number increased. The turbulence level was seen to die out close to the hole exit and almost resemble lower cavitation number cases.

Later on Andriotis et al.[23] in 2008, visualised and simulated 3-D cavitating flow to characterise the formation of cavitation inside transparent replicas of fuel injector valves used in low speed two stroke diesel engines. His design incorporated five hole nozzles on both real size and large scale models with cylindrical as well as tapered holes operating at various needle positions. The real size model nozzle injected into air, whereas the scaled model nozzle injected into liquid. Visualisations were made using two high speed cameras observing the two-phase flows structures in the nozzles. They revealed formation of unsteady vapour structures upstream (strings) of the injection holes inside the nozzle volume which were found in areas of flow circulation, originating from either pre-existing cavitation sites at sharp corners inside the nozzle or from the suction of outside air downstream of the hole exit, the later phenomena occurring in tapered hole nozzles low cavitation and Reynolds numbers were found to reduce the formation of string cavitation. Their computational predictions revealed that the stings structure formed inside the nozzle volume moved with a low circumferential velocity component relative to the nozzle axis.

A lot of information has been gained over the years through experimental studies on enlarged transparent diesel nozzles. Nonetheless, it cannot be argued that the actual timescales and length scales of cavitation as a phenomenon cannot be scaled, which of course points out the need for real-size nozzle experiments.

2.2.2.2 Real-size and other geometry nozzle flow investigations

This section will discuss literature in real size nozzle flows as well as flows in other small orifice nozzles diameter 1mm or less which tend to replicate single hole cavitation phenomena. Authors investigate simpler geometries than diesel nozzles due to the ease of carrying out quantitative measurements and the control of various hole to hole interacting phenomena.

Chaves et al. [92] used transparent real-size single-hole axisymmetric nozzles made of glass with refractive index matching between fuel and nozzle wall, to study hole cavitation using a steady-state flow rig. The authors were able to measure the flow velocity in the centreline of the nozzle by cross-correlating two light absorption signals with a laser- two-focus-velocimeter. The enhancing effect of cavitation on atomization was demonstrated by experimenting with a nozzle which on the upper part of the hole entrance was well polished, but ruffled in the lower part; the emerging spray appeared smooth in the upper part where no cavitation occurred inside the hole, but wrinkled in the lower part where cavitation was observed. The cavitation would initiate atomization in the lower part. They investigated that above an injection pressure threshold that depended on the nozzle geometry and chamber pressure, cavitation appeared at the sharp inlet corner of the nozzle. With increasing injection pressure the cavitation reached the nozzle exit (supercavitation). The discharge coefficient and the spray angle then level off at a value that was almost independent of any further increase of injection pressure. The authors' were successful in measuring the flow velocity in the nozzle hole centreline, close to the hole wall and in the emerging jet centreline. They found the centreline velocity inside the hole to be very high (close to the Bernoulli value) whereas close to the wall it would correspond to the calculated value of the mean velocity with the flow area taken to be at the nozzle hole. From the above the authors concluded that it

was wrong to consider that the whole geometric area of the hole is occupied by the cavitating liquid.

Badock et. al [3] used a laser light sheet and shadowgraph techniques to investigate cavitation phenomena, in the spray hole of real size single hole diesel injection nozzles and the break-up at the spray-hole exit, using a test rig that allowed for fully transient injection tests by utilising a Bosch common rail system with injection pressures up to 60 MPa. The authors modified the metal tip of the injector nozzle and replaced it with a transparent nozzle made from acrylic to be able to visualise and correlate the internal flow to the spray. The fuel was injected into a chamber that could be pressurised up to 1.5 MPa. They found that the laser sheet technique was not suitable to visualise both the internal flow and external spray. They observed that the phase boundary between the cavitation occurring and Perspex was limited by the surface roughness of the drilled holes. Secondary-break-up created stochastic roughness and wrinkles on the surface of the spray, which resulted in multiple light scattering. The latter resembled a milky haze lying in front of the observing plane. For this reason they only visualised the near exit part of the spray. Quasi-transient imaging of the injection event was done by taking images from multiple injections at later time instances, since it was not possible to record consecutive images from the same event with sufficient resolution. From the obtained images the various stages of cavitation development were analysed; at the beginning of the injection large gas bubbles could be observed, which even remained in the orifice during two subsequent injection events. An important observation was that continuous liquid core was visible at all times and it was surrounded by cavitation films. The authors observed no foam or any single accumulation of bubbles occurring. The cavitation films appeared to be irregular and quite thin initially, but at the point of highest velocity, these films became more regular. The authors observed that during the needle closing dissolved gas in the sac hole and the

spray hole in form of large bubbles survived the time between injections. They concluded that as the bubbles survived that long they could only possess a very small part of vapour. These bubbles would be partly sucked into the sac hole at the start of the injection and compressed as the pressure wave of the injection pushed them back out. They caused mushroom like structures on the emerging spray.

The above investigations have only been carried out in real size single nozzle hole studies. The visualization of the flow in realistic multi-hole diesel nozzles has unfortunately only been possible recently when Arcoumanis et al. [93] succeeded in visualizing the flow in one of the holes of a modified production conical sac nozzle by removing some of the material by accurate machining to ensure the hole characteristics remained the same; and fit a quartz window in its position. A CCD camera with a high magnification lenses attached was used to capture details of various flow regimes formed inside the injection hole. Due to the fact that the experiments were steady-state with a constant needle lift they could only attain moderate injection pressures, a limitation imposed by the high pressure pump. Two needle lifts and various back pressures were tested with the nozzle submerged, so that they could obtain results directly comparable with previously obtained results using the enlarged model. The comparison of the measured discharge coefficients showed that for high needle lift there was a better agreement between the large-scale and the real-size nozzle. It was confirmed for the real-size nozzle that after the onset of cavitation the discharge coefficient drops with increasing cavitation number, thus reaching asymptotically a minimum value. The authors' did not find any effects of varying Reynolds number under cavitating conditions. Another important finding was that string cavitation was observed in the real-size nozzle, but only in the high needle lifts case. Visual comparison of the various flow regimes between the two nozzles revealed similarities but also distinct differences. In the real-size nozzle and for low

Reynolds and cavitation numbers the observed structures collapsed inside the hole, which is in contrast to the large-scale nozzle's case, by which cavitation structures would always exit the hole. Nevertheless, the effect of increasing cavitation number was dramatic in both cases, with cavitation in the real-size exiting the nozzle hole in misty form. Finally, another important finding was that the observed structure sizes did not scale with the hole size. In the real-size nozzle they occupied a relatively larger volume fraction. This would support the claim that cavitation as a phenomenon cannot be scaled.

Desantes et al. [94] measured both the mass and the momentum flux of the injected spray emerging from a two-hole real-size research VCO nozzle at different pressures. They investigated the effects of cavitation on spray momentum and outlet velocity. They used a common rail system which could inject up to 1500 bar together with a high-pressure injection chamber for their investigations. For the momentum-flux measurements, the spray would impinge on a force sensor equipped with a piezo-electric pressure sensor and they would assume that the force measured by the sensor would be the same as the momentum flux due to conservation of momentum. They observed that when there wasn't any cavitation inside the nozzle holes (low cavitation numbers) the mass flux was found to be proportional to the pressure difference across the nozzle, and then when cavitation would initiate there would be choking of the flow i.e., the discharge coefficient would decrease. Varying the backpressure would not have any effect on the mass flux. The momentum flux, however, was not found to choke at any condition, and it continued to depend on the applied pressure difference. Nonetheless, no analysis was provided by the authors on what could be the causes for this phenomenon. They concluded that the outlet velocity increased when cavitation appeared due to the reduction of cross section of the liquid phase in the outlet section of the hole. This conclusion was deduced from the mass and momentum flux measurements. They also

concluded that there was a reduction in area coefficient of the hole once cavitation appeared and this resulted in an increase in the vapour phase in the outlet section of the nozzle hole.

Further on in 2009, Lockett et al. [28,67] employed two modified VCO nozzles to identify whether it was possible to employ simple optical techniques to discriminate between cavitating flows developed, and the physical attributes responsible. This was one of the first experiments to utilise a fully modified injector and recreate the full VCO geometry in Perspex, to be able to have a full view of all six holes simultaneously from the bottom view. This was also one of the first experiments to utilise high pressure (200-400bar) with Perspex nozzles. In contrast to all other reviews this author was looking to distinguish between different types of fuels by capturing and carrying out image analysis to correlate the cavitation to the fuel types. The fuels analysed had different physical properties and were secretly blended. The authors would study the cavitating flow occurring inside the nozzle holes by high resolution imaging of white light scattering from the cavitation. They employed a high power white light source and a high speed camera. In order to be able to verify their results and check for repeatability, they used two different techniques; utilise an unchanged bottom surface where the acrylic nozzle would attach (shiny surface) and; an anodised (blackened surface). The shiny surface produced bright background images and whereas the anodised surface produced dark background images which were processed separately and then compared.

A novel optical method for the assessment of diesel nozzle flow was developed in order to discriminate between the cavitation volume occupied by different diesel fuels during the fuel injection process based on high resolution, fast video photography of elastic scattering of the white light from the surface defining the liquid-vapour interface formed during nozzle

cavitating flow. They observed that the cavitation scattering area increased as a function of rail pressure for all the fuels tested, suggesting that the volume of vapour occupying the nozzle passages increased with increase in common rail pressure. They observed fuels containing FAME additives produced lower cavitation scattering areas than fuels without FAME concluding that the addition of FAME results in lower cavitation. They also observed the effects of an increase in cavitation leading to mass choke as the previous authors.

Sou et al.[95] in 2007 visualised cavitation in 2-D nozzles and near nozzle liquid jet using high speed cameras to investigate the effects of cavitation on liquid jet under various conditions of cavitation and Reynolds number. The nozzles investigated were large scale 2-D transparent models of single-hole nozzles with variable geometries. They used either tap water or light oil. The techniques used were imaging of internal nozzle flow patterns, cavitation structures and near hole exit spray structure with high speed digital video and LDV measurements inside the nozzle hole. Among other findings, an interesting relation between cavitation and spray structure was defined. Cavitation in 2D nozzles and liquid jet were classified into the following regimes: no cavitation and developing cavitation (wavy jet); super cavitation (spray); and hydraulic flip (flipping jet). It was also observed that cavitation and liquid jet near the nozzle exit were not strongly affected by the Reynolds number but by the cavitation number. Finally they concluded that strong turbulence induced by the collapse of cavitation clouds near the exit would play an important role in ligament formation. However ligaments did not always appear when a collapse took place, and some ligaments were also observed to appear when there was no collapse taking place.

Diesel injections with various nozzle geometries were investigated by Bae et.al [80] to obtain spray characteristics by optical imaging techniques. Sac and VCO type nozzles with single

guided needles coupled with rotary type mechanical pump were compared in terms of macroscopic spray development and microscopic behaviour using a common rail system. The authors also tested a variety of injection hole geometries, with different size holes and taper ratio represented as a K factor, in order to be able to give a conclusion on the best injector design. The authors used Mie scattering (spark light source and CCD camera) and shadowgraphy (Ar-ion laser and ICCD camera) techniques to observe the macroscopic behaviour. The microscopic images acquired by a microscopic lens system, strong light source and CCD camera. They observed that higher pressure injections produced smaller Sauter-Mean-Diameter (SMD) values, a longer spray-tip penetration due to higher spray momentum and had a small effect on spray angle. They found that the dominant variables influencing the spray droplet size were the injection pressure and nozzle size.

Blessing et al. [96] investigated the comparison of cavitation effects, spray characteristics and mixture formation when using different injection systems. The authors' test-rig comprised three different diesel injection systems namely: a conventional common-rail system (CR); a novel amplifier-piston-common-rail system (APCRS); and a pump-line nozzle system (PLN); with transparent metal 1-hole and 6-hole minisac real size geometry nozzles for internal nozzle observations and the metal equivalents for the spray investigation. The cavitation images were captured by a CCD camera illuminated by a light source using the shadowgraphy technique and used to measure the micro cone angle of fuel spray close to nozzle exit, spray tip penetration, needle lift, combustion imaging with soot formation inside optically accessible engine and then a comparison of CFD results to the experimental results carried out with a commercial package. They found that rounding the inlet edges from sac hole into the spray hole lead to a higher uniformity of the flow and a reduction in cavitation in the spray hole. One of the key findings was that conical shape of injection hole (K-factor) influences

cavitation behaviour and thus micro cone angle and spray breakup with 1-hole nozzles. The higher the K factor, the smaller the micro cone and spray angle, the less cavitation formation & spray break-up and the more tip penetration could be observed. Furthermore, the influence of K factor onto cavitation formation was also reproduced with CFD simulations.

Comparison of experimental and CFD results for 6-hole nozzle investigations showed fairly good agreement regarding cavitation pattern distribution and development. The flow inside the sac volume of the nozzle that was connected to the 'needle-lift controlled' CR system was identified to be responsible for strong fluctuations of cavities inside the injection holes during the early stage of injection, which led to increased micro- cone spray angles. Contrary to this, the flow inside the nozzle which was connected to the 'Pressure controlled' PLN system exhibited more stable flow behaviour and therefore a smaller spray angle. After the early stage of injection the compared injection systems showed similar cavitation and spray characteristics. The formation of thermal nitrogen monoxide was determined by the rate of injection and needle lift control. The performance of the CR system was poor compared to the PLN system in these areas since it was characterised by a longer needle opening phase and a smaller initial injection rate, these two effects leading to a less favourable air-fuel mixture and higher thermal NO production.

Payri et. al [22] carried out a study to find out the influence of cavitation on the internal flow and the macroscopic behaviour of a spray in diesel injection nozzles using two bi-orifice, one cylindrical and one conical nozzle. The authors initially determined the nozzle geometries by none destructive techniques based on silicon moulds. This was done so that they could determine the discharge coefficients and critical cavitation conditions. They initially used a cavitation test rig to hydraulically characterise the nozzle in order to determine the discharge

coefficient in cavitating and non-cavitating conditions. By controlling a pressure regulator in their modified injector cavitation test rig they could determine critical pressures. For analysing the macroscopic behaviour of the nozzle they setup a CCD camera illuminated by and electronic timed flash, synchronous with the injections. During the hydraulic testing it was observed that the critical cavitation conditions depended on the conicity of the nozzles; lower conicity and smaller rounding radii cavitates. They also concluded that these nozzles (with lower conicity) had lower mass discharge as compared to the larger conicity nozzles. They also observed an increase in spray cone angle and velocity coefficient, and a decrease in nozzle contraction coefficient, as a result of cavitation.

Later in 2009, [97] the authors R.Payri et al. carried out similar analysis to the one by F. Payri, by using eight steel drilled plates. The drilled holes had different diameters and degrees of conicity. They investigated the cavitation phenomena in different geometry nozzles and capturing the near nozzles spray behaviour under liquid pressurised ambient conditions using an ND:Yag laser for illumination. They observed hysteresis in the cavitation phenomena by measuring the back pressure needed for bubbles to appear or disappear while decreasing or increasing discharge pressure. They observed that once the cavitation bubbles had appeared, a pressure in the chamber higher than the value which corresponds to the conditions of bubbles appearing was necessary for its collapse.

2.2.3 Acoustic cavitation

Acoustic cavitation can be defined as any observable activity involving a bubble or a population of bubbles stimulated into motion by an acoustic field. A high concentration of acoustic energy results in localised stresses and temperature and/or fluid velocities. The high

energy acoustic waves create alternating regions of compression and expansion that can form cavitation microbubbles. The growth and collapse of these microbubbles focuses and transfers energy from the acoustic wave to the vapour inside the bubbles, producing extremely high localised pressures and temperatures. Acoustic cavitation is responsible for sonochemistry and sonoluminescence the former will be discussed in this section. Sonochemistry is defined as the chemistry associated with ultrasound. The focussing of acoustic energy has been seen to generate highly reactive free radicals that have been observed to significantly enhance chemical processing. During the expansion cycle a sound wave of sufficient intensity can generate cavities. A liquid is held together by attractive forces, which determine its tensile strength. In order to form a cavity, a large decrease in pressure associated with the expansion cycle of the sound wave is required in order to overcome the liquids tensile strength. The pressure drop required depends on the type and purity of the liquid [98] and its vapour pressure. The tensile strength of liquids is reduced by trapped gas in the crevices of small solid particles.

A bubble irradiated with ultrasound continually absorbs energy from alternating compression and expansion cycles of the wave. These cause the bubbles to grow and contract, striking a balance between the vapour inside the liquid and the surrounding liquid. In some cases the bubble will simply oscillate in size and in other cases it will increase in size. When it reaches critical size and can no longer absorb any more energy efficiently, the cavity implodes and the surrounding liquid rushes in. This implosive environment creates an ideal environment for chemical reactions [38,98,99]. The dynamics of cavity growth and implosion are strongly dependant on local conditions and the form of the material i.e., whether they are liquids, extended solid surfaces in liquids or solid particles in liquids. Suslick in 1983 stated that unlike all chemical reactions, most sonochemical reactions decrease in rate with increase in

ambient temperature, i.e. the temperature outside the cavity. The higher the ambient temperature is the more vapour there will be inside the cavity and this will cushion the implosions and lowers the temperature of implosion [32]. The ambient gas dissolved in the liquid is quite important because the thermal properties of these gases dissolved may vary and hence they may drive the temperatures occurring during implosion. A gas with a poor thermal conduction retains the heat of the collapsing cavity and thus generating higher implosion temperatures. The chemical effects of ultrasound cavitation have been related to bond breaking and radical formation in aqueous solutions forming hydrogen and acetylene and hydro-peroxide, hydrogen and hydro-oxy radicals [38,100–102].

In 1983, Suslick et al. [32] studied the chemical effects of high intensity ultrasound on alkane solutions using a collimated 20 kHz beam from a titanium horn. Reactions were performed in a glass sonification cell under Argon atmosphere. They found that acoustic cavitation on alkanes lead to carbon-carbon bond cleavage and radical rearrangements and the peak temperatures reached in cavities was controlled by the vapour pressure of the solvent. This was considered to be the consequence of high temperature regions developing in the multi-phase solution as a result of cavitation bubble collapse. The ultrasonic irradiation of decane produced hydrogen, methane, acetylene and other smaller 1-alkenes. They compared the process to a high temperature pyrolysis like event occurring. During their investigation it was found that a decrease in the solvent volatility caused: the intensity of cavitational collapse; the maximum temperature reached and; the rate of reaction, to increase.

Price et. al [34,33] have carried out high intensity ultrasound irradiation in automotive grade diesel fuels to study the formation of sediments. A filtered fuel sample was used in a temperature controlled bath, with 23 kHz ultrasound horn. The later analysed the fuels using

gas chromatography – mass spectrometry (GC-MC). They found that the filterability of the fuels was affected after only a few hours of ultrasonic treatment. The amount of insoluble sediment was shown to increase in a logarithmic scale with relation to the sonification time. They also observed the breakdown of alkane components similarly to [32]. The rate of alkane break down decreased with increase in carbon chain length and it was negligible at C_{20}. They concluded that this was due to the longer chained alkanes having a lower vapour pressure. Sonification promoted a polymerization reaction which incorporated nitrogen and other aromatic components in the fuels to form insoluble sediments.

Wheat et. al [103] investigated the effects of high intensity ultrasound on polycyclic aromatic hydrocarbons PAHs in aqueous solution. Two PAHs were chosen as contaminants i.e. biphenyl and phenanthrene, which were to be subject to high ultrasound intensity under a cooling bath. At the end the aqueous reaction mixture was placed into a separatory funnel and dried before being subject to analysis by Gas chromatography (GC) and Gas chromatography/mass Spectrometry (GC-MS). Hydroxyl radical substitution reactions in aqueous solutions were the primary constituents formed from hydroxyl groups under high intensity ultrasound irradiation.

Cataldo [104] observed that the sonication of benzene and toluene at room temperature caused the aromatic rings of the compounds to break down and lead to the formation of acetylene and coke. They also conducted sonification on naphthenic hydrocarbons namely decalin and tetralin and in both cases a dehydrogenation reaction occurred resulting from intense ultrasound at room temperature. Further analysis with Fourier transform infrared (FT-IR) showed that the compound produced was not coke but a cross linked polystyrene. Work done prior to Cataldo by Zeichmeister et. al and Currell et. al, as cited in their journal had observed

the formation of acetylene during the sonification of aromatic compounds like benzene, halo-benzenes, and heterocyclic compounds. Later work on benzene sonication [105] has also shown the formation of chars, and very recently the formation of traces of C_{60} fullerene was detected in sonicated benzene [106].

Katoh et. al [106] used ultrasound irradiation at 600 W and 20 kHz on 150 ml liquid benzene and found it produce approximately 1µg of C_{60} within one hour. Diedrich et. al [105] found that the polymers formed had characteristics of char, obtained from low temperature pyrolysis of hydrocarbons during ultrasound irradiation. They found that introducing elevated temperatures reduced their rate of reaction. The presence of solid impurities had little effect on the rate of reaction; however the presence of gas caused the rates of reactions to increase when compared to reactions where no gases were present. These lead them to conclude that the chemical reactions occurring were as a result of cavitation.

A study by Malykh et.al [107] found the possibility of an appearance of light hydrocarbon fractions after experiments on ultrasonic cavitation of model compounds of the middle fraction of petroleum such as; hexadecane, decanol, ethylcaprate and colza oil, in spherical and cylindrical resonators. They confirmed the appearance of light hydrocarbon fractions and colza oil interesterification. Preliminary results showed the cavitation cracking of model compounds of crude middle fractions and the conversion of colza oil into corresponding etheric fatty acids.

The results obtained here are suggesting certain chemical effects are likely to occur as a result of cavitation. The literature here has shown the impact of ultrasound induced cavitation is causing chemical changes. Chemical processes such as cracking and pyrolysis have also

been discussed thought to be occurring as a result of ultrasound cavitation. The work here will analyse whether hydrodynamic cavitation causes similar chemical effects on diesel fuels.

2.2.4 Atomisation, spray formation, and break up

Spray formation is the introduction of liquid into a gaseous environment through a nozzle such that the liquid, through its interaction with the surrounding gas and by its own instability breaks up into droplets. The process of atomisation is one in which liquid is disintegrated into drops and ligaments by the action of internal and external forces leading to spray formation. The process easily occurs if the liquid is present in a form that is more susceptible to disintegration i.e. the formation of thin jets or liquid sheets; because they have the highest surface energy and thus the greatest instability [108]. The performance of spray systems can be optimized and improved by achieving desirable spray properties, for example in engines, liquid fuels have to be sprayed into the injection cylinder in a manner that the stoichiometric air/fuel ratio is followed. This requires correct atomisation of the liquid fuel such that the desired droplet size, number density, velocity and repartition in the combustion chamber are obtained. Achieving the above allows an increase in fuel and energy efficiency whereas decreasing the emission of pollutants from combusting sprays.

The scientific interest in the fuel injection process has expanded due to an increased desire in fuel efficiency and pollutant emission control. In a lot of combustion systems fuels are used in their liquid form. Liquid fuels contain more energy per unit volume than gaseous fuels and are also easier to store and transport. Normal fuels in their liquid form are not volatile enough to produce vapour in the amounts required for ignition and combustion and therefore there is a requirement to atomize them into a large number of finer droplets. The atomisation process

allows the conversion of the liquid phase into vapour phase. The rate of evaporation of the fuels is inversely related to the size of the generated droplets i.e. smaller droplets yield a faster rate of evaporation. The surface to volume ratio of smaller droplets is larger than that of larger droplets and as evaporation occurs on the gas-liquid interface the decrease in size of the droplets enhances evaporation. The evaporation of fuel droplets in a spray involves a simultaneous heat and mass transfer processes, in which the heat for evaporation is transferred to the drop surface by conduction and convection from the surrounding air or gas, and the vapour is transferred by convection and diffusion back into the gas stream. The overall rate of evaporation depends on the pressure, temperature, and transport properties of the gas; the temperature, volatility, and diameter of the drops in the spray; and the velocity of the drops relative to that of the surrounding gas [109].

Arcoumanis et al. [110] has reported three different atomisation models: (1) Aerodynamic-induced atomisation: were waves develop on the surface of the liquid jet, and are caused by relative motion between the injected fuel and the gas. The Weber number is used to determine the growth rate of these waves and the disintegration of the jet into smaller droplets. The Ohnesorge number is used for the liquid viscosity effects. (2) Jet turbulence-induced atomisation: at fully turbulent flow conditions in the injector nozzle holes, the radial velocity component in the jet soon leads to disruption of the surface film, followed by general disintegration of the jet. Even when injected into vacuum, the jet will disintegrate under the influence of its own turbulence. (3) Cavitation-induced atomisation: where the liquid jet emerging from the injection hole disintegrates due to the collapsing of the cavitation bubbles present at the exit of the holes. Since the pressure around the emerging jet is much higher than the gas pressure inside the cavitating bubbles, these bubbles gradually collapse while they are convected by the internal jet turbulence. This process causes perturbation on the surface of the

liquid jet. The perturbations lead to jet disintegration and formation of smaller droplets at the time of total bubble collapse or at the time the bubble reach the jet surface.

In 2000, Smallwood et.al [111] provided a more in depth investigation into the mechanism of atomisation. The authors showed that the spray is completely atomised at or near the nozzle tip, where nozzle cavitation and turbulence-driven instabilities are the dominant break up mechanism. The influence of cavitation is twofold i.e. first the bursting and collapsing vapour cavities contribute to the disintegration of liquid masses at the exit of the nozzle hole, resulting in a mixture of bubbles and liquid occupying most of the cross sectional area; secondly, cavitation increased the turbulence intensity of the flow through the nozzle hole thus contributing to the instability of the liquid jet. The instabilities along with pressure fluctuations in the nozzle cause variation in the exit velocity of the droplets which resulted in temporal and spatial clustering of the droplets in the plume.

Internal cavitating flow occurring inside fuel injectors is believed to produce a number of effects on the internal fuel flow in the injector. Nozzle cavitation is believed to reduce the injected fuel mass in an unpredictable manner, which can result in poor fuel/air mixture formation in the engine, which in turn, can cause unstable combustion, and/or higher engine-out pollution emissions [2,22,84,94,112]. Nozzle cavitation is believed to affect the atomisation of the fuel jets into droplets as the jets enter the engine [88,91,113]. Cavitation occurring near injector surfaces may cause surface erosion, and ultimately injector failure [25]. Cavitation of the flow through the diesel nozzle has long been considered as a possible contributor to the breakup and atomisation process [114]. However it was not until the late nineties-early 2000's that several studies recognized and demonstrated the existence and the

influence of nozzle hole cavitation in diesel injection systems [2,92,115] and many have studied the effects of nozzle cavitation on atomisation and spray break up after this period.

Relevant properties for atomization		Spray illustration	Spray characteristics and geometrical aspects
Injected liquid	• Surface tension • Viscosity • Density • Temperature • Composition	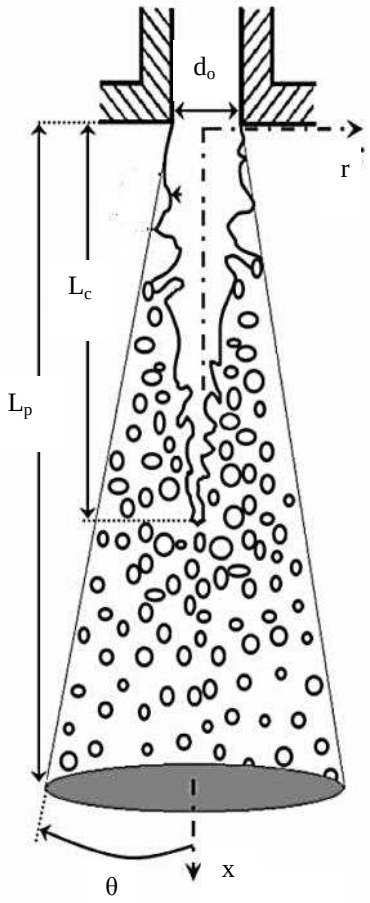	• Nozzle flow rate U_l • Radial and axial distances r and x • Length of liquid core L_c • Liquid jet or sheet thickness d_o • Distance of penetration L_p • Spray angle θ
Liquid flow	• Injection pressure • Injection rate • Injection duration • Quantity of fuel injected • Velocity • Turbulence in the liquid stream		
Ambient gas	• Gas temperature • Gas density/pressure • Gas composition		
Injector	• Orifice diameter • Orifice length • Orifice inlet geometry • Number of holes • Tip geometry (VCO, minisac etc.)		

Table 2.3 Most relevant properties for atomization with the related characteristics and geometrical aspects (adapted from[111])

The spray structure is influenced by various parameters including the properties of the injected fluid, the properties of the surrounding gas and the characteristics of the injector itself [116]. A summary of the properties affecting spray atomisation is seen in Table 2.3. Depending on the operating conditions and on the injector design, a wide variety of sprays can be produced. A spray is composed of: a liquid core corresponding to the extension of the

liquid body injected; the multiphase mixing layers characterised by irregular elements and large drops and created by atomisation; dispersed flow in which small round drops are well formed and; the vaporisation zone where the small droplets are evaporated as seen in Figure 2.11 [117]. Two main spray regions are defined i.e. the dense spray and the dilute spray regions.

The detaching of liquid core into ligaments and drops is known as primary breakup (primary atomisation). This occurs due to gas-liquid interfacial instabilities in the liquid core jet in the dense spray region. The liquid ligaments and large droplets further breakup into smaller droplets due to the interactions between liquid ambient gas or droplet collisions. This is known as secondary breakup (secondary atomisation) and occurs in the dilute spray region.

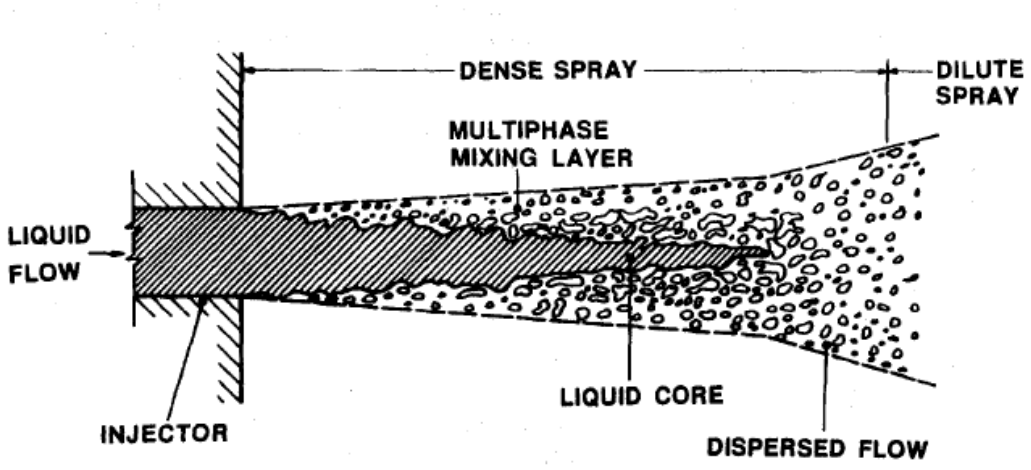

Figure 2.11 Illustration of the spray structure in the atomization regime [117]

The most relevant liquid properties to spray generation are viscosity, surface tension and density. The viscosity is a quantity that characterizes a fluid resistance to flow. It is the most important liquid parameter to atomization owing to its effect on droplet size, liquid flow rate and on the geometrical shape of the spray [118]. As liquid viscosity increases, flow rate is generally reduced and the development of instabilities in the liquid core is hindered. As a result, the disintegration process is delayed and a spray with a narrow spray angle and large

droplets is produced. Liquid viscosity is highly dependent on the temperature and decreases generally with increasing temperature [108]. Hiroyasu et.al [116] demonstrated the effect of kinematic viscosity and injection pressure of the liquid fuel on the spray cone angle and found that the spray angles θ were widened by a reduction in viscosity and an increase in injection pressure.

Ghuri et al [119] conducted an investigation to examine the effect of injection pressure and fuel type on the spray tip penetration length and the spray cone angle of sprays injected into an atmospheric chamber. They observed that the role of fuel viscosity seemed stronger before the break-up time than after break-up time. Before the break-up time, the spray had larger droplet diameter which meant higher spray momentum to penetrate the ambient air (longer break up length). The spray tip penetration developed quicker at the early stage of injection, and slower after the break up time when the spray atomization to the smaller droplets occurred. Most of the data showed the initial spray tip penetration of diesel fuel was always longer than biodiesel fuel. This was caused by the higher initial velocity of the diesel spray as consequence of its lower viscosity and density. The higher viscosity of biodiesel fuel resulted in higher resistance to break-up. However the higher viscosity also enabled the spray to have the higher momentum for a longer time after start of injection. As a result, the biodiesel spray could reach slightly longer penetration lengths in comparison to the diesel spray. They also concluded that the spray cone angle was mostly affected by changes in viscosity and not by changes in injection pressure. Increase in fuel viscosity leads to a decrease in spray cone angle.

Jankowski et. al [120] investigated the effects of fuel viscosity and injection pressure on the fuel droplet diameter and velocity distribution in a fuel spray in a constant volume chamber

using LDV, Phase Doppler Particle Analyser PDPA and PIV laser systems. The authors used diesel fuels with different viscosity in common rail powered compression ignition engines, varying injection pressure from 50 to 130 MPa. The test results showed that the lower viscosity fuels produce smaller droplet diameters than fuels with higher viscosity. They performed measurements of droplet velocity using LDV, the droplet diameter using PDPA and the droplets distribution using PIV and PDPA. They concluded that the physical process of generating the fuel sprays was strongly influenced by fuel viscosity, density and surface tension which depend on the fractional constitution and the process of crude oil refining and additives. Fuel viscosity affected the injection pressures similarly to those that have been discussed earlier. Increase in injection pressure resulted in decrease of droplets diameter. They observed a decrease in droplet velocity as the distance from the injection nozzle increased being caused as a result of turbulence.

Liquids of high surface tension are more difficult to disintegrate by aerodynamic, centrifugal or pressure forces comparing to those of lower surface tension. In general, the surface tension decreases as temperature increases for most pure liquids in contact with air. Break up processes in general are governed by a balance of energy between inertial forces and surface tension. Secondary droplet breakup occurs if the surface tension equals the effective aerodynamic force. The Weber number (We) is defined as the ratio of inertia forces to surface tension forces as:

$$We = \frac{\rho_l U_l^2 l_l}{\sigma_l}$$

Equation 2.6

Where ρ_l is the liquid density, U_l is the flow velocity of the fluid, l_l is the characteristic length scale of the liquid flow and σ_l is the surface tension of the liquid. The inertial forces tend to break apart the liquid core whereas the surface tension forces tend to hold it intact.

The other important dimensionless number of importance during atomisation is the Ohnesorge number defines as the ratio of inertial viscous forces to surface tension forces Equation 2.7.

$$Oh = \frac{\sqrt{We}}{Re} = \frac{\mu_l}{\sqrt{l\,\rho_l \sigma_l}}$$

Equation 2.7

Where μ_l is the liquid viscosity.

The fundamental parameters of the liquid flow are the injection pressure, liquid velocity and turbulence in the liquid stream**.** High pressure injection and high liquid velocity increase the formation of instabilities and disturbances at the nozzle exit and increase the atomization efficiency. Schweitzer [118] described the three regimes of turbulent flow and their effects on atomization as follows: The flow is called laminar when the liquids particles flow in streams parallel to each other and to the axis of the tube. When the paths of the liquid particles cross each other in a more or less disorderly manner having varying transverse velocity components, the flow is turbulent. If the centre of the flow is turbulent, and if its periphery is laminar, the flow is defined as semi-turbulent. The Reynolds number, previously defined in Equation 2.3 gives a good indication regarding the state of flow at the orifice exit. Spray disintegration is linked up with Reynolds number. The higher the Reynolds number the higher the level of turbulence in the flow and above a critical Re, a turbulent flow will remain turbulent. A laminar flow will turn turbulent if Re is increased, however if constant, a laminar flow will stay laminar. The level of turbulence imparted on a liquid flow influences its

atomisation process. Hiroyasu et. al [116] conducted an experiment with the aid of photographic techniques into the effects of ambient conditions and injection pressures on the spray tip penetration. They heated up a constant volume bomb filled with nitrogen to various temperatures. They concluded that the spray tip penetration was proportional to time in the early stages of injection (incomplete atomised region), and for later stages, they found the spray tip penetration was proportional to the square root of time. As a result, the initial stage of the spray evolved with a steady tip penetration equal to the injection velocity. During the complete atomisation stage, the jet was considered to disintegrate to form a spray with tip penetration length proportional to $t^{1/2}$.

Fath et. al [115] investigated the effects of different injection and chamber pressures for four different nozzle geometries on the internal cavitation structures and the spray break up close to the nozzle using a 2D measuring technique on the basis of Mie scattering. They concluded that the intact liquid core length decreased with an increase in injection pressure.

The density of the surrounding gas (generally air) is the final gas property of importance regarding spray formation. For a given distance from the nozzle, the size of droplets is smaller at higher air densities than lower air densities and the liquid jet disintegration is more efficient. The jet loses velocity more quickly at higher air pressures than at lower air pressures with less propagation along the axial axis. As a result, the spray penetration distance, L_p, and the liquid core length, L_c, are reduced (see Table 2.3). The spray cone angle also becomes wider with air density, changing the geometrical shape of the spray. Hiroyasu et. al [116] in their work reported an increase in spray cone angle and a decrease in spray tip penetration due to an increase in ambient gas pressure. They also observed that an increase in ambient gas

temperature resulted in a noticeable decrease in the spray cone angle which occurred as a result of the evaporation of droplets in the spray boundary.

Kennaird et. al [121] investigated the influence of in cylinder charge density varying between 10 kg/m^3 and 50 kg/m^3, injection pressure varying between 60-160 MPa and injector nozzle geometry on the behaviour of diesel sprays using high speed imaging. They observed that the leading edge of the vapour phase penetrated at a similar rate to the liquid core until the liquid core had reached its ultimate length. After that the vapour phase continued and penetrated deeper into the chamber due to the earlier liquid momentum transfer. They also observed the dependency of the vapour penetration on both gas density and injection pressure and that an increase in vapour pressure and a decrease in in-cylinder gas density resulted in a greater vapour penetration. Similar effects were observed by Naber et. al [122] as reported in the paper. Fath et. al [115] in their investigations concluded the liquid core decreased with increase in gas pressure.

Laguitton et. al [123] made an attempt to investigate the effects of in-cylinder density and fuel injection pressure on liquid penetration, vapour formation and auto ignition delay. They utilised two high speed video cameras to achieve pseudo 3D imaging of the spray and of auto ignition sites; and Schlieren imaging for the vapour phase analysis. The authors gathered data for in cylinder densities in the range of 10 – 50 kg/m^3 and injection pressures between 60 and 160 MPa. They observed that by increasing injection pressures and using small injector orifice sizes, the injected diesel droplets reduce in size and had a longer penetration hence increasing air utilisation, leading to faster evaporation rates and reduced ignition delay. Increasing the in cylinder density causes the spray penetration to reduce, however autoignition delay is also reduced, which indicate more favourable conditions for ignition.

The shape, size and flow state of the initial liquid body injected into a gaseous environment is mainly controlled by the nozzle geometry. Depending on nozzle characteristics, either a liquid jet or a liquid sheet is generated. The dimension of the liquid core is determined by the size of the nozzle orifice. Smaller nozzle orifices give rise to finer atomisation processes. The spray cone angle was found to be affected by the length and diameter of the nozzle orifice by Chaves et. al [92] and Schmidt et. al [81]. They concluded that an increase in nozzle L/D ratio gave rise to a decrease in the spray cone angle. Hiroyasu and Arai [116] reported that an increase in tip penetration occurred as a result of an increase in nozzle diameter. Smallwood et.al [111] conclude that the orifice diameter was the dominant injection parameter for spray penetration distance. Similarly to Hiroyasu they also concluded that a decrease in orifice diameter leads to a decrease in liquid penetration distance.

Su et al. [124] indicated that the nozzle configuration has an important effect on the fuel atomisation. The configuration included the following factors: the surface area of the nozzle hole, the entrance shape of the hole, the number of holes, the length to diameter ratio, the orientation of the nozzle holes with respect to the nozzle axis and the sac volume. The authors used a mini-sac injector with two types of nozzle hole entrances: sharp-edged and round-edged inlet. Higher injection pressures resulted in longer spray tip penetrations, narrower spray angles and smaller particle sizes for both nozzle entrance shapes. The sharp-edged inlet nozzle produced a wider spray dispersion angle, smaller SMD and a smaller value of particulate emission, compared to the round-edged inlet tip.

Bae et. al [80,125] investigated the spray characteristics of diesel injectors using various nozzle geometries. They observed the spray penetration of the sac nozzle to be lower than the VCO type nozzle at various injection conditions. A higher nozzle K factor led to smaller

spray penetration and spray angle when injected into atmospheric conditions. These effects however did not appear under pressurised environments.

Park et. al [126] investigated the effect of cavitation on the fuel flow and atomisation characteristics of bio diesel fuel using two different nozzles with different length to width (L/W) ratios. Their visualisation system captured the internal and external flow for investigating the formation and development of cavitation inside an orifice, and the internal and external flow characteristics were then analysed quantitatively using Reynolds, Weber, cavitation numbers and discharge coefficient. They had a droplet measuring system installed to measure the effects of cavitation on atomisation by measuring the mean droplet size and the axial and radial mean velocity. They revealed that the mean droplet sizes of biodiesel as compared to diesel fuel were larger. The droplet sizes became small when it formed the cavitation inside the orifice and in the case of the high L/W ratio nozzle; the droplet size was smaller than for the nozzle with the low L/W ratio. From these results they concluded that cavitation promoted the atomisation of fuels at the nozzle exit. The cavitating rate of biodiesel fuel was found to be lower than diesel fuel. When the nozzle L/W ratio was changed from 1.5 to 3, a higher pressure was required to visualize the occurrence of cavitation. On the basis of SMD and velocity measurements the cavitation in the nozzle orifice promoted the atomisation of fuels at the nozzle exit. They concluded that the energy generated during the formation, growth and rupture of cavitation enhances the energy for the atomisation of fuels.

2.3 Measurement Techniques and Diagnostics

So far the reviews on cavitation and atomisation have looked at various authors using a number of imaging and optical characterisation techniques. The ones important to this work will be reviewed in the current section namely: Mie scattering, Laser Induced Fluorescence (LIF), laser Sheet Dropsizing (LSD) and Structured Laser Illumination Planar Imaging (SLIPI)

2.3.1 Mie scattering and light scattering

When a particle (such as an atom, a molecule, a liquid or a solid particle) is illuminated by an electromagnetic wave, the discrete electric charges (the electrons and protons) are set into an oscillatory motion by the electric field of the incident wave. This oscillation causes the acceleration of the electric charges, which produces radiation of electromagnetic energy in all directions. This new radiation is called scattered radiation [127]. If a particle is divided into small regions such as each region is characterized by a dipole moment, then the oscillating field will cause the oscillation of the dipoles and a secondary radiation of scattered wavelets will be emitted by each region of the particle in all directions as observed in Figure 2.12. Scattering is thus the result of the sum of all these wavelets. During the emission of the new electromagnetic waves, the scattered wavelets interfere with each other, resulting in several preferential final scattering directions. Typically, back scattering and forward scattering are the dominant scattering directions. Both the size and the shape of a particle are responsible for the interference processes occurring. Depending also on the polarization state of the light an incident beam is scattered within preferential directions.

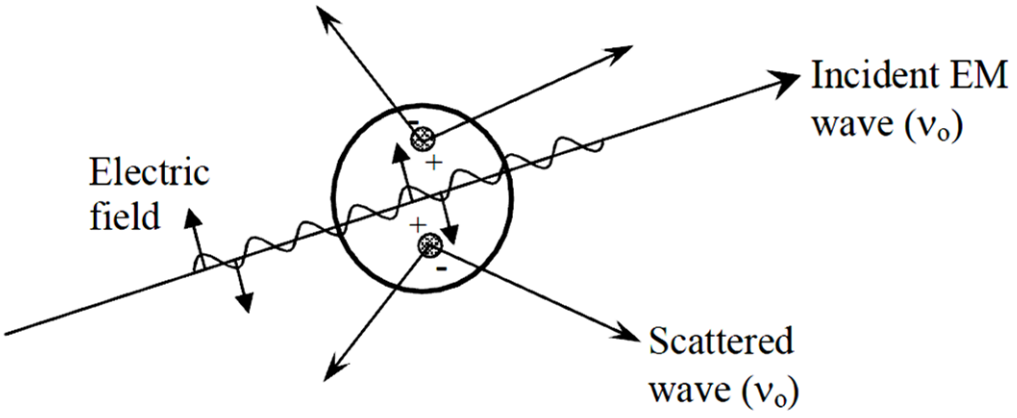

Figure 2.12 Light scattering by an induced dipole moment due to an incident electromagnetic wave [128]

The classical theory relating to particle scattering to diameter is called the Mie or more properly Lorenz-Mie theory. This theory is derived by solving Maxwell's equations describing electromagnetic radiation for the light scattered by a homogeneous sphere under uniform illumination. The theory forms the basis for the measurements of optical, particle sizing instruments based on measuring scattered light intensity. The key assumptions are that the particle is a sphere and homogeneous (characterised by a single refractive index at a given wavelength). The way of describing the light scattered from small spherical particles mainly depends on the ratio of the particle size and the wavelength of the incident light.

The dimensionless size parameter, is defined as follows [129] :

$$\chi = \frac{\pi dm}{\lambda}$$

Equation 2.8

In the equation, d is the particle diameter, λ is the laser wavelength and m is the refractive index of the particle. For χ << 1 the scattering process is described by the Rayleigh scattering,

for χ >>1 the geometric optics theory applies, whereas For $\chi \geq 1$ the scattering process is described by Lorenz Mie theory [127] named after the German physicist Gustav Mie (1869-1957). It is based on the application of the Maxwell equations on an isotropic, homogeneous, dielectric sphere. The model is equally applicable to spheres of all sizes, refractive indices and for radiation at all wavelengths. In the Mie formalism, Maxwell's equations are solved in spherical coordinates through separation of variables. The incident plane wave is expanded in Legendre polynomials so the solutions inside and outside the sphere can be matched at the boundary. The solution sought is at a distance much larger than the wavelength, in the so-called far-field zone. The far-field solution is expressed in terms of two scattering functions [130]:

$$S_1(\Theta) = \left| \sum_{n=1}^{\infty} \frac{2n+1}{n(n+1)} [a_n \pi_n(cos\ \theta) + b_n \tau_n(cos\ \theta)] \right|^2$$

Equation 2.9

$$S_2(\Theta) = \left| \sum_{n=1}^{\infty} \frac{2n+1}{n(n+1)} [a_n \tau_n(cos\ \theta) + b_n \pi_n(cos\ \theta)] \right|^2$$

Equation 2.10

Where $S_1(\Theta)$ and $S_2(\Theta)$ represents the angular intensity functions, θ represents the scattering angle, the functions τ_n and π_n are angular dependent functions expressed in terms of the Legendre polynomials by;

$$\pi_n(cos\ \theta) = \frac{P_n^1(\cos\theta)}{\sin\theta}$$

Equation 2.11

$$\tau_n(cos\ \theta) = \frac{dP_n^1(\cos\theta)}{\mathrm{d}\,\theta}$$

Equation 2.12

Where P_n^1 are the Legendre Polynomials of the first order. The coefficients a_n and b_n from Equation 2.9 and Equation 2.10 for a perfect sphere are defined as:

$$a_n = \frac{\Psi_n(\chi)\Psi_n'(m\chi) - m\Psi_n(m\chi)\Psi_n'(\chi)}{\xi(\chi)\Psi_n'(m\chi) - m\Psi_n(m\chi)\xi_n'(\chi)}$$

Equation 2.13

$$b_n = \frac{m\Psi_n(\chi)\Psi_n'(m\chi) - \Psi_n(m\chi)\Psi_n'(\chi)}{m\xi(\chi)\Psi_n'(m\chi) - \Psi_n(m\chi)\xi_n'(\chi)}$$

Equation 2.14

where the functions are the Riccati-Bessel functions [127]. The electric field in the far field is described by,

$$\begin{bmatrix} E_{\parallel S} \\ E_{\perp S} \end{bmatrix} = \frac{\exp(-ikR + ikz)}{ikR} \begin{bmatrix} S_2\ S_3 \\ S_4\ S_1 \end{bmatrix} \begin{bmatrix} E_{\parallel i}^0 \\ E_{\perp i}^0 \end{bmatrix}$$

Equation 2.15

Where the matrix $\begin{bmatrix} S_2\ S_3 \\ S_4\ S_1 \end{bmatrix}$ is the amplitude of the scattering matrix, exp (ikz) is the incident plane wave and $\frac{\exp(-ikR)}{ikR}$ is the outgoing scattering wave. The S-matrix relates the initial state and the final state of a physical system undergoing a scattering process. It describes the relationship between incident and scattered electric field components perpendicular and

parallel to the scattering plane as observed in the "far-field" [127]. The above expression simplifies in practical experiments:

(i) The exponential term, $\frac{\exp(-ikR+ikz)}{ikR}$ is a transport factor that depends on the distance between scatterer and observer. If one measures scattered light at a constant distance R from the scatterer, for example as a function of angle or orientation of polarization, then the transport factor becomes a constant.

(ii) The total field (E_{tot}) depends on the incident field (E_i), the scattered field (E_s), and the interaction of these fields (E_{int}). If one observes the scattering from a position which avoids E_i, then both E_i and E_{int} are zero and only E_s is observed.

(iii) For "far-field" observation of E_s at a distance R from a particle of diameter d such that $kR >> n_c^2$, $k = 2\pi/\lambda$, $n_c = d/\lambda$, the scattering elements S_3 and S_4 are equal to zero.

(iv) Practical experiments measure intensity, $I \leq E, E^* \geq (1/2)a^2$, where $E = a\exp(-i\delta)$, and a is amplitude and δ is phase of the electric field.

Hence for practical scattering measurements, the above equation simplifies to the following:

$$\begin{bmatrix} I_{\parallel S} \\ I_{\perp S} \end{bmatrix} = Constant \begin{bmatrix} |S_2|^2 & 0 \\ 0 & |S_1|^2 \end{bmatrix} \begin{bmatrix} I^0_{\parallel i} \\ I^0_{\perp i} \end{bmatrix}$$

Equation 2.16

For an unpolarised incident light source through a particle, the particle will scatter light that consists of polarised light in the plane of observation, parallel polarisation and perpendicular polarisation. The plane of observation is the plane formed by the incident light source transmitting. The scattering intensity depends on the polarisation orientation of the incident light. The scattered light from the different scattering modes also varied at different scattering angles as seen in Figure 2.13.

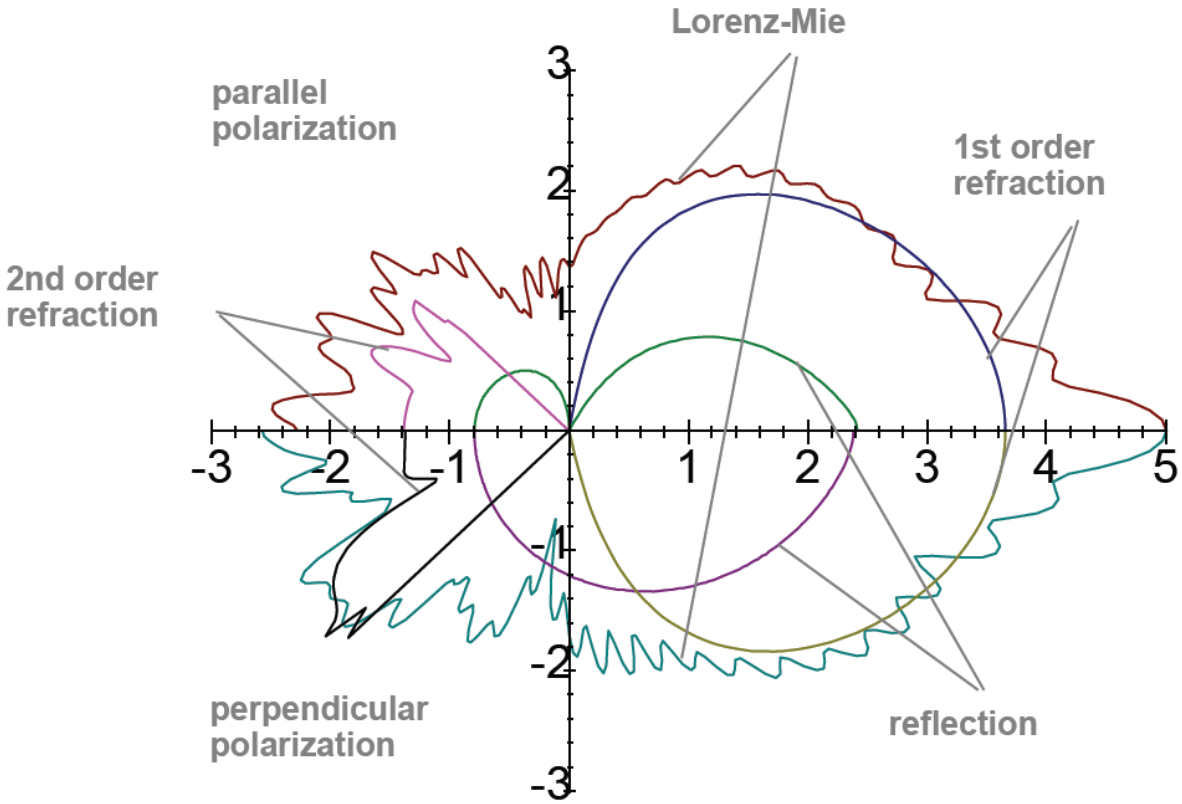

Figure 2.13 Diagram showing the intensity of scattered light from different scattering modes [131].

Scattering orders, optical depth and scattering regimes are parameters related to media containing a collection of scattering particles. The scattering order corresponds to the number of times that an individual photon interacts with the droplets (or other scattering particles) prior to spray exit. At a scattering order of 0 no interaction occurs, and the photons cross the spray keeping their initial direction. The scattering order 1 or single scattering is in optical measurement of sprays, the order of interest as the information obtained is directly related to the droplet characteristics (e.g. droplets size, concentration). The range of scattering order from 2 up to 9 is associated to the "snake" photons group (when assuming a forward scattering detection). These photons travel a longer path through the spray than the ballistic photons and exit the spray along approximately the same axis as the input light with a somewhat larger solid angle. Photons scattered more than 10 times are the diffuse photons and

exit the medium with a large solid angle after traveling long path in the spray [132]. Depending on the value of the optical depth and/or of the average scattering order, the scattering of light within a spray can be classified into 3 regimes i.e. single scattering regime (Optical depth OD≤1), intermediate scattering regime (2≤OD≥9) and multiple scattering regimes (OD≥10).

Planar Mie imaging corresponds to the detection of the elastic light scattered by the droplets and the irregular liquid elements of size comparable to the incident wavelength. By definition, elastic scattering is the term given when the light scattered from the illuminated particles has a wavelength identical to the incident radiation. When the scattered light is characterised by different wavelength than the incident radiation the process is known as in-elastic scattering. In laser diagnostics of non-combusting sprays Mie scattering is the natural and dominant scattering process from the interaction if the incident laser light with various liquids elements resulting from atomisation. For spherical and homogeneous droplets of size much bigger than the wavelength, the total amount of light elastically scattered in all direction (quantified by the scattering cross-section) is found to be linearly dependant to the square of the droplet diameter D^2. However, considering a given collection angle (e.g. for θ equal 90 or 60 degrees) and/or for small particles (D less than 10 μm), this dependence is not valid any longer and correction procedures are required [133]. Planar Mie images are generally used to provide information related to geometrical aspects of the spray structure. Many researches have used this technique to investigate diesel sprays as discussed in the earlier sections.

In spite of its whole field detection, sharp depth of field and simplicity, laser sheet imaging of sprays suffers from a number of limitations when the single scattering approximation is no longer valid and when intermediate single to multiple scattering regime applies. The first

limitation corresponds to the exponential attenuation of laser intensity as photon travel through the spray due to scattering and absorption along the incident direction. This is a well-known phenomenon called laser extinction and it is described in the Beer-Lambert law. Secondly the induced signal, regardless of the scattering process involved- elastic or inelastic; is reduced between the laser sheet used for illumination and the camera also according to the Beer-Lambert relation is referred to as signal attenuation or signal trapping. Finally depending on the optical thickness of the spray, photons can experience several scattering events within the sample prior to detection (multiple scattering). Errors by multiple scattering depend on the average deviation of the trajectory of the detected photons per scatter, and hence on the particle size distribution.

2.3.2 Laser Induced Fluorescence (LIF)

Laser induced fluorescence (LIF) is a powerful technique more and more commonly used by the chemical physicist for probing gas-phase atomic or molecular species, even in minute amounts, and determining their internal states distribution. By absorption of one or several photons from the laser beam, the probed species are pumped from an initial state i to an excited state e from which radiation is subsequently emitted as transitions take place to final states f. All or part of the emitted radiation is detected. Usually, each time it is possible that the light is detected at a wavelength different from the laser wavelength to eliminate any spurious signal due to scattered laser light [134]. Fluorescence results from a process that occurs when certain molecules called fluorophores, fluorochromes, or fluorescent dyes absorb light. The absorption of light by a population of these molecules raises their energy level to a briefly excited state. As they decay from this excited state, they emit fluorescent light. The

process responsible for fluorescence is illustrated by the electronic state diagram in Figure 2.14.

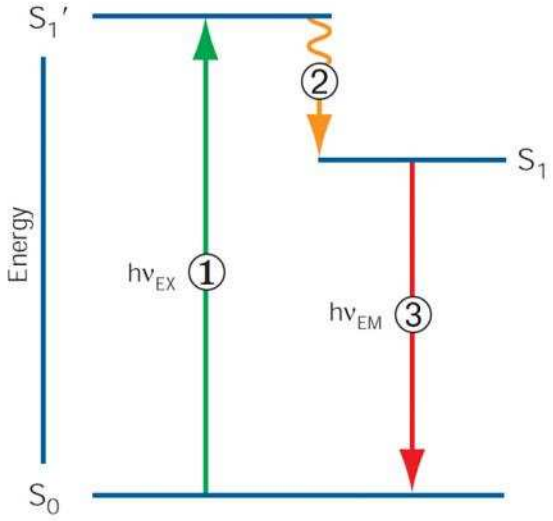

Figure 2.14 Jablonski diagram illustrating the processes involved in creating an excited electronic singlet state by optical absorption and subsequent emission of fluorescence. (1) Excitation; (2) Vibrational relaxation; (3) Emission.

When a photon of energy, $h\nu_{EX}$, supplied by an external source such as a lamp or a laser, is absorbed by a fluorophore, it creates an excited, unstable electronic singlet state (S1'). This process is distinct from chemiluminescence, in which the excited state is created by a chemical reaction. The excited state of a fluorophore is characterized by a very short half-life, usually on the order of a few nanoseconds. During this brief period, the excited molecules generally relax toward the lowest vibrational energy level within the electronic excited state Figure 2.14. The energy lost in this relaxation is dissipated as heat. It is from this relaxed singlet excited state (S1) that fluorescence emission originates. When a fluorochrome molecule falls from the excited state to the ground state, light is often emitted at a characteristic wavelength. The energy of the emitted photon ($h\nu_{EM}$) is the difference between the energy levels of the two states (Figure 2.14), and that energy difference determines the wavelength of the emitted light (λ_{EM}).

$$\lambda_{EM} = \frac{hc}{E_{EM}}$$

Equation 2.17

where E = the energy difference between the energy levels of the two states during emission (EM) of light, h is Planck's constant, c is the speed of light.

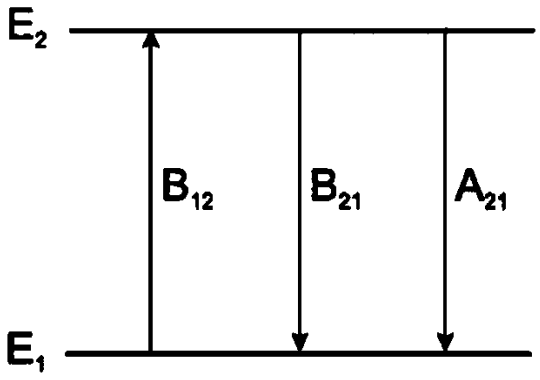

Figure 2.15 The probability of transition of a molecule between two energy levels

The Einstein coefficients characterize the probability of transition of a molecule between two energy levels E_1 and E_2 (Figure 2.15). B_{12} is the induced absorption coefficient, B_{21} is the induced emission coefficient and A_{21} is the spontaneous emission coefficient. The emission-induced process E2→E1 occurs at exactly the same rate as the absorption-induced process E1 →E2, so that $B_{12} = B_{21}$.

The number of molecules in states 1 and 2 is N_1 and N_2, respectively. These numbers must satisfy the Boltzmann Law:

$$\frac{N_1}{N_2} = exp\left[\frac{-(E_1 - E_2)}{kT}\right] = \exp\left(\frac{h\nu}{kT}\right)$$

Equation 2.18

Where h is Planck's constant. The rate of absorption from state 1 to state 2 is $N_1B_{12}\rho(\nu)$, where $\rho(\nu)$ is the energy density incident on the sample at frequency ν. The rate of emission from state 2 to state 1 is $N_2\,[A_{21} + B_{21}\,\rho(\nu)]$. At equilibrium, these two rates are equal, hence

$$\frac{N_1}{N_2} = \frac{B_{21}\rho(\nu) + A_{21}}{B_{12}\rho(\nu)} = 1 + \frac{A_{21}}{B_{12}\rho(\nu)}$$

Equation 2.19

The radiation density $\rho(\nu)$is given by Planck's black body radiation law:

$$\rho(\nu) = \frac{8\pi h\nu^3}{c^3 \exp\left(\frac{h\nu}{kT}\right) - 1}$$

Equation 2.20

The equations above (Equation 2.18 - Equation 2.20) lead to

$$A_{21} = \frac{8\pi h\nu^3}{c^3} B_{21}$$

Equation 2.21

The condition for observing induced emission (stimulated emission) is that the population of the first singlet state S_1 is larger than that of S_0. Induced emission is coherent, i.e. all emitted photons have the same physical characteristics – they have the same direction, the same phase and the same polarization. These properties are characteristic of laser emission. The term induced emission comes from the fact that the de-excitation is triggered by the interaction of an incident photon with and excited atom or molecule, which induces emission of photons having the same characteristics as those of the incident photon [135].

Not every absorbed photon is re-emitted as fluorescence light. There are several processes that lead to non-radiative dissipation of the absorbed energy. The ratio of absorbed energy and energy of emitted fluorescence photons is called fluorescence quantum yield φ_F:

$$\varphi_F = \frac{number\ of\ emitted\ photons}{number\ of\ absorbed\ photons} = \frac{N_F}{N_A}$$

Equation 2.22

φ_F measures the fluorescence efficiency. Its value is mostly determined by the molecular structure and the environment of the fluorescing dye molecule.

A laser-scanning instrument or a CCD-camera can be used to measure the intensity of the fluorescent light and subsequently create a digital image of the sample. Image analysis makes it possible to view, measure, render, and quantitate the resulting image.

The inelastic process of laser induced fluorescence is usually caused by the addition of a dye or tracer within the injected liquid or by natural fluorescence of the probed species. Some liquids of interest i.e. water, alcohols etc., do not fluoresce naturally and required an additional dope to be added to them. Fuels contain fluorescing compounds that can be excited in the ultra-violet spectral region, however the signal emitted is often difficult to quantify thus tracers are added in a manner that the fluorescing signal can selectively detected. LIF techniques are used for the visualization of the liquid phase in non-evaporating sprays and for the identification of both the liquid and vapour phase in evaporating sprays. The measurement of species concentration and temperature is also performed via LIF especially in combusting sprays. The principle of the technique is as follows: When the appropriate doped droplets or species cross the laser sheet, the incident optical excitation induced produces the emission of

an incoherent fluorescence signal which is optically filtered and detected. The signal intensity generated is a function of the absorber concentration, the temperature and the ambient pressure. In the past, a variety of fluorescent tracers have been used including acetone [136,137]; Rhodamine B [138] and Rhodamine 6G [139].

For small droplets containing the appropriate doping agent at correct concentrations, the emission of the fluorescence signal is isotropic and proportional to the incident light intensity. In such conditions, and for constant incident radiation, the fluorescence signal is volume dependant and linear to D^3 for spherical droplets. Increasing the size of the droplets and/or the concentration of the tracer leads to an increase in light attenuation within the droplets. In this case, the light emitted becomes anisotropic with a dominant back scattering.

To guarantee the proportionality of the Laser Induced Fluorescence (LIF) signal with the droplet volume, concentrations of tracer and laser light intensities must be then carefully chosen. A main strategy of LIF is to differentiate one phase from the other. This is performed by choosing the adequate doping agent which reduces the fluorescence signal in one phase while emitting a strong signal in the other.

Since fluorescent dyes are mostly applied in solution, various effects of the solvent must be discussed:

• Line broadening: Usually an organic dye molecule consists of many atoms, a fact that would lead to a distinctive vibrational line-emission spectrum. However, the solvation shell around each fluorescing molecule has a slightly different structure; therefore, the interaction between dye and solvent is not uniform. An emission spectrum, where we usually look at a whole ensemble of fluorescing molecules, consists of the contributions from each molecule. That

leads to strong broadening of the vibrational lines. At very low temperatures when the solvation shell cannot change its orientation within the fluorescence lifetime a line spectrum can nonetheless be observed.

• Relaxation: Electronic excitation leads to spatial expansion of the electron shell. In general this means an increased polarizability and decreased excitation energy. It also changes the dipole moment and therefore leads to a change in orientation of the nuclei and all the surrounding molecules. This process takes place within 10^{-10} s and is already finished when fluorescence occurs. Thus, the energy of the excited state is lowered at the time of emission compared to the time of absorption because of the solvent relaxation. The transition from the S_1 occurs according to the Franck-Condon law to a S_0 state with equal nuclear coordinates and equal orientation of the solvent molecules. This state is usually not in thermal equilibrium with its environment and therefore on a higher energy level then the S_0 ground state. Hence, the emission maximum always depends on solvent properties, such as viscosity and polarity.

In summary, a suitable tracer should be added to the liquid under investigation either directly or through a solvent. When selecting the solvent it should have similar evaporation and mass diffusion properties to the fuel it is being added to. It should also have a high fluorescence quantum yield when mixed with the tracer, at the excitation wavelength of the laser available.

2.3.3 Laser Sheet Dropsizing (LSD)

Laser Sheet Dropsizing produces instantaneous two dimensional images of spray Sauter Mean Diameter (SMD) by combining the well-established laser sheet techniques of Mie scattering and LIF. The general expression for the scattered signal S from a droplet of diameter D is given by Equation 2.23:

$$S = CD^n$$

Equation 2.23

where C is a constant containing experimental parameters including the laser fluence and signal collection solid angle, n is an index of dependence (expected to be constant for a fixed temperature). This expression is valid for D>>l (laser wavelength) and neglects any effects of Morphology Dependent Resonances.

Laser sheet dropsizing produces two-dimensional images of the Sauter mean diameter (SMD) distributions by combining the laser sheet techniques of Mie scattering and LIF [140]. These techniques can be used for qualitative and rapid measurement of fuel mass, spray geometry, and Sauter Mean Diameter. LSD thus allows a rapid spray characterisation. When a particle is illuminated by a laser light source, a portion of the incident light energy is absorbed by the excitable molecule that is then radiated as fluorescence (inelastic scattering). The remaining portion of the incident light experiences elastic light scattering. A laser induced fluorescence image of fluorescence from a fluorophore added to the spray, is captured.

The scattered light in the near forward direction has an angular distribution width, inversely proportional to the particle diameter. Figure 2.16 illustrates the different light scattering regimes in LSD.

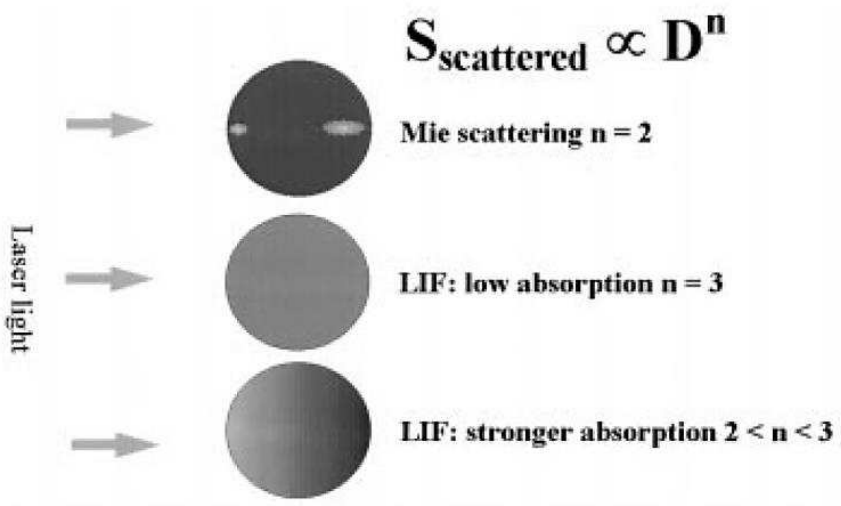

Figure 2.16 Different light scattering regimes for a spherical droplet [140]

The LIF signal S_{LIF} will be given by:

$$S_{LIF} = C_{LIF} \sum_{i=0}^{N} d_i^3$$

Equation 2.24

where d_i is the diameter of the droplet i and C_{LIF} is a calibration constant, which depends on the imaging system. The signal S for each pixel will represent the total intensity for all the droplets imaged within the measurement volume (pixel). To extract droplet sizes, the number of droplets must be known. However, the LIF signal gives the liquid volume fraction distribution.

An image is also captured using the elastic Mie scattering from the laser sheet incident on the spray. Since the fluorescence is red shifted, the two images can be taken without interference from the other scattering process. For liquid systems, the fluorescence signal is red-shifted

with respect to the laser wavelength and a spectral filter is used to discriminate it from the Mie scattered light. The elastic signal S_{MIE} is given by:

$$S_{MIE} = C_{MIE} \sum_{i=0}^{N} d_i^2$$

Equation 2.25

providing all the droplets scatter in the Mie regime. The ratio of intensity measured by one pixel in the LIF image, to the intensity measured by the same pixel in the Mie image is then given by:

$$\frac{S_{LIF}}{S_{MIE}} = \frac{C_{LIF}}{C_{MIE}} \frac{\sum_{i=0}^{N} d_i^3}{\sum_{i=0}^{N} d_i^2}$$

Equation 2.26

which is proportional to the Sauter Mean diameter SMD D_{32} defined by:

$$SMD = \frac{\sum_{i=o}^{N} d_i^3}{\sum_{i=o}^{N} d_i^2}$$

Equation 2.27

Thus by dividing the two images, a map of SMD distributions in the image plane is generated with high spatial resolution. The principle advantage of the laser sheet drop sizing technique is its ability to characterise dense sprays [140]. The above equations do not hold around the immediate vicinity of the nozzle exit, since the signals are not well defined due to the presence of ligaments.

According to Jermy et. al [141] the technique originates in a suggestion by Yeh et al. [142] and has been implemented by Yeh et al.[143], Sankar et al. [144], Le Gal et al. [140], and Lockett et. al [145]. Both Sankar and Le Gal used Mie-scattering calculations to confirm that, if morphology dependent resonances are neglected, the diameter-squared dependence of the Mie signal holds. Both authors validated the technique experimentally against PDA measurements in polydisperse sprays of moderate density. Le Gal et al. [140] and Domann et. al [133,146,147] checked the diameter dependence of the Mie and LIF signals experimentally, using streams of uniformly sized droplets and droplet-resolved imaging. This confirmed the diameter-squared dependence of the Mie signal, but showed that the assumption of a diameter cubed dependence of planar laser induced fluorescence (PLIF) signal held only at certain fluorophore concentrations. Domann and Hardalupas [146] developed a more sophisticated scattering calculation, which incorporates viewing angle and collecting aperture effects, and calculated both Mie and PLIF signals by ray tracing internal light paths, successfully reproducing the experimentally observed non uniform spatial distribution of fluorescence inside the droplet. In considering techniques for measuring droplet sizes in dense water sprays, LSD appears to offer accuracy in spray cores which are too dense for accurate PDA measurement. Since the technique can use a pulsed laser with a higher power than the continuous wave laser required for PDA measurements, it is expected to suffer less from signal attenuation by secondary scattering in the spray. The LSD technique measures a ratio of two intensities, and this measurand is expected to be more robust in the optically complex environment of a dense spray than the modulation phase difference measured by PDA. Further, the two intensities, PLIF and Mie, are each affected in a similar manner by sources of interference viz. non uniformity of the laser sheet profile and secondary scattering by the spray between the object plane and the camera. These interfering effects will to some degree cancel when the ratio of the images is taken.

PDA measurements of known size droplets are required for the calibration of SMD data. Since it is a laser sheet technique, mapping of the spray can be realised rapidly. Nevertheless, this technique is only capable of measuring Sauter mean diameters and the maximum measurable diameter is around 20 μm. Jermy et al [141] measured droplet diameters in a dense spray of ~20-μm water droplets by two optical techniques. In the core of the spray, they found that PDA suffers from signal attenuation resulting in overemphasis of larger droplets. LSD appeared to perform better with the data agreeing with more reliable PDA measurements and preserving the expected spray symmetry indicating that the LSD technique will perform more reliably than PDA in dense sprays.

2.3.4 Structured Laser Illumination Planar Imaging (SLIPI)

The techniques described above in sections 2.3.1 - 2.3.3 although use different properties of light scattering; they are all based on the single scattering approximation i.e. assuming that the detected photons have experienced only one scattering event prior to arrival at the detector. This assumption remains valid when the number density of the particles is low and the total photon path length within the probed medium is short. However, within optically thick media a large amount of photons are multiply scattered and the single scattering assumption is no longer valid. The multiple scattering blurs and attenuates the recorded images, introducing significant uncertainties in the detected optical signal.

Kristensson and Berrocal [148] investigated the possibility of suppressing the multiple scattering by employing structured illumination in a planar laser configuration on a dilute flow of water droplets generated by a nebulizer. This review is based on a technique developed by these authors to correct for multiple scattering. Structured illumination had been

used previously in fluorescence microscopy for image improvements and was first demonstrated for back scattering by Neil et al [149]. Neil et al. in their work presented an extremely simple modification to the conventional microscope illumination system that permitted optically sectioned images to be obtained and hence volume rendering of the thick structures in lily pollen grain to be obtained. However they found the specimens examined with their technique were substantially similar to those obtained with laser based confocal microscopes. This study was however for a static object where time was not a restrictive parameter. On the contrary the investigation of dynamic flows requires motion to be frozen in time.

Structured illumination is based on intensity modulation, in the spatial domain, of the excitation light, which can be created by projecting a grating onto the sample of interest. This enables blurring effects from multiple scattering to be suppressed in the image post processing. The main idea is that photons that have experienced several scattering events within the sample will lose the modulation information while singly scattered photons will not. Illuminating a grating leads to an image I(x,y) according to:

$$I(x,y) = I_C + I_S \times \cos(2\pi vy + \phi_0)$$

Equation 2.28

The light collected I (x,y) is divided into two different images denoted I_C and I_S. I_C would contain both singly and multiply scattered light and represents the conventional planar Mie image of the sample under investigation. I_S contains mainly singly scattered photons and represents the structured laser illumination image. In the equation the cosine term defines the fringe pattern which must be removed to obtain the true I_S image. This is achieved by recording three images with relative spatial phases (ϕ_0) 0, $2\pi/3$ and $4\pi/3$ denoted as I_1, I_2 and

I_3 respectively. These images correspond to a modulation shift of a third of a period between each image.

$$I_S = \frac{\sqrt{2}}{3}[(I_1 - I_2)^2 + (I_1 - I_3)^2 + (I_2 - I_3)^2]^{1/2}$$

Equation 2.29

$$I_C = \frac{I_1 + I_2 + I_3}{3}$$

Equation 2.30

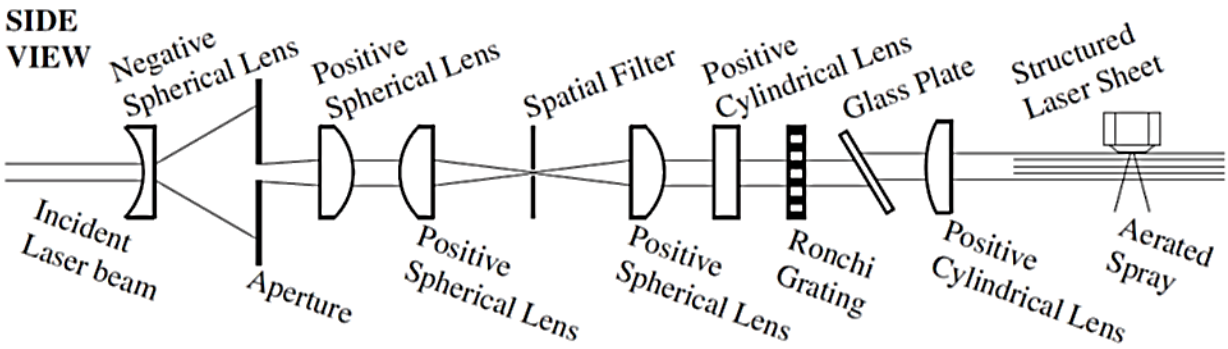

Figure 2.17 Optical arrangement to obtain line grating from a frequency doubled ND:Yag 532nm laser [150]

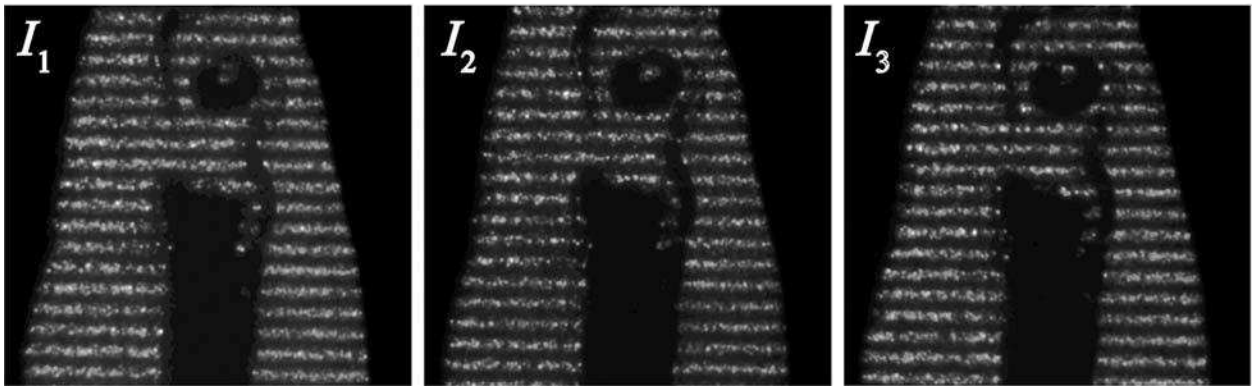

Figure 2.18 Illustration of the imaging part of the experimental setup together with three successive recorded images I_1, I_2 and I_3 [148].

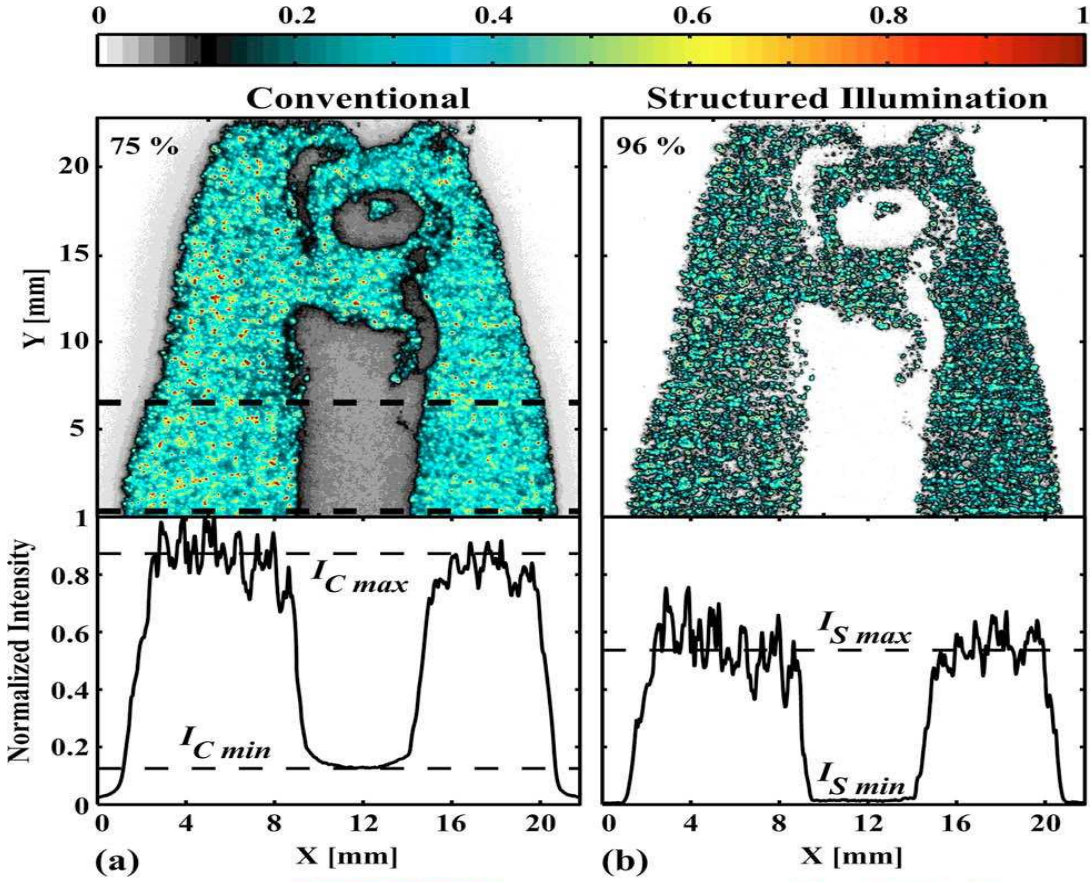

Figure 2.19 Comparison between I_C and I_S with a single nebuliser for dilute flow of water droplets [148]

The authors successfully demonstrated a new SLIPI technique for two phase flow visualisation in optically dense flows such as atomizing sprays where the single scattering theory no longer applies. They observed reduction in multiple scattering in images by a factor of 9 with the added benefit of an improved image contrast.

Berrocal and Kristensson [151–153] used the SLIPI technique to analyse dense regions of water and fuel sprays. They concluded that the 44% of light emission arising from secondary emission could be removed in a region where secondary breakups occurred. They also reported an increase in contrast as they had earlier. The technique enabled a more accurate accounting of the effects from laser extinction and could be implemented to other planar laser diagnostics, .i.e. planar liquid laser induced fluorescence and simultaneous Mie/LIF measurements. They also describe the SLIPI technique suitable for single shot images and for

averaged images. The capabilities of SLIPI could extend to studying primary and secondary breakup as well as full disintegration of the injected liquid if the images of the dense media are obtained at short enough time intervals enough to freeze the flow motion [153]. By recording data at successive depths with the SLIPI technique within an atomizing spray, light losses due to laser extinction and signal attenuation could be compensated for by post processing calculations and the Beer-Lambert law and an estimation of the local extinction coefficient is extracted within the three dimensions of an inhomogeneous cloud of droplets. [150,154].

2.3.5 Summary of measurement techniques

Many different measurement techniques for spray diagnostics and characterisation have been developed, each with its own advantages and constraints. It is clear that no single measurement method is totally satisfactory. The hypothesis developed in Chapter 1 was that hydrodynamic cavitation will result in similar effects as ultrasound cavitation in diesel fuels in forming particulates in suspension. In this case, an incident beam of light passing through the suspension will result in the particles scattering and absorbing the light resulting in a change in transmissivity of the light through the suspension. This technique is developed from the Beer-Lambert law which is discussed later in Chapter 3.

A non-intrusive measurement technique which is capable of measuring distribution of droplet sizes along a spray was required for the second set of analysis. The SLIPI technique is able to perform measurements for two phase flow visualisation in optically dense flows. However at the time the technique was relatively new and not much was known about it. The major concern was using this technique when it was in its early stage of development. For the above

reasons, the Laser Sheet Dropsizing (LSD) technique was opted for as it could measure the Sauter mean diameter distributions along the spray for a rapid spray characterisation. LSD appears to offer better accuracy in spray cores which are too dense for accurate Phase Doppler Anemometry (PDA) measurement and it is also capable of measuring spray distributions, whereas PDA is a point based measurement system [146]. The LSD technique requires a calibration to be performed by PDA measurements in order to mathematically quantify the results; however for a comparative analysis no calibration is required. The added advantage of the LSD system is that the images captured can be analysed collectively or individually i.e. collectively as a ratio of LIF/MIE images or individually as LIF and MIE light scattered images of the spray. For these reasons the LSD technique was selected to be used as the optical diagnostic tool for the measurement of spray distributions.

Due to a LIF based measurement system already in use on the spray it could not be replicated to characterise in-nozzle cavitation scattering unless a different source of fluorescence was added to the fuels and excited at a wavelength far apart from the current setup with LSD. The other drawback was the material of manufacture of the nozzle. Other researchers have used the elastic scattering technique in which the elastic white light scattering arising from the cavitation occurring in the nozzles is captured. This method will be used to characterise the flow in the nozzle holes. For the purpose of this thesis only a small part of the in-nozzle flow has been analysed.

Blank Page

Chapter 3 Effects of Sustained Hydrodynamic Cavitating Flow – Experimental and Calibration Tests Setup and Methodology

Modern common rail direct injection diesel engines operate with high pressure injection of diesel fuel into the engine combustion chamber. The injection of the diesel fuel occurs through small nozzle holes, located at the base of the injector. The actuation of the injector normally occurs through the forced movement of an electronically controlled injector needle, which is retracted as a result of activating a magnetic solenoid, or piezo-electric circuit, located inside the injector body. Diesel fuel maintained at high pressure in a common reservoir (called the common rail), is then able to flow into the injector, along the injector annulus, and out of the exposed injector nozzles into the engine.

A high pressure diesel pump is employed to maintain the diesel fuel at high pressure in the common rail. Modern common rail diesel pumps are capable of maintaining rail pressures in the operating range of 2,000 bar – 3,000 bar. The high rail pressure is maintained through phased multiple piston and one-way valve operation in the pump.

The diesel fuel contained in the pump and the common rail may experience cavitation during pumping and flow past sharp edges, creating localised vapour cavities. This type of flow is called cavitating flow, and is associated with unstable, unsteady vapour cavities forming inside the flowing fuel. Once formed, the vapour cavities may evolve in a number of different ways. They may attach themselves to particles in the flow, or onto adjacent surfaces. They

may grow or shrink in size, depending on internal temperature and pressure change due to flow conditions.

When vapour cavities collapse as a result of rapidly increasing local fluid pressure, the internal vapour temperature can rise to very large values as a result of local adiabatic compression. Consequently, complex hydrocarbon molecules found in diesel fuel may undergo pyrolysis reactions during cavitation bubble collapse. As a result, diesel fuel may experience a significant change in composition if exposed to sustained re-circulating cavitating flow.

As a result of these considerations, Shell Global Solutions began a research programme to investigate the impact of sustained hydrodynamic cavitating flow on the composition of diesel fuel. As part of this programme, Shell had funded a sub-programme to investigate the impact of sustained flow induced cavitation on the composition of diesel fuel.

The City University London research team designed and purpose-built a re-circulating flow cavitation rig, employing a continuous flow high pressure pump and a 5 hole diesel injector. Changes in composition in the diesel fuel due to hydrodynamic cavitation occurring across the injector and the high pressure pump are to be identified by the detection of time-dependent changes in the spectral transmissivity and linear attenuation coefficient of the diesel sample, measured continuously at 405 nm. The linear attenuation coefficient is a quantity that characterises how easily a material or medium can be penetrated by a beam of light. A large attenuation coefficient means that the beam is quickly weakened as it passes through the medium, whereas a small attenuation coefficient means that the medium is relatively transparent to the beam.

New diesel Fuels	Aged diesel Fuels	Model Fuels
BP Luton 29-01-11	BP Toddington 07-01-10	Paraffin blend
Texaco Leagrave 29-01-11	Texaco Milton Keynes 09-01-10	Paraffin-FAME mixture
Tesco Dunstable 29-01-11	Tesco Flitwick 07-01-10	(ParaffinB20)
Total Luton 29-01-11	Total 09-01-10	
Shell Flitwick 15-01-11		
ESSO A1 29-01-11		

Table 3.1 List of New and aged commercial fuels

The experimental programme undertaken involved the continuous measurement of sample spectral transmissivity over a sustained period, conducted on 10 commercial pump diesel bought from various fuel vendors, and a further 2 fuels which were paraffin based. Four of the commercial fuels were aged over a year. Of the paraffin based fuels one comprised of a paraffin blend of C_8 to C_{26}, whiles the second was a B20 diesel comprising of 80% paraffin blend and 20% fatty acid methyl ester (FAME) on a volume to volume ratio. The list of the fuels is seen in Table 3.1. In each test the diesel fuel test samples were exposed to sustained hydrodynamic cavitating flow for a period of 40 hours and the time resolved laser reference and transmission power intensities of the beam recorded. The experiment was continually monitored throughout the 40 hour run to ensure a stable injection pressure was maintained.

Further calibration tests were carried out to observe the effects of temperature on the change in spectral transmissivity and linear attenuation coefficient of the fuels. A water bath was employed in order to separate out the combined effects of cavitation and the release of internal compression energy during the diesel flow through the diesel nozzle into the receiver. This would identify and separate the magnitude of temperature and cavitation effects on the spectral transmissivity and linear attenuation coefficient of the fuels.

Corrections were then made to the laser intensity signals detected to take into account the laser absorption in the beam filter/splitter, the fused silica glasses and aluminium mirrors and obtain the corrected laser intensities of the beam inlet and outlet at the fuel. The description of the cavitation rig, the experimental programme and calibration tests are detailed below.

In order to quantify the overall chemical compositional changes, a 2D-Gas Chromatography (GC x GC) was be carried on the samples of fuels tested. This will be discussed in the chapter to follow.

3.1 Experimental Setup

The setup consisted of the cavitation rig which was linked to an external optical cylinder as shown in Figure 3.1. The set up consisted of two different elements, one being the continuous flow rig and the other the optical setup, i.e. the laser detector setup at the optical cylinder to measure the reference and transmission laser power measurements which will be discussed in section 3.2. This section details the continuous flow rig set up and describes the purpose of the analysis.

3.1.1 Overview of the continuous flow rig setup

The purpose of the experimental setup was to ensure a continuous flow of diesel fuel at high pressures through an injector nozzle with controlled pre-injection temperature. The setup consisted of a low pressure pump feeding diesel from a fuel tank through a 5 µm nylon fuel filter, then into a fixed displacement high pressure pump. The low pressure pump provided a head of a ~0.3 - 1.4 bar to feed the high pressure pump and an optical cylinder, at 550 bar

injection pressure. A diversion was created aft of the filter to feed fuel to an optical cylinder. The Dynex 1318H-10 high pressure pump was driven by a 4.2 kW variable speed motor. The motor can be driven to speeds up to 1800 r/min. The diesel fuel would then flow through a pressure gauge into a 5-hole injector and released into a fuel filled cylinder maintained at atmospheric pressure, flowing upwards into a heat exchanger. The Bosch 5 hole asymmetric nozzle had nozzle diameters of 0.22 mm.

The fixed displacement high pressure pump could provide flow rates up to 4.5 L/min at 1800 r/min measured for water glycol fluid with a viscosity of 1.9 cSt. The pump could provide pressures up to 630bar. This information was available in the pump specifications. The volume flow rate of the fuel circulating with an average density of 835 kg/m^3 can be estimated by calculating the Bernoulli velocity of the flow past five 0.22 mm diameter nozzles using $v_B = \sqrt{\frac{2\,(P_{rail}-P_{back})}{\rho_{fuel}}}$, where P_{rail} is the delivery pressure, P_{back} is the pressure at the receiving vessel and ρ_{fuel} is the density of the fuel. Finally the volume flow rate $\dot{V} = v_B \times A \times C_d$, where v_B is the Bernoulli velocity, A is the cross sectional area of the 5 holes and C_d is the coefficient of discharge. Using an estimated discharge coefficient of 0.8 (which is typical of diesel nozzles at approximately 550 bar pressure), an average diesel fuel density of 835kg/m^3, and a pressure difference equal to 549 bar, $v_B$can be calculated to be 362.625 m/s and $\dot{V}$ approximately 3.31 ± 0.01 L/min.

A pressure relief valve was installed aft of the high pressure pump to relief pressure surges back to the tank and prevent overpressures causing damage to the injector nozzles and body, and the high pressure piping. The relief valve could be manually set to the required maximum pressure. This could be done by first fully closing the valve then running the high pressure system and adjusting the pressure dial until there was no change on the pressure gauge. For

the experiments the relief valve was set to open at 630 – 650 bar and would empty into the tank.

The injector used was a pressure actuated 5-hole asymmetric nozzle with an inclined hole setup. The 5 holes were arranged asymmetrically and followed an inclination. The injector used is found in Mercedes Sprinters between years 1998 and 2000. The nozzle hole diameters for a new nozzle are 0.22 mm. As we required a continuous flow and not a pulsed flow the needle had been taken out of the injector to allow a continuous flow of fuel. The presence of the needle caused pressure surges in the high pressure pipes which travelled back into the pump. Figure 3.2 shows how the injector was setup vertically upright and injected into a 15 cm long cylinder. As observed in the image, just the tip of the nozzle, where the injection holes were located, was in the cylinder.

If the whole nozzle was in the cylinder as seen in Figure 3.4 there would be a possibility of stagnant fuel remaining in the bottom of the cylinder and re-circulating for long periods of time without joining the main flow of fuel. The current setup ensures all the liquid flows up and out of the cylinder. The high pressure cavitating fuel flow in the current setup will ensure all the liquid is pushed up into the cooler and back into the tank where the cycle can continue again.The motor speed required, to maintain an injection pressure of 550 bar at 70 °C, varied depending on the different diesel viscosities to between 1300 - 1600 rpm. The required injection pressures were achieved by manually adjusting the motor speed to reach the desired pressure after which it was read using a laser tachometer once the temperature had stabilised.

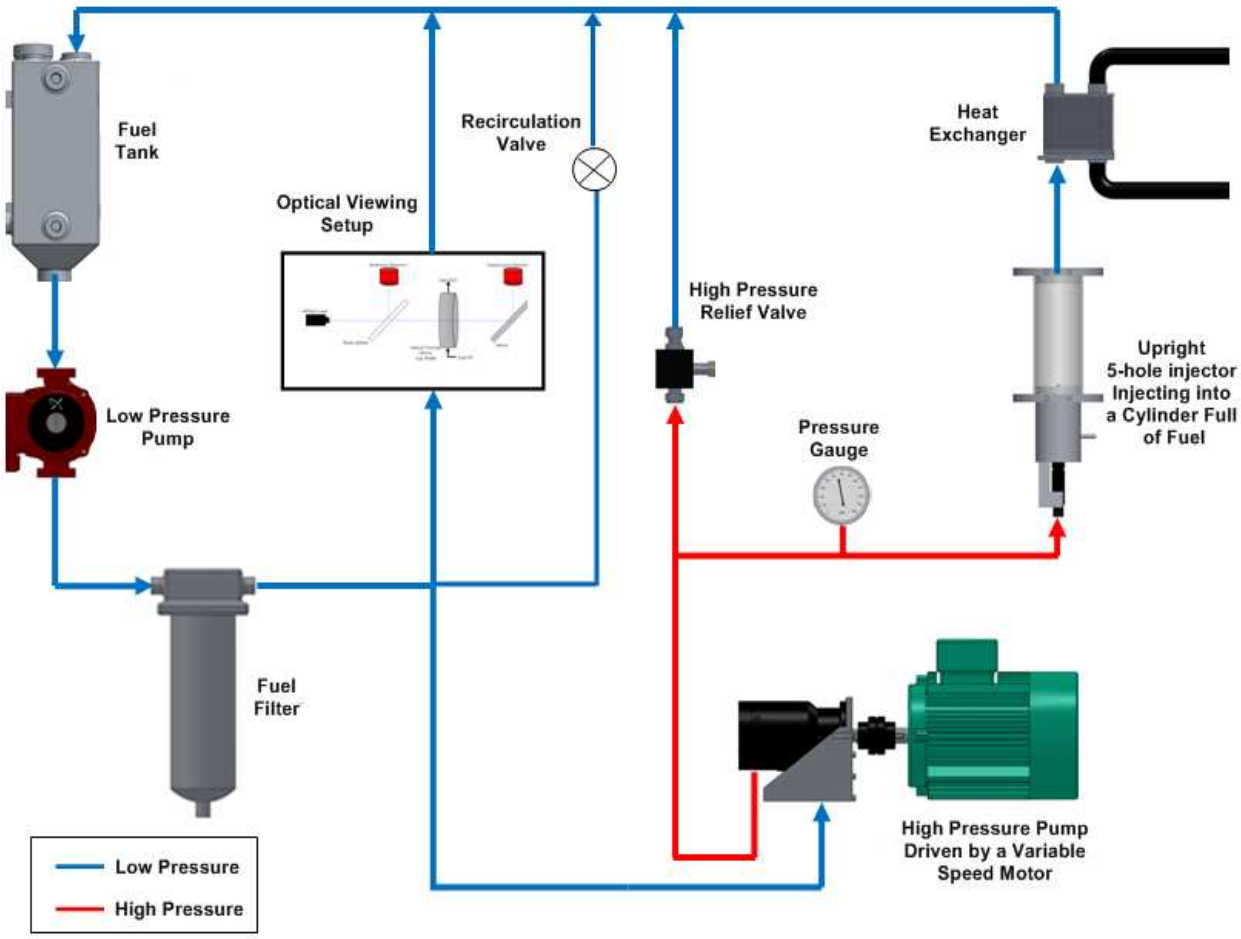

Figure 3.1 Overview of the continuous cavitating flow rig experimental setup

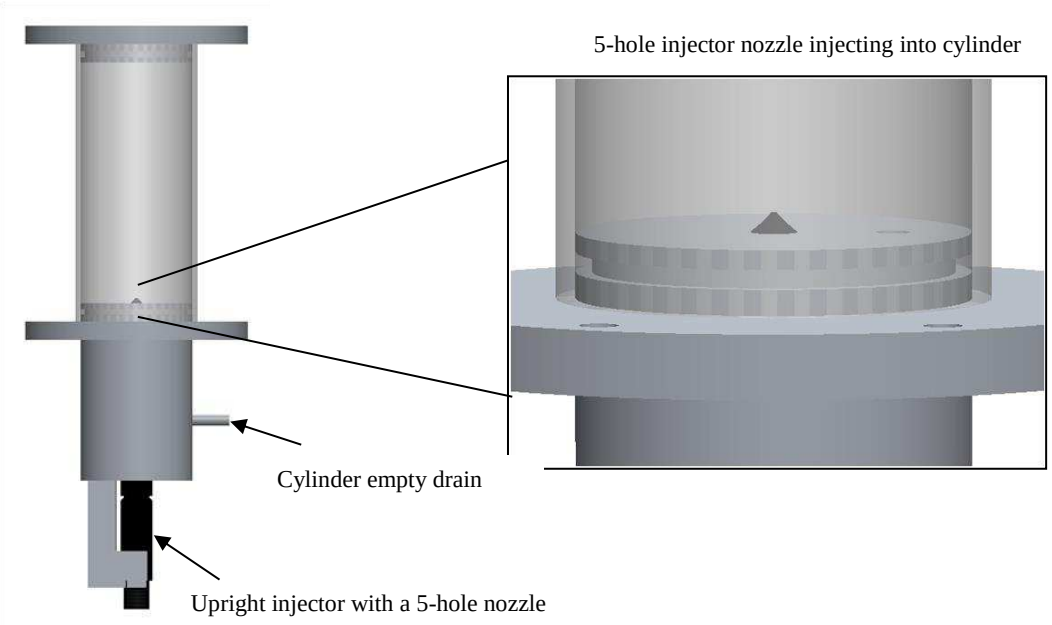

Figure 3.2 Injector setup

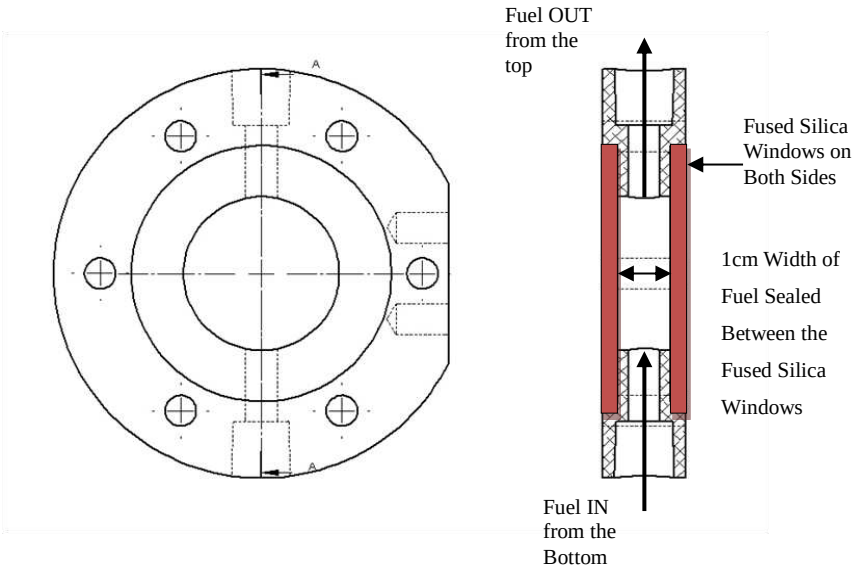

Figure 3.3 A section view of the optical cylinder

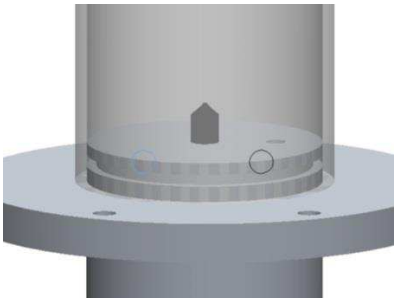

Figure 3.4 Raised nozzle in cylinder

Fuel flow aft of the filter was split to go into the high pressure pump and the optical setup. A section view of the optical viewing cylinder is shown in Figure 3.3. Fuel was fed into the cylinder from the bottom. It would then flow into the 1 cm width optical measuring section and out from the top, after which the fuel returned to the tank.

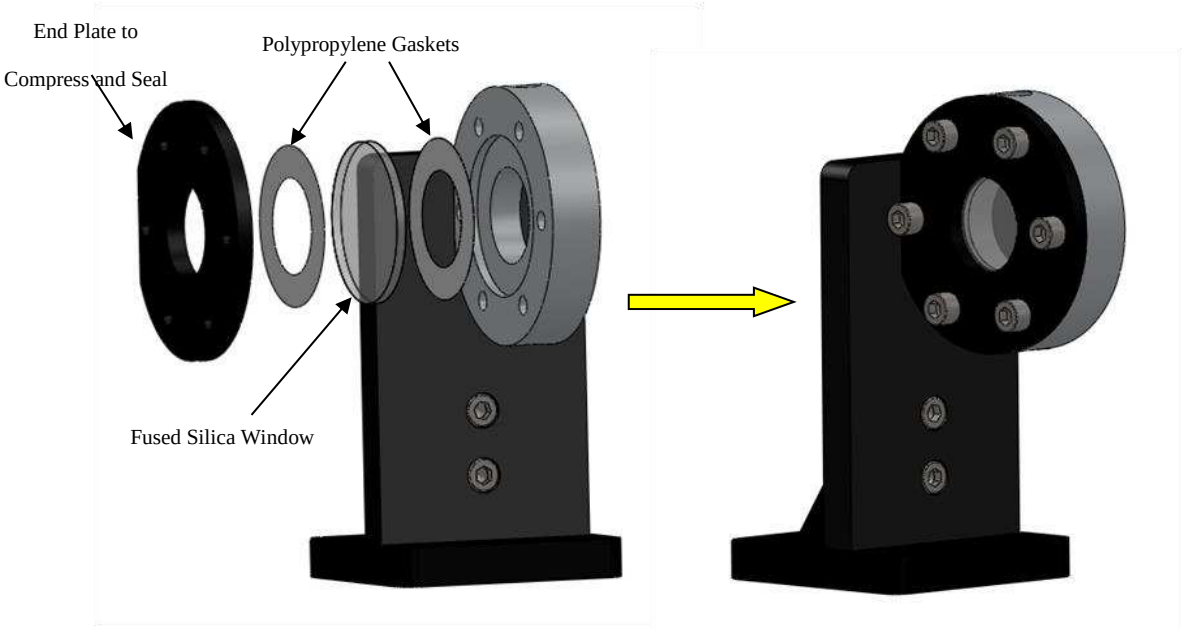

Figure 3.5 Fused Silica window insertion and sealing

The optical cylinder consisted of an aluminium body which was sealed with 3 mm thick optical grade fused silica windows on both sides using an aluminium end plate. This allowed for access to shine the laser through a 1 cm width of fuel. The windows were compressed with an aluminium plate and 6 M6 screws equally placed to ensure an equal compression force on the windows. Very thin polypropylene gaskets were used at the intersection between the aluminium plate and the fused silica, and between fused silica and the viewing cylinder in order to seal well and prevent any fuel leakages between intersections as seen in Figure 3.5.

There were four draining points in the high pressure cavitation rig. One drain valve under the fuel filter drains the tank, the low pressure pump, the fuel filter, the recirculation piping and the optical cylinder and piping. The second drain valve on the entry into the high pressure pump drains the high pressure pump and the low pressure piping from the filter to the high pressure pump entry. The third drain valve located on the high pressure exit of the high pressure pump drains the fuel in the high pressure piping between the high pressure pump and

the injector nozzle. The final drain point on the cylinder where the injector is located as seen in Figure 3.2 drains the cylinder, and the heat exchanger.

The continuous flow rig could hold up to 5 litres of fuel when full but for the purpose of the experiment 3.5 litres was used which was just above the minimum amount of fuel as a safety precaution in case of bursts or leaks. The setup ensured a continuous flow of diesel through the injector nozzle and optical cylinder.

Before running at high pressures, all the pipe work, pump, heat exchanger and cylindrical chamber aft of the injector were filled with the fuel to be tested using the low pressure pump. The recirculation valve was used at this stage, when filling up the system, to re-direct fuel flow and also to remove air bubbles from the system and the optical cylinder.

3.1.2 Electronics, safety and temperature control

The low pressure feed pump had to be turned on prior to the high pressure pump as the later required suction feed. To prevent damage to the high pressure pump an electronic cut-off was fitted to the low pressure pump that would prevent the high pressure pump running without feed. In case the feed pressure dropped drastically while the high pressure pump was running, they would both be cut-off. The cut off was set to 0.1 bar feed pressure.

The injection pressure was controlled by manually adjusting the motor speed by two dials, one for coarse and the other for fine adjustments of pressure. The adjustments showed up on the pressure gauge which measured from 1 - 1000 bar in increments of 10 bar. The pressure could be set with an error of ± 5 bar.

The reduction in pressure from injection, 550 bar, to aft injection, ~2 bar, will induce cavitation and thus boiling and increase the temperature of the fuel. The preponderance of this energy caused by the pressure drop is absorbed in the creation of vapour cavities. The induced cavities undergo formation, growth and implosive collapse. The collapse causes the internal vapour temperatures to be released into the surrounding liquid. A temperature control is required to prevent large rises in temperatures which would create no base for investigation and would destroy the experimental apparatus. It is essential to control the pre-injection temperature by cooling the flow aft of injection. A thermocouple attached to high pressure piping before the injector and temperature control system was used to control the pre-injection temperature by using the heat exchanger aft of injection to cool fuel. The temperature control system allowed sufficient fresh water flow to cool the fuel aft of the injector and maintain a controller set temperature. The cooling followed a cycle and controlled the pre-injection temperature to approximately +1 and -4 degrees of the set temperature. The cooled diesel would then flow back into the tank and the cycle continued.

3.2 The Beer-Lambert Law and the Optical Setup

The optical viewing set up was based on the Beer-Lambert Law of transmissivity through liquids. The Beer-Lambert Law or the Beer-Lambert-Bouger law relates the absorption of light to the properties of the material through which the light is travelling through. The transmission I_t of a light beam with the intensity I_o travelling through a substance is logarithmically dependent on the linear attenuation coefficient α and the distance it travels through the substance (path length) ℓ as seen in Equation 3.1.

$$\boldsymbol{I_t(\ell) = I_o e^{-\propto \ell}}$$

Equation 3.1

The transmissivity of the light is given as:

$$Transmissitance = \frac{I_t}{I_o}$$

Equation 3.2

Thus,

$$Transmsittance = \frac{I_t}{I_o} = \mathrm{e}^{-\propto \ell}$$

Equation 3.3

and therefore the attenuation coefficient α is given as,

$$\propto = \frac{\ln(Transmittance^{-1})}{\ell}$$

Equation 3.4

For a time resolved α,

$$\propto (t) = \frac{\ln(Transmittance^{-1}(t))}{\ell}$$

Equation 3.5

The linear attenuation coefficient α is a quantity that characterises how easily a medium can be penetrated by a beam of light. The linear attenuation coefficient and the absorption coefficient are usually used interchangeably. However in situations where large amounts of light is being scattered as it passes through the medium, they differ as the light can both be absorbed and scattered. In this case, the absorption coefficient would measure how quickly a

beam of light would lose intensity due to absorption, whereas the attenuation coefficient would measure the total loss of narrow beam intensity including scattering.

α is comprised of the scattering coefficient α_{sc} and the absorption coefficient α_{abs} i.e. $\alpha = \alpha_{sc} + \alpha_{abs}$. The linear attenuation coefficient α is related to the complex refractive index of the sample (specified by n = m + ik) by the relation

$$\alpha = \frac{4\pi k}{\lambda} = \frac{4\pi}{\lambda} lm(n)$$

Equation 3.6

where λ is the wavelength of the incident light [127]. In these experiments, the overall refractive index of the diesel samples is comprised of the overall refractive index of the blend of aliphatics, aromatics and additives making up the liquid content, taken together with the overall refractive index of any particles in suspension. The overall linear attenuation coefficient can be expressed in terms of a sum over the respective scattering and absorption terms

$$\alpha = \alpha_{sc} + \alpha_{abs} = \alpha_{sc}^{(l)} + \alpha_{sc}^{(p)} + \alpha_{abs}^{(l)} + \alpha_{abs}^{(p)}$$

Equation 3.7

Where, $\alpha_{sc}^{(l)}$, $\alpha_{abs}^{(l)}, \alpha_{sc}^{(p)} and\ \alpha_{abs}^{(p)}$ are the scattering and absorption coefficients for the liquid and the particle suspension respectively.

The linear attenuation coefficient will vary according to how many molecules there are in the in the path length of the beam. The larger the number of absorbing species, the larger the

attenuation or absorption coefficient. α is a function of the photon energy of light and the density and composition of the medium it passes through.

Path lengths through the fluid of 1 cm are usually accustomed. The light passing through a medium will follow an exponential decay law and the larger the path length the larger the decay in light. The light entering a liquid is proportional to that absorbed as a result of the chemical and physical characteristics of its contents, to the concentration of the absorbing medium and the length of the absorbing path. This study uses this law to present an analysis of the chemical changes in diesel fuel as a result of continuous cavitation cycles by using a 405 nm laser to characterise the cavitating flow.

A low power 405 nm World Star Tech. laser is passed through a beam splitter to reflect 10% of light to a reference detector measuring the reference intensity. The 90% transmitted through the splitter passes through the optical viewing cylinder and out, where it is reflected onto a transmission detector via an aluminium mirror. The transmission detector will measure the light after it has passed through 1 cm of fuel. The optical setup will enable the measurement of transmissivity of UV light through the fuel.

Figure 3.6 Laser power detector

The laser detectors commissioned were Laserpoint low power & energy sensors with high sensitivity, low noise and a high resolution measuring laser powers between 10 µW-200 mW. The detectors used a USB interface to record directly onto a computer or laptop via hardware boxes and PC-Link software. The program contained the possibility to calibrate under different light conditions before operation and also provide X10 measurement gain to enhance measurement flexibility of low power readings to

20 µW resolution. The software package logged 1-minute averaged laser power measurements for up to 12 hours non-stop, and the minimum and maximum powers per minute.

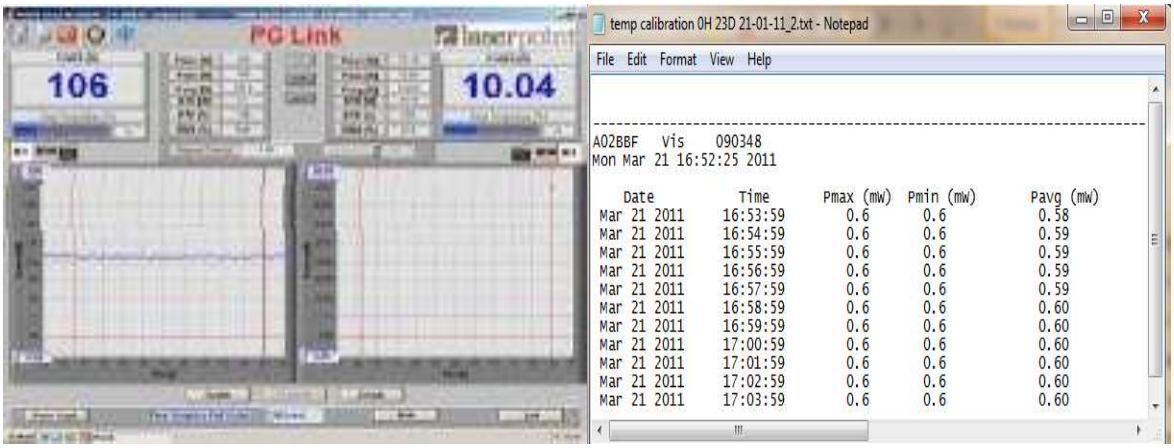

Figure 3.7 PC-Link Interface and the results produced for each detector.

Initially the raw transmission and reference readings will be used to a plot transmissivity versus time relationship of each fuel. The one minute Pavg (mW) measurements will be averaged over 15 minutes for both detectors before the analysis.

Each of these optical components will have their own absorption coefficients and these will later be calculated and calibrated to finally determine the intensity of light entering and exiting the fuel. This will be carried out in section 3.5. An overview of the setup can be seen in Figure 3.8. While running the analysis the laser detector setup was calibrated and kept under a box cover to prevent external light sources affecting the reference and transmission detector readings.

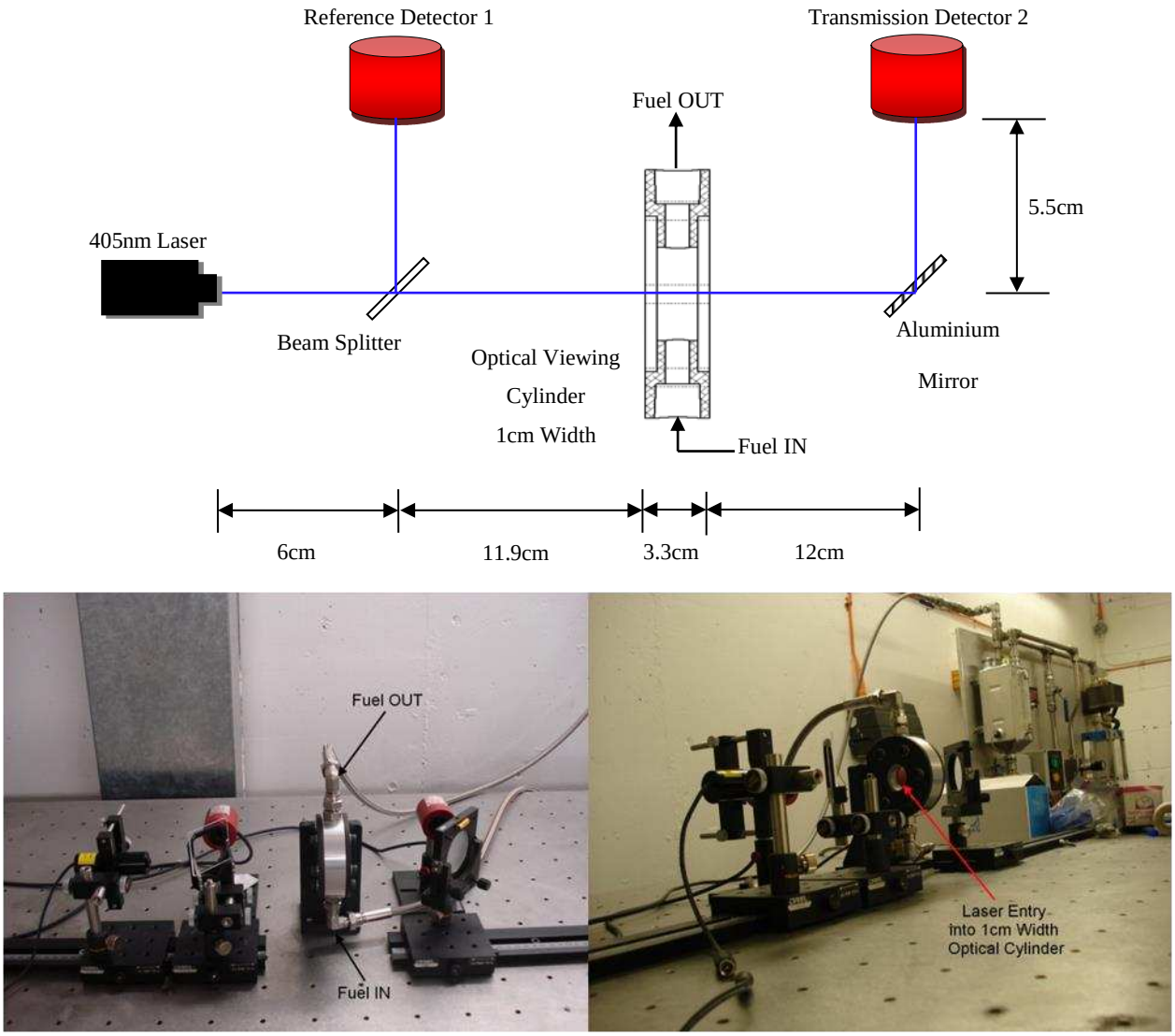

Figure 3.8 Laser-Detector setup with laser path through 1cm width of fuel at the optical viewing cylinder

3.3 Experimental Methodology

Each fuel in Table 3.1 was run for 40 hours over 4 days, i.e. 10 hours per day. Before each fuel was filled in the rig a flushing procedure with 95% hexadecane was carried out to prevent high levels of different fuels mixing. Following this a fuel filling procedure was used, followed by fuels experimental run procedure. After the 40 hour analysis was complete a drain procedure was followed. The laser power measurements were taken using power measurement software which was provided with the detectors to read a dual system. These procedures will be explained in this section, and they were carried out for all fuels. The fuel flushing, filling and draining procedures were followed whenever a fuel change was required, whenever a fill/drain was required whether it be for the flushing fuel or experimental fuel.

1. BP Toddington (Aged)
2. Texaco Milton Keynes (Aged)
3. Texaco Leagrave 29-01-11
4. Tesco Flitwick 07-01-10(Aged)
5. Tesco Dunstable 29-01-11
6. BP Luton 29-01-11
7. Shell Flitwick 15-01-11
8. Total Luton 29-01-11
9. ESSO A1 29-01-11
10. Total 09-01-10 (Aged)
11. Paraffinic fuel
12. ParaffinicB20

Table 3.2 Fuel analysis sequence

For each fuel, a new fuel filter and a new 5-hole nozzle were used. The reason for using a new nozzle was to keep consistency in the analysis. Cavitation in the nozzles causes the holes to wear out. Worn out holes will result in a flow with less cavitation intensity due to the sharp inlets to the nozzles being smoothened out. Using an old nozzle would create a different cavitation start profile and the cavitation intensity per test invalidating the results comparison. A flush filter was used during flushing procedure.

3.3.1 Fuel filling and draining procedure for analysis of fuels

The correct volume of fuel/flushing fuel was filled up. A volume of 3.5 L of fuel was used to fill up the cavitating flow rig for fuel analysis. The fuels were always filled up in new bottles to be poured into the cavitation rig. Initially approximately two litres was poured into the rig to soak the filter, fill the filter housing and piping circuit. The low pressure pump was run to fill up the optical viewing device. The rest of the fuel was poured into the rig and the rest of the piping circuitry and components were filled up.

Once the injection cylinder starts to fill the high pressure pump was switched on and run at about 10 – 20 bar to fill up the cylinder and cooler, the fuel would then flow back into the tank. Once circuitry and components were full, the high pressure pump was switched off and the fuel was circulated in the system using the low pressure pump.

In order to remove air bubbles, the recirculation valve was opened and closed immediately and bubbles were seen rising from the optical cylinder. Once the bubbles ceased appearing, the procedure of opening and closing the valve was ended. The fuel was circulated around the system for about 30 minutes to ensure no bubbles present and those present had escaped from the loosely screwed tank top.

Leak checks were carried out and all piping and extraction valves were checked to be shut. The tank level was checked to ensure a sufficient amount above the tank level sensor. A lot of fuel was not filled because if a leakage or burst appeared, only a small amount would empty before the electronics shut down the system because of low fuel. During draining, all electrical equipment was shut off and isolated. The first drain point was the under the filter.

This drain point as mentioned earlier would drain the tank, low pressure pump, filter and the optical cylinder. About 2 - 2.2 L of fuel was drained from this section.

The second draining point was at the injection cylinder. This would drain the cylinder and heat exchanger of fuel. To ensure the heat exchanger was drained fully, inert nitrogen at very low pressure was fed into the tank and the entry sealed. The only exit valve open for the nitrogen to leave the pressurized rig was the injection cylinder exit valve. The nitrogen would flow through from the tank to the heat exchanger and push the fuel out and into the cylinder to drain valve. This was done until no fuel was seen pouring from the heat exchanger back into the cylinder and exiting the valve.

Fuel was then drained from the high pressure exit and then the low pressure entry into, the high pressure pump. This would conclude the draining. The last 3 drain points would drain approximately 0.8 – 1 L in total. A total of 2.8 - 3.2 L was drained and the rest would be in the filter. The fuel drained was then labelled correctly.

3.3.2 Experimental analysis run procedure

Once the fuel was filled by following the fill procedure with 3.5 L of fuel and circulated through the system, a 200 ml pre analysis sample was acquired from the filter drain valve. This would give an initial analysis sample for chemical analysis. The pre-injection temperature is set to 55 degrees on the temperature control. The low pressure pump is switched on and an initial laser power reading is obtained, and then the high pressure pump is run. The pressure is slowly dialled up to 550 bar. Once the temperature reaches 55 degrees, one temperature cycle is allowed and once the cycle completes the temperature is increased to

the analysis temperature 69 degrees. The heat exchanger and the temperature control follows a cooling cycle as mentioned earlier. When the temperature reaches 69 degrees a further two cycles are allowed and then the time is noted for the laser power readings to commence. The analysis is run continuously for the rest of the day for 10 hours unless a shutdown occurs at which the time is taken and restart done.

The analysis run procedure is followed for the 40 hours, i.e. 4 days of analysis. During high pressure run, the tank cap was left loosely open, that is open to atmosphere. Once the 10 hours of run time are up the system was shut down and the fuel cooled overnight. The next day the run analysis procedure was restarted.

3.3.3 Flushing procedure

Initially two sets of 95% hexadecane of 3.5 L each were filled, flush one and flush two. Two flushes were carried out per flushing procedure, using first the flush one then the flush two. During filling and emptying flushes, the fill and drain procedures are followed.

Each flush was run for 30 minutes between 300 - 400 bar injection pressure and 40 degrees pre injection temperature. As expected the flush one would deteriorate faster than flush two. The transmission laser power was monitored before each flush set and once the power reached approximately 7 mW the flush one was discarded and replaced with flush two fuel and a new flush two of 95% hexadecane filled up. The initial transmission power reading for the pure unused 95% hexadecane was 11 mW. This gives a change of about 36% deterioration in flush one before it is changed.

3.4 Diesel Heating Calibration

Changes in fuel composition may also be affected by high temperatures. On one hand the high temperature facilitates the rate of cavitation whereas on the other it may be causing thermal decomposition in the fuel. The experiments were run at high temperatures thus a heat calibration was carried out to investigate the effects of high temperature on the fuel transmissivity and its linear attenuation coefficient and to try to separate out the effects of temperature to cavitation. Fuel samples were heat tested and then the laser transmission profile measures and the heat tested fuel sample later sent for 2D- GC analysis. The results of the heat calibration were to be later compared with the cavitation analysis results and further the chemical analysis to provide further conclusions. This section explains the setup and methodology used to carry out the heating calibration.

In order for a spectral attenuation analysis carried out on a heated fuel sample for comparison to the sustained cavitating flow analysis, a similar measurement methodology would have to be followed. However the fuel cannot be heated in the cavitation rig and thus the fuels have to be heated externally and then poured back in to the rig in order to obtain a comparable analysis of measurements. The sample fuel to be heat tested would first have to be poured in the rig and passed though the optical chamber to record its initial transmissivity. The fuel would then be emptied out from the rig into bottles which were placed in a modified urn to carry out the heat tests. Once the heat tests were complete, the sample was poured back into the rig to obtain a 40 hour heat test transmissivity measurement of the fuel. When carrying out both sets of transmissivity measurements in the rig, the fuel was only circulated past the optical chamber using the low pressure pump at approximately 0.5 bar gauge pressure. The high pressure pump was not switched on and thus no cavitating flow conditions took place.

The objective of the test was to heat and maintain the fuels at 70° C for 40 hours and poured back into the continuous flow rig for the laser transmission power signals to be acquired. Heat tests were carried out per fuel sample and in each tests new fuel samples of each test fuel were used. The heat tests employed the same time chronology to the parent analysis that is, 10 hours per day over 4 days.

For some of the fuels 3.5 L of fuel was heated up as the flow rig required this minimum amount to run the low pressure pump. This fuel amount would be filled into the rig and circulated with just the low pressure pump on, without running the high pressure pump. During the measurements carried out for these fuels, the injector was present however because the fuel was only circulated using the low pressure pump (at 0.5 bar gauge pressure), no cavitation would be induced past the injector. Later on, an adjustment was made to the continuous flow rig, where the high pressure side and the injector were isolated and thus the rig required a lesser amount of fuel to fill. For the rest of the fuels only 2.5 L was used for the heat test analysis. The fuel would flow from the filter back to into the tank. The adjustments were carried out once the cavitation analysis had ended.

Due to unfortunate circumstances there was not enough stock fuel of BP Toddington aged and thus heating tests were not carried out of this fuel.

3.4.1 Heating calibration setup and methodology

It is quite dangerous to heat fuels to temperatures up to 70 °C; a safe way had to be employed to keep the fuel vapours from developing and contacting a possible ignition source. The best way was to use a water bath with an adjustable temperature controller. A tea urn was modified

to contain a level gauge and a K-type thermocouple. A temperature control box allowed the heating temperature to be set and controlled to within 1 °C. The level gauge was employed as a safety device if the water evaporated beyond the level of fuel.

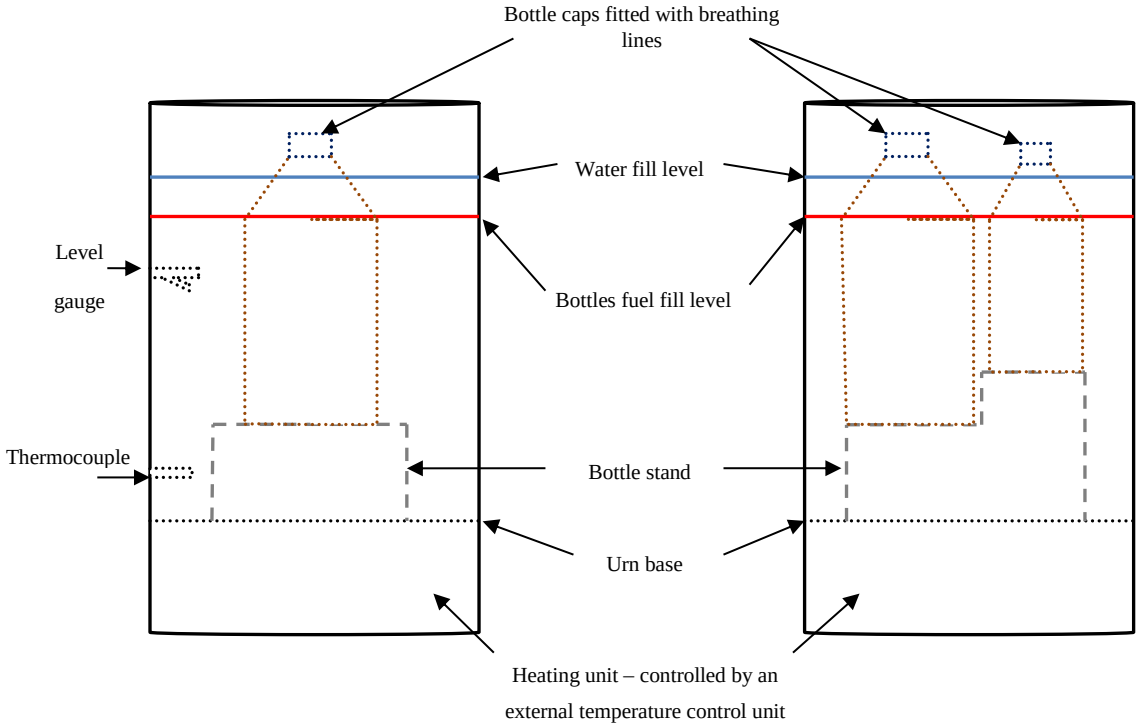

Figure 3.9 Heat calibration setup with modified tea urn and bottles used for the heat tests

Figure 3.9 shows the heating urn setup used to heat the fuel. In the image the blue lines are water fill levels and the red lines are fuel fill levels in the bottle. The water was always filled above the level of the fuel in the bottles. The urn could take either two 2.5L bottles or a 2.5 L and a 1.5 L bottle. A bottle stand was manufactured for that the glass bottles were not in direct contact with the heating unit base. Winchester glass bottles were used with modified caps to allow breathing to match the parent experiment breathing where the cap was loosely left open. The breathing will also be an advantage in that it will prevent excessive pressure build up inside the glass bottles. 1 mm diameter tubing was attached to each cap and leads to a ventilation duct to prevent pressure build up in the bottles.

Before the heat tests were carried out the 0 hour laser reference and transmission power readings were measured by pouring fuel at room temperature into the continuous flow rig and circulating it at low pressure at about 0.5 bar gauge pressure. Clean bottles were filled up with the fuels to test. During the tests, 3.5 L of fuel was used. One 2.5 L and 1 L bottle were filled up. During the tests which had 2.5 L bottles, two clean bottles were filled up with different fuels for example one filled with Shell and the other with Texaco and heat test conducted simultaneously in the urn. This enabled double the testing rate as otherwise heat tests would require a week's time per fuel analysis. Approximately 30 minutes water warm-up time to 70ºC was allowed. The water would reach the set temperature in 20 minutes and then a further 10 minutes were allowed to regulate the temperature evenly in the urn. Once the test was over, the bottles were taken out of the urn. Overnight, the bottles would be taken out of the urn to cool off, which would compare to the cavitation rig being switched off and the fuel undergoing the cavitation cooling overnight. When the test ended they were allowed to cool for a day before they were poured back into the rig at room temperature to measure their 40 hour reference and transmission power readings. This was carried out for all fuels apart from BP Toddington.

3.5 Laser Intensity Absorption/Transmission Calibration

In the laser-detector setup discussed in section 3.2, it is essential to calculate the laser intensity at the beam entry and at the beam exit to the fuel. The reference and transmission detector readings are available but the components that the laser beam travels through have their own transmission factors and the beam will decrease in intensity past each. The calculation is an approximation relative to these reference and transmission intensities acquired. The laser power reference and transmission readings previously obtained can be

used to obtain a reference transmissivity but have to be calibrated and the exit and entry laser intensities calculated if the linear attenuation coefficient of the laser light at 405 nm through the fuel is to be calculated precisely. The beam splitter transmissivity, the fused silica window transmissivity and the aluminium mirror transmissivity are to be calculated and replaced in Equation 3.1 to calculate the linear attenuation coefficient α.

The optical calibration procedures and results can be found in Appendix section A.1. The time resolved linear attenuation coefficient for the commercial fuels can be calculated using Equation 3.8 which is the same as Equation A.7 in the appendix.

$$\alpha(t) = \frac{ln\left(\frac{7.63 I_R(t)}{I_{T3(M)}(t)}\right)}{1.03} cm^{-1}$$

Equation 3.8

As the setup was adjusted for the two paraffinic model fuels used the time resolved linear attenuation coefficient was recalculated as in Equation 3.9 which is the same as Equation A.8 in the appendix.

$$\alpha(t) = \frac{ln\left(\frac{8.76 I_R(t)}{I_{T3(M)}(t)}\right)}{1.03} cm^{-1}$$

Equation 3.9

These two equations will be used further on in the next chapter to determine the fuels attenuation profiles

Blank Page

Chapter 4 Effects of Sustained Hydrodynamic Cavitating Flow - Results from Experimental Analysis and Chemical Analysis of Fuels

Visible light absorption is known to all of us, because this is what causes objects to be coloured. Visible light lies in the wavelength range of 400 - 700 nm. When light is absorbed by a material, valence (outer) electrons are promoted from their normal (ground) states to higher energy (excited) states. The promotion of electrons to different energy levels is not restricted to electromagnetic radiation in the visible part of the spectrum; it can also occur in the ultraviolet region.

Valence electrons can generally be found in one of three types of electron orbitals:

(i) Single, or σ, bonding orbitals;

(ii) Double or triple bonds (π bonding orbitals); and

(iii) Non-bonding orbitals (lone pair electrons).

Sigma bonding orbitals tend to be lower in energy than π bonding orbitals, which in turn are lower in energy than non-bonding orbitals. When electromagnetic radiation of the correct frequency is absorbed, a transition occurs from one of these orbitals to an empty orbital, usually an antibonding orbital, σ^* or π^* as seen in Figure 4.1. The exact energy differences between the orbitals depend on the atoms present and the nature of the bonding system. Most of the transitions from the bonding orbitals are too high a frequency (too short a wavelength)

to measure easily, so most of the absorptions observed involve only $\pi \rightarrow \pi^*$, $n \rightarrow \sigma^*$ and $n \rightarrow \pi^*$ transitions [155–157].

- $\pi \rightarrow \pi^*$ in alkenes
- $n \rightarrow \pi^*$ in molecules with carbonyl groups (ketones, aldehydes).
- $n \rightarrow \sigma^*$ in amines or alcohols
- $\sigma \rightarrow \sigma^*$ in alkanes (at vacuum UV- wavelength) [157].

Equations relating to absorption and the Beer-Lambert Law having developed in the preceding chapter, and calibrations have been carried out to obtain the reference laser power entering and exiting the fuel sample cell to enable the calculation of the spectral attenuation coefficient. The spectral attenuation coefficient is useful as it is independent of path length. The spectral attenuation coefficient is strongly influenced by the nature of the solvent, and for organic compounds, by the degree of substitution and conjugation.

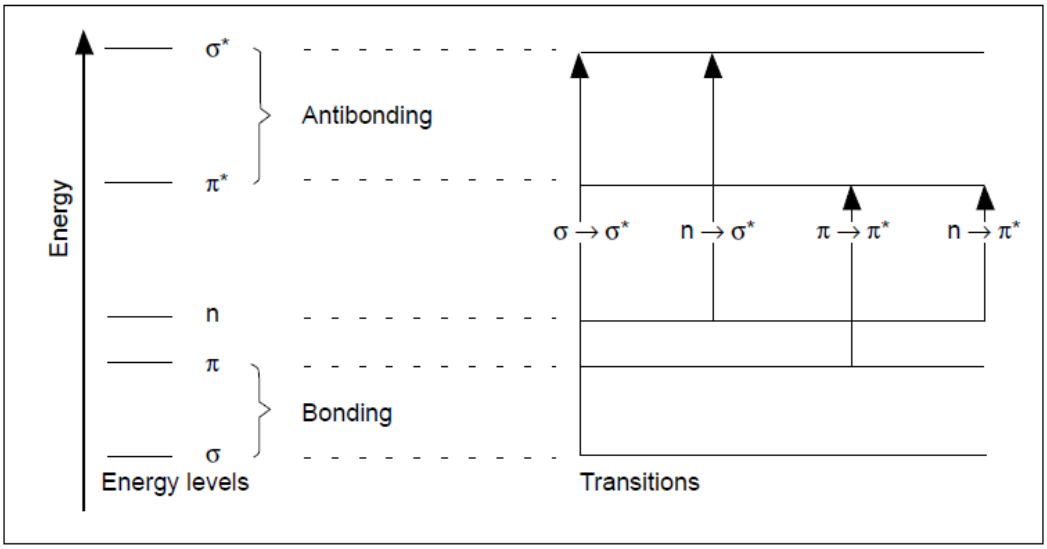

Figure 4.1 Electron transitions in ultraviolet/visible spectroscopy[155]

Many organic molecules absorb ultraviolet/visible radiation and this is usually because of the presence of a particular functional group. These groups that actually absorb the radiation are called chromophores. However there are various factors affecting the absorption:

(i) The solvent-the absorption in a polar solvent will be at a longer wavelength (lower energy, hence lower frequency) than in a non-polar solvent because the dipole-dipole interaction reduces the energy of the excited state more than the ground state.

(ii) Degree of conjugation-if carbon chain length is increased, the maximum wavelength absorption peak shifts slightly to a higher wavelength because the energy of the excited state is reduced. The longer the conjugated carbon chains in the absorbing system, the greater the intensity of absorption.

(iii) Acid-base indicators-absorption is advantageous in the acid-base indicators as a small change in the chemical structure of the indicator molecule can cause a change in the chromophores and it will absorb in different parts of the visible spectrum.

The absorption of visible or near ultraviolet light (> 2000A) only occurs when certain groups are present in the molecule. Examples of such groups, called chromophores, are:

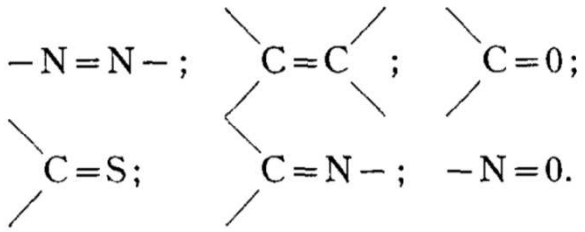

Figure 4.2 Examples of groups of chromophores [158]

It will be noticed that each of these groups possess an alternation of single and double bonds. In a coloured compound these groups occur conjugated with other double bonds. Although a

coloured molecule has many such conjugated double bonds, the colour does not depend upon the number of there alternations alone. The colour is strongly influenced by the way in which the chromophores are bound together i.e. upon the structure of the entire molecule [158].

In the work here, a single wavelength beam is being used and its absorption across various diesel fuels being cavitated over long periods of time being measured and used to calculate the spectral attenuation coefficient of the each fuel over time. This chapter analyses the results obtained from the optical arrangement of the long term cavitation experiment and the corresponding fuel heating tests carried out to subtract the effect of high temperature. Samples of the fuel were later sent for GC x GC analysis and will provide further information of the effects of hydrodynamic cavitation to the physical and chemical properties of the fuels.

4.1 Long Term Cavitation Experimental Results

4.1.1 Effects of temperature rise on the transmission signal

During the beginning of the experimental analysis on each day the temperature of the fuel was raised from room temperature to 69 ºC. It was observed that the transmittance of the 405 nm light through the fuel increased with increase in temperature. The change in transmittance for each fuel was different and dependant on the chromophores present in the fuel and the fuel temperature at the optical cell. Laser power reference and transmission readings were obtained at room temperature before the start of the experiment each day over the four days.

A temperature cycle was caused as an effect of cooling the fuel aft injection depending on its temperature prior to injection. As a result of this cooling temperature cycle, the temperature in the optical cell would vary between 55 – 65 ºC. As a result of this temperature variation, a

corresponding synchronised cycle was observed on the laser transmission through the fuel. As the temperature increased from 55 – 65 ºC, so would the power transmitted through the fuel and vice versa. This was observed for all fuels.

The reference and transmission readings at the optical cell temperature were obtained from the minute averaged readings saved during the course of the experimental analysis. The normalised laser power was calculated by a ratio of the transmission against reference for a selected hour in the middle of the cavitation run in a specific day. This cycle was observed to match the temperature of the fuel entering the optical cell however further quantitative analysis cannot be provided as the results were not synchronously recorded. For a quantitative analysis a precise temperature and a small time variation is required with a synchronous measurement of laser reference and transmission readings. The measurements taken here for the experiment were one minute averaged and thus the reference and transmission laser power has been averaged over the minute. Qualitatively the study is viable as the changes occurred were observed however they cannot be precisely quantified.

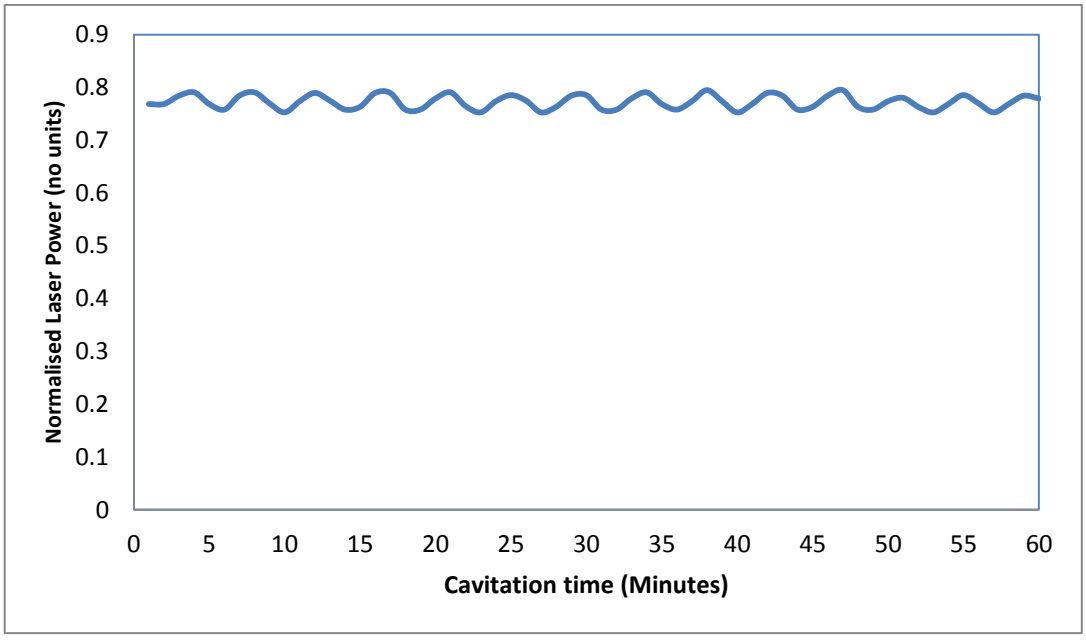

Figure 4.3 Normalised laser power against time (minutes) for Total Luton showing the variation of laser transmission

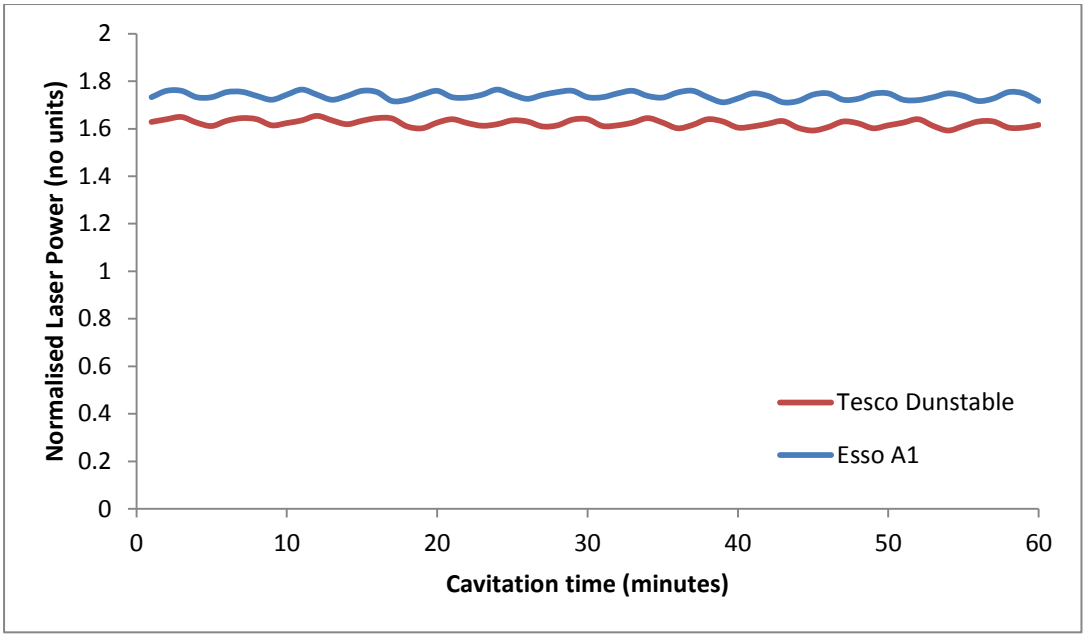

Figure 4.4 Normalised laser power against time (minutes) for Tesco Dunstable and Esso A1 showing the variation of laser transmission

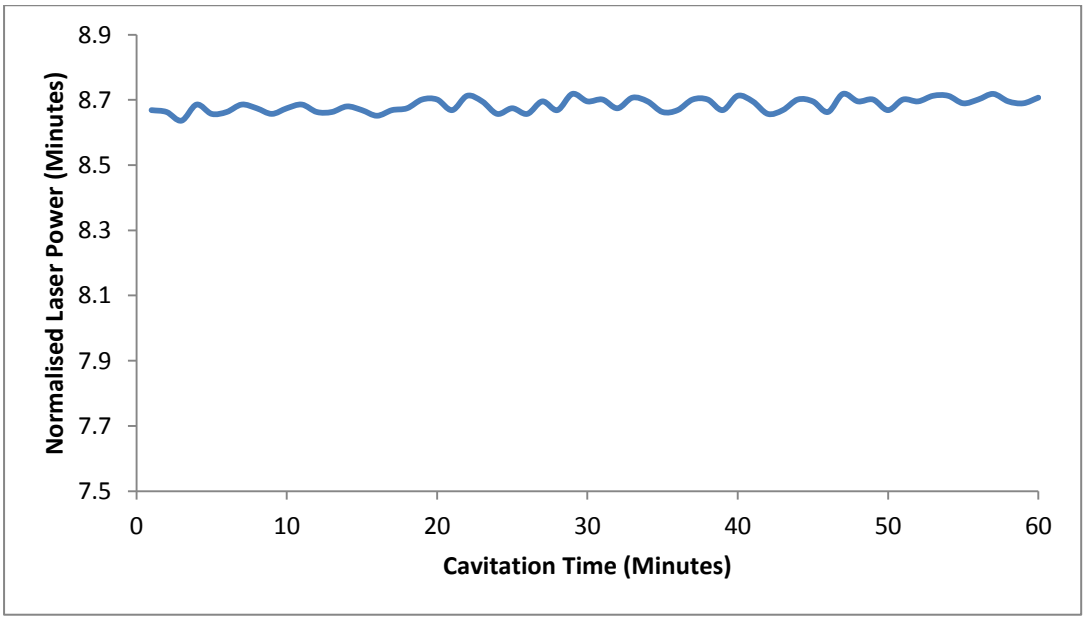

Figure 4.5 Normalised laser power against time (minutes) for the Paraffinic Model Fuel showing the variation of laser transmission

Figure 4.3 to Figure 4.5 show the changes in minute averaged normalised laser power over an hour of Total Luton, Esso A1, Tesco Dunstable and the paraffinic model fuel for an hour. The results show the effect of the cooling cycle on the measurements obtained. The temperature of the fuel exiting the heat exchanger is a factor that affects these cyclic variations. This in turn depends on the fuel thermal conductivity and the temperature of the coolant entering the heat

exchanger. The cycle time of the heat exchanger varied with the water inlet temperature, its flow rate and the temperature of the surrounding air and thus these curves and not purely cyclic as some temperature cycles may last longer than others. The other factor affecting the temperature of the fuels is the temperature gradient occurring throughout the rig.

It was observed that for all fuels the temperature cycle caused by the effect of the cooling post injection caused a synchronous change in transmission of laser power through the fuels. During analysis of the cavitation laser reference and transmission readings the one minute averaged will be averaged over 15 minutes to try and average out the effect of temperature on laser power transmission through the fuel. The full temperature cycle lasted between three to four minutes. The cycle seen in the figures above lasts four minutes this matched the cooling cycle observed. The maximum and minimum normalised laser power readings are 0.79 ± 0.01 and 0.75 ± 0.01 in Figure 4.3; 1.76 ± 0.01 and 1.72 ± 0.01 for Esso A1, 1.65 ± 0.01 and 1.61 ± 0.01 for Tesco Dunstable, in Figure 4.4; and 8.71 ± 0.01 and 8.66 ± 0.01 in Figure 4.5.

The cyclic variations occurring in the paraffinic model fuel is inconsistent in comparison to the commercial diesel fuels showing relatively sinusoidal cycles. These occurred due to the rate of heat exchanger performing inconsistently during the analysis of this fuel. This may have occurred due to the temperature or feed of the water supply varying largely as it was being used by elsewhere.

There are various factors that could affect the cooling cycle:

- The heat capacity of the fuel. The higher the heat capacity the higher the heat energy required to result in the same temperature difference. Thus the cooling cycle will take longer for higher heat capacity fuels.

- The temperature of the surrounding air in the room. If the air is cooler then the rig will lose more heat to the surrounding air and thus affect the cooling cycle time.
- The temperature of the inlet water supplied to the heat exchanger. The cooler the water at inlet to the heat exchanger the shorter the cycle and thus the cooler the temperature of the fuel exiting at the end of the heat exchanger.
- The inlet volume flow rate of water at the heat exchanger. If the volume flow rate is low the cooling cycle will be longer.

For the above reasons precise synchronous measurements of the temperature at inlet to the optical cell and the laser reference and transmission readings have to be carried out at shorter time periods, i.e. one second measurements, to obtain a quantitative conclusion.

The absorption spectra of molecules in the near visible to ultraviolet spectral region are known to change with temperature [158–161]. Among many kinds of temperature-dependent interactions, an interaction due to hydrogen bonding is the one most often encountered in usual absorption experiments [162]. A change in transmittance can be caused by a change in concentration of the absorbing species and this in turn may relate closely to the colour of the liquid. Grubb et.al [160] derived the term thermochromism for the change in colour of organic compounds with temperature. The following three important factors may be considered as causes of temperature dependant change in the absorption spectra [162]: 1) temperature effect on the refractive index of the solvent; 2) temperature effect in the Boltzmann distribution among vibrational and rotational energy levels of a solute molecule and 3) temperature dependant interactions among molecules in the system

4.1.2 Experimental analysis - 40 hours cavitation

One-minute averaged laser power measurements for the diesel samples that were subjected to cavitating flow tests were converted to fifteen minute averages. The continuous fifteen minute averaged laser transmission power data were ratioed against the synchronous reference laser power measurements, producing normalised transmission laser power data that would be independent of power fluctuations in the source 405 nm diode laser. A fifteen minute average was carried out to the raw one minute averaged intensity reference and intensity transmission data obtained during the experiment in order to average out the temperature variation occurring over the optical cylinder as a result of cooling and thus affecting the laser transmission as discussed in 4.1.1 above. The fifteen minute averaged results were then normalised with respect to the intensity reference signal and plot on a graph against run time.

Figure 4.6 Normalised transmitted laser power as a function of cavitation time (hours) for Shell Flitwick carried out to check optical setup consistency.Figure 4.6 to Figure 4.10 shows graphs of normalised transmission laser power profiles through the optical cell containing 1.1 cm thick layer of sample test fuel flowing upward through the cell, as a function of time during the forty hour cavitation test period. The first of the graphs shows the commercial diesel fuel tests whereas the second graph shows the model diesel fuels. The third curve consists of a combination of the above and the fourth graph consists of aged fuel test results. The graph in Figure 4.6 shows a consistency check carried out to in order check the repeatability of the measurements obtained. At this point the normalised transmission profiles have been displayed separately due to the reduced stability of diesel fuels over long term storage [36,163]. This will be discussed in detail further on. The fuels all show different transmitted laser profiles as a function of cavitation run time.

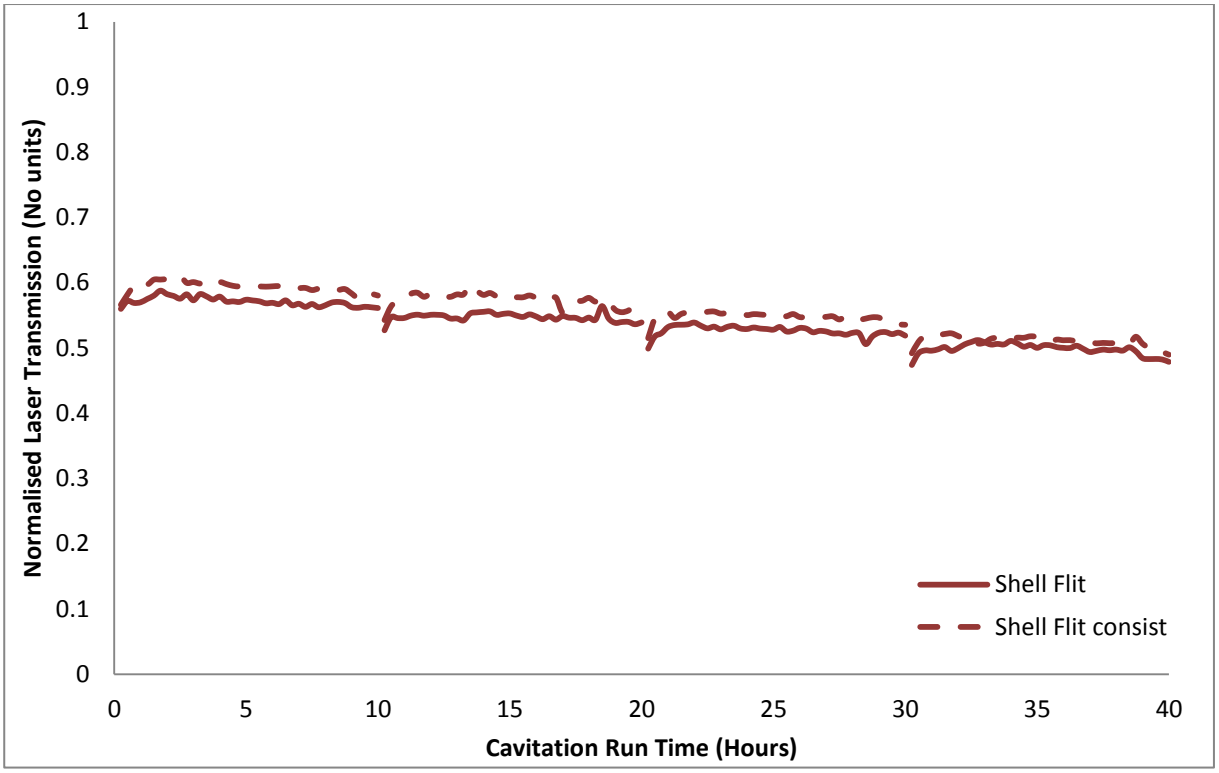

Figure 4.6 Normalised transmitted laser power as a function of cavitation time (hours) for Shell Flitwick carried out to check optical setup consistency.

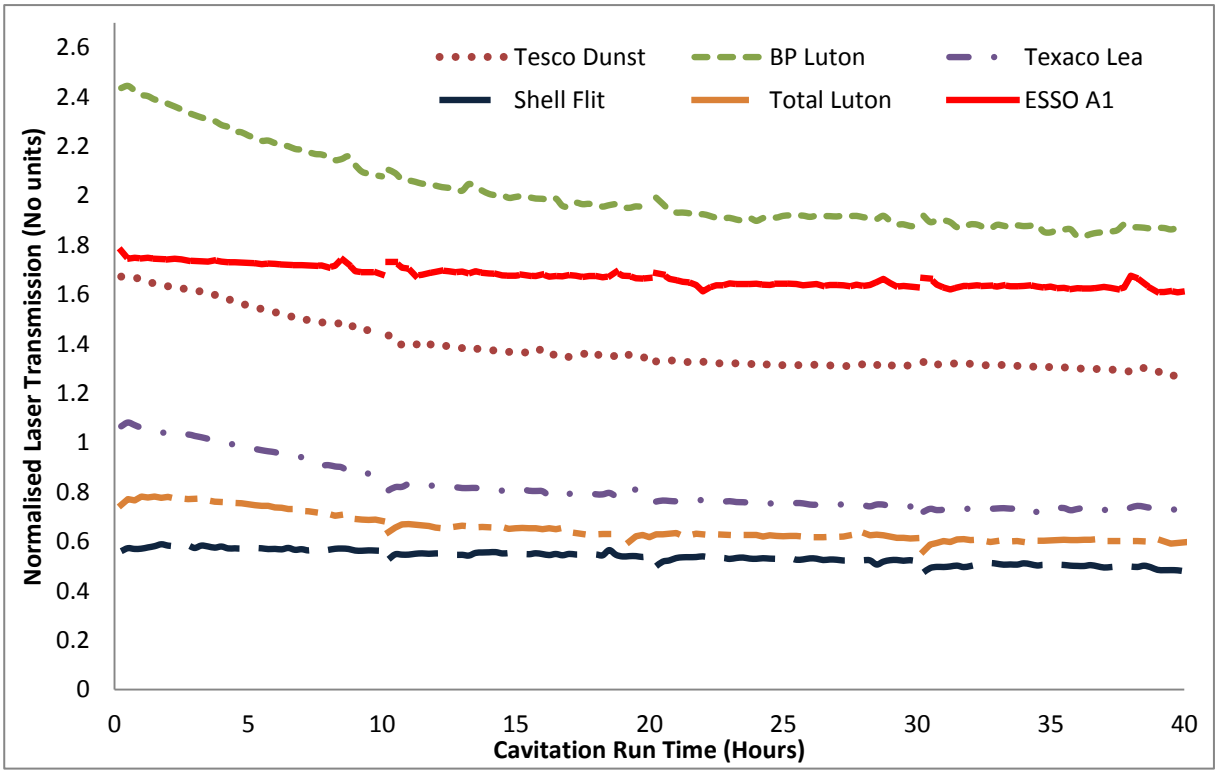

Figure 4.7 Normalised transmitted laser power as a function of cavitation time (hours) for NEW 6 commercial diesel samples

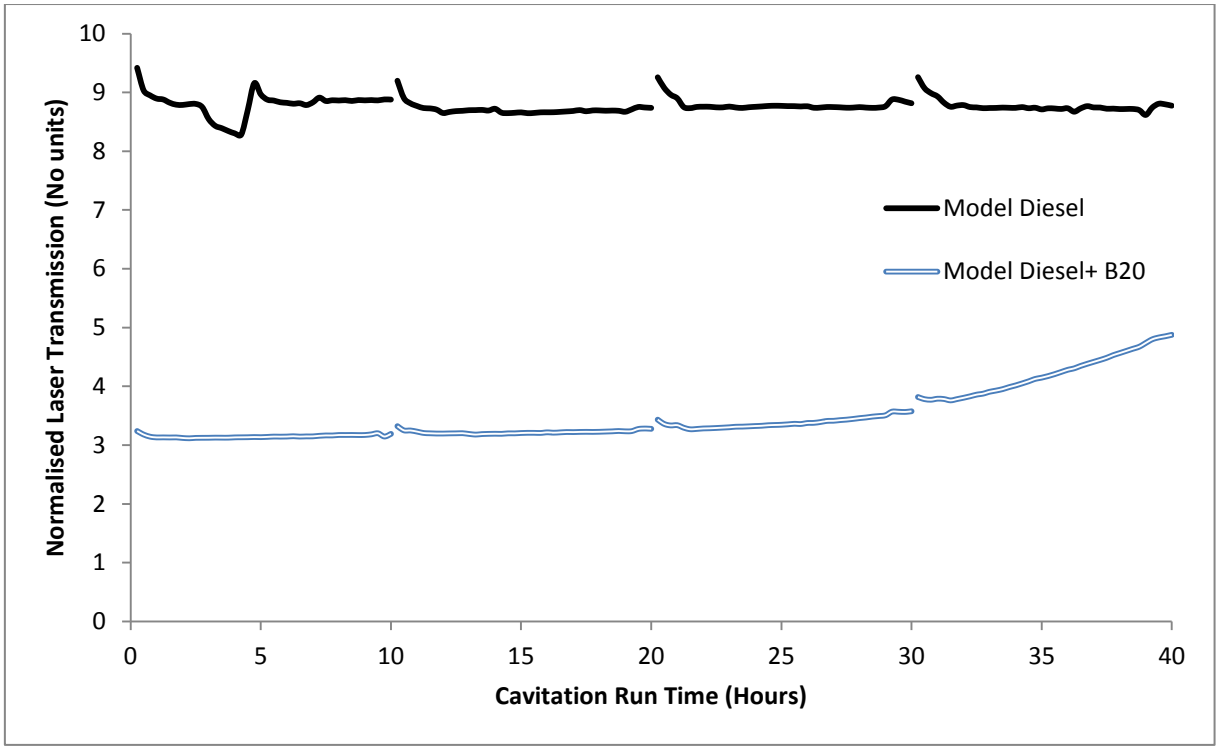

Figure 4.8 Normalised transmitted laser power as a function of cavitation time (hours) for 2 Paraffin-based Model diesels.

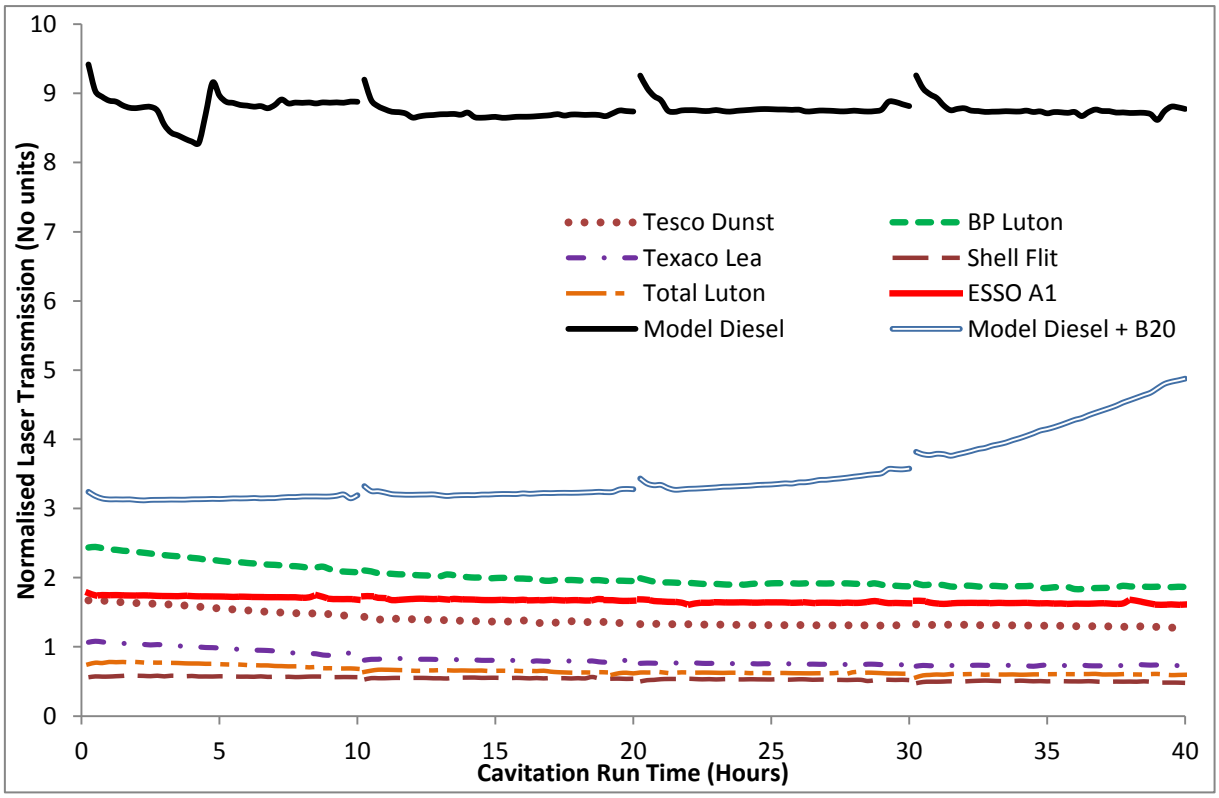

Figure 4.9 Normalised transmitted laser power as a function of cavitation time (hours) for 6 NEW commercial diesels samples and two paraffin-based model diesels

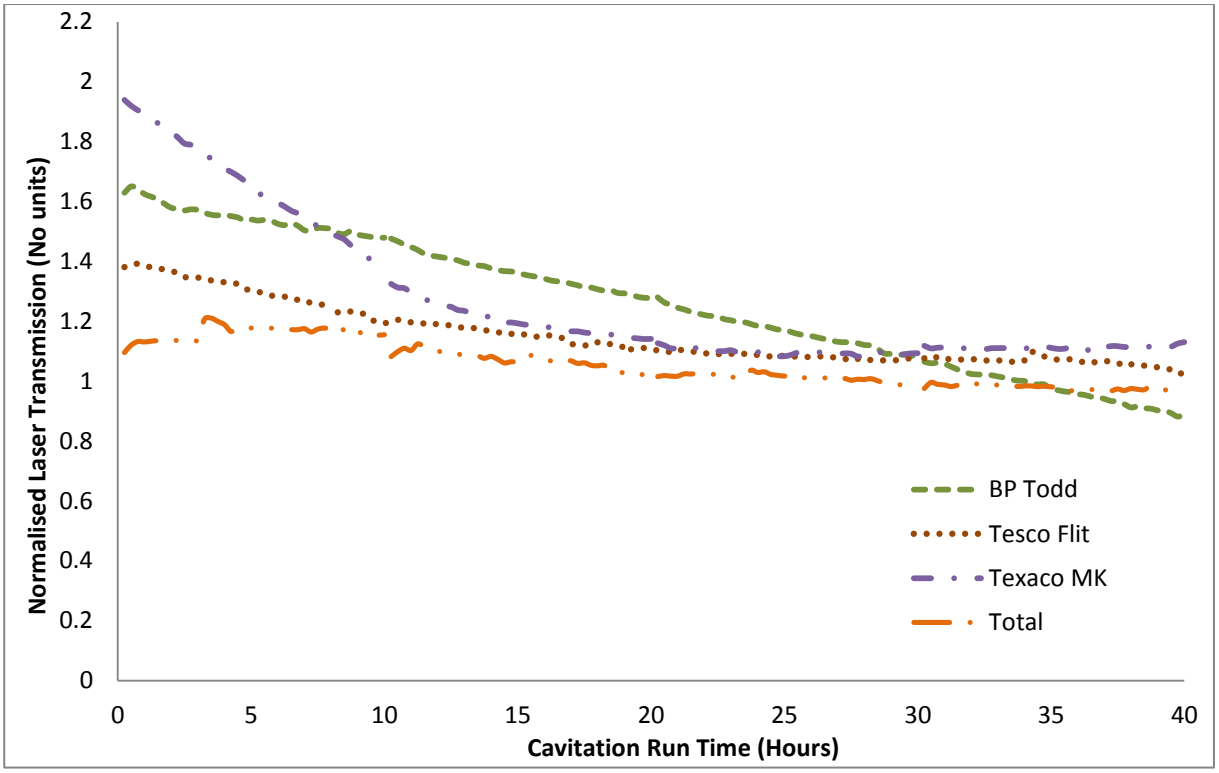

Figure 4.10 Normalised transmitted laser power as a function of cavitation time (hours) for 4 AGED commercial diesels

The normalised laser transmission obtained in Figure 4.6 is for Shell Flitwick run over forty hours on two separate occasions in order to check the laser power and optical measurement system consistency. Although carried out in exactly the same methodology, the consistency check run the second time utilized the same injector nozzle as the first case. The nozzle may have been worn out and thus the cavitation occurring over the injector nozzle may not be the same magnitude as the one run with a new nozzle. The reduction in cavitation magnitude occurring will have lower chemical consequences on the fuel and thus the normalised laser transmission will be higher. This is clearly observed in the graph as both curves start of at the same point and follow the same pattern to the end. The difference in normalised laser transmission at 1.25 hours and at 40 hours is 0.2 ± 0.1. The optical setup and measurements thus provide consistent results from fuel to fuel and the results obtained are comparable. The gaps in the histories of these graphs relate to day to day running. There are four sets of lines per fuel representing each day the fuel was run for 10 hours in the cavitation rig.

The normalised values at the beginning of the cavitation tests as observed in all graphs are different because the fuels individually have different attenuation coefficients depending on the concentration of absorbing species present in them. Shell Flitwick had the lowest normalised laser transmission signal at 0.58 ± 0.01 and is therefore lowest on the graph. A low normalised laser transmission relates to a large number of 405 nm laser power absorbing species present in the fuel. Of the commercial fuels, BP Luton had the highest laser normalised laser transmission signal at 2.43 ± 0.01. A high normalised laser transmission signal indicates a lower amount of 405 nm laser power absorbing species present in the fuel. The paraffin based model diesel was transparent to the incident laser light at 405 nm and had a normalised laser transmission between 8.83 ± 0.01 and 8.77 ± 0.01. In addition the model diesel attenuation coefficient was observed to remain unchanged over the forty hour cavitation period. There was negligible change in its absorption over the forty hour period. The initial glich seen in the curve at 2 hours is due to an emergency shut down and restart that had to be carried due to a fire alarm response. The fuel had then started to cool before it was restarted following the sequence to raise the temperature to 69 degrees. In contrast to this, all of the commercial diesel samples (fresh and aged) produce a decrease in normalised laser transmission power with time during the cavitation. The model diesel containing 20% RME produced a different variation. All the commercial diesels decreased in laser power transmission, whereas the RME-model diesel produced an increase in laser power transmission as a result of cavitation over time.

Figure 4.11 shows the overall changes in percentages as a result of the fuel under going forty hours of cavitation run time. From the bar plot showing percentage changes due cavitation run time in the rig, it can be observed that the model fuel under goes very little change in transmitted laser power over the forty hour period. By contrast the rest of the commercial

fuels produce a relative decrease in normalised transmitted power. Some of the aged fuels produce a large decrease in normalised transmitted laser power. The model diesel fuel containing RME produced a large increase in normalised transmitted laser power.

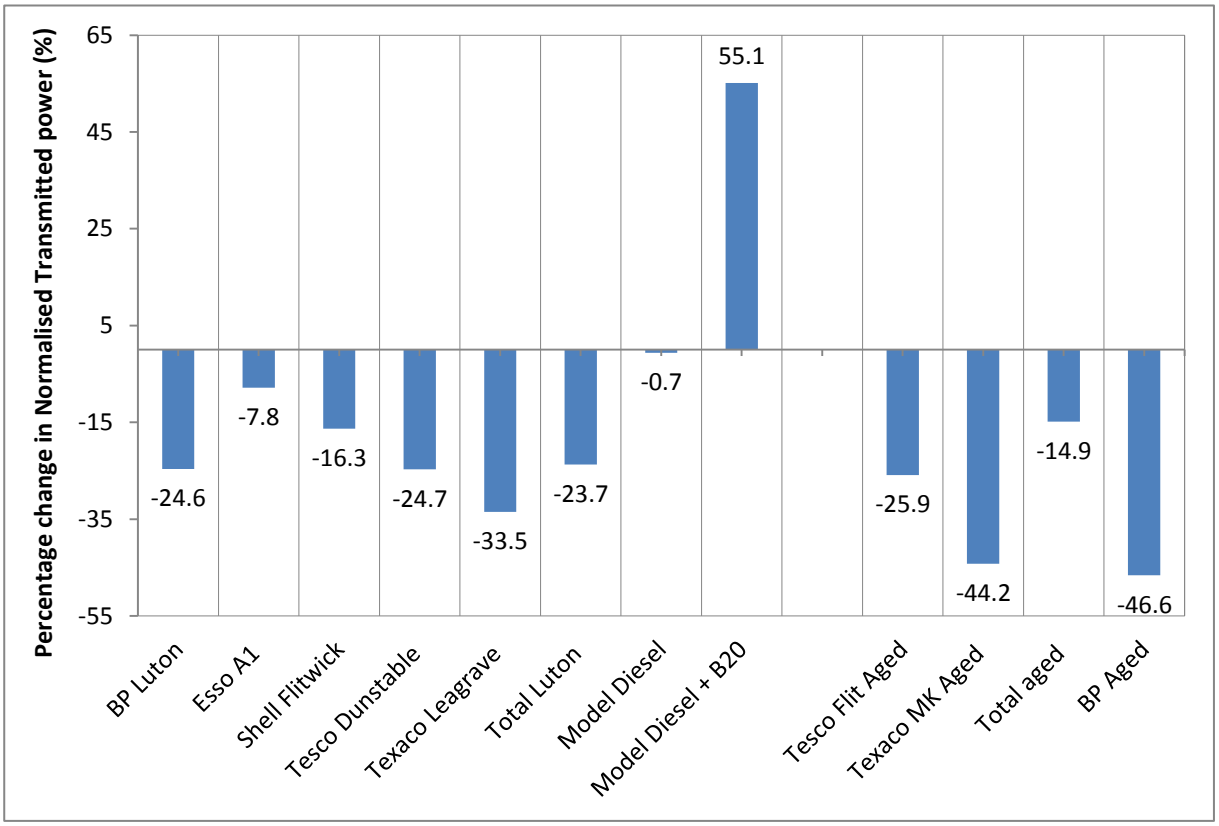

Figure 4.11 Percentage change in normalised transmitted laser power as a result of 40 hours cavitation

Two of the aged fuels display larger decreases in normalised laser transmission. One that sticks out and different to the rest of the commercial fuels is BP Toddington. In contrast to all the commercial fuels which display an initial sharp decrease in normalised laser transmission which levels out, the aged BP sample produces a linear decrease throughout the forty hours cavitation period. BP Toddington aged changed -46.6% ± 0.1%, whereas TEXACO MK changed -44.2% ± 0.1%. TESCO Flitwick and TOTAL aged produced changes in normalised transmitted laser power similar to that of fresh fuels. The stability of diesel fuels is reduced greatly as a result of long term storage leading to the formation of fuel sediments [163]. The

fuel instability maybe a factor creating this larger changes in optical transmission as a result of long term cavitation.

At the start of each day, there is a small rise/fall in laser transmission over time before the results stabilise. This was observed as an effect of temperature stabilisation during the start of the experiment and depended on the thermal properties of the fuels. For some of the commercial fuels a small rise in normalised laser transmission was observed at the start of each day until the 4 litre capacity of the rig had attained a stable temperature and a uniform temperature gradient entered the optical cylinder. The paraffinic model based fuels, BP Luton and ESSO A1 displayed a fall in normalised laser transmission at the start of each day until temperature stabilisation was achieved. This effect cannot be pinpointed as an effect of paraffins as the model fuel was comprised of paraffins and olefins.

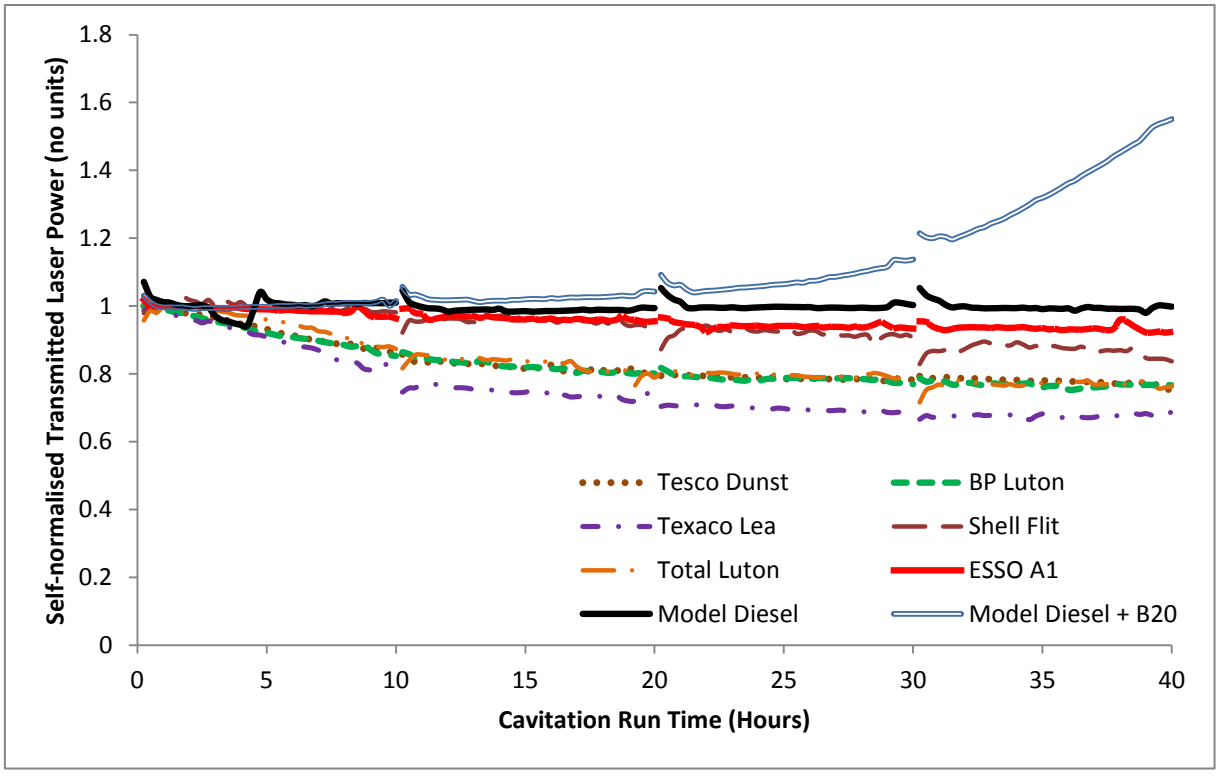

Figure 4.12 Self-Normalised Transmitted laser power as a function of cavitation time (hours) for 6 NEW commercial diesels samples and two paraffin-based model diesels.

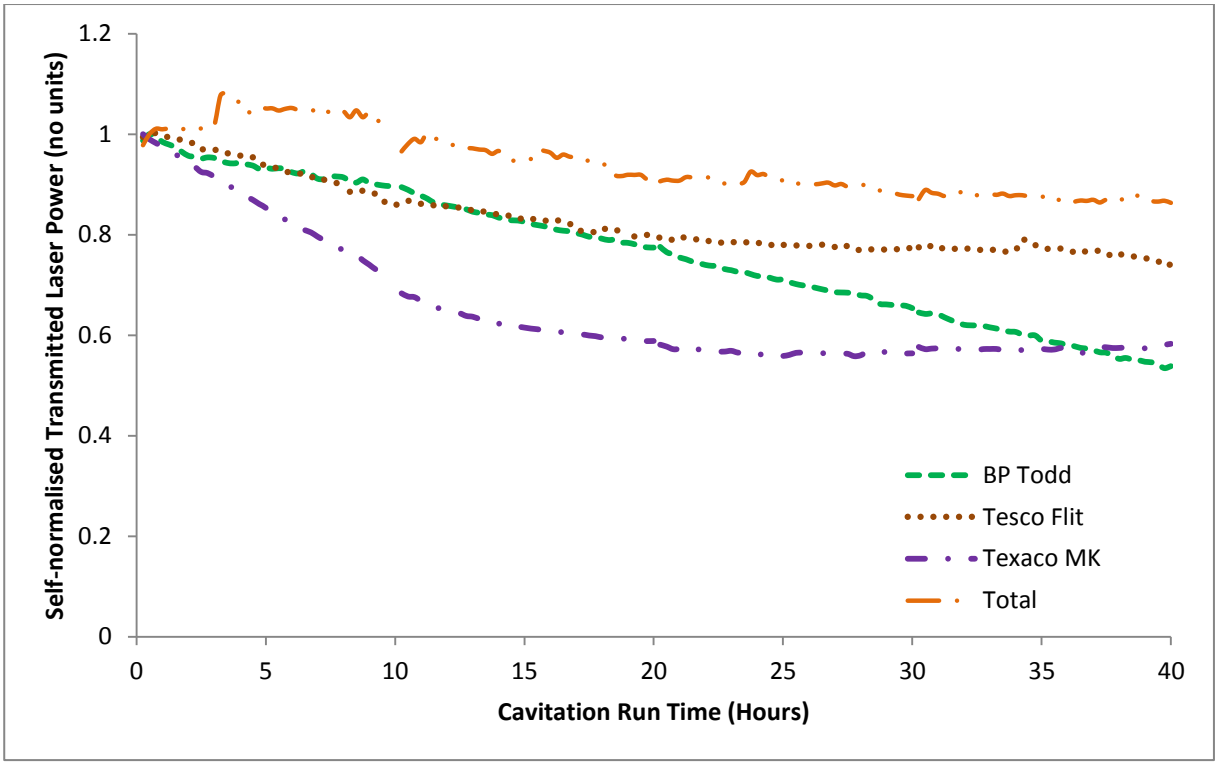

Figure 4.13 Self-Normalised Transmitted laser power as a function of cavitation time (hours) for 4 AGED commercial diesel samples

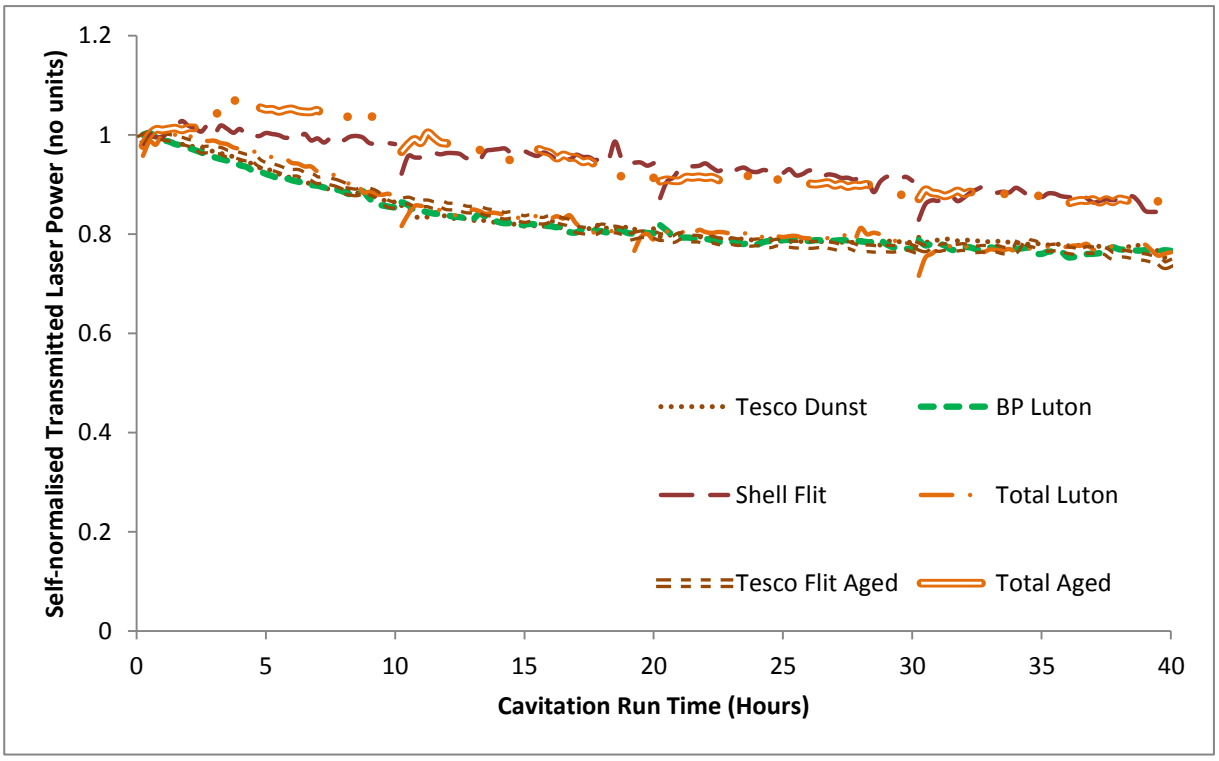

Figure 4.14 Self-Normalised Transmitted laser power as a function of cavitation time (hours) for 4 NEW commercial diesel samples and 2 AGED commercial diesel samples that have similar profiles.

The true scale of the change in normalised transmission power for all fuels can be observed in Figure 4.12 and Figure 4.13. These graphs show the relative variation in laser transmission through the respective diesel samples as a function of time and were determined by normalising the transmission profiles with the corresponding normalised transmission laser power at the beginning of the cavitation tests. From these it can be observed that the paraffinic model fuel under went negligible changes over forty hours of cavitation, -0.7 % ± 0.1%. The fresh commercial diesel fuels show a decrease in normalised laser transmittion over prolonged cavitation. TEXACO Leagrave overgoes the maximum overall change of -33.5% ± 0.1% whereas ESSO A1 displays the lowest change over the forty hours of cavitation with a change of -7.8% ± 0.1%.

In contrast to the other commerical fuel results the paraffinic-B20 model fuel displays an increase of 55.1% ± 0.1%. As the paraffinic model fuel without RME displayed no change in normalised laser transmission, the increase displayed by the RME containing paraffinic fuel can be pinpointed to the effects of RME. The effects of long term cavitation to the RME causes the amount of absorbing species contained within it to decrease and thus the normalised laser transmission increases. A discussion with scientists at Shell Global Solutions came up with the same conclusion with their analysis of the effects of ultrasound cavitation on RME containing fuel. Further investigation lead them to conclude that naturally occuring antioxidants in RME called tocopherols [164] are getting destroyed as a result of the impact of the sustained cavitation. It lead us to believe that these species was the major absorbing species in this mixture and thus its destruction would cause a decrease in laser power absorption and an increase in normalised laser transmission with prolonged periods of cavitation as seen in these figures. Visually observing the samples before and after the

cavitation gave further evidence as the after sample had gone much lighter after forty hours of cavitation.

The major issues with the usage of biodiesel are its susceptability to oxidation upon exposure to oxygen in the ambient air. This susceptibility is due to its content of unsaturated fatty acids chains. The oxidation process has been known to influence the stability of bio-fuels with factors such as the presence of air, light, elevated temperature, extraneous materials present in the container material, peroxides and antioxidants, as well as the size of the surface area between the biodiesel and air [165]. Approaches to improving the biodiesel oxidative stability include the delibrate addition of antioxidants. RME contains naturally occuring tocopherols and their destruction would result in its stability being compromised. However these naturally occuring and delibrately added antioxidants are probably getting destroyed by the effect of cavitation induced bubble collapse. The European diesel fuel standard EN 590:2009 includes diesel blends with up to 7 % (v/v) FAME [166].

So far it has been observed that prolonged cavitation has not affected the normalised laser power transmission through paraffinic model fuel diesel at 405 nm. The effects of prolonged cavitation on Rapeoilmethylester (RME), which is a fatty acid methyl ester (FAME), based paraffinic fuel have also been observed. It can be concluded that the presence of FAME causes and increase in normalised laser power transmission due to the destruction of the absorbing species contained in the FAME. Some fuels display a similar relative decrease of normalised transmitted laser power over time. Seen in Figure 4.14, SHELL Flitwick and Aged Total Luton produce a similar relative profile, whereas TESCO Dunstable, TESCO Flitwick (Aged), BP Luton and Total Luton also produce a relatively similar profile respectively. The magnitudes of the changes occuring in these fuels over the forty hours of cavitating run time

are the same, in the first set -15% ± 1% and in the second -25% ± 1%. The relative changes may be similar however the overall chemical changes occuring within the fuel may differ greatly due to the total concentration of absorbing species differing in each of these fuels and that is why they do not match up in Figure 4.7. The graphs in Figure 4.13 and Figure 4.14 were just plot to obtain an overal relative magnitude of change for comparison purposes between the fuels.

4.1.3 Spectral attenuation coefficient α

The equations obtained in section 3.5 as a result of the calibration of the optical system have been employed to calculate the spectral attenuation coefficients for all of the diesel samples as a function of the cavitation time. The results obtained are shown in Figure 4.15 to Figure 4.17. The paraffin blend model diesel was revealed to have an unchanged 405 nm spectral attenuation coefficient of 0.008 cm^{-1} ± 0.008 cm^{-1} during the cavitation period. Fresh commercial diesel fuels display a variation of spectral attenuation coefficients. SHELL Flitwick as expected from the normalised transmitted laser power has the highest spectral attenuation coefficient beginning at 2.38 cm^{-1} ± 0.01 cm^{-1}, increasing to 2.53 cm^{-1} ± 0.01 cm^{-1} at the end of the forty hour cavitation period. BP Luton had the lowest spectral attenuation coefficient beginning at 1 cm^{-1} ± 0.01 cm^{-1}, increasing to 1.26 cm^{-1} ± 0.01cm^{-1} at the end of the forty hour cavitation period.

The rest of the Fresh commercial fuels as seen from the figures had spectral attenuation coefficients between these beginning and end values. The point to note however is that the spectral attenuation coefficients all increase and are inversely related to the fuels normalised transmitted laser power. The spectral attenuation coefficient displays the measure of

absorption of radiation, as a function of frequency or wavelength, due to its interaction with the sample. The sample absorbs energy. The spectral attenuation coefficient quantifies the amount of 405 nm light absorbing species present in the fuel samples and provides a comparison to how this varies with time as a result of the cavitation it undergoes. Initially at the beginning of the experiment the amount of 405 nm light absorbing species present in the fuels determines it spectral attenuation coefficient at start. As a result of cavitation in the commercial diesel fuels, the amount of absorbing species increases and thus there is an increase in spectral attenuation over cavitation run time.

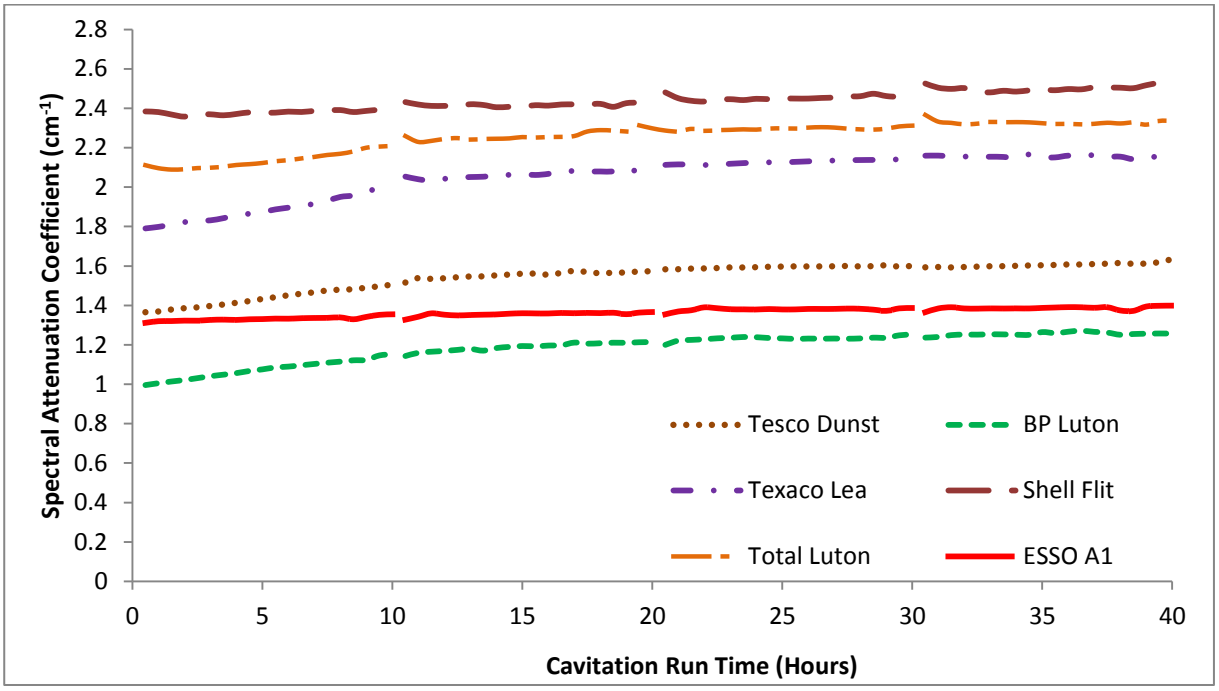

Figure 4.15 The Spectral Attenuation Coefficient (cm^{-1}) as a function of cavitation run time (hours) for New Commercial diesel Samples

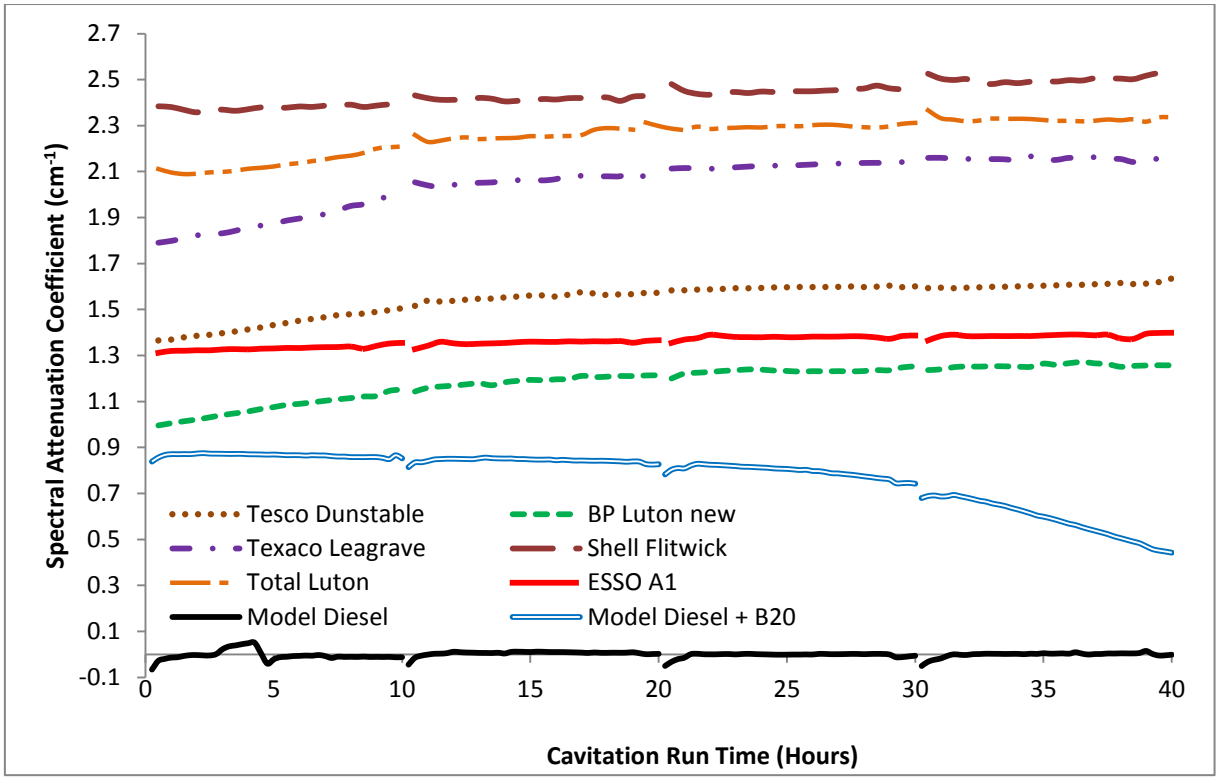

Figure 4.16 The Spectral Attenuation Coefficient (cm^{-1}) as a function of cavitation run time (hours) for New Commercial diesel Samples and the Paraffin based Model Sample

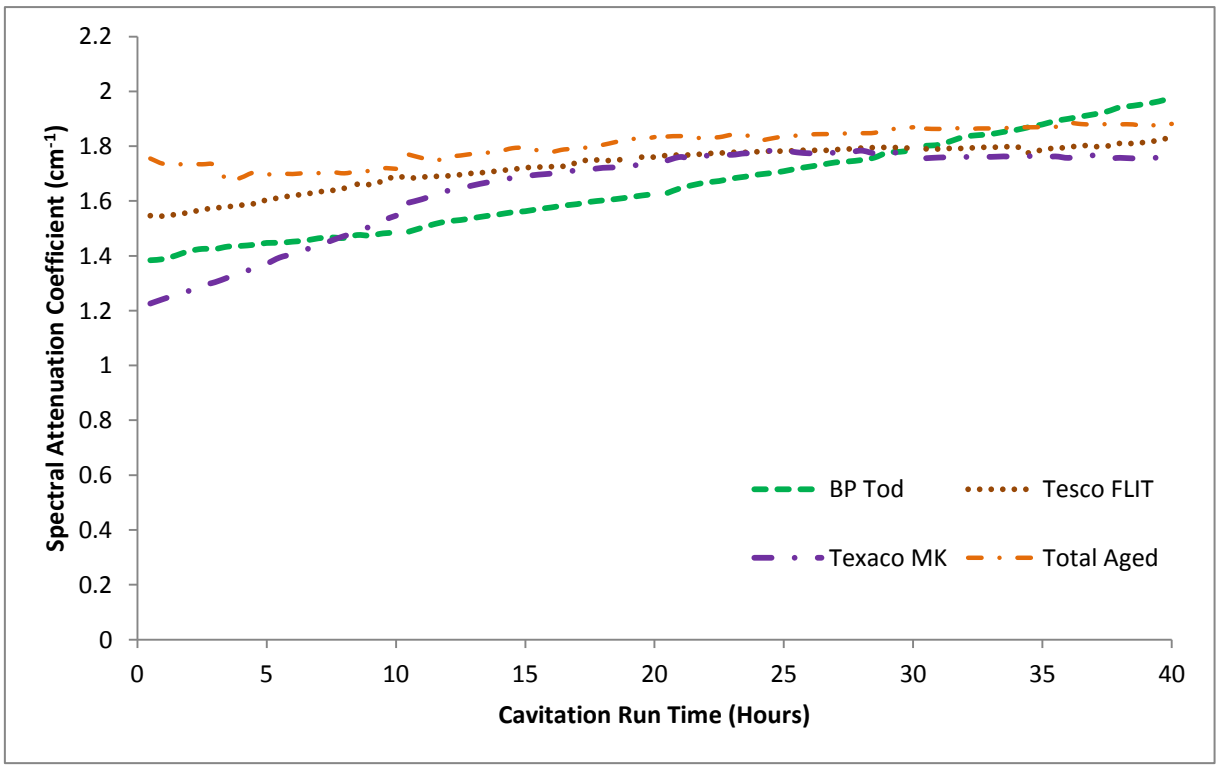

Figure 4.17 The Spectral Attenuation Coefficient (cm^{-1}) as a function of cavitation run time (hours) for Aged Commercial diesel Samples

Due to the fact that all the commercial fuels have different concentrations of absorbing species present in them, they have varying spectral attenuation coefficients at the beginning. Also observed is how the spectral attenuation coefficient of the RME - model fuel changes as a result of long exposure to cavitation. Commercial fuels containing RME or other biodiesel based contents maybe undergoing whole lot of formation and destruction of absorbing species. However due to the fact that commercial fuels only contain a maximum of 7% biodiesel fuels, the magnitude of the destruction of the absorbing species may not be as high as seen with the RME - model fuel which contained 20% RME. The results observed here consist of an overall timeline of the absorbing species. A rise in spectral attenuation coefficient shows that the rate of production of 405 nm absorbing species is greater than its destruction.

4.1.4 Separating effects of temperature and cavitation

All the fuels were subject to 40 hours discontinuous heat test replicating their run time on the cavitation rig apart from BP Toddington aged due to enough sample being unavailable. The tests were carried out to investigate the effects of high temperature on the chemical composition or rather the normalised transmitted laser power and signal attenuation coefficients to enable separate out the combined effects of cavitation and high temperature on the diesel samples. Although the release of internal compression energy due to cavitation in the diesel flow was responsible for the increase in temperature, the control temperature had been set at high temperature and thus the experimental results would show a combined effect of the raised temperature and cavitation effects on the diesel fuel. Therefore the diesel fuels were heated over forty hours synchronously in a water bath following the discontinuous profile. The laser transmission was denoted of the fuels before being placed in water bath as a

reference. After the 40 hours were complete the heated fuel was placed back into the cavitating flow rig and circulated at low pressure through the optically accessible cell at ambient temperature conditions. As there was no way of providing a full forty hour timeline similar to the cavitation experiment, only percentage changes with respect to the initial sample are provided from the results obtained. These will be compared with the percentage changes occurring as a result of the cavitation experiment with respect to the initial sample at zero hours. The results of the 40 hours discontinuous heat tests are displayed in Figure 4.18

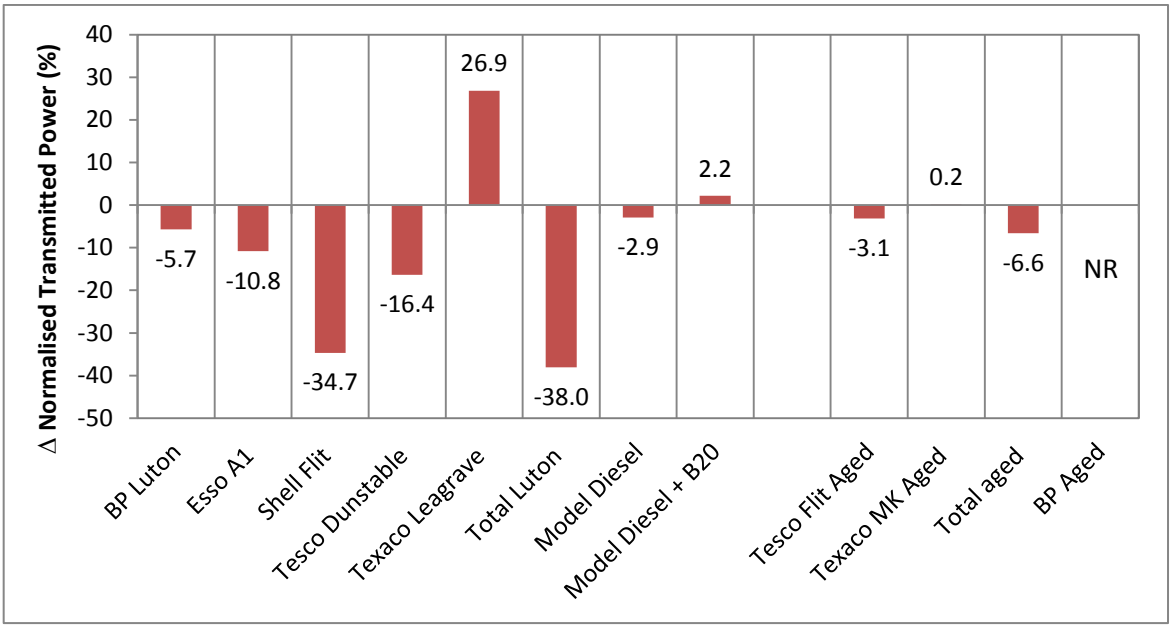

Figure 4.18 Percentage change in normalised transmitted laser power as a result of 40 hours discontinuous heat test

The overall percentage changes in normalised transmitted signal can be observed for each fuel with respect to its initial normalised transmitted laser power. SHELL Flitwick and TOTAL Luton produce the maximum decrease in transmitted power after heat test at 34.7 % ± 0.1 % and 38 % ± 0.1 % respectively. TEXACO Leagrave, model diesel+B20 and TEXACO MK show and increase in transmitted laser power of 26.9 % ± 0.1 %, 2.2% ± 0.1 % and 0.2% ± 0.1 % respectively. An increase in transmitted laser power corresponds to a decrease in the concentration of absorbing species in the fuel whereas decrease in transmitted laser power

corresponds to an increase in concentration of the absorbing species. The model diesel sample changed the least at 2.9% ± 0.1 %.

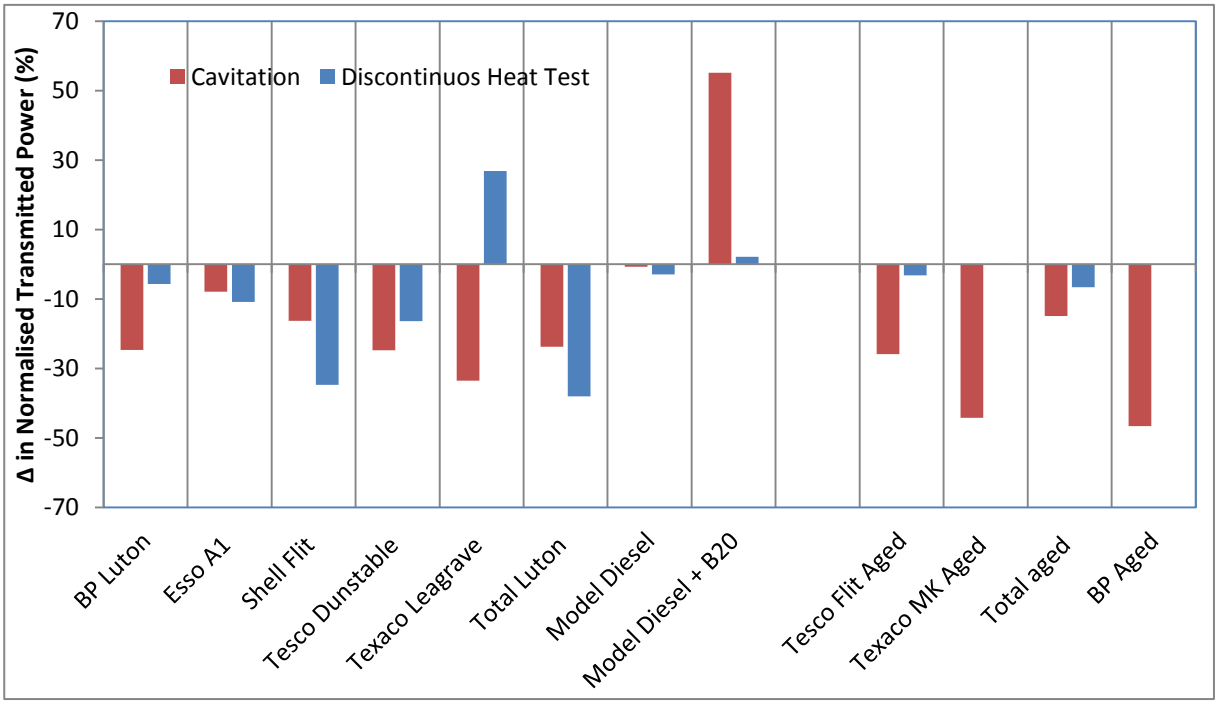

Figure 4.19 Percentage change in normalised transmitted laser power as a result of 40 hours cavitation and discontinuous heat test comparison

Figure 4.19 shows the comparison of the percentage changes from the cavitation experiment and the heat test with respect to their initial normalised transmitted laser power. In most cases the forty hour cavitating flow experiment related results cause a change larger in magnitude than that caused by the result of the forty hours of discontinuous heat test apart from SHELL Flitwick, ESSO A1, and TOTAL Luton. When comparing these results it can be noted that the changes caused by the forty hour cavitating flow are different to those caused by the discontinuous heat test. Overall for the majority of the fuels, the effects of the forty hours discontinuous heat tests can be subtracted from the effects of the forty hours cavitating flow to differentiate their effects. Two of these fuels namely SHELL Flitwick and TOTAL Luton had the lowest normalised transmitted powers and may have had additional absorbers been added

in by the manufacturers as fuel additives in the form of either winter fuel additives or fuel performance additives. ESSO A1 had the minimum changes observed to its spectral attenuation coefficient over the 40 hours of cavitation.

These fuels were all bought over winter months and different kinds of winter diesel fuel additives are added to stop the fuel from gelling and forming waxy deposits. The additives lower the temperature characteristics of the fuel. These additives may vary between fuel manufactures and may contain different amounts of absorbing species apart from aromatics and FAME species identified as absorbers here. These may react differently to cavitating flow and to temperature. The chemical composition of the fuel also determines the amount of additives added. Apart from the winter fuel additive, fuel manufacturers also add a lot of different secretive additives in their fuels to improve its performance. The hypothesis is that the different fuel additives added to the fuels may cause different effects to the amount of laser power being absorbed by the fuel as a result of different absorbing species present in the fuels. These additional fuel additives may be behaving in a different manner under cavitating flow conditions and as a result of heating. The different types of additives to fuels have been discussed in section 2.1.5. However this is just a hypothesis and nothing can be concluded by just looking at these figures as the story lies within the fuel composition and chemistry.

4.2 Experimental Results Summary

The composition of modern crude oil derived fuel is approximately 70 - 75% paraffins, and 25-30% aromatics consisting of 23 - 26% mono-aromatics, 2 - 3% di-aromatics, and 1% tri-aromatics [167,168]. Considering that the paraffinic model diesel was comprised of 100% paraffins and olefins, and that the forty hour cavitation period had no measurable effect on the 405 nm spectral attenuation coefficient The absence of any variation in the 405 nm spectral attenuation coefficient suggests that any compositional changes in the paraffins and olefins comprising the model diesel caused by the forty hour cavitation period had no effect on the overall spectral attenuation of the model diesel. The addition of RME to the model diesel produced results in conflict with the commercial diesel spectral attenuation results and thus the presence of bio-diesel/RME can also be excluded as producing an increase in spectral attenuation coefficient. However, the presence of biodiesel/RME may be inhibiting the overall effects by initially having additional absorbing species which are destroyed thereafter as a result of the effects of high local pressure and temperature release as a result of cavitation bubble collapse. This suggests that the rate of increase in absorbing species causing the increase in spectral attenuation at 405 nm is due to the presence of aromatics in the fuel.

The results from the experimental analysis using the 405 nm laser transmission through the fuels and monitoring their changes with time have shown that the concentration of the absorbing species increases with increase in time of the sustained cavitating flow. An increase in the concentration of the absorbing species results in a reduced power being detected at the fuel exit through a constant cross section in reference to its actual power being transmitted. This has been noted for all fuels.

The majority of the heat tests results show that the high temperature of the cavitating flow is maintained at may be a reason for an increase in spectral attenuation of the diesel fuels during the cavitating flow however cavitation in itself is also causing changes in the diesel fuel composition and properties as observed in the results comparison. It is not clearly observed using the results above however a chemical analysis would provide conclusive results of the changes occurring within the diesel fuel both chemically and physically. The results obtained from the sustained cavitating flow analysis in comparison to the heat test analysis show that the effects of the lowest temperature maintained in the rig does not have the same effects as the sustained cavitating flow results and thus leads to the conclusion that the thermal reactions may increase the reaction rate of the formation of absorbing species but are not the sole cause for the changes that have been observed in the sustained cavitating flow measurements.

Simple aromatics have a propensity to form complex poly-aromatic hydrocarbons (PAHs), leading to the formation of small soot-like particles suggesting the hypothesis that the increase in spectral attenuation coefficients of commercial diesels with cavitation time is caused by the aromatics comprising in the diesels undergoing pyrolysis like reactions during cavitation to form a particle like suspension, hence increasing the absorptivity of the cavitated samples.

The hypothesis also explains why some of the aged diesel samples both produced larger relative variations in their respective spectral attenuation coefficients than those produced from the fresh diesel samples. They would have been more susceptible to aromatic pyrolysis to form particulates than the fresh commercial diesel samples, due to their reduced fuel stability as a result of long term storage [35,36,163].

The results shown here give an indication of possibilities of the chemical changes occurring in the fuels. These changes can be pinpointed to the aromatics and FAME content of the fuel. However to come to a conclusion a chemical analysis of the fuels has to be conducted in order to derive the species present in the fuels before and after experimental analysis of cavitating flow and the heat tests. So far no physical attributes have been denoted and a chemical analysis would also give a firm conclusion to the effects of the cavitating flow on the physical properties of the fuels. Because the formation of soot-like particles is suspected, a particulate count could further this hypothesis to viable conclusion. Different changes are observed as a result of sustained cavitation and heat tests however in some cases the overall changes occurring as a result of the heat test exceed the relative changes occurring as a result of sustained cavitating flow. Different chemical changes maybe occurring to the fuels via the two processes and thus resulting in changes to different absorbing species. At this point further conclusions can only be obtained by performing a chemical analysis. However the study carried out here on analysing the normalised transmitted signal and spectral attenuation coefficient provide good histories of how changes in the concentration of the 405 nm absorbing species with time.

4.3 Two Dimensional - Gas Chromatography (GC x GC)

Chromatography was introduced by Martin and Synge in 1941 as a technique based on partitioning of chemical compounds between two liquid phases [169]. A possibility of a gaseous mobile phase was suggested at this time and actually introduced in 1952 to be known as Gas Chromatography [170]. Their work signalled the first time compounds could be separated chromatographically on the basis of their volatility and has become one of the most important and widely applied analytical techniques in modern chemistry.

Chromatography is a technique used to separate mixtures of compounds, so that the individual components can be identified and/or quantified. The mixture being analysed is dissolved in a fluid called the mobile phase (gas) which is then forced through an immobile, immiscible stationary phase. The mobile gas at first was nitrogen; recently helium and hydrogen are also used. A list of the stationery phases is provided in [171]. The phases are chosen such that components of the sample have differing solubility in each phase. A component which is quite soluble in the stationary phase will take longer to travel through it than a component which is not very soluble in the stationary phase but very soluble in the mobile phase. As a result of these differences in mobility, sample components will become separated from each other as they travel through the stationary phase. GC uses columns: narrow tubes packed with the stationery phase, through which the mobile phase gas is forced. The mixture is transported through the column by continuous addition of the mobile phase gas. This process is known as elution. A detector then monitors the composition of the gas stream as it emerges from the column carrying separated components.

The quality of the separation achieved by the whole system can be that of the column only and thus it is at the centre of the analytical gas chromatograph. Earlier packed columns were used; however their resolution was limited by their length, which is itself restricted by the pressure drop occurring as a result of gas flow. This restriction was removed by the invention of capillary columns. In a capillary column, the stationery phase is coated on the inner wall, either as a thin film or impregnated into a porous layer on the inner. The differing paths taken by solute molecules as they pass through the non-uniform bundle of capillaries is replaced by a single channel. It has the advantage over packed columns of greatly increased separation efficiency, lower operating temperature and better separation efficiency in equal times. The downside of the capillary columns is that they have small amounts of stationery phase which

limits their capacity. This can be corrected by special sample-introduction methods (on column, loop type and programmed temperature vaporization) and sensitive detectors (flame ionisation detector, mass spectrometer, helium ionisation detector, flame photometric detector etc.) [172]. Columns are recently being made from fused silica.

In a flame ionisation detector (FID), the effluent undergoes combustion in a hydrogen/synthetic air flame which ionizes the analyte molecules. Ions and free electrons are formed in the flame. The charged particles produce a measurable current flow in the gap between two electrodes in the detector. The resulting current flow is of greater strength than the signal produced by the pure carrier gas and the fuel gas flame alone. This signal differential provides information about the sample. The current is proportional to the ion formation which depends on the composition of the separated sample. FID is preferred for general hydrocarbon analysis with detection from 0.1 ppm to almost 100%, but also for organic substances containing hydrocarbons and for volatile organic compounds

GC can be applied to the analysis of mixtures, which contain compounds with boiling points from near zero to over 700 K, or which can be heated sufficiently without decomposition to give a vapour pressure of a few millimetres of mercury (mmHg) [172]. GC fails when under complex mixtures. This is caused by the limited peak capacity of any chromatographic column. Bands travelling along the column undergo broadening. As a result, the number of individual bands that can be fully resolved at the outlet of the column is finite, even if the initial injection band width is infinitely small. This fundamental limitation cannot be overcome by simply modifying the chromatographic parameters. The only solution to the problem is to subject the sample separated by the GC column to additional separation based on a different mechanism, which results in two-dimensional separation.

Comprehensive two-dimensional gas chromatography (GC x GC) is one of the most powerful analytical tools for the analysis of organic compounds in complex matrices. There must be two orthogonal GC columns in the system that are coupled by some interface or modulator that is capable of either sampling or collecting the effluent from the first column and periodically introducing it to the second column. The interface must perform its task of sampling/collecting followed by injection at a rate that allows the original first dimension separation to be preserved. The technique is based on collecting continuous samples from a GC column and periodic injection, through a modulator, of small portions of the samples collected into a second GC column of different properties. The first column samples the components in time creating a primary retention time axis, then presenting them to the secondary column either individually or in greatly simplified sub mixtures. The secondary column provides an independent analysis of the dispersed sample eluting from the first column and disperses simplified sub-mixtures along a secondary retention time axis. This modulator collects material for a certain period of time, and then injects the entire fraction that it has collected into the second dimension column as a short chromatographic pulse. It then collects another fraction of effluent from the first column while the previous fraction is being separated on the second dimension column. This process of effluent collection and injection repeats itself throughout the entire analysis [173]. The secondary column disperses the sample along an axis orthogonal [174] to the first columns retention time axis to form a 2-D data space. The process is repeated at a rate fast enough that each peak from samples coming out of the first column is sampled at least three times with a flow modulator, preserving the separation achieved in the first column and providing samples for analysis in the secondary column. Results from the analysis have to be converted from the linear form to a 2-D representation using software algorithms.

Orthogonality occurs when two different and independent separation mechanisms are used. It is ideally achieved when there is no correlation between the retention in each of the columns. For example, separation on the first column may be achieved as a result of boiling points whereas in the second column medium polar, polar or shape selective separation can occur, resulting in two separation methods. In practice however perfect orthogonality is not achieved. From the example above the separation in the second column is partially achieved as a result of boiling point differences. The amount of orthogonality is however enough to separate very complex mixtures.

A modulator is the most important instrumental device in GC x GC [175]. Modulation is necessary to transfer the sample from the first column to the second, acting as a continuous injector for the second column. The main aims of the modulator are to trap/accumulate and refocus narrow adjacent fractions of the first column effluent and release them rapidly into the second column [176]. An overview of modulators used in GC x GC is also given in [175,176]. Without the modulator to sample the first column/dimension periodically, the bands may recombine in the second column and coelute at the detector or they may change their elution order. This will render the system to perform a 1D-GC analysis [177].

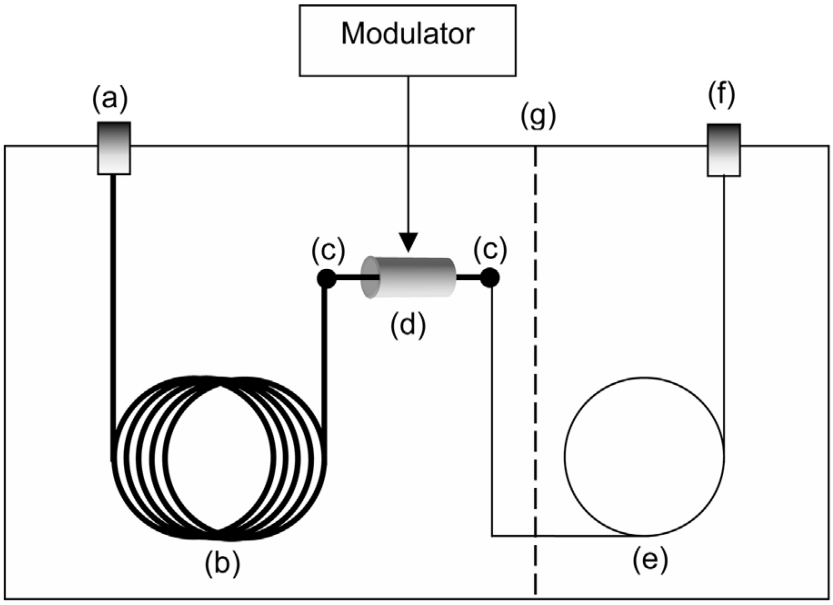

Figure 4.20 Block diagram of a GC x GC system. (a) injector; (b) primary column; (c) column connectors (at least one is necessary; multiple may be required depending on the exact configuration); (d) GC x GC interface; (e) secondary column; (f) detector; (g) optional division for secondary oven

Figure 4.20 shows a schematic of a GC x GC system obtained from [177]. Figure 4.21 also from the same reference gives representations of how GC x GC data is obtained. The observation at the detector is a series of second-dimension chromatograms that elute one after the other from the secondary column. If each peak sample is sampled at least 3 times, it will show up in at least 3 consecutive second dimension chromatograms. This data is usually plot on a 3 Dimensional plot and then displayed as a top down view in the form of a contour plot with primary retention time plot in the x axis and secondary retention time plot on the y axis. The peaks appear as spots of varying colour or contour lines. This is all done by software algorithms provided for analysis. The software usually uses the modulation period of the interface and the times to which pulses t1, t2 and t3 occur as seen in Figure 4.21, to slice the original chromatographic signal into its component second dimension chromatograms. The chromatograms are then aligned side by side to from the GC x GC retention plane which is plotted as seen in Figure 4.21 (D). Methods of calculating retention time are given in the reference. The resulting image for the GC x GC analysis can be seen in Figure 4.22.

GC x GC displays many advantages as discussed by Phillips et.al [174]. First, peak capacity is very larger than one dimensional GC i.e. the number of peaks that can be separated in either one or two dimensions is high. The peak capacity is ideally the product of the peak capacity of each column. Second, the retention in the second dimension is independent thus a measure of the secondary molecular property. Third, each compound/substance is identified by two independent retention measures and can be distinguished and identified better. Fourthly, the 2D chromatograph provides a more complete picture

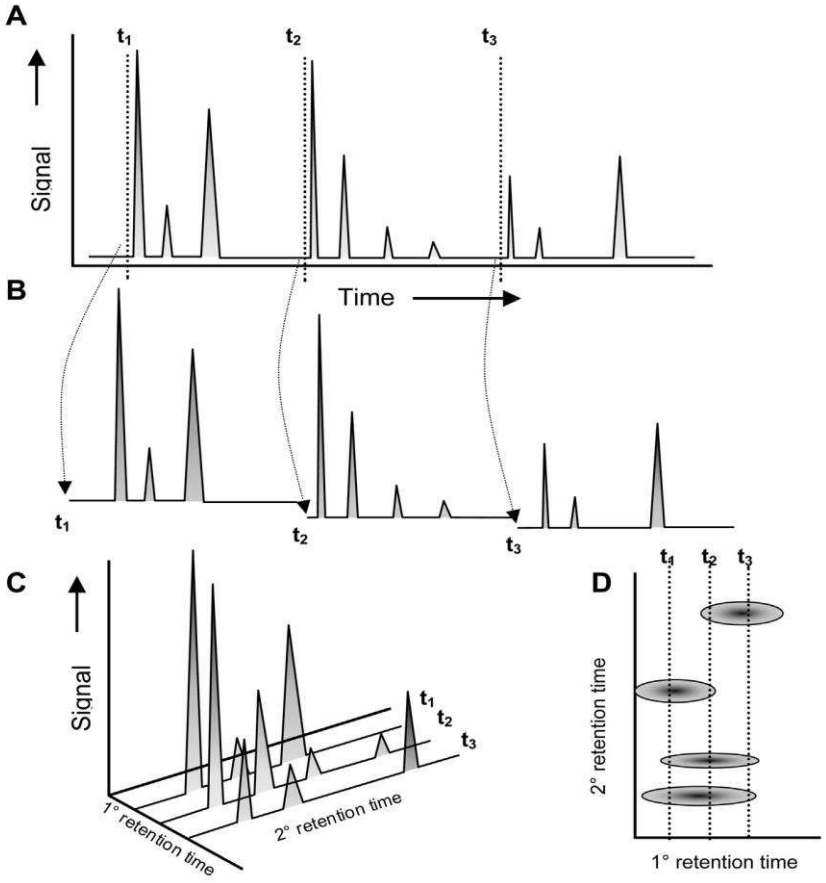

Figure 4.21 The interpretation of GC x GC data and generation of contour plots. (A) The raw GC x GC chromatogram consisting of a series of short second dimension chromatograms. t1, t2, and t3 indicate the times when injections to the second dimension column occurred. The computer uses these injection times to slice the original signal into a multitude of individual chromatograms (B). These are then aligned on a two dimensional plane with primary retention and secondary retention as the X and Y axes, and signal intensity as the Z-axis (C). When viewed from above, the peaks appear as rings of contour lines or colour-coded spots (D).

GC x GC finds applications in many areas, including; petroleum analysis, environmental analysis, forensics and many others. Vendeuvre et. al [178] and Mühlen et.al in 2006 [179] use comprehensive two-dimensional gas chromatography to characterise samples derived from petrochemicals. Westhuzen et.al in 2010 uses GC x GC on the analysis of Fisher-Tropsch oil products [180].

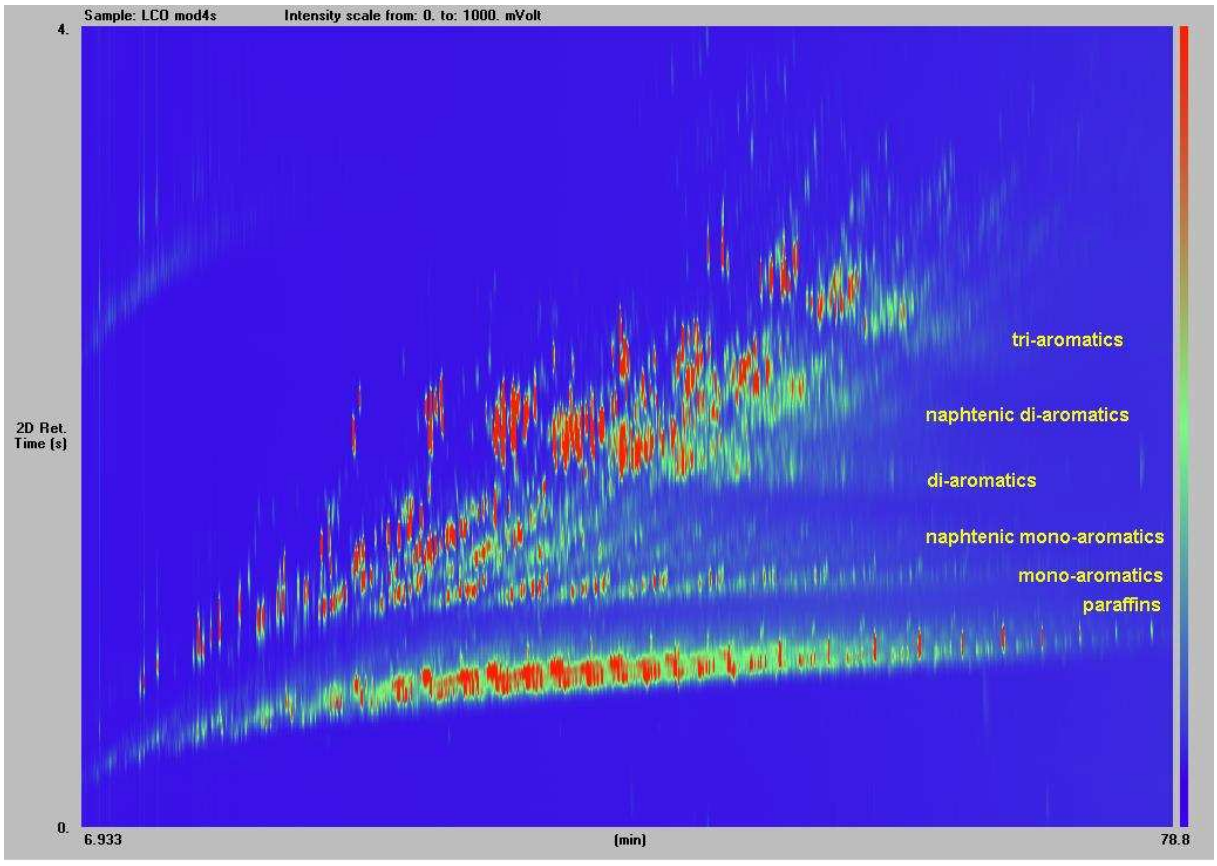

Figure 4.22 GC x GC analysis with FID of light cycle oil obtained from thermo electron corporation-Flavio Bedini.

4.4 GC x GC and Particle Counter Analysis and Results

Mixtures of hydrocarbons, such as those resulting from oil refining processes, i.e. diesel fuels form extremely complex molecules. The almost invariably contain very large numbers [181] of different components on all or most of the following classes:

(i) Saturated hydrocarbons (together known as alkanes or paraffins, and consisting of n-alkanes and branched alkanes; the latter are also called iso-alkanes)

(ii) Cyclic alkanes (known as napthenes and consisting of mono-, di- and multi-cyclic structures with various degrees of substitution)

(iii) Aromatics (consisting of mono-, di- and multi-ring structures with various degrees of substitution)

(iv) Components containing heteroatoms, such as sulphur, nitrogen, or oxygen. The first is easily the most abundant and it is present in several component classes (sulphide, disulphides, mercaptanes, thiophenes)

(v) Unsaturated hydrocarbons (known as alkenes or olefin, possibly divided into n-alkenes, iso-alkenes, cyclic alkenes, etc.)

(vi) Combined structures (components, that cannot be classifies in one of the above classes, containing for example, both aromatic and naphthenic rings).

Unsaturated hydrocarbons do not occur in natural oils, but they are formed in substantial amounts in thermal and catalytic cracking processes.

It is quite complex to analyse all these compounds together and thus the GC x GC was carried out to identify different classes of hydrocarbon mixtures in the fuels, i.e. paraffins, aromatics (mono-, di- and tri-), FAME and residuals. In addition to this, a particle count analysis was carried out to the ‘before’ and ‘after’ experimental fuel samples. The particle counter would

place the hypothesis discussed previously that soot/particulates were being formed as a result of aromatics pyrolysis like effect. Other physical properties of the fuels obtained from the results will also be analysed, i.e. density, flash point and viscosity.

The instrument used for the GC x GC analysis was an Agilent HP7890 GC, with dual column capability with a flame ionisation detector FID. The two columns used were (a) a boiling point column and (b) a column separating via polarity, thus giving 2D GC, boiling point separation on the x axis and polarity (double bonds) separation on the y axis. Switching between the two columns took place via a micro fluidic switch which was situated in the GC oven. An FID is a scientific instrument that measures the concentration of organic species in a gas stream. The operation of the FID is based on the detection of ions formed during combustion of organic compounds in a hydrogen flame. The generation of these ions is proportional to the concentration of organic species in the sample gas stream. Hydrocarbons generally have molar response factors that are equal to number of carbon atoms in their molecule, while oxygenates and other species that contain heteroatoms tend to have a lower response factor. The sample gas is introduced into a hydrogen flame inside the FID. Any hydrocarbons in the sample will produce ions when they are burnt. Ions are detected using a metal collector which is biased with a high DC voltage. The current across this collector is thus proportional to the rate of ionisation which in turn depends upon the concentration of HC in the sample gas. Carbon monoxide and carbon dioxide are not detectable by FID.

The software package used to evaluate the data produced was developed by a company called ZOEX. The results carried out here both of the GC x GC and particle count were done at SHELL GLOBAL SOLUTIONS using their equipment. Their scientists performed the measurements and provided the results back to us. In the analysis the changes are calculated

by subtracting the tests results minus the results of the fresh sample before experiment (Test sample results – Result of sample before test). The relative changes have been calculated as $\frac{test\ sample\ results - results\ of\ sample\ prior\ to\ test}{results\ of\ sample\ prior\ to\ test}$. The tests samples are obtained from the GC analysis of the sustained cavitation and heat test fuels after 40 hours each whereas the initial results sample are the GC results of the samples obtained prior to these tests.

The results will also show repeatability as dotted lines in the plots. The repeatability (r) is the variation in measurements taken by the instrument on the same sample under same conditions. Repeatability conditions occur when analyses are performed by the same analyst on the same day with the same instrument in the same laboratory. The relative standard deviation (RSD), or coefficient of variance, is used to compare the uncertainty between different measurements of varying absolute magnitude. The RSD is calculated from the standard deviation (σ), and is commonly expressed as a percentage (%):

$$\%RSD = \frac{\sigma}{\bar{x}} \times 100\%$$

Equation 4.1

where σ is the standard deviation of measured data and $\bar{x}$ is arithmetic mean of the data. These measurements have not been performed here but are available with the measurement equipment specifications.

4.4.1 Change in physical properties

Fuel Name	Density (g/cm^{-3})	Flash point (°C)	Viscosity (cSt)
BP Luton	0.8323	61.0	2.471
Esso A1	0.8331	60.0	2.175
Shell Flitwick	0.8392	60.0	2.699
Tesco Dunstable	0.8333	67.0	2.832
Texaco Leagrave	0.8323	59.0	2.513
Total Luton	0.8325	66.0	2.723
AGED			
BP Toddington	0.8324	60.0	2.643
Tesco Flitwick	0.8338	67.0	2.645
Texaco MK	0.8286	63.0	2.502
Total Luton	0.8382	62.0	2.824

Table 4.1 Physical properties of the initial commercial fuel samples before the tests were carried out

Various physical properties of the diesel fuels were obtained from the analysis, namely: density, flash point and viscosity. The effects of forty hours cavitating flow and forty hours heat test on the physical properties of the fuel will be compared is the section to follow. Table 4.1 shows the density (g/cm^{-3}), flash point (ºC) and viscosity (cSt) of the commercial diesel fuel samples obtained prior to the experimental analysis of forty hours cavitating flow and forty hours heat test.

4.4.1.1 Density

The density of a fuel can indicate certain fuel composition ranges. This information can provide predictions of fuel economy, power, deposits, wear and exhaust smoke [62]. For example, a diesel fuel with increased density contains more energy per gallon (heating value). Such a fuel would tend to improve fuel economy. However an excessively high density could result in increased engine deposits and smoke. Density however is not the sole determining factor in predicting such performance parameters, but it is a useful test as it can be performed

very easily by a hydrometer. SHELL Flitwick and TOTAL Luton Aged have the highest initial density at 0.8392 g/cm^{-3} and 0.8382 g/cm^{-3} respectively as seen in Table 4.1.

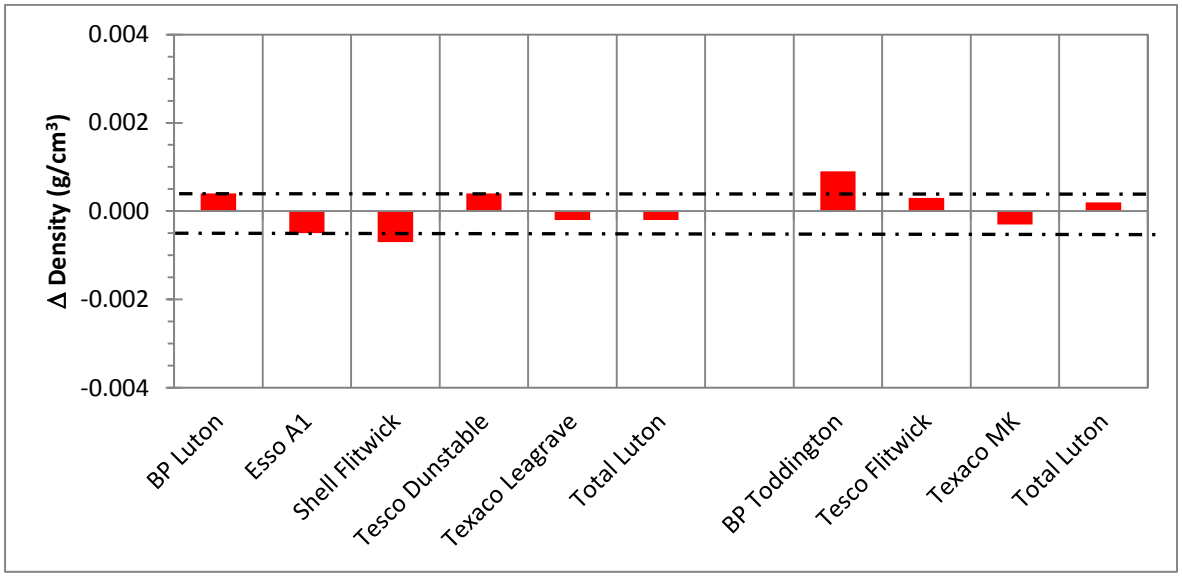

Figure 4.23 Change in Density (g/cm^{-3}) for commercial fuels as a result of forty hours of cavitating flow

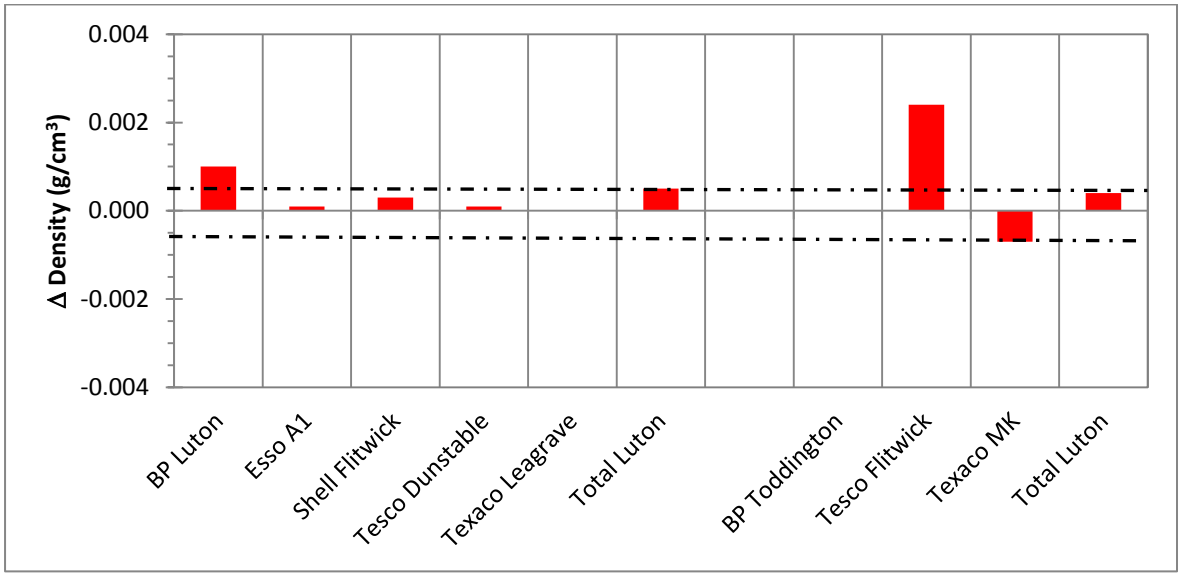

Figure 4.24 Changes in Density (g/cm^{-3}) for commercial fuels as a result of forty hours of discontinuous heat tests

Figure 4.23 and Figure 4.24 show changes in density in g/cm^{-3} for all the commercial diesel fuels as a result of forty hours cavitating flow tests and forty hours of discontinuous heat tests with a %RSD of ±0.0005. The dashed lines on these graphs and the graphs to follow in this chapter represent measurement repeatability in %RSD. The changes in density were

calculated by subtracting the density obtained from the test from the density of the initial sample tested. It can be observed that the changes in density occurring as a result of the forty hours of cavitating flow are different to the ones observed from the forty hours heat tests.

There is no consistent change observed in the case of the forty hours cavitating flow. The density of 5 commercial fuels increases whereas it decreases for the rest. The largest change occurring in BP Toddington of which increased by 0.0009 g/cm^{-3} and in SHELL Flitwick which decreased in density by 0.0007 g/cm^{-3}.

The changes in density from the forty hours heat test show a more consistent change. All fuels increase in density as a result of forty hours of discontinuous heat tests apart from TEXACO MK which decreases in density by 0.0007 g/cm^{-3} as a result of forty hours of discontinuous heat tests. The maximum increase in density occurred in TESCO Flitwick of 0.0024 g/cm^{-3}.

Overall, the changes in density of the commercial fuels as a result of forty hours of cavitating flow and heat tests were very small but a change nonetheless. Both experiments displayed different changes occurring in density as a result of the processes undergone under cavitation and under heat tests. The relative changes in density with respect to the initial value before the tests were very small in the ranges of less than 0.01 % (BP Toddington) for the cavitating flow tests and 0.3 % (TESCO Flitwick) for the heat tests. However these are both aged samples.

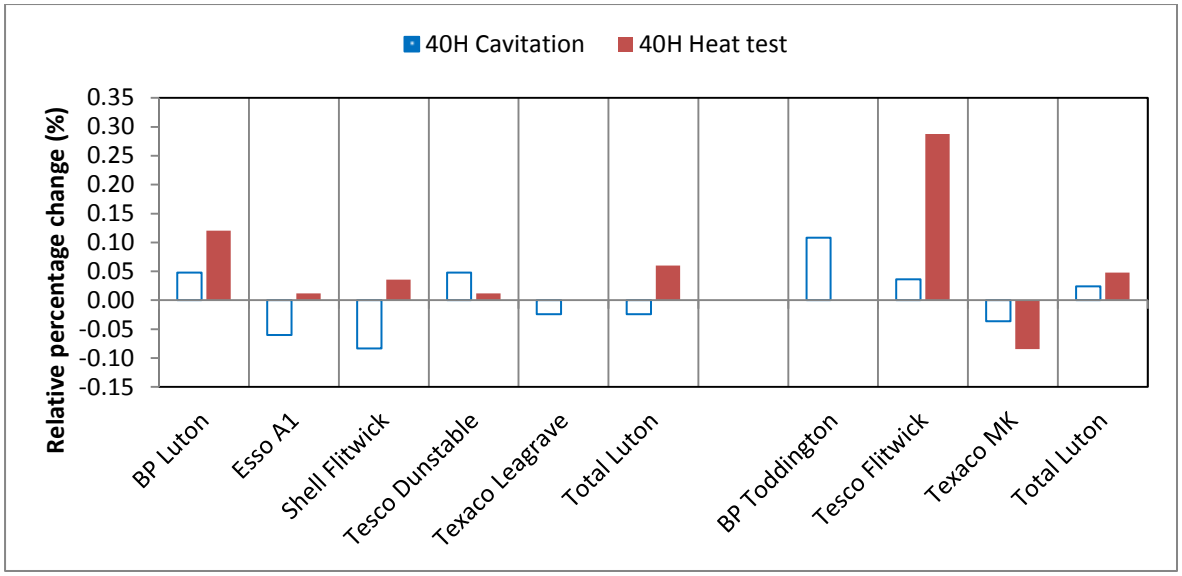

Figure 4.25 Relative percentage changes in density of the commercial diesel fuels with respect to the initial density prior to sustained cavitation and heat tests.

Figure 4.25 show the relative percentage changes of both 40 hour sustained cavitating flow and 40 hour heat tests. The results show no consistent change in density over the samples tested. Depending of the constituents of the fuels, various changes maybe occurring in the fuels and this will be different per fuel. The highest relative change in density observed was 0.288 % ± 0.001% in TESCO Flitwick aged. Apart from TEXACO MK results, all the other sustained heat test results show a positive relative change. There is a 50:50 count for the sustained cavitation results where half show positive changes whereas the other half undergo negative changes in density.

Injection equipment as mentioned earlier meters fuel on a volume basis and thus any variations will affect the power output. Fuel with higher density will have a higher mass flow rate for the same injection conditions. However the data here suggests a very small change in density and thus the effects may not be significant.

4.4.1.2 Flash point

Flash point of a fuel is important in connection with its safety, storage and handling. The minimum flash point standard as observed in Chapter 2 for diesel fuels is 55 ºC. The flash point of a fuel does not directly affect its engine performance. The flash points displayed below have repeatability of 1.8 ºC and as guidance the dotted lines have been placed on the graph. The results in Figure 4.26 show a positive change in flashpoint as a result of forty hours of cavitating flow with a %RSD of ±1.8. BP Luton undergoes no change in flash point as a result of forty hours of cavitation. The maximum change observed is by SHELL Flitwick of 3 ºC.

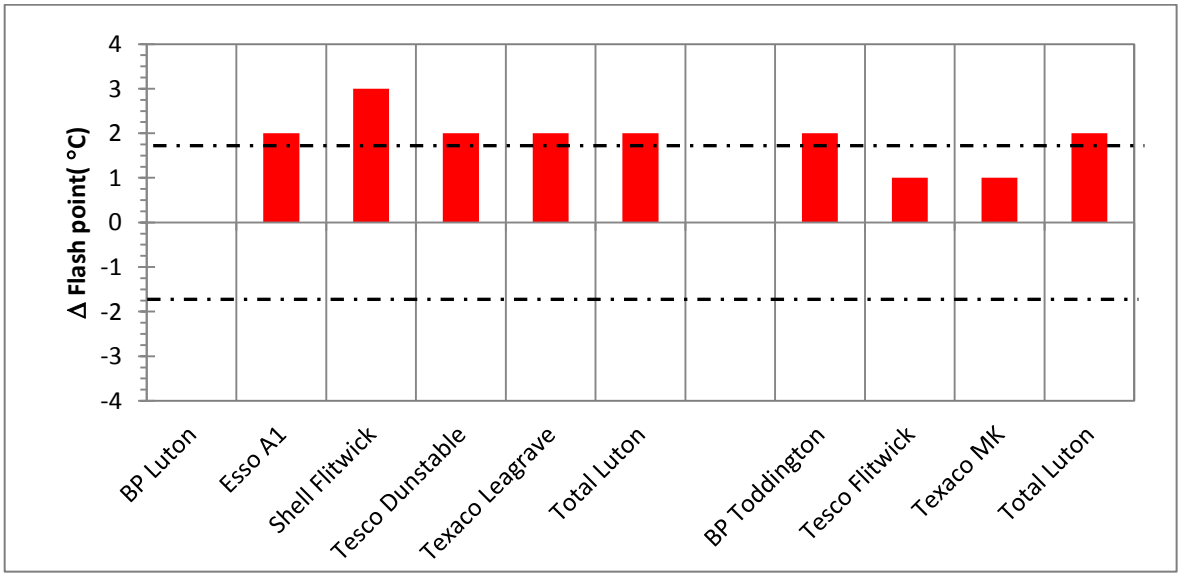

Figure 4.26 Change in Flash Point (ºC) for commercial fuels as a result of forty hours of cavitating flow

The results in Figure 4.27 show changes in flashpoint as a result of forty hours of discontinuous heat tests. The results display changes in flash point are lower than those displayed by the forty hours cavitation tests. In contrast the flash point of BP Luton changed by 0.5 ºC as a result of forty hours heat test to no changes occurring over the forty hours cavitating flow. Negative changes are also observed in the aged fuels, the flash point of TEXACO MK and TESCO Flitwick decreases by 0.5 ºC and 1.5 ºC respectively.

Positive relative changes in flash point were observed from Figure 4.28 apart from the results obtained form 40 hour heat tests for TESCO and TEXACO aged fuels. The maximum relative change observed is 5 % ± 0.001% by SHELL Flitwick. All sustained cavitation results show a positive relative increase in flash point.

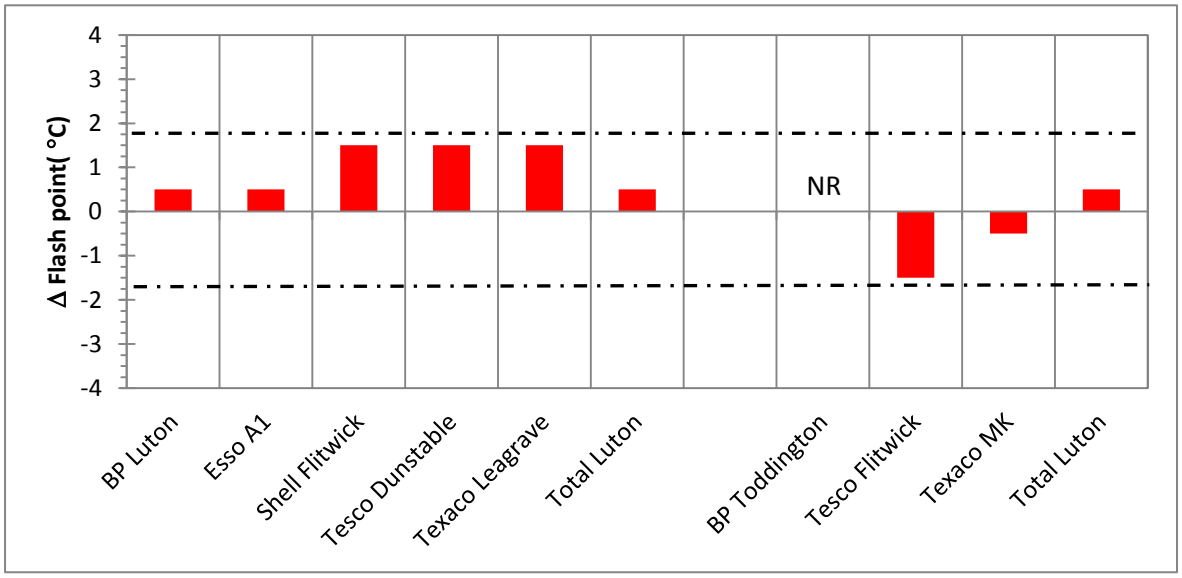

Figure 4.27 Changes in Flash Point (°C) for commercial fuels as a result of forty hours of discontinuous heat tests

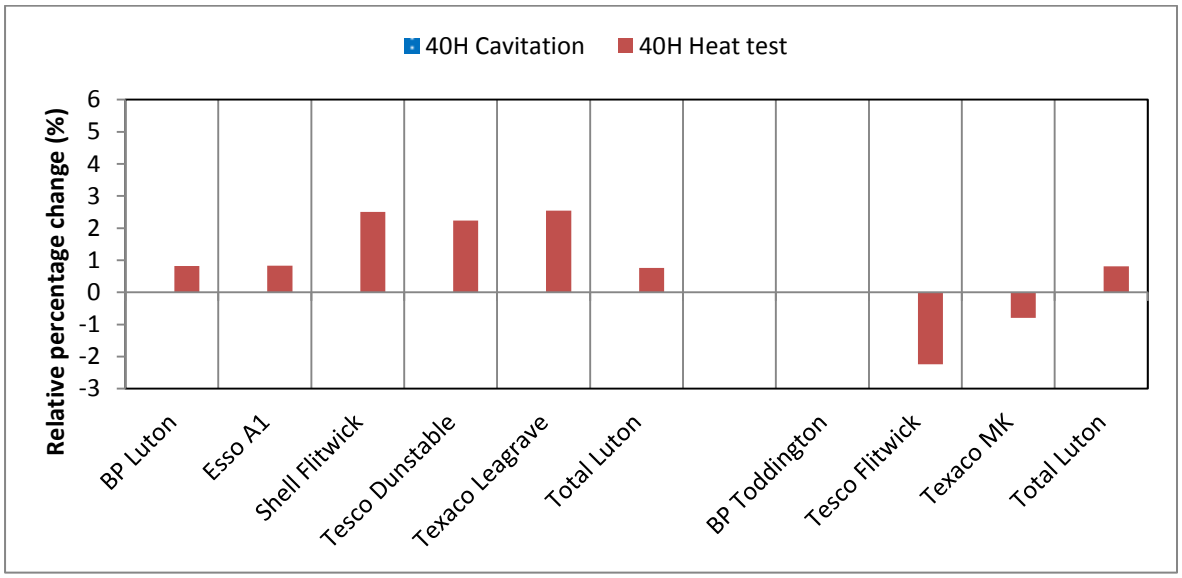

Figure 4.28 Relative percentage change in flash point of the commercial diesel fuels with respect to the initial flash point prior to sustained cavitation and heat tests.

As the initial flash points of all fuels started off higher than the 55 ºC limit and most of the changes displayed an increase in flash point, the fuels would still deemed to be safe for storage and handling either in the fuel tank of the car or otherwise.

4.4.1.3 Viscosity

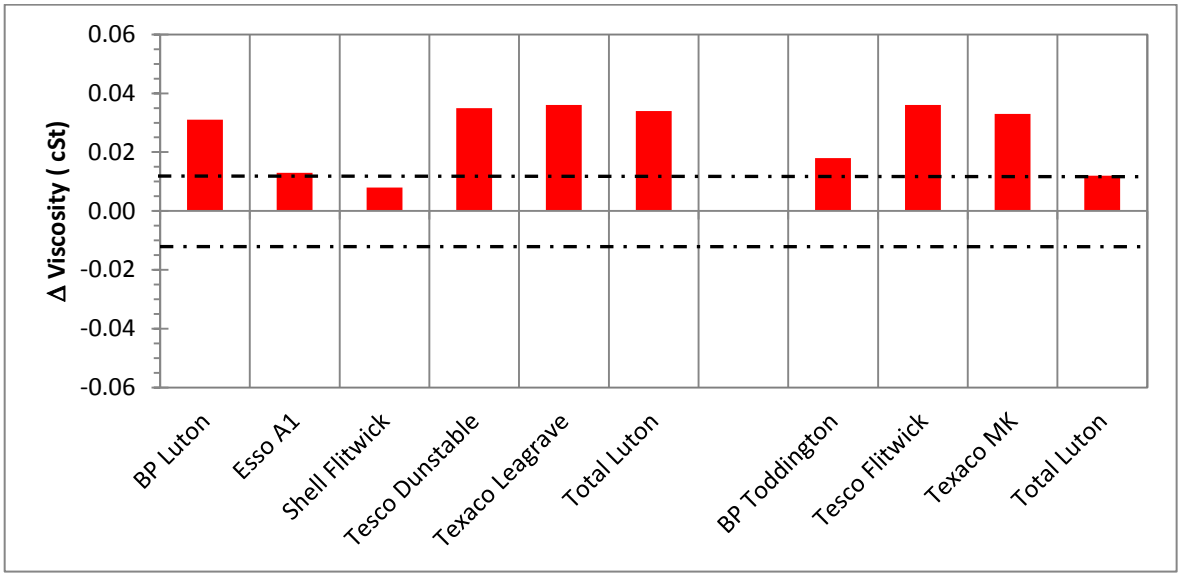

Figure 4.29 Change in Viscosity (cSt) for commercial fuels as a result of forty hours of cavitating flow

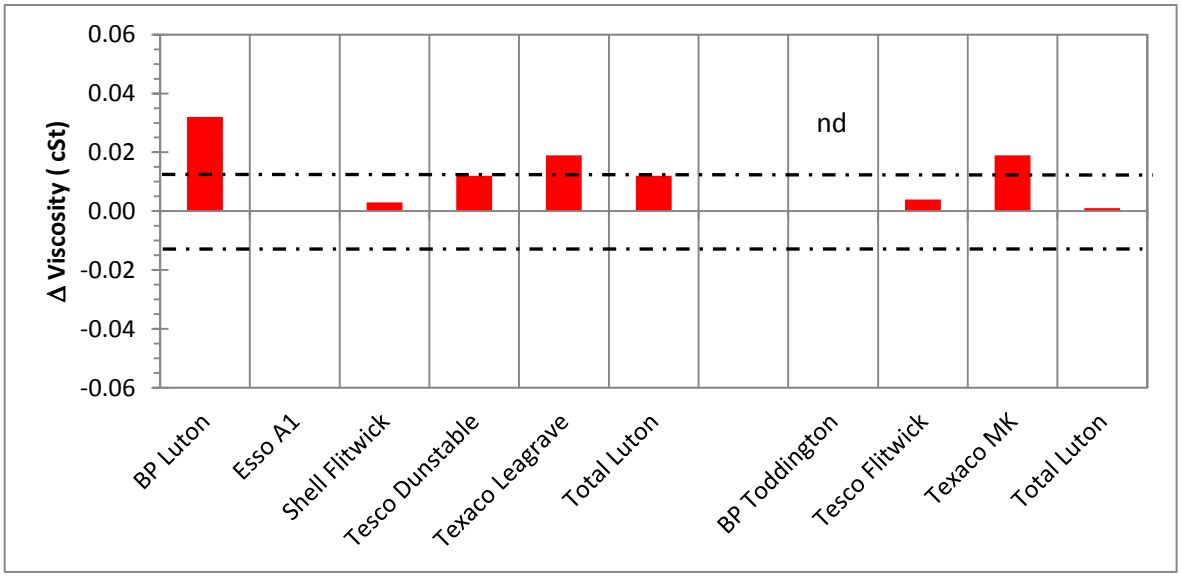

Figure 4.30 Change in Viscosity (cSt) for commercial fuels as a result of forty hours of discontinuous heat tests

Viscosity of diesel fuels is an important property and impacts the performance of fuel injection systems. If too low, it may cause excessive wear and power loss in injector pumps due to injector or pump leakages. If too high, it may cause too much pump resistance and adversely affect fuel spray patterns. The minimum and maximum viscosity as per requirements for emission control are 2 mm^2/s and 4 mm^2/s respectively. 1 mm^2/s is equal to 1 cSt.

Figure 4.29 show the effects on viscosity due to forty hours of cavitating flow with a %RSD of ±0.016. All changes occurred were positive increases in viscosity. The maximum changes in viscosity as a result of forty hours cavitation were displayed by BP Luton, TESCO Dunstable, TEXACO Leagrave, TOTAL Luton (new), TESCO Flitwick and TEXACO MK in excess of 0.03 cSt.

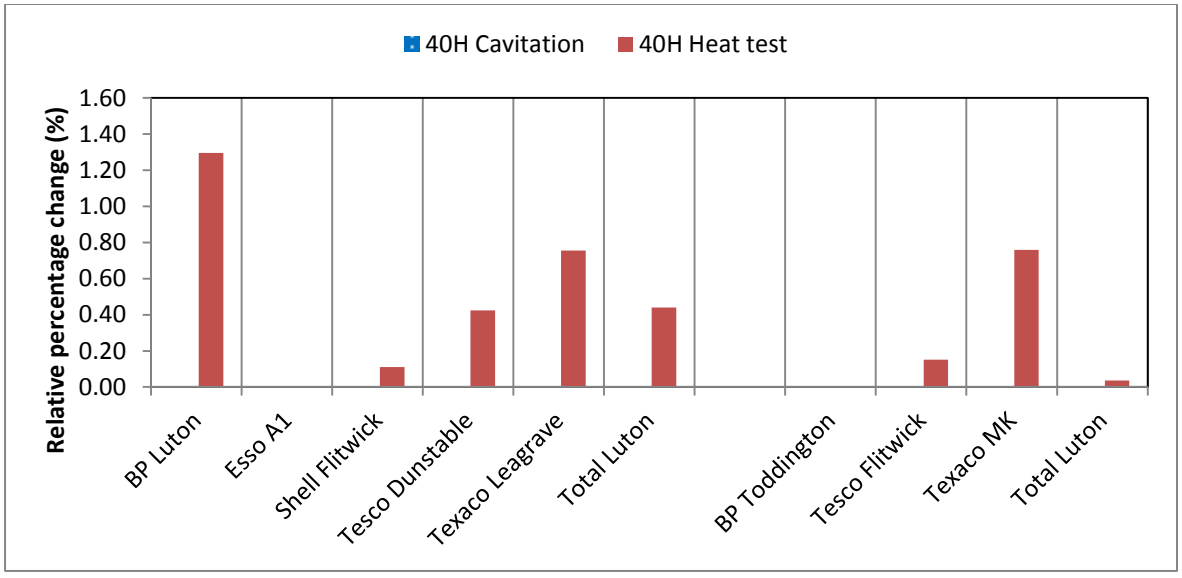

Figure 4.31 Relative percentage changes in viscosity of the commercial diesel fuels with respect to the initial viscosity prior to sustained cavitation and heat tests.

Figure 4.30 shows the effects on viscosity due to forty hours of heat tests. All changes occurring hear are also positive but are very low in comparison to the effects on viscosity due

to forty hours cavitation. The maximum change in viscosity observed as a result of forty hour heat test was in BP Luton of 0.032 cSt.

Sustained cavitating flow causes relatively higher changes in viscosity when compared to the 40 hour heat test results as seen from Figure 4.31. There is a positive relative change observed in both test cases for all fuels and no changes were observed from the ESSO A1 heat test result.

The changes in viscosity observed are all positive and because all the fuels had an initial viscosity above the minimum 2 cSt, they are still within the requirements for emission control and market demand. Temperature may have had some effect in the increase in viscosity of the fuels; however the impact of cavitating flow still caused more increase in viscosity of the commercial fuels than the impact of temperature only. The effects of high fuel viscosity have been discussed in Chapter 2. Effects of viscosity on internal nozzle cavitation and atomisation are well known and have been discussed in the same chapter. An increase in fuel viscosity would result in reduction in cavitation in nozzle passages due to resistance of flow. Increase in viscosity also results in thinning of spray angles, and lower spray tip penetration. Fuels of lower viscosity also result in smaller droplet diameters than fuels with higher viscosity as observed by [120].

Viscosity is a measure of a fluid's resistance to flow. It describes the internal friction of a moving fluid. A fluid with large viscosity resists motion because its molecular composition gives it a lot of internal friction. A fluid with a low viscosity flows easily because its molecular composition results in very little friction when it is in motion. The changes in chemistry of the fuels are discussed in the section 4.4.2 below. Section 4.4.3 discusses the

formation of particles as a result of these experiments. It is thought that a change in composition of the fuels and the formation of particles is the result of the increase in viscosity observed of the fuels. The formation of particles in the fluid maybe resulting in an increased internal friction in a moving fluid and thus it has a higher viscosity.

4.4.2 Chemistry and chemical structure

The two dimensional plots obtained from the GC x GC analysis contained individual species in each sample are too complex to identify in all the individual peaks and thus the samples are generically classified i.e. by aromatic, FAME, paraffins and residuals as mentioned previously based on percentage peak volumes. This was done by the company carrying out the analysis. Software enables the creation of class and subclass regions in the acquired chromatogram based on retention times. Classification then grouped the compounds into the structure based chemical classes and quantified peak/compound groups precisely by peak areas. The chromatograms showed retention time in the first dimension in the x axis and retention time in the second dimension in the y axis. The compounds classifications were then colour coded to enable easy determination. The aromatics were further classified into mono-, di- and tri-aromatics. The FAME was identified by ester components present.

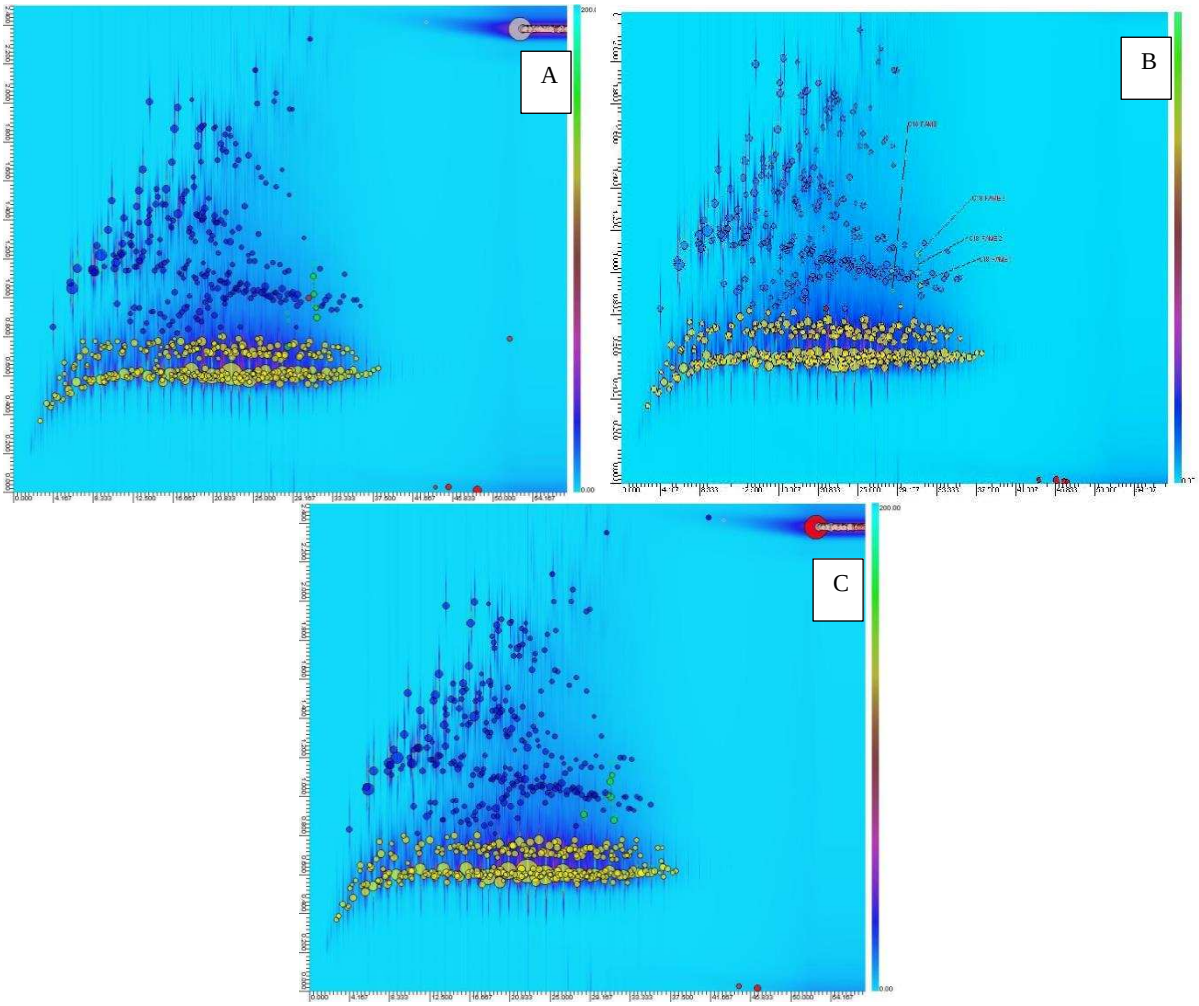

Figure 4.32 Figures obtained from the GC x GC analysis of Shell Flitwick A-initial sample, B- forty hours cavitating flow sample an C- forty hour discontinuous heat test sample.

Figure 4.32 shows the results of SHELL Flitwick obtained from the initial sample, the sample after forty hours cavitation and the sample after forty hours of discontinuous heat test. The bubbles were colour coded: Green represented paraffin species; blue/dark blue represents aromatic species. The FAME species were labelled in (B). This was carried out for all the diesel fuel samples apart from the 2 model fuels. The model fuels could not be sent to analyses due to non-disclosure of its detail composition. As it is observed from these figures, it is very complex to identify specific species and how they change over the different tests. This is the reason for their grouping. This does take out the quantitative analysis of each component, but gives us an overview of what is happening to the overall classes of

compounds. The peak area percentages of each class were obtained and will be displayed in the later sections of this chapter.

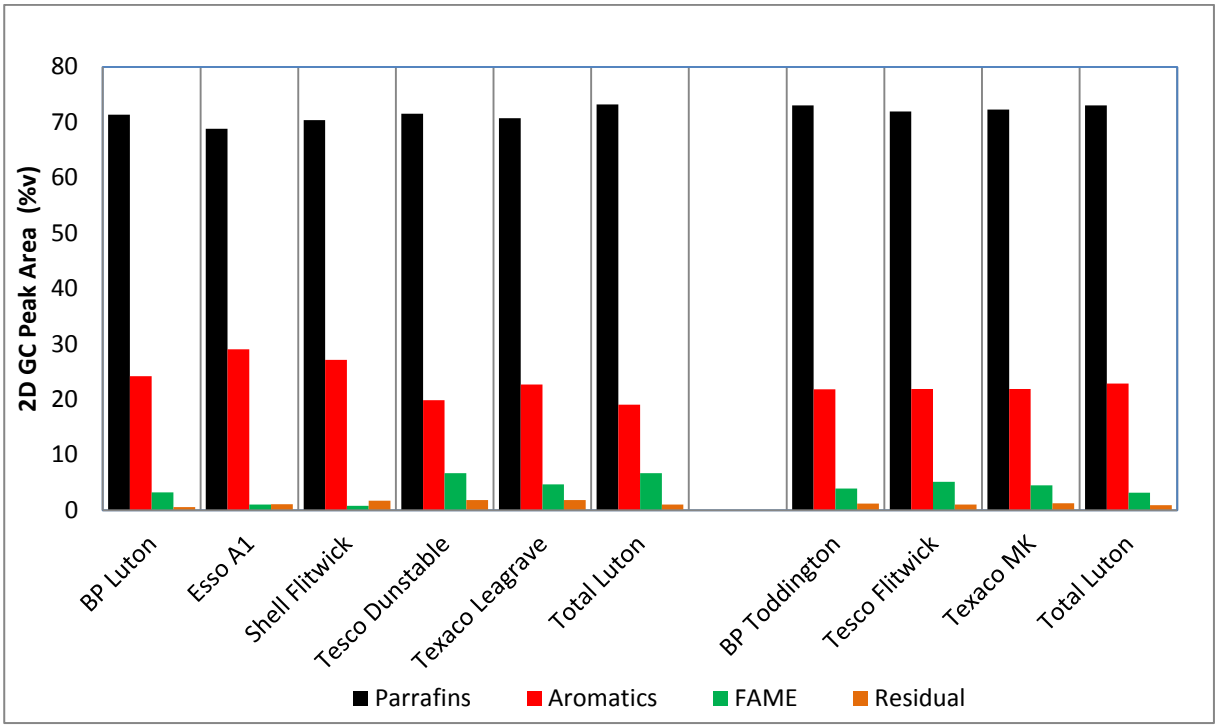

Figure 4.33 The initial composition of the fuels prior to cavitation Obtained from the GC x GC peak area (%v)

Figure 4.33 shows the initial diesel sample before experiment peak area percentages (%v) for all the commercial diesel fuels in their classes. The fuels consist on average 71 % paraffins, 23 % aromatics, 5 % FAME and 1 % residuals on a volume to volume (v/v) basis. Table 4.2 shows the initial aromatics breakdown in the fuels before any tests were carried out. The table shows the percentage mono-aromatics, di-aromatics and tri(+)aromatics in the fuels. The fuels contain between 21-30 %v/v total aromatics

Fuel Name	Mono aromatics (% v/v)	Di aromatics (% v/v)	Tri (+) aromatics (% v/v)	Total aromatics (% v/v)
BP Luton	23.4	2.7	0.3	26.4
Esso A1	22.1	4.9	0.3	27.3
Shell Flitwick	24.8	4.6	0.5	29.9
Tesco Dunstable	19.2	2.3	0.2	21.7
Texaco Leagrave	22.8	3.1	0.4	26.3
Total Luton	18.6	2.4	0.3	21.3
AGED				
BP Toddington	20.6	2.2	0.3	23.1
Tesco Flitwick	19.6	2.4	0.3	22.3
Texaco MK	20.6	2.2	0.3	23.1
Total Luton	20.7	3.3	0.4	24.4

Table 4.2 Initial Aromatics composition break down of the commercial diesel fuels obtained from the GC x GC analysis

4.4.2.1 Paraffins

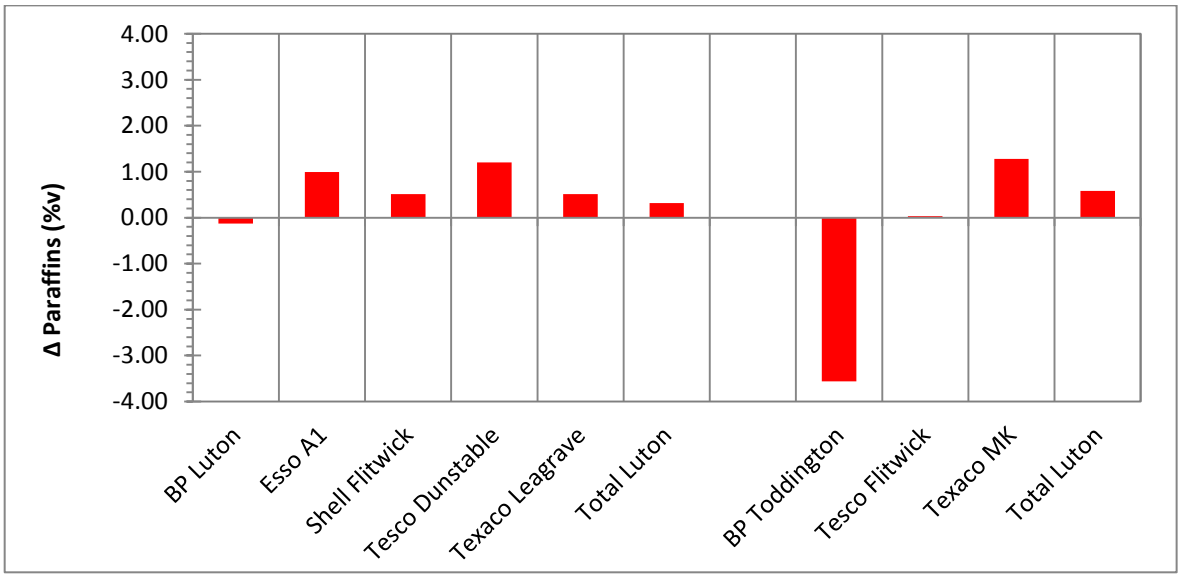

Figure 4.34 Relative changes in Paraffins (%v) for commercial fuels based on GC x GC peak area as a result of forty hours of cavitating flow

Figure 4.34 shows the changes in paraffin composition due to the effects of cavitating flow. The results show that most commercial fuels display an increase in the percentage volume of paraffins as a result of the effect of sustained cavitating flow. BP Toddington, an aged fuel, shows a large decrease in paraffins by 3.56 % volume as a result of sustained cavitating flow. The percentage volume has been determined by the percentage peak area occupied by paraffins as a result of GC x GC on the samples before and after cavitation. The largest

increase in paraffins is by TESCO Dunstable (1.20 %v) and TEXACO MK Aged (1.28 %v). TESCO Flitwick aged and BP Luton displayed negligible changes in paraffins as a result of forty hours of sustained cavitating flow.

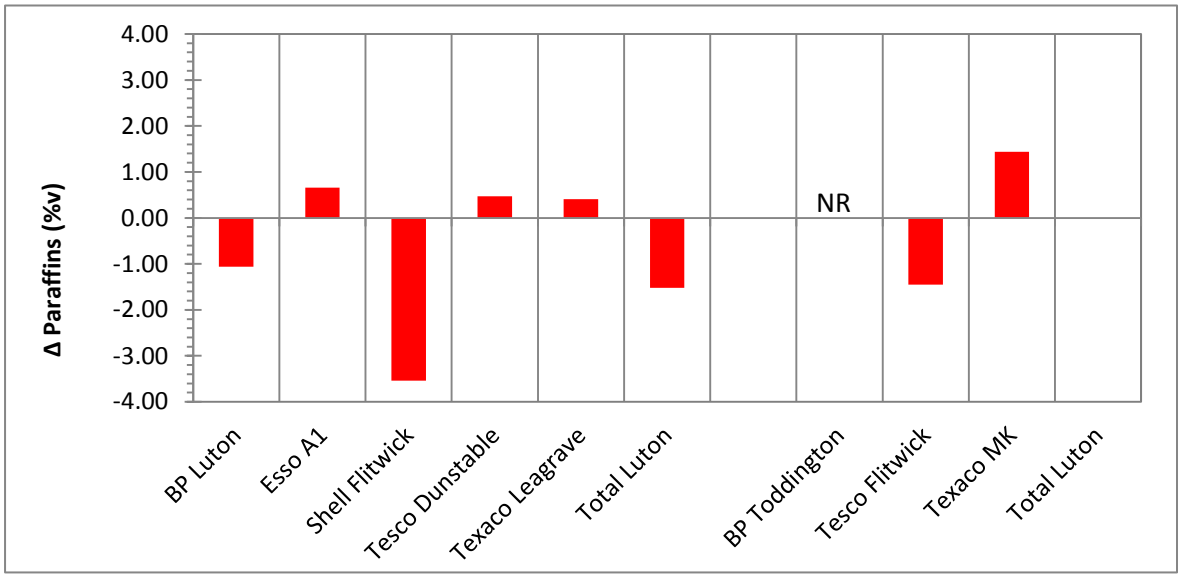

Figure 4.35 Relative Change in Paraffins (%v) for commercial fuels based on GC x GC peak area as a result of forty hours of discontinuous heat tests

Figure 4.35 shows the changes in paraffins from GC x GC peak area percentage obtained of the heat tests on the commercial fuels. The results show no relation to the results obtained of the change in paraffins as a result of forty hours of sustained cavitating flow. SHELL Flitwick underwent a large decrease in the percentage volume of paraffins (-3.54%v) as a result of discontinuous heat tests. The same amount of decrease was observed by BP Toddington as a result of forty hours of sustained cavitating flow. TEXACO MK and TEXACO Leagrave underwent the similar changes in percentage volume of paraffin in both cases but had an increase/decrease as a result of heat tests by 0.16 % v and 0.1 %v respectively.

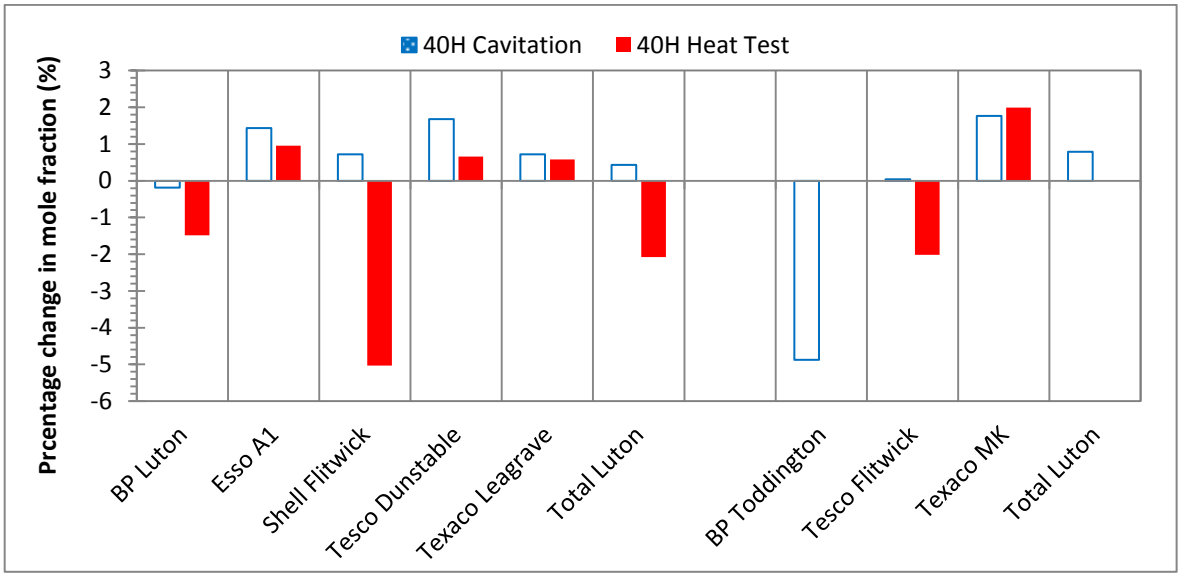

Figure 4.36 Relative percentage change with respect to the initial percentage volume in Paraffins of the commercial diesel fuels prior to sustained cavitation and heat tests.

Figure 4.36 shows the relative percentage changes in paraffins to the original composition. The results show quite different changes in paraffins as a result of cavitation and heating tests of the commercial diesel fuels. This depends on the chemical reactions occurring and whether there is formation or consumption of paraffins from other species. It is observed that the changes show a large decrease in relative percentage volume of paraffins as high as 4.87 % ± 0.01 % occurring as a result of sustained cavitation in aged BP Toddington and 5.03 % ± 0.01 % as a result of 40 hours of heat tests in SHELL Flitwick. The maximum increase in relative percentage of paraffins occurred as a result of 40 hours heat test in Texaco MK aged which also showed the highest positive change in paraffins as a result sustained cavitation.

Paraffins show a relatively small change as a result of both sustained cavitation and heat tests carried out apart from aged BP Toddington as a result of cavitation and SHELL Flitwick as a result of heating. These two fuels display a surprisingly large result. Unfortunately the tests could/cannot be repeated to verify the results. If the results are correct then the changes in paraffins may be due to various factors i.e. fuel stability of the aged fuel undergoing

cavitation; the composition of paraffins in the fuel (iso-, n-, cyclic); or possibly lighter paraffin fractions content in both fuels which may have evaporated during the tests. There is also a possibility that heavier fractions may have broken down into lighter fractions as a result of the tests and these lighter fractions may have evaporated during the tests. The exact paraffin content in the fuels is not known and thus it is not possible to exactly identify the cause of the large change in paraffin of the two fuels. Cyclo-paraffins generate less unsaturated low boiling point hydrocarbons than n-paraffins and form relatively more benzene, thought to be the result of dissociation of C-H bonds in the direct benzene formation process [182]. For the Naphthene and iso-paraffinic hydrocarbons, the temperature at the start of decomposition is lower than for n-paraffins, and decomposition ratio is higher. The lower fraction hydrocarbon content formed as a result of thermal decomposition, increases in all fuels and there are differences in the temperature where it begins to decrease as well as in the start of formation temperature, the quantity and the temperature of the start of reductions for the different compounds. The cause is thought to have been due to different compositions of paraffin content i.e. n- paraffins, iso-paraffins, napthenes; in the fuels disintegrating/decomposing into aromatics/lighter fraction paraffins.

4.4.2.2 Mono-aromatics

Figure 4.37 shows the change in aromatics obtained from the GC x GC peak area as a result of forty hours sustained cavitating flow with a %RSD of ± 0.59. The results show a significant decrease in relation to the initial composition of mono-aromatics for all the fuels up to 0.9 % v for SHELL Flitwick and 0.8 %v for BP Luton. A decrease is observed for all commercial fuels in mono-aromatics between 0.3 % v to 0.9 %v. The only increase observed is in aged TEXACO MK by 0.1 %v.

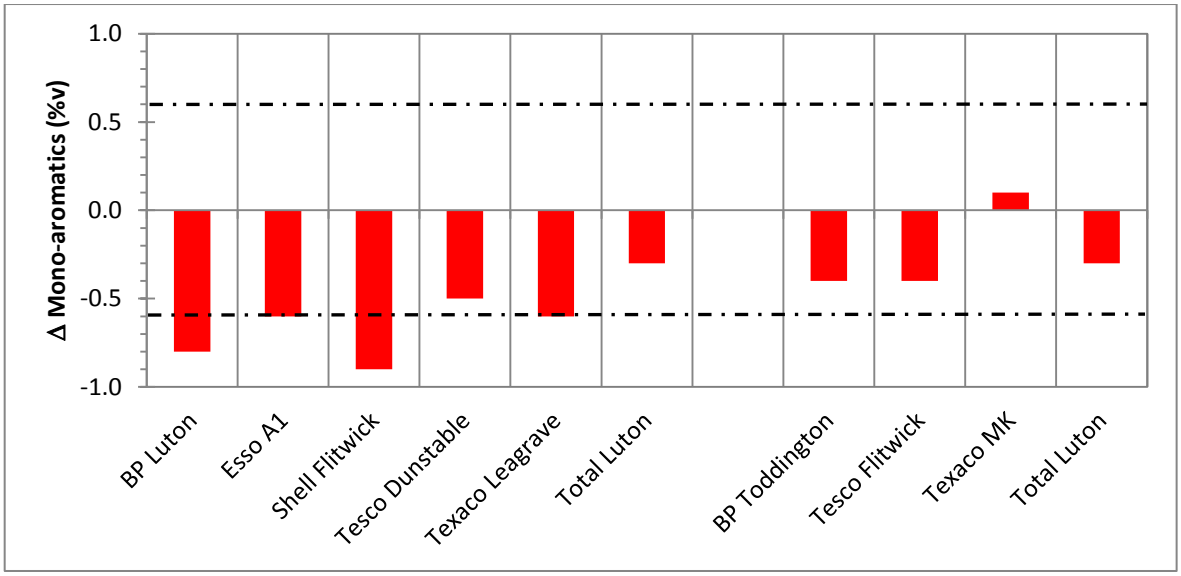

Figure 4.37 Change in Mono-Aromatics (%v) for commercial fuels as a result of forty hours of cavitating flow

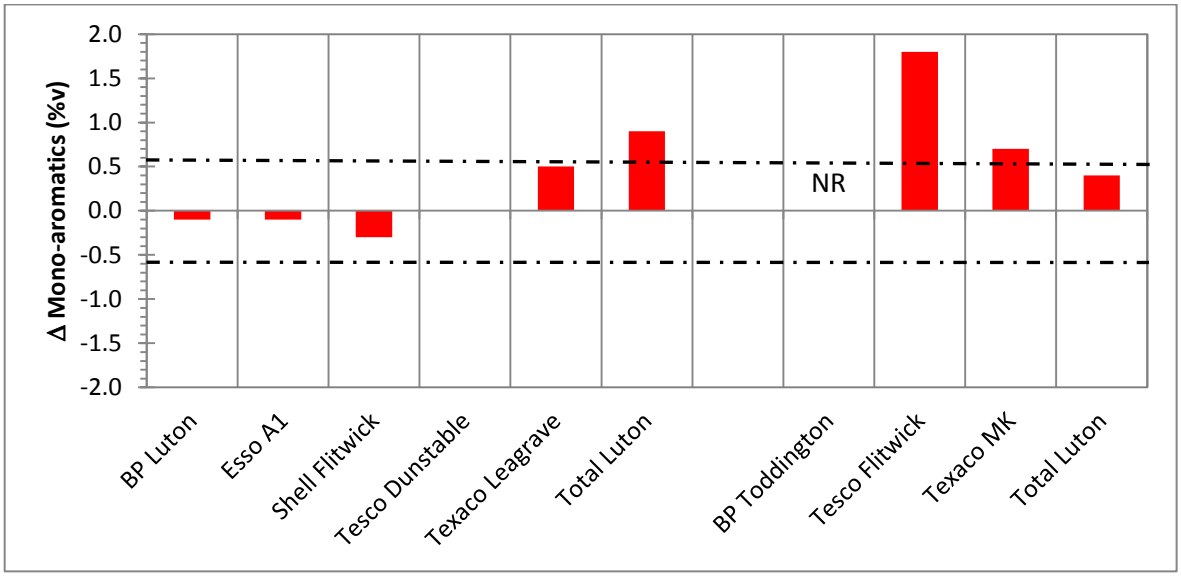

Figure 4.38 Change in Mono-Aromatics (%v) for commercial fuels as a result of forty hours of discontinuous heat tests

The heat tests conducted on the fuels show an overall increase in the percentage volume of mono-aromatics as observed in Figure 4.38. The largest increase in percentage volume of aromatics was observed in aged TESCO Flitwick of 1.8 %v. The increases in mono-aromatics varied from 0.4 %v in Aged TOTAL Luton to 1.8 %v in TESCO Flitwick. The only decrease observed was in BP Luton (0.1 %v), ESSO A1 (0.1 %v) and SHELL Flitwick (0.3 %v).

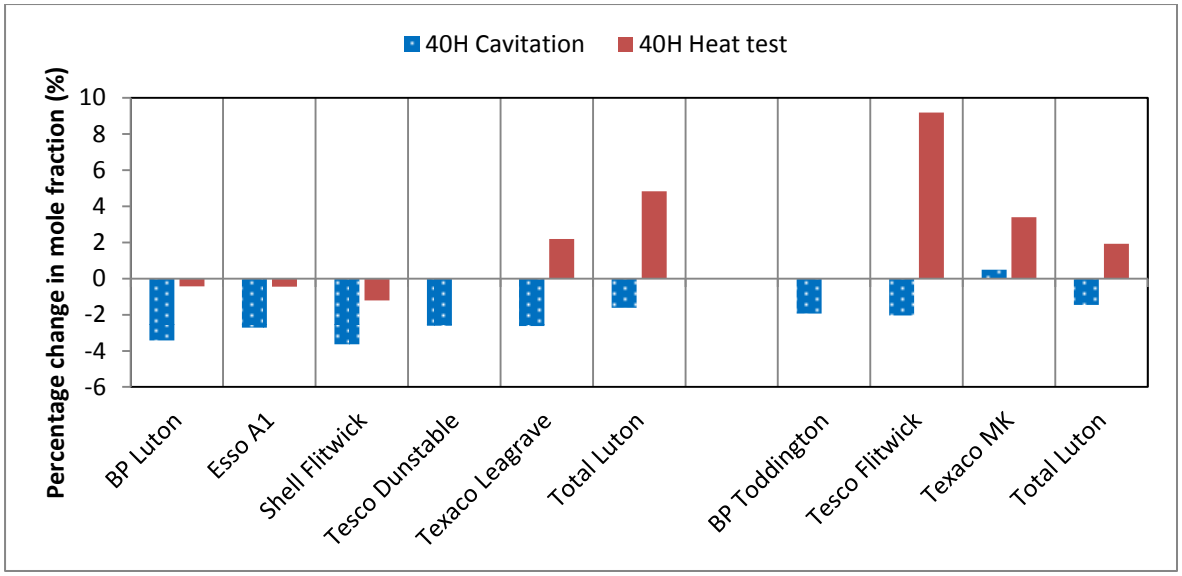

Figure 4.39 Relative percentage change with respect to the initial percentage volume in mono-aromatics of the commercial diesel fuels prior to sustained cavitation and heat tests.

The changes observed in mono aromatics as a result of forty hours of cavitation defers from the changes occurring as a result of forty hours of discontinuous heat tests which once again suggest that they are undergoing totally different chemical changes. This is seen by the comparison of Figure 4.37 to Figure 4.38. As a consequence of hydrodynamic cavitation, the mono- aromatics content in the fuel is observed to decrease for all the fuels, however the change is not consistent as a consequence of the heat test. The results from the heat tests are observed to cause small changes either negative or positive for the new fuels and positive for the aged fuels. This suggests that they may be undergoing different chemical processes. The repeatability of both results is 0.59 %v as marked on the graphs by the dotted lines.

Relative percentage changes in mono aromatics composition can be observed in Figure 4.39. Fuels tested from the sustained cavitating flow analysis display negative relative changes of up to 3.63 % ± 0.01 % with respect to the original composition by volume. The increase in the formation of mono aromatics was observed in the results from TESCO Flitwick aged of 4.84 % ± 0.01 %. This however was the only change occurring from heat tests analysis that resulted in a large change in mono aromatics than sustained cavitation results.

4.4.2.3 Di-aromatics

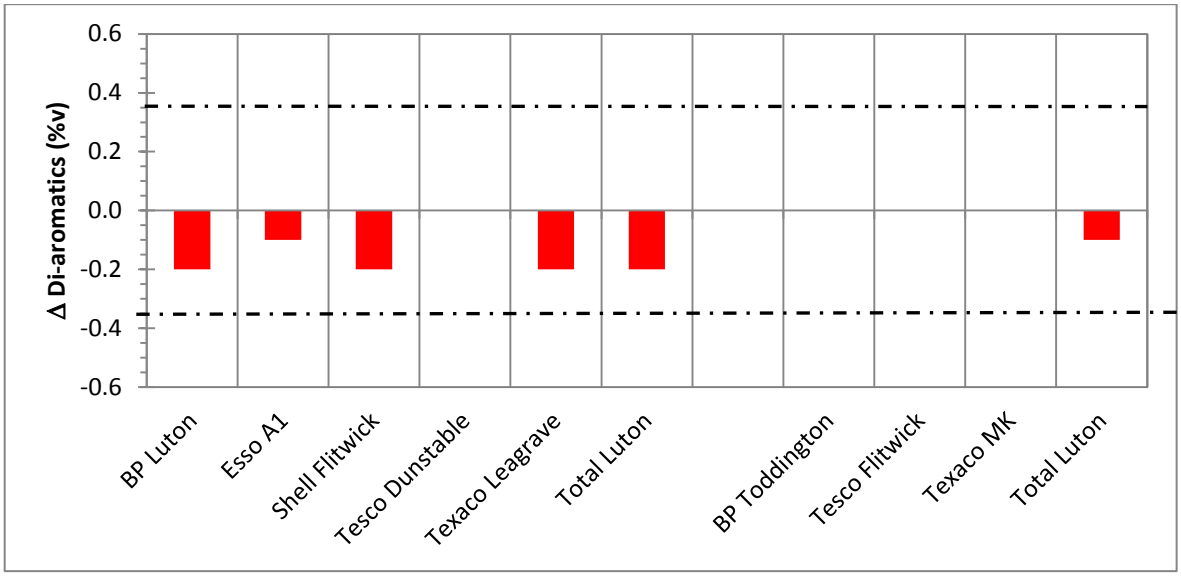

Figure 4.40 Change in Di-Aromatics (%v) for commercial fuels as a result of forty hours of cavitating flow

The effect of forty hours of cavitation on the di-aromatics can be observed in Figure 4.40 with a %RSD of ±0.37. The effect of long periods of cavitation causes the percentage volume of di-aromatics in the commercial fuels to decrease. No change was observed in TESCO Dunstable, and aged BP Toddington, TESCO Flitwick and TEXACO MK. A decrease was observed in all the other commercial diesel fuels: BP Luton, SHELL Flitwick, TEXACO Leagrave and TOTAL Luton decreased by 0.2 %v; ESSO A1 and aged TOTAL Luton decreased by 0.1%v. This is a large significant decrease in comparison to their original percentage volumes prior to the heat and cavitation tests being carried out which were in the range of between 2.2 %v to 4.9%v. TOTAL Luton, TEXACO Leagrave and BP Luton show changes of 8.33 % ± 0.01 %, 6.45 % ± 0.01 % and 7.41 % ± 0.01 % respectively in di-aromatics with respect to the values before tests. SHELL Flitwick, ESSO A1 and aged TOTAL Luton undergo changes of 4.35 % ± 0.01 %, 2.04 % ± 0.01 % and 3.03 % ± 0.01% respectively on di-aromatics with respect to the values before tests.

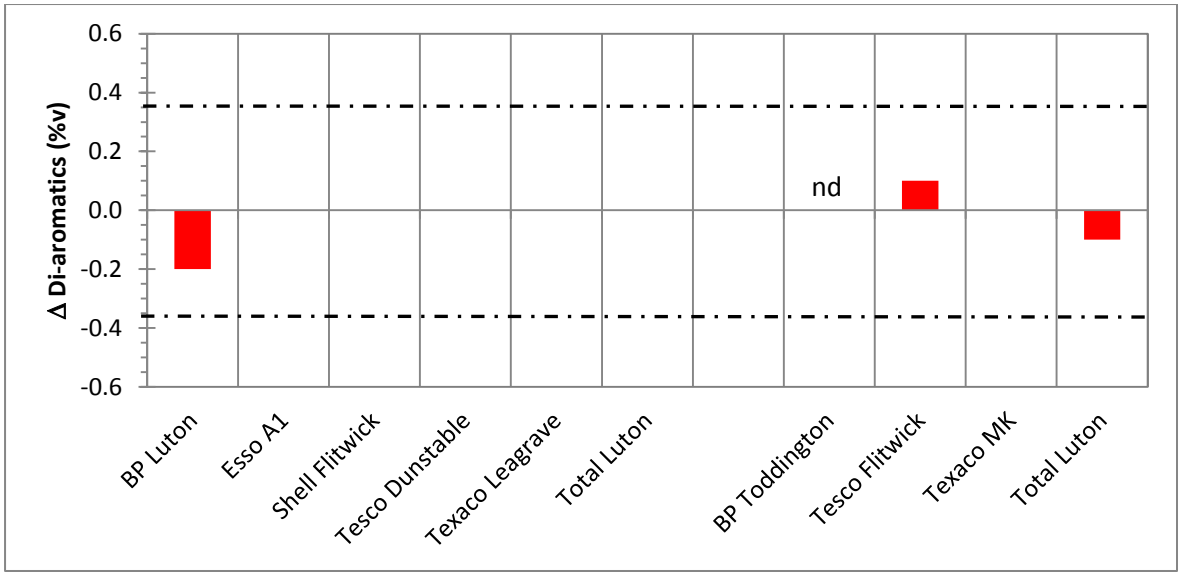

Figure 4.41 Change in Di-Aromatics (%v) for commercial fuels as a result of forty hours of discontinuous heat tests

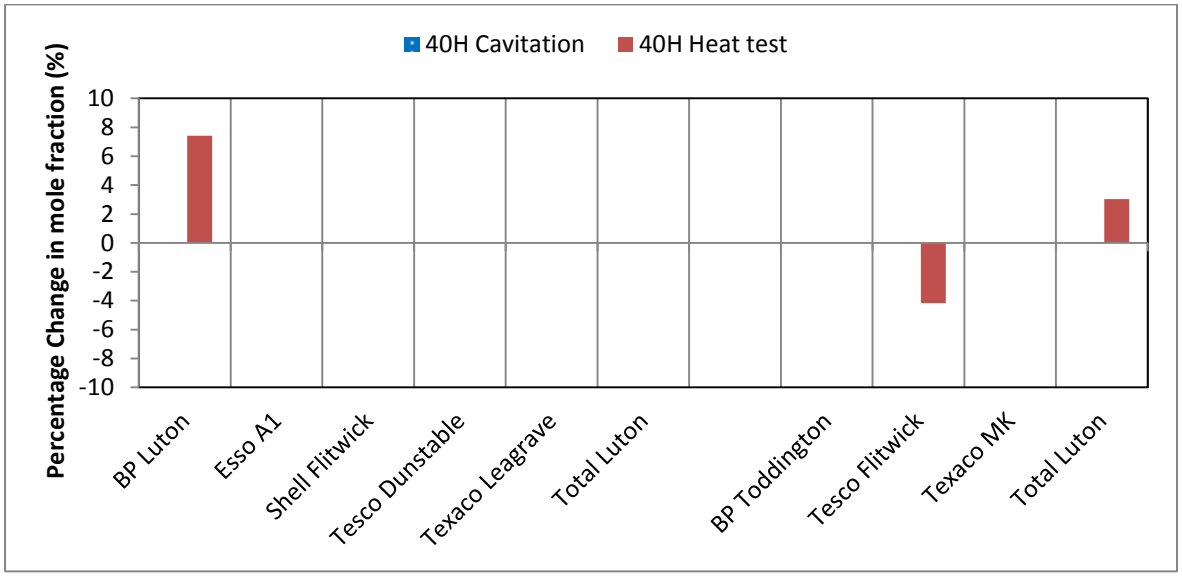

Figure 4.42 Relative percentage change with respect to the initial percentage volume in di-aromatics of the commercial diesel fuels prior to sustained cavitation and heat tests.

The results obtained from the GC x GC analysis of the forty hours heat tested samples undergo changes in di-aromatics observed in Figure 4.41. BP Luton and aged TOTAL Luton decreases in percentage volume of di aromatics by 0.2 %v and 0.1 %v, whereas Aged Tesco Flitwick shows an increase in the percentage volume of di-aromatics by 0.1 %v. BP Luton and aged TOTAL Luton undergo the same magnitude of changes as observed in the GC x GC tests of the forty hour cavitating flow samples testing changes in di-aromatics.

Similarly to the changes observed in the consumption of mono-aromatics as a result of sustained cavitating flow, the di-aromatics composition also undergoes relative decreases in percentage which relate to the consumption of di-aromatics as seen in Figure 4.42. The fuels undergoing heat tests did not have large changes and most of them had no changes at all in the composition of di-aromatics.

4.4.2.4 Tri (+)-aromatics

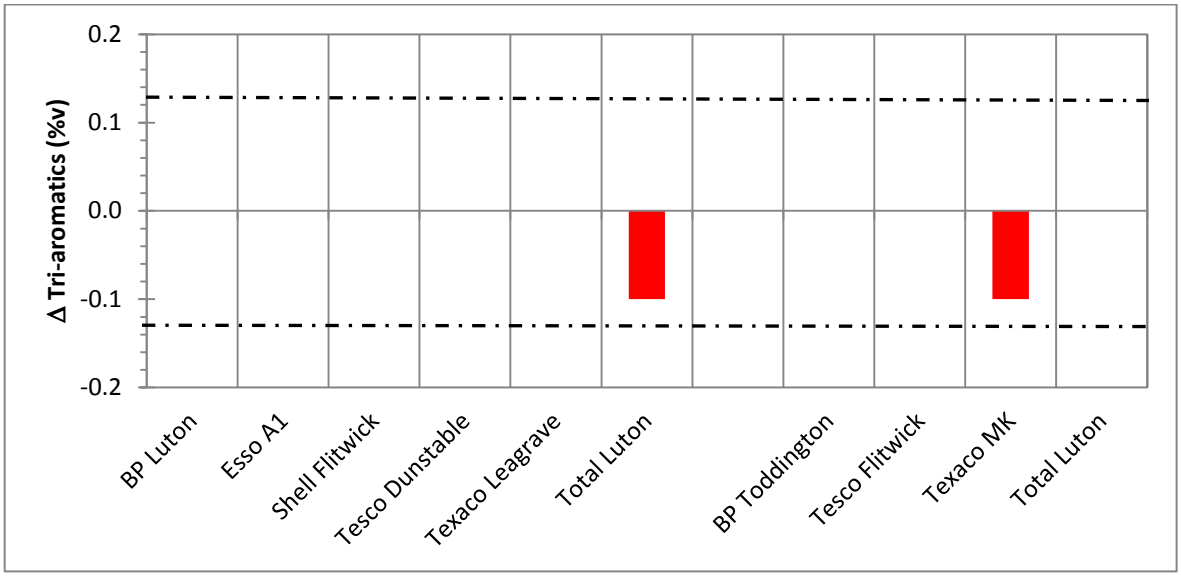

Figure 4.43 Change in Tri-Aromatics (%v) for commercial fuels as a result of forty hours of cavitating flow

The results obtained from the GC x GC analysis of the commercial fuels samples showing changes in tri(+)aromatics as a result of forty hours cavitating flow are seen in Figure 4.43 with a %RSD of ±0.13. Only two fuels undergo changes in percentage volume of tri (+) aromatics as a result of cavitating flow and these are TOTAL Luton and TEXACO MK Aged. These changes are significantly high when compared to the initial values before cavitation of these fuels. Both fuels undergo 33.33 % ± 0.01 % when compared to their GC x GC results of the initial commercial fuel samples. The results show no other fuels underwent any changes in tri (+) aromatics as a result of forty hours cavitating flow.

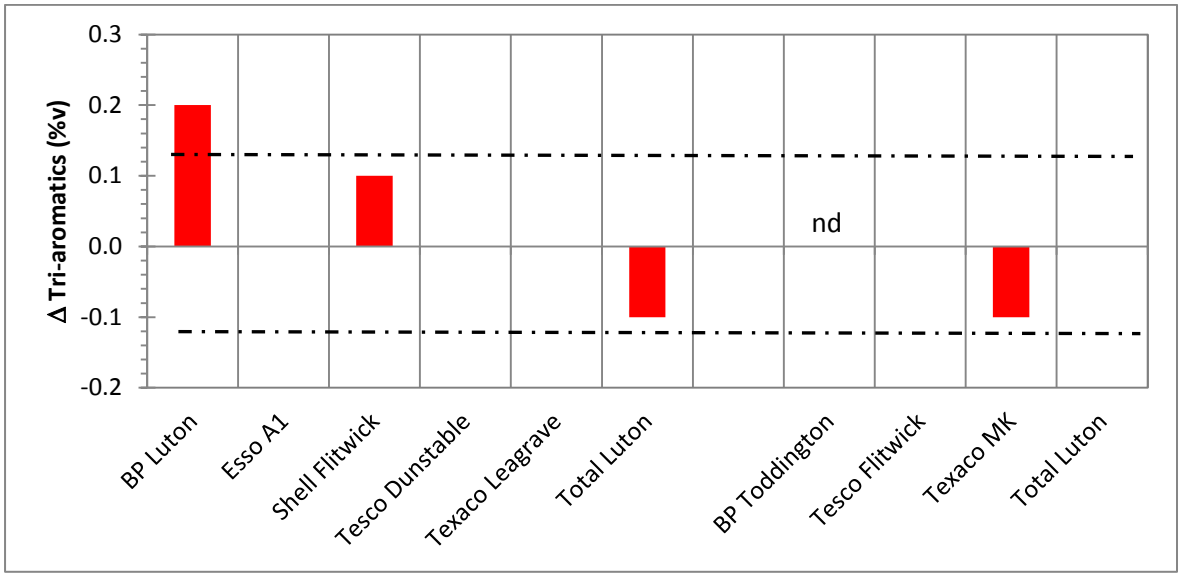

Figure 4.44 Change in Tri-Aromatics (%v) for commercial fuels as a result of forty hours of discontinuous heat tests

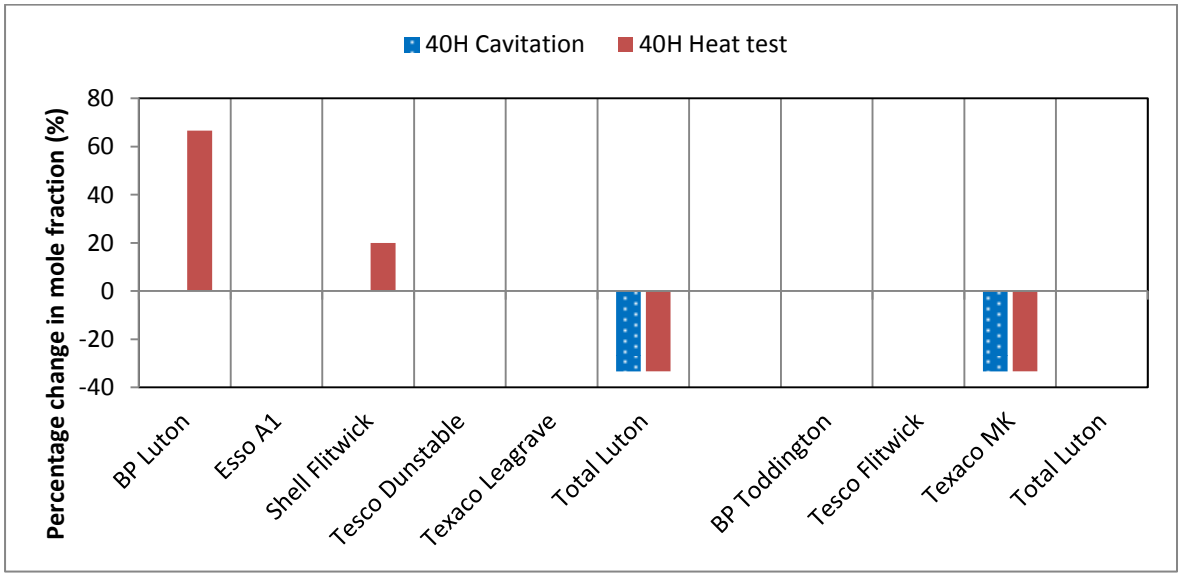

Figure 4.45 Relative percentage change with respect to the initial percentage volume in tri (+)-aromatics of the commercial diesel fuels prior to sustained cavitation and heat tests.

The results obtained from the GC x GC analysis of the commercial fuels samples showing changes in tri (+) aromatics as a result of forty hours of heat tests are seen in Figure 4.44. Four fuels are observed to undergo changes in tri (+) aromatics as a result of forty hours of heat tests and these are: BP Luton and SHELL Flitwick showing increase in percentage volume of tri (+) aromatics by 0.2 %v and 0.1 %v respectively; and TOTAL Luton (new) and aged TEXACO MK decreasing in percentage volume of tri (+) aromatics by 0.1 %v each.

A large amount of tri (+) aromatics were formed as a result of 40 hours of heat test as seen in Figure 4.45. TOTAL Luton new and Texaco MK aged show similar changes in tri (+) aromatics over both experimental analysis.

4.4.2.5 FAME

The changes in percentage volume of FAME obtained from the GC x GC peak area percentages of the commercial fuels as a result of forty hours of cavitation is shown in Figure 4.46. FAME found in biodiesel occupy a region that is also populated by numerous cyclic alkanes and mono-aromatics found in petroleum. Fortunately, the intensities of the petroleum hydrocarbon peaks are far lower than the intensities of the FAME peaks, even for blends with low biodiesel content. This allows the FAMEs to be accurately quantitated by modulation processes during the GC measurement [183]. The commercial fuels undergo large changes in the FAME peak area percentage and thus percentage volume. All commercial fuels undergo a decrease in percentage volume of FAME as a result of forty hours of cavitating flow apart from ESSO A1 which shows a very small increase of 0.05 %v. The largest change in percentage volume occurs in aged TESCO Flitwick of 0.83 %v. BP Luton, TESCO Dunstable and BP Toddington undergo a decrease in percentage volume by 0.33% each, however in comparison to the GC x GC peak areas of the initial samples before cavitation they undergo a percentage change of 10.25 % ± 0.01 %. Aged TESCO Flitwick changes by 25.78 % ± 0.01 %. SHELL Flitwick, TEXACO Leagrave, TOTAL Luton, aged TEXACO MK and aged TOTAL Luton decreased in percentage volume of FAME by 0.2 %v, 0.37 %v, 0.12 %v, 0.23%v and 0.11 %v respectively. The changes in percentage in FAME with respect to before cavitation are 6.21 % ± 0.01 %, 11.49 % ± 0.01 %, 3.73 % ± 0.01 %, 7.143 % ± 0.01 % and 3.42 % ± 0.01 % respectively.

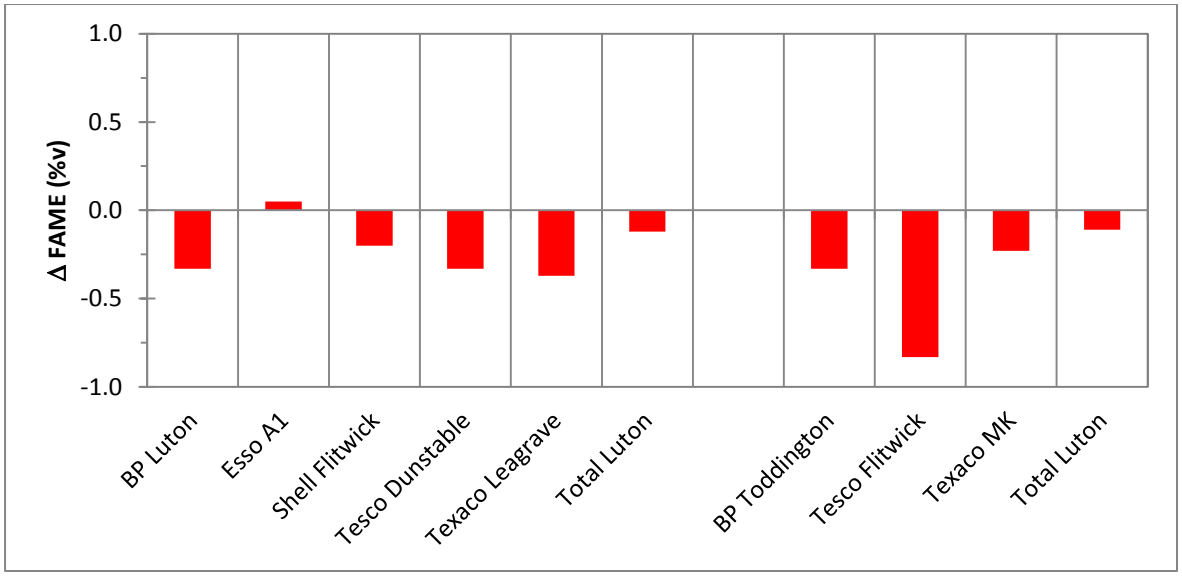

Figure 4.46 Change in FAME (%v) for commercial fuels based on GC x GC peak area as a result of forty hours of cavitating flow

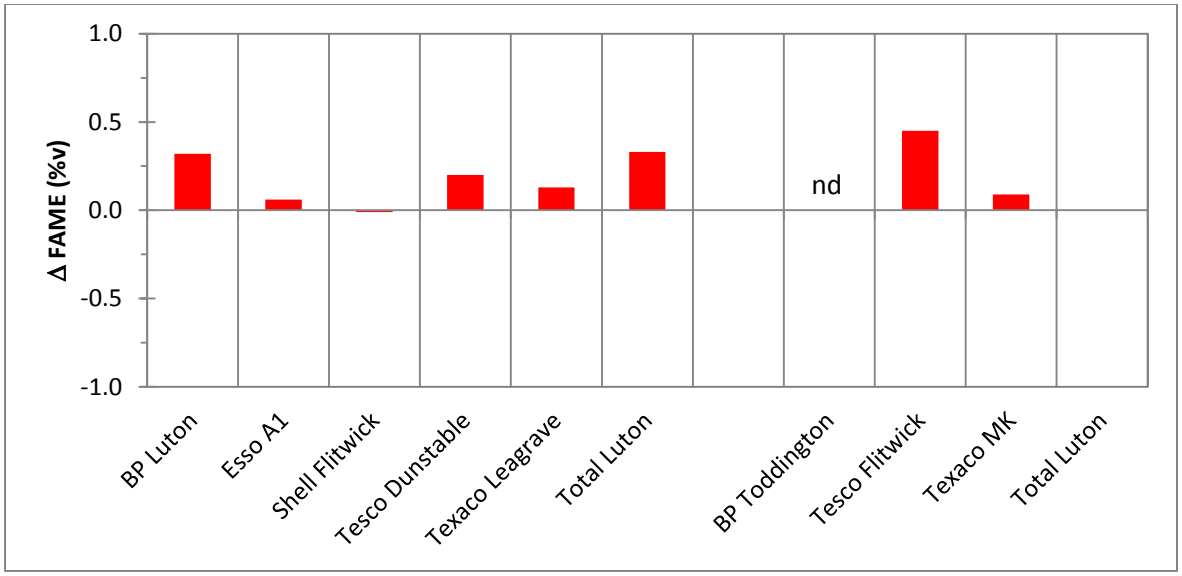

Figure 4.47 Change in FAME (%v) for commercial fuels based on GC x GC peak area as a result of forty hours of discontinuous heat tests

In contrast to the results obtained from the GC x GC analysis of FAME after forty hours cavitation, the commercial fuels show an increase in FAME as a result of forty hours of heat tests as observed from Figure 4.47. The largest increase observed in percentage volume of FAME was in TESCO Flitwick of 0.45%v. BP Luton and new TOTAL Luton showed similar changes in FAME percentage volume increase of 0.33 %v and 0.33 %v respectively. ESSO A1, TESCO Dunstable, TEXACO Leagrave and aged TEXACO MK undergo increases in

percentage volume of FAME of 0.06 %v, 0.2 %v, 0.13 %v and 0.09 %v respectively. SHELL Flitwick underwent a decrease in percentage volume of FAME by 0.01 %v as a result of forty hours of heat test.

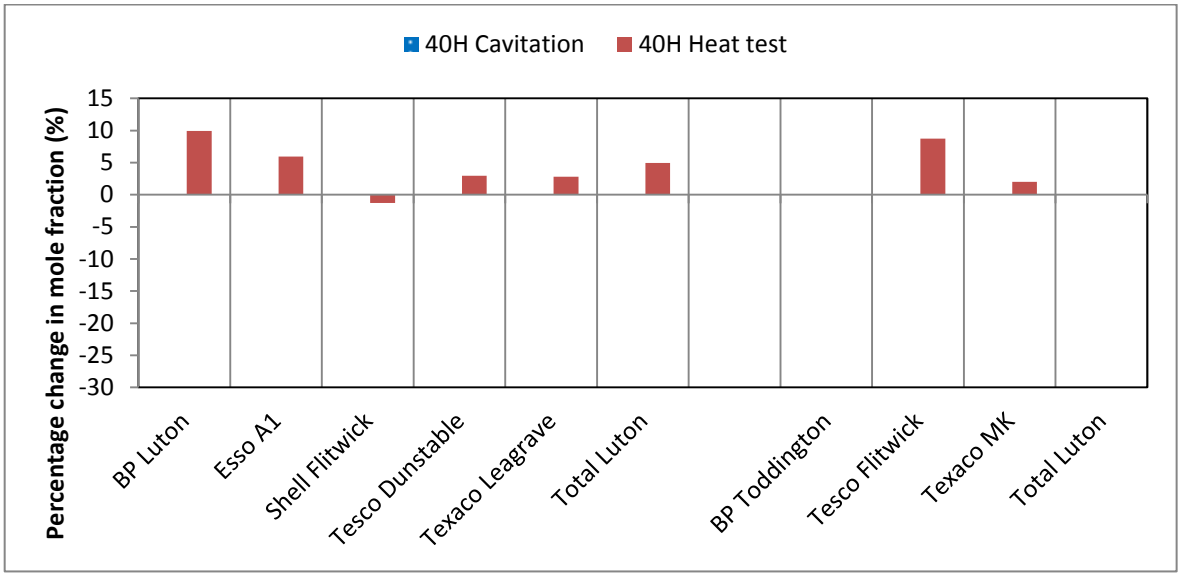

Figure 4.48 Relative percentage change with respect to the initial percentage volume in FAME of the commercial diesel fuels prior to sustained cavitation and heat tests.

The largest relative change in FAME occurred in aged TESCO Flitwick which decreased in composition of FAME by 8.74 % ± 0.01 % as a result of sustained cavitation tests as seen in Figure 4.48.

4.4.2.6 Residual

The effects on the percentage volume of residuals in commercial diesel samples as a result of forty hours of cavitation are shown in Figure 4.49. The results show aged BP Toddington had the largest change of 5.41 %v in residuals as a result of forty hours of cavitation. The rest of the fuels had less than 1 %v change in residual composition as a result of forty hours of cavitation. The overall changes in residual volume with respect to the percentage volume of residual in the initial fuel sample before cavitation was extremely high. The relative increase

in BP Toddington was 4339.84 % ± 0.01 % whereas the relative increase for aged TESCO Flitwick aged TOTAL Luton and new BP Luton was 100.99 % ± 0.01 %, 26.60 % ± 0.01 % and 91.67 % ± 0.01 % respectively. ESSO A1, SHELL Flitwick, TESCO Dunstable, TEXACO Leagrave and aged TEXACO MK had a relative decrease in residual percentage volume with reference to its initial volume prior to cavitation by 0.93 % ± 0.01 %, 24.56 % ± 0.01 %, 18.82 % ± 0.01 %, 20.00 % ± 0.01 %, and 37.98 % ± 0.01 % respectively.

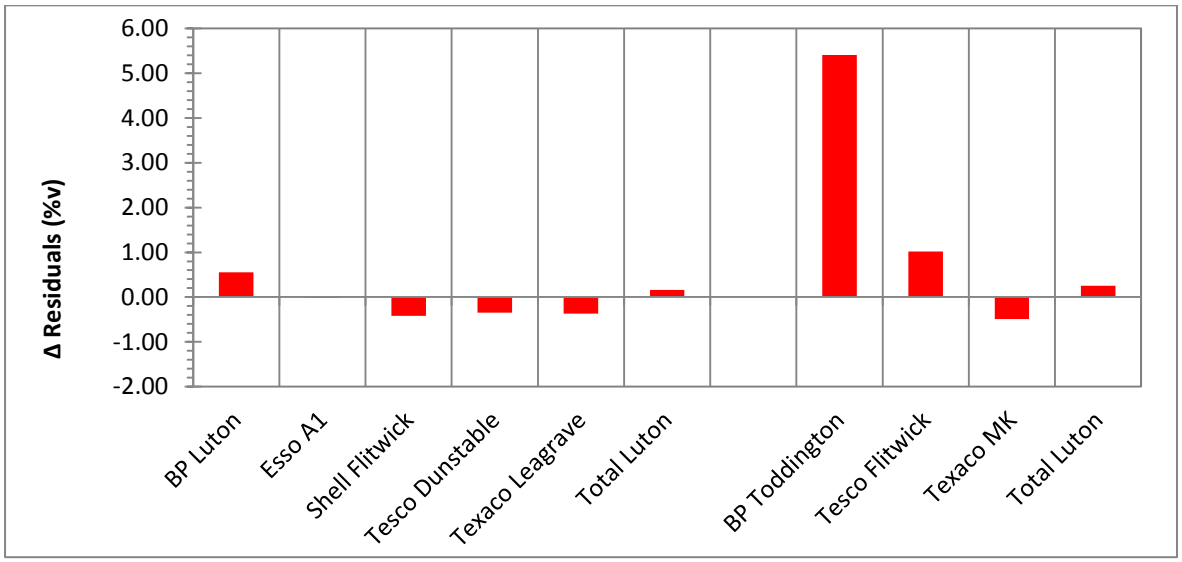

Figure 4.49 Change in Residual (%v) for commercial fuels based on GC x GC peak area as a result of forty hours of cavitating flow

The effects on the percentage volume of residuals in commercial diesel samples as a result of forty hours of discontinuous heat test are shown in Figure 4.50. The results show the maximum change occurred in SHELL Flitwick which increase in percentage residual composition by 4 %v. the rest of the fuels had an increase/decrease of residual volume by less than 1 %v. the relative changes in percentage volume with respect to the initial volume of residuals before cavitation was not as high in magnitude as seen in the results of the cavitation tests. SHELL Flitwick, BP Luton, and aged TESCO Flitwick increased in relative residual volume by 233.92 ± 0.01 %, 75 % ± 0.01 % and 4.95 % ± 0.01 % respectively. ESSO A1, TESCO Dunstable, TEXACO Leagrave, TOTAL Luton, and aged TEXACO MK decreased

in relative percentage volume by 23.15 % ± 0.01 %, 55.91 % ± 0.01 %, 56.76 % ± 0.01 %, 12.75 % ± 0.01 % and 50.39 % ± 0.01 % respectively. ESSO A1, TESCO Dunstable, TEXACO Leagrave and aged TEXACO MK underwent larger relative changes in residual composition as a result of forty hours of heat tests than those in forty hours of cavitating flow. Aged TOTAL Luton displayed no changes in residual volume as a result to forty hours of heat tests.

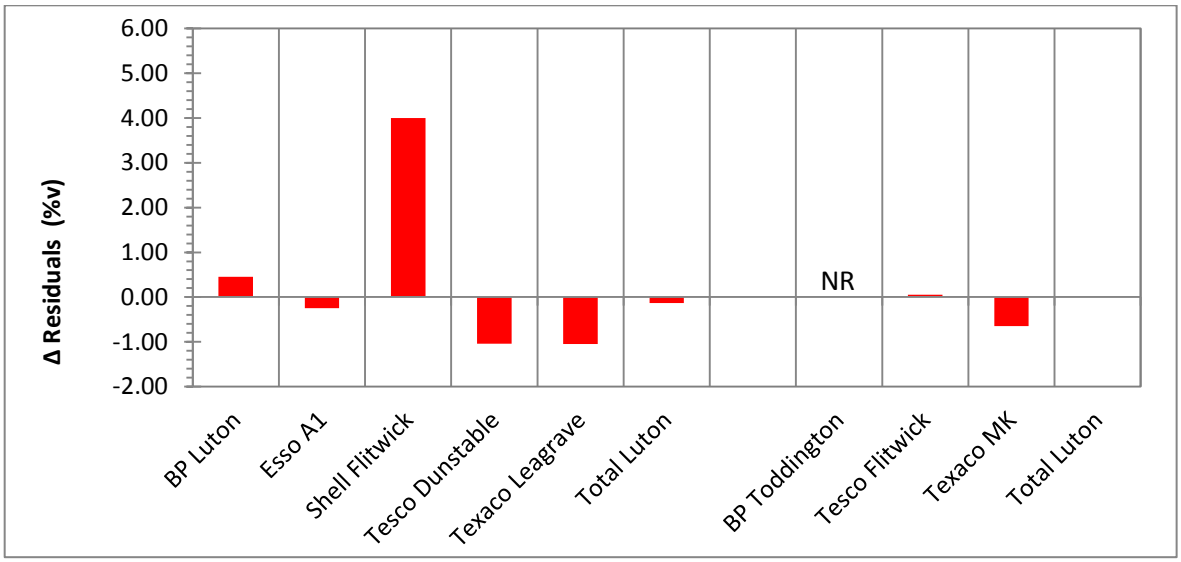

Figure 4.50 Change in Residual (%v) for commercial fuels based on GC x GC peak area as a result of forty hours of discontinuous heat tests

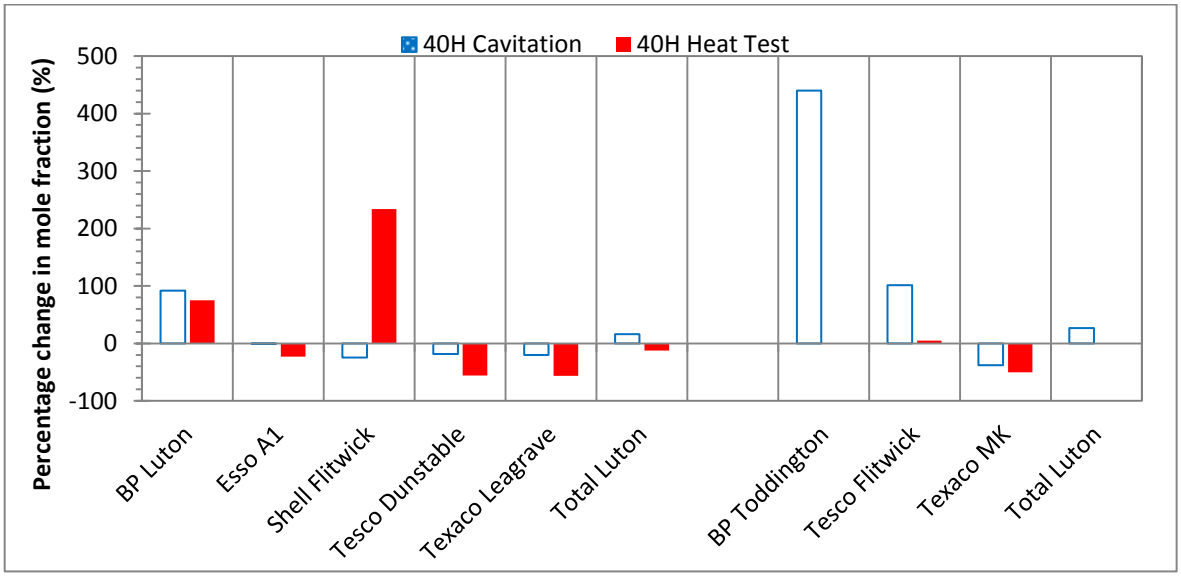

Figure 4.51 Relative percentage change with respect to the initial percentage volume in residual of the commercial diesel fuels prior to sustained cavitation and heat tests.

The changes in residuals can be seen in Figure 4.51, which shows increases as large as 400% in residual volume as a result of sustained cavitation tests. Most of the Aged fuels have resulted in large changes in residual volume when compared to the newer fuels.

4.4.2.7 Overall changes in chemical composition

The overall changes in composition of paraffins, Mono-aromatics, di-aromatics, tri (+)-aromatics, FAME and residual volume as a result of forty hours of cavitating flow and forty hours of heat tests can be observed in Figure 4.52 and Figure 4.53 respectively. It can be observed from the charts that the chemical changes occurring as result of forty hours of cavitating flow are different to the changes chemical composition caused by 40 hours of heat tests. The increased temperature in the cavitating flow may be increasing the rates of reaction occurring but the changes are not solely due to the elevated temperature maintained.

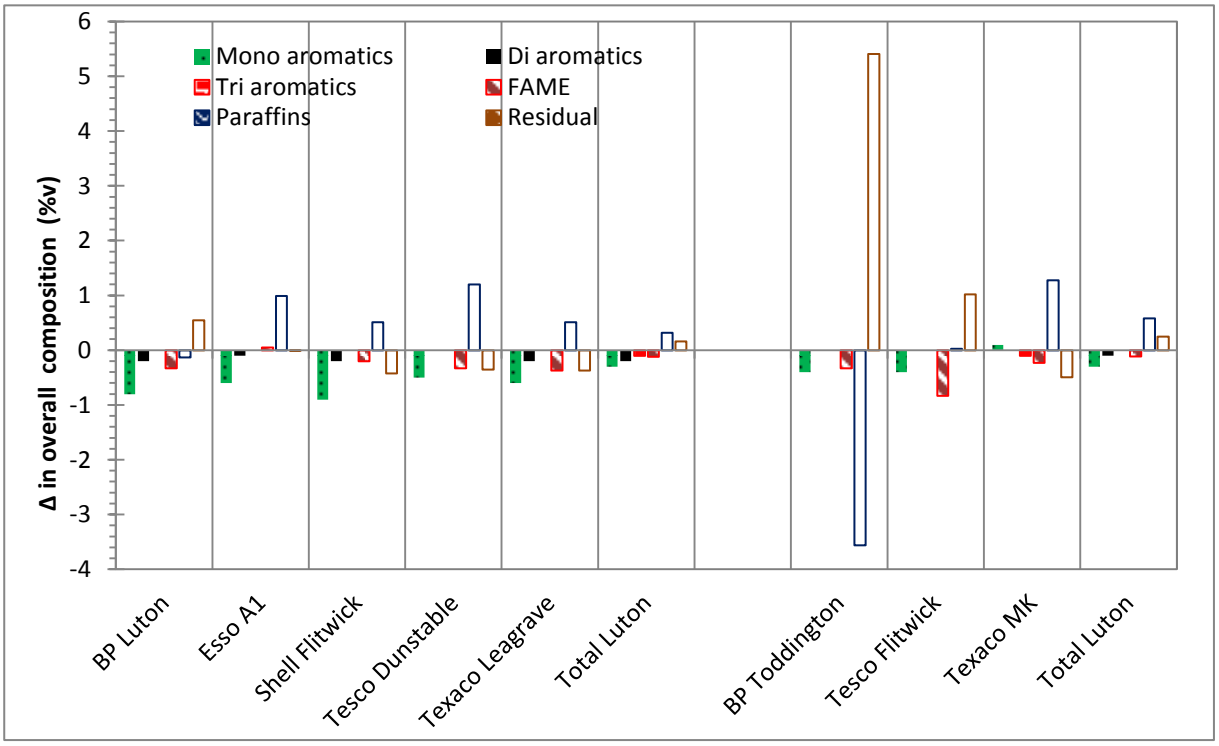

Figure 4.52 Overall change in hydrocarbons and residuals (%v) for commercial fuels obtained from the GC x GC analysis as a result of forty hours of cavitating flow

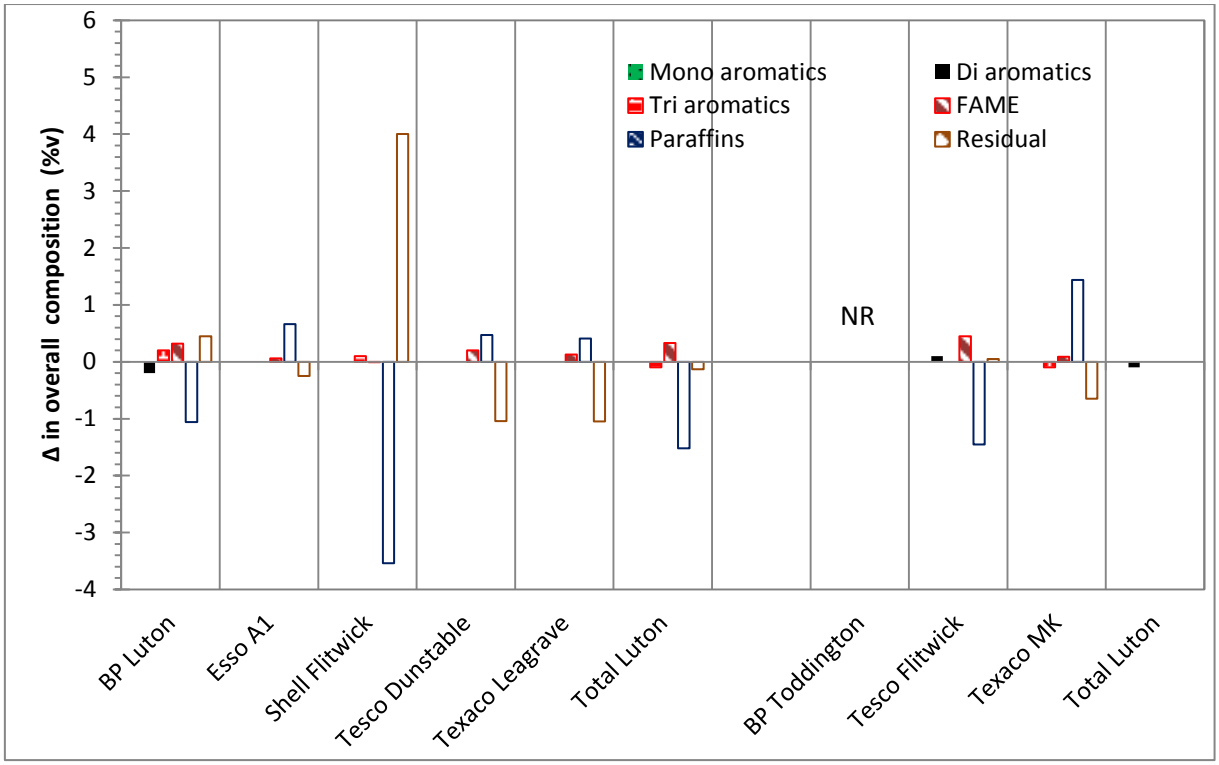

Figure 4.53 Overall change in hydrocarbons and residuals (%v) for commercial fuels based on GC x GC peak area as a result of forty hours of discontinuous heat tests

From Figure 4.52, the maximum change in composition occurring due to sustained cavitating flow is in BP Toddington Aged where there is a large increase in residual volume and a relatively large decrease in paraffins composition observed. The maximum change in composition occurring due to sustained elevated temperatures occurs in SHELL Flitwick which undergoes an increase in its percentage composition of residuals and a decrease in percentage composition of paraffins.

4.4.3 Particle number

Particle analysis was carried out using a Spectrex LPC-2200 laser particle counter which makes measurements based on the principle of near-angle scattering. A revolving laser beam is passed through walls of a glass container; any particles present in the fuel sample cause the beam to scatter. The extent of scattering is proportional to the number and size of the

particles. The mode of operation is shown schematically in Figure 4.54, with details of the laser optics given in Figure 4.55.

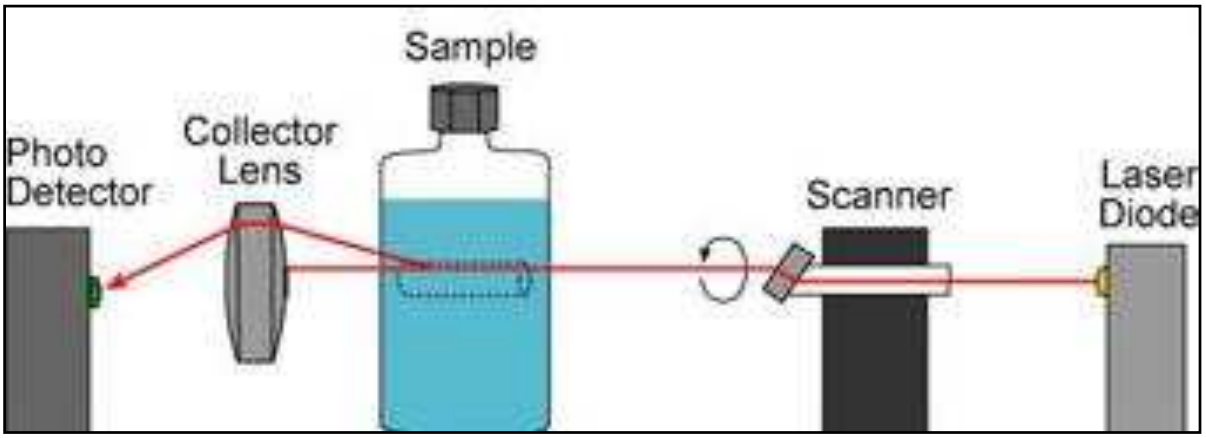

Figure 4.54 Schematic showing the operation of the Spectrex LPC-2200 particle counter.

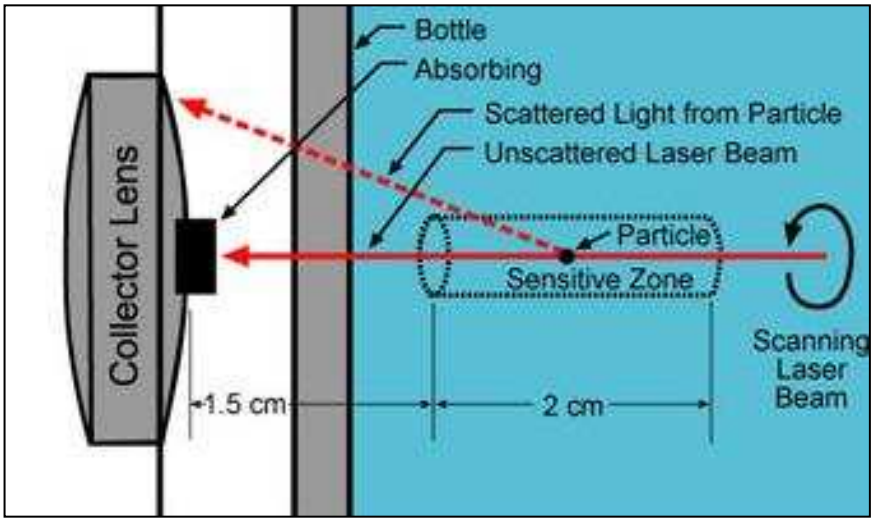

Figure 4.55 Details of the laser optics in the Spectrex LPC-2200 particle counter.

The instrument can determine the number and size of particle in the 0.5 to 200 µm range, although only particles between 1 and 100 µm are detected reliably and sized with a suitable level of precision. The standard operating procedure for the analyser involves:

(i) Agitating the sample on a mechanical shaker at 300 rpm for 1 minute

(ii) Wiping the sample vial with propan-2-ol to remove any marks and finger grease

(iii) Allowing for settling of any air bubbles

(iv) Measuring the particle count over the 1-100 µm range three times and taking mean values.

Sample dilution becomes necessary if the particle count exceeds, 1000 cm^{-3}. When the particle number concentration is higher than this there is a risk of overlap between particles in the third dimension (i.e. closer to or further from the detector) which may lead to two or more small particles being counted as a single particle. Then dilution of the fuel is needed to reduce the particle count this is done using chromatography grade n-heptane which has a very low background particle count (<20cm^{-3}). The dilution factor is automatically corrected for by the instruments software.

The results obtained from the particle analysis are shown in Figure 4.56. The figure shows particle number concentration in cm^{-3} against the different commercial fuels for three sets of data obtained: a) from the commercial fuels before tests carried out; b) the results after the forty hour cavitation tests and; c) the results after forty hours of heat tests.

The results of particle number concentration from the initial results show a very low concentration for all the fuels. The highest particle number concentration was observed in the aged BP Toddington sample of 46554 cm^{-3} and TESCO Dunstable of 10829 cm^{-3}. Two of the new fuels and one aged fuel had results above 1000 cm^{-3}: SHELL Flitwick (5872 cm^{-3}); new TOTAL Luton (7437 cm^{-3}) and aged TEXACO MK (6000 cm^{-3}). All the rest of the fuels had initial sample particle number concentration below 1000 cm^{-3}.

The particle number concentration increases largely as a result of forty hours of cavitation as observed in the figure. As a result of forty hours of cavitation, BP Toddington had a final

particle number concentration of 232,064 cm^{-3}, whereas TOTAL Luton and TESCO Dunstable had final particle counts after forty hours of cavitation of 151,663 cm^{-3} and 106,175 cm^{-3} respectively. These results are real and not changes or relative results. All commercial fuels apart from ESSO A1 and SHELL Flitwick show increases in particle number. However this may be due to the particle counter system not being able to efficiently count particles above 100 µm. The fuels may have had larger particles present in them. BP Luton, TEXACO Leagrave and aged TEXACO MK had similar particle counts after forty hours of cavitation of 47,915 cm^{-3}, 47,248 cm^{-3} and 43,676 cm^{-3} respectively. Aged TESCO Flitwick and aged TOTAL Luton showed particle number counts of 21,979 cm^{-3} and 8,628 cm^{-3} respectively after forty hours of cavitating flow.

The magnitude of particle number concentration for most fuels is much higher due to the forty hours of cavitation than the forty hours of heat test. The results from the heat tests show a low concentration of particle number concentration of particle size between 1-100 µm, whereas the forty hours cavitating flow results show a much higher particle number concentration of particle size 1 - 100 µm. There is a high probability that the particles formed as a result of forty hours of cavitation could have been larger than 100 µm due to coagulation of particles resulting in larger sizes.

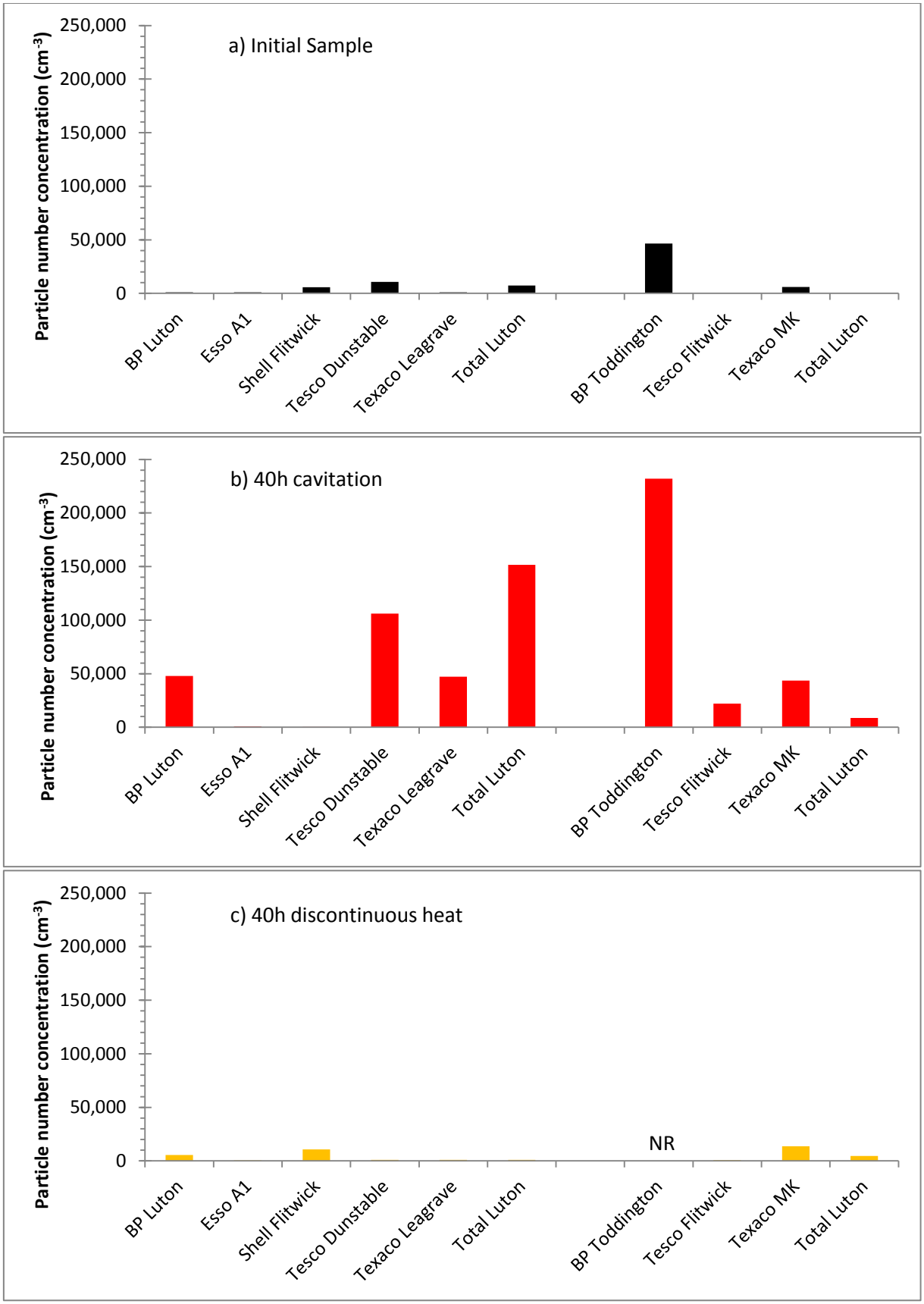

Figure 4.56 Particle numbers of commercial fuel obtained: a) Initial/Before Tests; b) After Forty Hours Cavitating flow and; c) After Forty Hours Heat Test

4.5 Overall Discussion and Conclusions of Experimental Results

In the Table 4.3 and Table 4.4, the nomenclature of the measuring parameters is as follows: CNTP – 40 hours of sustained Cavitation Normalised Transmitted Power results, HNTP - 40 hours of Heat test Normalised Transmitted Power results, ρ- Density, VC - VisCosity, FP - Flash Point, PF - ParaFfins, FAM – FAME, MA- MonoAromatics, DA – DiAromatics, TA - Tri(+)Aromatics, R – Residuals, PC – Particulate Count. The results are a summary of the previously seen experimental analysis, GC x GC and Particulate count results for 40 hours sustained cavitation analysis and 40 hours of heat test analysis compiled together.

Fuel Name	Experimental results		GC x GC and Particulate count									
	(% change w.r.t 0 hours)		(% change w.r.t. initial sample)									(Δ)
	CNTP	HNTP	ρ	VC	FP	PF	FAM	MA	DA	TA	R	PC
Model	-0.66	-2.91	NR									
Model + B20	55.11	2.21										
BP Luton	-24.64	-5.70	0.05	1.25	0.00	-0.18	-10.25	-3.42	-7.41	0.00	91.67	46,941
Esso A1	-7.84	-10.81	-0.06	0.60	3.33	1.44	1.55	-2.71	-2.04	0.00	-0.93	-200
Shell Flitwick	-16.30	-34.71	-0.08	0.30	5.00	0.72	-6.21	-3.63	-4.35	0.00	-24.56	-5,535
Tesco Dunstable	-24.71	-16.39	0.05	1.24	2.99	1.68	-10.25	-2.60	0.00	0.00	-18.82	95,345
Texaco Leagrave	-33.48	26.86	-0.02	1.43	3.39	0.72	-11.49	-2.63	-6.45	0.00	-20.00	46,354
Total Luton	-23.69	-38.04	-0.02	1.25	3.03	0.44	-3.73	-1.61	-8.33	-33.33	15.69	144,216
BP Toddington	-46.56	NR	0.11	0.68	3.33	-4.87	-10.25	-1.94	0.00	0.00	439.84	185,510
Tesco Flitwick	-25.88	-3.15	0.04	1.36	1.49	0.04	-25.78	-2.04	0.00	0.00	100.99	21,333
Texaco MK	-44.18	0.18	-0.04	1.32	1.59	1.77	-7.14	0.49	0.00	-33.33	-37.98	37,677
Total Luton	-14.86	-6.60	0.02	0.42	3.23	0.79	-3.42	-1.45	-3.03	0.00	26.60	8,081

Table 4.3 Table showing a summary of the changes from the experimental analysis, the 2D GC results and the particle count analysis for fuels from the 40 hours sustained cavitation analysis

Fuel Name	Experimental Results (% change w.r.t 0 hours)		GC x GC and Particulate count (% change w.r.t initial sample)									(Δ)
	CNTP	HNTP	ρ	VC	FP	PF	FAM	MA	DA	TA	R	PC
Model	-0.66	-2.91	NR									
Model+B20	55.11	2.21										
BP Luton	-24.64	-5.70	0.12	1.30	0.82	-1.49	9.94	-0.43	7.41	66.67	75.00	478.99
Esso A1	-7.84	-10.81	0.01	0.00	0.83	0.96	5.94	-0.45	0.00	0.00	-23.15	-41.77
Shell Flitwick	-16.30	-34.71	0.04	0.11	2.50	-5.03	-1.28	-1.21	0.00	20.00	233.92	82.68
Tesco Dunstable	-24.71	-16.39	0.01	0.42	2.24	0.66	2.98	0.00	0.00	0.00	-55.91	-91.71
Texaco Leagrave	-33.48	26.86	0.00	0.76	2.54	0.58	2.79	2.19	0.00	0.00	-56.76	9.01
Total Luton	-23.69	-38.04	0.06	0.44	0.76	-2.08	4.95	4.84	0.00	-33.33	-12.75	-86.14
BP Toddington	-46.56	NR	NR									
Tesco Flitwick	-25.88	-3.15	0.29	0.15	-2.24	-2.02	8.74	9.18	-4.17	0.00	4.95	33.34
Texaco MK	-44.18	0.18	-0.08	0.76	-0.79	1.99	1.99	3.40	0.00	-33.33	-50.39	129.26
Total Luton	-14.86	-6.60	0.05	0.04	0.81	0.00	0.00	1.93	3.03	0.00	0.00	726.27

Table 4.4 Table showing a summary of the changes from the experimental analysis, the 2D GC results and the particle count analysis for fuel from the 40 hours heat test analysis.

The model fuel which consisted of mainly long chained paraffins some olefins underwent the least changes as a result of 40 hours sustained cavitation. This leads to the conclusion that the sensitivity of the paraffin contents in the fuels to the attenuation results is not high and thus paraffins are the least affected by sustained cavitation.

Sustained cavitation resulted of the model fuel+B20 shows positive changes and thus this relates to a decrease in absorptivity of the laser power through the fuel. Considering the model fuel underwent very little change, these effects can be pinpointed to be caused by the FAME content in the fuels. As mentioned previously, oxygenates in the FAME are being destroyed and thus leading to an increase in 405nm laser transmissivity. However changes observed in signal transmissivity as a result of 40 hours of cavitation tests lead to a decrease in

transmissivity of the 405nm laser. From the above, the paraffin and FAME content cannot be held accountable for these changes in transmissivity with time. It is observed from the 2D-GC analysis that changes in FAME as a result of 40 hours of cavitation are relatively higher than the other fuel components, however from the model fuel results obtained, the decrease in laser transmissivity and thus an increase in laser attenuation through the fuels is not caused by the FAME content. The FAME content in fuel has shown an increase in fuel transmissivity and a decrease in laser attenuation through it. Overall changes in laser transmissivity and laser attenuation may have been lowered by the FAME content in the rest of the fuels.

The relative changes occurring as a result of cavitation are different to those caused by heating only as can observed in both Table 4.3 and Table 4.4. Thus it can be concluded that the high initial temperature set for the fuels is not the sole cause of the changes in transmissivity and laser spectral attenuation through the fuels. However the temperature may be acting as a catalyst to increase the rates of reactions occurring in the fuels.

All the commercial fuels show a decrease in laser transmissivity and an increase in laser attenuation through then during the 40 hours of sustained cavitation. A large decrease in the aromatic content of the fuels is also observed as a result of the cavitation. However the number of particles in the fuels is increasing the largest relative to the initial sample particle counts. These counts are in the orders of thousands as a result of cavitation compared to a few hundreds as a result of heat tests. This is the major finding of this work that fuels are forming large number of particles as a result of sustained cavitating flow and this is purely not an effect of heat but an effect of cavitation bubble collapse on the chemical change in the fuels. The added heat maybe increasing the rate of formation of the particles; however is not the sole cause of its formation as observed in the results. Many authors have related the formation

of these particles to the aromatic species as seen in Appendix B. The cause of the changes in spectral attenuation and laser transmissivity through the fuels can be identified as been caused by a decrease in aromatics leading to the formation of large PAHs and further on particulates and soot.

It is important to know the pathways to the formation of particulates from the aromatic species and thus Appendix B will show the pathways from chemical kinetics which maybe be involved in the formation of particulates from both aromatics and paraffins as combustion of solely paraffinic fuels have also been observed to for soot and particulates in the exhaust although not as high as commercial diesel fuels containing aromatics. The pathways analysis is carried out by using two combined kinetic models which has not been validated, however the pathways leading to the formation of soot (BIN in the models) can be used to approximate the possible pathways to the formation of soot

The particle counter could only measure accurately particles of sizes between 1- 100 µm. Very small and very large particles may not have been included in this count. Some of the fuels, i.e. Shell Flitwick and ESSO A1 showing negative particle counts may have been an effect of additives in the fuels suppressing the formation of particles and this may have led to formation of smaller particles in the fuels; smaller than the capability of the machine to be able to produce a count.

Blank Page

Chapter 5 Simultaneous External Spray Sizing and Nozzle Hole and Sac Imaging - Experimental Apparatus and Calibration

In the preceding chapters the effect of cavitation and cavitation bubble collapse on different diesel fuels has been discussed. The subsequent chapters will discuss effects of fuel density and distillation profile on its SMD distribution and thus its atomisation. The atomisation profiles are relative to the external spray drop size distribution. The degree of atomisation in the spray is related to its combustion characteristics and thus formation of particulates and emissions. The degree of atomisation can be controlled by increase in injection pressure, change in nozzle characteristics and changes in fuel volatility and distillation characteristics. The objective of this study was to obtain a spray drop-size distribution of fuels with varying distillation profiles. The Fuels of different distillation profiles (High, gap and low) were provided by Shell Global solutions with an objective of obtaining their drop size distribution using optical characterisation techniques. The quality of diesel spray is very important in direct injection diesel engines. The spray characteristics are strongly influenced by the nature of flow inside the injection hole [124]. The internal flow is largely dependent on the presence of the cavitation phenomenon [2,92]. Payri et. al [22] carried out an investigation on the influence of cavitation on the internal flow and the macroscopic behaviour of the spray in diesel injection nozzles. Cavitation and turbulence generated inside the nozzle is known to influence the primary breakup of the fuel, especially in the near nozzle region. However it is unknown how properties of the fuel affect the in nozzle cavitation and thus the external atomization and spray formation.

Initially the purpose of this work was to correlate the external spray formation to the internal nozzle hole cavitation. However the scope of this work contained a large dataset and thus for the purpose of the work here, this analysis will not be carried out. The internal nozzle images will still be used to analyse a phenomena which was observed in the sac of the nozzle. This will be discussed later on. The work here covers this analysis and the fuel SMD distribution analysis for the three fuels.

Synchronised white light scattering images from the internal nozzle scattering were captured simultaneously with the spray images. This chapter aims to describe the high pressure injection rig and the laser-sheet dropsizing optical setup. The fuels had to be seeded with Rhodamine-B which would then be excited by a 527 nm laser sheet and the fluorescence captured at > 560 nm. Mie scattering from the spray would also simultaneously be captured on the same camera, on different halves of its sensor. The seeding is briefly described here so that the reader is familiar with the seed before it is explained in detail after the high pressure rig setup.

A second camera would capture white light scattered from fuel cavitation inside the injector holes and sac simultaneously and thus the spray captured can be linked to the internal nozzle cavitation occurring. Each fuel was repeated with a new minisac nozzle tip made from acrylic to maintain consistency. Also the tips were reused for the next fuel as to calibrate the manufacture. The experimental setup will be discussed in detail in this chapter.

5.1 High Pressure Injection Rig

5.1.1 Fuel delivery system

The function of the fuel injection system was to introduce accurately a quantity of fuel into the injector, at a predetermined rate and pump angle position. The high pressure injection rig described here was custom manufactured at City University and could generate injection pressures of up to 600 bar. A schematic of the rig can be seen in Figure 5.1. The fuel was delivered from the tank to the high pressure pump by an electrical fuel pump. After filtration the fuel flowed into the high pressure pump. The high pressure pump was driven by an electric motor running at 1490 rev/min (24.833 rev/s) directly coupled. The fuel here was compressed (300-1800 bar) and then discharged to the common rail. Fuel accumulated under high pressure in the common rail and from there, it was injected into the atmosphere each time the injector opened.

The injection is controlled by an external control box which sent a discharge signal to the injector electronic driver unit. Independent control of the number of skip cycles (injection rate), injection duration, number of injections per cycle and injection delay was achieved by a custom built controller unit. The injector timings and the electronic control unit will be discussed in detail later in this chapter. A Kulite ETMER-1-375M-3500BARSG pressure transducer installed prior to the injector measures the pressure during discharge. The transducer had a rated pressure of 3500 bar SG (Sealed Gauge), a sensitivity of 1.189 mV/bar and a zero balance of 500 mV ± 50 mV. The zero balance was acquired prior to each test and the required pressure calculated to narrow down the zero balance error. A modified Denso injector was used for the experiments and the modifications are described in 5.1.3.

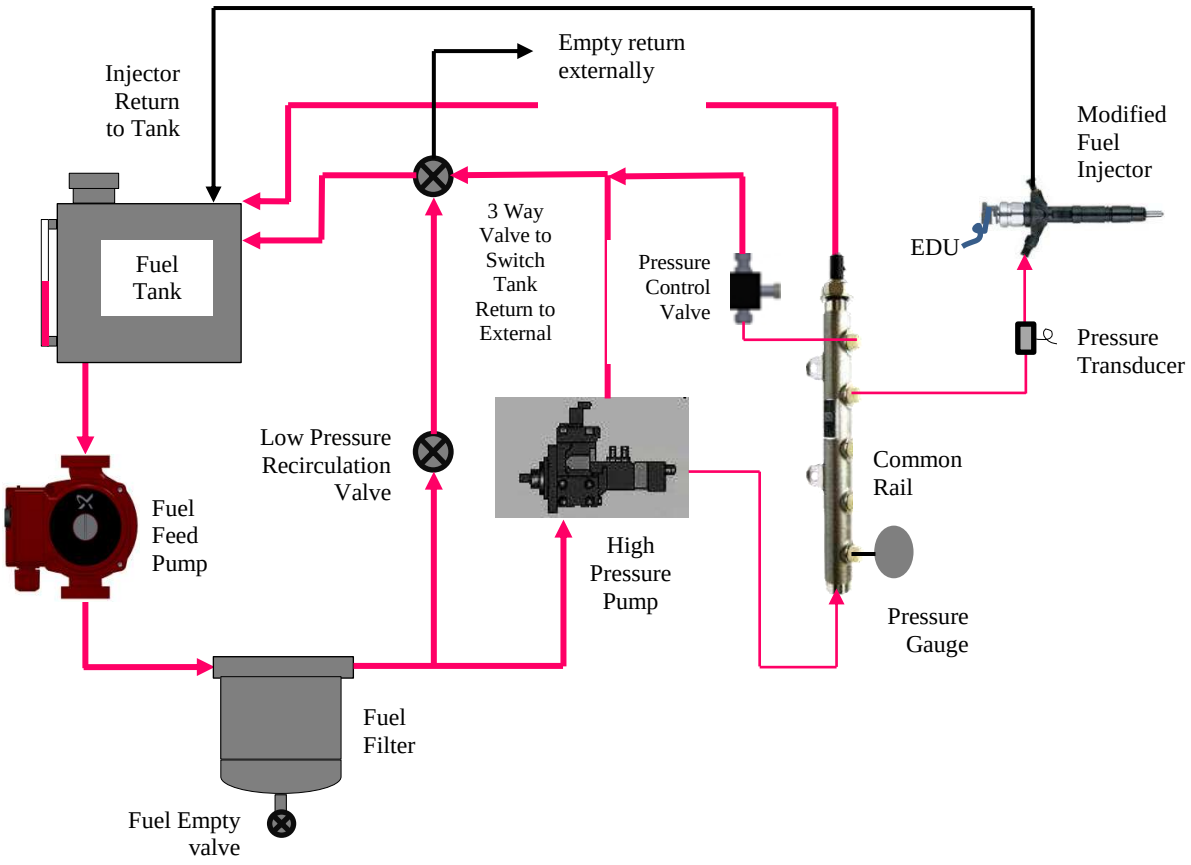

Figure 5.1 Schematic of the high pressure injection rig

Past the filter, there was a valve to select the direction of the flow either back into the tank or into the high pressure pump. The flow back into the tank was required as a vent during the filling/emptying procedures. The high pressure pump, common rail and injector had fuel return lines back into the tank. The return line on the high pressure pump and the common rail was to relief pressure and excess fuels back into the tank during pumping and when the rig was stopped. The return line on the injector was for excess fuel not injected to return back to the tank. This line was also used as fuel sampler to collect fuel during experimental analysis. This fuel sample obtained would be later calibrated for its fluorescence yield to be able to form a comparison between the fuels

The common rail pressure is measured by a high pressure gauge attached to the common rail. The fuel pressure at the common rail is controlled by an adjustable pressure control valve.

The pressure control valve is located on the common rail. It can be adjusted to the required pressure measured on the gauge attached to the common rail and relieved back into the tank. The pressure control valve is adjusted to the required injection pressure by reading the output from the pressure transducer and opening/closing the valve as required.

The temperature of the fuel at the inlet of the high pressure pump could be monitored. A K-type thermocouple was mounted in the pump to measure the inlet fuel temperature into the pump. This was displayed on the rig. The thermocouple was also connected to a cooling system which passed cold mains water into a cylindrical input into the tank to cool the fuel as required and dumped the heated water to a sink. The temperature could be set between 40 and 70 degrees centigrade at the control. By cooling the fuel in the tank, cold fuel would enter the high pressure pump. It was ideal to cool the tank because all the high pressure discharge would flow into the tank. When the common rail was not charged all of the high pressure liquid would empty into the tank and circulate back into the pump.

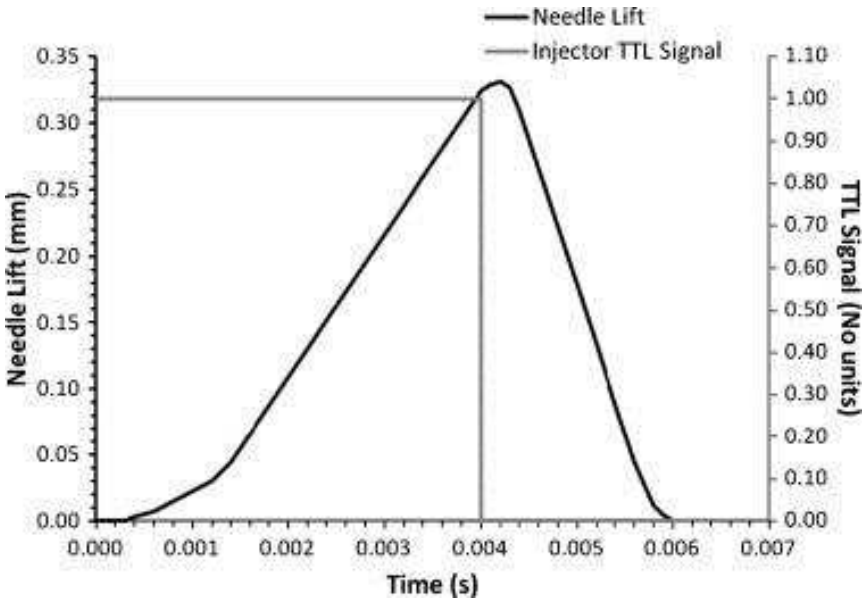

Figure 5.2 Needle lift and injection pulse obtained by Dr. Liverani [184] using the modified Denso injector and EDU

An electronic injector driver sent a high voltage square wave pulse to a magnetic solenoid, located in the injector. The switching of the magnetic solenoid actuated the injector needle, allowing high pressure fuel to pass through the injector. The mean time-resolved needle lift for this type of injector was measured using an inductive sensor, and is shown on the timing diagram presented Figure 5.2. This profile was measured in [67,184] using the same injector and electronic driver unit for providing the same voltage pulses to drive the injector and can be utilised during this study.

The needle lift appeared to be gradual with an approximately constant lift rate of 0.118 mm/ms for approximately 4 ms, followed by a short period of approximately 0.3 ms in the neighbourhood of maximum lift, followed by an approximately constant rate of needle return for a period of approximately 1.6 ms. The needle reached its final seal position at approximately 6 ms after the electronic start-of-injection signal. This lift profile was due to the relatively low common rail pressure of 200 – 400 bar, and is typical for engines operating at idle, or low/part load, when the common rail pressure remains relatively low (400 – 600 bar).

The injectors employed in this study were designed for maximum rail pressures of approximately 1200 – 1400 bar. During high load operation, the high fuel pressure normally facilitates the development of a large needle lift rate. The needle normally reaches its highest point within 0.5 ms, and remains open at its highest position until the magnetic circuit is turned off.

Initially it was decided to use a very fine 5 micron stainless steel filter element in order to prevent large particles damaging the pump. But during pre-tests sample mixtures were

prepared with Rhodamine-B and fuel with different mixtures. But the Rhodamine seemed to disappear somewhere and did not appear in injections. A bright pink fluid placed into the rig was injected much lighter in colour (very light pink). This was troubling as somehow the Rhodamine-B was getting lost and may have been coagulating somewhere. It was discovered after some careful thought that flow past the metal filter was creating a potential and the Rhodamine was attracted to this and thus stuck to the metal filter. On removing the metal filter and dipping it into Ethanol, a bright pink mixture formed which only became lighter only after 3 flushes of Ethanol ~ 1 L per flush. The filter was then changed to a polypropylene filter. This filter would initially be soaked in 1 L of 120 mg/L Rhodamine-Fuel solution so that it had been discoloured and would not be dyed further by the experimental fuel.

5.1.2 The injection control unit

The pump had an encoder fitted that would output a pulse every 5 degree rotation. This was necessary to control timing of injections to occur at a selected pump angle each time in order to prevent large fluctuations in pressure. This signal was sent to the control unit and the injections were triggered by controlling the number of skips of the pump revolution. The skip rate could be manually set on the control unit. A skip rate of 8 (skip 8 revolution and inject) was used during the experimental acquisition which provided and injection rate of 3 Hz. One revolution of the pump took 40.268 ms, thus an injection occurred every 322.144 ms. The injection duration would also be set manually on the control unit, ranging from 1 - 5.5 ms.

The control box, on receipt of the injection signal, would send a dialled delay signal to the injector of the size of the duration set. The injection delay between the start pulse and the pulse sent to the injector could be set between 100 - 500 μs. So once the trigger was received

the injection would start after the set delay. The start pulse would be the start trigger and synchronisation pulse for image acquisition and synchronisation for the cameras and synchronisation of the laser fire pulse at 10 kHz.

The pump encoder signal was the master signal for the control box and it would provide the synchronised injection, laser and camera signals with respect to the pump angle. The outputs for the laser and camera synchronisation were set to 10 kHz with respect to the rise of the TTL signal. The unit was used to provide acquisition signals for the cameras and synchronised trigger signals at 10 kHz to synchronise the laser.

5.1.3 Optically accessible injector nozzle design

The injector nozzle is of the most important parts of a diesel engine. Nozzle geometry affects spray characteristics and therefore atomisation behaviour [22]. In order to perform real size analysis on the nozzle holes they have to be modified to be optically accessible. The injector nozzle was modified to have its holes machined out and replicated in clear acrylic to enable a good view of the internal holes.

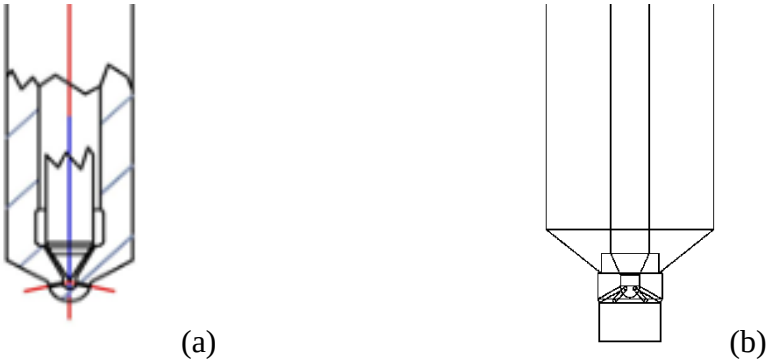

Figure 5.3 (a) Non-modified nozzle (b) Modified nozzle with new tip

In [184] a mini-sac tip with the exact internal dimensions as the section cut was designed and manufactured. The same internal nozzle hole and minisac dimensions are used, but the exterior has been modified to a 4 profile nozzle. The hole angles have also been modified from 12.5 degrees to 25 degrees. Figure 5.4 shows the nozzle previously used and Figure 5.5 shows the redesigned 4 profile nozzle. In both figures the nozzle hole diameter/length (d/l) ratio at hole centreline is 0.134 ± 0.001. The nozzle hole diameter is 0.136 ± 0.001 mm and the nozzle hole length 1.018 ± 0.001 mm. The difference between them is the length of the lower end as seen in Figure 5.4 is slightly longer due to the outer surface having a cylindrical cut, whereas in Figure 5.5 it has been profiled so that the hole is symmetrical about its centre.

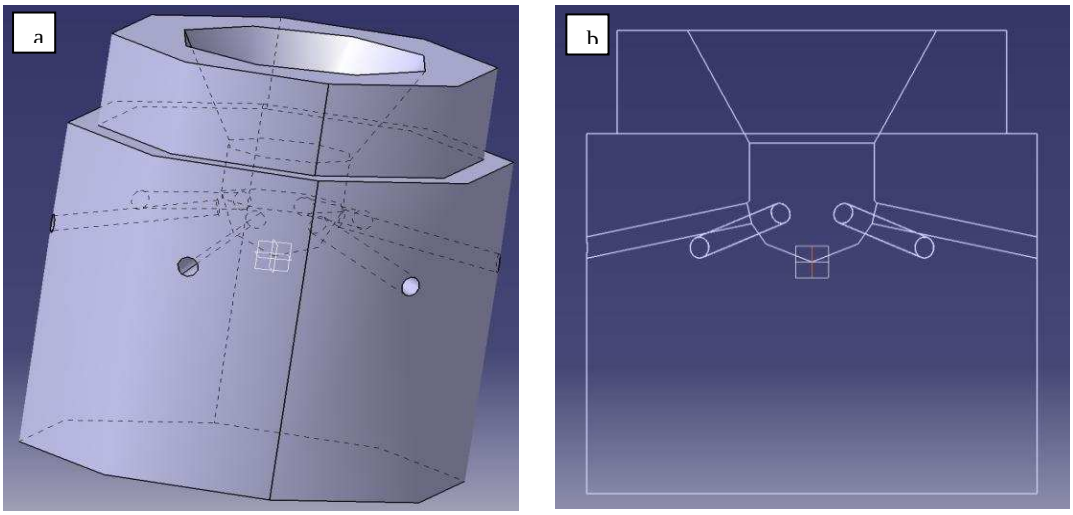

Figure 5.4 (a) Exterior image of the Mini-sac tip used previously (b) The interior image of the tip previously used

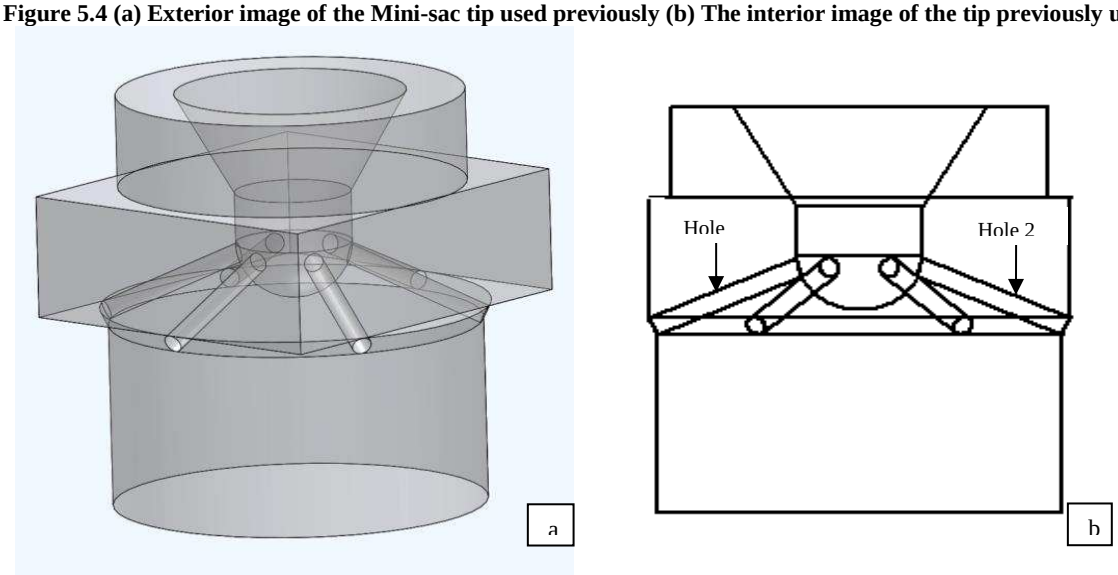

Figure 5.5 (a) Image showing current nozzle design (b) Nozzle interior image showing increased nozzle hole angle

Only two of the nozzle holes can be viewed for best results these two holes are designed to be manufactured on opposite faces marked hole 1 and 2 in Figure 5.5 (b). It can be observed in Figure 5.4 (b), that a nozzle hole angle of 12.5 degrees from the horizontal caused part of it at the inlet to be obstructed. The nozzle hole angle was doubled from 12.5 degrees from the horizontal, to 25 degrees. This was carried out to have a better view of the whole nozzle and especially the inlet from the sac to the holes. The side view in Figure 5.5 (b) shows the modified nozzle with full side view. As seen both hole 1 and 2 can be viewed fully from the side.

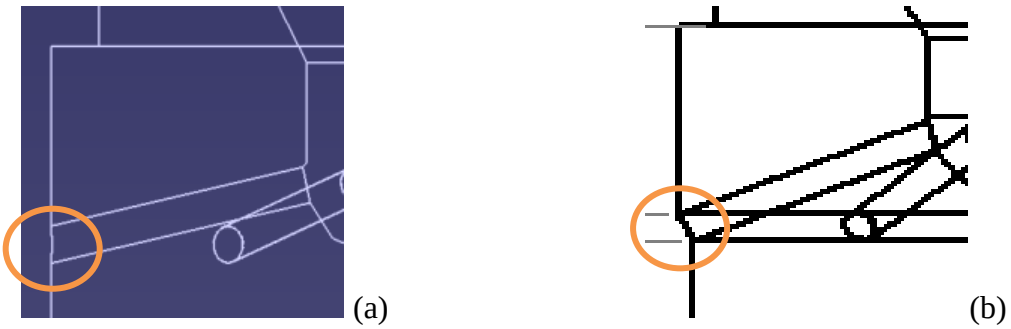

Figure 5.6 (a) Exit of the previous nozzle (b) the exit of the new nozzle hole

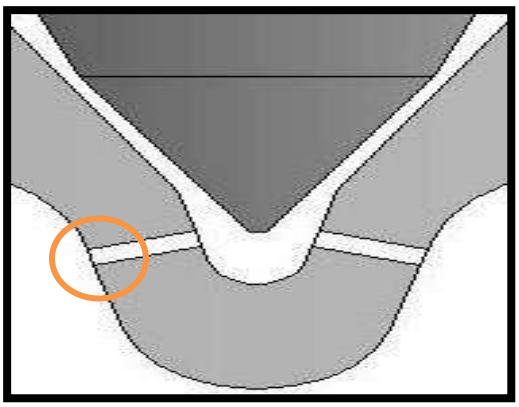

Figure 5.7 A representation of the nozzle hole exit profile of an actual injector

The nozzle hole lengths have also changed in the new design and are more closely matched to real size nozzles. The previous nozzles holes ended horizontally and this is not the case for real size injector nozzle holes. These holes end at an angle to the horizontal making near perfect cylindrical holes. The changes in design are shown in Figure 5.6. Figure 5.7 shows the nozzle hole exit on non-modified mini-sac injector nozzle.

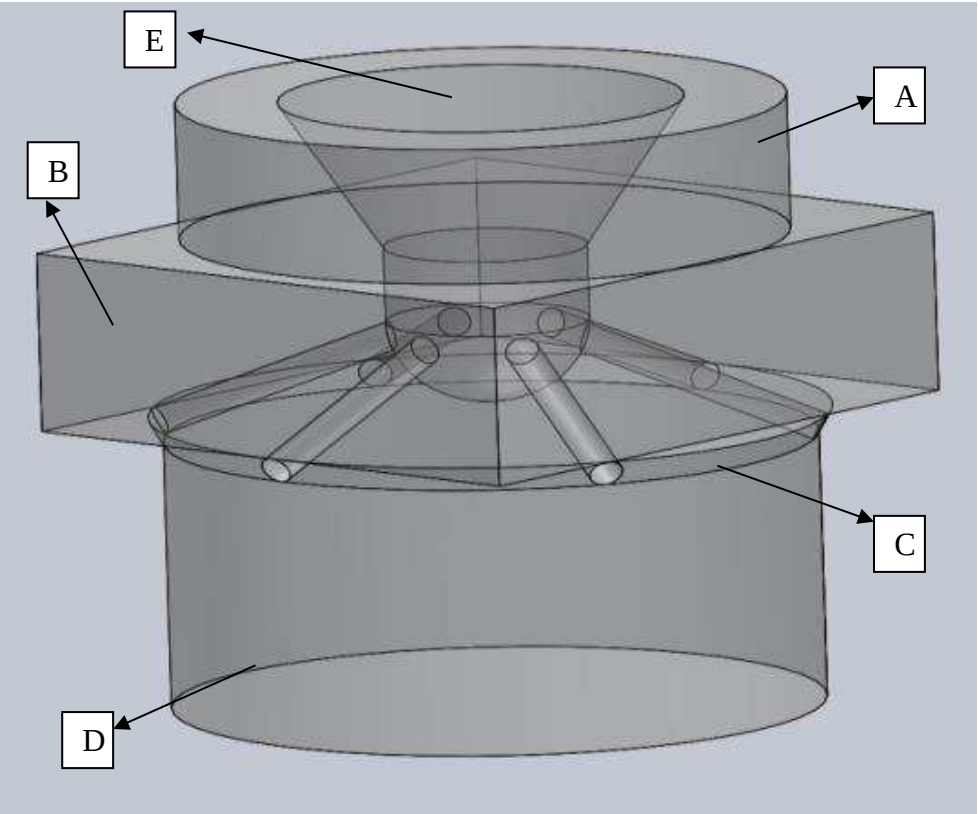

Figure 5.8 Injector tip transparent image

Figure 5.8 shows other modifications made to the exterior of the nozzle. The nozzle was made to be a 4 profile nozzle from the previous 2 profile. Section A in the figure has been unmodified. Its dimensions and size are the same as the previous design as this section attaches to the same injector nozzle used previously. Any modifications to part A would mean the attachment section in the nozzle on the injector would have to be modified or else it would not seal properly.

Part B is a rectangular section and has been modified to suit the current nozzle angle. The longer side reaches the edges of the two holes that could be viewed. The shorter side has been shortened to prevent the other four nozzle holes to be covered by a roof. If it was the same size as the longer length it would cover the top of the other four holes and would create a roof over the spray. This could cause changes to the geometric cavitation inside the nozzles and the changes may affect the two holes in view and the spray atomisation.

Part C refers to the nozzle hole exit modification discussed earlier. Part D is an extension to prevent the spray hitting the spray cone and the attachment unit to compress it onto the modified injector. The spray cone design is discussed in detail later. The overall length of the new modified injector tip was the same as the old injector tip which was 3 mm.

Initially during redesign of the injector nozzle an error was made and the design had slightly longer holes because of their position on the sac. This was realised after they had been manufactured. The error was corrected and the nozzles re-manufactured. However during initial testing, the entire correct aspect ratio nozzles were consumed/fractured due to pressure testing. It was decided that the slightly larger aspect ratio nozzles to be used due to time and manufacture expense. If consistently used, the comparison of the data would be unaffected. During testing, the combination of 400 W focused white light heat, nozzle compression and the force of injection the nozzles would deteriorate after about 500 injections. The actual d/l ratio was 0.134 ± 0.001, whereas the larger length nozzle d/l ratio is 0.126 ± 0.001. The later was used throughout this study. Figure 5.9 shows the differences between the two nozzles.

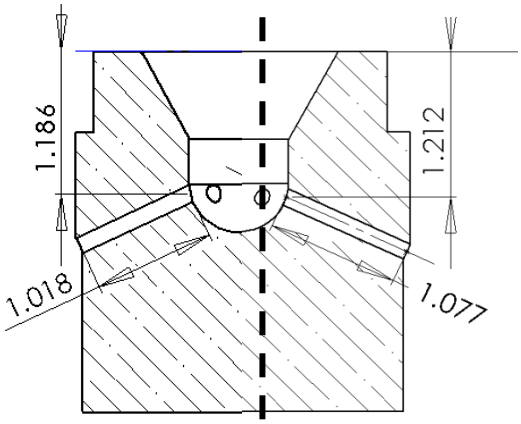

Figure 5.9 RHS original hole length of the nozzle, LHS larger hole length of the nozzle.

After manufacture the nozzles were placed under great scrutiny to identify the best nozzles by looking at features such as; hole alignment from the bottom and side, hole entry into the sac, hole parallelism and hole exit, before they were selected to be used. Nearly 60 - 70% of the

nozzles were discarded. In total the larger aspect ratio nozzles used in the test were manufactured thrice. The manufacture of the first 2 sets was the same (hole hand drilled), but the third had to be changed slightly due to unavailability of certain core components required for manufacture.

The holes which were previously hand drilled required a precision drill bit of 0.136 mm. The bits used in the first two manufactures had a shank and could be held well in a chuck. Unfortunately these drill bits were unavailable and ceased from being manufactured. Custom manufacturing them would be prohibitively expensive. The new drill bits in the market of diameter 0.136 mm did not have a shank as seen in Figure 5.10 and thus could not be held well by a chuck and would also bend on impact to the acrylic due to the force of drilling. It was then decided to machine these 6 holes by holding the drill bit in a CNC machine for accuracy and control of the force at drilling. But this did not suceed as the hole drilled would start curving after a certain point and would therefore not be parallel. Finally a solution came up. Drill bits with a shank were still available in 0.13 mm size. These were used to pre-drill the holes and the holes would be re drilled with the 0.136 mm thin drill. The pre-drilling would prevent the 0.136 mm thin drill bending. This process was carried out on a CNC machine for accuracy of hole location during the double drilling. The nozzles marked in alphabets are from the first to manufactures whereas the nozzles marked in Roman numeral are from the third manufacture.

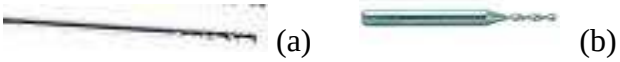

Figure 5.10 (a) drill with no shank (parallel) (b) drill bit with shank

Prior to the experiment, the nozzles went through thorough scrutiny to check for correct features and to select the best nozzles as mentioned earlier. Initially the nozzles were polished at the two perpendicular sides to the holes to be imaged and the bottom surface. This was done to optimize the light entering the nozzle and also to get better images. The polishing was done on rotating polishers initially with 1micron paste to coarse polish then with a 0.5 micron solution for finer polishing. The nozzles were imaged over a microscope at 4X zoom to look at the internal hole structures from the base and from the two sides and a 10X zoom to look at the hole diameters and shape at exit.

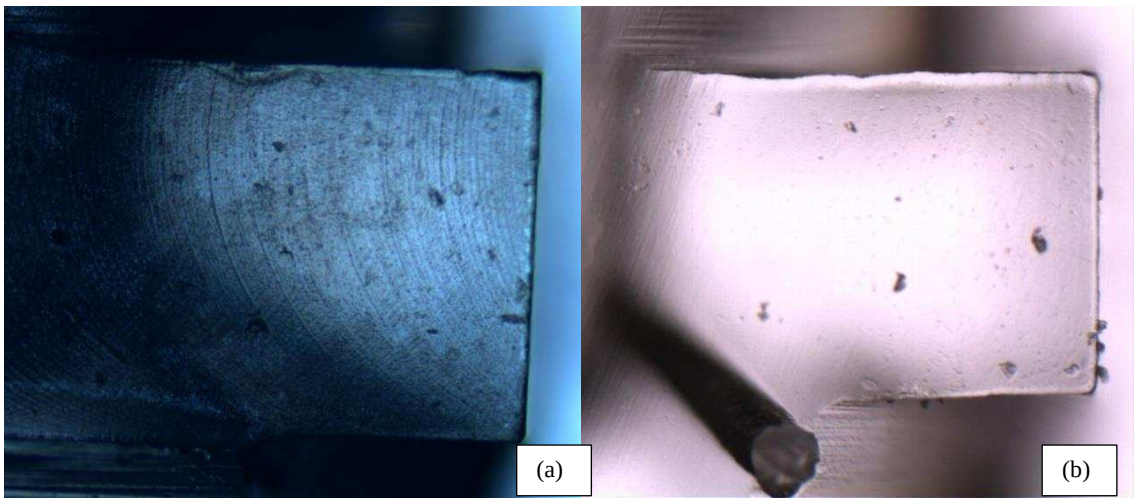

Figure 5.11 (a) unpolished side showing grains (b) polished side

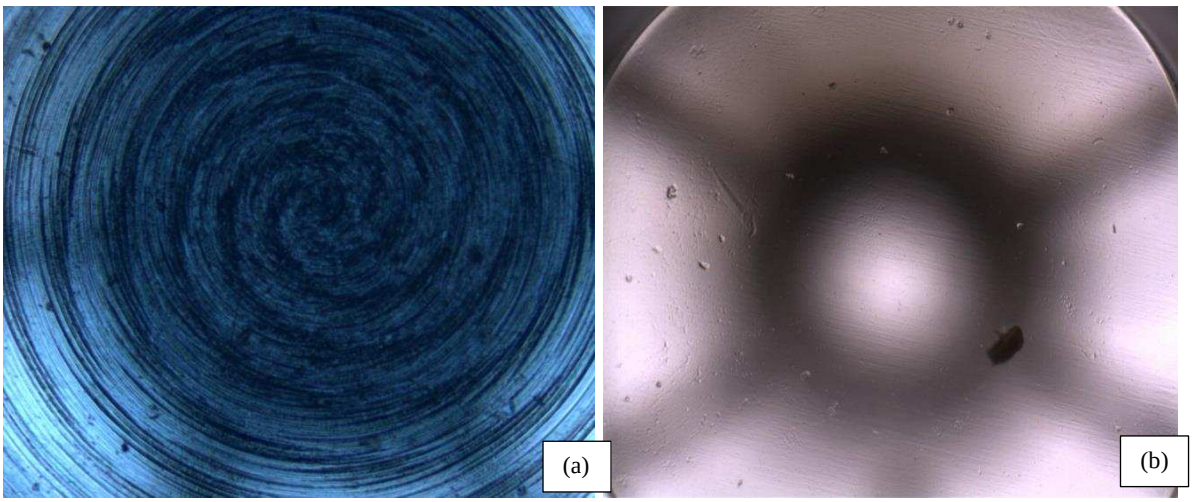

Figure 5.12 (a) Unpolished Bottom surface (b) polished bottom surface

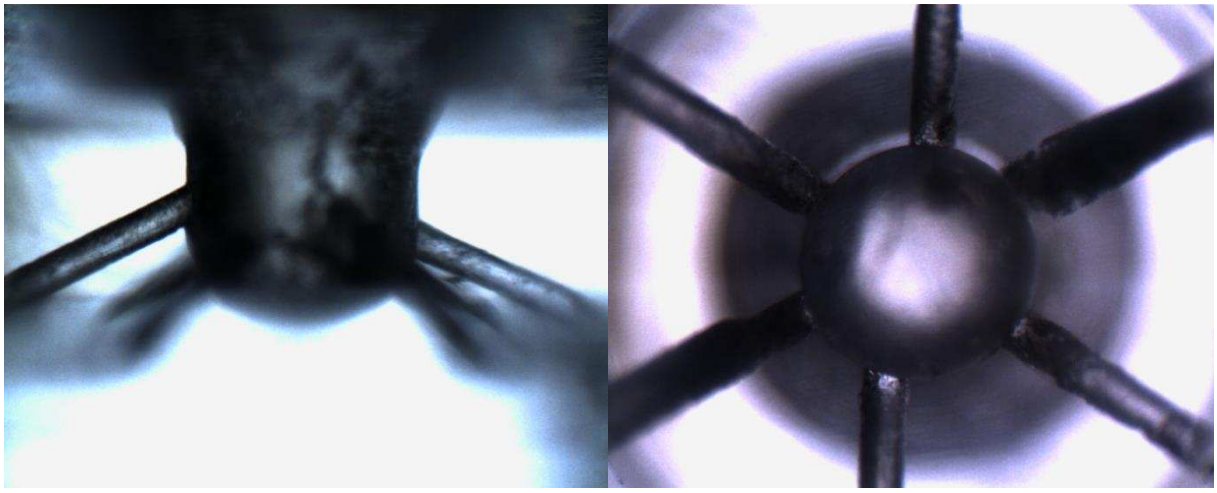

Figure 5.13 Microscopic images from the side and bottom of discarded acrylic nozzles (non-selected)

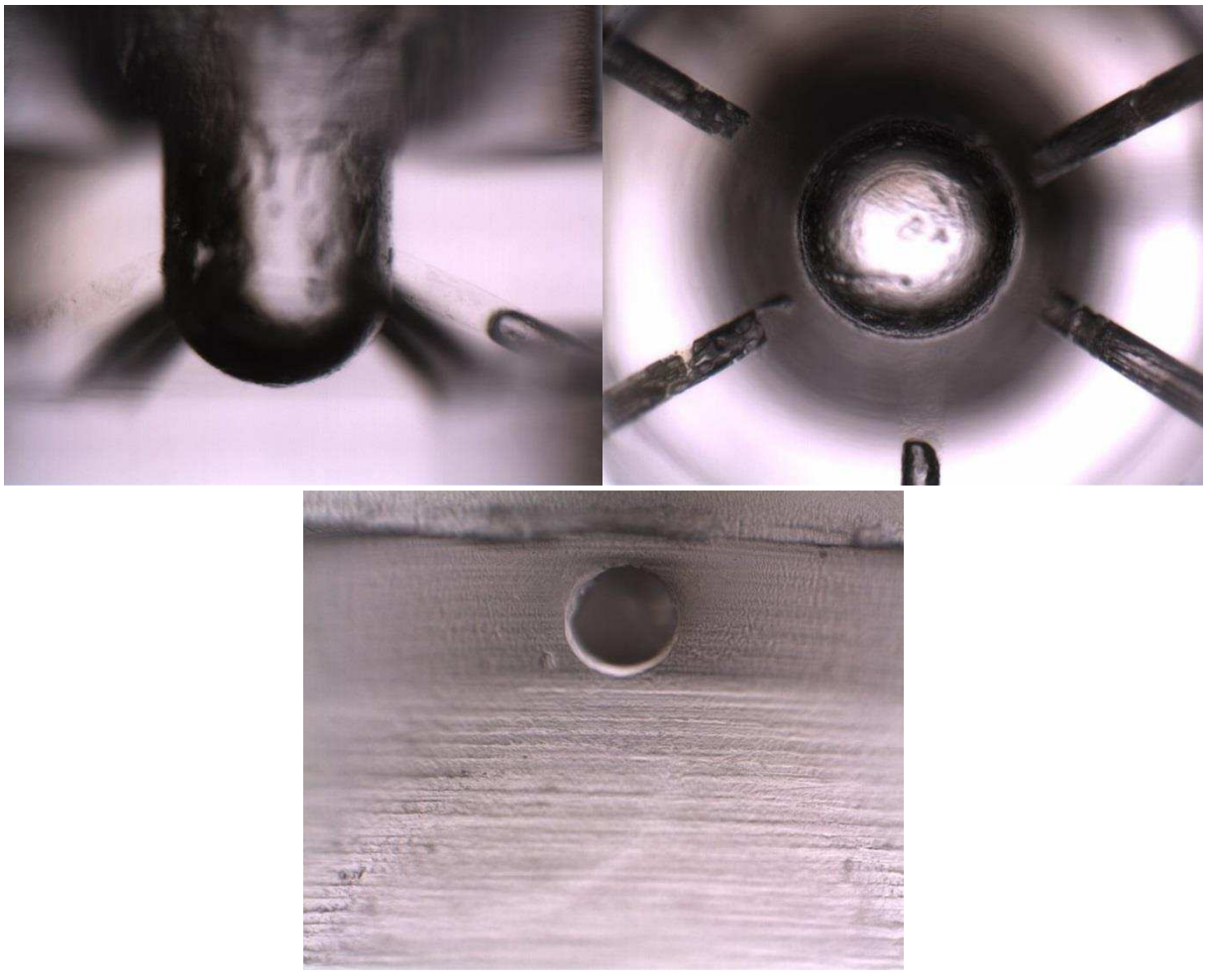

Figure 5.14 Microscopic images of the selected acrylic nozzles

Figure 5.13 and Figure 5.14 shows the criteria for acrylic nozzle selection. The holes in Figure 5.13 were observed to be entering the sac at different levels whereas images taken

from the bottom show holes not being parallel and some larger than others. Figure 5.14 shows the criteria for a near perfect nozzle. As seen nozzle holes are entering at the same height in the sac and they are symmetrical and parallel from the bottom images. The holes also have a circular exit. These are the criteria used for selection as nozzle geometry has a significant effect on the in-hole cavitation and in turn its external spray formation and structure.

It is also important to determine a way to seal the injector nozzle tip to injector. Glues will not help due to the high pressure force causing the temperatures to rise. It would be difficult to apply and during compression it may spread into the inside of the Mini-sac and also cause thickness geometry on contact and possibly block the holes. The only other feasible way is to use compression forces. Previous users [184] have used high spring constant springs compressed by screw mechanism to provide a compression force. The effect of using a spring is that sudden high pressure forces cause small movements in the spring which tend to cause leaks and movement of the injector nozzle tip. Once the impact of the start of the injection is gone and the injection force is stable, there is a constant force application. The screw mechanism also causes slight errors as it would have to be tightened in order to produce a compression on the spring to overcome the force of injection without any exact measure.

It is critical to the experimental setup and to obtain good images to have a good system to seal the nozzle tip to the injector nozzle. The fuel injection pressure for experimental analysis is set to 350bar. To calculate the forces on face E which in the inner circle of the face (diameter - 1.597 mm) a 1.5 safety factor was used by increasing the pressure in the calculation to 550 Bar. Using the standard pressure formulae (force per area), the force of fuel impacting the 0.8 mm diameter minisac would be 99 N. A mass of approximately 10 kg will be acting on the

small surface and thus a good compression system will be required to attach the nozzle tip to the modified injector.

A double acting hydraulic cylinder which uses a controllable air pressure via pressure regulator to control a piston attached to a rod was used to provide a compression force to seal the nozzle tip onto the injector nozzle.

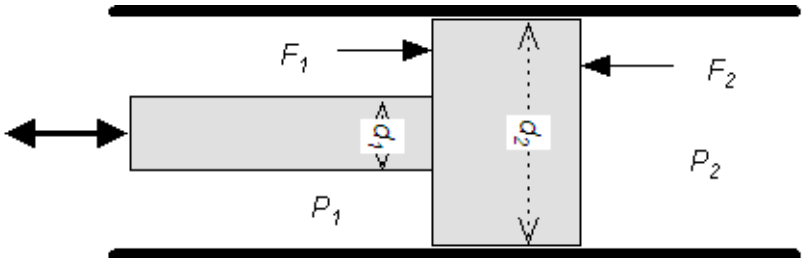

Figure 5.15 Principles of a compact cylinder

$$\mathbf{F_1} = \frac{\mathbf{P_1 \pi (d_2^2 - d_1^2)}}{\mathbf{4}}$$

Equation 5.1

Figure 5.15 shows the basic principles of a double acting hydraulic cylinder. Equation 5.1 represents the force-pressure relationship of the double acting cylinder on the rod side. In the equation F represents the rod pull force, P is the pressure in the cylinder (rod side), d_1 is the rod diameter and d_2 is the piston diameter. Table 5.1 shows the dimensions of the hydraulic air ram.

Piston Rod Diameter (d_1)	16 mm
Piston Diameter (d_2)	40 mm
Piston Stroke	50 mm

Table 5.1 Notable dimensions for the double acting ram

Due to a balancing screw, the force that was required to compress the nozzle tip doubles to 200 N. This is because due to the position of the balance screw being located the same distance between the centres of the injector and ram, on the opposite side. It will take half the force created by the ram; hence the force is doubled so the half needed for the nozzle tip compression (99 N) still acts on it. The pressure required to produce a force of 200 N using the dimensions in Table 5.1 and Equation 5.1 is 2 bar.

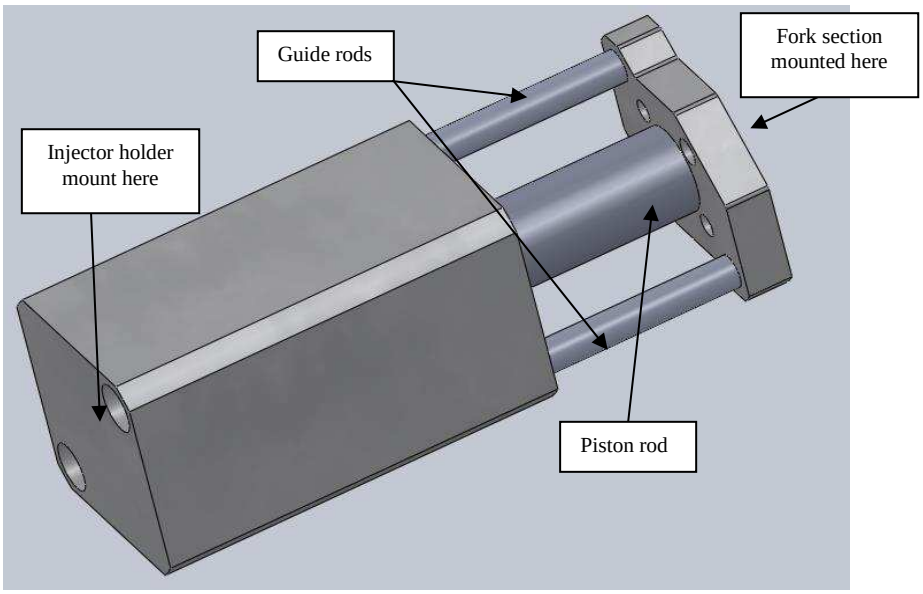

Figure 5.16 Image representation of the double acting hydraulic ram

A fork section which held a cuboid Fused Silica glass section was attached to one end of the hydraulic air ram. The other end was attached to the injector holder mount. The Fused Silica cuboid was designed to fit firmly into the fork section and flush with the conical injector tip stand. Further discussions of the fork cuboid section are continued in the assembly.

5.1.4 Injector nozzle assembly and spray extraction

A rigid injector design was necessary in order to mount the injector horizontally at high pressure. The other important criterion to be taken into consideration is that, all the

components namely; the injector and mount, injector nozzle tip and hydraulic pressure ram, would not be in the path of the fuel spray to be imaged. If any of these were in the fuel spray path then it would hit these components and rebound back. This would influence the spray imaging and cause misinterpretation of results. The injector mount was therefore designed to stand at an angle of 60 degrees from the horizontal from one side as observed in Figure 5.17. One fuel spray was required to be spraying vertically upwards at an angle of 25 degrees. This other spray opposite would spray downwards, and the rest to the sides. The spray directed downwards would hit the double acting hydraulic air ram attached below the injector to the same mount. As the sprays are at 60 degrees to each other it was essential to rotate the mount at 60 degrees as will be observed and discussed later in the assembly section. The injector was then clamped into this mount and held firmly. The whole mount was firmly screwed to an optical table.

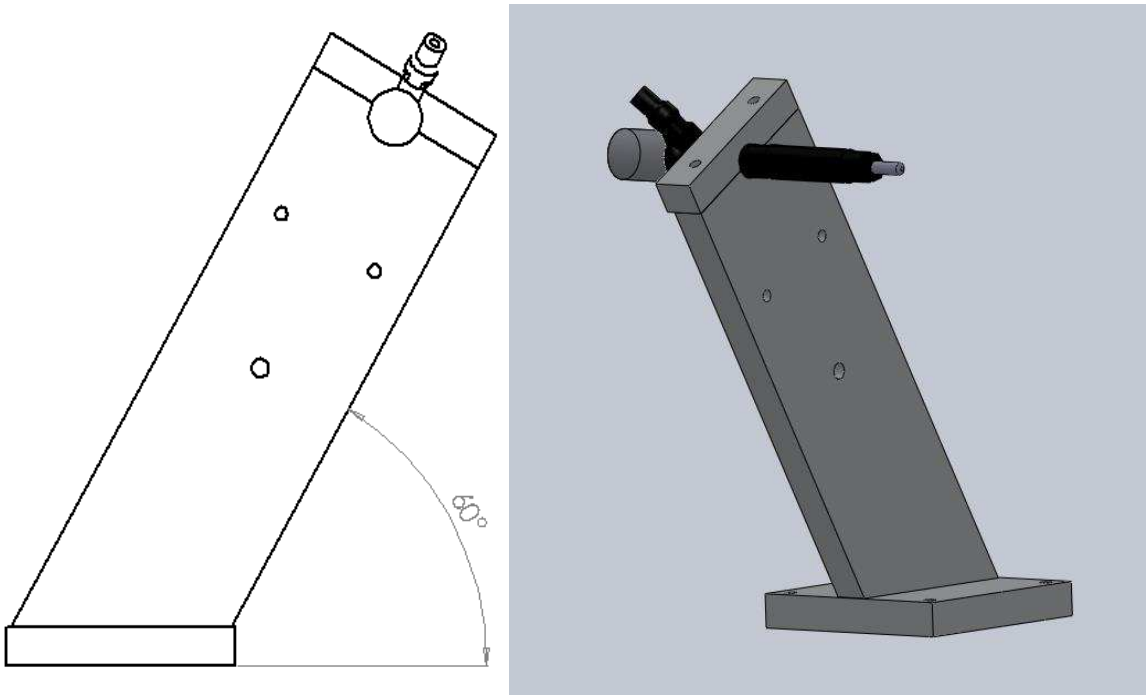

Figure 5.17 Injector holder mount

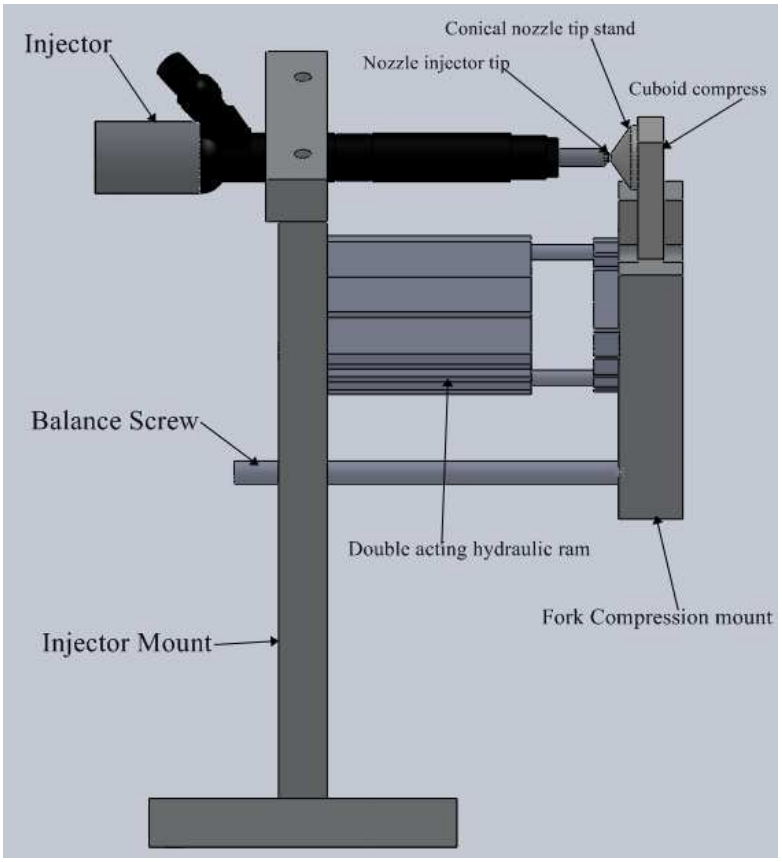

Figure 5.18 Assembly of fuel injection components

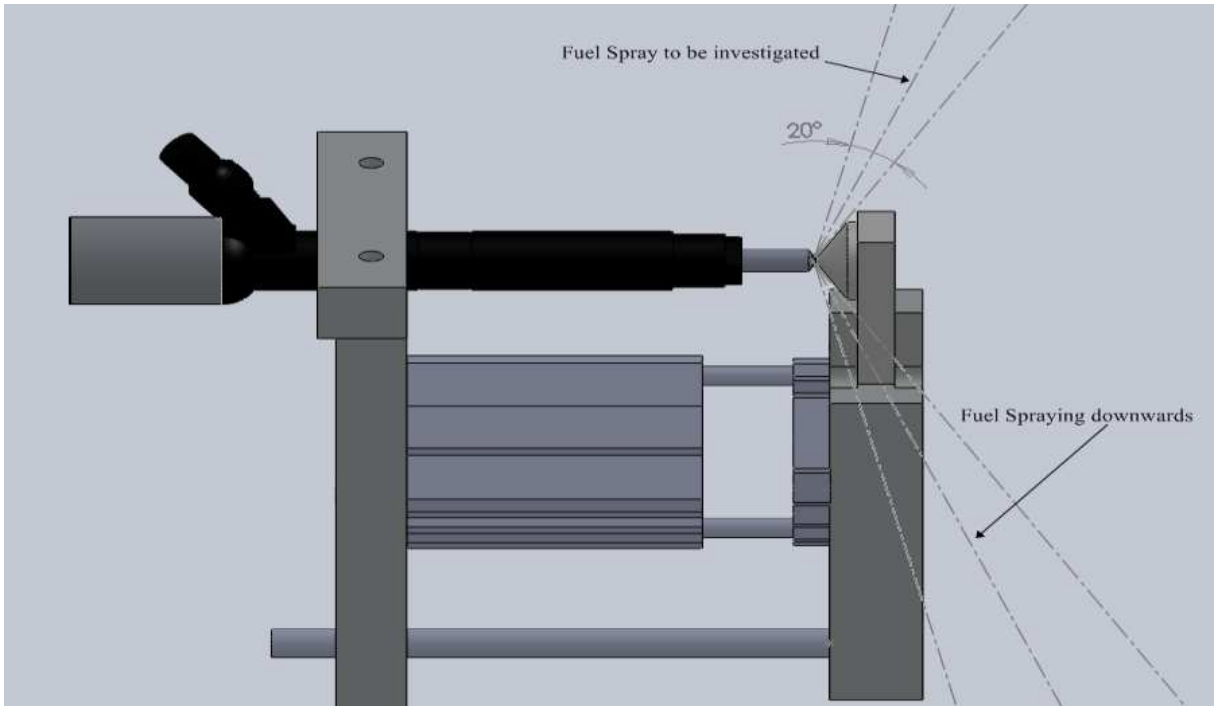

Figure 5.19 Assembly showing 2D spray path

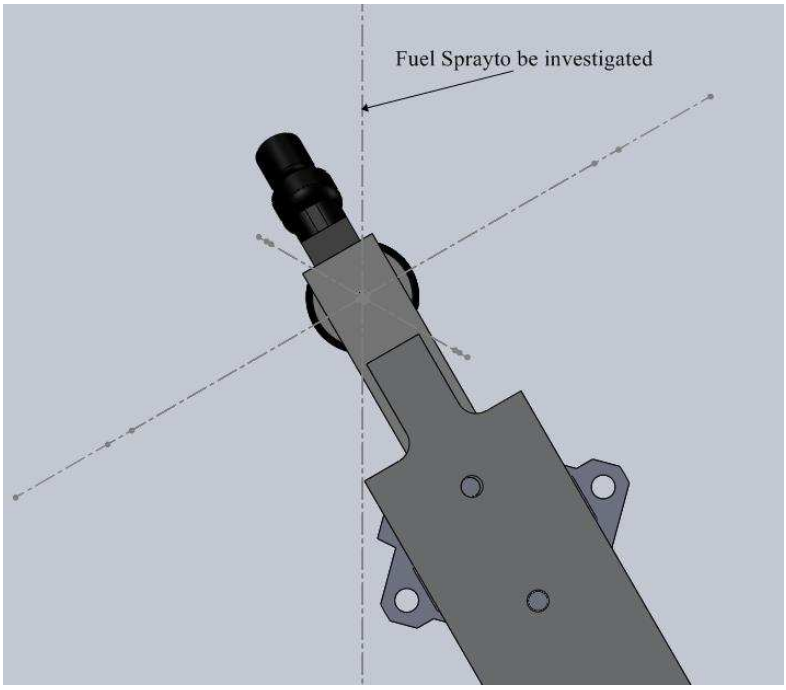

Figure 5.20 Assembly showing all 6 sprays directed out of the page

Figure 5.18 shows the assembly of the components all mounted. A 2D representation of the fuel spray path can be observed in Figure 5.19. As discussed earlier in the injector mount design, the spray downwards in Figure 5.19 would hit the hydraulic air ram and thus the mount had to be angled at 60 degrees. Figure 5.20 shows all the 6 fuel sprays, spraying out of the page. All 6 sprays paths do not collide with any parts/components mounted, thus there will be no rebounds of spray droplets covering any optics.

The cuboid compress section and the conical nozzle tip stand observed in Figure 5.19 are made from acrylic and Fused Silica respectively. Both these components had to be optically accessible as they were in the white light path into the acrylic injector nozzle. The later was made in fused silica to prevent it from burning as it was near the focal point of the laser sheet

The fuel spray contains Rhodamine-B which is a skin irritant and also causes breathing difficulties if inhaled. The fuel spray atomises into a very fine aerosol which will be spread in

the air and breath easily. A fuel spray exhaust extract design was created to use an exhaust tunnel to draw the fuel spray through an air filter (to filter the Rhodamine by dyeing the element) then in to the exhaust tunnel. The design had 6 holes which would be lined up with the six sprays from the injector nozzle tip. It was also designed so that at least 2 cm of the spray length could be captured with the laser sheet dropsizing camera.

The design of the extract was mostly dependent on the distance away from the injector nozzle tip. Placing it further back would mean increasing its diameter due to the spray penetration causing a wider spray cone angle. The spray angle would also increase, and thus the side flaps would have to be thicker. An optimum distance was determined that enabled a 2 cm spray to be viewed and the spray also to be captured before the spray and spray cone angle got too wide. The inner radius of the extract was 60 mm. This was optimised to collect all the spray exiting whereas giving ample space for the Laser sheet dropsizing optics and large magnification of the inside of the nozzle for the imaging of the internal flow.

Each hole in the extract was connected to pipe. All six pipes were connected to a suction being created by a compressor drawing air from the cell past an air filter in an exhaust tunnel. This would filter out the fuel and the Rhodamine-B. The clean air is then extracted to the exhaust tunnel. The air filter would be changed often to ensure the air was not contaminated. The hole in the centre of the fuel spray exhaust extract is a cut out to allow passage to white light which will illuminate the acrylic nozzle.

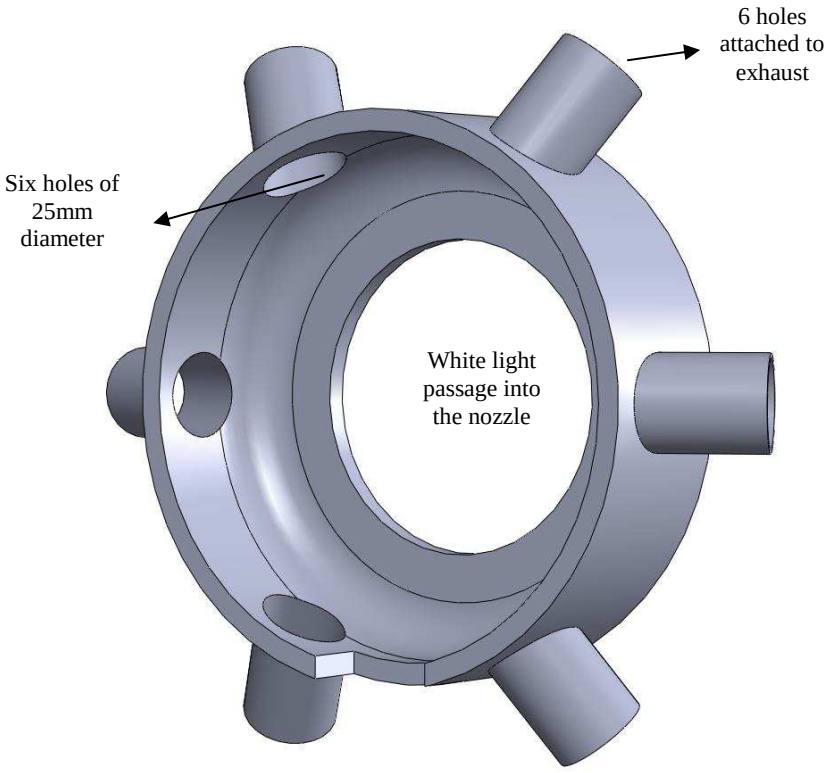

Figure 5.21 Fuel spray exhaust extract

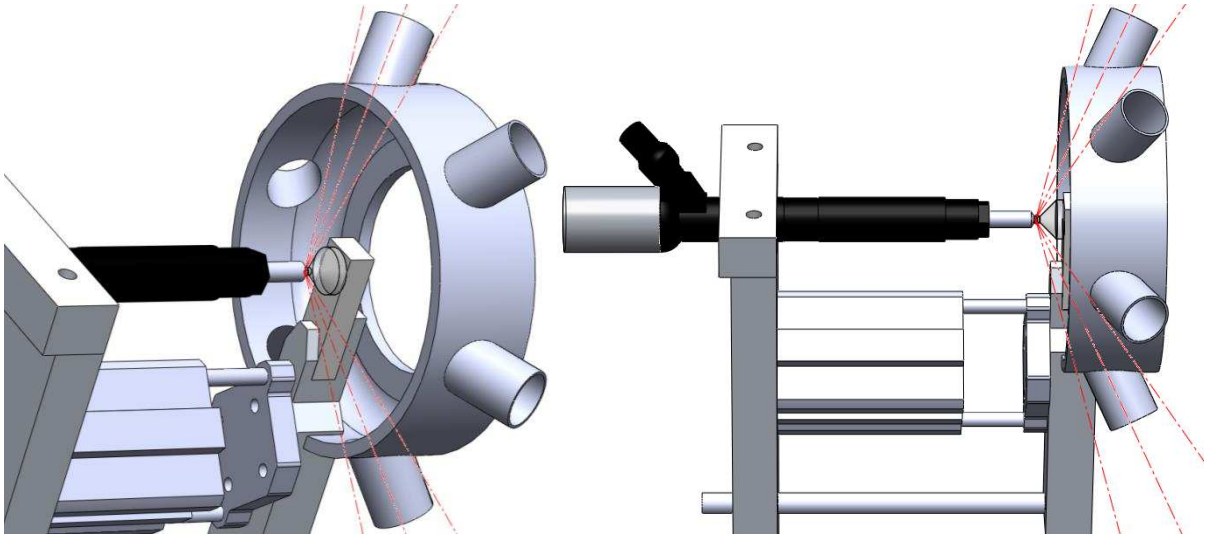

Figure 5.22 Fuel sprays into the six extract holes.

5.2 High Speed Image Acquisition and Optical Setup

The fuel was seeded with Rhodamine-B as the fluorescing particle. The nozzle and corresponding spray to be imaged will be set to spray at an angle of 25 degrees from the vertical. The setup uses:

- 10 kHz Pegasus Nd:YLF Laser at 527 nm, 1.5 mm beam diameter, ~1mJ per pulse, Gaussian profile and a pulse width of 180 ns at Full Width Half Maximum (FWHM). The laser had an energy stability of <1% rms after a 10 minute warm up. The laser is used to illuminate about 2 cm of the external fuel spray which has been seeded with Rhodamine-B. A microscopic lens setup will be used to form about 2 cm width of laser sheet which will be directed perpendicular to the centre of the spray.

- 400W ARRILUX 400 "Pocket PAR" white light source. The white light is used to illuminate the acrylic injector nozzle from its bottom. It will create a good illumination inside the nozzle holes which will be captured from the side.

- 2 x Photron SA1.1 cameras at 10 kHz. 1 camera is going to image a combination of the Laser Induced Fluorescence (LIF) scattering and Mie Scattering images of the external spray (LSD Camera). The second camera will capture the white light elastic scattering from the insides of the nozzle simultaneously (INF camera). Both cameras will use an 85 mm Nikon lens. The two cameras will take synchronised images throughout the injection with a delay between the laser firing and the image acquisition set with a delay to prevent laser illumination interfering with the internal nozzle imaging.

5.2.1 Laser sheet dropsizing of external spray

Laser induced fluorescence/Mie scattering also known as Laser Sheer Dropsizing (LSD) was proven to be a useful diagnostic for the measurements of Sauter Mean Diameter (SMD) in non-evaporating sprays. It is a method to determine the two dimensional droplets size distribution in a spray and is different from the point-wise measurement techniques such as Phase Doppler Anemometry (PDA). The principles of LSD have previously been discussed in the literature review.

Rhodamine-B doped fuel would be injected upwards at an angle of 25 degrees from the vertical. The Rhodamine in the fuel will excited at 527 nm for the LIF images. This section will discuss the laser optics and the image acquisition optics. The laser optics section discusses the formation of the laser sheet and its direction towards the sprays exiting vertically upwards with and angle of 25 degrees. This is followed by the discussion of the doubling optics which take light scattered from the spray and split it into LIF and MIE by filtering and then focussed on different halves of the LSD camera.

5.2.1.1 Laser optics

The laser was initially brought to the height at which it would be angled into the spray at by periscope like arrangement with two mirrors. To maximise the reflection of the laser beam it was ensured that the beam would contact the mirror at its centre. The sheet forming optics used within this study consisted of a planar convex lens and 2 cylindrical lenses. The laser beam first enters a 1 m focal length planar convex lens to create a converging beam. The beam then passes onto a -25 mm planar concave cylindrical lens where it forms into a diverging vertical sheet. A +150 mm cylindrical lens expands the beam sheet from about 2

mm high to 12 mm. This lens is located closer to the planar concave cylindrical lens to produce a gently expanding beam. The divergence and height of the beam could be varied by adjustments on the sheet forming optics. Fine adjustments were made by rotating thumb wheels on the lens mounts and adjusting the distance between the final 2 lenses to achieve the optimum beam sheet. The sheet travelled a distance of ~50 cm from the final cylindrical lens to the spray position and increased from ~12 mm to ~20 mm in height. The sheet is then reflected by a mirror onto the spray path. The sheet at the spray was approximately 20 mm high and 0.2 mm wide at focus.

To ensure maximum potential of the laser sheet, proper positioning of the mirrors and the sheet forming optics are essential. Furthermore, failure in correct positioning of the optics results in a Non-Gaussian beam profile. By careful alignment, the laser beam will follow the central axis of lens in the sheet forming optics. Once sheet was positioned and set the optics were tightened so they could not be moved. It was critical that these sheet forming and directing optics were not move during the experiment.

5.2.1.2 Image doubler, filters and LSD camera

The current study involves simultaneous imaging of LIF and MIE scattering methods and for this reason an image doubling, filtering and acquisition of two views of the same subject on a single image, with each view being individually filtered to provide LIF and Mie images on 2 halves of a single image. The optics consisted of a beam splitter, a 527 nm band pass filter with neutral density filter for attenuation, an aluminium mirror and a high OD neutral density filter as mirrors and a 550 nm long pass filter with a neutral density filter for light attenuation.

The light scattered from the spray would first pass a 50:50 Beam splitter. 50% pass and 50% reflect. The pass light would go through onto an aluminium mirror which reflected it passed an OD 0.3 neutral density filter and a 527 nm band pass filter. The light would then travel through an OD 2 neutral density filter onto one half of the camera. Both neutral density filters on this half were to attenuate the intensities to the correct signals to be captured in the camera.

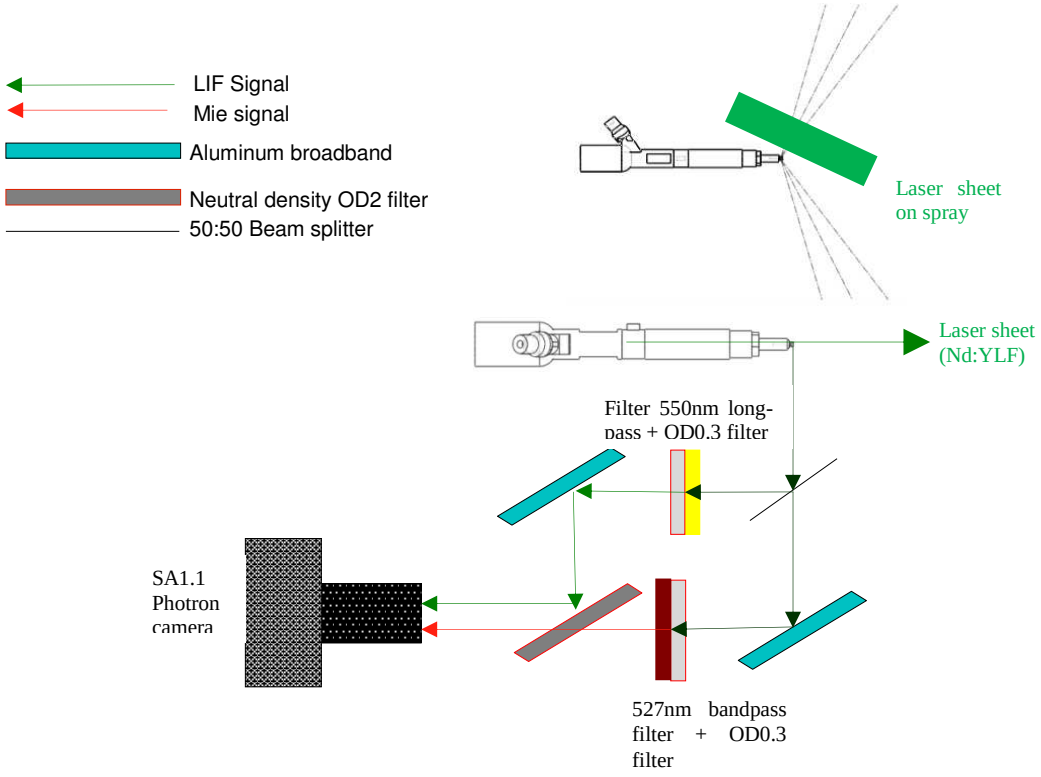

Figure 5.23 The image doubler, filter and camera setup

The reflected light would pass through a 550 nm long pass filter and neutral density filter OD 0.3 to attenuate the intensity of the light and then reflected by an aluminium mirror onto the OD 2 neutral density filter and onto the other half of the camera. The images were attenuated such that the Mie spray image and the LIF spray image had similar intensities, the LIF attenuated to intensity slightly lower.

Figure 5.23 shows the image doubler setup with the camera. The figure shows the principles and pathways of the separated light which are then filtered and directed on different halves of the camera sensor.

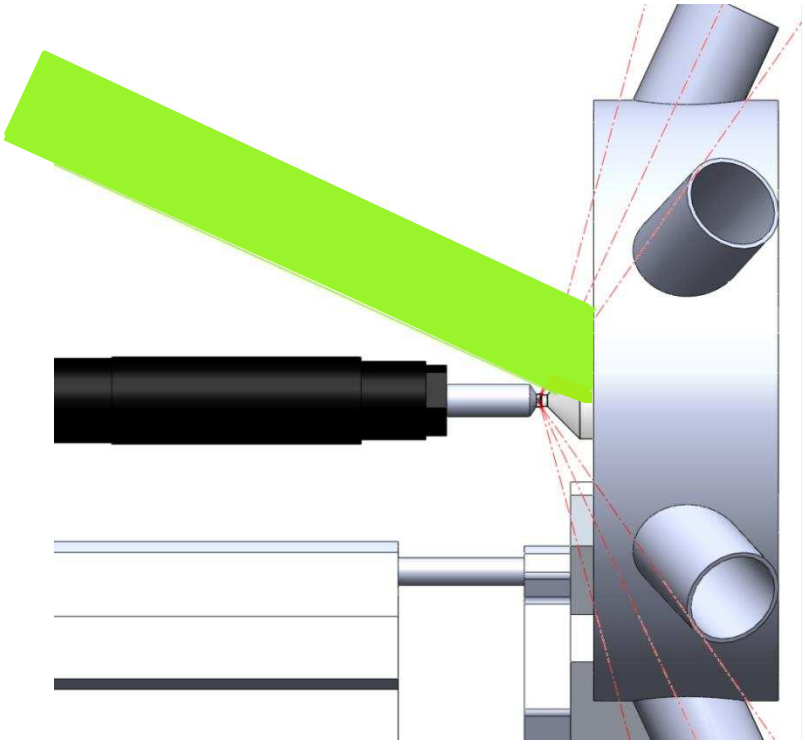

Figure 5.24 Laser sheet illuminating the spray

The LSD camera had a Nikon 85 mm f1.4 camera lens, reverse coupled to 65 mm extension tubes. The images captured had a resolution of approximately 28 µm/pixel. The resultant image was of magnification 0.7. For the experimental acquisition, the lens was set f1.4, the camera setup to image 1024 x 512 pixels acquired at a synchronised delay of 30 µs from the INF camera at a frame rate of 10 kHz, an exposure of 370 ns, and a dynamic range of 12 bits (0 - 4095). During the experiments the camera would be set to acquire 100 frames (10 ms) per acquisition pulse. This would produce approximately 17 frames prior to injection, 50 frames (5.0 ms) during the injection and 33 frames post injection.

5.2.2 Elastic scattering inside nozzle holes

Continuous white light obtained from a collimated Arri 400W POCKET PAR lamp was passed through a hot mirror to direct away 'Hot' UV light and then into a 150 mm diameter planar convex lens with 50 cm focal length. The converging light was reflected using a 45 degrees mirror on to a 50 mm diameter biconvex lens with 150 mm focal length, passed through the fuel extract and then the compressing cuboid and the fused silica conical section and focused onto the acrylic injector nozzle. Figure 5.25 shows and overview of the setup. Back-scattered light obtained from the cavitating diesel in the nozzle passages was reflected onto a high speed Photron SA1.1 camera (INF camera) using a Nikon 85 mm f1.4 camera lens, reverse coupled to 230 mm extension tubes. This arrangement facilitated high resolution imaging of approximately 8 μm/pixel. The INF camera was configured to obtain 768 pixel x 768 pixel images with a 1μs shutter speed and the camera lens at f2.4 taking images at a frame rate of 10 kHz. The use of this camera in this manner facilitated real-time capture of individual injection events. Figure 5.26 shows a view of the image that would be captured by the INF camera. The camera was configured to begin capturing images synchronous with the leading edge of the electronic pulse sent to the injector with a 500 μs delay. On receipt of the trigger pulse, the camera took 150 frames at 10 kHz frame rate for 15 ms duration. Each frame had exposure duration of 1.0 μs. The camera also provided a 30 μs general out- delay signal for the start of acquisition of the LSD camera.

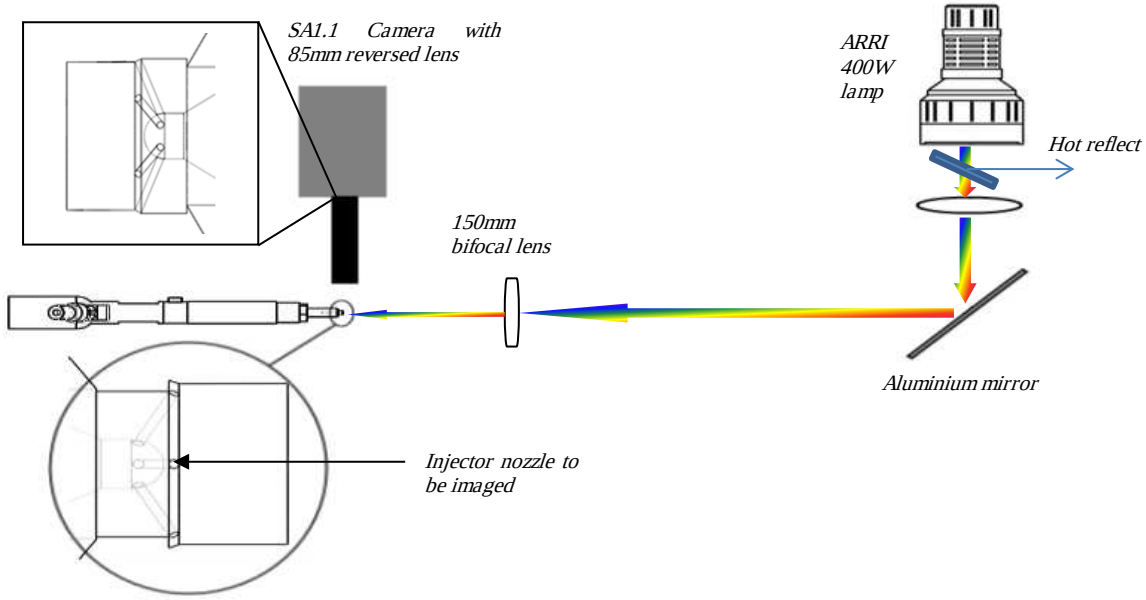

Figure 5.25 The internal nozzle hole flow imaging setup

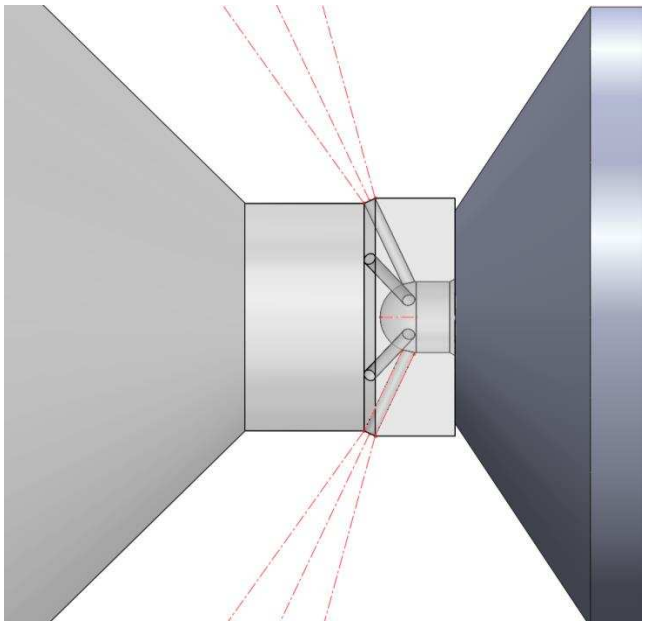

Figure 5.26 Image the INF camera would capture.

Initially images were set to be obtained over 10ms duration, but during testing there seemed to be a lot of large and small cavities forming when the needles had subsided. They may have been formed by cavitation in the small passage created when the needle is near seated. These cavities behaved in a violent vortex like structure in the sac when the needle had subsided.

This motion had high angular velocity initially which decayed with time. Small cavities were also seen either going down the holes towards the sac or out wards towards the exit in the two holes in focus. The bubbles either travelled in the same direction i.e. both towards the sac or both towards the hole exit, or in opposite directions i.e. either one towards the sac and the other towards the exit. This phenomenon was seen as interesting and thus the time to image was increased from 10ms from the trigger input to 15ms. This would give approximately 14 frames prior to injection, 50 frames during injection and about 86 frames after injection to capture this phenomenon. However due to the synchronised LSD camera only being able to store 10914 frames at 1024 x 512 pixels, the internal nozzle flow images were taken in 2 sets of 50 injections each.

During pre-experimental setup it was seen that the laser illumination was causing interference with the white light illumination. But because they both had very short exposure they could be set to capture one after the other. The INF (internal nozzle flow capturing) camera was set to be the master and it provided a 30 µs delay trigger for the LSD (dual image LIF-MIE capturing) camera. This would enable capture of the internal nozzle flow pre- laser fire. Calculating the Bernoulli velocity at 350 bar to be 295 m/s for a fuel with density of 801.9 kg/m^3, in 30 µs the spray would travel approximately 10 mm and thus the cavitation observed in the middle of the nozzle would be captured in the middle of the external spray for the same frame number.

5.3 High Speed Data Acquisition and Control

5.3.1 Synchronisation and control setup

A reference synchronisation clock at 10 kHz was provided to the INF camera. The clock was synchronised to the start trigger. A delayed sync out of 30 µs was output from the INF camera and fed to synchronise the laser at a delayed clock. This was done to stop the laser light interfering with the internal nozzle imaging. During initial tests it was established that the laser firing in synchronisation with the INF camera acquisition was affecting the quality of the images. The delay would mean that the laser fired 30 µs plus the internal camera delay to translate a sync output, of 160 ns. This delayed sync signal was also sent to a pulse generator where the sync to the LSD camera could be varied to up to 5 µs.

During setup it was discovered that the SA1.1 cameras wait for a sync pulse and then a trigger pulse to start acquisition. The variable delay was necessary to synchronise LSD camera acquisition to the laser firing. The delay sync out signal from the INF camera and the variable delay signal were sent to an oscilloscope. The laser was then fired and a delay between the signals was obtained for when the laser started to brighten the images and again when the image started to dim. This was known as the laser ON and laser OFF signals. The variable sync was set to the average of these two delay times obtained which was approximately 1.6 - 1.7 µs from the start of the laser pulse for 370 ns exposure duration. This was checked prior to each test before images were obtained to see whether the LSD camera exposure and the laser firing timing were precise.

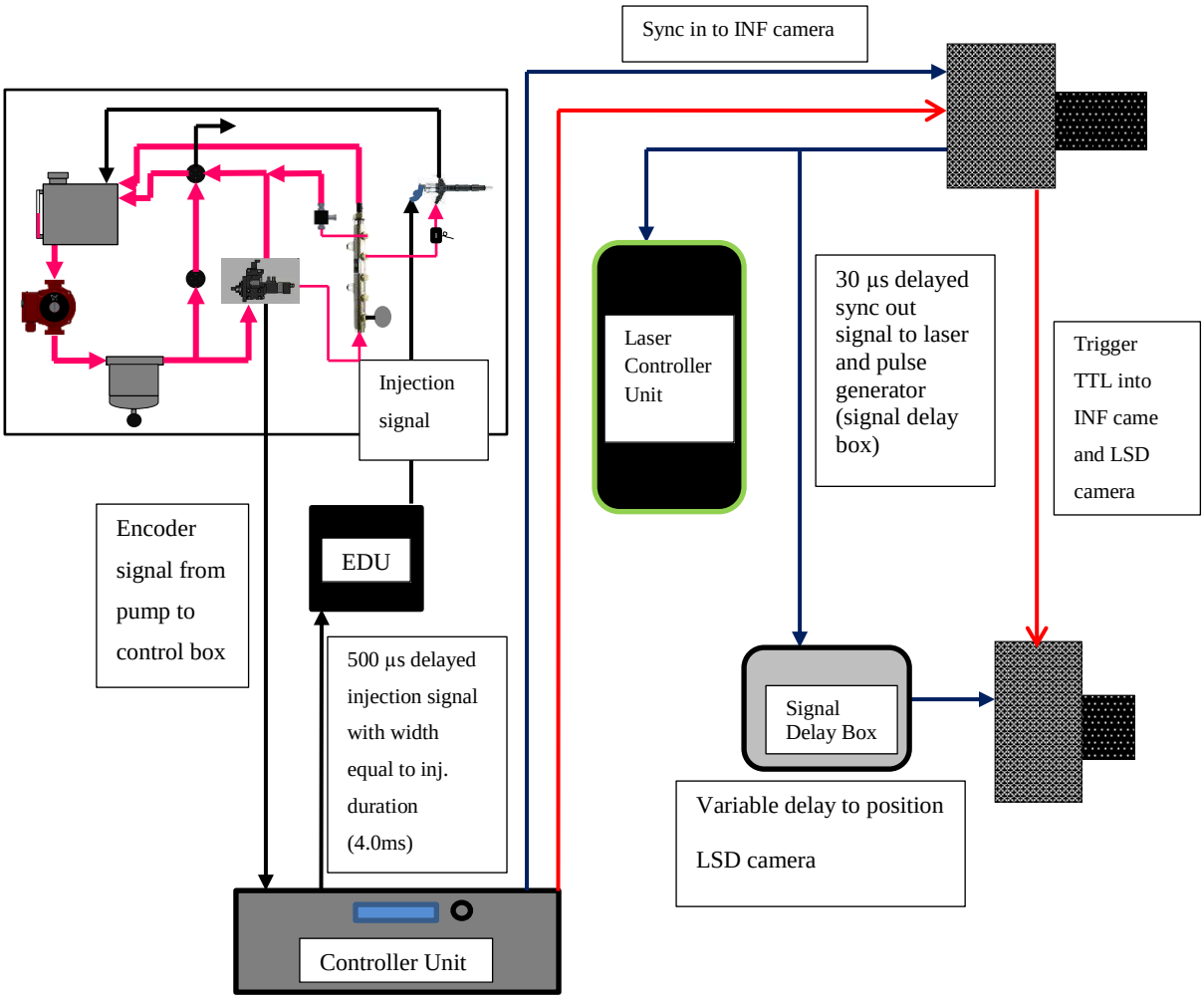

Figure 5.27 Synchronisation set up

The control box provided a trigger signal at 10 kHz synchronous with the start of injection. This was input into the INF camera TTL trig in. The camera provided and output to the TTL trig in (TTL trig out) which was input into the LSD camera. This set the acquisition start times of both cameras to the start of the TTL for the injection pulse.

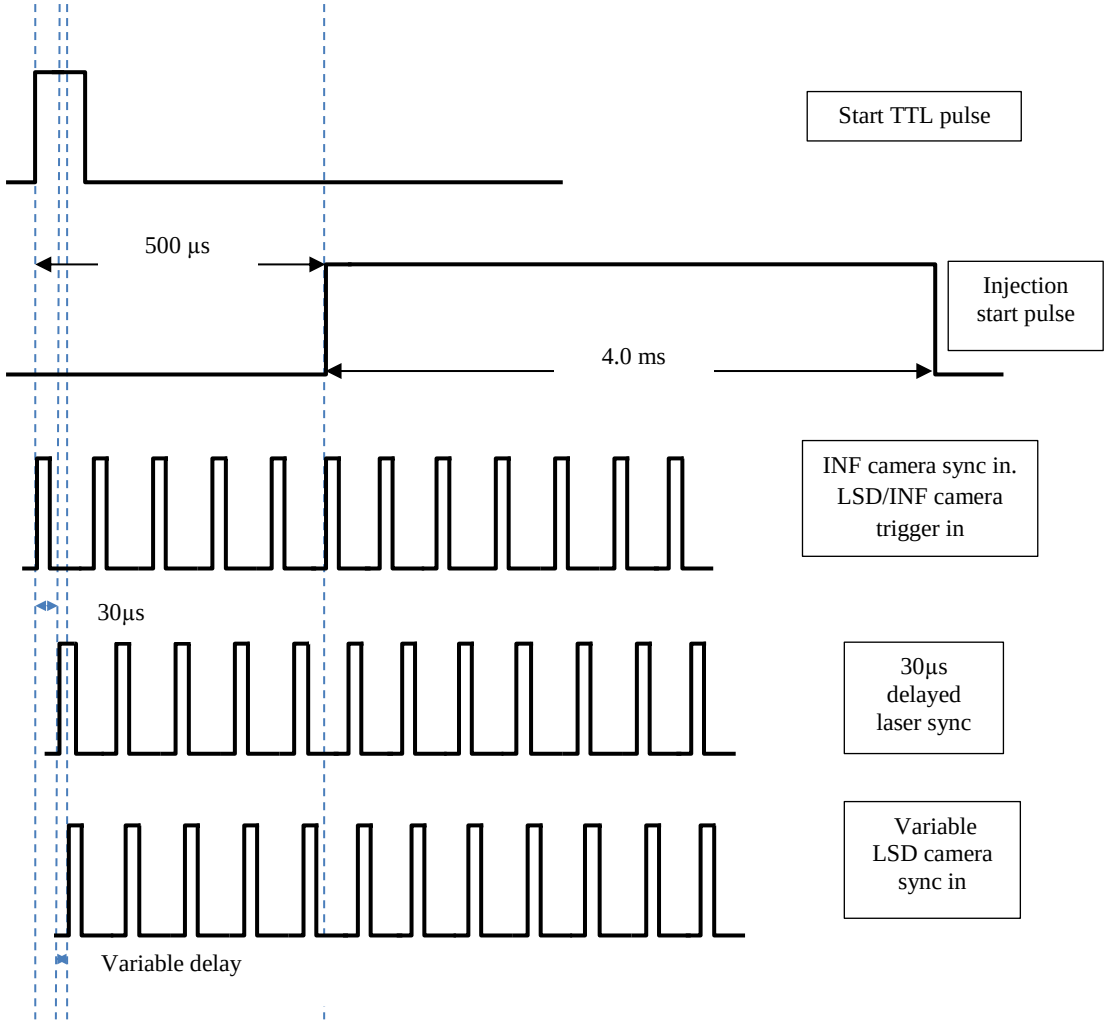

Figure 5.28 Start, injection, camera and laser synchronisation signals

5.3.2 Acquisition setup

The injection duration pulses and the laser fire pulses were recorded on to a PC by NI data acquisition systems 200,000 sample per second for 6.0 ms duration from the start of injection for every injection. Data was recorded every 5 µs equalling to 3000 samples over the 6ms period (200,000 samples/second).

Both the LSD and INF cameras were set to output their exposure digital pulses. The pressure transducers produced an analogue voltage signal which had to be calibrated to convert it into pressure. These together with the digital laser pulse signal and the injector trigger signal were

recorder in an excel comma separated file via a LabView code written to acquire data synchronously on the rise of the injection pulse. Both camera exposure pulses were expanded to a pulse width of 25 µs from their rise position so that they could be registered by the acquisition cards. The INF camera had an exposure pulse width of 1 µs whereas the LSD camera had an exposure pulse width of 370 ns. These pulses would have been missed otherwise as we were recording every 5 µs.

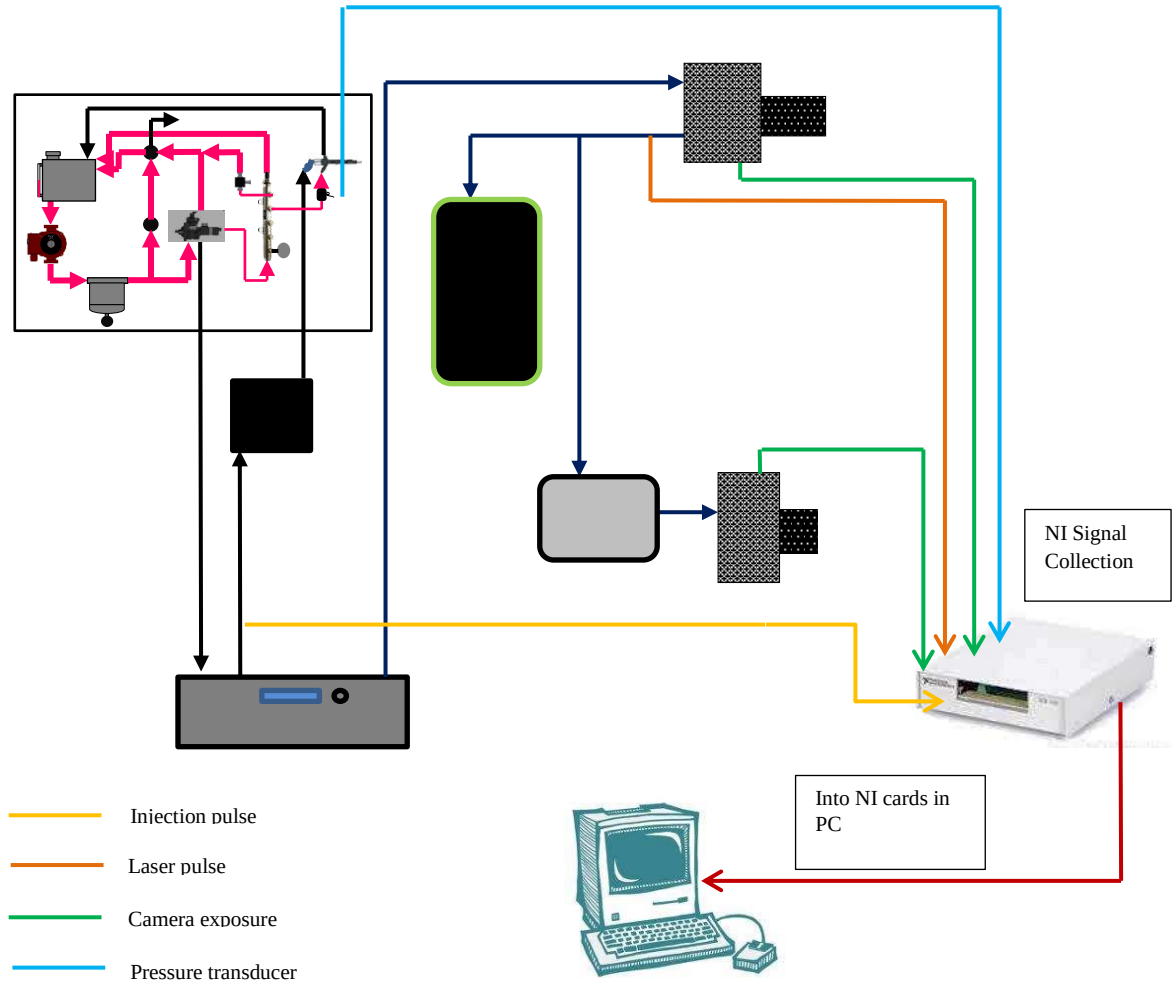

Figure 5.29 Data acquisition of laser pulse, camera exposure pulse, injection pulse and pressure analogue.

Blank Page

Chapter 6 Simultaneous External Spray Sizing and Nozzle Hole and Sac Imaging - Experimental Methodology

It is important to employ a consistent methodology during experimentation to enable correct comparison of data. This chapter provides a description of the diesel fuels used, the details for the fluorescent dye and seeding, the experimental methodology followed and finally the calibration work necessary is described. The calibration work was done to check nozzle manufacturing consistency and also mass injection variation per set. The laser profile across the imaging zone and the fuels fluorescence profile are also provided.

6.1 Fuels and Fluorescent Seeding

Fuels named A, B, D and a paraffinic model fuel were provided by Shell Global Solutions. The data for fuels A, B and D are known however their paraffinic model fuel is a secret blend and is only shown in this thesis as it was used for nozzle manufacture calibration. Information for this fuel can be approximated from its distillates between branched and linear chains of C8 - C26. From this data it is assumed the distillation range lies between 200 – 360 ºC. Table 6.1 shows some of the known physical properties of the fuels. From the table it can be noted that Fuels A and B have the highest densities with B having the higher viscosity. Paraffinic model fuel and Fuel D have lower densities. Fuel D has the lowest flash point and this can be further seen in its d profile. From the fuels, A is a fame free fuel with no additives. Fuel B is a ‘gap’ fuel, that is, some fractions around the 40 - 60% distillation point are missing being referred

to as the gap. This is observed by the sudden rise in the distillation profile of fuel B between the 40 - 60% distillation points in Figure 6.1. Fuel D is kerosene based fuel.

Fuel Name	Density @ 15°C IP 365 (kg/m^3)	Flash point IP 34 (°C)	Viscosity @ 40°C IP 71 (mm2/s)
A (Fame Free)	825		2.078
B	826.1	56.5	2.102
D	800.3	45	1.664
Paraffinic model fuel	780	-	-

Table 6.1 Physical properties of the fuel samples to be tested

Fuels A and B have a high distillation profile and will be referred to has heavy fuels (Boiling range between 150 – 350 ºC). Fuel D has a low distillation profile with a boiling range between 150 - 210 ºC and is thus referred to as the light fuel.

In order to obtain quantitative results from the fluorescence, it has to come from a single component. The simultaneous detection of the fluorescence from various species leads to a complicated dependence of the integrated signal intensity on the variables of that species such as species concentration, temperature, pressure and local gas composition [157]. Various fluorescing compounds may also differ in boiling points, diffusion and transport coefficients. Therefore systems are preferred where the fluorescence signal can be attributed to a single species for a quantitative LIF analysis.

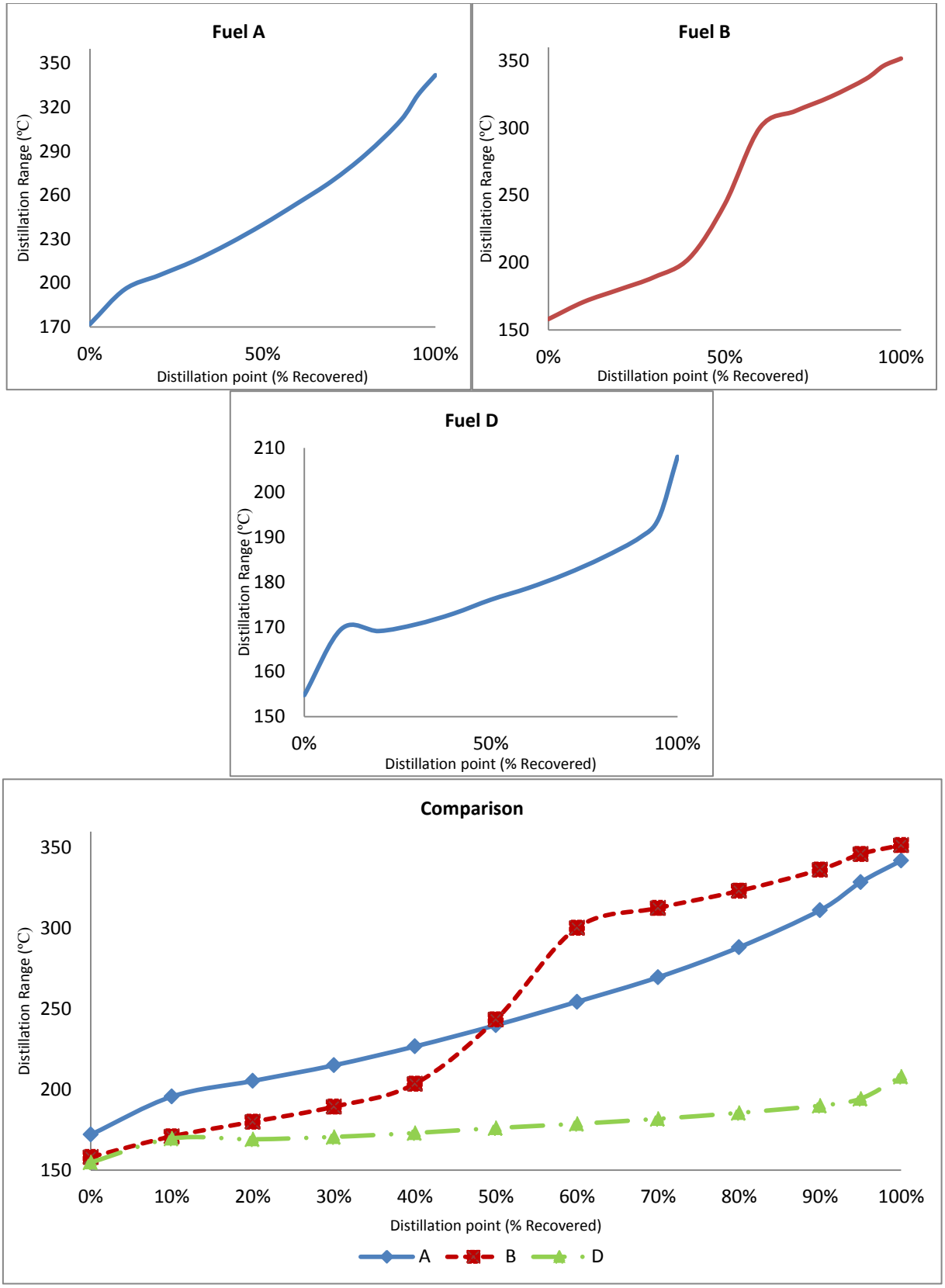

Figure 6.1 Distillation curves of the fuels A, B and D.

To generate fluorescence, excitation laser light delivered to the spray emerging from the injector must be within the absorbance spectrum of the dye. The closer the excitation wavelength is to the peak absorption wavelength of the dye, the greater the excitation efficiency. Optical filters that are suitable for the emission profile of the tracer dyes are then used to refine the emitted fluorescence such that only desired wavelengths are passed on to the imaging camera. The key was matching a tracer dye with a suitable excitation source and emission filter to obtain optimal detection efficiency.

The fluorescent tracer dye chosen was Rhodamine B (RhB) with an excitation wavelength at 543 nm and an emission wavelength of 568 nm in Ethanol [185]. Selecting a filter near the emission peak of the tracer dye generally improves the sensitivity and linear range of the measurement. A 560 nm long pass filter is used on the fluorescence channel. A long pass filter passes light longer than its specified wavelength and rejects all light shorter than that wavelength. The reason for selection of a 560 nm long pass filter is that we would like to separate out the Mie scattering at 527 nm. The chemical formula of RhB is $C_{28}H_{30}N_2O_3$. Its molecular structure is shown in Figure 6.2.

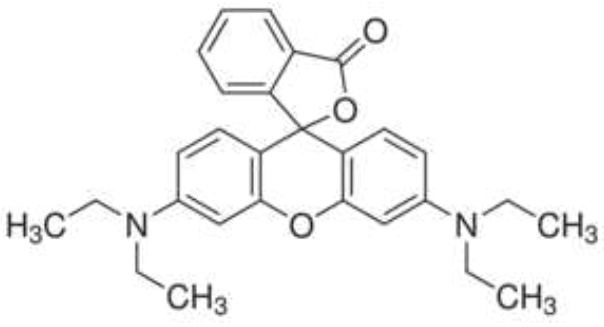

Figure 6.2 Molecular structure of RhB

RhB was not readily soluble in the diesel fuels provided thus a solvent matching the mid-distillation profiles was selected to premix it before being added to the fuels. The selection of

the solvents depended on its boiling point match to approximately the mid-distillation profile of the fuels to be tested. 1-Decanol was selected as a pre-mixer solvent for fuels A, B and paraffinic model fuel as it matches their distillation profiles. 1-Octanol was selected as a pre-mixer solvent for fuel D because of its lower distillation profile. The relevant properties of the solvents are given Table 6.2. The solvents were purchased from Sigma-Aldrich and the data had been obtained from the product data sheets provided. The different solvents used may cause the fluorescence yields to differ and will thus be a yield calibration of the mixtures will be performed.

Solvent	1-Decanol	1-Octanol
Chemical Formula	$CH_3(CH_2)_9OH$	$CH_3(CH_2)_7OH$
Initial Boiling Point (ºC)	231	196
Density @ 25 ºC (kg/m^3)	829	827

Table 6.2 Physical properties of dye solvents obtained from Sigma Aldrich

The RhB would be mixed into these solvents using an ultrasound bath to break up and completely dissolve it. The concentration of RhB to be used was determined during the pre-testing period. For a 12bit image (0 - 4095 counts) the Mie image count was initially attenuated to give a maximum between 3200 - 3500 counts. Solvents of different dye concentrations were then mixed into the fuel until it matched this and then was attenuated to be slightly lower (about 3000 - 3200 counts) by using a neutral density filter of attenuation 0.03.

The optimum concentration of RhB in solvent was 0.6 g/L (stock solution). This was then mixed to a ratio of 4:1 (fuel:stock) to create a mixture with an overall dye concentration of 120 mg/L in fuel. The fuel had overall 20% solvent and 120 mg/L dye concentration. 1 litre (±

2.5 ml) of solvent is measured using a measuring cylinder and poured into a bottle. 600 mg of RhB powder is then measured using a measuring scale with readout of 1mg and an accuracy of ± 0.5 mg. The dye was then poured into the solvent and then left in an ultrasound bath to breakup lumps of the dye powder and dissolve in the solvent for 30 - 60 minutes. The final solvent-dye solution is 1 litre of stock solvent solution with a dye concentration of 0.6 g/L. This would later be mixed to 4 litres of fuel to create a final dye concentration of 120 mg/L and a fuel to solvent ratio of 4:1. Four out of the five litres would be used for experimental analysis. The remaining one litre was used to pre-soak the fuel filters so that it absorbs and discolours RhB dye to saturation and not further absorbing any dye from the fuel-solvent mixture for the analysis.

6.2 Experimental Methodology

It was important for the experimental analysis and to be true to the results that there was minimum fuel to fuel change contamination. The steps here show how this was minimised by applying the correct procedures of filling, emptying and flushing the rig from fuel to fuel changes.

6.2.1 Fuel fill and empty

The system was filled in from the tank mouth. There were three empty points; one under the filter and the second was the injector return. The third was controlled by a 3 way valve which fed the fuel from the high pressure pump and common rail return either into the tank or to an external empty (controlled by the valve). This was vital when flushing out the high pressure pump and common rail containing previous fuel. The fuel filter capacity was 1.1 litres, the

common rail 15 ml and the high pressure pump case volume 150 ml. The full capacity of the tank was 2.5 litres. As there was a heat exchanger inside the tank a minimum level was set just for fuel to be filled just above the heat exchanger. This volume is approximately 1.1 litres. It was estimated that the un-drainable piping/components in the rig held approximately 300 ml. This was made up of 150 ml in the high pressure pump, 15ml in the rail and approximately 100 ml in the piping. The piping volume has been exaggerated by 50%.

For filling procedures, the 3-way valve was set to empty externally to a large measuring cylinder. The fuel filter was then changed to either the metal filter for a flush or a new filter for analytical fuel. 4 litres of analytical/flush fuel would be filled into the rig and the initial mixture of previous and current fuel would empty out and not back into the tank by running the feed pump. Air was released from the system by switching the control valve to return the low pressure feed to empty externally rather than go into the high pressure pump. The high pressure pump was then switched on and the pump and rail flushed to empty externally to a volume of 500 ml. This was done by constantly charging and discharging the rail to empty externally through the 3 way valve. Once approximately 500 ml of fuel was pumped out from this valve, it was switched back to empty into the tank.

For emptying procedures, the fuel would be drained from the empty valve under the filter. This would drain from; the tank, the filter, the piping into the high pressure pump, and the circulation piping. The injector return line was also emptied. For flush fuels, a sample was taken and the rest discarded as waste. The analytical fuels emptied were marked and stored away.

6.2.2 Rig flush

The maximum contamination was estimated to be 300 ml. The rig would first be flushed with 4.2 L of unmixed fuel. The unmixed fuel would be the next analytical fuel i.e. if analytical fuel is Fuel A, an unmixed Fuel A would be used to flush out the previous fuel in the rig. The maximum contamination in the flush sample would be (300/4000 ml) 7.5%. Four litres of analytical fuel is then filled into the rig, as the rig filling procedure above. The maximum contamination in the analytical fuel of previous fuels is now (7.5% x 300 ml) 21 ml in 3.8 L of fuel which is 0.55%.

Once the fill procedure was complete as 6.2.1 above, the high pressure pump would circulate the rig for 1hour constantly while charging and discharging the rail manually to ensure a thorough mix of the fuel in the rig.

In order to ensure the fuel being injected was the analytical/current flush fuel a series of 7500 injections were carried out with injection duration of 5ms. Injector return fuel was collected throughout the injection sequence but only kept as samples for the final 2500 injections. This was observed closely to match the initial fuel poured into the rig (whether seeded or un-seeded). This process was carried out for both the flush and analytical fuels. The injections would be carried out with the injection spray exhaust switched on.

Injection pressure (bar)	Injection duration (ms)	Injection Skip rate (count)	Injector-trigger delay (µs)	Injections per cycle (count)
150	5.0	8 (3Hz)	400	150

Table 6.3 Variables setting during flush

6.2.3 Analysis procedure

Once the previous fuel was flushed out and the next/new analytical solution mixture prepared and filled into the high pressure rig, its analysis would commence. A brand new filter element and acrylic injector nozzle tip were employed for each fuel set. For the Shell analysis measurements for each fuel were conducted at an injection pressure of 350 and 250 bar. The dataset of the later and a comparison between the two pressure sets will form part of a paper which will be published separately. This thesis will dwell on the 350 bar injection pressure fuel analysis.

The first step was setting up the injector nozzle holes such that the spray from the hole under investigation is in line with the laser sheet. This was done by lightly screwing on the 0.136 mm drill bits with a shank into the hole. Once placed on the injector body and lightly held in place by the compression system, the nozzle could be rotated by means of a mini spanner specifically designed to fit the along the rectangular cross section of the tip. It would then be rotated as required and aligned with the laser sheet. The position of the laser sheet remained untouched. Once the drill bit was in place, the laser was run a very low power to check the alignment with some photo paper placed in the path past the bit to note the position of the bit relative to the laser. The drill bit inserted would model the spray injected. When aligned the laser sheet illuminating the paper would look have a very small bright green section and then a dark section covered shaded by the drill bit and then another small green section as pictured in Figure 6.3. This figure is only an animation of what this looked like unfortunately a camera photograph could not be taken. The alignment of the spray to the laser sheet would later be tested by imaging a few pilot injections.

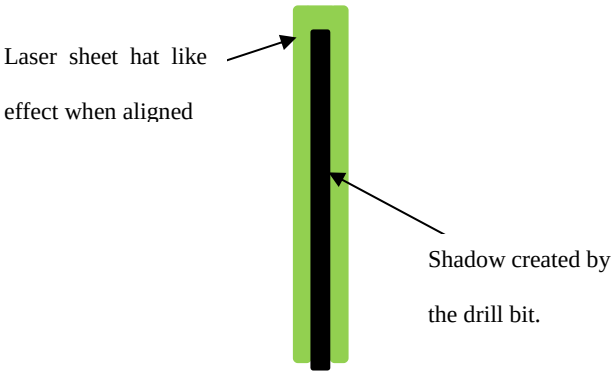

Figure 6.3 Aligned drill bit in nozzle to laser sheet

While the drill bit was still in place, the INF and LSD camera focus were checked by turning on the white light. This was just a check as it turned out no change was required for all analysis from what it was refined to and set during pre-testing. The drill bit was then taken off the nozzle. The fused silica cone well aligned on the tip, it was compressed. The air pressure required to seal as discussed previously was regulated to 3.5 bar. Once this pressure was set this was not changed until the end of testing. Changing this pressure would cause the cone to misalign on the injector nozzle and thus having to further recalibrate the camera and obtain new background images.

The injection control unit settings were adjusted as required. For experimental analysis, the number of injection would be set to 100 injections for a laser only analysis and to 50 injections for a laser plus white light analysis. The trigger-injection delay set to 500 µs and the revolutions skip rate set to 8. The synchronisation transfer units and the pulse generator were switched on. The cameras then synced with the 10 kHz sync pulse. Both cameras were set to their image size and exposure settings (Table 6.4). The lens F-stop was then full closed, the lens covered and calibrated for zero light. Laser pulse is then aligned to the LSD camera exposure timing by turning the laser onto full power, noting the laser appear and disappear delays by adjusting the manual delay on the pulse generator. The laser appear/disappear could

be seen on the LSD camera. An average of these values obtained and laser fire-LSD camera exposure signal adjusted to the average value on the pulse generator. This ensured the laser pulse and the LSD camera exposure were synced.

Software Settings	**INF camera**	**LSD Camera**
Exposure	1/1000000	1/2700000
Frame size	768 x 768	1024 x 512
Camera lens setting	85mm f 2	85mm f 1.4
Sync in	Sync pulse from control box	Delayed e sync from INF camera
Sync out delay	30µs	-
Trigger out	To LSD camera	-
Exposure out	To NI acquisition	To NI acquisition

Table 6.4 Camera inputs and software settings

Injection pressure (bar)	Injection duration (ms)	Injection Skip rate (count)	Injector-trigger delay (µs)	Injections per cycle (count)
350	4.0	8 (3Hz)	500	100 (Laser only), 50 x 2 (Laser + white light)

Table 6.5 Pressure and injector control input

Laser only background obtained next for the LSD camera with the laser on full power. This was followed by laser + white light backgrounds for both INF and LSD cameras with both the laser and white light on full power setting.

A zero pressure voltage reading was obtained for the pressure transducer via the NI acquisition system. This was in the range of 500 mv ± 50mv. The pressure setting for 350 bar injection pressure was calculated taking into account the sensitivity of the transducer which was 1.189 mV/BAR. The injection pressure was regulated to this value.

To check everything was up to speed a couple of pilot injections were carried out to check the spray-laser sheet alignment and focus on the LSD camera and the internal flow focus on the INF camera. During the injection process, injection spray exhaust suction was switched on. Data would be obtained for 100 injections at 350 bar, 4.0 ms for the laser only condition, with the corresponding inlet temperature to the high pressure pump. The images saved, and then data obtained in two sets of 50 injections at 350 bar, 4.0 ms for the laser + white light condition. The fuel inlet temperature to the high pressure pump was noted throughout the injections for both conditions. This would conclude the data and image acquisition for the analysis for a brand new nozzle.

The injector nozzle used in the previous fuel analysis was then placed in and aligned. Injections were carried out at 350 bar 4.0 ms for laser only and laser + white light with 50 injections per conditions. As an example, the nozzle used in the current fuel would be used in the next fuel as a calibration nozzle. This was carried out so that the effect of variations in nozzle profile could be minimised between fuels analysed. The nozzle manufacture and selection will later be calibrated.

Fuel name	**B**	**A**	**D**	**Paraffinic model fuel**
Nozzle	Nozzle B	Nozzle E	Nozzle P	Nozzle J
Calibration nozzle	Nozzle F	Nozzle B	Nozzle K	Nozzle x

Table 6.6 Fuel chronology and nozzle used.

Table 6.6 shows the fuel analysis order and the corresponding new and previous fuel nozzles used. Note that the exact order is not as above as the order only shows the fuels with publishable data, there were 4 other classified fuels tested. Sometimes data could not be obtained for the internal nozzle flow for the calibration nozzle as it burst during the laser only

testing. The calibration nozzles here are only used for viewing purposes and final checks to look at the spray profile with a nozzle used on the previous fuel and a new fuel and to check whether they were comparable. Manufacturing consistency calibrations on the sprays were carried out using four new nozzles using the paraffinic model fuel and the results on the spray analysis will be discussed later.

6.3 Calibration

6.3.1 Laser profile

In order to measure the laser profile a high concentration fuel-RhB solution was diluted with more fuel in order to prevent the laser power from attenuating highly in the imaging region and have enough seeds to create fluorescence but not to over-seed so that the laser power is absorbed in the mixture over a shorter length. The solution of paraffinic fuel mixture with rhodamine B in solution with decanol was diluted with additional diesel fuel to create a 56 ml overall mixture of paraffinic fuel with 4% Decanol and 24 mg/L rhodamine B.

The mixture was placed in a 2 cm x 2 cm x 45 cm laser profile cuvette. The cuvette was placed in the laser path in the location approximately where the injections would be captured. The laser was run at full power, 10 kHz to capture approximately 3500 images varying with time. The images were averaged to produce a laser Gaussian profile. Figure 6.4 shows the Gaussian nature of the laser sheet profile captured with the laser entering from the right hand side at an angle of 25 degrees from the horizontal (similarly to the spray imaging).

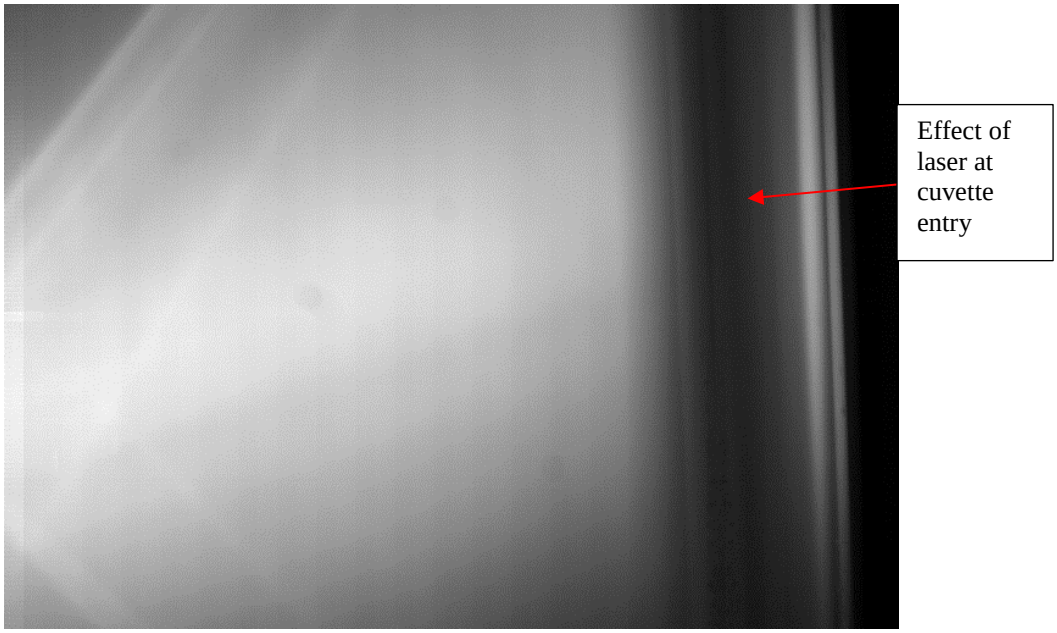

Figure 6.4 Mean laser profile at 10 kHz, 1mJ/pulse laser power.

This profile has been produced here as a completion for the results obtained, however it will not be used in the basis of the worked produced here. The results shown here are on the basis of the dropsizing which shows a LIF to MIE ratio. Correcting both the LIF and MIE images with the laser profile is essentially causing itself to divide out and thus there is no real need for the correction, both the LIF and Mie image will be produced from the same profile and thus dividing them outright without the laser profile correction does not change the final outcome.

6.3.2 Fuel fluorescence yield profile

The mixture calibration is important for the basis of this work, as the fluorescence yield of a fluorophore changes depending on the solution they are in. The work here required 3 sets of mixture calibrations, i.e. fluorophore-decanol mixture in diesel FDD, fluorophore octanol mixture in light diesel FOLD and fluorophore- decanol mixture in purely paraffinic fuel FDP. A similar set up to the laser profile was used however; the measurements were obtained at

low laser power as the original mixtures used during the experiment and collected from the injector return were used during this procedure. The sheet forming optics were taken out and thus the laser at the imaging plane was no longer a sheet. After the measurements were done per set, the laser power was measured using a power meter to be able to calibrate the final yield profile against laser power.

Mixtures were filled into the cuvette and placed in the line of the laser-imaging path and similar place where the sprays were imaged, a low power laser sheet produced and images of the fluorescence yield obtained at lens f-stop of f16. The f stop was increased to reduce the aperture, as there as high amounts of fluorescence scattering at the lower f stop and this was producing images which were saturating in pixel intensity. An average of a 1000 images obtained per set was carried out. The images were then compared to each other with the RhB mixture in diesel Fuel A as the reference. The yield images per fuel set had small amounts of translation which was corrected before being divided by the fluorescence yield image of fuel A.

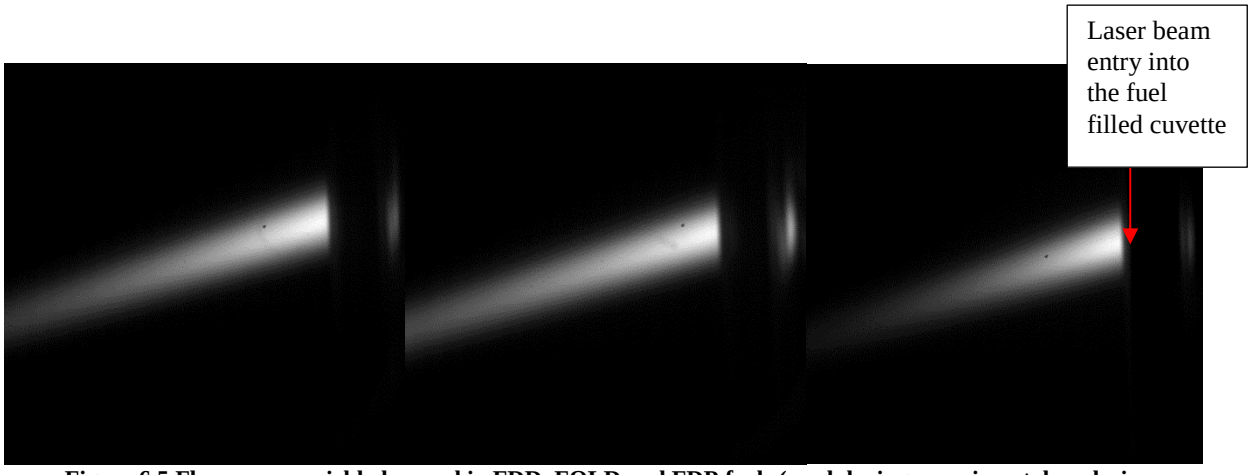

Figure 6.5 Fluorescence yield observed in FDD, FOLD and FDP fuels (used during experimental analysis.

The images captured showed high fluorescence scattering at the entry to the cuvette however this decreased further down. For this reason a high intensity region was selected for Fuel A-

RHB mixture, and the same region was selected for the rest of the translated yield images and an average intensity in this region obtained for all the sets. These average ratios would be compared between the fuels and a calibration constant calculated. FOLD and FDD yields were obtained at the same laser power at 360 mw, FDP yield was obtained at a laser power of 340 mw and it was thus adjusted linearly to match a corresponding yield at 360 mw. FDD mixtures thus required no calibration. The FOLD and FDP fuels fluorescence images were calibrated with ratios found in Table 6.7.

	FOLD/FDD	FDP/FDD
Calibration ratio (power corrected)	1.04	1.7

Table 6.7 Fluorescence yield calibration ratios for the fluorescence yield of Rhodamine B in different mixtures.

6.3.3 Nozzle manufacture consistency calibration

Four new nozzles were used for the purpose of the manufacturing calibration to check nozzle manufacture consistency and how it affects the external spray sizing. The validation was done to check whether there was variation in injections between different nozzles used as a result of manufacture. A new nozzle was used for every set of fuels and could not be re-used for every fuel case as a result of nozzle wear. A nozzle manufacture consistency check was carried out to observe the variation and repeatability of the sprays from each new nozzle manufactured. Previously the nozzles had undergone a selection procedure; however their performance and repeatability factors of the different nozzles have not been tested as certain aspects, for example the nozzle hole entry sharpness and hole roughness, cannot be measured. Thus a calibration was performed to check how 4 new nozzles, which had passed the previous stage of selection, performed using the same fuel under the same injection conditions.

Four sets of nozzles were used with a single set of fuel at 350 bar to analyse the effects of manufacture. Henceforth these will be referred to as cases 1-4, referring to the nozzles used. The nozzles were brand new, polished on the sides and checked for hole accuracy. For the purpose of calibration and wear, and because a calibration was also required for the internal nozzle flow, the tests were carried out with laser and white light conditions, i.e. both laser + white light were on but the laser was adjusted relative to its acquiring camera post white light camera acquisition, so that there was no interference from the laser to the internal nozzle acquisition. A full analysis was carried out as described in 6.2.3. 50 injections were carried out for each case.

The external spray images obtained were analysed and Sauter mean diameter distributions obtained for each case, time resolved over the 50 injections. For SMD distributions between intensity of 0 and 1.5, frequencies over 100 SMD bins (between 0-1.5 SMD) were obtained which showed a frequency of the SMD in each bin size. A time resolved intensity frequency was obtained over the number of injections. For example over the hundred injections containing 100 frames per injection, the bin number frequencies obtained in each set of frames over the hundred injections was cumulatively summed. The frequencies obtained per bin in frame 1 injection 1, were added to frame 1 injection2, frame 1 injection 3 and so on. Each bin size frequency was then divided by the sum of the frequencies over 100 bins per frame to compensate for the overall spray sizing and to enable comparison between cases. A time resolved intensity frequency distribution was obtained per frame over the number of injections which was then divided by the total sum of frequencies in each frame. The results were then plot for time steps 2.1 - 2.4 ms (frames 25 - 29) at the start of injection, 3.9 – 4.5 ms (frames 43 - 50) at peak lift condition and 5.1 – 5.5 ms (frames 56 - 60) at the end of injection.

Then for each bin size from 1 – 100, the average was obtained per bin over the four nozzles, i.e. an average of bin 1 to 100 in nozzles 1-4 per frame. These were then plot with their standard deviation. This result would show how the injections deferred between the four different nozzles used. Total frequency sum per frame related time resolved intensity frequency for frame 49 (4.5ms) can be observed in Figure 6.6.

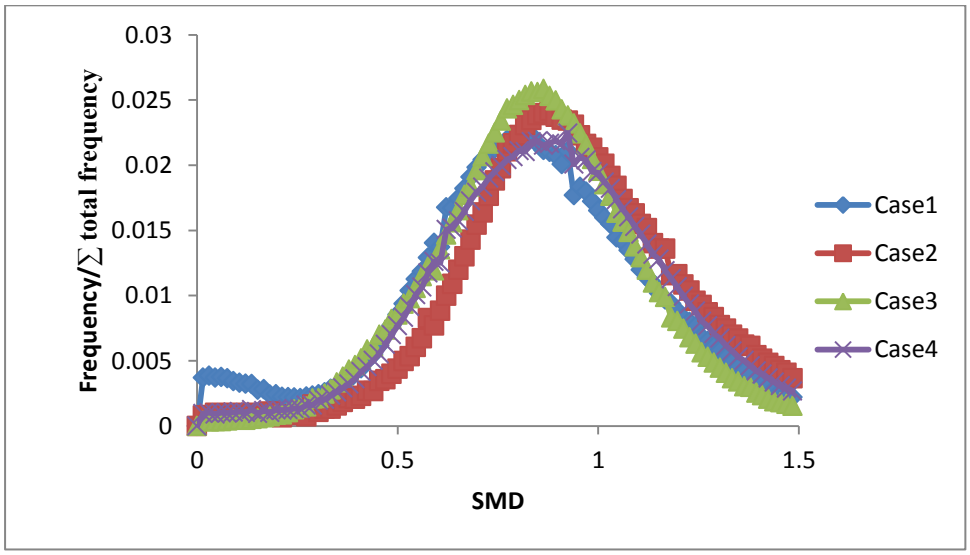

Figure 6.6 Total cumulative frequency relative time resolved intensity frequency distributions of SMD obtained at the peak needle lift at 4.4 ms for cases 1 – 4

The corresponding mean and standard deviation chart can be observed in Figure 6.7 below.

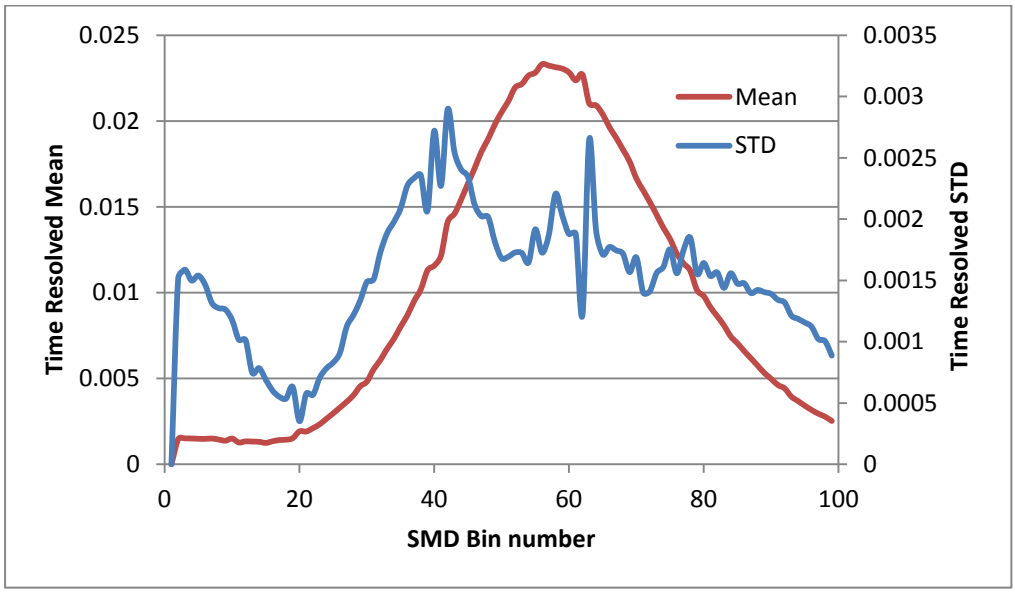

Figure 6.7 Mean and standard deviation analysis on Figure 6.6

The full range of charts can be observed in section Appendix C. From Figure 6.6 it can be denoted that the peaks occurring over the cases are in very close bin proximity and the mean and standard deviation images obtained show the variation of the sprays injected from different nozzles from their combined mean. Figure 6.7 shows a mean and standard deviation calculated using data from all cases at each time step per bin intensity i.e. the mean and standard deviation at each time step at individual bin intensities of the combined frequencies of all the cases. The same was carried out for the remaining time steps. This analysis would produce a mean distribution of all four cases. The standard deviation graph shows a sudden drop. This occurs at the point where the frequencies in all for cases are matching of closely their mean frequency.

Frame	Time (ms)	Maximum Standard deviation
26	2.1	0.003962168
27	2.2	0.004059841
28	2.3	0.00456388
29	2.4	0.004976035
30	2.5	0.00508287
43	3.8	0.003570223
44	3.9	0.003773651
45	4	0.003202199
46	4.1	0.003460236
47	4.2	0.003648961
48	4.3	0.003598789
49	4.4	0.002896895
50	4.5	0.003672651
56	5.1	0.003754758
57	5.2	0.003878625
58	5.3	0.003120713
59	5.4	0.002697834
60	5.5	0.00336565

Table 6.8 Maximum standard deviation values obtained at the beginning, maximum and end sections of needle lift.

Table 6.8 shows the maximum standard deviations obtained per time resolved intensity frequency distribution at various points in the injection cycle i.e. start of injection (26-30 ms), peak lift(43-50 ms) and end of injection (56-60ms). The time resolved intensity frequency

distributions as shown in the appendix will be compared to the ones obtained from the experimental analysis of fuels and thus a conclusion obtained of whether the changes occurring in sprays are as a result of the nozzle manufacture inconsistency or from the changes in distillation properties of the fuels. If the time resolved intensity frequency distributions obtained from the nozzle consistency data are matching or are relatively similar to the time resolved intensity frequency distributions obtained from the fuels analysis the conclusion will lead to the fact that the changes in fuel are not causing significant changes in the fuel spray. However if they are significantly different this would lead to the conclusion that the fuels are causing these changes in spray Sauter mean diameter.

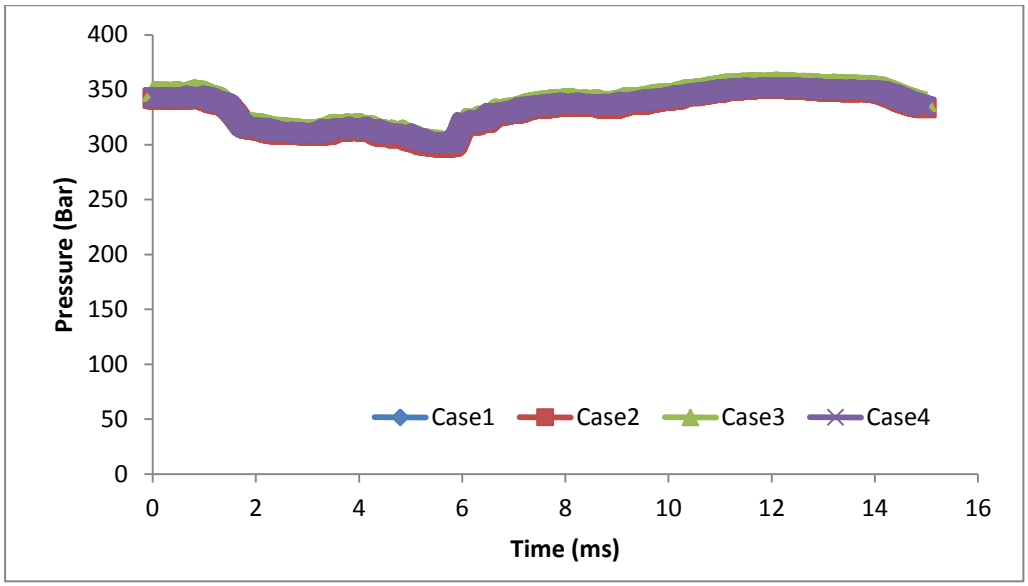

Figure 6.8 Time resolved mean pressure distributions for cases 1-4 over the 50 injections.

Figure 6.8 shows the pressure distributions for the case 1 – 4 over 50 injections at 350 bar. The pressure distributions were a maximum of ± 5 bar of the average of the four cases at each time step.

6.3.4 Injected fuel mass measurement and consistency

With the current setup of the injector and nozzle requiring compression, it is difficult to capture/collect all of the spray from all 6 holes and obtain its mass. Even if a method established, each test would require a brand new nozzle to be able to consistently match mass injected between fuels as mass injected from nozzles having gone through different number of injections would be inconsistent due to the short life time of the nozzles at high pressures. Furthermore the manufacture of the nozzles was very expensive and time strenuous.

Replacing the modified injector nozzle body for the original non modified full metal body would make it much easier to measure the fuel mass injected as the need for the compression ram, cone and compression acrylic is no more. A lot more space is created to be able to fit a small bottle onto the injector and collect the spray. However because of modifications on the nozzle angle and the hole length from the original this would not replicate the correct mass injected. If a way to measure the mass injected using the acrylic nozzle was determined, a few tests could be run with two different fuels and compared to the mass injected from the full metal body injector for the same two fuels. A constant factor could be obtained by comparing the mass injected from the acrylic nozzle and the mass injected by the full metal body nozzle. This constant factor could be used to estimate the mass injected by the acrylic nozzle already having the mass injected by the metal nozzle.

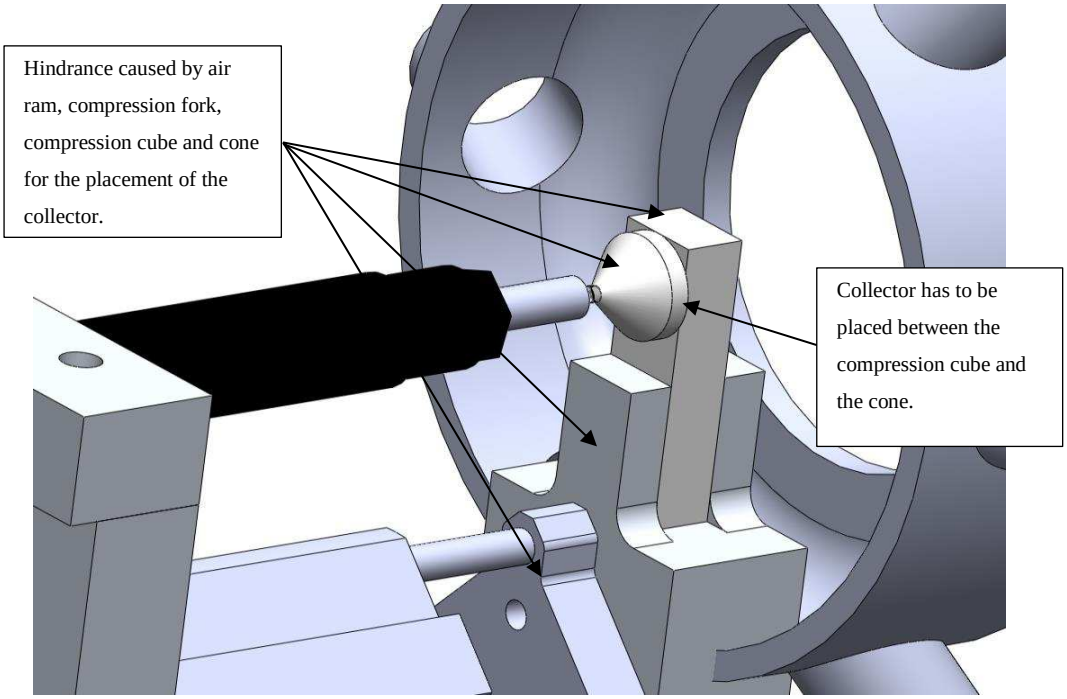

Figure 6.9 Drawbacks to spray capture with the modified nozzle body setup

Collecting all the liquid injected would require the collector being compressed together with the cone and nozzle onto the injector body (placed between the cone and compression cube). Also it would have to be closed off so that none of the fuel being injected would be lost. It should also be able to sustain the momentum of the spray and not rupture. A rigid body like a bottle if placed, but one which is small enough and has a flat base would have to be custom manufactured. This would be quite expensive plus it would be extremely difficult to contain the liquid when removing the bottle after the injections. Careful thought lead to the discovery of another use for a condom. It fit the specifications perfectly and 2 or 3 could be combined for reinforcement. They are highly elastic and would stretch to take the impact of the spray. They could be wrapped around the injector and the mouth tied so no spray escaped.

Fuels	Density @ 15oC Fuel only using IP 365 (kg/m3)	Estimated Density Fuel +20% Decanol/**Octanol** (kg/m3)	Estimated Density Fuel + 20% Decanol/**Octanol**+120mg/l RhB (kg/m3)
A	825	825.94	826.06
B	826.1	826.82	826.94
D	800.3	**805.64**	**805.76**
Paraffinic model fuel	780	789.94	790.06

Table 6.9 Fuel-Solvent mixture density (fuel only, fuel plus solvent, analytical mixture)

Four new nozzle tips manufactured in the 3rd batch would be used to measure the mass injected for two different fuels (2 new nozzles per fuel) and then the nozzle body replaced by the non-modified body and mass injected measured. The two would then be compared and a constant factor obtained to be able to estimate the mass injected from the modified nozzle tip from the injected mass measured of the non-modified nozzle body. The mass injected from the rest of the fuels would be measured using the non-modified injector nozzle body. The non-modified nozzle body is a fully metal nozzle with no modifications made to adapt the acrylic nozzle. Table 6.9 shows the estimated densities of the Fuel-solvent mixtures with and without RhB.

6.3.4.1 Injected fuel mass measurement using an acrylic nozzle (modified injector)

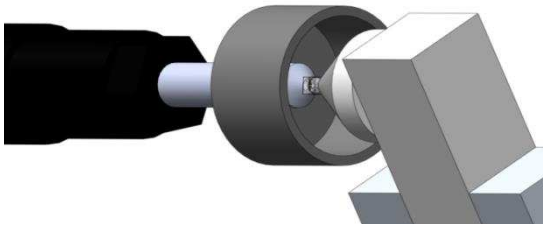

Figure 6.10 Soda bottle cap on the injector body

A pre-weighed soda bottle cap was cut to fit over the modified nozzle body. This would reduce the impact of the momentum of the spray onto the condom walls. Pre weighed unrolled condoms with the cone were held onto

the cube and the air ram pressurised minimally to be able to move the cube, cone and condoms onto the tip. The cone was aligned so that its base fit concentrically with the base of the pre-weighed acrylic nozzle tip. The condoms were then unwrapped to fit around the cone, minisac tip and soda bottle cap. They were fully unwrapped and tied at the mouth with a small breathing pipe. The breathing pipe would allow air in the setup to escape once liquid from the injection filled up the space. No spray escaped. The condoms were set to form a sac like feature on the bottom surface so that the liquid condensed from the spray would collect here. The injections were carried out at high pressure pump inlet temperatures of 24-29ºC. The air ram was set to compress and release just before the injections were started and as soon as they were complete to prevent prolonged compression rupturing the condoms.

Injection pressure (bar)	Injection duration (ms)	Injection Skip rate (count)	Injector-trigger delay (µs)	Injections per cycle (count)
350	4.0	8 (3Hz)	500	100 (Paraffinic model fuel) 50 (Fuel A)

Table 6.10 Pressure and control box settings for injected mass measurements

Injector control box and pressure settings were set as seen in Table 6.10 to replicate the spray analysis. The pressure throughout the injections was recorded using NI software for 6.0ms duration on receipt of every injection pulse, as done during the spray analysis. The exhaust extraction was turned on in case of condom rupture. Both Fuels used for this test had been mixed with 20% Solvent and 120mg/l RhB.

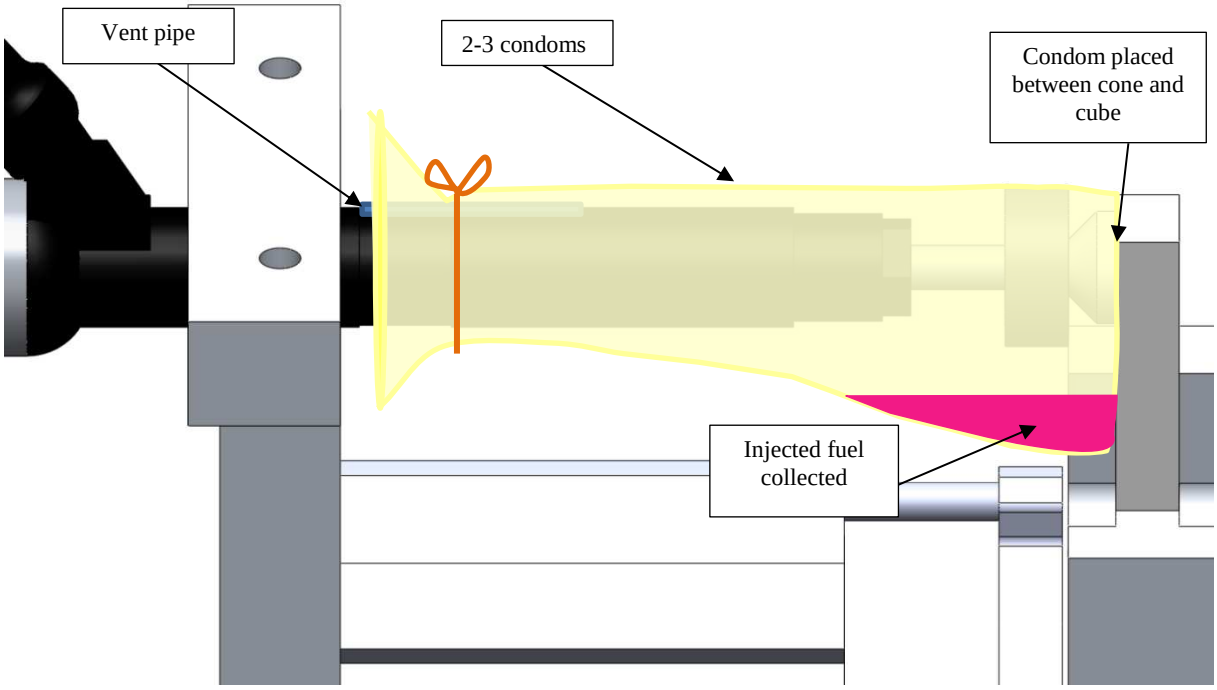

Figure 6.11 Modified nozzle injector-condom injected mass collection setup

Mass injected per 100 injections-Nozzle viii (g)	5.204
Mass injected for 100 injections-Nozzle ix (g)	5.187
Total Mass for 200 injections (g)	10.391
Mass per injection (mg)	51.955

Table 6.11 Mass injected for analytical Paraffinic model fuel using the acrylic nozzle (modified injector)

The vapour-liquid mixture was allowed to settle for 15 minutes before being taken off the injector. The condom containing the minisac nozzle tip, cone and bottle cap were taken off and weighed. The mass injected was obtained by subtracting this mass by the initial empty mass of the components. The measurements were obtained for analytical paraffinic model fuel and Fuel A. Two nozzles (viii and ix) were used during the paraffinic model fuel tests. Each nozzle was wrapped around with 2 condoms and 100 injections carried out. Table 6.11 shows the results per acrylic nozzle and the overall mass per injection from 6 holes. Figure 6.12 shows the similarity of the time resolved injection pressure profiles of both nozzle used.

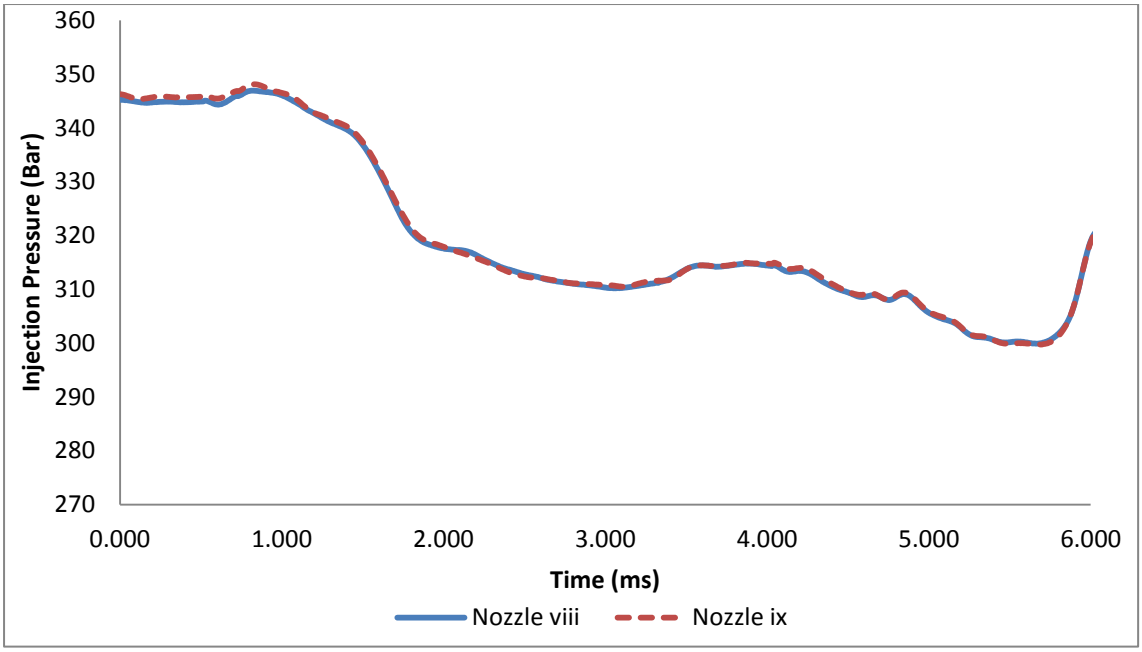

Figure 6.12 Time resolved average injection pressure profile for acrylic nozzle viii and ix used in injected mass measurements of paraffinic model fuel - solvent mixture

When testing Fuel A with a 2 condom combination wrapping the nozzle, it seemed to be bursting for both 50 and 100 injections per set and thus 3 condom combinations were used and the test carried out in sets of 50 injections as seen in Table 6.12. There may be two reasons for these:

1. Either the fuel is reacting with the condoms and causing weakness at points of impact
2. Or the heavier Fuel A has a larger spray momentum due to its higher density and this is causing the rupture

Mass injected per 50 injections - Nozzle iv (g)	Set 1	2.781
	Set 2	2.802
Mass injected per 50 injections - Nozzle i (g)	Set 1	2.788
	Set 2	2.801
Total Mass for 200 injections (g)		11.172
Mass per injection (mg)		55.86

Table 6.12 Mass injected for analytical Fuel A using the acrylic nozzle (modified injector)

During the mass injected tests for Fuel A using the acrylic nozzles it is seen that the mass injected increases per nozzle set as the number of high pressure injections carried out using

that nozzle increases. For both nozzles iv and i, the mass for the first 50 injections was lower than the second 50 injections by on average 0.34 mg/injection (0.017g over 50 injections). This may be due to the amount surface roughness in the holes caused during the drilling process during manufacture decreasing as a result of the cavitating flow. The in-hole surface friction increases cavitation in the holes and the cavitation occurring in turn choked the flow resulting in a decrease in injected mass. Once this surfaces are smoothed out by the in-hole cavitating flow occurring during the injections the mass injected increases by approximately 0.6% per set of 50 injections. The decreased cavitation caused by the wall surfaces smoothening is also accompanied by a very small decrease in the time resolved injection pressure profile as seen in Figure 6.12.

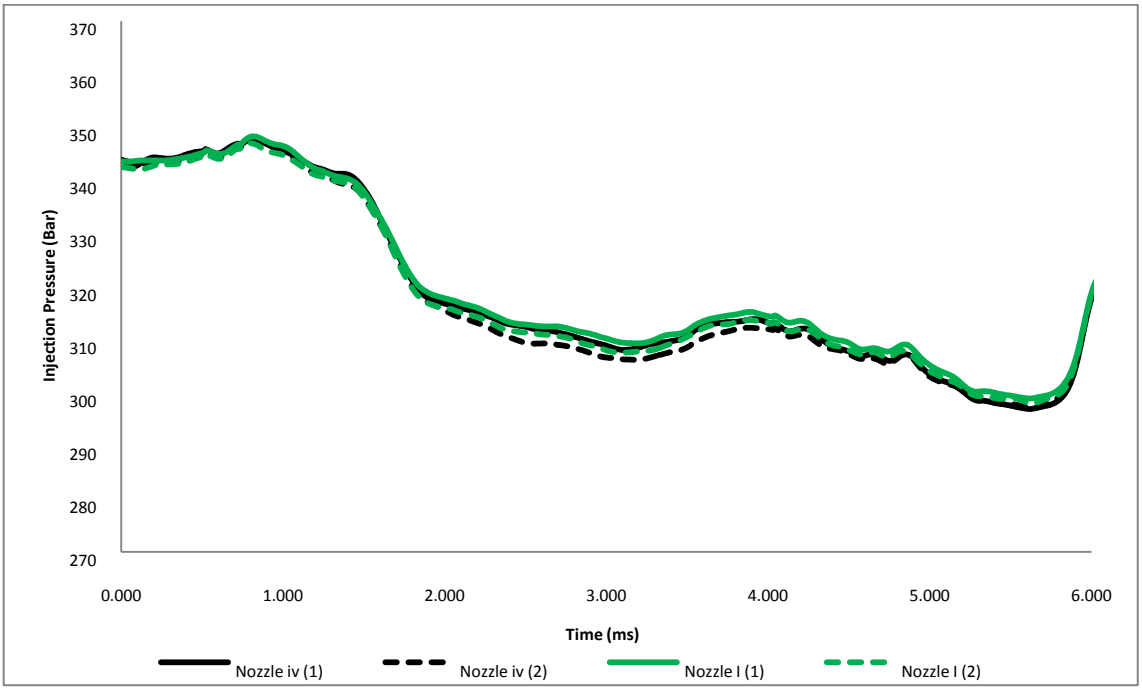

Figure 6.13 Time resolved average injection pressure profile for acrylic nozzle iv and i used in injected mass measurements of Fuel A - solvent mixture containing RhB

The hole smoothing is causing the surface are of the holes to increase and thus the pressure to decrease especially seen during high needle lift. This observation holds for both nozzles used for this test. During testing, to minimise the effects of this phenomena on the results, the total

number of injections were kept to a maximum of 200 injections per nozzle. This phenomenon would occur during testing however the effects over time would be comparable between nozzles (fuels tested) as observed here. New nozzles were used for each test and at the same injection pressure they would degrade similarly and thus the results obtained using a new nozzle for each fuel would be comparable. Figure 6.13 shows the time resolved pressure profile for the injections carried out using fuel A.

The case is also replicated in the paraffinic model fuel tests. Nozzle viii underwent 50 more injections at the beginning due to an error of not setting the correct pressure on the air ram. Nozzle viii went through initial 50 injections where the injector had not been sealed correctly. A further 100 injections were done after resetting with new set of condoms and the mass measured. Nozzle ix underwent 100 injections straight. This may be the reason for the 0.017g difference between the two sets. If each set of 50 injections as seen with the mass injected results of Fuel A injects 0.017g more, this may be occurring at the start of the paraffinic model fuel study where the ram was not pressurised correctly and thus the difference over the 2 nozzles as seen in Table 6.11. There was not any significant injection pressure variation between these nozzle tests as seen in Figure 6.12 and thus this difference cannot be a result of injection pressure variations. It is not known what the relationship is with further increments with 50 injections. This result is consistent with the difference in the first two sets of 50 injections.

6.3.4.2 Injected fuel mass using a non-modified injector

Fuels	A	B	D	Paraffinic model fuel
Viscosity - Fuel only (mm^2/s)	2.078	2.102	1.664	
Density @ 15ºC [IP 365] (kg/m^3)	825	826.1	800.3	780
Density of Fuel solvent mixture (kg/m^3)	826.06 (+120mg/l RhB)	826.82	805.64	789.94
Mass injected per 100 injections- Set1 (g)	7.019	6.939	7.127	6.688
Mass injected per 100 injections-Set2 (g)	7.017	6.939	7.127	6.696
Total Mass (g)	14.036	13.878	14.254	13.384
Mass per injection (mg)	**70.18**	**69.39**	**71.27**	**66.92**
Volume per 200 injections (ml)	16.992	16.785	17.693	16.943
Volume per injection (ml)	0.08496	0.08392	0.08846	0.08472

Table 6.13 Fuel injected mass using non modified nozzle

The modified nozzle was replaced by the original non-modified nozzle and injections carried out for all the fuels with a modified bottle in place to capture all the spray. The injections were carried out in two sets of 100 injections for all the fuels and mass injected weighed, as shown in Table 6.13. As the rig contained Fuel A-Solvent mixture containing 20% Decanol and 120mg/L RhB, this was carried out first and thus it is the only mixture to contain RhB for these measurements. The rest of the fuel solutions were mixed with 20% solvent as previously done during the LSD tests but without RhB. From the Table 6.13, Fuel D had the highest injected mass whereas paraffinic model fuel had the lowest. In comparison, all fuels injected approximately 17ml over the 200 injections.

6.3.4.3 Injected fuel mass consistency

A consistency check was performed on the non- modified injector nozzle to test its injected mass consistency over a number of sets. Fuel A mixed with 20% solvent containing 0.6 g/l RhB was used as the test mixture. Five sets of 100 injections were carried out at 350 bar pressure and 4.0 ms injection duration and the injected mass calculated for each set. Injected mass was calculated by subtracting the empty bottle mass from its containing 100 injections. The results from the five sets are shown in Table 6.14.

Injection set	1	2	3	4	5
Mass injected per 100 injections (g)	7.018	7.017	7.018	7.018	7.022
Mass injected per injection (mg)	0.07018	0.07017	0.07018	0.07018	0.07022
Average fuel per injection (mg)	0.070186				
Consistency per injection (%)	-0.00855	-0.0228	-0.00855	-0.00855	0.0484

Table 6.14 Injected mass consistency of Fuel A mixture using the non-modified injector.

The results show the non-modified nozzle had an injection consistency of ± 0.05% per injection which in turn would give rise to a maximum difference in 0.04 µg per injection over five sets of 100 injections at 350 bar injection pressure and 4.0 ms injection duration. Comparing these results with Figure 6.14, it is seen that the results from set 5 had a lower injection pressure whereas set 2 had a slightly higher average injection pressure over the 100 injections. Increase in pressure causes an increase in cavitation and this may choke the mass flow in the nozzles thus injecting a lower mass. Thus at constant pressures as seen in sets 1, 3 and 4, the non-modified injector produced a consistent mass injection.

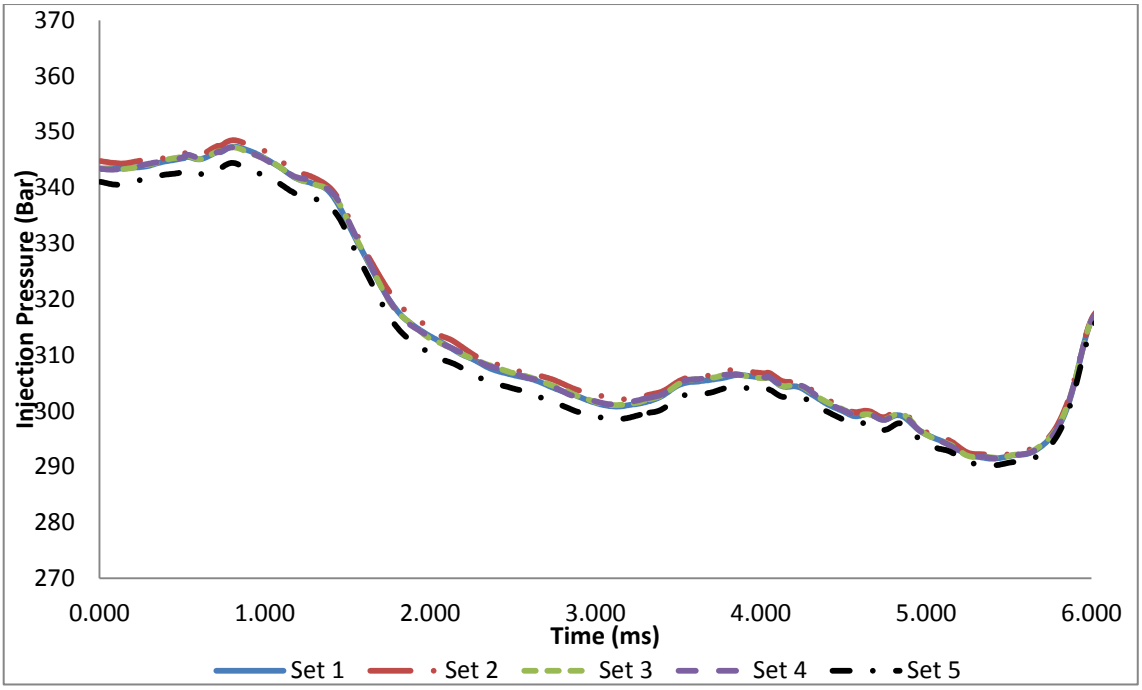

Figure 6.14 Average time resolved injection pressures acquired during Fuel A injected mass consistency measurements using the non-modified injector nozzle

The consistency of the mass injected using the modified injector nozzle with the acrylic tip end has been covered above in 6.3.4.1. Table 6.11 and Table 6.12 show the consistency of two different nozzles. For the acrylic nozzles it is not possible to obtain an injection consistency of a longer period of time however the mass injected can be calibrated for various nozzles. The nozzle holes in the acrylic nozzles erode as a result of cavitation as discussed above and thus each set of injections will have a slightly higher injected mass. It is important to keep the nozzle usage within its limits to prevent error induced as a result of a change in nozzle profile. For this reason injections at 350 bar injection pressure were carried out first. Fuels could thus be matched due to the nozzles having to go through a similar wear. Table 6.14 shows that for each fuel, the mass injected for each nozzle per set of injections is similar.

6.3.5 Imaging errors (signal to noise ratio) on spray images

For any electronic measuring system, the signal-to-noise ratio (SNR) characterizes the quality of a measurement and determines the ultimate performance of the system. With a CCD (charge-coupled device) image sensor, the SNR value specifically represents the ratio of the measured light signal to the combined noise, which consists of undesirable signal components arising in the electronic system, and inherent natural variation of the incident photon flux. Because a CCD sensor collects charge over an array of discrete physical locations, the signal-to-noise ratio may be thought of as the relative signal magnitude, compared to the measurement uncertainty, on a per-pixel basis. Photon noise (sometimes referred to as shot noise) results from the inherent statistical variation in the arrival rate of photons incident on the CCD. Photoelectrons generated within the semiconductor device constitute the signal, the magnitude of which is perturbed by fluctuations that follow the Poisson statistical distribution of photons incident on the CCD at a given location. The photon noise, or measurement variation, is therefore equivalent to the square-root of the signal.

$$\mathrm{SNR}_{\text{photon noise}} = \frac{\mu_{\text{signal}}}{\mathrm{STD}_{\text{signal}}}$$

Equation 6.1

where μ_{sig} is mean of the background-subtracted intensity and STD_{signal} is the standard deviation, or noise, contained by the background subtracted intensities.

In order to calculate the SNR a highest intensity region of 25 x 25 pixels of ten consecutive images from the laser profile images were selected. The mean and standard deviation of the

intensity in that region was determined and the SNR calculated using Equation 6.1 for the selected section in the 10 images.

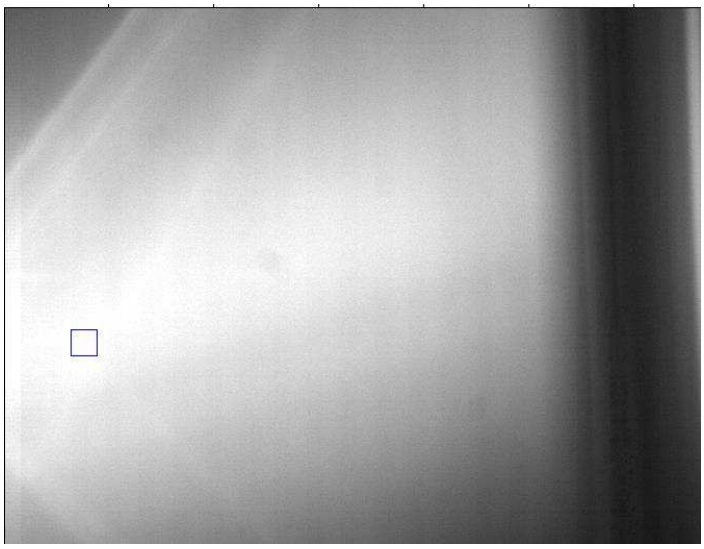

Figure 6.15 Region selected from the laser profile images sequence for SNR ratio calculation

A key feature of Poisson statistics is that the standard deviation is equal to the square-root of the number of individual particles. That is, if there are P particles in each pixel, the mean is equal to P and the standard deviation is equal to √P. This makes the signal-to-noise ratio equal to P/√P, or simply, √P. Thus the number of photons can be calculated as;

$$SNR = \sqrt{Photons}, \qquad Photons = SNR^2$$

Equation 6.2

Image number	1	2	3	4	5	6	7	8	9	10
Mean	1174.62	1201.53	1172.41	1197.78	1181.03	1193.39	1172.22	1187.07	1184.97	1169.65
STD	17.58	17.98	17.01	18.45	18.45	17.95	18.37	16.81	17.66	17.86
SNR	66.80	66.84	68.91	64.93	64.00	66.47	63.81	70.63	67.10	65.50
Photons	4461.91	4467.21	4748.23	4215.38	4096.53	4417.91	4071.15	4989.27	4502.07	4290.15

Table 6.15 Mean STD, SNR and Photons count for the base analysis of the laser profile

Table 6.15 shows the results from the base analysis of the laser profile. The results are from each image where the mean and standard deviation were calculated over the 25 x 25 pixels per image. Table 6.16 shows the mean and standard deviation compiled over the 10 images with data points 25 x 25 x 10.

Mean	1183.468
STD	20.83226
SNR	56.80937
Photons	3227.305

Table 6.16 The overall Mean STD, SNR and photon count from the 25 x 25 pixels over 10 images

The laser profile was carried out with a diluted solution of paraffinic fuel-decanol mixture and thus will require adjustment to match the experimental concentration of dye. The number of photons can be adjusted linearly to match the experimental concentration of dye in fuel by a constant factor i.e. (120 mg/l)/(0.024mg/l) = 5000 and a SNR ratio recalculated. A linear adjustment can also be made for the fluorescence yield in different solutions i.e. decanol-fuel and octanol-fuel mixtures. The current calculation was for a FDP mixture. Table 6.7 shows the conversion factors from a FDD to a FOLD and FDP mixture. The factor to convert from a FDP to a FDD is 1/1.7. The photons and the corresponding SNR are then recalculated. The photons from FDD are then used to calculate the photons in the FOLD mixture and followed by the SNR. Noise could be determined by determining the inverse of the SNR.

Table 6.17 show the photons, SNR and Noise over the 10 images corrected for the fuel type FDD.

DECANOL-FUEL	Photons	SNR	Noise
1	13123266	3622.605	0.000276
2	13138847	3624.755	0.000276
3	13965373	3737.027	0.000268
4	12398191	3521.106	0.000284
5	12048605	3471.11	0.000288
6	12993841	3604.697	0.000277
7	11973972	3460.343	0.000289
8	14674314	3830.707	0.000261
9	13241396	3638.873	0.000275
10	12618085	3552.194	0.000282
Overall	9492072	3080.921	0.000325

Table 6.17 Photons, Signal to noise ratio and Noise for a FDD mixture

OCTANOL-FUEL	Photons	SNR	Noise
1	13648197	3694.35	0.000271
2	13664401	3696.54	0.000271
3	14523988	3811.04	0.000262
4	12894119	3590.84	0.000278
5	12530550	3539.85	0.000282
6	13513595	3676.08	0.000272
7	12452931	3528.87	0.000283
8	15261286	3906.57	0.000256
9	13771052	3710.94	0.000269
10	13122809	3622.54	0.000276
Overall	9871755	3141.93	0.000318

Table 6.18 Photons, Signal to noise ratio and Noise for a FOLD mixture

Table 6.18 show the photons, SNR and Noise over the 10 images corrected for the fuel type FDD. The numbers in the tables are for a 25 x 25 pixel region. The overall parameter has been calculated by compiling the full range of data i.e. 25 x 25 pixels x 10 images and determining the mean intensity and its standard deviation for both mixture cases.

The results show a signal to noise ratio in the range of 3200. i.e. for every 3200 signal counts there is 1 noise count. In comparison to the photons level captured, the noise level is relatively low. Some degree of noise is always present in any electronic device that transmits or receives

a "signal." For digital cameras, the signal is the light which hits the camera sensor. Even though noise is unavoidable, it can become so small relative to the signal that it appears to be non-existent. The signal to noise ratio (SNR) is a useful and universal way of comparing the relative amounts of signal and noise for any electronic system; high ratios will have very little visible noise whereas the opposite is true for low ratios.

The ratio determined here is high and thus the noise is very low. A good comparative measure is the decibel range. Images are considered excellent if their decibel range is above 30 db [186]. Decibels can be calculated by determine the $\log_{10}$ of the SNR and multiplying it by 10. Thus the FDD mixture image overall result has a decibel value of 34.89 db and the FOLD mixture image has a decibel value of 34.97 db. This results show the quality of the images is good with a very low noise.

Chapter 7 Sac Vortex Flow Effects and External Spray Drop Sizing

7.1 In-Nozzle and Sac Flow Analysis

For the basis of this work and its relation to deposit formation inside injector nozzle holes, the in-nozzle flow analysis consists of phenomena observed occurring towards the end and post injection only. The observations made show possible in-nozzle deposit formation mechanisms which have not been observed so far. The analysis is mostly qualitative and efforts have been made to quantify certain parameters where possible.

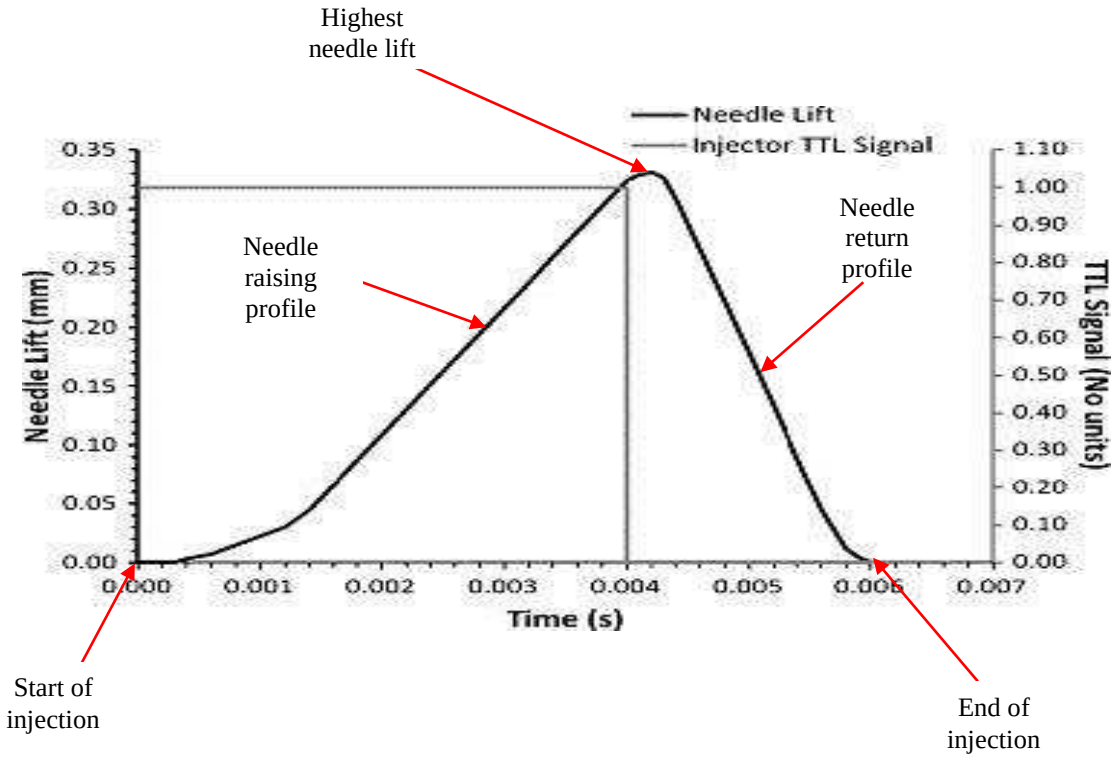

Figure 7.1 Image defining needle profile with annotations (reproduction of Figure 5.2)

Figure 7.1 shows the needle lift profile and terms that will be used in conjunction with the needle profile throughout this chapter. The images were acquired at 10 kHz. Needle lift began on the TTL trigger pulse, 500 µs after the image acquisition trigger pulse thus 5 images were obtained prior to injection. The profile has been discussed in the preceding chapters. The needle is observed to start moving at around frame 13, which represents a time of 0.8 ms after the injection trigger signal, however spray only emerges at frame 18 in both internal nozzle and external dropsizing images representing a time of 1.3 ms after injection trigger. The injection continues until the 65th frame which represents the 6 ms after injection trigger. The spray in the LSD images resides at the 64th frame as the needle returns – close to sealing, and the cavitation in the nozzle holes has resided. Internal nozzle images were captured in sets of 150 frames where frames 1-5 were pre-injection trigger, 6 - 65 were of the injection and 66 - 150 were of post injection bubble movement. External nozzle images were captured in sets of 100 where 1 - 5 frames were pre-injection trigger images, 6 - 65 were injection images and 66 - 100 were blank images post injection.

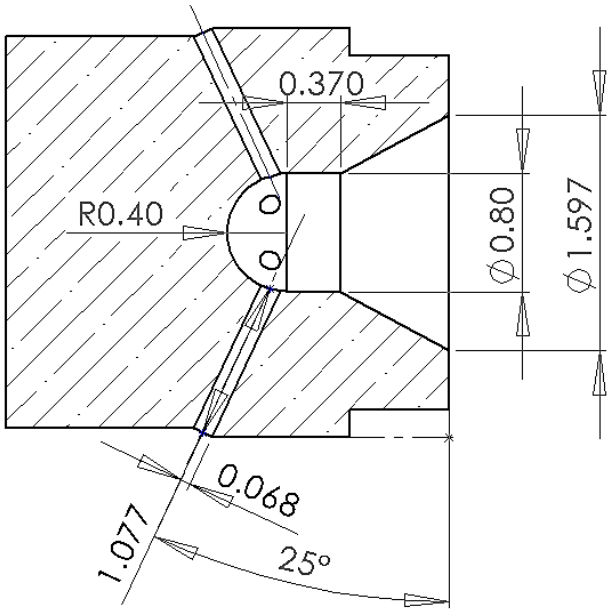

Figure 7.2 Dimensions of the nozzle sac and holes (measurements are in mm with a tolerance of ±0.01mm)

Figure 7.2 shows real measurements of the injector tip geometry with the dimensions of the sac and the nozzle holes. This was captured on the INF camera with a resolution of ~8µm/pixel.

7.1.1 Sac vortex flow post injection

During the end of the needle return, bubbles were observed to be forming in the sac. These bubbles were not observed during the injection. Similar bubbles in the sac region and nozzle hole region have been observed by Badock et. al [3]. They describe them as dissolved gas bubbles. They appear just as the needle seals any further flow of fuel into the sac during the end of its return phase. The bubbles then form a circumferential vortex flow inside the sac which initially has high radial velocity but then quickly subsides with time post injection, as angular momentum of the flow decreases. Flow around the needle and in the sac has vorticity [23,26,27,82–86,187] and the bubbles retain the angular momentum resulting from this vorticity when the needle has sealed on to the minisac tip. The bubbles are formed as a result of needle cavitation occurring during the end stages of needle return. When the needle is just about to seal, very small gaps between the needle and the injector body/the minisac tip occur which result in the formation of the bubbles observed. At 5.6 ms from injection no bubbles appear however in the next frame which displays images at 5.7 ms from injection bubbles start forming as a result of needle cavitation. At this point the needle is approximately 0.02 mm from its end of travel. The bubbles are two phase mixtures of fuel and fuel vapour.

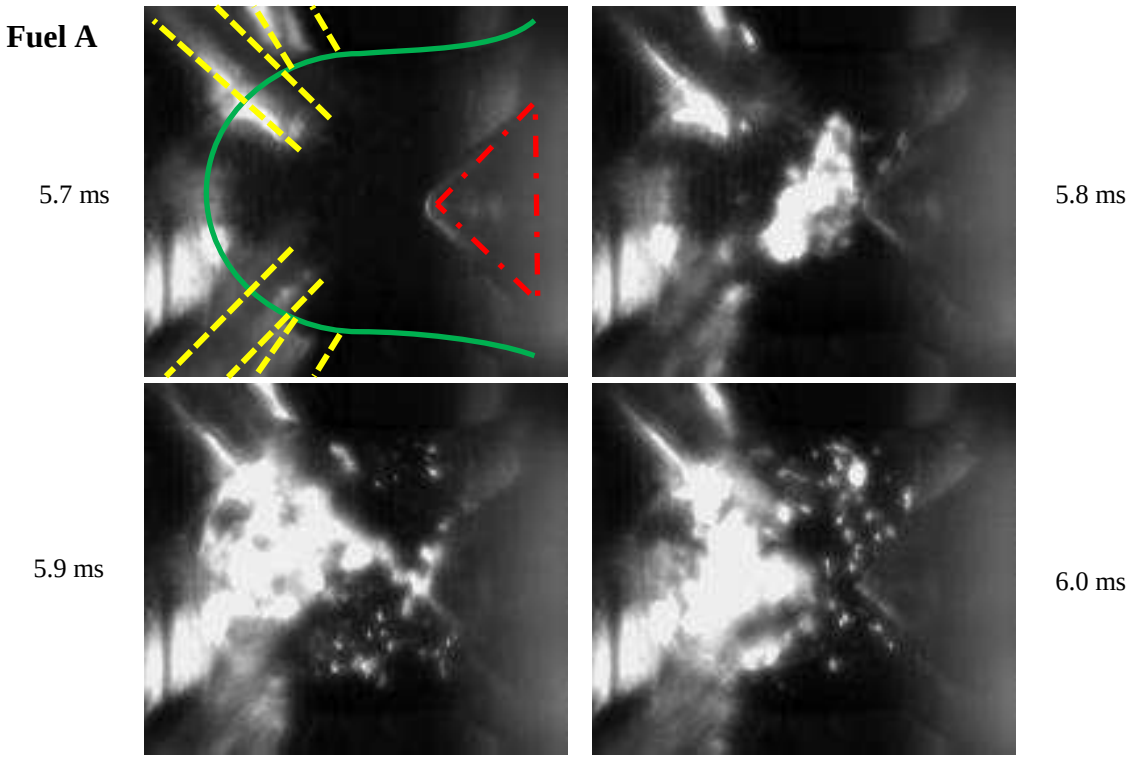
Fuel A
5.7 ms
5.8 ms
5.9 ms
6.0 ms

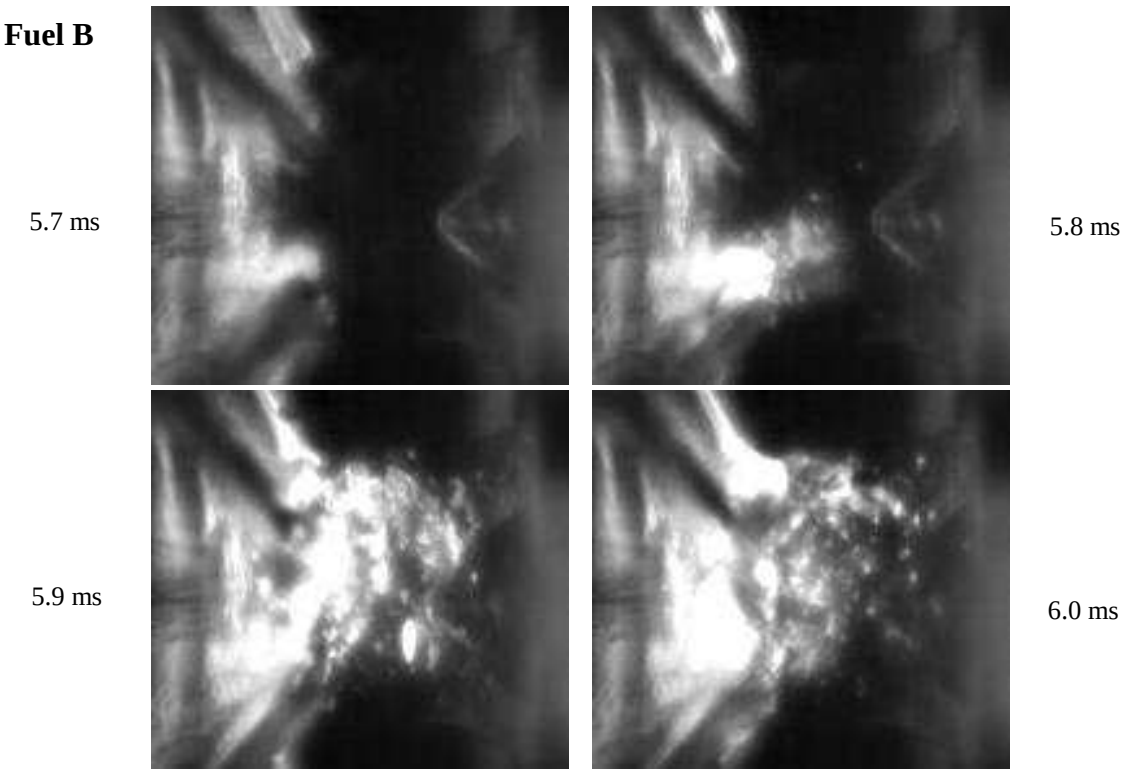
Fuel B
5.7 ms
5.8 ms
5.9 ms
6.0 ms

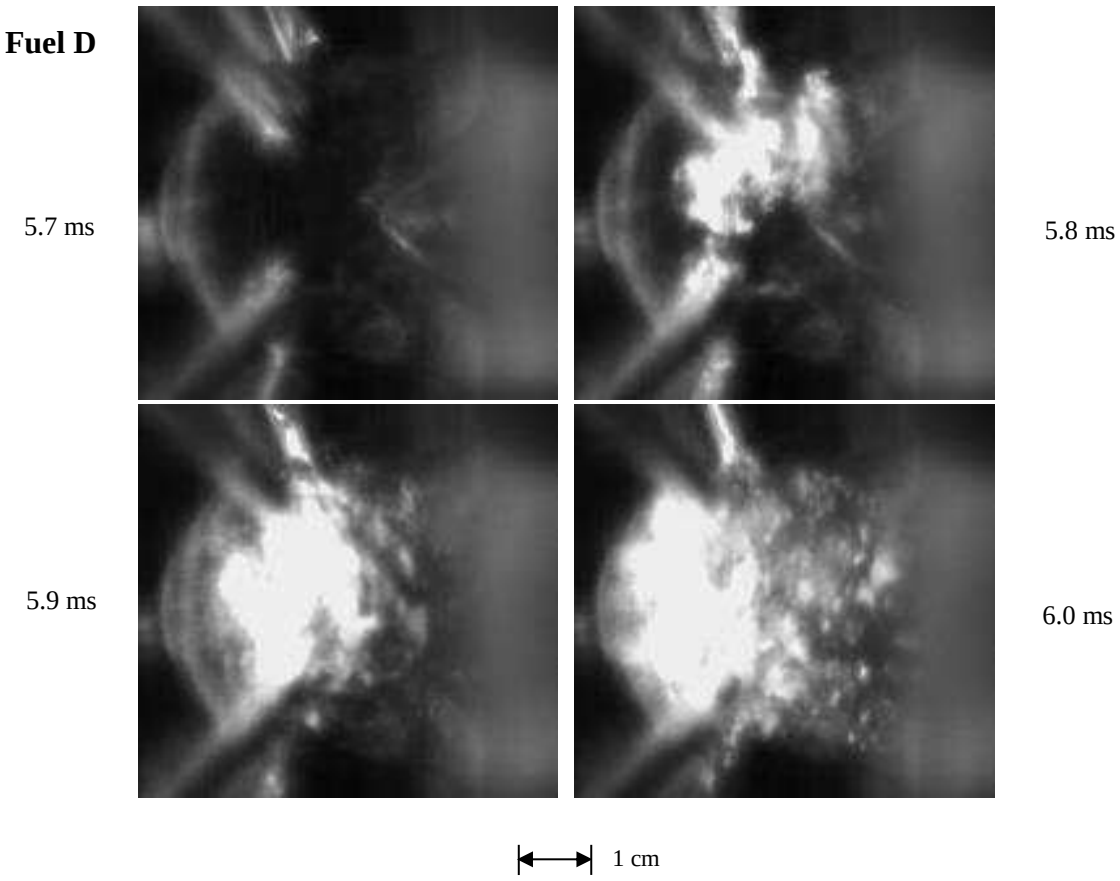

Figure 7.3 Images from 5.7 - 6 ms injection lift time (left to right), for Fuels A, B and D showing the formation of bubbles in the sac depicted by the bright spots occurring in the sac due to elastic scattering of white light from the bubble surfaces [Scale: 1cm=0.23mm]

The images in Figure 7.3 are unprocessed images of fuels A, B and D between times 5.7 – 6 ms during the end of needle return. Processing the images by background light subtraction resulted in the needle shape profile and the sac volume profile to become close to invisible and thus to preserve their existence the images have been produced unedited. In the image for 5.7 ms of fuel A, the green full profile is the sac volume, whereas the red dotted dash profile is showing the needle shape and finally the yellow dashed profiles are the nozzle holes. Two of the four nozzle holes are directed towards the foreground of the image whereas the other two are the nozzle holes in focus injected along the image plane. The images show the formation of bubbles in the sac at the final stages of needle return (near closure), due to the very small gaps between needle and the minisac tip body. This small gap results in needle cavitation as seen in the 5.8-6 ms images for all fuels. At 5.7 ms no bubbles are seen in the sac

and in the next step they appear due to needle cavitation. The bubbles are visible as they surface scatter light elastically and are seen as the white sections in the sac. During images 5.8 – 6 ms the needle has not fully sealed and thus the amount of bubbles in the sac volume increase up to this point until the needle has fully sealed the fuel flow from the sac volume.

There was a lot of saturation of light in the sac because of large amounts of light been scattered by the bubbles and thus it was not possible to determine variation of bubble sizes in the sac. Toward the bottom of the sac (hemispherical section) at entry to the focused white light the bubbles scattered highly and thus the images show saturated regions in this sections. The other issue of this angle of capture is that the size of the bubbles in the background of the images would appear slightly smaller than when they would appear in the foreground of the image and their focus and definition would also differ. Thus it was not possible to carry out a review of the diameters of theses bubbles

The liquid fuel in the sac post injection had an angular momentum. Due to the formation of bubbles in the sac, this motion was observable due to the fuel motion transporting these bubbles formed. As a result of this motion the bubbles would collide with each other and coalesce as seen in Figure 7.4. This phenomenon was captured during the later stages when the vorticity in the sac is subsiding due to the bubble movement being traceable. The images shown are successive images at 10 kHz observed on three separate occasions.

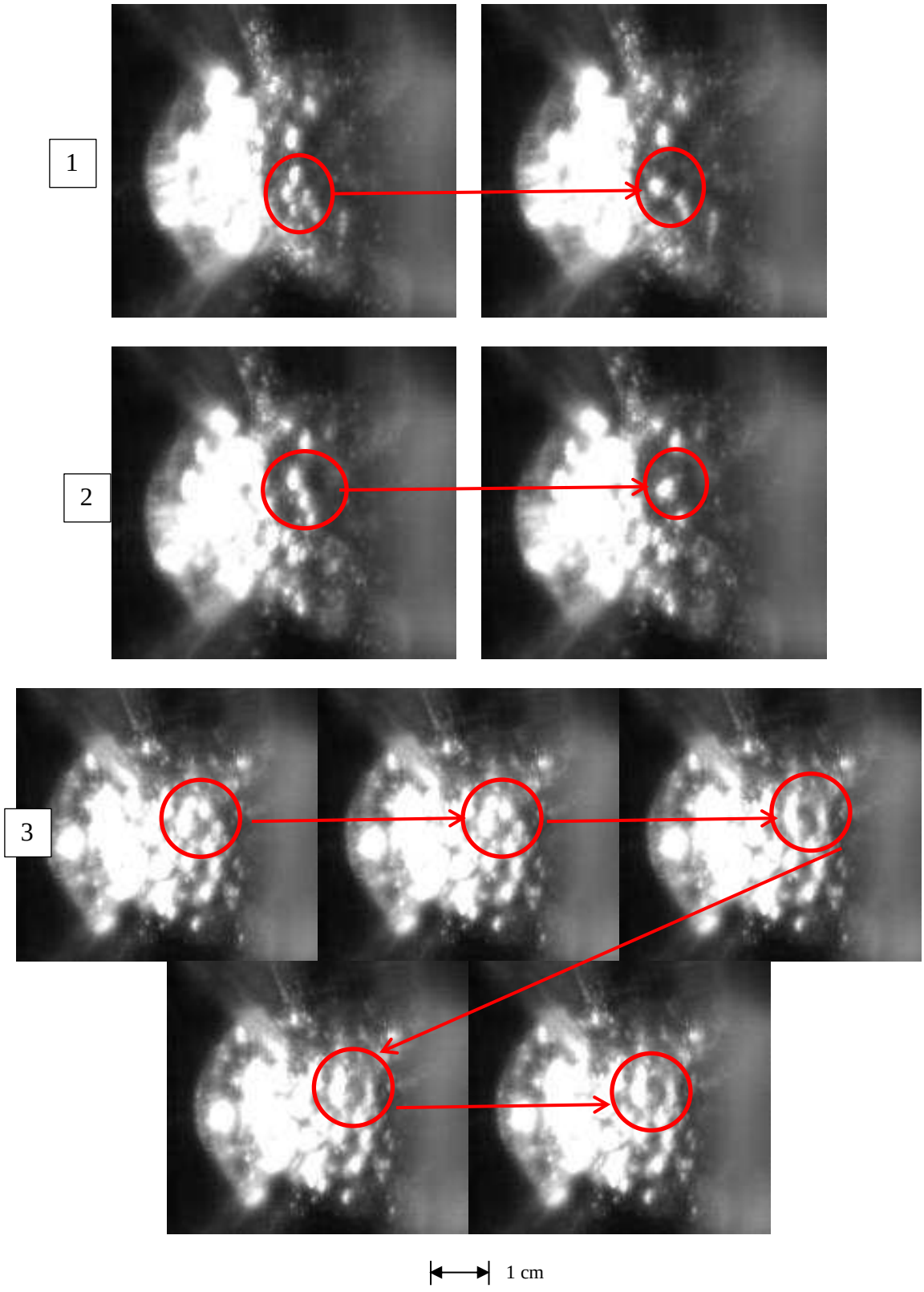

Figure 7.4 Growth/coagulation of bubbles in the sac volume as a result of coalescence (images are continuous frames at 10 kHz observed for different injections), [Scale (1&2) 1cm=0.23mm, Scale (3) 1cm = 0.26mm]

The angular momentum of the liquid fuel in the sac transporting these bubbles is an important parameter to be able to quantify its vorticity. It is possible to be able to determine the flow vorticity in the sac by determining the vorticity of the bubble it is carrying. Immediately post injection, the flow angular momentum is too high for the image acquisition speed and thus the bubbles cannot be tracked individually. There are various factors that are disadvantageous for this view of capture in order to measure the flow vorticity i.e. the saturation of light intensity at the sac and; the centre of vorticity and the direction of vorticity cannot be identified. Thus it has not been possible to obtain a quantifiable angular momentum of the flow.

7.1.2 In-nozzle hole bubble flow

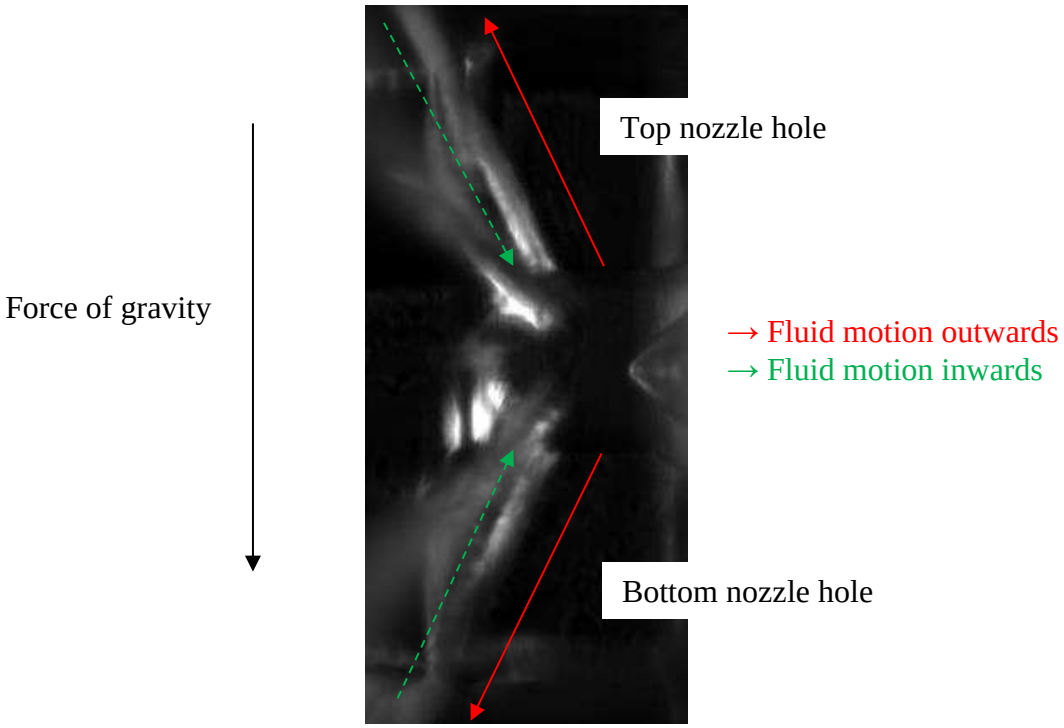

Figure 7.5 Description of flow directions to be used with regards to in-nozzle bubble formation and flow.

During the end of the injection period, bubbles are also seen to appear in the nozzle holes. They may be formed as a result of the reduction in flow velocity reducing the amount of shear in the liquid entering the nozzles and thus nucleation resulting in the formation of large

bubbles; or as a result of bubbles appearing from needle cavitation entering the nozzle holes. The bubbles would initially have outward momentum as a result of the initial direction of the flow; however this would quickly change in some cases and result in the flow coming back towards the sac volume or continue flowing out. Figure 7.5 shows the flow descriptions that will be used in the bubble movement analysis in both vertically upwards and downwards injecting nozzle holes.

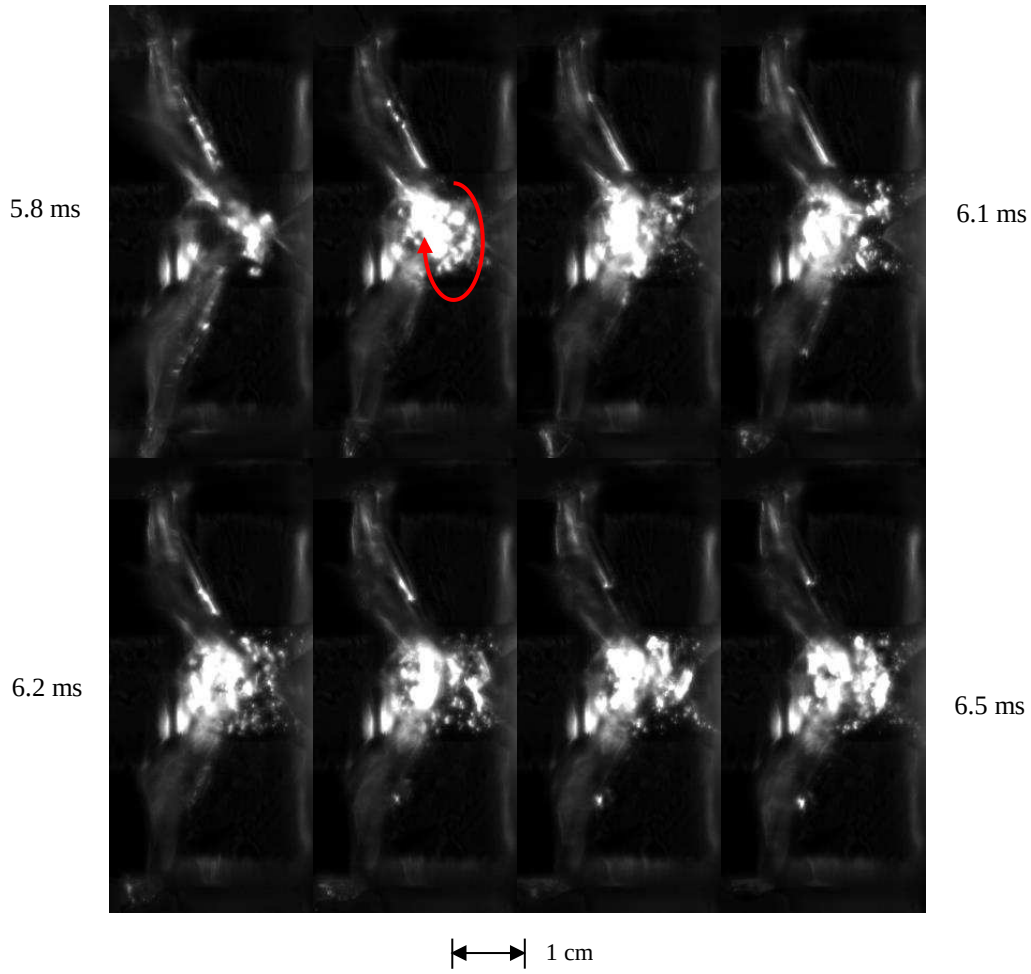

Figure 7.6 The formation of bubbles in the nozzle holes during the end of needle return (5.8 - 6 ms) and the initial momentum of bubble travel in both holes (6.1 - 6.5 ms) being out ward. (Left to right 5.8 -6.5 ms) [Images scale 1cm=0.568mm]

Figure 7.6 shows the formation of the bubbles in the nozzle holes and their initial flow momentum driving them outwards in both nozzle holes. The 5.8 ms image shows similar structure to Rayleigh breakup however occurring inside the nozzle holes as a result of

axisymmetric surface waves formed by the interaction of primary disturbances in the liquid and surface tension forces at low velocities. These bubbles appear due to a reduction in flow velocity (as a result of the needle nearing closure) reducing the shear stress in the liquid and with the low shear stress acting on the liquid, bubbles are formed rather than cavities which occur at high flow velocity (thus higher shear stress on the liquid). This is the initial formation of the bubbles as observed in the 5.8 and 5.9 ms images. At 6.0 ms the injector seals and thus any bubbles appear after this maybe as a result of bubbles in the sac volume flowing into the nozzles.

Once these bubbles had formed their initial momentum would be outward as due to the flow momentum of the liquid carrying these bubbles being in that direction, however sometimes a sudden change in momentum would be observed that would pull the bubbles back into the nozzle hole. If this was the case the bubbles travelled with a velocity that dampened down synchronous to the flow with vorticity occurring in the nozzle holes. Bubbles would either continue with their momentum exiting the hole or return back in towards the sac volume. The observations of the bubble movement were not always the same and could not be predictable i.e. sometimes the bubbles in both holes move outwards, sometimes they both move inwards and at other times they move in opposite directions to each other (i.e. top hole being sucked inwards into the sac whereas bottom hole bubble outwards and vice versa). The movements however were synchronous to the vorticity inside the sac volume and as soon as this dampened down so did the bubble movements in the sac volume. This leads to the hypothesis that the flow with vorticity ω ($\omega = \frac{1}{2} curl\, V$) contains regions of high and low pressure gradient. Regions of low pressure tend to cause suction in the nearby holes whereas the regions of higher pressures result in ejections/outward motion. The suction may be of very

low pressure however it is enough to cause the change in momentum of a bubble travelling outwards and pull it inwards.

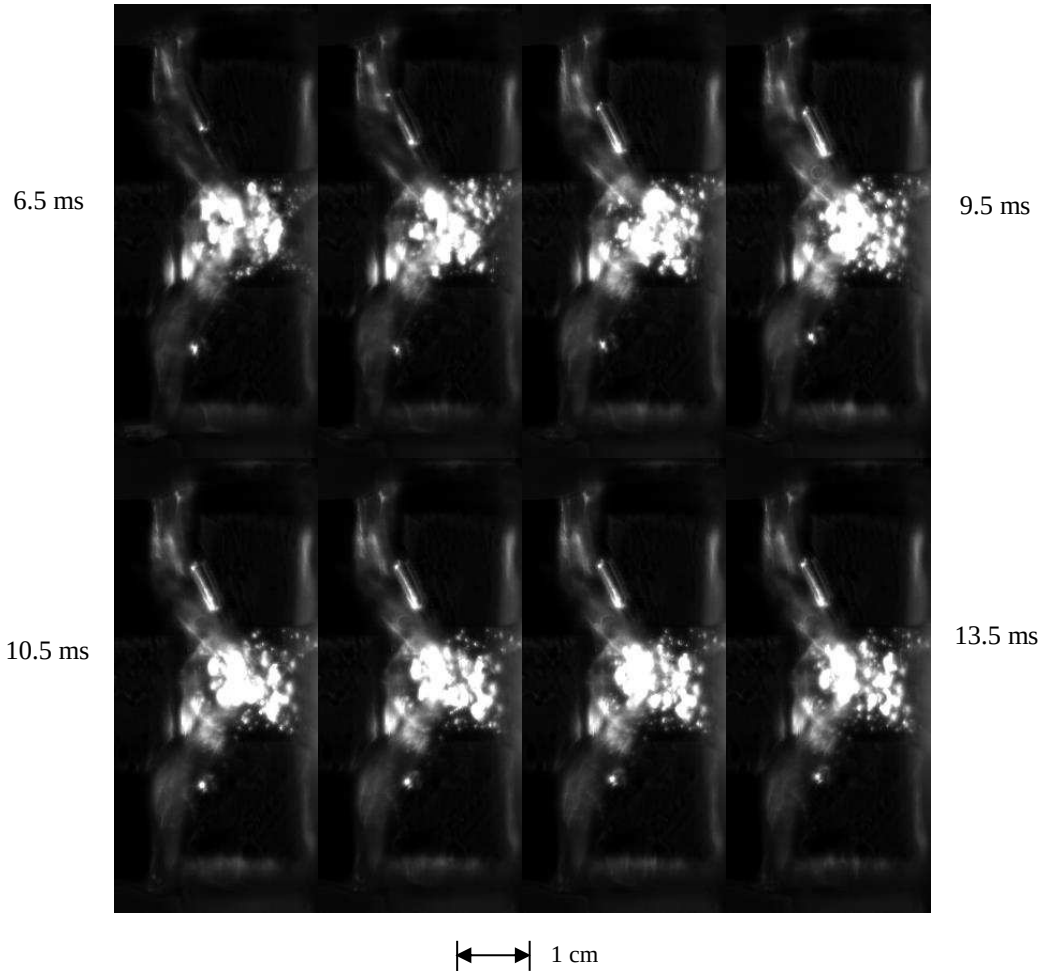

Figure 7.7 Continuation of images in Figure 7.6 from 6.5 - 13.5ms (left to right) in times steps of 1 ms, showing bubble motion in nozzle holes inwards towards sac volume [Images scale 1cm=0.568mm]

Figure 7.7 shows a continuation of the sequence of images see in Figure 7.6 from 6.5 ms in steps of 1 ms to 13.5 ms (6.5 ms post injection). The previous set shows outwards movement of bubble flow in both top and bottom nozzle holes, however as observed in Figure 7.7 bubbles in both holes change direction and flow inwards to the sac volume. The bubble in the top hole ceases motion after about 10.5 ms however the bottom hole bubble continues its journey inward towards the sac slowly as the fluid in the sac rotates. The sizes of the bubbles vary as seen in the figures. The top hole bubble is elliptical, of diameter 16 pixels ± 1 pixel

(~131 micron) along the nozzle diameter and elongating 50 pixels ± 1 pixel (~404 micron) across the hole length. The bottom bubble is more spherical of diameter 16 pixels ± 1 pixel (~131 micron) covering the hole diameter.

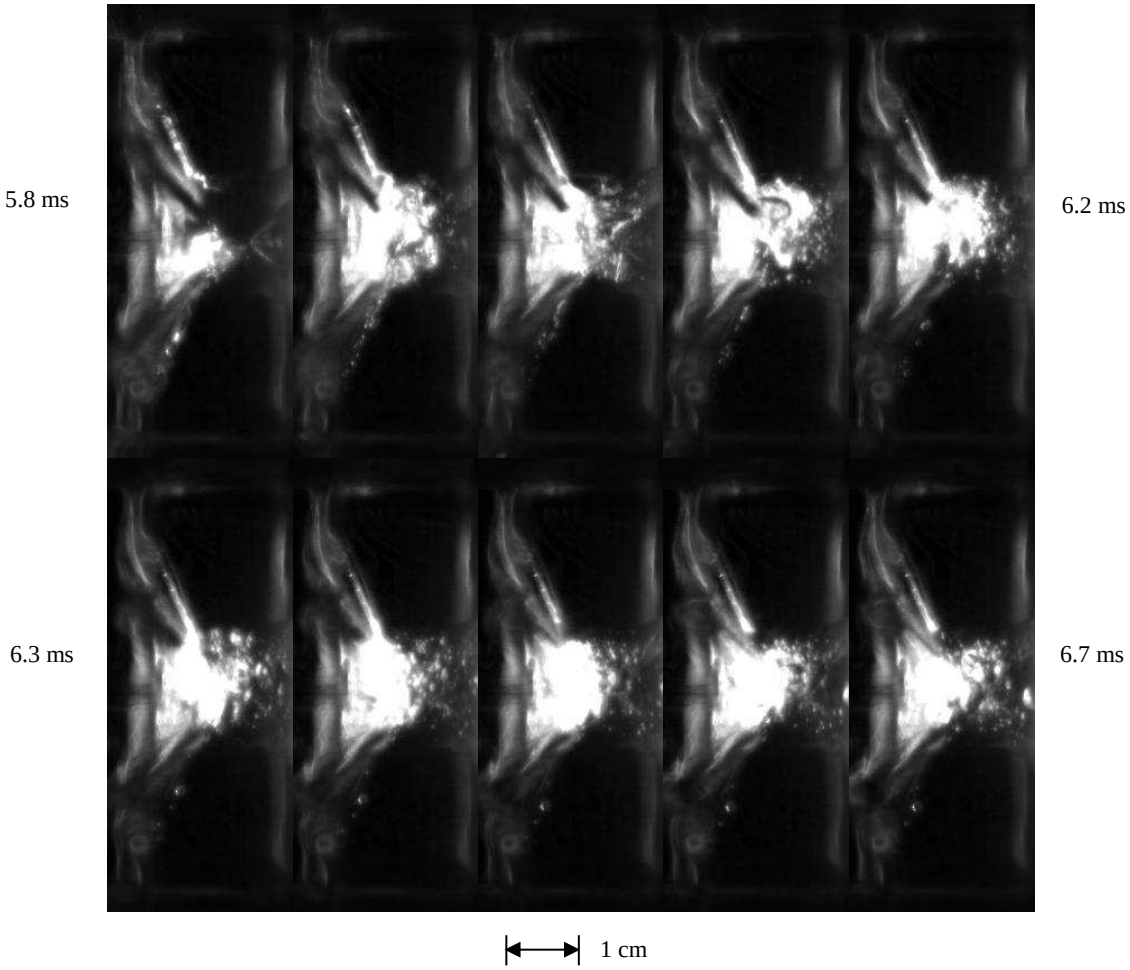

Figure 7.8 Bubble formation in sac and nozzles between 5.8 – 6.7 ms (left to right) showing bubble exit and re-entry and final exiting top hole [Images scale 1cm=0.542mm]

Figure 7.8 shows an observation were the bubble in the top hole initially exited the sac volume at 6.5 ms time and then re-entered the sac at 6.6 ms to re-exit at 6.7ms and continue flowing outwards as observed in Figure 7.9.

The bubble in the top hole seen in Figure 7.8 and Figure 7.9 is initially covering the length of the nozzle hole before it is pushed out. These images show bubble movement in opposite

directions. The bubble in the top hole moves outwards, however the bubble in the bottom hole moves inwards towards the sac volume and is quite close to re-entering the sac volume. More bubbles appear from the exit of the bottom hole flowing inwards towards the sac.

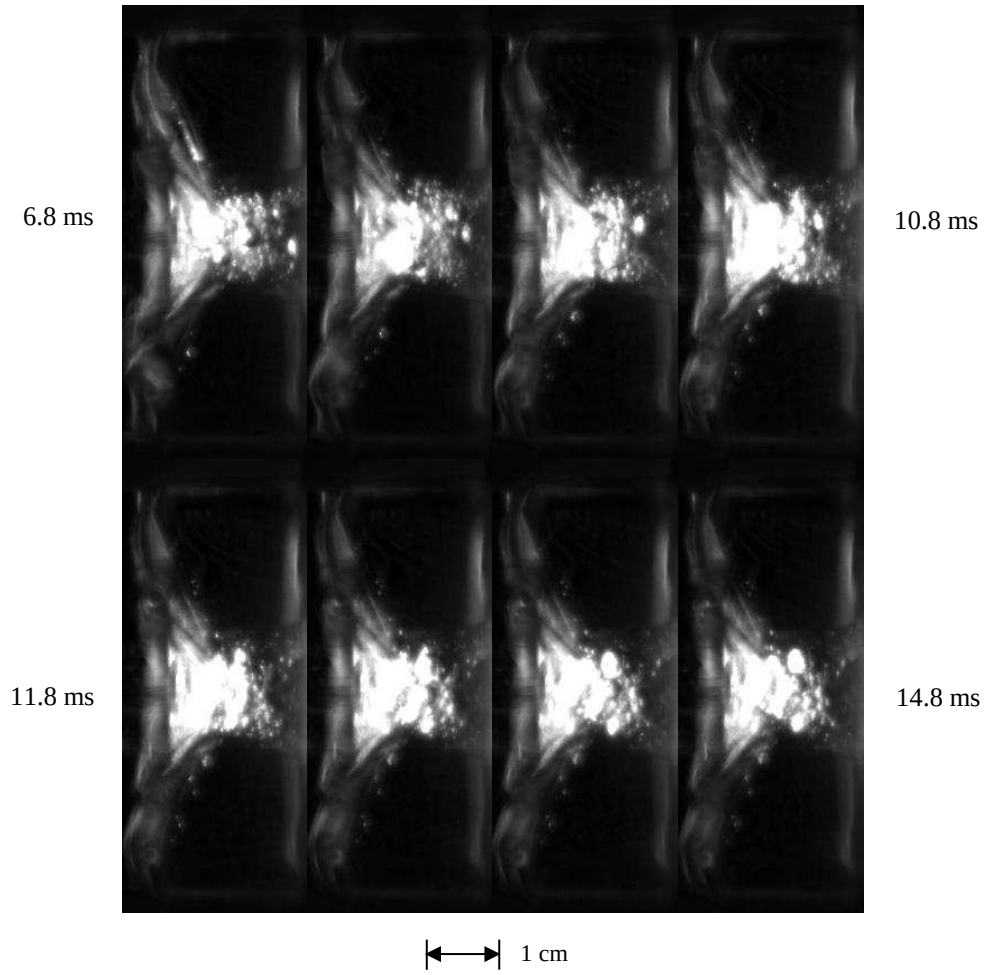

Figure 7.9 Continuation of Figure 7.8 between 6.8 -14.8 ms (left to right) in time steps of 1ms showing bubble movement in opposite directions [Images scale 1cm=0.542mm]

In Figure 7.10 bubbles entering the nozzle hole are observed as a consequence of the angular momentum of the flow in the sac volume, these bubbles enter the hole 2 ms after the end of injection and move outwards of the nozzle hole. A bubble in the bottom hole travels close to the sac volume.

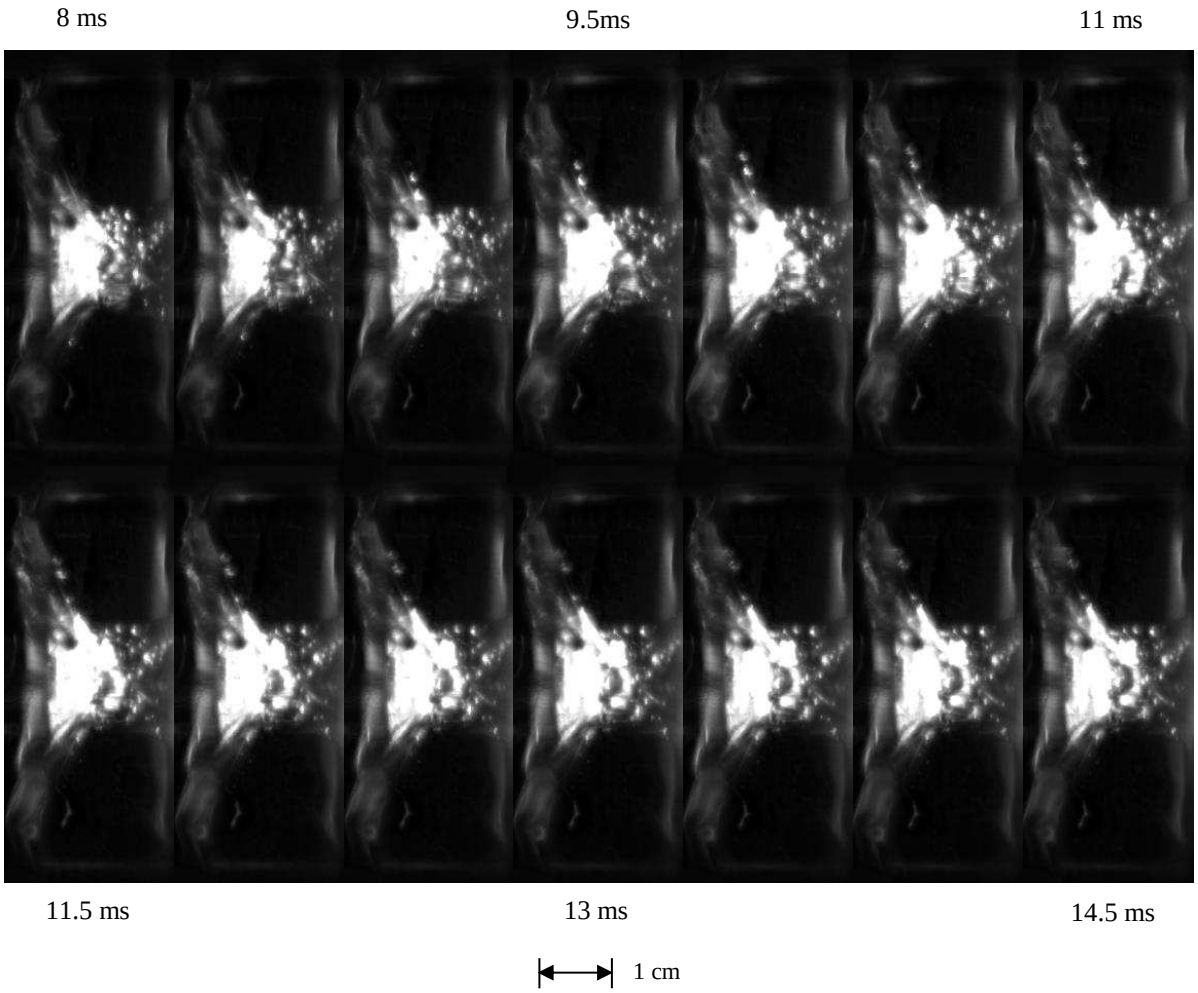

Figure 7.10 Images taken 2 ms after end of injection showing bubble entry from sac volume into top hole in steps of 0.5 ms (left to right) [image scale 1cm=0.59mm]

Some bubbles were observed flowing back into the sac in both top and bottom holes. Figure 7.11 and Figure 7.12 show suction of bubbles into the sac volume in the top and bottom holes respectively.

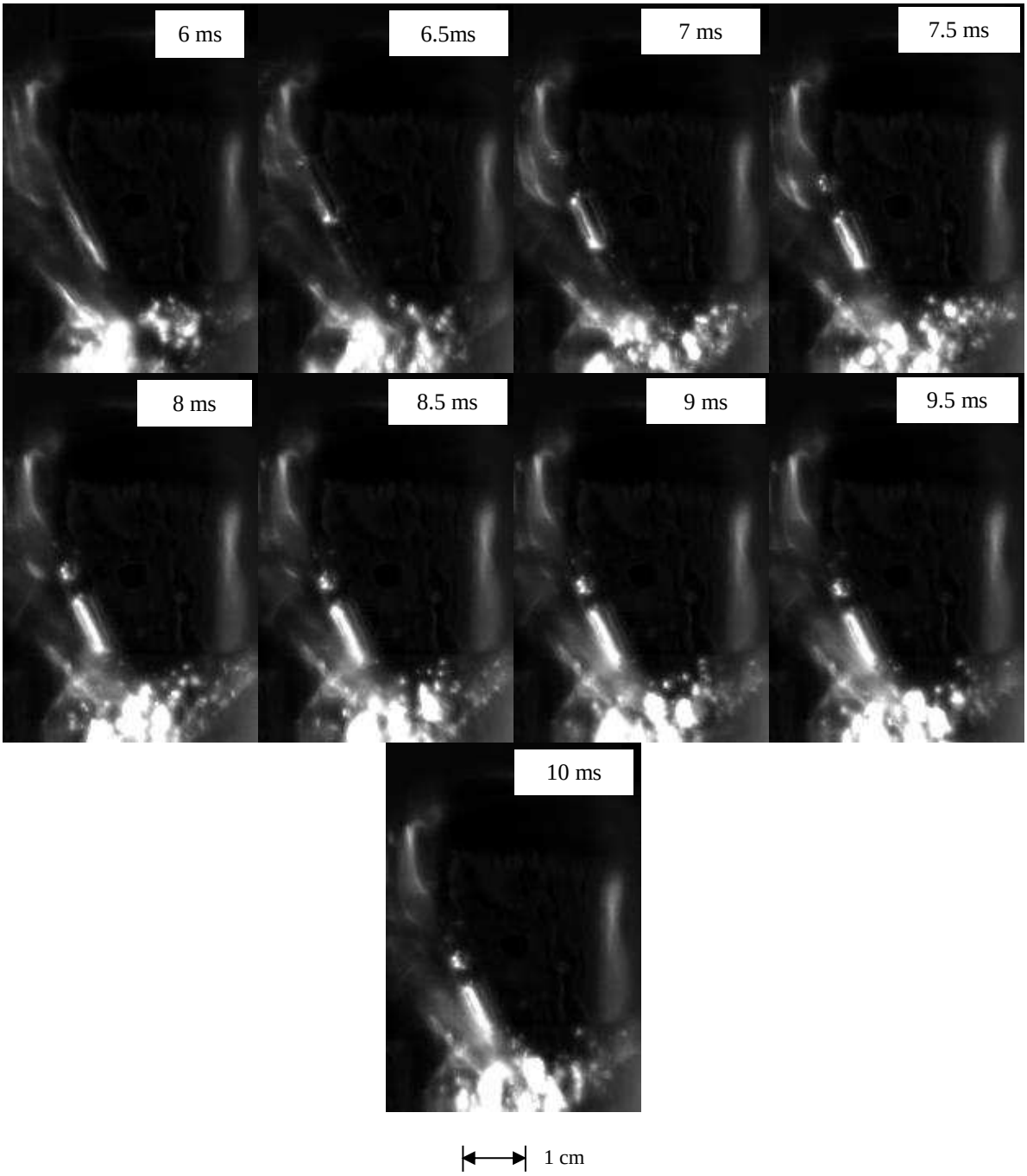

Figure 7.11 Observations showing bubbles re- entering the sac volume in the top hole taken from 6 ms – 10 ms (on needle seal) in steps of 0.5ms (left to right) [Image scale 1cm =0.32mm]

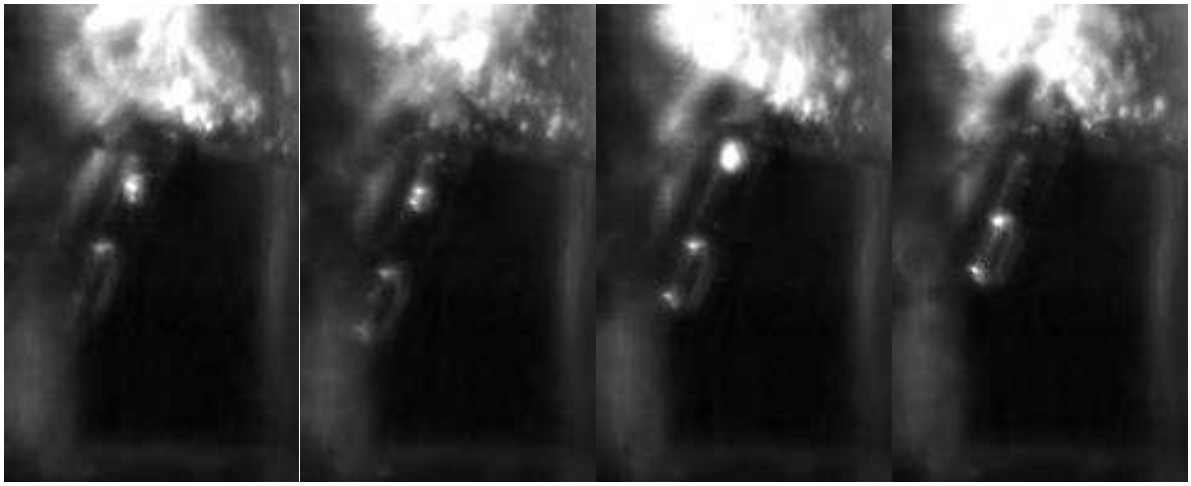

Figure 7.12 Observations showing bubbles re- entering the sac volume in the bottom hole taken from 6.3 ms – 7.8 ms (on needle seal) in steps of 0.5ms (left to right) [Image scale 1cm =0.248mm]

7.1.2.1 Statistical analysis of bubble travel

In order to get an overview of the travelling bubbles in each holes, a statistical analysis was carried out to determine:

- Percentage of bubbles travelling inwards per nozzle hole
- Percentage of bubbles travelling outwards per nozzle hole
- Proximity to the nozzle hole entrance
- Direction of bubble travel comparison in both holes (opposite travel, both inwards and both outwards.).

Initially a post processor programme developed by BETA CAE systems [188] with videos compiled between 6.0 ms and 14.5 ms (needle return to end of recording) of the end of injections was used. The post processor allowed tracking of selected bubble movements and produced x and y coordinates outputs of the motion of the bubble. Each video per fuels A, B and D was uploaded on to the post processor. The bubbles selected per hole (i.e. top and bottom holes) and then allowed the software to track its motion. The software would then

output x and y coordinates from start to finish of the bubble track. $BubT_{op}(x,y)(t)$ which is the top hole bubble travel with time and $Bub_{Bot}(x,y)(t)$ the bottom hole bubble travel with time.

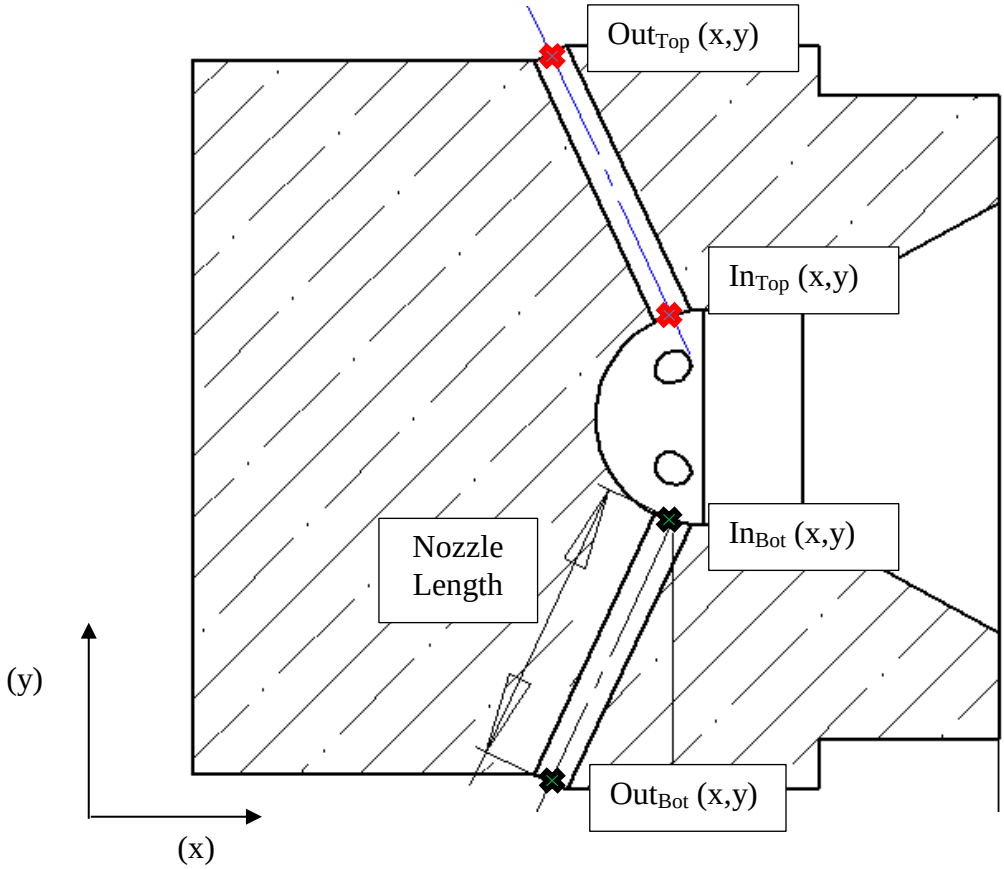

Figure 7.13 Hole inlet and outlet positions definition per hole

Bubbles were selected per hole when their boundary could be best defined. Using the time varying coordinate output from the post processor, change in bubble displacement was calculated between each subsequent time step. For the top hole, if the bubble increased in y coordinate with time it was termed to be positive, whereas a decrease in y coordinate with time was termed as negative. For the bottom hole, and increase in y coordinate would result in negative travel whereas a decrease in y coordinate would result in positive travel. Positive travel refers to travel out of the holes whereas negative travel refers to bubble travel towards the sac, for both top and bottom nozzle holes.

$$\Delta d_{(hole)}^{i,n,f}(t)$$

$$= \sqrt{\left[Bub_{hole}^{i,n,f}(x)(t+1) - Bub_{hole}^{i,n,f}(x)(t)\right]^2 + \left[Bub_{hole}^{i,n,f}(y)(t+1) - Bub_{hole}^{i,n,f}(y)(t)\right]^2}$$

Equation 7.1

Where Δd represents the change in displacement, superscript i refers to number of frames (85 to 150), superscript n refers to the injection event, superscript f represents the fuel name, subscript hole refers to the hole (top or bottom), Bub(x) represents the coordinates of the bubble at time t and t+1. After the calculation in Equation 7.1 a check of the y coordinates in both holes was carried out and if negative travel with relation to the previous logical statements determining negative travel, the result of Δd would be multiplied by -1. The overall displacement would be obtained for each hole (top and bottom) and the changes in displacements summed per injection event as in Equation 7.2.

$$overall\ displacment_{hole}^{n,f} = \sum_{i} \Delta d_{hole}^{n,f}(t)$$

Equation 7.2

The result from Equation 7.2 would be put through another logical to test to check whether the number was positive or negative to depict the direction of travel. The numbers were then summed to obtain an overall percentage of injections travelling outwards or inwards during the end of injection events per nozzle hole depicted by their overall displacement being either negative or positive. Holes with no bubbles observed were subtracted and presented separately.

$$if\ overall\ displacement_{hole} < 0, Overall\ disp\ logic_{hole}(n) = 0\ , else = 1$$

Equation 7.3

Injection sequence summation (n)	Result	Logic	Logic interpretation
n	>0	1	Positive travel (outwards)
n	<0	0	Negative travel (inwards)
n	-	-	No bubble

Table 7.1 Logic interpretation for the summation of overall displacement per injection

From Equation 7.3, results positive were summed and an overall positive percentage obtained, the negative motion was obtained by subtracting the injections with no bubbles observed from the positive displacement bubbles.

The logic obtained in Equation 7.3 was then compared for both top and bottom holes. The logics were summed per injections and then another logical analysis performed on the summation obtained.

$$comparison\ logic(n) = overall\ displacement\ logic_{Top}(n) + overall\ displacement\ logic_{Bot}(n)$$

Equation 7.4

If comparison logic was found to be equal to 0, then this would mean that bubbles in both nozzle holes are travelling inwards to the sac; if equal to 1, then the bubble motion in both holes was in the opposite direction (i.e. top hole bubble moving outwards whereas bottom hole bubble moves inwards and vice versa; and if equal to 2 then bubble in both holes are moving outwards in the positive direction.

Injection number n	Top hole logic	Bottom hole logic	(Summation) and direction
n	0	1	(1) Opposite travel
n	1	0	(1) Opposite travel
n	1	1	(2) Both outwards
n	0	0	(0) Both inwards
n	1	No bubble	(-) No comparison

Table 7.2 Interpretation of top and bottom hole logic summation per injection event.

In the final analysis the bubble motions were analysed with respect to the entrance to the hole and the nozzle length and checked for their proximity to the hole entrance (Equation 7.5).

$$\Delta origin\ relative\ d_{hole}^{i,n,f}(t) = \frac{\sqrt{\left[In_{hole}^{f}(x) - Bub_{hole}^{i,n,f}(x)(t)\right]^2 + \left[In_{hole}^{f}(y) - Bub_{hole}^{i,n,f}(y)(t)\right]^2}}{nozzle\ length}$$

Equation 7.5

As the bubble coordinates were subtracted from the hole inlets, the value from Equation 7.5 would provide the length relative, entrance relative bubble position. That is it would pinpoint how close the bubble was to the nozzle hole entry. Values less than 0.05 were presumed to be closer to the hole entry or have entered the sac. A value of 1 would mean the bubble is near the nozzle exit. The focus here was how close the bubbles got to the sac as this would then mean there was a possibility of the hole travelling into the sac volume. A logical analysis was carried out on the results from Equation 7.5, if the value of $\Delta origin\ relative\ d_{hole}^{i,n,f}(t)$was <0.05 then it would result in a logical 1. A summation of the 1's was carried out over the injections and a bubble count close to the sac proximity produced over the number of injections. A sequence of 100 injections were analysed for fuels A and B whereas 70 for Fuels D. The results are shown in Table 7.3 - Table 7.5.

Table 7.3 and Table 7.4 show the overall two phase bubble motion directions in the top and bottom nozzle holes as a percentage and a comparison of the bubbles in two holes in synchronous injections. Table 7.5 provides information about the bubble proximity to the sac volume.

Fuel Name	**Overall Motion**						**Overall percentage (%)**	
	Top Hole (%)			Bottom Hole (%)				
	Outwards	Inwards	No Bubble	Outwards	Inwards	No Bubble	Outwards	Inwards
A	43	51	6	7	85	8	25	68
B	100	0	0	11	67	22	55.5	33.5
D	60	23	17	7	79	14	33.5	51

Table 7.3 Overall bubble motion per hole

Fuel name	**Top/Bottom relative motion (%)**		
	Opposite	Both Inwards	Both Outwards
A	42	40	4
B	67	0	11
D	49	20	3

Table 7.4 Relative motion of bubbles in both holes

Fuel name	**Proximity to sac volume** (count/no. of injections)	
	Top Hole	Bottom Hole
A	2/100	11/100
B	0/100	3/100
D	10/70	26/70

Table 7.5 Bubble proximity to sac volume count

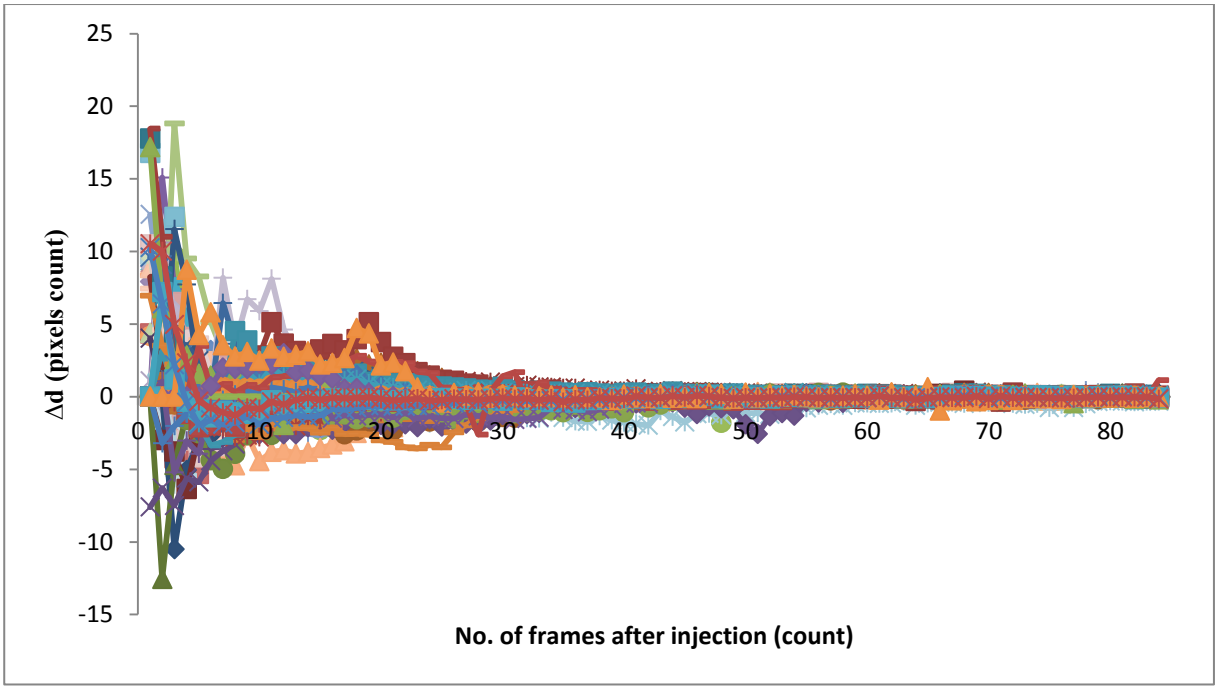

Figure 7.14 Displacement distributions of bubbles with time for Fuel A showing the change in displacement per 0.1 ms time steps after injection for 100 injections for bubbles observed in the top hole

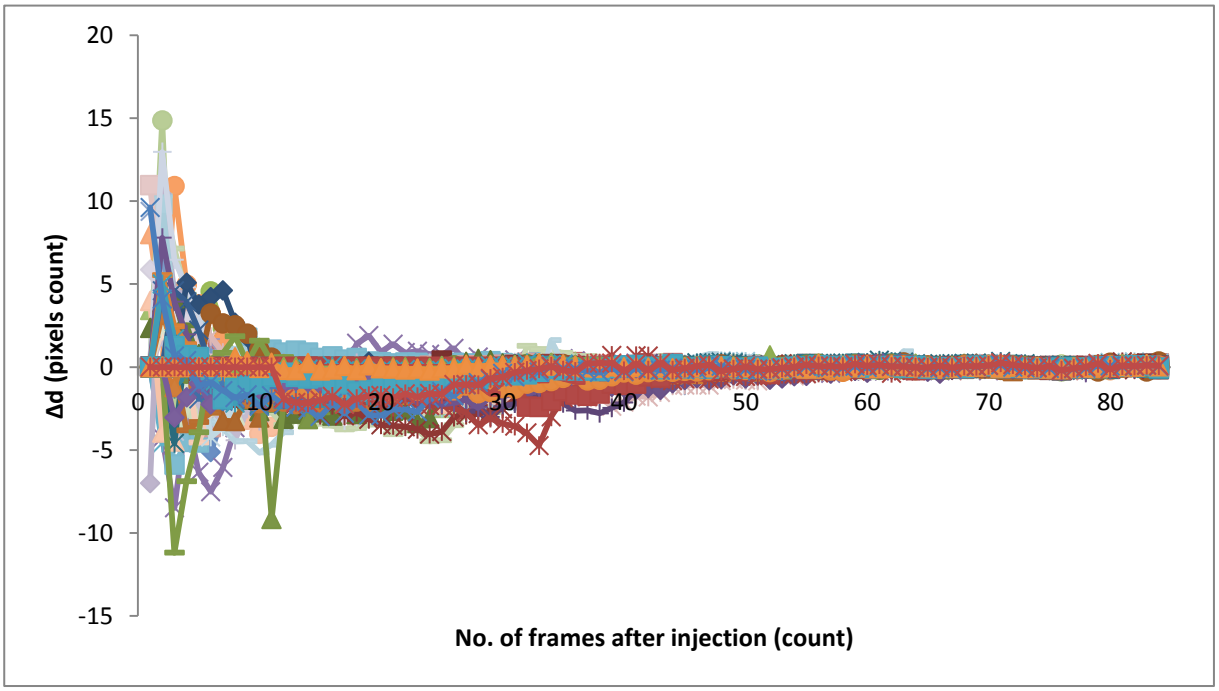

Figure 7.15 Displacement distributions of bubbles with time for Fuel A showing the change in displacement per 0.1 ms time steps after injection for 100 injections for bubbles observed in the bottom hole

Results obtained from Fuel A show that 43% of bubbles in the top hole travelled outwards whereas 51 % travelled inwards towards the sac. 7 % of bubbles in the bottom hole were

observed to travel outwards whereas 85 % travelled back inwards towards the sac volume. From Table 7.5, 2 of the bubbles from the top hole whereas 11 bubbles in the bottom hole travelling inwards reached close proximity or entered the sac volume. Most of the bubbles travelled in opposite directions or inwards. Only in 4% of cases in both holes combined were observed to travel out wards. Overall 68 % of bubbles found in the nozzle holes after injection were observed to travel inwards. Figure 7.14 and Figure 7.15 shows the change in displacement against time for the top and bottom holes respectively. The figures show high initial changes in displacement which decay with time. The figures show a distribution of the changes in displacement against time using Equation 7.1 for 100 end injections of fuel A.

Results from Fuel B show a very biased account especially with respect to the top hole. This is because the bubble boundaries could not be defined until later due to phenomena observed in Figure 7.8 occurring for a long period. The motion could not be properly defined however it was noticed that the large bubbles spent a long time in the sac-hole intersection. They seemed to be initially traveling into the sac as observed in the Figure 7.8 after which they start moving outwards. This was only observed in the top hole. 11 % of fuel B bubbles in the bottom hole travelled outwards whereas 67% travelled back towards the sac volume however only 3 bubbles came to close proximity of the sac volume entrance. A high number percentage of bubbles were observed travelling in opposite directions. The overall motion is dominated by the outward motion in the top hole and only 33.5% of bubbles observed travel outwards.

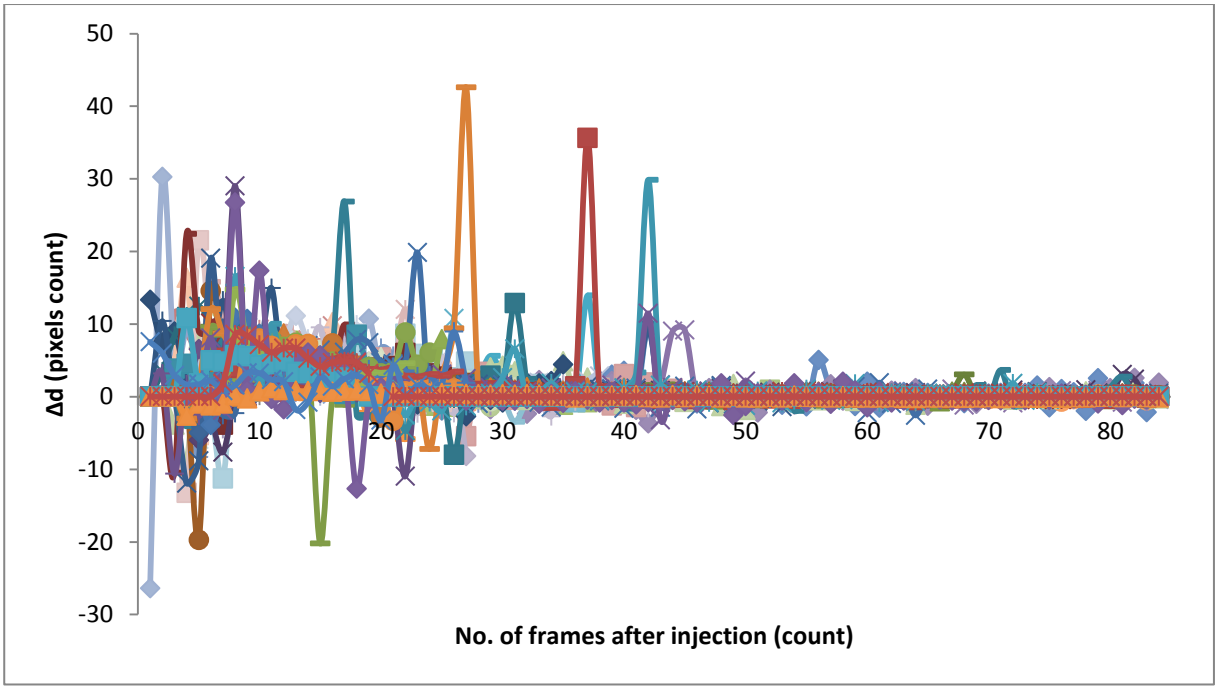

Figure 7.16 Displacement distributions of bubbles with time for Fuel B showing the change in displacement per 0.1 ms time steps after injection for 100 injections for bubbles observed in the top hole

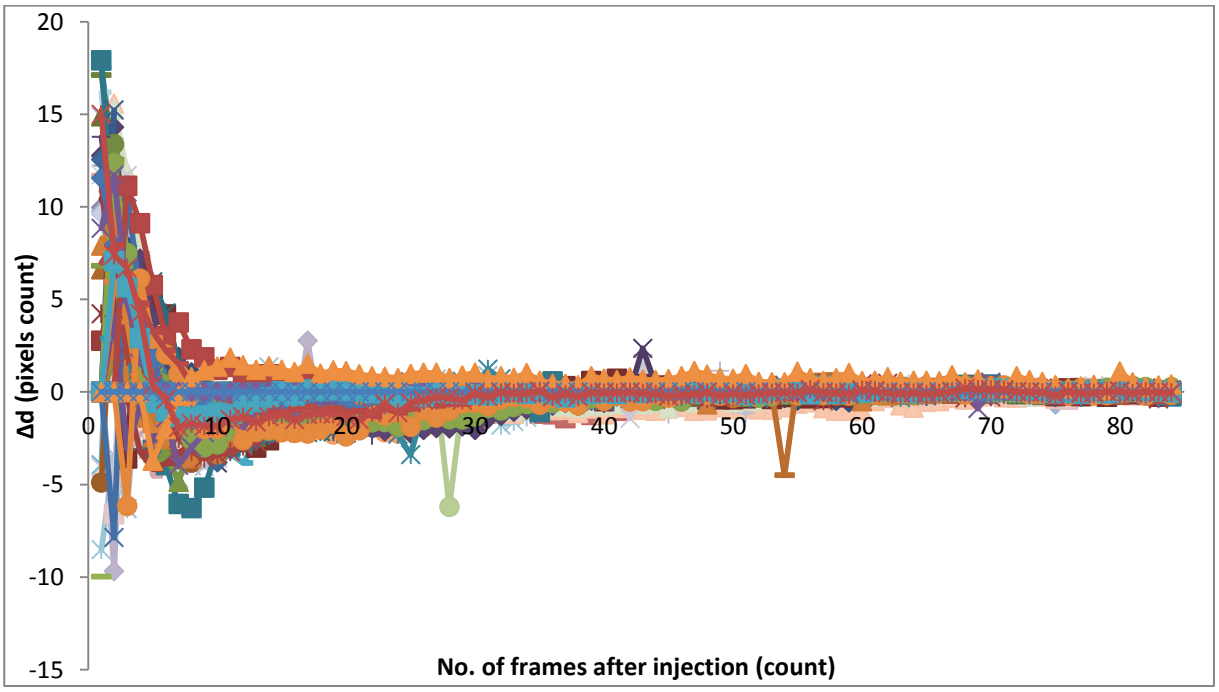

Figure 7.17 Displacement distributions of bubbles with time for Fuel B showing the change in displacement per 0.1 ms time steps after injection for 100 injections for bubbles observed in the bottom hole

Figure 7.16 and Figure 7.17 show change in displacement distributions for fuel B in the top and bottom hole respectively. The top hole figure identifies the phenomena written in the

earlier paragraphs where the bubble edge is only defined later and this is shown by the later peaks occurring in the graph. These do not appear in the consequent bottom hole figure. Some bubbles also display motion described earlier where the bubble exits the sac and re-enters and then re-exits these are shown by the later negative peaks in the chart which represent inwards motion after which the bubble slowly flows outwards. The top hole figure also clearly identifies the positive motion bias of the holes described earlier. The bottom hole has a more mixed distribution of negative and positive motions parameterised earlier as percentages. The effects maybe occurring as a result of a possible fuel separation occurring between the light and heavy components present in the gap fuel. The lighter components are evaporating and the heavier components setting downwards into the nozzle sac. The interaction between these maybe resulting in the phenomena observed where the bubble is seen to move in and out of the nozzle due to the opposing forces of the bubble trying to sink and float combined by the effects of vorticity in the sac volume. Once the heavier components of the fuel have settled into the sac, the lighter components continue to evaporate and thus the bubble is observed to move upwards in the hole towards the exit. This phenomenon is not observed in the bottom hole as motion of the heavier fuel dominates the outwards pull of the bubble. The momentum of the heavier fuel over the lighter fuel drives the bubble out of the bottom nozzle.

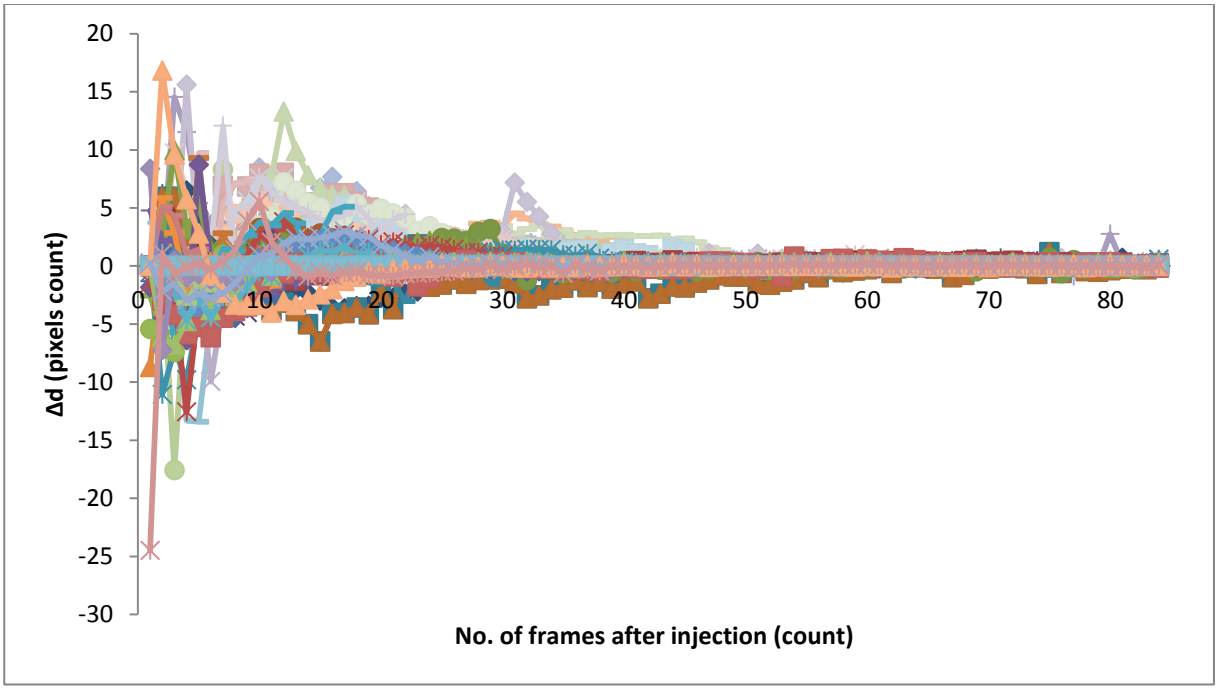

Figure 7.18 Displacement distributions of bubbles with time for Fuel D showing the change in displacement per 0.1 ms time steps after injection for 100 injections for bubbles observed in the top hole

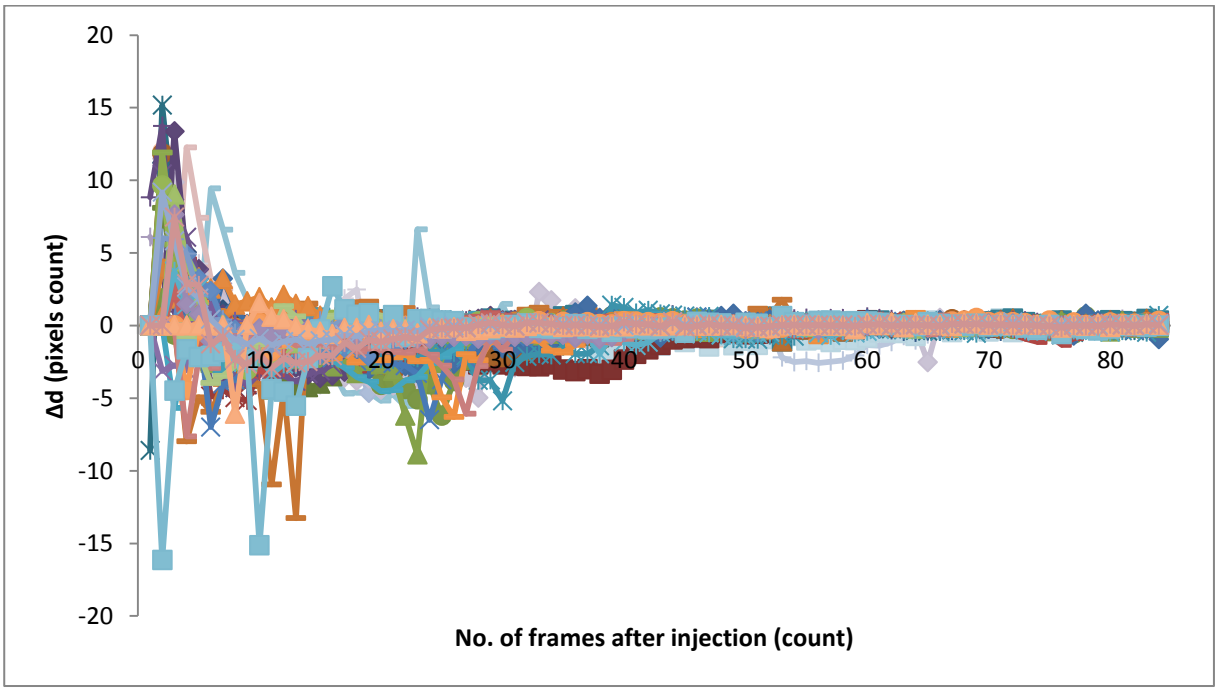

Figure 7.19 Displacement distributions of bubbles with time for Fuel D showing the change in displacement per 0.1 ms time steps after injection for 100 injections for bubbles observed in the bottom hole

The results from Fuel D show a high number of inwards bubble travel toward the sac volume. Of the bubbles travelling into sac volume or into close proximity of the sac volume 10 were from the top hole whereas a large 26 were from the bottom hole out of the 70 injections.

Around 46% of the bubbles in the bottom hole ended up near or into the sac volume taking into account the number of occasions bubbles were not observed. 60% of bubbles in the top hole travelled outwards whereas 23% travelled in the direction of the sac. In the bottom hole, 7% of bubbles were observed to travel outwards where 79% travelled inwards. A large number of bubbles still travel in opposite direction in the relative hole travel comparison.

The observations here again relate to its lower distillation profile. Fuel D has a very low distillation profile and thus a lower evaporation point. The fuel vapour fractions in the bubbles created are lighter than the surrounding fuel and thus they are largely influenced by the sac vorticity which further drives their movement. Most bubbles in the bottom hole move inwards towards the sac whereas the bubbles in the top hole move outwards towards the hole exit.

Fuel D injections were blurring the side of the imaging section and providing blurred views of the interior holes. Each image seemed to worsen the view and thus only 70 images could be viewed over two sets of nozzles. The blurring also caused problems with tracking programme as unwanted scattering from the coating occurring outside disrupted bubble view. Only clear hole views of both top and bottom nozzles have been selected. Figure 7.18 and Figure 7.19 show the change in displacement distributions of the bubbles observed with time per injection.

In the figures above (Figure 7.14-Figure 7.19) the distributions show the high initial change in displacement of the bubbles decreasing with time. This was observed similarly in the sac volume where the initial vorticity of the liquid was high but dissipated its energy with time as a result of the liquid viscosity. A number of liquid properties such as liquid viscosity and liquid surface tension, and nozzle characteristics such as nozzle wall friction, may be affecting

the travel of bubbles in the nozzle holes. High liquid viscosity and high wall friction will resist liquid flow. The wall friction impact however depends on the surface area of the bubble in contact with the nozzle walls.

The hypothesis developed as a result of the above observation is that the vorticity in the sac is causing a lot of high and low pressure gradients which in turn are causing suction and extraction points in the nozzle holes as observed by the movements of the bubbles in the nozzle holes. The pressure gradients may be constantly changing as observed during some injections whereby the bubble travel direction constantly changes. The properties of the fuels are supplementing this motion where the lighter fractions require a lower force to be displaced, while heavier components which require higher force thus sink into the sac from the top hole or move outwards from the sac in the bottom hole.

7.1.3 In-nozzle bubble flow conclusions

It has been observed that during needle return and seal, the vorticity of the flow is retained in the sac volume even after injector seal. The flow angular momentum is high immediately post injection but subsides over time. The vorticity in the sac volume has been observed to cause points of suction and discard in the nozzle holes by creating regions of high and low pressure. The effect of a region of low pressure induced by the vorticity in the sac near an injection hole results in a suction of bubbles as observed, whereas regions of high pressure induced by the vorticity in the sac volume in the vicinity of an injection hole results in the bubble being pushed outwards.

The suction observed may be drawing external gases (exhaust) from outside to at least inside the nozzle holes or maybe even as far as the sac volume. The vorticity effect causes suction and expulsion as observed in two holes however four other holes are out of view in the imaging plane. For the vorticity drawing in bubbles mechanism to be true, it also has to expel them and this may be occurring in the other holes as well as the ones in the imaging plane as has been shown by the results. The bubbles formed are a two phase gas-liquid mixture of highly reactive fuel vapour and degased air. A mixture of hot air and a volatile gas-liquid bubble on a very hot injector metal surface in an engine situation is the ideal place for reactions to occur. Furthermore it has been observed that pyrolysis like effects may occur in the fuels at higher temperatures leading to the formation of particulates.

Carbon deposit formation from diesel fuels mainly involves the chemical conversion of precursors to species of higher molecular weight with limited fuel instability. The precursors include nitrogen and sulphur containing compounds, organic acids, and reactive olefins. Pedley et al. [189] established a mechanism by which insolubles are formed in the acid-catalysed conversion of phenalenones and indoles to complex indolylphenalene salts. Phenalenones are formed by oxidation of certain reactive olefins; indoles occur naturally in certain blend components of diesel fuel. Certain dissolved metals, especially copper, contribute by catalysing oxidation reactions. Venkataraman et. al [190] analysed solid deposits from commercially available high pressure diesel injectors to study the solid deposit formation and compared it to the deposits formed by thermal oxidative stressing of n-hexadecane. Both deposits formed contained PAH with oxygen moieties. The formation of PAH from n-hexadecane showed that aromatization of straight chain alkanes and polycondensation of aromatic rings was possible at temperatures as low as 160°C in the presence of oxygen. They suggest the cycloalkanes form aromatics with the presence of

oxygen and heat and this was responsible for the deposit formation. Heat would be present in an engine as a result of the continuous combustion raising the temperature of the surfaces through conduction and convection.

In an engine situation where higher pressure exists in cylinder, the motion of the piston to exert exhaust gases maybe pushing and enhancing in the nozzles that draw the bubbles in, with the possibility of exhaust gases being drawn in as well. For a four-stroke diesel engine running at various speeds as shown in r/min, the time between injection, combustion and exhaust stroke (piston moving 1 complete revolution) is 24 ms. In 12 ms the combustion gases start being ejected outwards. The time for reaction is sufficient at all engine run speeds per cylinder as seen in Table 7.6

Engine speed (r/min)	Injection to exhaust (1 rev) (ms)	Injection to injection (2 revs) (ms)
1800	33.33	66.67
2000	30	60
2500	24	48
3000	20	40
3500	17.14	34.28
4000	15	30

Table 7.6 The time between injection and full exhaust cycle and injection to injection cycle for a four stroke engine running at different speeds.

A possible mechanism for the entry of air into the nozzle passages as a result of the vorticity in the sac volume creating low pressure regions in the vicinity of passages inducing suction of reactive bubbles towards the hole is presented here. There is also a possibility of the formation of highly reactive fuel-gas bubbles in the sac volume as a result of needle cavitation (sheet cavitation occurring on the lower surface of the needle). The bubble formation in the nozzle holes is as a result of nozzle cavitation evolving and is as a result of receding stress on bubble nuclei. The result may be a formation of gas bubbles rather than a cavitation bubbles.

Gas bubbles would be bubbles with gas/air entrained in liquid fuels whereas a cavitation bubble would be fuel vapour entrained in fuel. The hypothesis is that these bubbles formed maybe highly reactive vessels as they may contain fuel vapour and degassed air. The presence of the fuel vapour plus the thermal effects in an engine situation in the presence of oxygen may lead to the formation of deposits. The deposits formation may take place post engine switch off where the bubbles in the nozzle hole and sac are susceptible to longer periods of thermal stressing.

Diesel fuel contains a certain amount of air dissolved in it depending on the fuel temperature, pressure on the fuel, density and the amount of aeration to which the fuel has been subjected. A reduction in pressure on the fuel or an increase in the temperature of fuel releases the air from the fuel. The amount of release depends on the degree of fuel saturation with air and the magnitude of pressure reduction or temperature increase. This could happen in the fuel tank, fuel filters or fuel pumps. There are many reasons for the fuel tank being a problem area: hot fuel under pressure being dumped into the tank via the fuel injection return lines; fuel sloshing around in the tank while driving; less-efficient pumps (suction type, inline pumps); and the fact that most fuel tanks are mounted below the height level of the injectors. All of these things contribute to agitation, which then leads to additional unwanted air particles becoming trapped in the fuel. The solubility of air in hydrocarbons is discussed in by Battino et al in [191,192].

During this phase of needle cavitation, the air dissolved in the fuels may be coming out of solution. If this is the case then this would create an ideal reaction sequence where there is the presence of fuel, air and high temperature (combustion temperature in the engines). The combination leads to reactions in the fuels which maybe leading to the formation of deposits

in the sac and further into the injector. Needle cavitation occurring during the final moments of needle closure is the mechanism to bring out the dissolved air from the fuel. This occurs as there is a sudden decrease of pressure and the presence of high temperatures in these regions. Once the air is out of solution and present in the sac, the higher combustion temperature on the walls of the sac and injector nozzle holes form ideal places for deposit formation reactions to occur.

The formation of deposits can impact on the quality of the combustion process leading to: - power loss, increase in smoke, higher noxious emissions level and a reduced fuel economy [12]. Recent technical advances in fuel injection systems require components to be smaller and lighter to ensure highly dynamic response. They need to be manufactured to very exacting tolerances and have to operate within very small clearances to minimise any leakage at the very high pressures encountered in modern systems. Therefore, it is essential that the FIE is kept free from deposits of any kind and is operated with fuel which is fit for purpose, otherwise problems of power loss, emissions non-compliance, reduced fuel economy, poor driveability and difficulty in starting are likely to be observed.

7.1.4 Observation of string cavitation

During the initial testing period where the focusing of the nozzle holes onto the camera was being carried out. A test was carried out with the camera focus slightly on the foreground of the two holes in the plane. The camera was focusing close to the entry of two holes injecting to the foreground of the images as seen in Figure 7.20 and Figure 7.21 below. As a result, two different occasions of hole to hole string cavitation in a real size replica of an injector nozzle was captured occurring at the inlet of the two holes injecting on the foreground as seen in

these images. The injection pressure at this point was 400 bar as this was still the test and setup phase. The strings are thins line of light scattering observed joining two holes at the entrance.

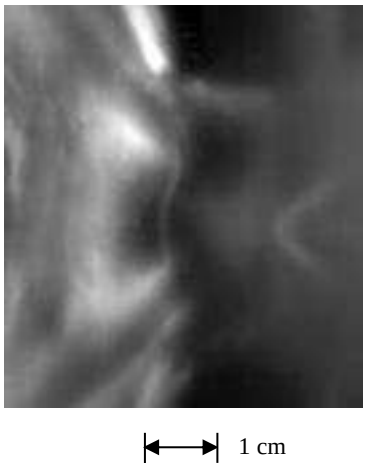

Figure 7.20 Hole to hole cavitation at 400 bar injection pressure observed during 1.5ms after needle lift began [Image scale 1cm=0.227]

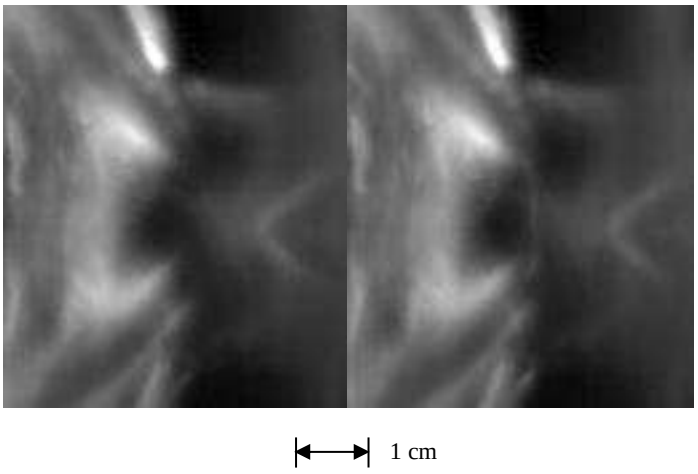

Figure 7.21 Hole to hole string cavitation at 400 bar injection pressure observed at 1.3ms after needle lift began (Successive images at 10kHz) [Image scale 1cm=0.227]

Figure 7.22 and Figure 7.23 show two single events showing the occurrence of string cavitation between two holes. These images were obtained during pilot testing of a new nozzle. It was observed that one nozzle hole next to the bottom hole on the foreground was blocked. And thus the string came in to focus as it went from the hole close to the top hole in

the foreground into the bottom hole as seen in these images. It was observed for long periods of time as seen in Figure 7.23.

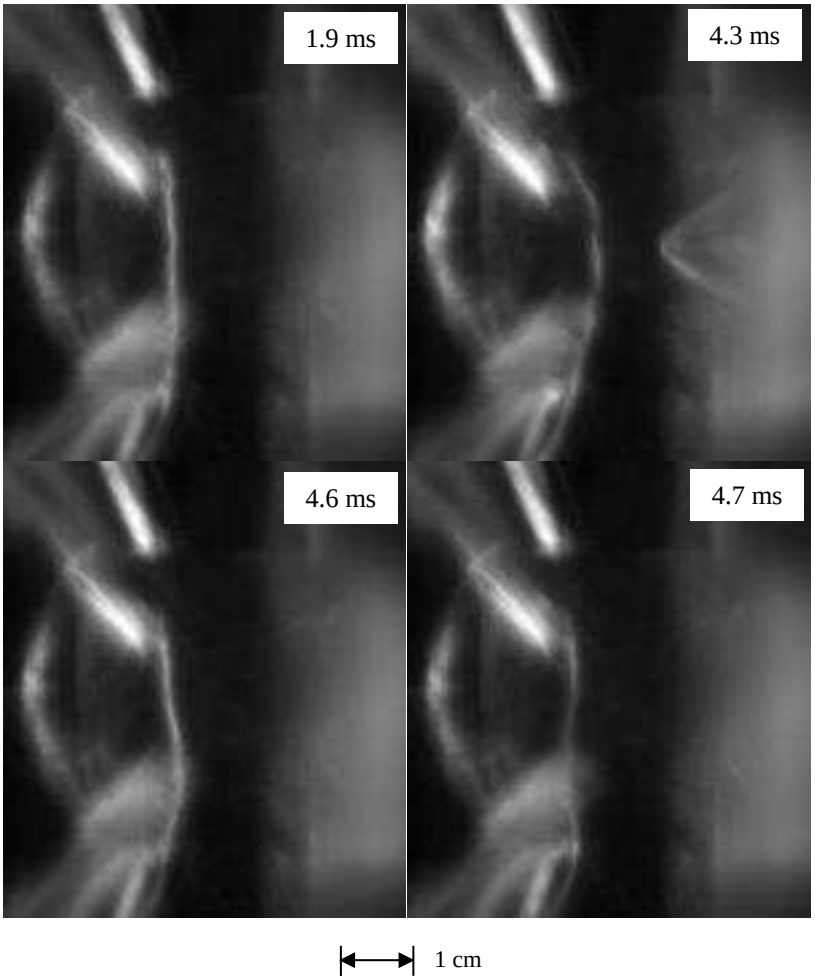

Figure 7.22 Hole to hole String cavitation observed at 350 bar injection pressure at 1.9 ms, 4.3ms, 4.6ms and 4.7ms after needle rise begun occurring during a single injection event [Image scale 1cm=0.227]

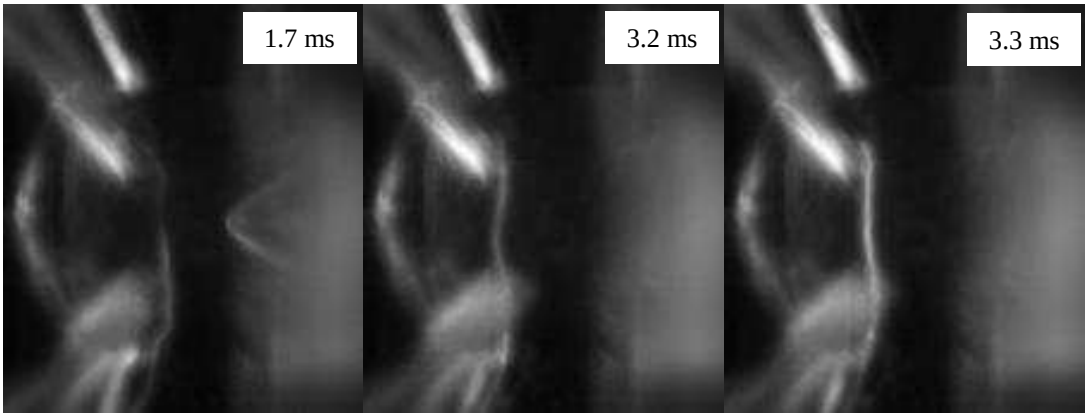

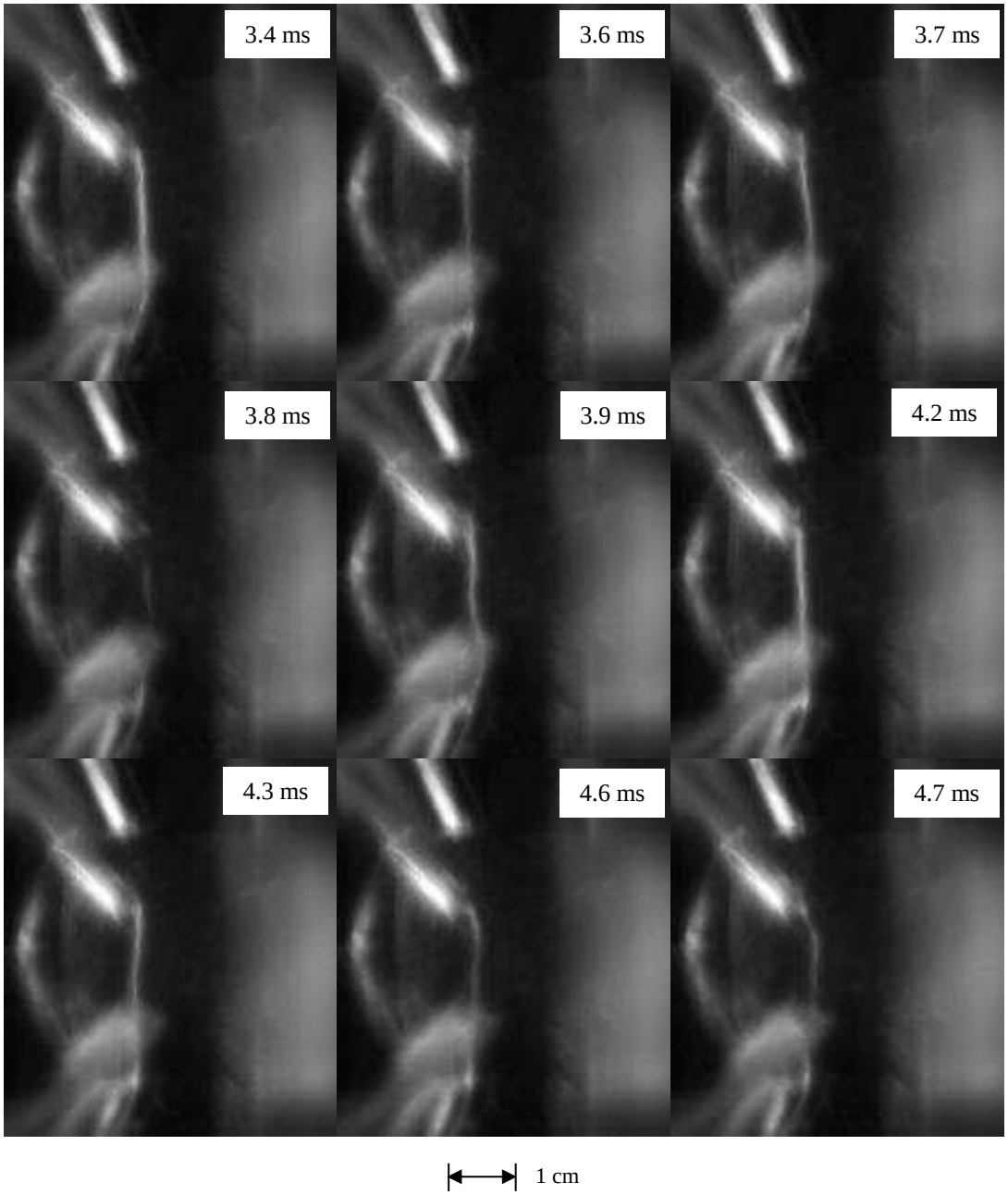

Figure 7.23 Hole to hole String cavitation observed at 350 bar injection pressure at 1.7 ms, 3.2-3.4 ms, 3.6- 3.9ms, 4.2-4.3 ms and 4.6-4.7 ms (left to right after needle rise begun occurring during a single injection event following Figure 7.21. [Image scale 1cm=0.227]

Strings are found at the core of recirculation zones. They originate either from pre-existing cavitation sites forming sharp corners inside the nozzle where the pressure falls below the vapour pressure of the flowing liquid, or even from suction of outside air downstream of the hole exit [23]. The frequency of appearance of the strings has been correlated with the Strouhal number of the vortices developing inside the sac volume; the latter has been found to be a function of needle lift and hole shape. The presence of strings significantly affects the

flow conditions at the nozzle exit thus influencing the injected spray. The presence of strings results in the alteration of cavitation structures in the nozzle hole and a variation in the instantaneous fuel injection quantity. String cavitation and their implications have been observed and discussed by [23,26,27,82–86].

7.2 External Spray Dropsizing Distribution

From the images obtained on the LSD camera, Sauter mean diameter distributions were calculated by determining a ratio of LIF to Mie image for fuels A, B and D to enable a comparison of the fuels.

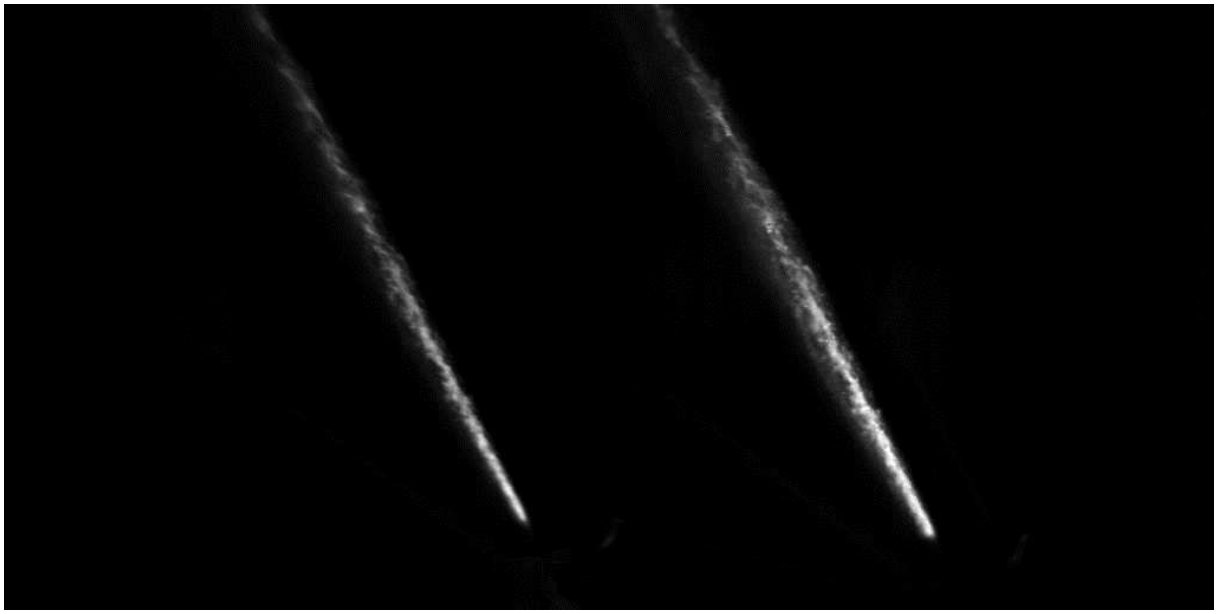

Figure 7.24 A LIF-MIE combined image captured in the LSD camera showing LIF scattering from the dye on the left and Mie scattering from the spray on the right hand side.

The 1024 x 512 images captured had both sets of LIF and Mie image as observed in Figure 7.24. A mean background was obtained from the range of background images obtained prior to experiment. The mean background images were then subtracted from the experimental

images and then the images were separated into two 512 x 512 pixel images of LIF and Mie images.

In order to express the processing of the data images mathematically, the pixel intensity on the raw data images was represented by S_{ij}^{klm}, where S_{ij}^{klm} represented the intensity of the pixel located on the CCD chip at the position defined by the row index i and the column index j, $i \in \{0,1,2,3...1024\}$, $j \in \{0,1,2,3...512\}$. The index number k represents the frame number within a set of 100 images at 10 kHz for a single injection event, ranging from frame 1 to frame 100; while the index number l refers to the specific injection event, ranging from injection 1 to injection 100. The index number m refers to the diesel fuel sample tested, and ranges from A, B and D. A thousand background images were obtained for each experimental session. The pixel intensity data are represented by the indexed intensity variable B_{ij}^{mq}, where the index numbers i, j, and m retain their meaning from above, while the index number q refers to background image 1 to 1000. A mean background image was calculated for each experimental session. This is expressed by Equation 7.6

$$\overline{B_{ij}^{m}} = \frac{1}{1000}\sum_{p=1}^{N} B_{ij}^{mq}$$

Equation 7.6

The mean background subtracted image is represented as I_{ij}^{klm} and is equal to $S_{ij}^{klm} - B_{ij}^{m}$. The image I_{ij}^{klm} is then split into two images of $i, j \in \{0,1,2,3...512\}$ namely, LIF_{ij}^{klm} and Mie_{ij}^{klm} respectively.

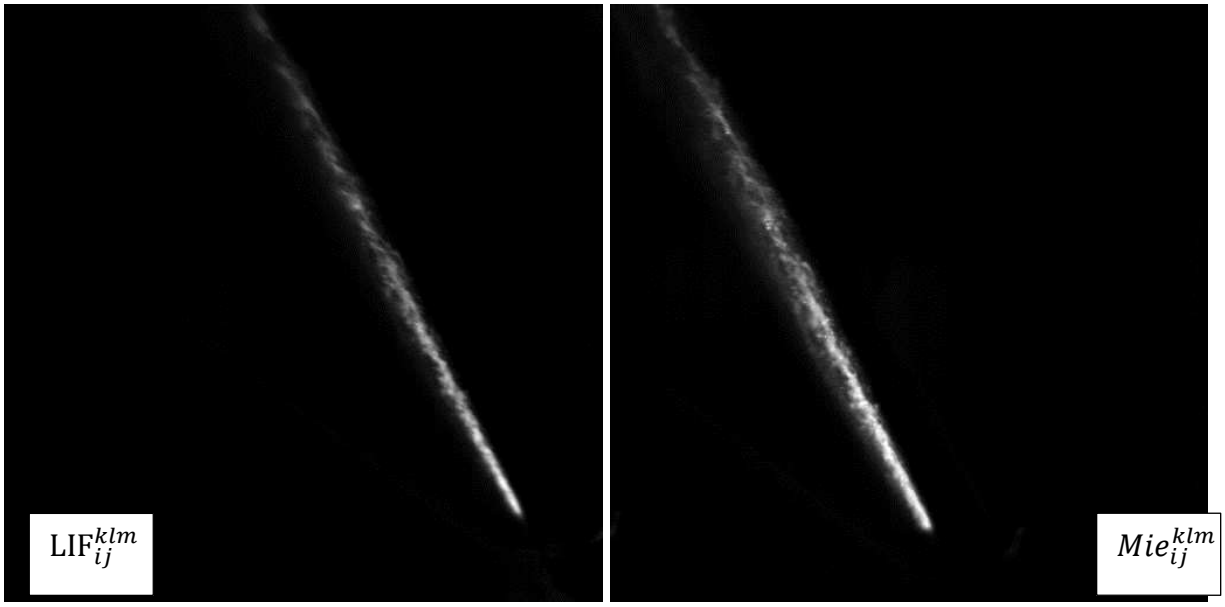

Figure 7.25 Split LIF and Mie images into two 512 x 512 images

As it can be observed from the above images the ratio cannot directly be taken as the Mie image is translated with respect to the LIF image. The image was translated with reference to the LIF image. However even after translation, the ratio still cannot take place as the images are homographically incorrect. The images are being reflected onto the camera chip via mirrors which act independently to each other and thus cause projective (homography) transformations having 8 degrees of freedom. The transformations will be carried out on the Mie image using the LIF image as a reference. The 8 degrees of freedom are translation, rotation, shear and scaling across both the i and j axis of the image.

A 2D point (x; y) in an image can be represented as a 3D vector x = (x1; x2; x3) where $x = \frac{x_1}{x_2}$ and $y = \frac{x_2}{x_3}$. This is called the homogeneous representation of a point and it lies on the projective plane P^2. A homography is an invertible mapping of points and lines on the projective plane P^2. Hartley and Zisserman [193] provide the specific definition that a homography is an invertible mapping from P^2 to itself such that three points lie on the same line if and only if their mapped points are also collinear. They also give an algebraic

definition by proving the following theorem: A mapping from $P^2 \rightarrow P^2$ is a projectivity if and only if there exists a non-singular 3x3 matrix H such that for any point in P^2 represented by vector x it is true that its mapped point equals Hx. This tells us that in order to calculate the homography that maps each x_i to its corresponding x_i' it is sufficient to calculate the 3x3 homography matrix, H. It should be noted that H can be changed by multiplying by an arbitrary non-zero constant without altering the projective transformation. Thus H is considered a homogeneous matrix and only has 8 degrees of freedom even though it contains 9 elements. This means there are 8 unknowns that need to be solved for. Typically, homographies are estimated between images by finding feature correspondences in those images. The most commonly used algorithms make use of point feature correspondences. Since the work is being carried out in homogeneous coordinates, the relationship between two corresponding points x and x´ can be re-written as: $x' = Hx$ where:

$$x' = \begin{pmatrix} x_1' \\ x_2' \\ x_3' \end{pmatrix}, H = \begin{bmatrix} h_{11} & h_{12} & h_{13} \\ h_{21} & h_{22} & h_{23} \\ h_{31} & h_{32} & 1 \end{bmatrix}, x = \begin{pmatrix} x_1 \\ x_2 \\ 1 \end{pmatrix}$$

In H, h_{11}-h_{32} represents the 8 degrees of freedom and this matrix has to be solved to be able to map two images. Evangelidis and Psarakis [194,195] have developed an enhanced correlation coefficient ECC algorithm to map between coordinate systems of two or more images. The references define their code which is freely available on their website and on the mathworks file exchange [196,197]. It is a gradient based image registration algorithm which achieves high accuracy in parameter estimation. Its performance is invariant to global illumination changes since it considers the correlation coefficient as an objective function. The algorithm uses gradient based iterative optimization techniques for optimum estimation of the parameters. The parametric image alignment problem consists of finding a transformation

which aligns two image profiles. In order to match image transformations of the projective/ homographic nature, the algorithm produces with an appropriate performance measure which when optimized will yield optimum parameter estimation using gradient based non-linear optimization techniques. It applies a Gaussian filter to the images to compensate for photometric distortions in contrast and brightness. Further information on the algorithm can be found in the references provided.

The only change made to the algorithm is an addition of an iteration check that if achieved would end the iteration and continue to the next one. In the original algorithm the amount of iterations had to be specified, however for aligning the enormous dataset acquired here would create either too little or too many iterations. Thus a check was employed to find the difference in all 8 parameters at the current and previous iteration and if the difference divided by the value at the previous iteration approached to 10^{-6}, the iteration would be stopped and the next image sets loaded.

The programme allowed a template image and the image to be transformed to be input and it would then compute the transformation of the input image with respect to the template. It would then output the transformed image with its corresponding H matrix of transform linking it to the template image. The LIF sequence of images LIF_{ij}^{klm} was used as the template image with its corresponding time step Mie image Mie_{ij}^{klm} as input to be transformed to $MieHOM_{ij}^{klm}$.

The algorithm was then input into a wider programme written in matlab. The programme was a colloquial one to allow storage of important parameters. The programme also carried out a double image ratio of the LIF image over the corresponding time resolved Mie image in

double precision to calculate the Sauter mean diameter distribution and stored in the same format for later use.

$$LSD_{ij}^{klm} = \frac{LIF_{ij}^{klm}}{MieHOM_{ij}^{klm}}$$

Equation 7.7

The LSD image was later loaded up and converted into false colour in the Sauter mean diameter range of 0 – 1.5 pixel intensity of the LSD image which was converted to Black – Blue – Cyan - Green – Yellow – Orange – Red – Magenta – White; equally from 0 – 1.5, where 0 starts is black and 1.5 is white.

LIF scattering intensity depends on the fluorophore which in turn will have different fluorescent yields depending in the solution it is in. Thus the LIF images have to be calibrated with this yield factor in different solutions. From the Rhodamine B in solution calibration results obtained previously, the calibrations of the Rhodamine B in decanol and Rhodamine B in octanol were carried out and the transmission intensity with respect to laser power obtained. The calibration was carried out for diesel – RhB – decanol mixtures and kerosene like light diesel-RhB- octanol mixture. Using the diesel-RhB-Decanol (Fuel A-decanol-RhB mixture) reading as reference, the Fuel D-octanol-RhB was divided by 1.04.

$$LSD_{ij}^{kl\ FUELD} = \frac{\frac{LIF_{ij}^{kl\ FUELD}}{1.04}}{MieHOM_{ij}^{kl\ FUELD}}$$

Equation 7.8

As Fuel B was a mixture of diesel-RhB-decanol, and thus no calibration would be required. The calibration would enable a comparison between fuels with respect to their fluorescence

yields using the fluorescence yield of Rhodamine B in decanol as a reference. Thus the Sauter mean distributions plotted in false colour and any other post processing past this calibration is comparable between the fuels.

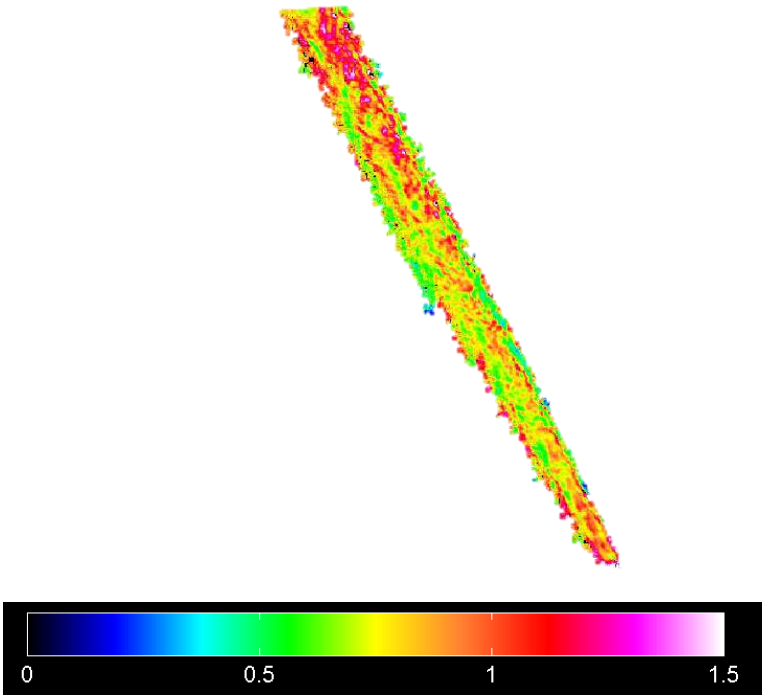

Figure 7.26 A false colour image in the range of 0- 1.5 pixel intensity at 4.1 ms after needle lift began for Fuel A.

Before the conversion into false colour, the real image which had multiple scattering effects had to be eliminated along the edges of the spray. This was done by applying a Gaussian edge detection which finds edges by looking for zero crossings after filtering the image with a Gaussian filter. After applying the Gaussian edge detection to define the spray boundary, the LSD_{ij}^{klm} image is reproduced in false color as defined above and seen in Figure 7.26.

Intensity frequency histograms of the LSD_{ij}^{klm} images produced with 100 SMD bins between 0.015 and 1.5 for each injection frame over a complete set of injections i.e. 1, 101, 201, 301……9901, frames 2, 102, 202, 302, … 9902, frames 3, 103, 203, 303, … 9903, and so on up to frames 100, 200, 300, … 10000, for all fuels; to produce probability density histograms over a time resolved analysis. The frequency of occurrence of the SMD bin would be carried

out in each time resolved frame for all the injections. The histograms were produced for 100 injections for fuels A and B, and 65 injections for Fuel D as seen in Figure 7.27 which shows the probability density histogram of 4.0 ms time after needle lift began for 100 injections combined. The histograms were plotted between 1.5 ms after needle lift to 5.9 ms after needle lift. Figure 7.27 shows the probability density distribution at 4.1 ms for 100 injections. These histograms contain spray image intensity data compiled at the time set over the total number of injections.

Lastly a time resolved mean was obtained for LSD_{ij}^{klm} images for a set of 100 injections by finding the mean images associated with frames 1, 101, 201, 301……9901, frames 2, 102, 202, 302, … 9902, frames 3, 103, 203, 303, … 9903, and so on up to frames 100, 200, 300, … 10000, for all fuels. This is expressed mathematically by

$$\overline{LSD_{ij}^{km}} = \frac{1}{100}\sum_{l=1}^{100} LSD_{ij}^{klm}$$

Equation 7.9

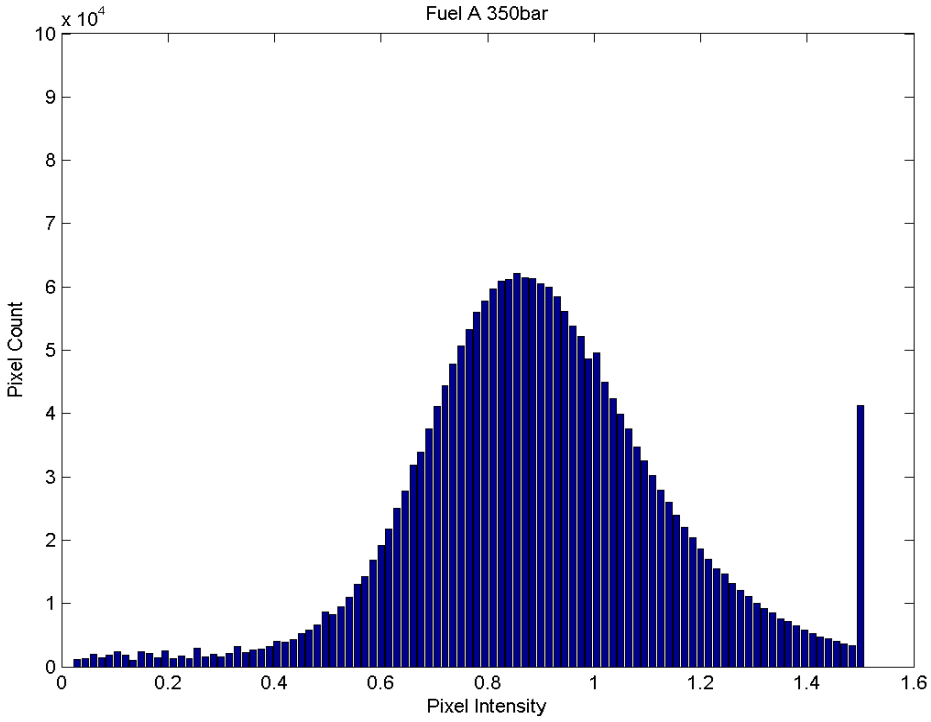

Figure 7.27 Intensity frequency histogram showing pixel frequency in SMD bins of 0.015 counts from 0.015-1.5 at time 4.1ms for 100 injections

7.2.1 External spray Sauter mean diameter distribution

The results obtained above of the dropsizing distribution, time resolved histograms and time resolved mean dropsizing images produced will be analysed herewith. In order to make a comparison between fuels, the dropsizing images were reproduced in false colour. For the purpose of this work, only images obtained in the regions of maximum needle lift between 3.9 - 4.5 ms are analysed of the full spray. The results at high lift will produce a good comparison for the spray characteristics between the different fuels. As there were hundreds of injections captured, it will be a good place to begin the analysis with time resolved mean images between times 3.9 - 4.5 ms over the 100 injection for fuels A and B and 65 injections for Fuel D.

The time resolved mean images between 3.9 ms and 4.5 ms at maximum needle lift show differences in the spray dropsizing as observed in Figure 7.28. The colour bar here represents the relative Sauter mean diameter through the LIF-Mie ratio. The images seen do not show any spray structure as seen in the single time event images (Figure 7.26), however they give an overview of the drop sizing distribution throughout the time event over the number of injections carried out for comparison between the fuels.

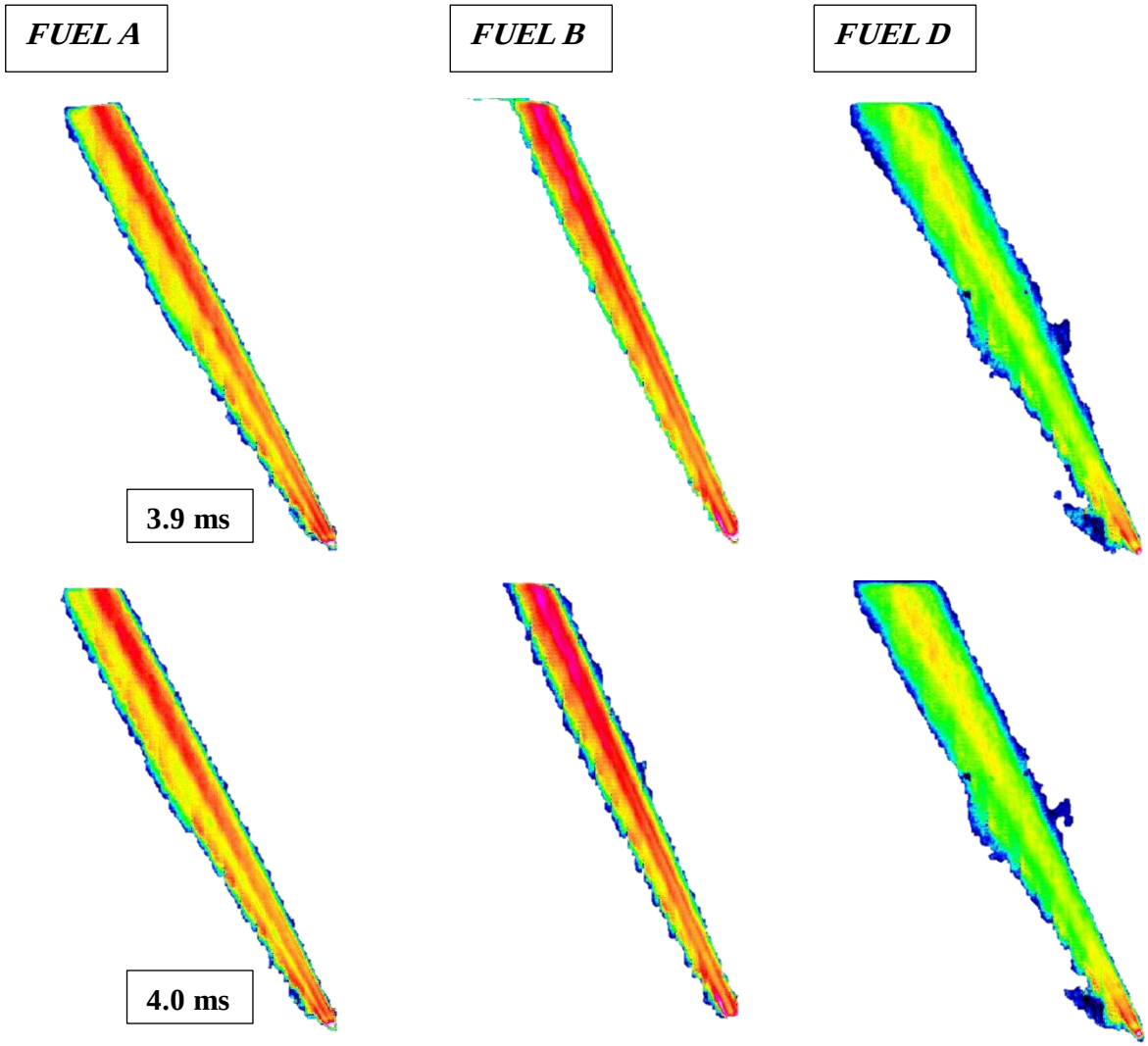

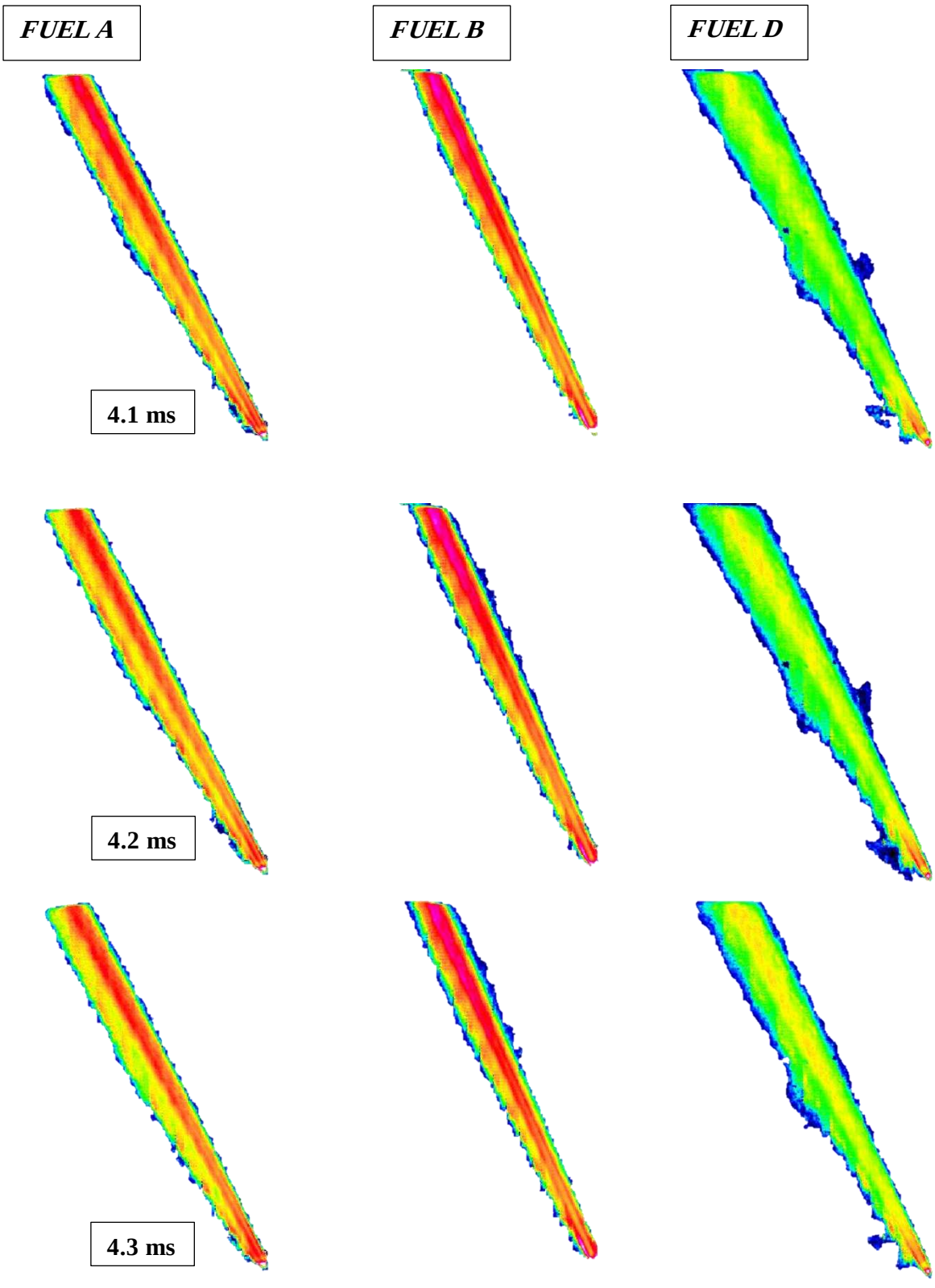
FUEL A
FUEL B
FUEL D
4.1 ms
4.2 ms
4.3 ms

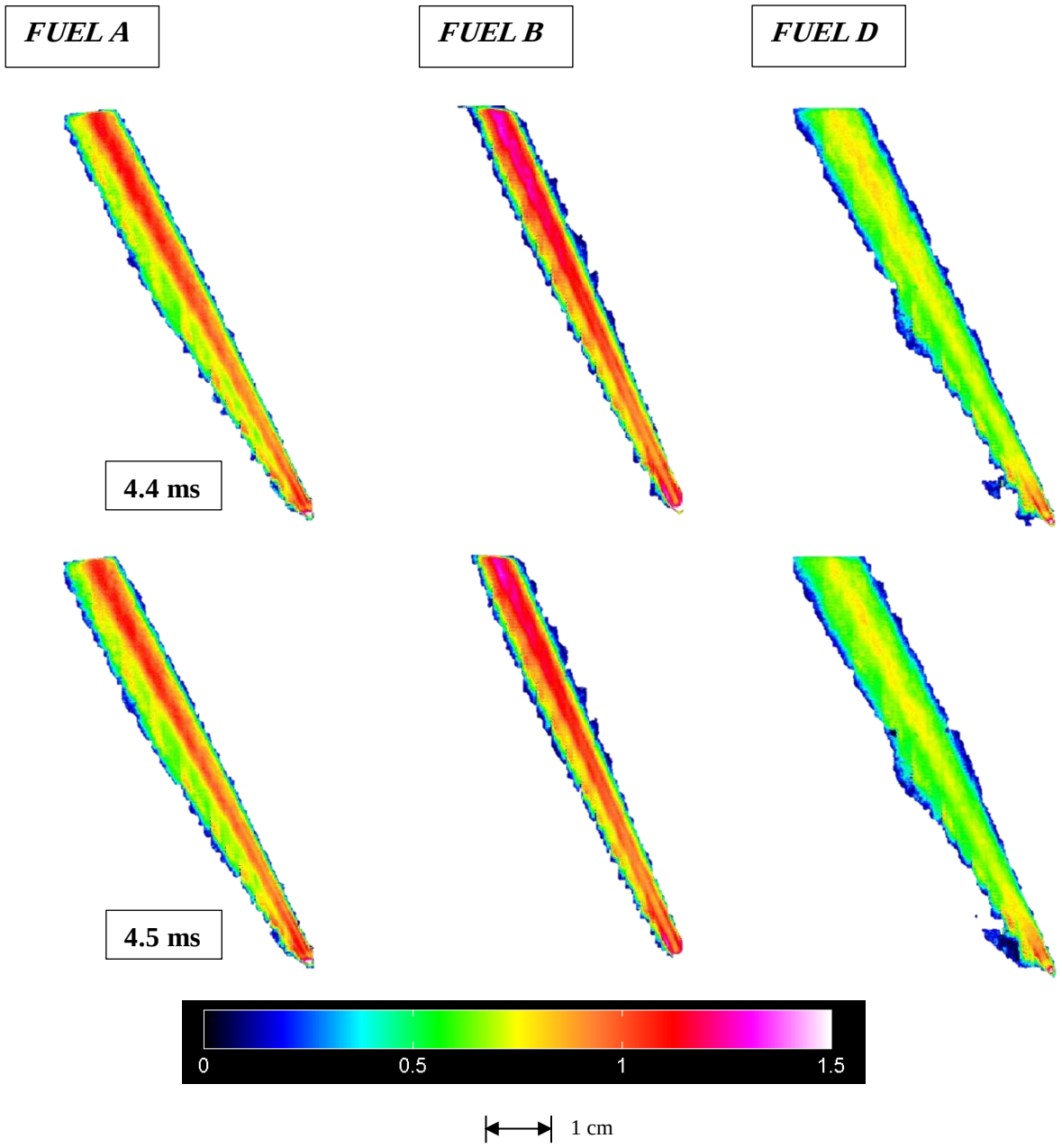

Figure 7.28 Time resolved mean images of time 3.9 - 4.5 ms (in rows) after injection trigger showing Fuels A, B and D in columns 1, 2 and 3 respectively. False colour range 0 – 1.5 as shown at the end of image [Image scale 1cm =2.69mm]

Fuel A displays a more consistent drop size distribution as observed from images in Figure 7.28. The drop size distribution ranges from approximately 1 count in the core spray region and decreasing towards finer drop sizes towards the spray boundary. Sprays for fuel B on the other hand contain a much larger drop size distribution in the spray core in the region of 1 -1.5 counts and finer- much smaller drop sizes in the spray boundary region. The sprays for Fuel D

consist of even finer drop size distributions in the spray core in the range of 0.5 - 1 counts and finer spray boundaries.

The spray jet images observed are non-symmetrical about their centres. This is consistent for all fuels. The asymmetry of the jet occurs as a result of the geometric cavitation occurring inside the nozzle holes causing instabilities in the spray. Geometric cavitation occurs due to the sharp edges at nozzle hole entry and develops into the nozzle hole. The geometric cavitation leads to the formation of turbulence and instabilities in the nozzle hole which travel outwards on to the external spray. Sheet cavitation resulting from the upper edge of the hole creates a spatial asymmetry. Further on, this gives to the rise in an asymmetric spray structure. This phenomenon in combination with the vortex flow occurring in the nozzle holes [84,86] flowing outward into the spray results in an asymmetric spray formation.

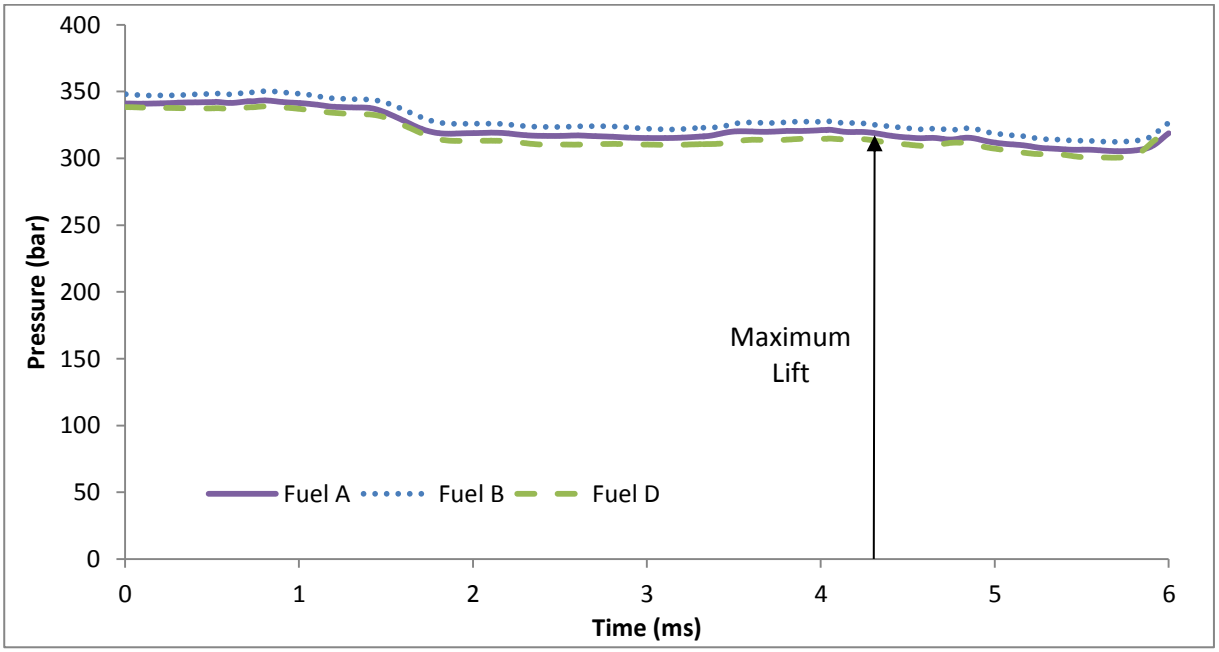

Figure 7.29 Injection pressure profile of Fuel A, B and D from injection trigger to 6.0ms covering the injection duration

Figure 7.29 shows the time resolved mean injection pressure averaged over the total number of injections per time event comparison pinpointing the point of maximum needle lift. The

pressure variation is of 12 bar between the fuels B and D. The time resolved mean pressure was calculated by averaging the pressure at each time point over the total number of injections. Injection pressures observed were consistent for all fuels and thus the results obtained would be independent of the injection pressure variation between the fuels.

The histograms of the corresponding time resolved mean drop size images are in Figure 7.30 - Figure 7.32. The histograms quantify the distributions seen in Figure 7.28 with respect to the frequency of the dropsizing over the injection events per frame captured. The distributions shown in these figures have been obtained from the whole of the spray image captured. The x axis labelled pixel intensity is the SMD whereas the y axis is the count of this SMD from the whole of the spray region.

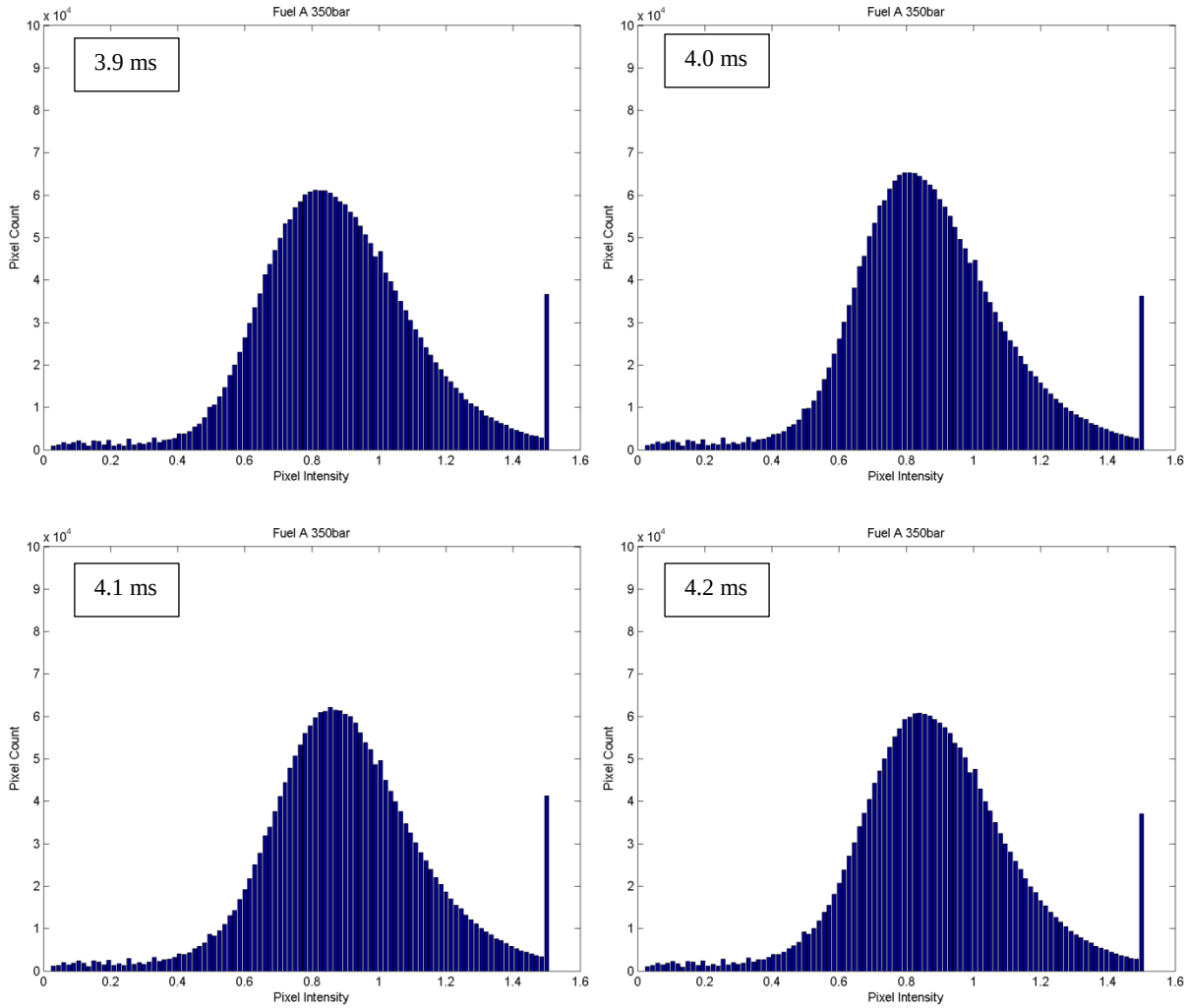

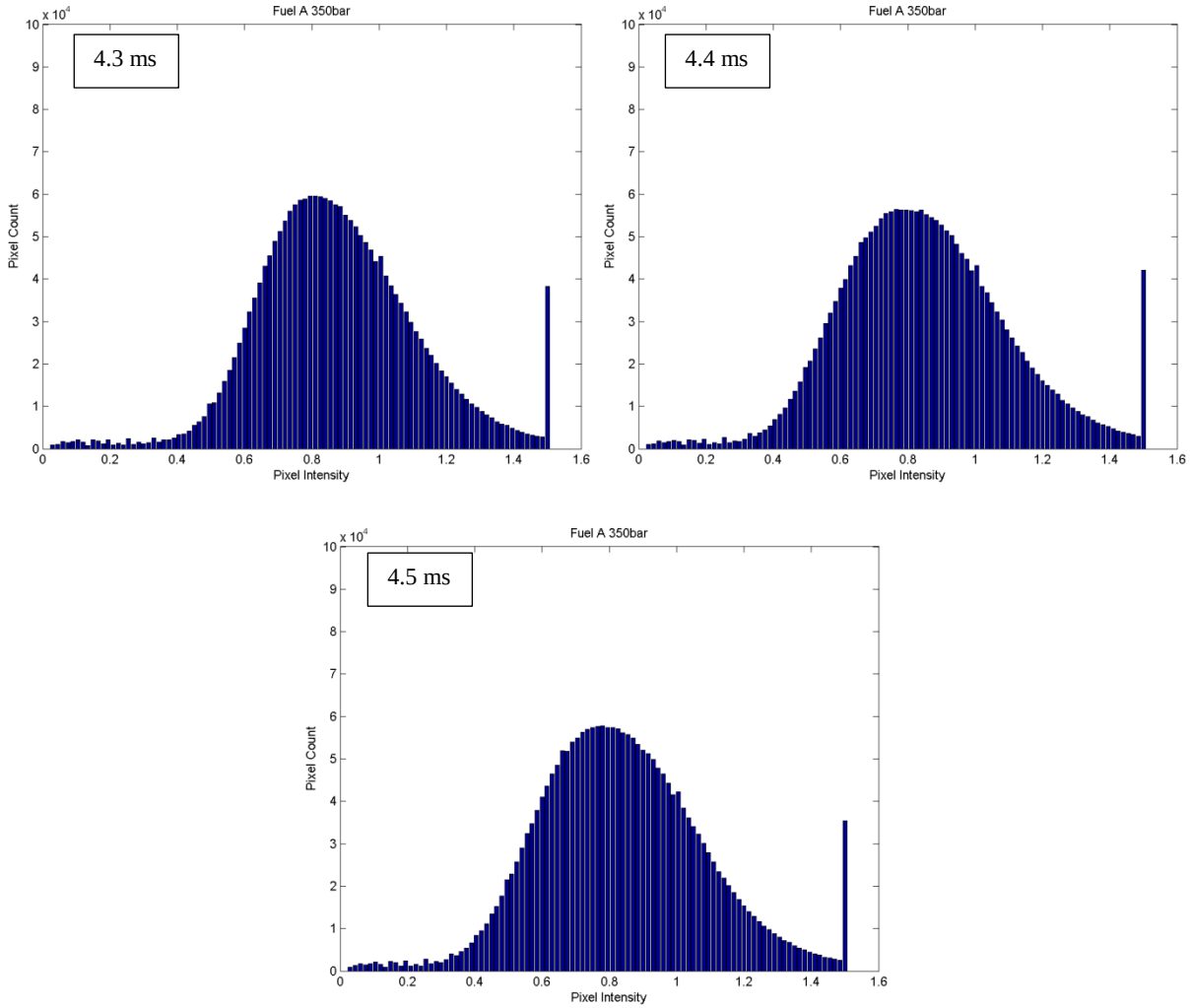

Figure 7.30 Intensity frequency histograms for 3.9 - 4.5ms (left to right) over 100 injections for fuel A showing the distribution of drop sizes against drop size frequency

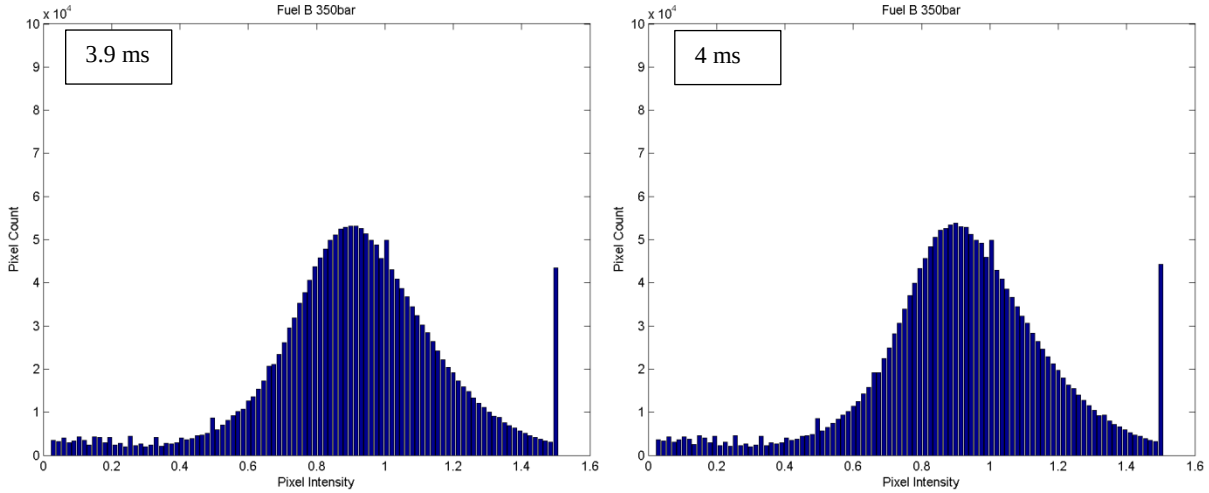

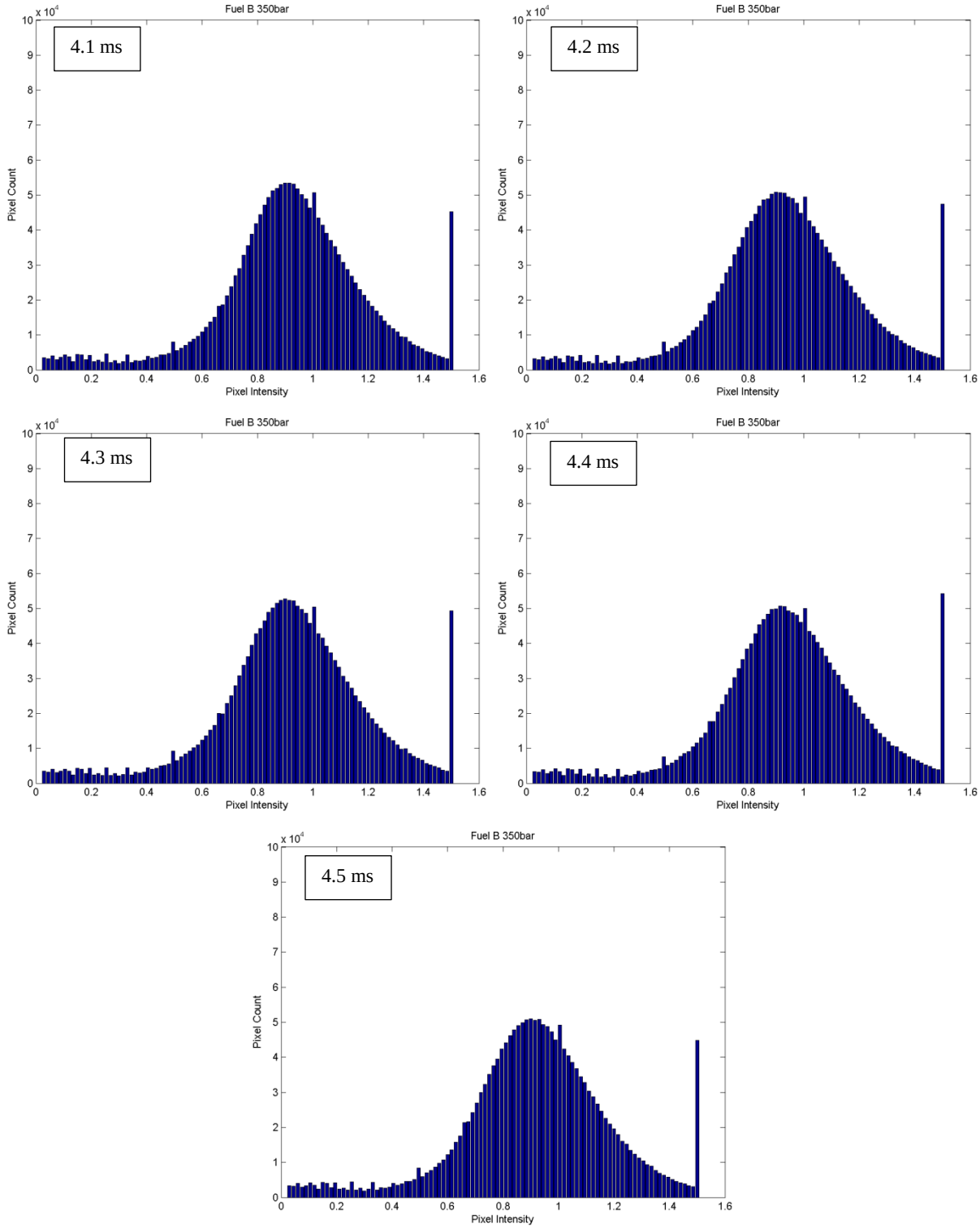

Figure 7.31 Intensity frequency histograms for 3.9 - 4.5ms (left to right) over 100 injections for fuel B showing the distribution of drop sizes against drop size frequency

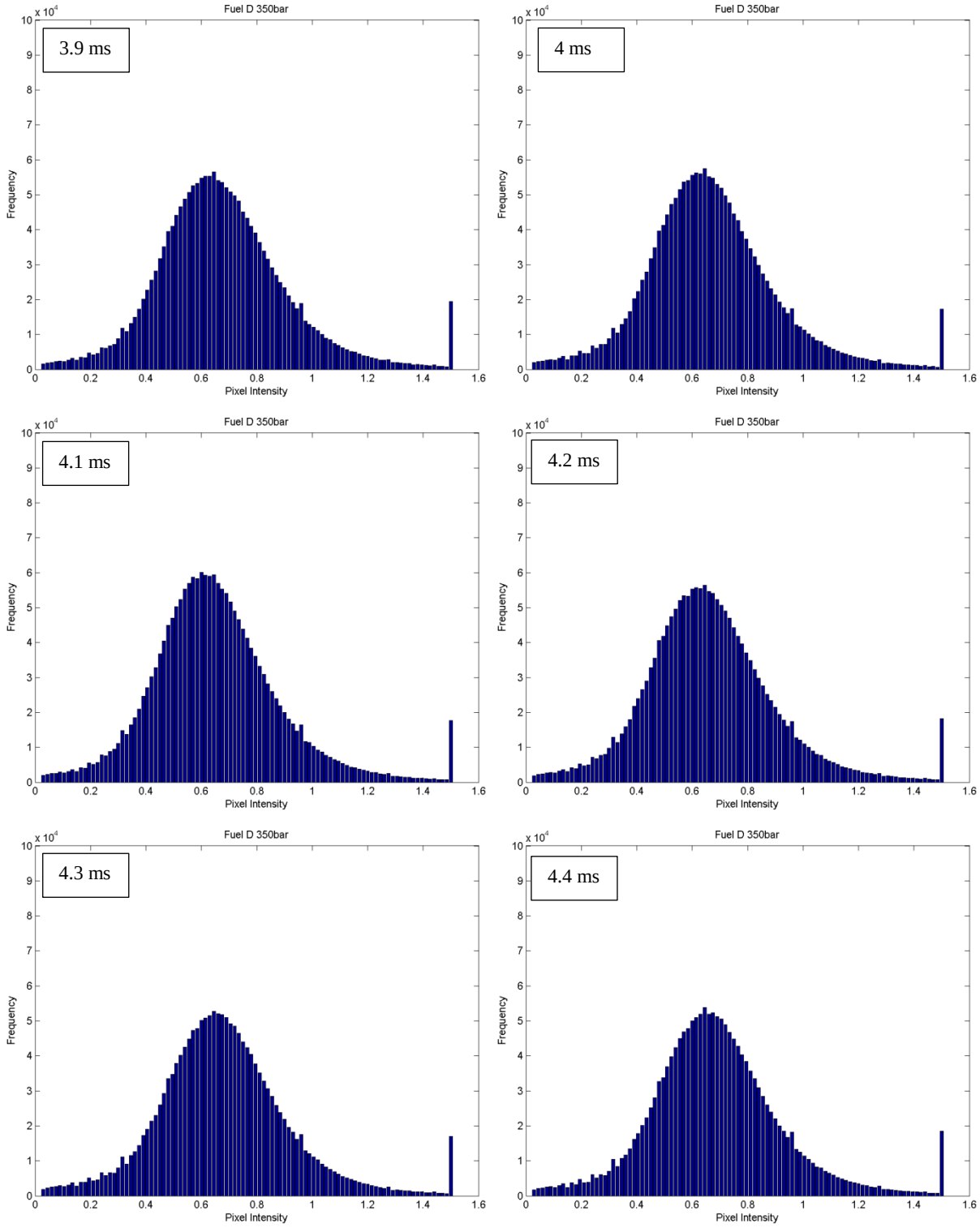
Fuel D 350bar
3.9 ms
4 ms
4.1 ms
4.2 ms
4.3 ms
4.4 ms
Frequency
Pixel Intensity
x 10^4

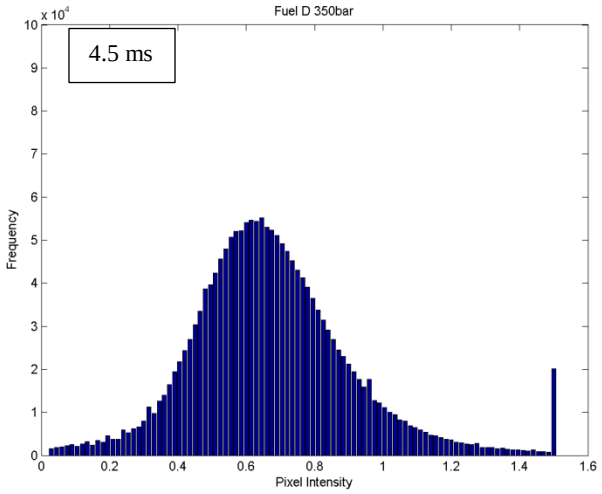

Figure 7.32 Intensity frequency histograms for 3.9 - 4.5ms (left to right) over 100 injections for fuel D showing the distribution of drop sizes against drop size frequency

The histograms in Figure 7.30 - Figure 7.32 agree with the above statements. Histograms for Fuel A show a normal distribution with the maximum frequency (mode) of SMD at approximately 0.85 counts at 4.1 ms after injection pulse (Figure 7.30). The frequency of the much higher SMD (between 1 - 1.5) is larger than the very SMD (between 0 - 0.5) observed at the tails of the distribution. This is consistent with the fuel distillation profiles discussed in the earlier chapter were Fuel A had a more linear distillation profile ranging from 170 – 340 ºC.

Histograms from Fuel B show a mode occurring at larger Sauter mean diameters of approximately 1 count. Fuel B had a gap distillation profile with smaller distillation components between 160 – 205 ºC (0 – 20 % distillation recovery), a mid-point at 240 ºC (50% distillation recovery) and then larger distillation components between 300-350 ºC (60-100% distillation recovery). In comparison to Fuel A it has lower distillation components and thus has the frequency of the small drop sizes has increased in comparison. The time resolved mean sprays for the fuel show very large regions of high intensity in the core region and then finer particles in the spray boundary. The spray size distribution is not as evenly distributed as

observed in the Fuel A sprays. The time resolved sprays of Fuel A show a spray core with high intensity which gradually decreases to the spray boundaries. The difference occurring may be due to there being a gap in the Fuel B distillation and thus the spray images show this step from a large drop size spray core to much finer boundary edge, whereas the images of Fuel A which has a near linear distillation profile shows gradual changes in drop size from the spray core to the boundary.

Fuel D histograms in Figure 7.32 show much lower Sauter mean drop size distribution as compared to the other two fuels A and B. From the histograms it shows a SMD mode occurring at around 0.65 counts at 4.3 ms after needle lift. The histograms also show a very low frequency of large SMDs between 1 -1.5. The highest frequency of drop sizes is between 0.4 and 1. The fuel also has a more linear distillation profile and thus the time resolved spray images similarly to those of Fuel A show a gradual change in drop sizes from the spray core to the spray boundary. However the spray core in Fuel D is much finer (lower SMD) than Fuel A.

The distributions show how the full width of half maximum (FWHM) of the fuels vary and this is observed well in Figure 7.33. The FWHM of the fuel distribution is very similar; however the location of the SMD mode is changing. The mode occurs at lower SMD intensities for the lighter fuel and at higher SMD intensities for the heavier fuels. The difference occurring between fuels A and B can be further supported as a result. This evidence adds to the observations that there is a gradual change in intensity distribution from the spray core to the boundary, which are shown in the distribution. However for a similar FWHM, fuel B has shift to higher spray drop sizes.

From the above results, histograms and time resolved images between 3.9 - 5ms after the start of injection, it can be concluded that fuels with lower distillation profile curves demonstrate smaller spray drop size distribution and thus smaller drop sizes, whereas fuel with higher distillation profiles curves have shown large drop sizes distributions in the spray and thus overall larger drop sizes. The mean time resolved images clearly distinguish between drop sizes and distillation profiles where larger distillation profile fuels (heavier fuels) had a larger drop size distribution in the spray core and a less large drop size distribution along the spray boundary.

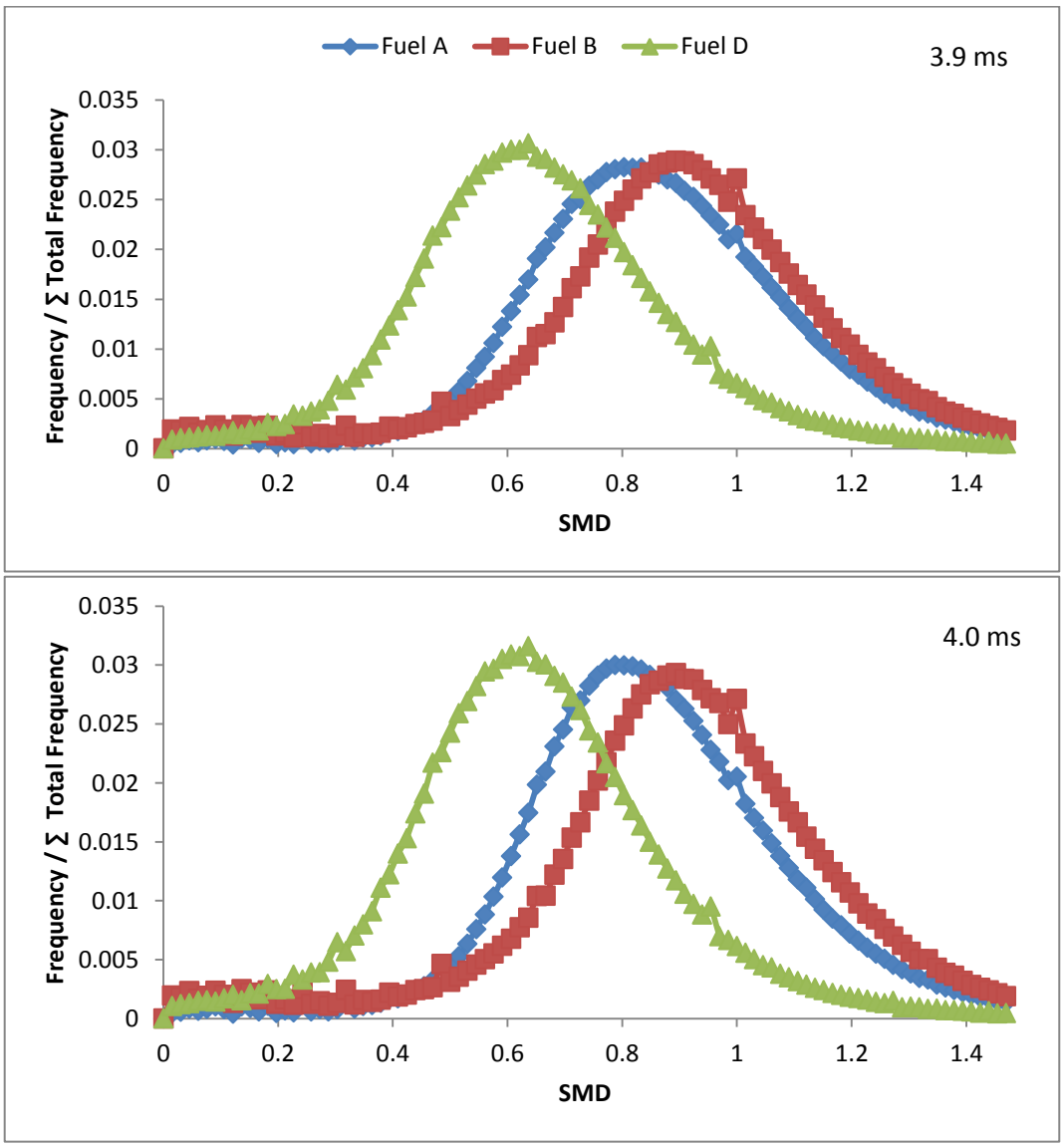

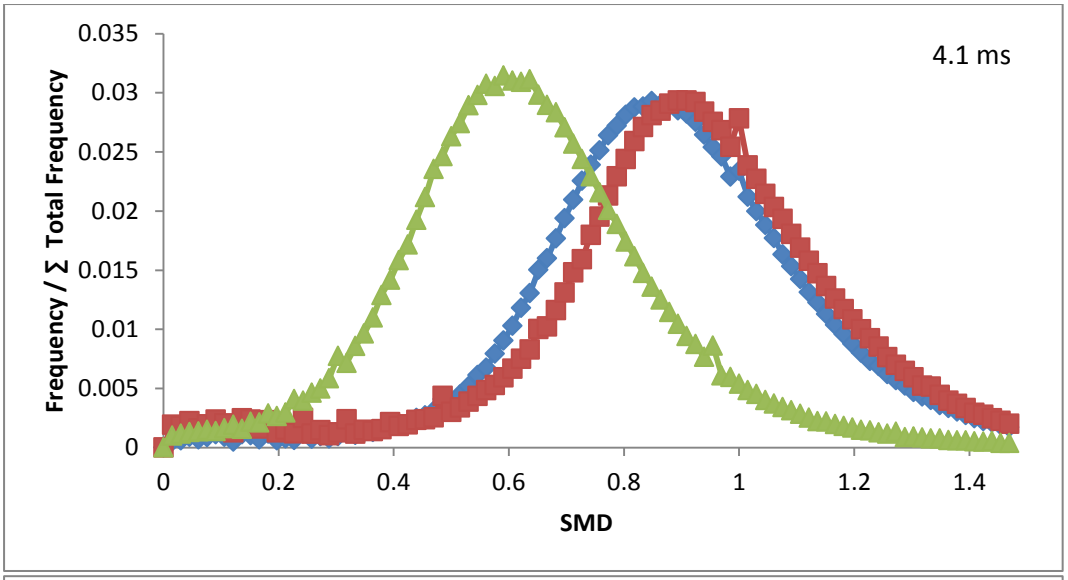
4.1 ms
Frequency / ∑ Total Frequency
0.035
0.03
0.025
0.02
0.015
0.01
0.005
0
0
0.2
0.4
0.6
0.8
1
1.2
1.4
SMD

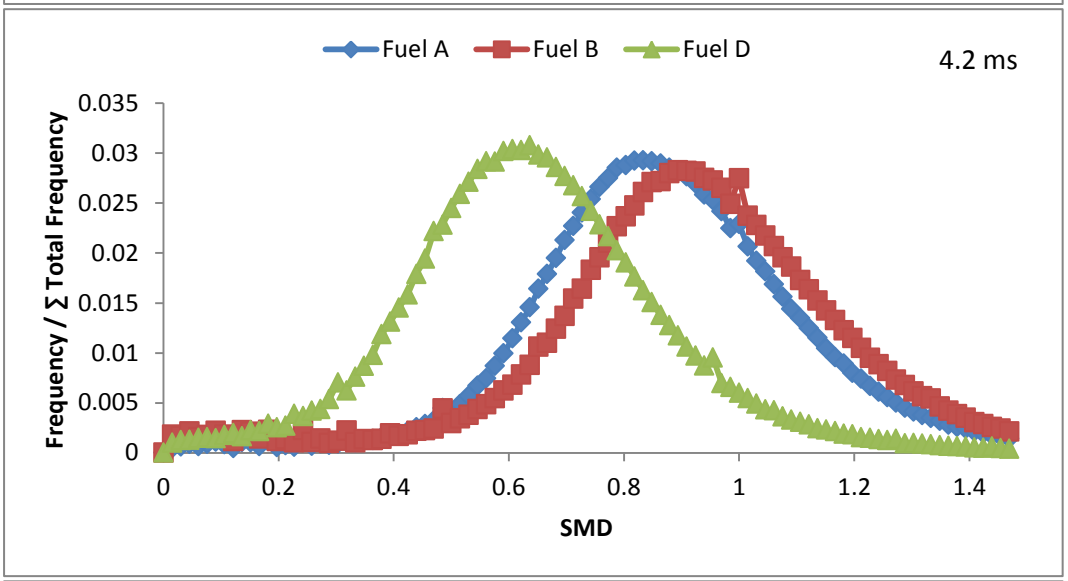
Fuel A
Fuel B
Fuel D
4.2 ms
Frequency / ∑ Total Frequency
0.035
0.03
0.025
0.02
0.015
0.01
0.005
0
0
0.2
0.4
0.6
0.8
1
1.2
1.4
SMD

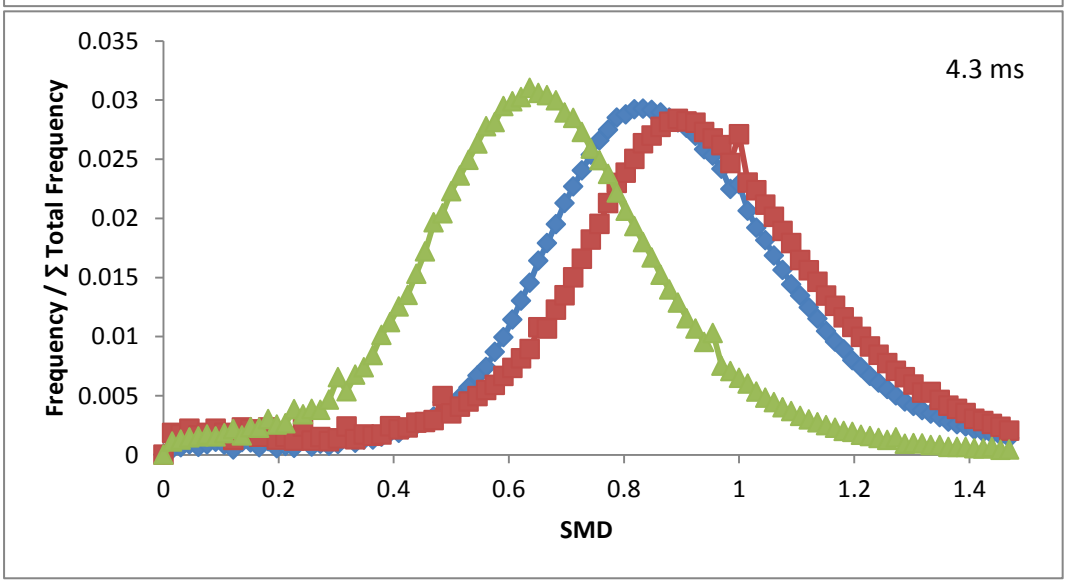
4.3 ms
Frequency / ∑ Total Frequency
0.035
0.03
0.025
0.02
0.015
0.01
0.005
0
0
0.2
0.4
0.6
0.8
1
1.2
1.4
SMD

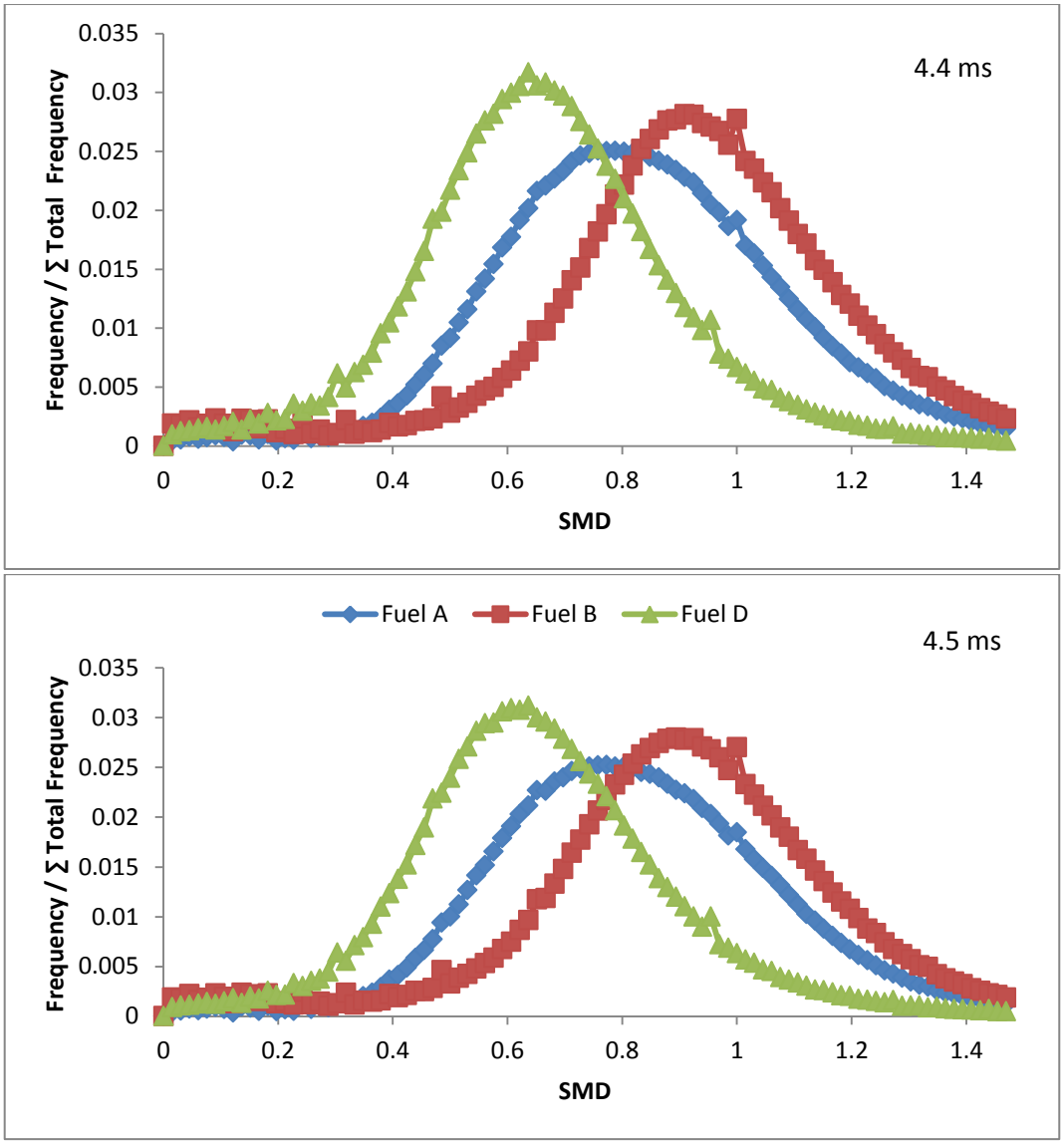

Figure 7.33 Comparisons of distributions of time resolved intensity frequency relative to the sum intensity frequency over the SMD between 0-1.4 for each fuel against pixel intensity count for fuel A, B and D over 3.9 - 4.5ms at peak lift (top to bottom).

The distributions in Figure 7.33 show the comparisons of the drop size distributions of the fuels. The distributions plots earlier have been compiled into one plot showing the maximum frequency profile per SMD intensity of the fuel distributions. It can be observed that the fuels have distinguishable drop size distributions. Figure 7.34 shows the fuel relative mean and standard deviation across the fuels samples at each SMD intensity bin in the time step over the peak lift. The difference in the fuels drop size distributions is clearly identifiable. Fuel D lies on the lower SMD size range throughout. Fuel B shows the largest drop size distributions

owing to its higher maximum distillation point, and Fuel A lies in the middle. There are some occurrences where the profiles of Fuel A and Fuel B show similar spray size distributions

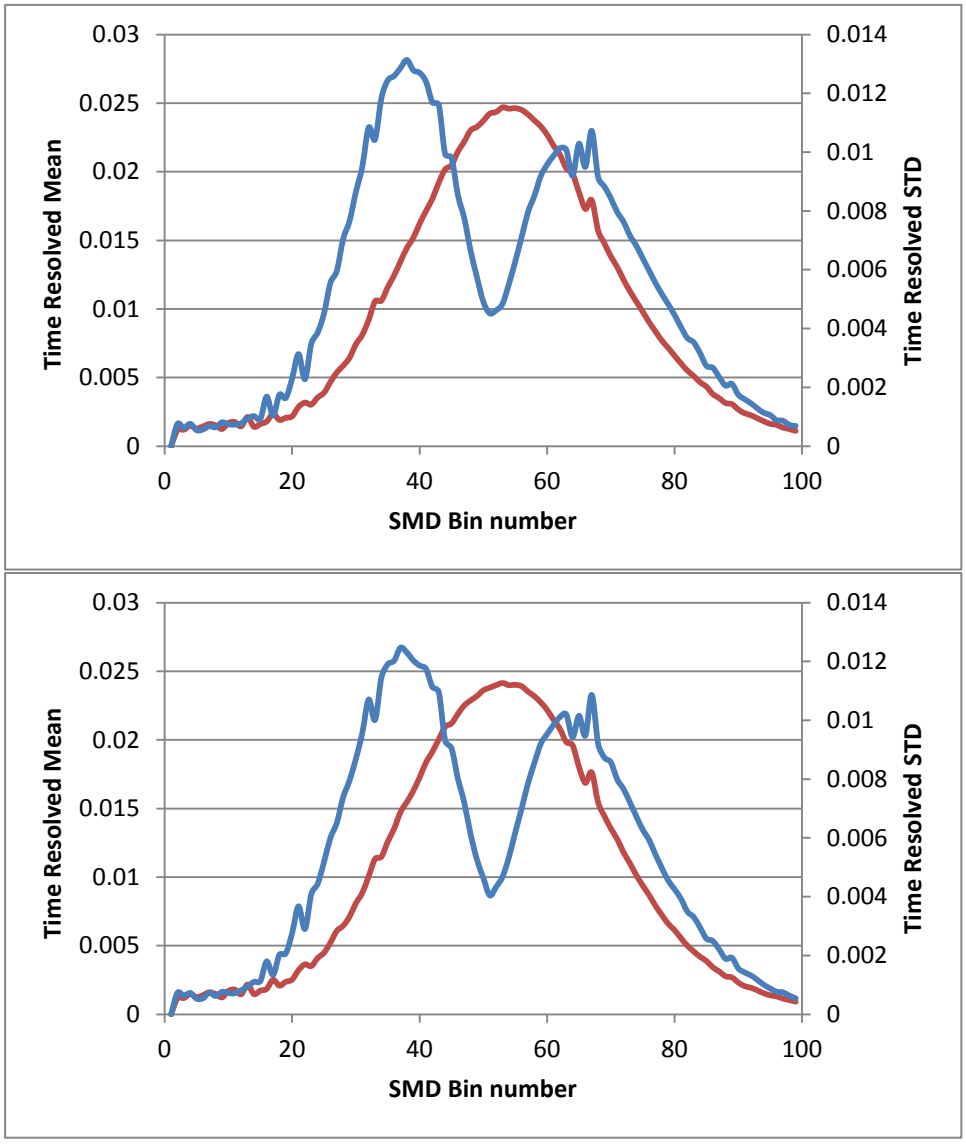

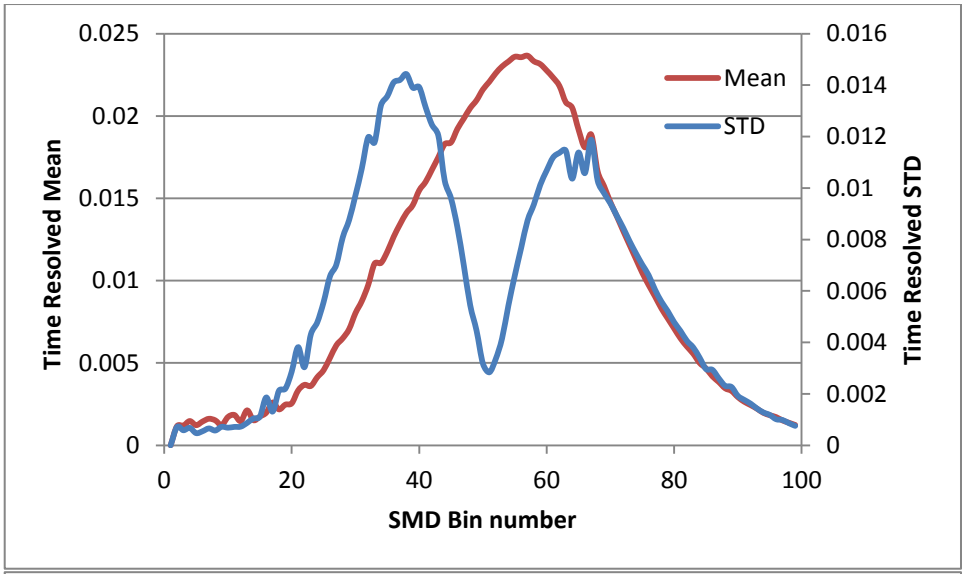
Mean
STD
Time Resolved Mean
Time Resolved STD
SMD Bin number
0.025
0.02
0.015
0.01
0.005
0
0.016
0.014
0.012
0.01
0.008
0.006
0.004
0.002
0
0
20
40
60
80
100

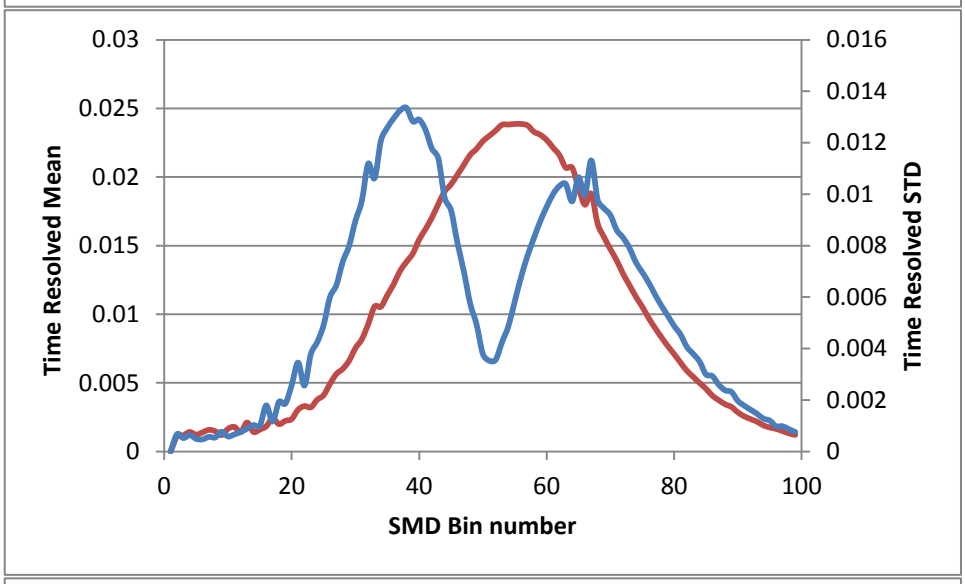
Time Resolved Mean
Time Resolved STD
SMD Bin number
0.03
0.025
0.02
0.015
0.01
0.005
0
0.016
0.014
0.012
0.01
0.008
0.006
0.004
0.002
0
0
20
40
60
80
100

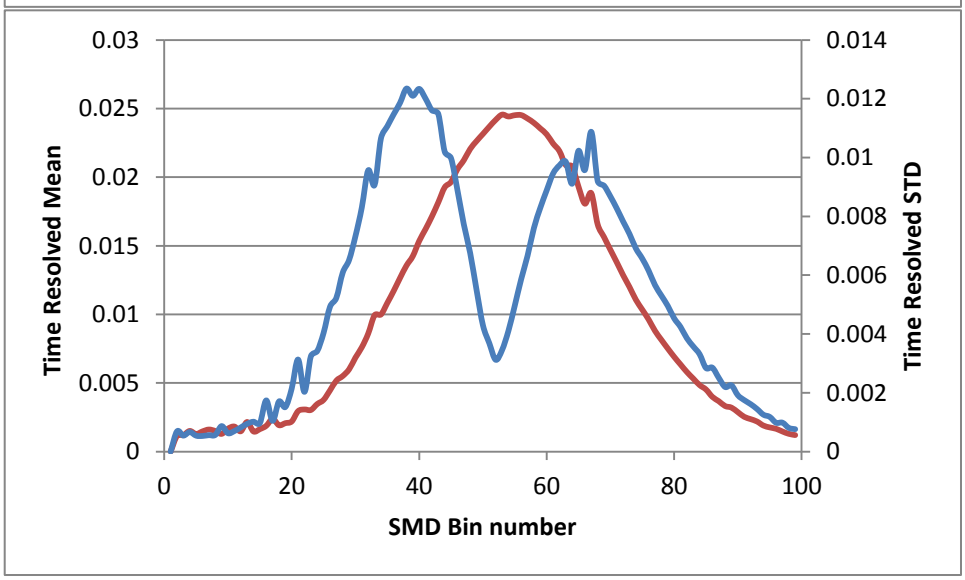
Time Resolved Mean
Time Resolved STD
SMD Bin number
0.03
0.025
0.02
0.015
0.01
0.005
0
0.014
0.012
0.01
0.008
0.006
0.004
0.002
0
0
20
40
60
80
100

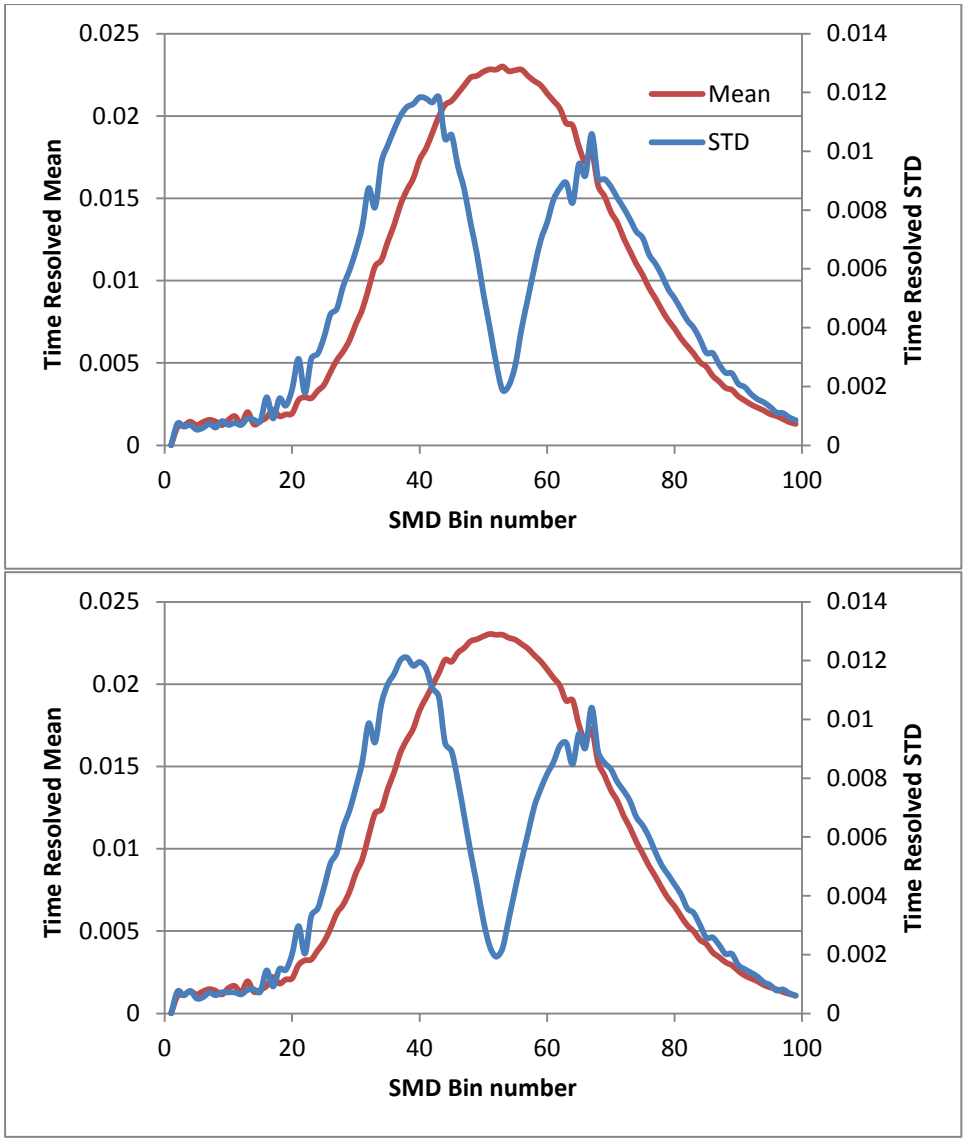

Figure 7.34 Mean and standard deviation comparisons of fuels from charts in Figure 7.33 between 3.9 - 4.5ms at peak needle lift over 100 SMD Bins (top to bottom).

The time resolved intensity frequency distributions in Figure 7.33 show a comparison of the distributions of the fuels relative to the overall frequency count per image. The charts show that fuels A and B are quite similar up to needle return from maximum lift. Both these fuels are significantly different to fuel D which has lower peak intensity as compared to fuels A and B over the peak needle lift analysis. Fuels A and B have peaks occurring at higher SMD intensities. Fuel D has a peak at a lower SMD distribution than fuels A and B. Fuel B has a slightly larger SMD distribution than fuel A. Thus the lighter fuels result in lower SMD distributions and heavier fuels have displayed larger SMD distributions.

Frame	Time (ms)	Maximum Standard Deviation between fuels
43	3.8	0.0125
44	3.9	0.0124
45	4	0.0131
46	4.1	0.0144
47	4.2	0.0134
48	4.3	0.0123
49	4.4	0.0118
50	4.5	0.0121

Table 7.7 Maximum standard deviation values obtained at maximum needle lift of fuels A, B and D

Figure 7.34 is just for comparison to the nozzle manufacturing consistency results. The results showed a standard deviation of 0.0035 over peak lift whereas the distribution seen in Figure 7.34 show standard deviations as shown in Table 7.7 which is significantly larger. The sudden drop observed in these graphs occurs as a result of the fuel drop size matching the fuels average profile, however this occurs at varying frequencies.

Lower distillation profile fuels (lighter fuels) have shown smaller drop sizes distributions in the spray core and even smaller drop size distributions at the spray boundary. The result is not because of the difference injection pressure of max. 12 bar lower than the other fuels tests, as an increase in injector pressure would result in an increase in atomisation efficiency [115,120] and thus smaller drop size distributions.

The results here have been distinguished by their distillation profiles, however their viscosities also vary similarly, i.e. the heavier fuels (Fuel B) have a higher viscosity, the medium fuel (Fuel A) has a medium viscosity in comparison and the light fuel (Fuel C) has the lowest viscosity as in Table 6.1. As liquid viscosity increases, flow rate is generally reduced and the development of instabilities in the liquid core is hindered. As a result, the disintegration process is delayed and a spray with a narrow spray angle and large droplets is

produced. Liquid viscosity is highly dependent on the temperature and decreases generally with increasing temperature [108]. Lower viscosity fuels produce smaller droplet diameters than fuels with higher viscosity [120]. Thus in this situation of non-evaporating spray conditions, it cannot be determined without further analysis whether the changes in SMD distributions are as a result of the change in distillation profile of the fuels or as a result of viscosity differences. There has been insufficient time at this stage to analyse the internal nozzle cavitation images. The hypothesis will require relating the spray to the internal nozzle hole cavitation to deduce the cause of the changes in SMD. Preliminary visual observations of the images showing cavitation occurring in the nozzle holes for the fuels shows differences however this yet has not been quantified and will form part of further publications. The sprays are also in non-evaporating conditions (injecting into atmospheric pressure) and thus the spray atomisation is most likely cavitation induced. If this is the case and the cavitation structures in the nozzle holes can be identified to be deferring between the fuels then it may form a strong case that the effects observed in the Sauter mean diameter distributions of the spray are as a result of the differences in distillation profile of the fuels.

Chapter 8 Conclusions and Further Work

This body of work examined here has been achieved by using two novel diesel injection rigs that have been developed at City University London for the novel experimental investigations of the effects of cavitation on fuels by using optical techniques. The following sections summarise the key conclusions and findings

8.1 Effects of Sustained Hydrodynamic Cavitating Flow

A novel recirculation, continuous cavitating flow rig was designed and manufactured in order to test the effect of high pressure cavitating flow on the chemical stability of diesel fuels. The novelty lies in the design of the rig to examine fuels under long term cavitating flow conditions to test their robustness. To date, this is the only type of rig built for the purpose of investigating the effects of sustained cavitating flows for diesel fuels. The change in composition and/or stability of the fuel was determined through the continuous measurement of the spectral attenuation coefficients of the cavitated diesel samples at 405 nm as a function of the cavitation time. A commercial tea urn was modified in order to immerse diesel samples in heated water, in order to mimic the temperature history of the diesel samples in the cavitating flow rig. This was carried out in order to differentiate the effect of temperature from the effect of cavitation on the diesel samples.

Commercial diesel samples were tested in the cavitating flow rig and immersion in the water bath. Two model fuels were also tested as above. The commercial diesels consisted of fresh samples that were subjected to cavitating flow testing within three months of purchase, and

aged samples that were stored in a fuel store for twelve to fifteen months, and then subjected to cavitating flow testing and water bath immersion. The model diesel tested comprised of a paraffinic blend and a 20% FAME paraffinic fuel.

The fresh commercial diesel samples were observed to undergo a continuous increase in spectral attenuation coefficients during cavitating flow, leading to 8 % to 25 % increase in spectral attenuation over forty hours. The aged commercial diesel samples were observed to undergo an even greater increase in spectral extinction during the cavitation period, leading to a 14 % to 50 % increase in spectral attenuation coefficient after forty hours cavitation. These results show that the fuels are undergoing chemical breakdown which is causing their attenuation to increase.

The paraffinic model diesel produced almost no variation in spectral attenuation coefficient, and hence almost no variation in spectral absorption and scattering during and after the forty hour cavitation period. This suggests that any variation that occurred in the composition of the model diesel sample during cavitation had a negligible effect on the spectral attenuation coefficient of the model diesel sample. The model diesel containing FAME produced a decrease in spectral attenuation coefficient, which suggests that the FAME content of the fuels does also not result in an increase in spectral attenuation coefficient. However the presence of FAME affects the overall change in spectral attenuation coefficient.

A comparison of the composition of the paraffin-rich model diesel, together with the absence of variation in spectral attenuation during cavitation, with the composition of the commercial diesels and the consistent increase in the spectral extinction coefficients of these samples during cavitation, leads to the conclusion that the cavitation affected the aromatics in the

commercial diesels. It is likely that the aromatics were undergoing pyrolysis-like reactions during cavitation to form complex polycyclic aromatic hydrocarbons (PAHs), and even small particles in suspension. This hypothesis would explain the relative increase in the spectral extinction produced by the aged diesel samples when compared with that produced by the fresh commercial diesel samples, in terms of the reduced chemical stability of the aged samples when compared with the fresh samples.

The GC x GC results show a mixture of changes in the paraffinic content of the fuels, where some fuels show an increase in paraffin content. This is described by the chemical modelling in Appendix B and could be the effect of aromatics and FAME in the fuels breaking down to form paraffins. The chemical modelling carried out in the Appendix has also shown a possible pathway leading from paraffins to aromatics and soot formation without any initial presence of aromatics. This agrees with the GC results that aromatics are leading to the formation of soot particles.

The key result from this experiment is the large increase in particles/soot as a result of long hours of cavitating flow on the fuels. A similar change has not been observed in the heat test analysis, leading to the conclusion that the effect of cavitation on the fuels is leading to a formation in particulates. The key component of the fuel identified in the formation of particulates is the presence of aromatics, however even during its absence, at higher pressures and temperatures, paraffins have the propensity to from particulates and soot.

In relation to engine cycles discussed in Chapter 1, a lot of high pressure fuel is recirculated and constantly cavitates on release to lower pressure at the exits of orifices at the high- low pressure interfaces in the system. The high-low pressure systems release high pressures from

the pumps, common rails and injectors into low pressure sides via valves. During this release past the valves the fuel on return is constantly cavitating. The observations made here, that the impacts of sustained cavitation on diesel fuels is leading them to pyrolysis like reactions forming particulates opens areas for further development of these fuels by fuel manufacturers to either improve the stability of the fuels by varying fuel components or by developing further additives to prevent the degradation into particulates as a result of sustained cavitation.

The work here has described the effects on the fuels by the constant recirculation under cavitating conditions. This could also be identified as a cause for the appearance of deposits on the fuel filters. There is also a possibility of prior air dissolved in the fuel (if any) to come out of solution in the form of bubbles, due to a very sudden decrease in pressure in the sac volume, at the end of injection. The combination of high temperature surfaces and gases and the presence of an air-fuel mixture for durations depending on the engine speed form the ideal points for reactions to occur.

Pyrolysis modelling of a model fuel bubble collapse approximating polytropic conditions ranging from atmospheric conditions to temperatures and pressure of 2000 K and 1.37 GPa respectively has shown the pathways to the formation of particulates and soot molecules from both aromatics presence in the fuels and paraffins presence. This has been presented in the appendix section as it as a very qualitative approach and a non-validated kinetic model. The objective of this study was to show how imposing likely pressure and temperature conditions and a creating a gaseous model of a collapsing cavitation bubble with a temperature and pressure history. The result of a high temperature and pressure history may lead to pyrolysis and particulate formation.

The reaction leading to formation of particulates from pyrolysis is the formation of the phenyl group C6H5 and methane via the hydrogen subtraction reaction of benzene and methyl radicals. Phenyl would then react with benzyl (C7H7) radicals formed as a break up of ethyl benzene to form benzyl benzene (C13H12). Mono-aromatic benzene would react with methyl radicals formed during paraffin break up to form toluene. It would also break down to form C4H5 and acetylene which at higher residence time saw the reverse process dominate and more benzene produced. The phenyl radical reacts with acenaphthylene to form small particulates. Furthermore reactions in di-aromatic naphthalene with methyl radicals form 1- and 2-naphthylacetylene which was another precursor onto the formation of small particulates. It would react with biphenyl, acenaphthylene, pyrene, phenanthrene already present in the diesel model for kinetics to form these particles. Methyl-naphthalene and biphenyl have been identified as soot precursors. Reaction of primary particles with phenyl leads to the formation of larger particulate classes. Reactions between phenyl and biphenyl would also lead to the formation of particulates. Naphthylacetylene species start forming at 5 µs and continue till the end of analysis by the reaction. The evidence to particulate formation in diesel fuels as a result of cavitating flow conditions over a sustained period have been observed by the decrease in laser attenuation of fuels undergoing cavitating flow conditions and the particle count results of these fuels. Particles in the laser path would lead to attenuation of laser light as measured. Seen here is a summary of the possible routes to the formation of particulates from aromatics and even paraffins at higher residence times, pressures and temperatures. The kinetic model is not validated and thus this is just a qualitative hypothesis of the possible routes.

Various soot precursors have been identified in the pyrolysis of diesel fuel as a result of sustained high pressure cavitation. These soot precursors react with mono and di-aromatics to

form particulates. The particulates formed later increase in size due to coagulation of particles. Paraffinic fuels could also result in the formation of particulates however they would have to form aromatics first which was a slightly longer process and would only occur at higher residence times. The move towards higher injection pressures in diesel FIE means that these residence times will easily be achieved as a result of the higher injection pressures which will further increase the local temperatures and pressure occurring at bubble collapse.

8.2 Sac Vortex Flow effect and External Spray Drop Sizing

A novel high pressure, common rail injection rig was manufacture at City University London which could adopt a modified injector body. The novelty of the experiment lies in the optical setup to simultaneously capture internal flow cavitation and external spray dropsizing at 10 kHz. The design of the injector-nozzle compression using the double acting hydraulic arm with a balance and the spray extraction system was novel too. The modified injector body had its sac end cut-off and replicated in acrylic for optical access into the nozzle holes and sac. The elastic light scattering technique was used to observe the cavitation phenomena in the nozzle holes from one side. On the other side a novel laser sheet drop sizing setup enabled the capture of LIF and MIE images of the external near nozzle spray on two halves of a single camera. A dual camera system was utilised which was synchronised with the laser and injection timings. One camera captured the internal nozzle cavitation whereas the other captured the LIF-Mie images of the external spray. During initial setup, key features were discovered occurring in the sac volume and thus the imaging was setup to capture a side view of two nozzle holes and the sac through the injection period and 8.5 ms post injection to be able to observe these phenomena.

Three different fuels were analysed at 350 bar injection pressure, 4.0ms injection duration. Synchronised images of the internal nozzle flow cavitation and the corresponding external spray were obtained. However for the purpose of this thesis, only the bubble formation in the sac and a very brief analyse of the laser sheer dropsizing distribution of the fuels has been reported. The remainder will be published in due course.

8.2.1 Sac vorticity effects on bubble movement in the nozzle holes

During the final stages of injector needle return, needle cavitation occurred which resulted in the formation of bubbles in the sac volume and possibly in the nozzle holes. Due to the initial momentum and vortex structure of the flow, this was maintained once the needle had sealed and the bubbles were observed to move with high initial angular momentum which slowly resided. The effect of this vorticity in the sac volume was that it created regions of high and low pressure in the vicinity of the hole entries and this resulted in suction and extraction of bubbles observed in the nozzle holes. Initially the pressures would be high enough to suddenly change the momentum of an out flowing bubble and draw it inwards to the sac. With the observations of bubble motions into the sac volume, there is a possibility of external gases entering as well. In engine conditions this would be hot combustion exhaust gases at high temperature entering the nozzle holes and possibly into the sac volume. Reactions of the bubbles at the high temperature with the added exhaust gas mixture may lead to the formation of particulates in the nozzle holes and sac volume. In addition the bubbles may have degassed air inside them and may not be purely fuel vapour. Air may have dissolved within the fuel in the fuel filters and fuel tanks where conditions arise as a result of pressure differences and high temperature fuel returning into the tank. The air comes out of solution during the sudden decrease in pressure at needle return to form bubbles inside the sac volume. These bubbles

form a highly reactive air, fuel vapour mixture in the presence of hot surfaces which may lead to the formation of deposits on the nozzle surfaces and sac volume. This may also lead all the way inside the injector volume as deposits have been observed on the needle surface itself.

8.2.2 External spray drop sizing

The three fuels analysed had different distillation profiles. LIF-MIE images obtained were homographically aligned by software and checked for validation by matching structures on the matched images. False colour images were produced of time resolved LIF over MIE ratioed images showing the spray SMD distributions. Probability distributions were then plot to show the ranges in SMD drop size for the fuels with different distillation profiles between 0-1.5 SMD intensity. In conclusion, the fuel D with the lower distillation ranges showed lower spray Sauter mean diameter distributions in comparison to the heavy/higher distillation point fuels A and B. Fuels A and B which both had higher distillation profiles also differed in their SMD distributions observed of the sprays. The probability distribution at high needle lift showed large differences in SMD distributions of the fuel sprays relative to their distillation profiles.

The effects of viscosity differences in the fuels on the spray SMD distribution have thus far not been investigated as they are beyond the scope of the thesis and will form part of further publications. It is thought that the atomisation occurring is cavitation induced, due to the spray ejecting into non-evaporative conditions. Thus further clues of the cause the differences in the SMD lies in the images captured of the cavitation occurring inside the nozzle holes.

The work here has shown different pathways onto deposit formation as a result of cavitation occurring in the fuels using various optical techniques to characterise cavitation and deposit formation resulting from cavitation. It has also shown the spray Sauter mean diameter distributions of fuels will different viscosities and distillation curves. The distinction on whether the resulting Sauter mean distributions are as a result viscosity or distillation profiles will form part of future publications post analysis of the internal nozzle cavitation images.

8.3 Further Work

The work reported here, the sustained cavitating flow analysis has been conducted at medium pressure of 550 bar. A higher pressure evaluation is required for further analysis of fuels under sustained cavitation in order to match current FIE injection pressures. The effects of higher pressure on paraffinic fuels is of interest as long term cavitating flow conditions at 550 bar did not show any effects on the laser attenuation through the fuel. It is also of interest on the GC analysis of the paraffinic fuels post sustained cavitating flow conditions. This would confirm the changes occurring in the paraffinic fuels and whether they react to form particulates as a result of sustained cavitation.

The temperature effects on the laser attenuation were observed in 4.1.1. The analysis was very brief; however a more detailed time resolved temperature profile relation to the temperature at measurement point is of interest. If the results are comparable to those seen here, the laser attenuation measurement setup could be used effectively as a thermometer once calibrated for a specific liquid.

In order to confirm the routes to the formation of particles in diesel fuels undergoing cavitating flow conditions, a validated kinetic model containing a range of species is required. Once obtained, this will also allow a comparable quantitative analysis where the laser attenuation could be worked back to from the results of the kinetic modelling. A comprehensive GC x GC analysis with the full set of results would provide a comprehensive analysis of the breakdown of the species. The results obtained here were summarised to class and the results were provided as images as in Figure 4.32 obtained without any detailed information. If the full comprehensive information was available it would be possible to observe the detailed changes in hydrocarbon species and also possibly calibrate a kinetic model.

It has been observed here that long term cavitating flow conditions are leading to the formation of soot particles in suspension, however it is unknown how these fuels will perform under combusting conditions. It is also not known how these cavitated fuels containing particles will defer to the non cavitated fuels in the characterisation of the internal nozzle flow and external spray dropsizing. It would have been ideal to test the cavitated fuels in the LSD experiment and how the external spray dropsizing would have deferred to that of the original non-cavitated version of the fuels. That is, test FuelX in the LSD rig, then put a fresh sample of fuel X in the sustained cavitation rig and after 40 hours place this fuel in the LSD rig. It was not possible here due to sponsor obligations. It has been shown here that the fuels may change composition chemically and physically; however it is of interest on how these fuels would perform when injected. The comparison would involve carrying out the analysis described in Chapter 5 to Chapter 7 with a non-cavitated fuel and then running the non-cavitated fuel in the analysis as in Chapter 3 to Chapter 4 to produce a sustained cavitating flow fuel sample and then running this fuel back to the analysis in Chapter 5 to Chapter 7. The

comparison of these two fuels would be of great interest in the quality of spray formation and internal nozzle cavitation. The particulates formed in the fuels as a result of sustained cavitating flow conditions may form additional nucleation sites for the formation of nuclei and result in cavitation occurring over a larger are of the hole thus increasing flow choking and thus resulting in lower fuel mass injected.

Further analysis of the vortex flow in the sac volume in order to correctly match its vorticity to the bubble motion in terms of speed is required for a quantitative analysis. A better characterisation of the sprays using the LIF images has to be conducted with the remaining data which will give more conclusive evidence of flow conditions observed in the sprays relative to the distillation profiles, which so far have not been reported but will be published later. It is also of interest whether these bubbles formed post injection are degassed bubbles of air in the fuel. This setup may provide the thinking here, however the results will confirm the hypothesis that if this is the case then engine conditions, in the presence of high temperatures, they may form sites for particle formation.

The results of the external spray sizing as seen in 7.2 do not distinguish clearly whether the effects are as a result of distillation profile differences of the fuels or the differences in viscosity of the fuels. Further analysis of the cavitation in the internal nozzle hole captured simultaneously to the spray and providing a link to the cause of the drop size distributions may lead to a conclusion. These results are readily available and the analysis may be carried forward and form future publications.

Blank Page

Publications

Lockett R. D., and Jeshani M., *"An Experimental Investigation into the Effect of* Hydrodynamic Cavitation on Diesel," International Journal of Engine Research 10.1177/1468087413497005, pp. 606–621, 2013.

Lockett R. D., Liverani L., Thaker D., Jeshani M., and Tait N. P., *"The characterisation of* diesel nozzle flow using high speed imaging of elastic light scattering," Fuel, vol. 106, pp. 605–616, 2013.

References

[1] Heywood J., Internal Combustion Engine Fundamentals, McGraw-Hill Science/Engineering/Math, 1988.

[2] Soteriou C., and Andrews R. J., *"Direct injection* diesel sprays and the effect of cavitation and hydraulic flip on atomization," 950080 SAE Technical Paper, 1995.

[3] Badock C., Wirth R., Fath A., and Leipertz A., *"Investigation of cavitation in real size* diesel injection nozzles," International Journal of Heat and Fluid Flow, pp. 538–544, 1999.

[4] Cook S., and Richards P., *"Possible Influence of High Injection Pressure on Diesel* Fuel Stability: A Review and Preliminary Study," SAE Technical Paper 2009-01-1878, 2009.

[5] Barker J., Richards P., Goodwin M., and Wooler J., Influence of High Injection Pressure on Diesel Fuel Stability: A Study of Resultant Deposits, SAE International, Warrendale, PA, 2009.

[6] Bosch, Diesel Fuel Injection System Common Rail, 1995.

[7] FTI meters, *"Diesel Fuel Flow Measur*ement – Avoiding Common Pitfalls"[Online]. Available: http://www.ftimeters.com/downloads/wp_diesel_fuel_flow_measurement_avoid_pitfalls.pdf.

[8] Caterpillar, *"DIESEL FUELS & DIESEL FUEL SYSTEMS*" [Online]. Available: http://www.cat.com/cda/files/3375312/7/.

[9] Lockett R. D., and Jeshani M., *"An Experimental Investigation into the Effect of* Hydrodynamic Cavitation on Diesel," International Journal of Engine Research 10.1177/1468087413497005, pp. 606–621, 2013.

[10] Tang J., Pischinger S., Lamping M., Körfer T., Tatur M., and Tomazic D., Coking Phenomena in Nozzle Orifices of Dl-Diesel Engines, SAE International, Warrendale, PA, 2009.

[11] Lepperhoff G., and Houben M., Mechanisms of Deposit Formation in Internal Combustion Engines and Heat Exchangers, SAE International, Warrendale, PA, 1993.

[12] Caprotti R., Bhatti N., and Balfour G., *"Deposit Control in Modern Diesel Fuel* Injection Systems," SAE Paper, p. 2250, 2010.

[13] Barker J., Richards P., Snape C., and Meredith W., Diesel Injector Deposits–An Issue That Has Evolved with Engine Technology, SAE Technical Paper Series, 2011-01-1923, JSAE 20119126, 2011.

[14] Ullmann J., Geduldig M., Stutzenberger H., Caprotti R., and Balfour G., *"Effects of* Fuel Impurities and Additive Interactions on the Formation of Internal Diesel Injector Deposits," 7th International Colloquium Fuels, pp. 377–388, 2009.

[15] Ullmann J., Geduldig M., Stutzenberger H., Caprotti R., and Balfour G., Investigation into the Formation and Prevention of Internal Diesel Injector Deposits, SAE International, Warrendale, PA, 2008.

[16] Caprotti R., Breakspear A., Graupner O., Klaua T., and Kohnen O., Diesel Injector Deposits Potential in Future Fueling Systems, SAE International, Warrendale, PA, 2006.

[17] Pehan S., Jerman M. S., Kegl M., and Kegl B., *"Biodiesel influence on tribology* characteristics of a diesel engine," Fuel, pp. 970–979, 2009.

[18] Abu-Jrai A., Rodríguez-Fernández J., Tsolakis A., Megaritis A., Theinnoi K., Cracknell R. F., and Clark R. H., *"Performance, combustion and* emissions of a diesel engine operated with reformed EGR. Comparison of diesel and GTL fuelling," Fuel, pp. 1031–1041, 2009.

[19] Arifin Y. M., Furuhata T., Saito M., and Arai M., *"Diesel and bio*-diesel fuel deposits on a hot surface," Fuel, pp. 1601–1609, 2008.

[20] Arifin Y. M., and Arai M., *"The effect of hot surface temperature on diesel fuel deposit* formation," Fuel, pp. 934–942, 2010.

[21] Barker J., Richards P., Snape C., and Meredith W., *"A Novel Technique for* Investigating the Nature and Origins of Deposits Formed in High Pressure Fuel Injection Equipment," SAE International Journal of Fuels and Lubricants, pp. 38–44, 2010.

[22] Payri F., Bermudez V., Payri R., and Salvador F. J., *"The influence of cavitation on the* internal flow and the spray characteristics in diesel injection nozzles," Fuel, pp. 419–431, 2004.

[23] Andriotis A., Gavaises M., and Arcoumanis C., *"Vortex flow and cavitation in diesel* injector nozzles," Journal of Fluid Mechanics, pp. 195–215, 2008.

[24] Badock C., Wirth R., and Tropea C., *"The influence of hydro grinding on cavitation* inside a diesel injection nozzle and primary break-up under unsteady pressure conditions," Proc. 15th ILASS-Europe, pp. 5–7, 1999.

[25] Asi O., *"Failure of a diesel engine injector nozzle by cavita*tion damage," Engineering Failure Analysis, pp. 1126–1133, 2006.

[26] Hartwig Roth, *"Experimental and Computational Investigation of Cavitation in Diesel* Injector Nozzles," 2004.

[27] Roth H., Gavaises M., and Arcoumanis C., *"Cavitation Initiation, Its D*evelopment and Link with Flow Turbulence in Diesel Injector Nozzles," 2002-01-0214 SAE Technical Paper, 2002.

[28] Lockett R. D., Liverani L., Thaker D., and Arcoumanis C., *"The characterisation of* diesel cavitating flow using time-resolved light scattering," Injection Systems for IC Engines[Online]. Available: http://openaccess.city.ac.uk/2070/. [Accessed: 12-Feb-2013], 2009.

[29] He Y., Zhao Z., Liu J., Du H., Li M., and Zong Y., *"Two*-phase flow of liquid-gas in diesel fuel injection system and their effect on engine performances," Journal of Thermal Science, pp. 223–227, 2013.

[30] Bosch, *"Diesel Systems Common Rail Systems CRSN3 with 2,000 to 2,500* bar"[Online]. Available: http://www.bosch-automotivetechnology.com/media/db_application/downloads/pdf/antrieb/en_3/DS-Datenbl_CRSN3_20_25_EN_20130212.pdf.

[31] Shinohara Y., Takeuchi K., Herrmann O. E., and Laumen H. J., *"3000 bar Common* Rail System," MTZ worldwide eMagazine, pp. 4–9, 2011.

[32] Suslick K. S., Gawienowski J. J., Schubert P. F., and Wang H. H., *"Alkane* sonochemistry," The Journal of Physical Chemistry, pp. 2299–2301, 1983.

[33] Price G. J., and McCollom M., *"The effect of high*-intensity ultrasound on diesel fuels," Ultrasonics Sonochemistry, pp. S67–S70, 1995.

[34] Price G. J., and McCollom M., *"Use of high*-intensity ultrasound as a potential test method for diesel fuel stability," Fuel, pp. 1394–1397, 1995.

[35] Pedley J. F., Hiley R. W., and Hancock R. A., *"Storage stability of petroleum*-derived diesel fuel: 3. Identification of compounds involved in sediment formation," Fuel, pp. 1124–1130, 1988.

[36] Kalitchin Z. D., Ivanov S. K., Tanielyan S. K., Boneva M. I., Georgiev P. T., Ivanov A., and Kanariev K., *"Chemical stability of diesel fuels and sediment formation therein:* 1. Evaluation of the chemical stability of diesel fuels by following the kinetics of sediment formation," Fuel, pp. 437–442, 1992.

[37] Suslick K. S., and Flannigan D. J., *"Inside a collapsing bubble: sonoluminescence and* the conditions during cavitation," Annu. Rev. Phys. Chem., pp. 659–683, 2008.

[38] Suslick K. S., and Crum L. A., *"Sonochemistry and sonoluminescence,"* Encyclopedia of Acoustics, Volume One, pp. 271–281, 1997.

[39] Richter H., and Howard J. B., *"Formation of polycyclic aromatic hydrocarbons and* their growth to soot—a review of chemical reaction pathways," Progress in Energy and Combustion Science, pp. 565–608, 2000.

[40] Jones A. R., *"Light scattering for particle characterization,"* Progress in Energy and Combustion Science, pp. 1–53, 1999.

[41] Horváth I. T., and Vetrano M. R., *"Development of the Multi Wavelength Light* Extinction Technique for the characterization of nanoparticles-Data inversion."

[42] Hoge F. E., *"Laser measurement of the spectral extinction coefficients of fluorescent,* highly absorbing liquids," Applied Optics, pp. 1725–1729, 1982.

[43] Yamamoto G., and Tanaka M., *"Determination of aerosol size distribution from* spectral attenuation measurements," Applied optics, pp. 447–453, 1969.

[44] Barker J., Richards P., Goodwin M., and Wooler J., *"Influence of High Injection* Pressure on Diesel Fuel Stability: A Study of Resultant Deposits," 2009.

[45] Birgel A., Ladommatos N., Aleiferis P., Zülch S., Milovanovic N., Lafon V., Orlovic A., Lacey P., and Richards P., *"Deposit Formation in* the Holes of Diesel Injector Nozzles: A Critical Review," SAE Technical Paper 2008-01-2383, 2008.

[46] Lubrizol, *"Internal Diesel Injector Deposits"*[Online]. Available: http://www.lubrizol.com/9040Zer0/Performance/DieselInjectorDeposits.html.

[47] Garrett T. K., Automotive fuels and fuel systems: Diesel, Pentech Press, 1994.

[48] *"http://www.dieselnet.com/tech/images/fuel/diesel/~refinery.png."*

[49] Cuvelier D. H., Evaluation of Diesel Fuel Cetane and Aromatics Effects on Emissions from Euro-3 Engines, CONCAWE, 2002.

[50] Steinbrink R., Cahill G. F., Signer M., and Smith G., *"European Programmes on* Emissions, Fuels and Engine Technologies (EPEFE) - Vehicle/Engine Technology," SAE Technical Paper 961067, 1996.

[51] Hublin M., Gadd P. G., Hall D. E., and Schindler K. P., *"European Programmes on* Emissions, Fuels and Engine Technologies (EPEFE) - Light Duty Diesel Study," SAE Technical Paper 961073, 1996.

[52] *"WORLDWIDE FUEL CHARTER Fifth edition,"* 2012.

[53] Doel R., CONCAWE, Automotive Emissions Management Group, CONCAWE, Fuels Quality and Emissions Management Group, and Special Task Force FE/STF-12, Evaluation of automotive polycyclic aromatic hydrocarbon emissions, CONCAWE, Brussels, 2005.

[54] Payri R., García J. M., Salvador F. J., and Gimeno J., *"U*sing spray momentum flux measurements to understand the influence of diesel nozzle geometry on spray characteristics," Fuel, pp. 551–561, 2005.

[55] Boudy F., and Seers P., *"Impact of physical properties of biodiesel on the injection* process in a common-rail direct injection system," Energy Conversion and Management, pp. 2905–2912, 2009.

[56] Som S., E. D., I. A., and Aggarwal S., *"Influence of Nozzle Orifice Geometry and Fuel* Properties on Flow and Cavitation Characteristics of a Diesel Injector," Fuel Injection in Automotive Engineering, K. Lejda, ed., InTech, 2012.

[57] Hoekman S. K., Broch A., Robbins C., Ceniceros E., and Natarajan M., *"Review of* biodiesel composition, properties, and specifications," Renewable and Sustainable Energy Reviews, pp. 143–169, 2012.

[58] Katherine O. Blumberg, Michael P. Walsh, and Charlotte Pera, *"low*-sulphur petrol and diesel; the key to lower vehicle emmisions," 2003.

[59] Ali Y., Hanna M. A., and Borg J. E., *"Optimization of diesel, methyl tallowate and* ethanol blend for reducing emissions from diesel engine," Bioresource Technology, pp. 237–243, 1995.

[60] Shi X., Yu Y., He H., Shuai S., Wang J., and Li R., *"Emission characteristics using* methyl soyate–ethanol–diesel fuel blends on a diesel engine," Fuel, pp. 1543–1549, 2005.

[61] Sharp C. A., Howell S. A., and Jobe J., *"The Effect of Biodiesel Fuels on Transient* Emissions from Modern Diesel Engines, Part I Regulated Emissions and Performance," SAE Technical Paper 2000-01-1967, 2000.

[62] Robert Reynolds, and et.al, *Changes in Diesel Fuel, The Service Technician's Guide to* Compression Ignition Fuel Quality., 2007.

[63] Zuleta E. C., Baena L., Rios L. A., and Calderón J. A., *"The oxidative stability of* biodiesel and its impact on the deterioration of metallic and polymeric materials: a review," Journal of the Brazilian Chemical Society, pp. 2159–2175, 2012.

[64] Westbrook S. R., Evaluation and Comparison of Test Methods to Measure the Oxidation Stability of Neat Biodiesel, United States. Department of Energy, 2005.

[65] McCormick R. L., Ratcliff M., Moens L., and Lawrence R., *"Several factors affecting* the stability of biodiesel in standard accelerated tests," Fuel Processing Technology, pp. 651–657, 2007.

[66] Terry B., McCormick R. L., and Natarajan M., *"Im*pact of Biodiesel Blends on Fuel System Component Durability," SAE Technical Paper, 2006.

[67] Lockett R. D., Liverani L., Thaker D., Jeshani M., and Tait N. P., *"The* characterisation of diesel nozzle flow using high speed imaging of elastic light scattering," Fuel, vol. 106, pp. 605–616, 2013.

[68] Joseph W. ROOS, Larry J. CUNNINGHAM X. F., *"Fuel Additives for Future Fuel* and Vehicle Technologies," Journal Of Automotive Safety And Energy, p. 107, 2010.

[69] Brennen C. E., Cavitation and bubble dynamics, Oxford University Press, 1995.

[70] Knapp R. T., Daily J. W., and Hammitt F. G., Cavitation, McGraw-Hill, 1970.

[71] Gogate P. R., Tayal R. K., and Pandit A. B., *"Cavitation: A technology on the* horizon," 2006.

[72] Lorimer J. P., and Mason T. J., *"Son*ochemistry. Part 1—The physical aspects," Chemical Society Reviews, pp. 239–274, 1987.

[73] Rayleigh, Lord, *"VIII. On the pressure developed in a liquid during the collapse of a* spherical cavity," Philosophical Magazine Series 6, pp. 94–98, 1917.

[74] Plesset M., *"The dynamics of cavitation bubbles,"* Journal of Applied Mechanics, pp. 277–282, 1949.

[75] Plesset M. S., and Prosperetti A., *"BUBBLE DYNAMICS AND CAVITATION,"* Annu. Rev. Fluid Mech., pp. 145–85, 1977.

[76] De Bosset A., Obreschkow D., Kobel P., Dorsaz N., and Farhat M., *"Direct effects of* gravity on cavitation bubble collapse," 2007.

[77] Lauterborn W., and Bolle H., *"Experimental investigations of cavitation*-bubble collapse in the neighbourhood of a solid boundary," Journal of Fluid Mechanics, pp. 391–399, 1975.

[78] Suslick K. S., Mdleleni M. M., and Ries J. T., *"Chemistry induced by hydrodynamic* cavitation," Journal of the American Chemical Society, pp. 9303–9304, 1997.

[79] Stinebring D. R., Billet M. L., Lindau J. W., and Kunz R. F., *"D*eveloped Cavitation-Cavity Dynamics," 2001.

[80] Bae C., Yu J., Kang J., Kong J., and Lee K. O., *"Effect of Nozzle Geometry on the* Common-Rail Diesel Spray," 2002.

[81] Schmidt D. P., Rutland C. J., and Corradini M. L., *"A Fully Compressible, Two-*Dimensional Model of Small, High-Speed, Cavitating Nozzles," Atomization and Sprays, 1999.

[82] Arcoumanis C., Gavaises M., Flora H., and Roth H., *"Visualisation of cavitation in* diesel engine injectors," Mécanique & Industries, pp. 375–381, 2001.

[83] M. Gavaises and C. Arcoumanis, *"Advances in cavitation research in Automotive fuel* injectors," Munich, Germany, 2009.

[84] Arcoumanis C., Gavaises M., Nouri J. M., Abdul E., and Horrocks R. W., *"Analysis of* the Flow in the Nozzle of a Vertical Multi-Hole Diesel Engine Injector," 980811 SAE Technical Paper, 1998.

[85] Afzal H., Arcoumanis C., Gavaises M., and Kampanis N., *"Internal flow in diesel* injector nozzles: modelling and experiments," IMechE Paper S, pp. 25–44, 1999.

[86] Gavaises M., Andriotis A., Papoulias D., Mitroglou N., and Theodorakakos A., *"Characterization of string cavitation in large*-scale Diesel nozzles with tapered holes," Physics of Fluids, 2009.

[87] Arcoumanis, C. & Gavaises, M., *"Cavitation in diesel injectors: modelling and* experiments.," Proc. ILASS-EUROPE, Manchester, UK, 1998.

[88] Kim J. H., Nishida K., and Hiroyasu H., *"Characteristics of the Internal Flow in a* Diesel Injection Nozzle," International Journal of Fluid Mechanics Research, 1997.

[89] Arcoumanis C., Nouri J. M., and Andrews R. J., *"Application of Refractive Index* Matching to a Diesel Nozzle Internal Flow," 1992.

[90] Arcoumanis C., Flora H., Gavaises M., Kampanis N., and Horrocks R., *"Investigation* of Cavitation in a Vertical Multi-Hole Injector," 1999-01-0524 SAE Technical Paper, 1999.

[91] SOTERIOU C., SMITH M., and ANDREWS R., *"Diesel injection : laser light sheet* illumination of the development of cavitation in orifices," pp. 137–158, 1998.

[92] Chaves H., Knapp M., Kubitzek A., Obermeier F., and Schneider T., *"Experimental* Study of Cavitation in the Nozzle Hole of Diesel Injectors Using Transparent Nozzles," 950290 SAE Technical Paper, 1995.

[93] Arcoumanis C., Flora H., Gavaises M., and Badami M., *"Cavitation in Real*-Size Multi-Hole Diesel Injector Nozzles," SAE Technical Paper 2000-01-1249, 2000.

[94] Desantes J. M., Payri R., Salvador F. J., and Gimeno J., *"Measurements of Spray* Momentum for the Study of Cavitation in Diesel Injection Nozzles," 2003-01-0703 SAE Technical Paper, 2003.

[95] Sou A., Hosokawa S., and Tomiyama A., *"Effects of cavitation in a nozzle on liquid jet* atomization," International Journal of Heat and Mass Transfer, pp. 3575–3582, 2007.

[96] Blessing M., König G., Krüger C., Michels U., and Schwarz V., *"Analysis of Flow and* Cavitation Phenomena in Diesel Injection Nozzles and Its Effects on Spray and Mixture Formation," SAE Technical Paper 2003-01-1358, 2003.

[97] Payri R., Salvador F. J., Gimeno J., and de la Morena J., *"Study of cavitation* phenomena based on a technique for visualizing bubbles in a liquid pressurized chamber," International Journal of Heat and Fluid Flow, pp. 768–777, 2009.

[98] Suslick K. S., *"The chemical effects of ultrasound,"* 1990.

[99] Suslick K. S., Ultrasound: its chemical, physical, and biological effects, VCH Publishers, 1988.

[100] Crum L. A., Mason T. J., Reisse J. L., and Suslick K. S., Sonochemistry and sonoluminescence, Springer, 1998.

[101] Suslick K. S., and Flint E. B., *"Sonoluminescence from non*-aqueous liquids," 1987.

[102] Flint E. B., and Suslick K. S., *"Sonoluminescence from nonaqueous liquids: Emission* from small molecules," Journal of the American Chemical Society, pp. 6987–6992, 1989.

[103] Wheat P. E., and Tumeo M. A., *"Ultrasound induced aqueous polycyclic aromatic* hydrocarbon reactivity," Ultrasonics Sonochemistry, pp. 55–59, 1997.

[104] Cataldo F., *"Ultrasound*-induced cracking and pyrolysis of some aromatic and naphthenic hydrocarbons," Ultrasonics Sonochemistry, pp. 35–43, 2000.

[105] Diedrich G. K., Kruus P., and Rachlis L. M., *"Cavitation*-induced Reactions in Pure Substituted Benzenes," Canadian Journal of Chemistry, pp. 1743–1750, 1972.

[106] Katoh R., Yanase E., Yokoi H., Usuba S., Kakudate Y., and Fujiwara S., *"Possible new* route for the production of C6 by ultrasound," Ultrasonics Sonochemistry, pp. 37–38, 1998.

[107] Malykh N. V., Petrov V. M., and Mal'tzev L. I., *"ULTRASONIC AND* HYDRODYNAMIC CAVITATION AND LIQUID HYDROCARBON CRACKING."

[108] Lefebvre A. H., Atomization and Sprays, Hemisphere Publishing Corporation, 1989.

[109] LEFEBVRE, A., and Ballal, D., Gas Turbine Combustion, 3rd Ed, Taylor and Francis Group, 2010.

[110] Arcoumanis C., Gavaises M., and French B., *"Effect of Fuel Injection Processes on the* Structure of Diesel Sprays," SAE Technical Paper 970799, 1997.

[111] Smallwood G. ;Gulder O. O. L., *"VIEWS ON THE STRUCTURE OF TRANSIENT* DIESEL SPRAYS," Atomization and Sprays, 2000.

[112] Soteriou C., Andrews R., Smith M., Torres N., and Sankhalpara S., *"The Flow Patterns* and Sprays of Variable Orifice Nozzle Geometries for Diesel Injection," 2000-01-0943 SAE Technical Paper, 2000.

[113] Nishida K., Ceccio S., Assanis D. N., Tamaki N., and Hiroyasu H., *"Characterization* of Cavitation Flow in a Simple Hole Nozzle," International Journal of Fluid Mechanics Research, 1997.

[114] Bergwerk W., *"Flow Pattern in Diesel Nozzle Spray Holes,"* Proceedings of the Institution of Mechanical Engineers, pp. 655–660, 1959.

[115] Fath A., Fettes C., and Leipertz A., *"Investigation of the Diesel Spray Break*-Up Close to the Nozzle at Different Injection Conditions," Fourth International Symposium on Diagnostics and Modeling of Combustion in Internal Combustion Engines, Kyoto, Japan, JSME, pp. 429–434, 1998.

[116] HIROYASU H., and ARAI M., *"Structures of fuel sprays in diesel e*ngines," SAE transactions, pp. 1050–1061, 1990.

[117] Faeth G. ., Hsiang L.-P., and Wu P.-K., *"Structure and breakup properties of sprays,"* International Journal of Multiphase Flow, pp. 99–127, 1995.

[118] Schweitzer P. H., *"Mechanism of Disintegration o*f Liquid Jets," Journal of Applied Physics, pp. 513–521, 1937.

[119] Ghurri A., Kim J.-D., Kim H. G., Jung J.-Y., and Song K.-K., *"The effect of injection* pressure and fuel viscosity on the spray characteristics of biodiesel blends injected into an atmospheric chamber," Journal of Mechanical Science and Technology, pp. 2941–2947, 2012.

[120] Jankowski A., Siemińska-Jankowska B., Sandel A., and Bocheński C., *"Investigation* of the fuel spray atomization spectrum in common-rail system for diesel engines," Journal of KONES, pp. 53–64, 2003.

[121] Kennaird D. A., Crua C., Lacoste J., Heikal M. R., Gold M. R., and Jackson N. S., *"In-*Cylinder Penetration and Break-Up of Diesel Sprays Using a Common-Rail Injection System," SAE Technical Paper 2002-01-1626, 2002.

[122] Naber J. D., and Siebers D. L., *"Effects of Gas Density and Vaporization on* Penetration and Dispersion of Diesel Sprays," SAE Technical Paper 960034, 1996.

[123] Laguitton O., Gold M. R., Kennaird D. A., Crua C., Lacoste J., and Heikal M. R., *"Spra*y development and combustion characteristics for common rail diesel injection systems," 2002.

[124] Su T. F., Farrell P. V., and Nagarajan R. T., Nozzle Effect on High Pressure Diesel Injection, Wisconsin Univ., Madison, WI (United States), 1995.

[125] Bae C., Yu J., Kang J., Kong J., Cuenca R., and Lee K. O., *"The influence of injector* parameters on diesel spray," Proc. THIESEL 2002, pp. 55–66, 2002.

[126] Park S. H., Suh H. K., and Lee C. S., *"Effect of Cavitating Flow on the Flow and Fuel* Atomization Characteristics of Biodiesel and Diesel Fuels," Energy and Fuels 2008, pp. 605–613, 2008.

[127] Bohren C. F., and Huffman D. R., Absorption and scattering of light by small particles, Wiley, 1983.

[128] Hahn D. W., *"Light scattering theory,"* Department of Mechanical and Aeorospace Engineering, University of Florida, 2006.

[129] Lee Black D., McQuay M. Q., and Bonin M. P., *"Laser*-based techniques for particle-size measurement: A review of sizing methods and their industrial applications," Progress in Energy and Combustion Science, pp. 267–306, 1996.

[130] Hulst H. C., and Hulst H. C. van de, Light scattering: by small particles, Courier Dover Publications, 1957.

[131] Luis Le Moyne, *"LIF & MIE spray characterisation.*"

[132] Edouard Berrocal, *"Multiple s*cattering of light in optical diagnostics of dense sprays and other complex turbid media," Ph.D. Thesis, Cranfield Universiyy, 2006.

[133] Domann R., and Hardalupas Y., *"Quantitative measurement of planar droplet Sauter* mean diameter in sprays using planar droplet sizing," Particle & Particle Systems Characterization, pp. 209–218, 2003.

[134] Bras N., *"Laser Induced Fluorescence,"* Laser Chemistry, pp. 405–412, 1990.

[135] Valeur B., Molecular fluorescence: principles and applications, John Wiley & Sons, 2013.

[136] Thurber M. C., and Hanson R. K., *"Simultaneous imaging of temperature and mole* fraction using acetone planar laser-induced fluorescence," Experiments in fluids, pp. 93–101, 2001.

[137] Berckmüller M., Tait N. P., Lockett R., Greenhalgh D. A., Ishii K., Urata Y., Umiyama H., and Yoshida K., *"In*-cylinder crank-angle-resolved imaging of fuel concentration in a firing spark-ignition engine using planar laser-induced fluorescence," Symposium (International) on Combustion, pp. 151–156, 1994.

[138] Lavieille P., Lemoine F., Lavergne G., Virepinte J. F., and Lebouché M., *"Temperature* measurements on droplets in monodisperse stream using laser-induced fluorescence," Experiments in Fluids, pp. 429–437, 2000.

[139] Düwel I., Schorr J., Wolfrum J., and Schulz C., *"Laser*-induced fluorescence of tracers dissolved in evaporating droplets," Applied Physics B, pp. 127–131, 2004.

[140] Le Gal P., Farrugia N., and Greenhalgh D. ., *"Laser Sheet Dropsizing* of dense sprays," Optics & Laser Technology, pp. 75–83, 1999.

[141] Jermy M. C., and Greenhalgh D. A., *"Planar dropsizing by elastic and fluorescence* scattering in sprays too dense for phase Doppler measurement," Applied Physics B, pp. 703–710, 2000.

[142] Yeh C.-N., Kosaka H., and Kamimoto T., *"Fluorescence/scattering image technique* for particle sizing in unsteady diesel spray," Transactions of the Japan Society of Mechanical Engineers, Part B, pp. 4008–4013, 1993.

[143] Yeh C.-N., Kosaka H., and Kamimoto T., *"Measurement of drop sizes in unsteady* dense sprays," Recent advances in spray combustion: Spray atomization and drop burning phenomena., pp. 297–308, 1996.

[144] Sankar S. V., Maher K. E., Robart D. M., and Bachalo W. D., *"Rapid Characterization* of Fuel Atomizers Using an Optical Patternator," Journal of Engineering for Gas Turbines and Power, pp. 409–414, 1999.

[145] Lockett R. D., Richter J., and Greenhalgh D. A., *"The characterisation of a diesel* spray using combined laser induced fluorescence and laser sheet dropsizing," Lasers and Electro-Optics Europe, 1998. 1998 CLEO/Europe. Conference on, pp. 148–148, 1998.

[146] Domann R., and Hardalupas Y., *"Evaluation of the Planar Droplet Sizing(PDS)* technique," ICLASS-2000, pp. 131–138, 2000.

[147] Domann R., and Hardalupas Y., *"Special Issue: Laser Diagnostics. Evaluation of a* Planar Droplet Sizing(PDS) Technique.," Atomization, pp. 7–17, 2000.

[148] Kristensson E., Berrocal E., Richter M., Pettersson S.-G., and Aldén M., *"High*-speed structured planar laser illumination for contrast improvement of two-phase flow images," Optics letters, pp. 2752–2754, 2008.

[149] Neil M. A. A., Juskaitis R., and Wilson T., *"Method of obtaining optical sectioning by* using structured light in a conventional microscope," Optics letters, pp. 1905–1907, 1997.

[150] Kristensson E., Berrocal E., Wellander R., Ritcher M., Alden M., and Linne M., *"Structured illumination for 3*-D Mie imaging and 2-D attenuation measurements in optically dense sprays," Proceedings of the Combustion Institute, pp. 855–861, 2011.

[151] Berrocal E., Kristensson E., Richter M., Linne M., and AldÚn M., *"Application of* structured illumination for multiple scattering suppression in planar laser imaging of dense sprays," Optics Express, pp. 17870–17881, 2008.

[152] Berrocal E., Kristensson E., Sedarsky D., Aldén M., and Linne M., *"Analysis of the* SLIPI technique for multiple scattering suppression in planar imaging of fuel sprays," Proceeding of the 11th ICLASS, Vail, USA, 2009.

[153] Kristensson E., Richter M., and Alden M., *"Nanosecond structured laser illumination* planar imaging for single-shot imaging of dense sprays," Atomization and Sprays, 2010.

[154] Berrocal A., Wellander R., and Kristensson E., *"Accounting for mulitple scattering* signal attenuation and laser extinction using structured laser illumination planar imaging," Proceedings ILASS-Europe, 2010.

[155] The Royal Society of Chemistry, *"Ultraviolet/visible spectroscopy,"* Modern Chemical Techniques[Online]. Available: http://media.rsc.org/Modern%20chemical%20techniques/MCT4%20UV%20and%20visible%20spec.pdf.

[156] *"Visible and Ultraviolet Spectroscopy*"[Online]. Available: http://www2.chemistry.msu.edu/faculty/reusch/virttxtjml/spectrpy/uv-vis/spectrum.htm.

[157] Schulz C., and Sick V., *"Tracer*-LIF diagnostics: quantitative measurement of fuel concentration, temperature and fuel/air ratio in practical combustion systems," Progress in Energy and Combustion Science, pp. 75–121, 2005.

[158] Sklar A. L., *"Theory of Color of Organic Compounds*," The Journal of Chemical Physics, pp. 669–681, 1937.

[159] Yarborough V. A., Haskin J. F., and Lambdin W. J., *"Temperature Dependence of* Absorbance in Ultraviolet Spectra of Organic Molecules," Analytical Chemistry, pp. 1576–1578, 1954.

[160] Grubb W. T., and Kistiakowsky G. B., *"On the Nature of Thermochromism,"* Journal of the American Chemical Society, pp. 419–424, 1950.

[161] Passerini R., and Ross I. G., *"Temperature Dependence of the Ultraviolet Absorption* Spectrum of Naphthalene in Solution," The Journal of Chemical Physics, pp. 1012–1016, 1954.

[162] Ito M., *"The effect of temperature on ultraviolet absorption spectra and its relation to* hydrogen bonding," Journal of Molecular Spectroscopy, pp. 106–124, 1960.

[163] Pedley J. F., Hiley R. W., and Hancock R. A., *"Storage stability of petroleum*-derived diesel fuel: 1. Analysis of sediment produced during the ambient storage of diesel fuel," Fuel, pp. 1646–1651, 1987.

[164] Fröhlich A., and Schober S., *"The Influence of Tocopherols on the Oxidation* Stability of Methyl Esters," Journal of the American Oil Chemists' Society, pp. 579–585, 2007.

[165] Knothe G., *"Some aspects of biodiesel oxidative stability,"* Fuel Processing Technology, pp. 669–677, 2007.

[166] *"DIRECTIVE 98/70/EC OF THE EUROPEAN PARL*IAMENT AND OF THE COUNCIL of 13 October 1998 relating to the quality of petrol and diesel fuels and amending Council Directive 93/12/EEC 1998L0070— EN— 25.06.2009 — 004.001— 1," 2009.

[167] J. Erwin, *"Assay of Diesel Fuel Components Properties and Perfor*mance," Symposium on Processing and Product Selectivity of Synthetic Fuels, Division of Fuel Chemistry, American Chemical Society, Washington DC, USA, pp. 23 – 28, 1992.

[168] *"Agency for Toxic Substances & Disease Registry:-* http://www.atsdr.cdc.gov/toxprofiles/tp75-c3.pdf."

[169] Martin A. J. P., and Synge R. L. M., *"A new form of chromatogram employing two* liquid phases," Biochemical Journal, pp. 1358–1368, 1941.

[170] James A. T., and Martin A. J. P., *"Gas*-liquid partition chromatography. A technique for the analysis of volatile materials," Analyst, pp. 915–932, 1952.

[171] Adahchour M., Beens J., Vreuls R. J. J., and Brinkman U. A. T., *"Recent developments* in comprehensive two-dimensional gas chromatography (GC × GC): I. Introduction and instrumental set-up," TrAC Trends in Analytical Chemistry, pp. 438–454, 2006.

[172] Bartle K. D., and Myers P., *"History of gas chromatography,"* TrAC Trends in Analytical Chemistry, pp. 547–557, 2002.

[173] Marriott P., and Shellie R., *"Principles and applications o*f comprehensive two-dimensional gas chromatography," TrAC Trends in Analytical Chemistry, pp. 573–583, 2002.

[174] Phillips J. B., and Xu J., *"Comprehensive multi*-dimensional gas chromatography," Journal of Chromatography A, pp. 327–334, 1995.

[175] Pursch M., Sun K., Winniford B., Cortes H., Weber A., McCabe T., and Luong J., *"Modulation techniques and applications in comprehensive two*-dimensional gas chromatography (GC×GC),*"* Analytical and Bioanalytical Chemistry, pp. 356–367, 2002.

[176] Adahchour M., Beens J., Vreuls R. J. J., and Brinkman U. A. T., *"Recent developments* in comprehensive two-dimensional gas chromatography (GC × GC): II. Modulation and detection," TrAC Trends in Analytical Chemistry, pp. 540–553, 2006.

[177] Górecki T., Harynuk J., and Panić O., *"The evolution of comprehensive two*-dimensional gas chromatography (GC×GC),*"* Journal of Separation Science, pp. 359–379, 2004.

[178] Vendeuvre C., Bertoncini F., Duval L., Duplan J.-L., Thiébaut D., and Hennion M.-C., *"Comparison of conventiona*l gas chromatography and comprehensive two-dimensional gas chromatography for the detailed analysis of petrochemical samples," Journal of Chromatography A, pp. 155–162, 2004.

[179] Von Mühlen C., Zini C. A., Caramão E. B., and Marriott P. J., *"Application*s of comprehensive two-dimensional gas chromatography to the characterization of petrochemical and related samples," Journal of Chromatography A, pp. 39–50, 2006.

[180] Van der Westhuizen R., Crous R., de Villiers A., and Sandra P., *"Comprehensive two*-dimensional gas chromatography for the analysis of Fischer–Tropsch oil products," Journal of Chromatography A, pp. 8334–8339, 2010.

[181] Schoenmakers P. J., Oomen J. L. M. M., Blomberg J., Genuit W., and van Velzen G., *"Comparison of comprehensive two*-dimensional gas chromatography and gas chromatography – mass spectrometry for the characterization of complex hydrocarbon mixtures," Journal of Chromatography A, pp. 29–46, 2000.

[182] Tosaka S., and Fujiwara Y., *"The characteristics of chemical reaction of di*esel fuel," JSAE Review, pp. 463–468, 2000.

[183] Seeley J. V., Seeley S. K., Libby E. K., and McCurry J. D., *"Analysis of* biodiesel/petroleum diesel blends with comprehensive two-dimensional gas chromatography," Journal of chromatographic science, pp. 650–656, 2007.

[184] Liverani L., *"Cavitation in Real*-Size Diesel Injector Nozzles," City University, SEMS, 2010.

[185] Chang T.-L., and Borst W. L., *"Effect of solvent polarity on a rotational isomerization* mechanism of rhodamine-B in normal alcohols," The Journal of Chemical Physics, pp. 4724–4729, 1990.

[186] *"Sensor scores*"[Online]. Available: http://www.dxomark.com/index.php/About/Sensor-scores/Use-Case-Scores. [Accessed: 23-Sep-2013].

[187] Gavaises M., and Andriotis A., *"Influence of vortex flow and* cavitation on near-nozzle diesel spray dispersion angle," Atomization and Sprays, pp. 247–261, 2009.

[188] *"Beta CAE Systems,"* BETA CAE systems[Online]. Available: http://www.beta-cae.gr/.

[189] Pedley J. F., Hiley R. W., and Hancock R. A., *"Storage stab*ility of petroleum-derived diesel fuel: 4. Synthesis of sediment precursor compounds and simulation of sediment formation using model systems," Fuel, pp. 27–31, 1989.

[190] Venkataraman R., and Eser S., *"Characterization of deposits formed on diesel injec*tors in field test and from thermal oxidative degradation of n-hexadecane in a laboratory reactor," Chemistry Central Journal, p. 25, 2008.

[191] Battino R., Rettich T. R., and Tominaga T., The solubility of nitrogen and air in liquids, American Chemical Society and the American Institute of Physics for the National Bureau of Standards, 1984.

[192] Battino R., and Clever H. L., *"The Solubility of Gases in Liquids,"* Chemical Reviews, pp. 395–463, 1966.

[193] Hartley R., and Zisserman A., Multiple View Geometry in Computer Vision, Cambridge University Press, 2003.

[194] Evangelidis G. D., and Psarakis E. Z., *"Projective Image Alignment by Using ECC* Maximization.," VISAPP (1), pp. 413–420, 2008.

[195] Evangelidis G. D., and Psarakis E. Z., *"Parametric imag*e alignment using enhanced correlation coefficient maximization," Pattern Analysis and Machine Intelligence, IEEE Transactions on, pp. 1858–1865, 2008.

[196] *"ECC Image Alignment Algorithm,"* ECC Image Alignment Algorithm[Online]. Available: http://xanthippi.ceid.upatras.gr/people/evangelidis/ecc/.

[197] *"Mathworks file exchange,"* Matlab central[Online]. Available: http://www.mathworks.it/matlabcentral/fileexchange/27253-ecc-image-alignment-algorithm-image-registration.

[198] Davies P. C. W., *"Quantum tunne*ling time," American journal of physics, p. 23, 2005.

[199] Hayashi S., Hisaeda Y., Asakuma Y., Aoki H., Miura T., Yano H., and Sawa Y., *"Simulation of soot aggregates formed by benzene pyrolysis,"* Combustion and Flame, pp. 851–860, 1999.

[200] Krestinin A. V., *"Detailed modeling of soot formation in hydrocarbon pyrolysis,"* Combustion and Flame, pp. 513–524, 2000.

[201] Ono K., Yanaka M., Saito Y., Aoki H., Fukuda O., Aoki T., and Yamaguchi T., *"Effect* of benzene–acetylene compositions on carbon black configurations produced by benzene pyrolysis," Chemical Engineering Journal, pp. 128–135, 2013.

[202] Naydenova I., Vlasov P. A., and Warnatz J., *"Detailed kinetic modeling of soot* formation in pyrolysis of benzene/acetylene/argon mixtures," Proceeding of the European Combustion Meeting, 2005.

[203] Agafonov G. L., Naydenova I., Nullmeier M., Vlasov P. A., and Warnatz J., *"Detailed* kinetic modeling of PAH growth and soot formation in shock tube pyrolysis of benzene and ethylene," Proceedings of the 20th ICDERS, Montreal, Canada, 2005.

[204] Ivie J. J., and Forney L. J., *"A numerical model of the synthesis of carbon black by* benzene pyrolysis," AIChE journal, pp. 1813–1820, 1988.

[205] Frenklach M., and Wang H., *"Detailed modeling of soot particle nucleati*on and growth," Symposium (International) on Combustion, pp. 1559–1566, 1991.

[206] Kennedy I. M., *"Models of soot formation and oxidation,"* Progress in Energy and Combustion Science, pp. 95–132, 1997.

[207] Mendiara T., Domene M. P., Millera A., Bilbao R., and Alzueta M. U., *"An* experimental study of the soot formed in the pyrolysis of acetylene," Journal of Analytical and Applied Pyrolysis, pp. 486–493, 2005.

[208] Lahaye J., and Ehrburger-Dolle F., *"Mechanisms of carbon black formation.* Correlation with the morphology of aggregates," Carbon, pp. 1319–1324, 1994.

[209] Lahaye J., Prado G., and Donnet J. B., *"Nucleation and growth of carbon black* particles during thermal decomposition of benzene," Carbon, pp. 27–35, 1974.

[210] Ono K., Yanaka M., Tanaka S., Saito Y., Aoki H., Fukuda O., Aoki T., and Yamaguchi T., *"Influence of furnace temperature and residence time on configurations of carbon* black," Chemical Engineering Journal, 2012.

[211] Herbinet O., Marquaire P.-M., Battin-Leclerc F., and Fournet R., *"Thermal* decomposition of n-dodecane: Experiments and kinetic modeling," Journal of analytical and applied pyrolysis, pp. 419–429, 2007.

[212] Guillaume Blanquart, *"CHEMICAL AND STATISTICAL SOOT MODELING,"* STANFORD UNIVERSITY, 2008.

[213] Wang H., and Frenklach M., *"Calculations of Rate Coefficients for the Chemically* Activated Reactions of Acetylene with Vinylic and Aromatic Radicals," The Journal of Physical Chemistry, pp. 11465–11489, 1994.

[214] Frenklach M., *"Reaction mechanism of soot formation* in flames," Physical Chemistry Chemical Physics, pp. 2028–2037, 2002.

[215] Okada T., Iwai Y., and Awazu K., *"A study of cavitation bubble collapse pressures and* erosion part 1: A method for measurement of collapse pressures," Wear, pp. 219–232, 1989.

[216] Richter H., Granata S., Green W. H., and Howard J. B., *"Detailed modeling of PAH* and soot formation in a laminar premixed benzene/oxygen/argon low-pressure flame," Proceedings of the Combustion Institute, pp. 1397–1405, 2005.

[217] Ergut A., Granata S., Jordan J., Carlson J., Howard J. B., Richter H., and Levendis Y. A., *"PAH formation in one*-dimensional premixed fuel-rich atmospheric pressure ethylbenzene and ethyl alcohol flames," Combustion and Flame, pp. 757–772, 2006.

[218] *"http://web.mit.edu/*anish/www/MITcomb.html."

[219] Maly R. R., *"Effect of GTL Diesel Fuels on Emissions and Engine Performance,"* presentation at 10th Diesel Engine Emissions Reduction Conference, Coronado, Calif, 2004.

[220] Wu T., Huang Z., Zhang W., Fang J., and Yin Q., *"*Physical and Chemical Properties *of GTL−Diesel Fuel Blends and Their Effects on Performance and Emissions of a* Multicylinder DI Compression Ignition Engine," Energy & Fuels, pp. 1908–1914, 2007.

[221] Soltic P., Edenhauser D., Thurnheer T., Schreiber D., and Sankowski A., *"Experimental investigation of mineral diesel fuel, GTL fuel, RME and neat soybean* and rapeseed oil combustion in a heavy duty on-road engine with exhaust gas aftertreatment," Fuel, pp. 1–8, 2009.

Appendix A

A.1 Laser Absorption Calibration for Optics

The optical calibration of the absorption of laser light through the optics will be presented here. The laser power incident on the diesel samples I_0 has to pass through the reference beam splitter, followed by the fused silica window into the optical cell, i.e. $I_0 = t_f t_{fs1} I_T$, where t_f is the transmission factor through the OD 0.03 filter, t_{fs1} is the transmission factor through a fused silica window and I_T is the total laser power emitted. I_T can be expressed in terms of the laser power reflected from the neutral density filter onto the reference detector I_R.

$$I_o = \frac{t_{fs1}(1 - r_f)}{r_f} I_R$$

Equation A.1

where r_f is the reflectivity of the OD 0.03 neutral density filter being used as a beam splitter.

The laser power exiting the diesel samples passes through a fused silica window before being reflected onto the transmission power detector. The laser power measured at the detector is denoted by $I_{T3\,(M)}$ and it is related to the laser power exiting the diesel sample in the optical cell I_E by,

$$I_{T3(M)} = t_{fs2} r_m I_E$$

Equation A.2

where t_{fs2} is the transmission coefficient for the exit fused silica window and $r_m$is the reflectivity of the final mirror. The time derived spectral attenuation coefficient is then derived from Equation 3.5 to be,

$$\alpha(t) = \frac{ln\frac{I_O(t)}{I_E(t)}}{l} = \frac{ln\frac{t_{fs1}t_{fs2}r_m(1-r_f)I_R}{r_f I_{T3(M)}}}{l}$$

Equation A.3

where l is the optical path length of the laser through the diesel fuel sample in the optical cell. This was measured to be 1.03 cm ± 0.01 cm.

The calibrations were carried out with no fuel present in the optical cylinder in the setups it was utilized in, apart from the fused silica transmissivity test where, room temperature paraffinic model fuel was used. The windows were cleaned of any fuel and dirt that would cause any small errors. The measurements were calibrated and run under a covering box similar to the cavitation analysis measurement runs.

Three different setups were used in the approach. These setups are seen in Figure A.1. The first setup was the actual setup that replicated the cavitation analysis optical setup. The second setup replicated the first excluding the end mirror that reflected the laser beam onto the transmission detector. An analysis between these two approaches and changing the beam intensity by changing the beam splitter to a lower transmitting filter enables the calculation of the mirror absorbance. An equation will be developed to relate the intensity measured at the transmission detector $I_{T3\,(m)}$ and the intensity of the beam prior to the mirror I_{T3}.

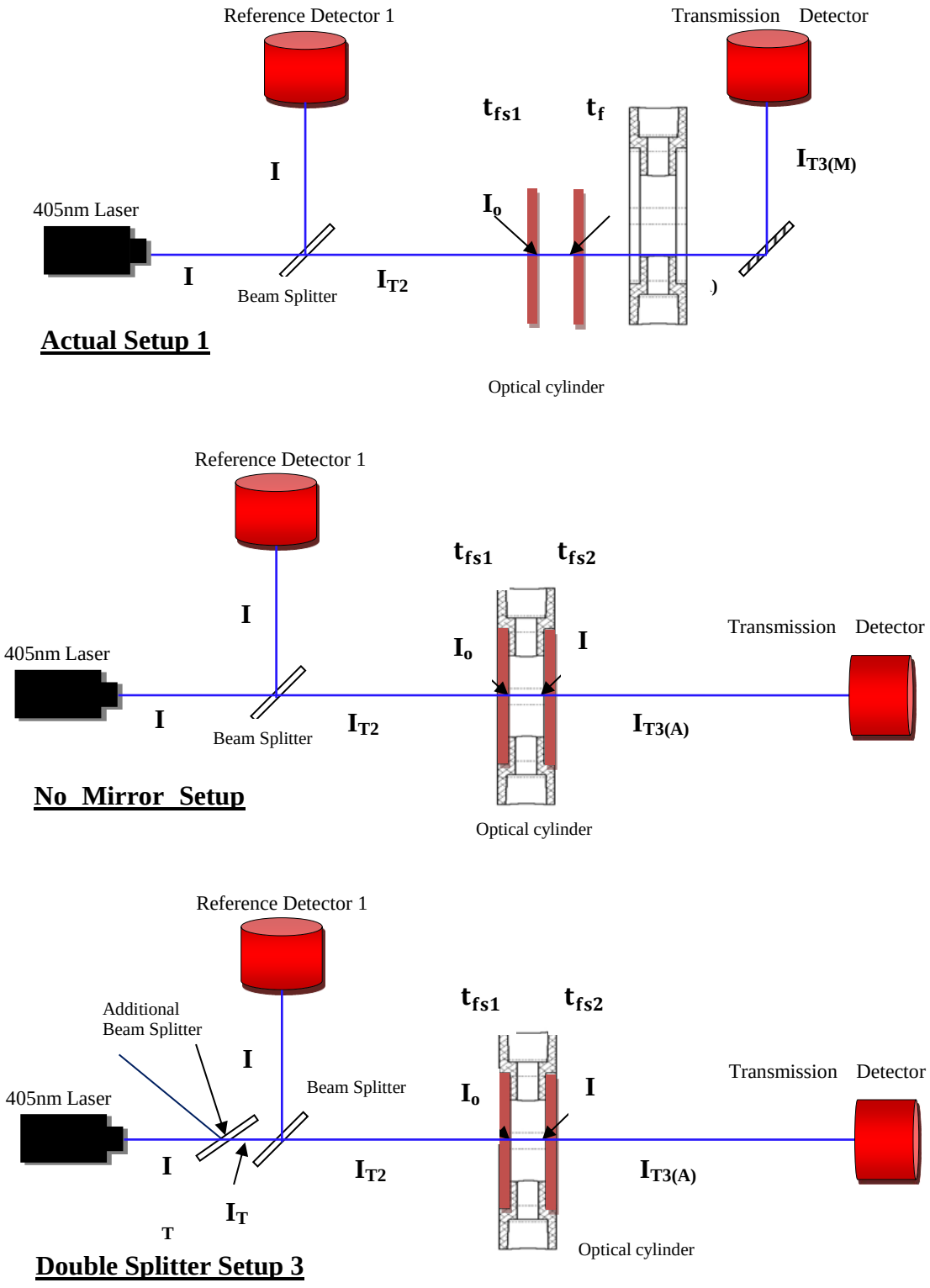

Figure A.1 Laser beam detector setup and nomenclature (1)Actual setup, (2) No mirror Setup (3) Double splitter setup

The nomenclature in the Figure A.1 denotes intensities at different beam regions and is as follows:

Actual Setup

$\mathbf{I_T}$ - Total intensity emitted by laser

$\mathbf{I_R}$ - Part of Intensity $\mathbf{I_T}$ reflected to by beam splitter

$\mathbf{I_{T2}}$ - Part of intensity $\mathbf{I_T}$ transmitted through filter/splitter

$\mathbf{t_{fs1}}$ - Intensity $\mathbf{I_{T2}}$ absorbed by window 1

$\mathbf{I_o}$ - Intensity at laser entry into fuel

$\mathbf{I_E}$ - intensity before window 2

$\mathbf{t_{fs2}}$ - Intensity absorbed by window 2

$\mathbf{I_{T3\,(M)}}$ - Final intensity into detector 2 (mirrored)

No Mirror Setup

$\mathbf{I_{T3\,(A)}}$ - Final intensity onto detector 2 (un-mirrored)

Double splitter setup

$\mathbf{I_{T1}}$ - Laser intensity past First beam splitter

In the second and third setup, the transmission detector was repositioned so that the beam would travel the same distance as in setup 1 past the fuel exit, i.e. 17.5 cm. The third setup replicated the second and included an extra beam splitter placed before the actual splitter that was used in the experimental analysis setup. This setup will be used solely to calculate a relationship between the reference detector intensity readings I_R and the intensity transmitted past the splitter I_{T2}.

By using second approach solely through only one window in the optical cylinder and changing the beam intensities would give an approximation of the window absorbance. An

equation that relates the laser beam intensity past the beam splitter I_{T2} and the window absorbance I_{abs1} will be developed to determine the laser beam intensity I_o at the entry to fuel. One that relates the intensity prior to the mirror $I_{T3(A)}$ and the exit window will be developed to calculate the fuel exit laser beam intensity I_E.

In setups 1-2, three beam splitters were used to create a change in beam intensities. Beam splitter 1 was a neutral density filter that transmitted approximately 90% and reflected approximately 10% of the incident laser beam. This splitter/neutral density filter is the same one used in the optical setup during the cavitation analysis. Beam splitter 2 was also a neutral density filter that transmitted ~85% and reflected ~15% of the incident beam. The third one is an actual 50:50 beam splitter and transmitted ~50% of the incident light.

During setup 3, splitter 1 was placed in its original position and splitter 2 and splitter 4 placed simultaneously ahead of this to create a change in incident beam. Splitter 2 has been described in the earlier paragraph. Splitter 4 is a neutral density filter that transmits ~55% of incident beam.

The following subchapters will elaborate on the development of the beam relationships to eradicate the absorbance through the components and finally a formula developed to calculate the time resolved linear attenuation.

A.1.1 Mirror absorption (relationship between $I_{T3(m)}$ and $I_{T3(A)}$)

By following setup 1 six measurements were obtained as seen in Figure A.2 by changing the components in the laser path. Tests 1, 4 and 5 were repeated with two other neutral density

filters, each transmitting less than the other. The first beam splitter used was splitter 1, followed by splitter 2 and then splitter 3. The beam splitter/neutral density filter characteristics have been described earlier. Different transmission filters enables a change in incident laser beam intensity and further analysis of the mirror absorption can be carried out relative to the incident intensities.

Signal test 1 replicates the optical setup used in the cavitation analysis. In signal tests 2, 3 and 6 the beam splitters are absent. Signal test 3 measures the full mirrored beam power and signal test 4, both the reference and transmission detector powers, both setups without the optical cylinder. Signal tests 5 and 6 are intensity measurements with one fused silica window on the optical cylinder.

Following these measurements, no mirror setup 2 was employed to carry out further laser intensity signal tests as seen in Figure A.3. As earlier described, three splitters were used to change the incident laser beam. The splitters used were the same as the ones used when carrying out signal tests using the actual setup, i.e. Splitters - 1, 2, and 3. The difference in these tests is that the end mirror that reflects the laser beam past the optical cylinder has been omitted.

Simultaneously comparing the transmission detector intensity readings for each test carried out following the actual setup and the corresponding test with the no mirror setup, and plotting these values on a graph for comparison will inhibit the development of a relationship between the $I_{T3(A)}$ and $I_{T3(m)}$. Comparing the transmission detector results for tests from both setups, for example test 1 will give one result with a mirror present and the other without a mirror present, and a relationship can be developed to calculate $I_{T3(A)}$ using $I_{T3(m)}$.

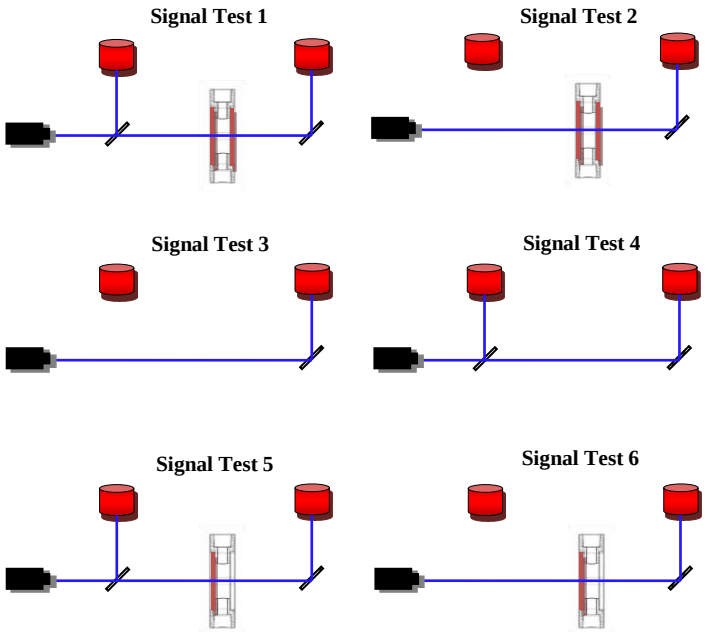

Figure A.2 Laser intensity signal intensity tests carried the actual setup 1

Table A.1 shows the results obtained. These will be plot on a graph as $I_{T3(A)}$ vs. $I_{T3(m)}$, and a trend line with a zero XY intercept plot to determine the line equation and thus their relationship. The zero intercept was set as with no incident intensity there would be no transmission intensity and thus there would be no absorption of the incident laser intensity by the optical component. That is at $I_T = 0$, there would be no laser absorption as there is no incident laser beam.

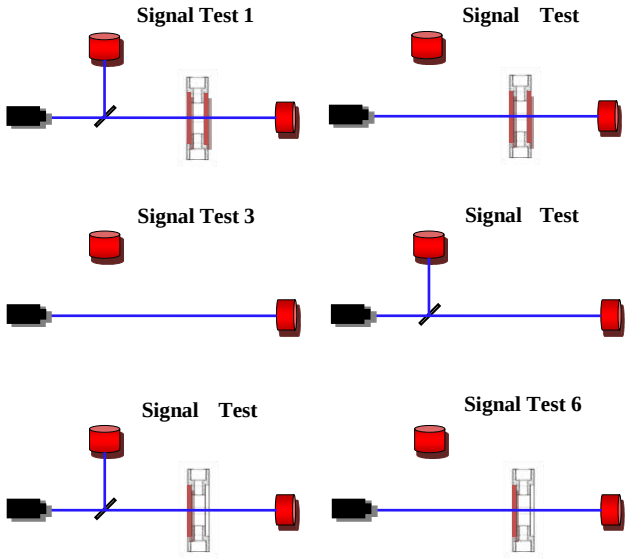

Figure A.3 Laser intensity signal test setups following no mirror setup

Test No.	Splitter 1		Splitter 2		Splitter 3	
	Actual Setup Test Results- $I_{T3(m)}$ (y)	No Mirror Setup Test Results-$I_{T3(A)}$ (x)	Actual Setup Test Results- $I_{T3(m)}$ (y)	No Mirror Setup Test Results-$I_{T3(A)}$ (x)	Actual Setup Test Results- $I_{T3(m)}$ (y)	No Mirror Setup Test Results- $I_{T3(A)}$ (x)
1	12.02	13.89	10.11	11.59	6.37	7.3
2	13.5	15.26	-	-	-	-
3	15.56	17.82	-	-	-	-
4	13.84	15.91	11.65	13.43	7.36	8.55
5	12.78	14.72	10.81	12.4	6.81	7.91
6	14.35	16.48	-	-	-	-

Table A.1 Comparison of Mirrored and no mirrored data using three different beam splitters

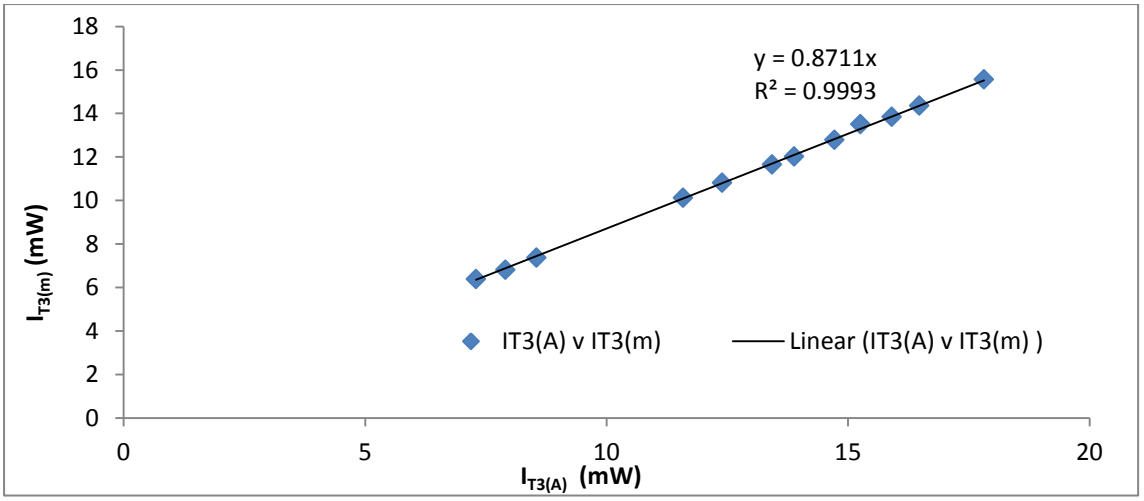

Figure A.4 Graph of $I_{T3(A)}$ vs. $I_{T3(m)}$ with a equation trend line

From the trend line equation as seen in Figure A.4,

$$I_{T3(m)} = 0.871\ I_{T3(A)}$$

Equation A.4

Therefore,

$$I_{T3(A)} = \frac{I_{T3(m)}}{0.871}$$

Equation A.5

With a linear correlation of R^2=0.993. Using Equation A.5 and known value of $I_{T3(m)}$, $I_{T3(A)}$ can be calculated. Using Equation A.3 and $I_{T3(m)}$ results obtained, $I_{T3(A)}$ values were calculated and compared to the previously determined values of $I_{T3(A)}$ via calibration setup to approximate the errors created. From Table A.2 a comparison between the values of derived and actual $I_{T3(A)}$ produced a mean relative error of 0.5%. The final mirror is determined to reflect 0.871 ± 0.001 of the incident laser power on it, therefore r_m = 0.871.

Actual No mirror $I_{T3(A)}$ (mW) (±0.01)	Calculated $I_{T3(A)}$ (mW) (±0.01)	Error (%)
13.89	13.80	0.644
15.26	15.49	-1.549
17.82	17.85	-0.211
15.91	15.89	0.148
14.72	14.67	0.402
16.48	16.48	0.009
11.59	11.61	-0.158
13.43	13.38	0.398
12.40	12.41	-0.099
7.30	7.31	-0.222
8.55	8.45	1.185
7.91	7.82	1.118

Table A.2 Comparisons of actual and calculated $I_{T3(A)}$.

A.1.2 Beam splitter transmission-reflection (relationship between I_R and I_{T2})

The splitter transmissivity can be determined by predicting a relationship experimentally between the reflected intensity I_R and the transmitted intensity I_{T2}. Out of these two, I_R is the only known value from cavitation experiments, thus a relationship of beam I_R and I_{T2} will enable the determination of the later by this relationship. Signal tests 3 and 4 as seen in Figure A.3 were used in conjunction with intensity signal tests 7 and 8 seen in Figure A.5 below. Test 7 and 8 had two beam splitters, the first splitter was to decrease the incident laser intensity arriving on to the second beam splitter which the reflected light onto the reference detector and allowed transmission onto the transmission detector. The beam splitter that split between the reference and transmission detectors was splitter 1, that is, the splitter used in the cavitation analysis optical setup. Two neutral density filters were used i.e. splitter 2 and 4 to vary light onto splitter 1. The objective was to determine a relationship between the reflected and transmitted light of splitter 1 with varied incident intensity. Splitters 2 and 4 filtered light at different magnitudes.

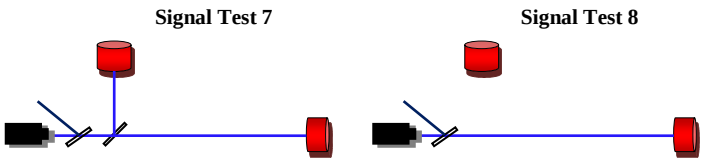

Figure A.5 Laser intensity signal tests following double splitter setup

The above tests were repeated thrice to reduce errors and results are shown in Table A.3 below.

For the signal tests with 2 splitters, I_T is determined using the transmission detector reading of signal test 8. I_R and I_{T2} are determined using signal test 7. For single beam splitter tests 3 and

4, the I_T is determined by test 3 and the later test determines intensities I_R and I_{T2}. A scatter graph of I_R vs. I_{T2} with a trend line to determine the equation of their relationship was plot.

Repeat number	Intensity Signal Test number	I_T (mW) (±0.01)	I_R (mW) (±0.01)	I_{T2} (mW) (±0.01)
1	Splitter 4 test 7 & 8	9.65	0.95	8.68
	Splitter 2 test 7 & 8	14.02	1.40	12.56
	Test 3 & 4	17.81	1.77	16.02
2	Splitter 4 test 7 & 8	9.56	0.96	8.62
	Splitter 2 test 7 & 8	13.93	1.37	12.46
	Test 3 & 4	17.68	1.78	15.82
3	Splitter 4 test 7 & 8	9.56	0.94	8.59
	Splitter 2 test 7 & 8	13.98	1.37	12.58
	Test 3 & 4	17.77	1.77	15.98

Table A.3 I_T, I_R, I_{T2} obtained from setup tests 3

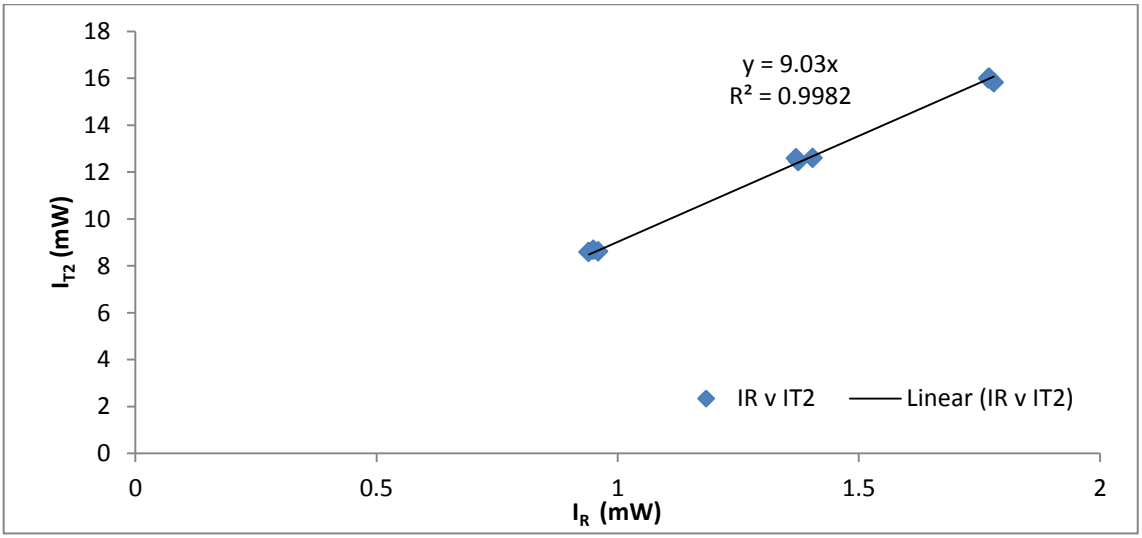

Figure A.6 Graph of I_R vs. I_{T2} with a trend line

From the graph and trend line,

$$I_{T2} = 9.03\, I_R$$

Equation A.6

with a linear correlation coefficient of R^2=0.9982. Replacing I_R values from Table A.3 and inserting them into Equation A.6 will provide calculated data for $I_{T2.}$ Comparing these calculated values to actual values from Table A.3 will give an estimation of errors created by

using this equation to estimate I_{T2} given I_R. A comparison between the values of I_{T2} derived from the proportional relationship with the measure values produced a mean relative error of 0.8%. The neutral density OD0.03 filter reflected 0.099±0.001 of the incident laser power on it, onto the reference detector. Therefore, in Equation A.3, $\frac{(1-r_f)}{r_f}$ = 9.03.

I_{T2} (mW) (±0.01)	Calculated I_{T2} (mW) (±0.01)	Error (%) (±0.01)
8.68	8.58	1.214
12.56	12.68	-0.7
16.02	15.98	0.227
8.62	8.67	-0.573
12.46	12.41	0.376
15.82	16.07	-1.612
8.59	8.49	1.178
12.58	12.37	1.654
15.98	15.98	0.055

Table A.4 Comparison of actual and calculated I_{T2}, and an estimate of errors.

A.1.3 Fused silica window transmissivity T_{fs}

The fused silica windows had to be calibrated with a transparent fluid flowing through the optical cell during calibration measurements, with the transparent fluid having a refractive index matching those of the diesel samples. This was in order to calibrate the effect of the laser passing from air into the fused silica window then into the diesel sample, to be followed by the laser exiting the fuel and entering the fused silica window and into the air.

Paraffinic model fuel blend was employed as a model diesel in order to calibrate the optical transmission of the laser through the fused silica windows sealing the optically accessible cell. The fuel was almost transparent to the diode laser light at 405nm. Intensity signal tests 3-6, shown in Figure A.3 were used as the experimental arrangement necessary to calibrate the transmission through the fused silica windows.

The transmission through the fused silica windows were measured using Signal setup 3 and Signal setup 7 in Figure A.3. The beam power transmitted through the fused silica windows were compared with the beam incident directly on the transmission detector. The transmission through the fused silica windows and the transparent cold paraffinic model fuel was determined to be 0.970±0.001. Therefore the combination effect of the two windows $t_{fs1}t_{fs2}$ as seen in Equation A.3 is 0.970.

A.1.4 Determination of linear attenuation coefficient α

The optical setup during the cavitation analysis only provides I_R and $I_{T2(m)}$ as a function of time. The linear attenuation coefficient Equation 3.5 requires the inputs I_o and $I_{E.}$ Using the calibration analysis in sections A.1.1 to A.1.3 above these values can be calculated to determine the linear attenuation coefficient. Replacing the values obtained in sections A.1.1 to A.1.3 in Equation A.3 gives,

$$\alpha(t) = \frac{ln\left(\frac{7.63I_R(t)}{I_{T3(M)}(t)}\right)}{1.03} cm^{-1}$$

Equation A.7

This will be used with time resolved reference and transmission detector readings to calculate a time resolved linear attenuation coefficient for the commercial fuels.

When carrying out measurements for paraffinic model fuel and paraffinic model fuel - B20, the setup had been changed by removing the mirror and having the final transmission laser power detector directly in line with the laser. The calibrations were redone without having to calibrate for the reflectivity of the mirror. The linear attenuation coefficient equation for these two fuels is,

$$\alpha(t) = \frac{ln\left(\frac{8.76 I_R(t)}{I_{T3(M)}(t)}\right)}{1.03} cm^{-1}$$

Equation A.8

Appendix B

B.1 Kinetic Modelling for the Pyrolysis of a Surrogate Fuel

Chemical kinetics deals with the rates of reactions. In order for a reaction to occur, a collision must occur; the collision must be of sufficient energy to break the necessary bonds and be of proper orientation. This is the basis of reaction rates. Factors effecting reaction rates are concentration of the reacting species found in the rate law, temperature and the presence or absence of a catalyst. The reaction rate is defined as the change in concentration of a reactant with time. Consider a reaction:

$$A \rightarrow B$$

Equation B.1

The rate of reaction with respect to A is,

$$Rate = -\frac{\Delta[A]}{\Delta t}$$

Equation B.2

Whereas with respect to B is,

$$Rate = \frac{\Delta[B]}{\Delta t}$$

Equation B.3

In the equations, the squared brackets represent the concentration or the number of moles of the species present. The negative sign seen in Equation B.2 represents a species being consumed.

Now consider a reaction,

$$aA + bB \rightarrow cC + dD$$

Equation B.4

Where the lowercase letters represent the concentration or the number of mole of the higher case species.

$$Rate = -\frac{1}{a}\frac{\Delta[A]}{\Delta t} = -\frac{1}{b}\frac{\Delta[B]}{\Delta t} = \frac{1}{c}\frac{\Delta[C]}{\Delta t} = \frac{1}{d}\frac{\Delta[D]}{\Delta t}$$

Equation B.5

The rate law of the chemical equation is however,

$$Rate = k[A]^x[B]^y$$

Equation B.6

Where x and y are the reactant orders determined from experiment and k is the rate constant. The rate law is an equation that tells us how fast the reaction proceeds and how the reaction rate depends on the concentrations of the chemical species involved. There are several types of orders of reaction described powers or sum of powers of the rate law equation as seen in Table B.1

Rate law	Order
Rate = k	Zero
Rate= k[A]	First order with respect to A First order overall
Rate= k$[A]^2$	Second order with respect to A Second order overall
Rate= k[A][B]	First order with respect to A First order with respect to B Second order overall
Rate= k[A][B][C]	First order with respect to A First order with respect to B First order with respect to C Third order overall

Table B.1 Relationship between Rate law, order and rate constant k

Only a small fraction of the collisions between reactant molecules convert the reactants into the products of the reaction. Another factor that influenced whether reaction will occur is the energy the molecules carry when they collide. Not all of the molecules have the same kinetic energy. This is important because the kinetic energy molecules carry when they collide is the principal source of the energy that must be invested in a reaction to get it started. Before the reactants can be converted into products, the overall collision energy must overcome the activation energy for the reaction. However this is not always the case, even if collision energy does not surpass the activation energy the reaction may still go ahead by a process known as quantum tunnelling. Quantum tunnelling is the quantum-mechanical effect of transitioning through a classically-forbidden energy state. To understand the phenomenon, particles attempting to travel between potential barriers can be compared to a ball trying to roll over a hill; quantum mechanics and classical mechanics differ in their treatment of this scenario. Classical mechanics predicts that particles that do not have enough energy to classically surmount a barrier will not be able to reach the other side. Thus, a ball without sufficient energy to surmount the hill would roll back down. Or, lacking the energy to penetrate a wall, it would bounce back (reflection) or in the extreme case, bury itself inside the wall (absorption). In quantum mechanics, these particles can, with a very small probability, tunnel to the other side, thus crossing the barrier. Here, the ball could, in a sense, borrow energy from its surroundings to tunnel through the wall or roll over the hill, paying it back by making the reflected electrons more energetic than they otherwise would have been [198].

The activation energy E_a is the minimum energy that must be input into a chemical system in order for a chemical reaction to occur. The Arrhenius equation gives the quantitative basis of the relationship between the activation energy and the rate at which a reaction proceeds.

$$k = Ae^{\frac{-Ea}{RT}}$$

Equation B.7

Where A is the frequency factor for the reaction, R is the universal gas constant and T is the temperature in Kelvin.

Many factors influence rates of chemical reactions, and these are summarized below.

- Nature of Reactants- Acid-base reactions, formation of salts, and exchange of ions are fast reactions. Reactions in which large molecules are formed or break apart are usually slow. Reactions breaking strong covalent bonds are also slow.
- Temperature- Usually, the higher the temperature, the faster the reaction. The temperature effect is discussed in terms of activation energy.
- Concentration Effect- The dependences of reaction rates on concentrations are called rate laws. Rate laws are expressions of rates in terms of concentrations of reactants. Keep in mind that rate laws can be in differential forms or integrated forms. They are called differential rate laws and integrated rate laws.
- Heterogeneous reactions- reactants are present in more than one phase. For heterogeneous reactions, the rates are affected by surface areas.
- Catalysts- substances used to facilitate reactions. By the nature of the term, catalysts play important roles in chemical reactions. Catalysts increase the rate of reaction and are not consumed by the reaction

The experimental results have led to hypothesis of particulate/soot formation which may be the results of a pyrolysis like process occurring as a result of sustained cavitating flow. Many researchers have studied and modelled the formation of soot/particulates as a result of poly

aromatic hydrocarbon PAH formation [182,199–205]. The particles formed then grow by coagulation and surface reactions. From a study by Tosaka et. al [182], they found that n-hexadecane disintegrated into low boiling point hydrocarbons as a result of thermal pyrolysis, and subsequently formed Benzene and alkyl-benzenes by the Diels-Ader reaction. Heating n-hexadecane to temperatures between 600-1200ºC created polycyclic compounds by condensation polymerization which then formed PAHs. They concluded that the carbon-carbon bonds in aliphatic hydrocarbon (paraffin, olefin, and napthenes) are thermally decomposed to low boiling point hydrocarbons, and benzene rings are then formed by dehydrogenation, condensation polymerization and polycyclization. This may be the basic process of primary particle formation passing through polycyclic aromatic hydrocarbons to become primary particles. The bond dissociation energies of aliphatic hydrocarbons depend on carbon links, and the dissociation energies are small. The temperature where fine particle formation is initiated may be lower when the formed amounts are higher. They found the thermal decomposition process of aromatic hydrocarbons clearly different from that of aliphatic hydrocarbons. The benzene ring was not decomposed and the formation of particulate took place by condensation polymerization via PAH.

Soot is mostly carbon and it is produced during the high temperature pyrolysis or combustion of hydrocarbons. As hydrocarbons pyrolyze, they produce primarily smaller hydrocarbons, in particular acetylene. The initial step in the production of soot is the formation of the first aromatic species from these aliphatic hydrocarbons [206]. The aromatic species grow by the addition of other aromatic and smaller alkyl species to form larger PAHs. Continued growth of the PAH leads eventually to the smallest identifiable soot particles with diameters of the order of 1 nm and with masses of around 1000 amu. Once soot particles are formed through

the inception process, they can grow by two mechanisms i.e., collisional coagulation and surface growth. The former process is physical while the latter process is chemical in nature.

When particles are small and surface growth is active, collisions between particles generally lead to the formation of a larger spheroid via the process of coalescence. Older particles undergo agglomeration in which the individual spheroids are retained in long chains with a fractal like geometry. The formation of large amounts of PAH and aromatics compounds is troublesome as these species are precursors of the formation of soot and even coke at high temperature [207] which generate solid deposits in the injection channels and a fouling in the combustion chamber.

In the furnace process, carbon black is produced by the continuous pyrolysis of hydrocarbons, which are sprayed into a high-temperature field (1500–2000 K) inside the furnace. The process is complicated owing to the fact that chemical reactions occur rapidly with heat and mass transfer, and therefore, it is difficult to control the aggregate shape. The formation mechanism for carbon black is considered to be as follows. Large molecules are considered to be the precursors of carbon black particles. Although various theories have been proposed for the reaction mechanism of pyrolysis, all of the recent studies conclude that in both pyrolytic systems and flame systems, PAHs are the precursors of carbon nuclei [208,209]. The primary soot particles expand either by the addition of molecules from a gas phase, such as acetylene, or by reaction with smaller PAHs [39]. At the start of the reaction, a large number of particles are produced. These particles collide to produce larger spherical particles, which then aggregate into final carbon black clusters. The particles are converted into amorphous Carbon and a progressively more graphitic material in the furnace. This is because graphite is the

most thermodynamically stable form of carbon. With a long residence time, it is believed that aggregate growth occurs as a result of fusion among primary particles [210].

Herbinet et. al [211] found the production of hydrogen, methane, ethane, 1,3 butadiene and 1-alkenes from ethylene to 1 undecene in the thermal decomposition of n-dodecane in a jet stirred reactor at temperatures from 793 K to 1093 K, for residence times between 1 and 5 seconds at atmospheric pressure. For higher temperatures and residence time's acetylene, allene, propyne, cyclo-pentene, 1, 3 cyclo-pentadiene and aromatic compounds from benzene to pyrene through naphthalene were also observed by the author.

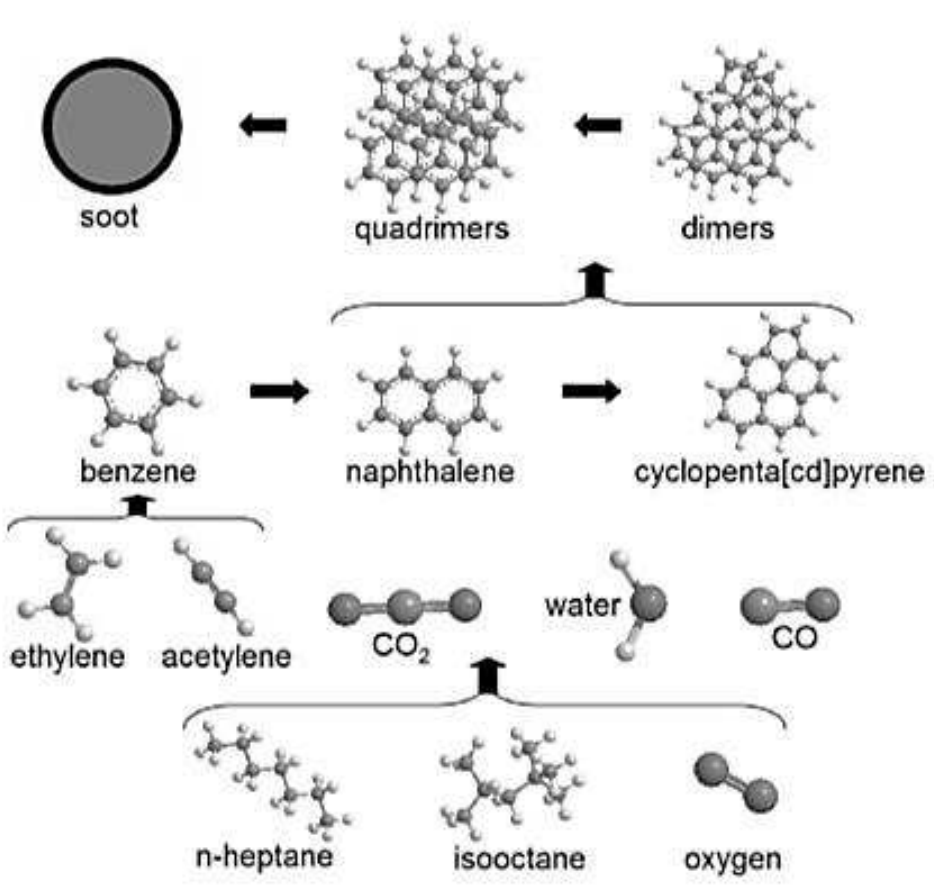

Figure B.1 Sketch of the main pathways from the fuel components to the formation of the first soot particle [212]

The chemical mechanism, depicted in Figure B.1 describes the decomposition of the different molecular components, the oxidation of the smaller species, and the formation of larger hydrocarbon molecules.

The processed involved in PAH and soot formation are summarised as in [39]:

- Formation of molecular precursors of soot- the molecular precursors of soot are thought to be heavy PAHs of molecular weight 500 - 1000 amu. The growth process from small molecules such as benzene to larger and larger PAH appears to involve both addition a C_2, C_3 or other small units, among which acetylene has received much attention, to PAH radicals, and reactions among the growing aromatic species, such as PAH–PAH radical recombination and addition reactions. The relative contribution of the different types of growth reactions seems to depend on the fuel. In the case of aromatic fuels such as benzene, acetylene and other active reactants for aromatics formation are formed in relatively large concentrations in the breakdown of the fuel, whereas in the case of aliphatic fuels such as acetylene, ethylene or methane, the first aromatic ring must be formed from fuel decomposition products by a sequence of elementary reactions in which the active ring formation reactants are in lower concentrations than in the aromatics flames.
- Nucleation or inception of particles from heavy PAH molecules- in this process mass is converted from molecular to particulate systems, i.e. heavy PAH molecules form primary soot particles with a molecular mass of approximately 2000 amu and an effective diameter of about 1.5 nm. PAH of increasing size are mainly formed by sequences of chemical reactions of radicals of smaller PAH with acetylene, PAH or PAH radicals. At some size, PAH species react with each other while individual PAH keep on growing; particle inception (nucleation) occurs.

- Mass growth of particles by addition of gas phase- After the formation of the primary soot particles their mass is increased via the addition of gas phase species such as acetylene to the PAH, including PAH radicals. PAH growth via the addition of acetylene to the initial adduct may play a significant role in the formation of larger and larger PAH, especially at high pressure and relatively low temperature. In addition molecule size may favour the stabilization of the initial PAH–C2H2 adducts and therefore their contribution to the growth process. Wang and Frenklach [213] as reviewed by Ritcher [39], addressed not only the issue of acetylene addition to PAH radicals containing up to three aromatic rings but also the formation of acenaphthalene in competition with the formation of 1-naphthylacetylene or the corresponding 1-$C_{10}H_7C_2H_2$ adduct. Another key reaction investigated by Wang and Frenklach was the second step of the H-abstraction/ C2H2-addition sequence which leads from the first to the second aromatic ring, i.e. the reaction of the 2-phenylacetylene radical followed by cyclization.
- Coagulation via reactive particle-particle collisions- Sticking collisions between particles during the mass growth process significantly increases particles size and decreases particle number without changing the total mass of soot present. Particle sizes increase further by collision of growing soot particles. Initially, colliding particles coalesce completely yielding new spherical structures while later they agglomerate into, chainlike structures [214].
- Carbonization of particulate matter - At higher residence times under pyrolytic conditions in the post flame zone, the polyaromatic material comprising the yet formed particles undergoes functional group elimination, cyclization, ring condensation and ring fusion attended by dehydrogenation and growth and alignment of polyaromatic layers. This process converts the initially amorphous soot material to

a progressively more graphitic carbon material, with some decrease in particle mass but no change in particle number.

Blanquart [212] analysed the effects of temperature between 450K to 2000K, on the prediction of soot volume fraction in flames and found that the soot model predicted a bell shaped curve. The soot volume fraction increases until a threshold temperature and then decreases as the temperature is further increased. It was found that nucleation and condensation dominate at low temperatures while growth by surface reaction is more active at intermediate to high temperatures. The chemical composition of soot particles has been investigated by considering the surface reactivity and the volumetric carbon-to-hydrogen ratio. As postulated in many soot models, the surface reactivity was shown to decrease with increasing temperature. However, the reactivity of large aggregates was found to be much larger than that of small spherical particles. On the other hand, large aggregates exhibit a larger C/H ratio characteristic of a more carbonized particle resulting from strong surface reactions.

Diesel fuels as discussed in earlier sections consist of paraffins, napthenes and aromatics. As per the references above, given the right conditions, any of these constituents can break down to form aromatics and thus PAHs.

B.1.1 Kinetic model and setup

The purpose of this study was to investigate soot formation from the pyrolysis of a kinetic model. The study is not qualitative as it is not possible to work backwards to work out the absorptivity determined earlier. The model has not being validated and is used here just as a

indicative tool. The composition of the model fuel was developed using various references found in the literature review section and the GC x GC analysis results. Kinetic mechanisms were obtained from two sources and thereafter combined to include a wider set of chemistry as will be discussed later in this section. The model fuel was input into chemical kinetics software and a chemical kinetics analysis carried out to detect the formation of soot/particulates from the pyrolysis of the fuels. The temperature and pressure profiles were modelled as polytropic process (n=1.25) as an approximation of bubble collapse using time steps of 1 microsecond as seen in Table B.2. The volume was modelled to half at each time step to try and replicate a bubble collapsing. The polytropic relationships of pressure and temperature to volume ratio are as follows:

$$p(t) = \left(\frac{V_o}{V_{(t)}}\right)^n \times p_o$$

Equation B.8

$$T(t) = \left(\frac{V_o}{V_{(t)}}\right)^{n-1} \times T_o$$

Equation B.9

Where p(t) and T(t) represents the pressure and temperature at time t seconds respectively, n is the polytropic constant, the subscript o represents the values at time 0 s, $V_o/V_{(t)}$ represents the volume ratio which double at every time step (halves with respect to the initial volume at time t= 0 s). The pressure and temperature at t= 0s were taken to be ambient i.e. 1 atm and 300 K respectively. The polytropic process was modelled up till the pressure reached 1 GPa as observed by many researchers theoretically and experimentally as the collapse pressure [215]. The polytropic constant was chosen that would link peak pressure of about 1 GPa to about 2000K temperature.

Time (s)	Temperature(t) (K)	Pressure(t) (atm)	v_0/v (t)
0.0E+00	300.00	1.00	1
1.0E-06	356.76	2.38	2
2.0E-06	424.26	5.66	4
3.0E-06	504.54	13.45	8
4.0E-06	600.00	32.00	16
5.0E-06	713.52	76.11	32
6.0E-06	848.53	181.02	64
7.0E-06	1009.08	430.54	128
8.0E-06	1200.00	1024.00	256
9.0E-06	1427.05	2435.50	512
1.0E-05	1697.06	5792.62	1024
1.1E-05	2018.15	13777.25	2048

Table B.2 Polytropic profile for the analysis of pyrolysis caused as a result of bubble collapse

The pressure and temperature time profile were entered into kinetics software which would model the pyrolysis in a gas reactor given the kinetic reaction mechanism and thermodynamic input file. The software allows simulation of both transient and steady-state reactor systems. For transient systems, the user may specify controlling conditions that vary as a function of time. The programme requires an input gas-phase kinetics reaction file and a corresponding thermodynamics file containing the thermodynamics data for species present in the reaction file. The thermodynamics file contains: the species identification information; its phase; 7 coefficient polynomials at two temperature ranges for fitting the Cp_o / R, H_o / RT and S_o / R equations in the kinetics.

Researchers from the Massachusetts Institute of Technology MIT have carried out detailed modelling of soot particles with diameters of up to 0.7 nm and provided chemical reaction mechanisms files for atmospheric pressure conditions taking into account pressure dependence of chemically activated reactions. The model is discussed in detail in [216] by

Richter et. al and used by Ergut et. al [217] in flame conditions. Their model is presented on a website link [218]. To gain more quantitative insight, detailed reaction networks describing the formation and depletion of PAH have been extended to particle formation. Most mechanisms are based on the above outlined scheme, i.e., they assume PAH of a certain size to be soot nuclei. However, also rapid polymerization of acetylene was advocated as route leading to carbon structures of increasing size. Two major concepts have been applied: the method of moments and the sectional approach. In the discrete sectional technique, the particle ensemble was divided into classes (BINs), properties such as mass, the numbers of carbon and hydrogen atoms are averaged within each section. The word BIN here refers to soot particles and not class sizes as in the distributions in chapters 6-7. An appealing feature of the sectional approach is the similarity of the description of gas phase and aerosol chemistry, they are directly coupled and are both written in the common form $A + B \rightarrow C + D$. The main objective of the creators of this mechanism was to provide a reliable predictive tool for PAH and soot based on a realistic understanding of the formation process. They have not made any steady state assumptions in the kinetic model. Further references and information of this reaction mechanism can be found on [216]. This chemical kinetic mechanism however does not include paraffins. It is solely based on the formation of poly aromatic compounds from aromatics. The mechanism also had very large compounds of soot formed as a result of aggregation and this could not be supported by the software version used. They were removed from the kinetic code and thus this would mean only small emerging soot particles will be considered. In order to concentrate solely on pyrolysis process and not oxidation as this was not a flame condition, oxygenated compounds in the mechanism were removed. This included any oxygen containing species and reactions.

A separate reaction mechanism for the pyrolysis of n-hexadecane to aromatics was obtained from Olivier Herbinet at Nancy. The author is found in reference [211]. He was unable to provide us with the mechanism found in the reference however he was kind enough to generate a model for the pyrolysis of n-hexadecane using EXGAS. This initially did not have any aromatics formation in it however the author was once again kind enough to add the chemistry leading to the formation of aromatics.

This reaction mechanism from Nancy was combined with the mechanism from MIT carefully. The reaction files were checked to identify identical species and reactions in both files. Any duplication was removed from the NANCY mechanism before they were both merged. The thermodynamic data was then compared and combined eliminating species that had been previously removed keeping constant care that the property data was consistent.

The combined NANCY-MIT chemical reaction file was then used with the corresponding thermodynamic data of the species to perform the modelling. The combined file consisted of 447 different gas phase species and 3796 possible gas phase reactions for these species. A set of the original and merged mechanisms and their thermodynamic data is provided in the supplementary CD pack.

The detailed kinetic model describes the formation and consumption of PAH and soot developed by MIT now includes hexadecane pyrolysis species and reactions. In the mechanism large PAH and carbonaceous particles with diameters of up to ~70nm are defined as classes (BINs) covering given mass ranges. BIN radicals are denoted by BINJ are formed by Hydrogen abstraction from the parent BIN molecule. Classes (BINs) of very large PAH and of particles covering certain mass ranges have been defined. The average molecular mass

and the number of carbon and hydrogen atoms are assigned to each BIN. Characteristics of the BINs are given in Table B.3. Diameters have been determined based on the assumption of spherical structures and a density of 1.8 g/cm^3. BINs 4 and larger are considered as ‘‘particles’’ while BINs 1 to 3 are conceptually treated as ‘‘large PAH.’’ This description is consistent with the definition of species with a molecular mass of 2000 amu and a diameter of 1.5 nm as primary soot particles and the definition of soot as ‘‘unextractables’’ in the case of gravimetric determination of its concentration [216].

BIN	Mass (amu)	C_xH_y	Diameter (nm)	H/C
1	201–400	C24H12	0.85	0.500
2	401–800	C48H24	1.07	0.500
3	801–1600	C96H48	1.34	0.500
4	1601–3200	C193H84	1.69	0.435
5	3201–6400	C388H144	2.13	0.371
6	6401–12,800	C778H264	2.68	0.339

Table B.3 Definition of classes of molecules (BINs) describing large PAH molecules and soot particles [216].

As mentioned earlier, due to the capability of the older freeware version of Chemkin not being able to handle large mass species, BINs larger than BIN6 have been eliminated and thus the analysis will show the formation of smaller soot particles of diameters between 1.69 - 2.68 nm, and very large PAHs.

The model fuel constituents are described in Table B.4. The table shows reactant names as present in the kinetic mechanism. The process was modelled to be a transient case. The polytropic pressure and temperature model were varied in time steps of 1 microsecond (Table B.2) with the fuel reactants being input as seen in Table B.4 and results obtained.

Model fuel		
Class	Reactants	Number of moles
Paraffins (75% v/v)	C16H34-1 (n-hexadecane)	0.75
Mono- aromatics (20% v/v)	C8H10 (Ethyl-Benzene)	0.1
	C6H6 (Benzene)	0.03
	C7H8 (Toluene)	0.01
	Indane	0.03
	Indene	0.03
Di-aromatics (4% v/v)	C10H8 (Naphthalene)	0.01
	A2CH3-1 (Methyl-naphthalene)	0.02
	C12H10 (Biphenyl)	0.005
	A2R5 (Acenaphthylene)	0.005
Tri(+) aromatics (1% v/v)	A3L (Anthracene)	0.002
	Pyrene	0.003
	A3 (Phenanphthrene)	0.004
	A4 (Tetraphene)	0.001

Table B.4 The constituents of the model diesel fuel used to model the formation of soot particulates under pyrolysis.

B.1.2 Model results

The results here are based on kinetic modelling carried out using the aurora code of Chemkin software package using the polytropic pressure and temperature profile with respect to 1 μs time steps described in Table B.2, the diesel fuel model in Table B.4, the modified chemical reaction database and modified thermodynamic data files. The reaction files are provided in a separate CD attached herewith. The CD contains the NANCY and MIT mechanisms and the combined mechanism used in the modelling here.

Changes in mole fractions as a result of the polytropic modelling can be seen in Figure B.2 - Figure B.5, and the percentage changes in species with respect to their initial mole fractions can be found in Table B.5.

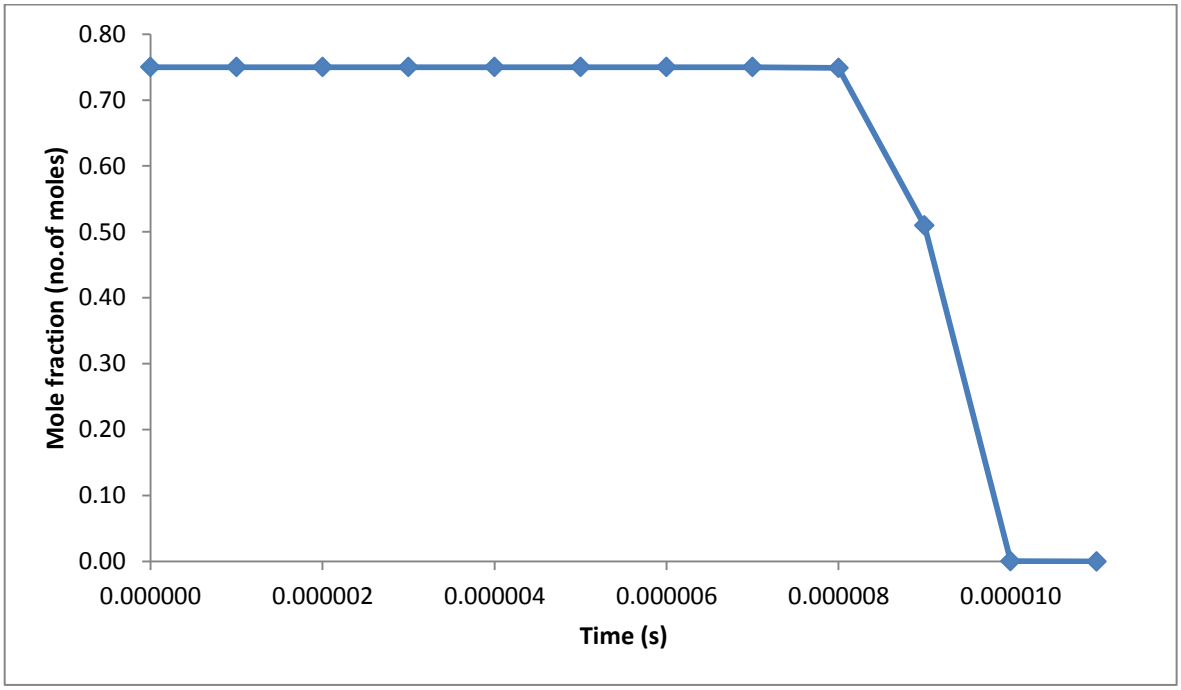

Figure B.2 Change in mole fractions of Paraffins

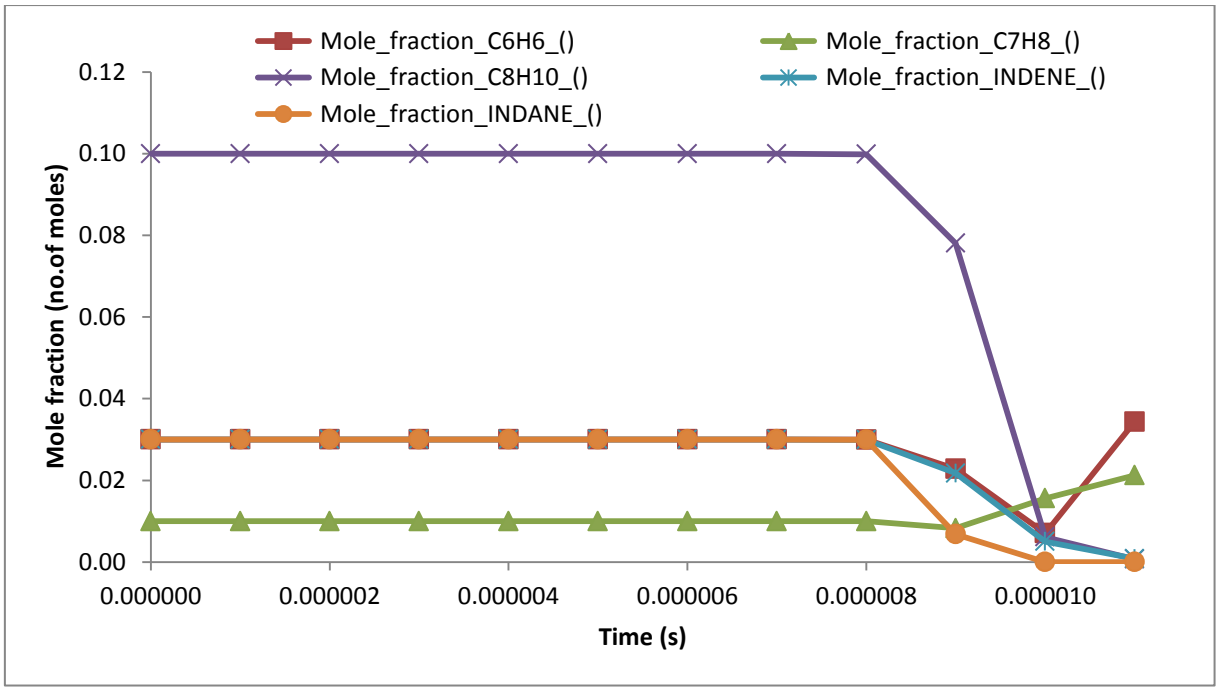

Figure B.3 Change in mole fractions of mono aromatics present in the model fuel

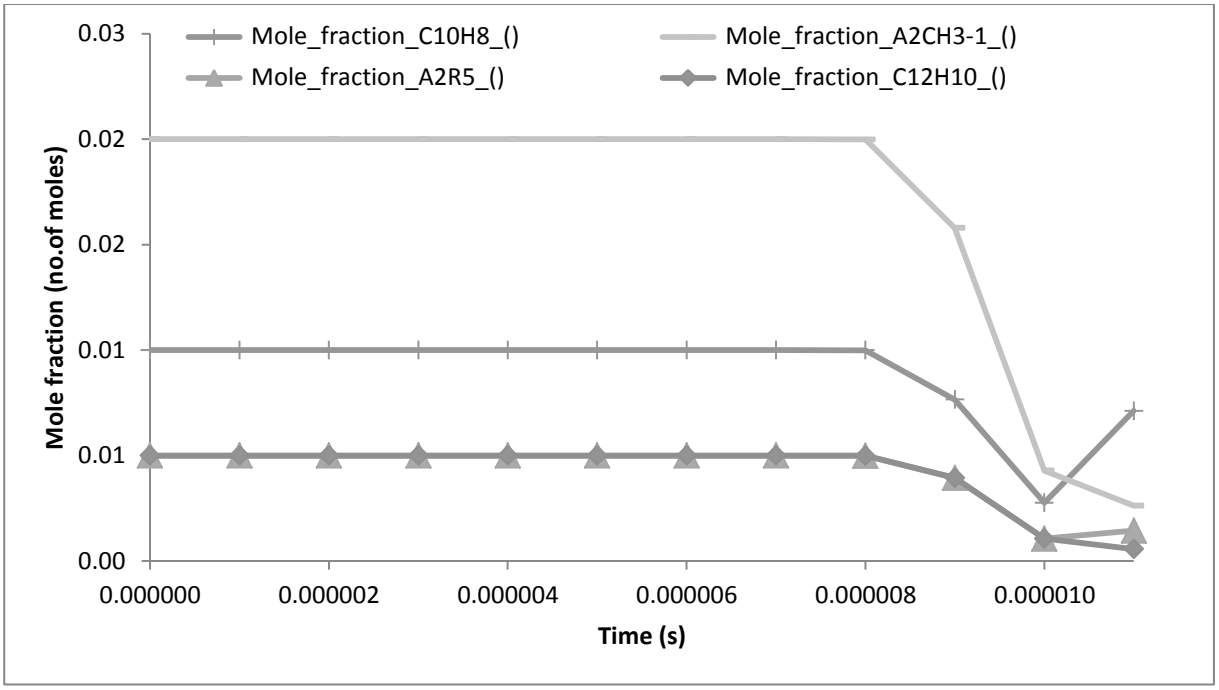

Figure B.4 Change in mole fractions of di- aromatics present in the model fuel

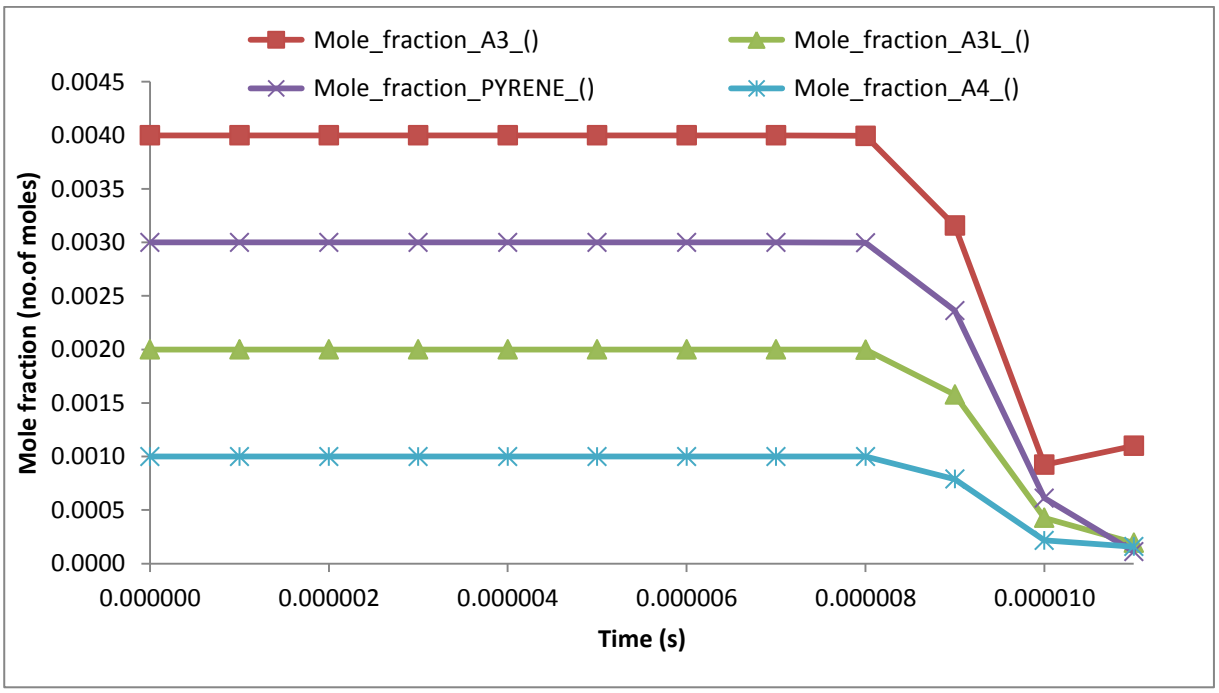

Figure B.5 Change in mole fractions of tri (+) aromatics present in the model fuel

Model fuel		
Class	Reactants	Percentage change in moles decrease/increase (%)
Paraffins (75% v/v) Overall change 38.69%	C16H34-1 (n-hexadecane)	100.00 / 0
Mono- aromatics (20% v/v) Overall Change 72.41%	C8H10 (Ethyl-Benzene)	99.30 / 0
	C6H6 (Benzene)	76.51 / 387.2
	C7H8 (Toluene)	17.35 / 157.1
	Indane	100.00 / 0
	Indene	97.35 / 0
Di-aromatics (4% v/v) Overall change 41.257%	C10H8 (Naphthalene)	72.35 / 157.3
	A2CH3-1 (Methyl-naphthalene)	86.86 / 0
	C12H10 (Biphenyl)	88.54 / 0
	A2R5 (Acenaphthylene)	78.68 / 35.16
Tri(+) aromatics (1% v/v) Overall change 38.75%	A3L (Anthracene)	90.29 / 0
	Pyrene	96.27 / 0
	A3 (Phenanthrene)	76.90 / 18.99
	A4 (Tetraphene)	84.22 / 0

Table B.5 Percentage change species mole fractions present in the model fuel with respect to the initial mole fractions present

As seen in the figures above displaying the changes in mole fraction of species present in the model diesel fuel, changes only start occurring after 8 µs due to the temperature and pressure aft this point being high (past 1000K and 1700atm). Hence the graphs start changing post 8 µs. The highest overall changes occurred in the mono-aromatics and di-aromatics species present in the model fuel. Some of the species present show a sudden increase in mole fraction in the last two time steps i.e. Benzene, toluene, naphthalene, acenaphthylene and phenanthrene, as observed in Figure B.2 - Figure B.5. In Table B.5, the percentage decrease has been calculated with respect to the minimum mole fraction reached and the mole fraction of the species at the start. The percentage increase has been calculated between the minimum mole fraction reached and the following increase in mole fractions of species in the following

time step as observed in the graphs. An increase in mole fraction of the species occurs if the rate of production of the species is higher than its rate of consumption. Hexadecane and Indane are totally consumed as shown in the table. These results however do not show the full picture. The changes overall changes occurring may be high but the detail of the species break down and, their rate of productions and consumption and furthermore, the pathway leading is leading to the formation of the BIN (Soot) particles is important.

The classification of the BIN classes 1 - 6 is described in Table B.3. Table B.6 shows the increase in BINs with time due to the polytropic model of bubble collapse. Mole fractions of all BINs are increasing with time showing formation of large PAHs and particles. There are particulates forming at lower temperature and pressures however they are in very small amounts as seen in the table.

Time (s)	Temperature (K)	Pressure (atm)	Mole fractions of BINs					
			BIN1	BIN2	BIN3	BIN4	BIN5	BIN6
0	300.00	1.00	0.00E+00	0.00E+00	0.00E+00	0.00E+00	0.00E+00	0.00E+00
1.00E-06	356.76	2.38	3.68E-53	9.06E-61	1.16E-110	8.14E-157	3.35E-203	8.90E-250
2.00E-06	424.26	5.66	6.50E-43	7.93E-51	2.81E-91	2.29E-128	1.09E-165	3.31E-203
3.00E-06	504.54	13.45	3.66E-34	2.42E-42	1.54E-74	1.07E-103	4.29E-133	1.10E-162
4.00E-06	600.00	32.00	1.39E-26	5.71E-35	7.38E-60	5.59E-82	2.44E-104	6.80E-127
5.00E-06	713.52	76.11	1.49E-20	4.76E-29	6.79E-48	3.22E-64	7.84E-81	1.07E-97
6.00E-06	848.53	181.02	1.49E-15	1.34E-23	1.80E-37	5.50E-49	8.73E-61	7.87E-73
7.00E-06	1009.08	430.54	1.38E-11	3.38E-18	1.54E-18	4.61E-19	5.91E-20	1.08E-21
8.00E-06	1200.00	1024.00	9.56E-08	3.90E-13	1.84E-18	4.87E-19	2.10E-19	4.74E-21
9.00E-06	1427.05	2435.50	1.01E-05	4.24E-09	5.74E-13	9.00E-15	7.77E-17	4.03E-19
1.00E-05	1697.06	5792.62	1.87E-05	4.54E-07	2.01E-09	1.05E-09	3.18E-10	6.32E-11
1.10E-05	2018.15	13777.25	9.55E-04	1.37E-04	1.36E-06	1.72E-06	3.66E-07	5.27E-06

Table B.6 Increase in mole fractions of BINs 1-6 with reaction time

The analysis that proceeds was carried out by the analysis of the rate of production of species function in software. This analysis also provided the chemical equation breakdown of the

production or the consumption of all the species. Hexadecane started to break up at a time early on between 1-4 µs to a variety of C_nH_{2n+1} (n=3 to 16), ethyl (C2H5) and methyl (CH3) radicals. The hexadecane at later time steps reacted with previously formed methyl radicals, via hydrogen subtraction to form Methane (CH4) and large $C_{16}H_{33}$ radicals. These breakdown reactions were sustained up till 7 µs at which the hexadecane further broke up into propane (C3H8), butane (C4H10) and large $C_{16}H_{33}$ radicals by reacting with previously formed propyl and butyl radicals (at 4 µs). It carried on its breakdown at the next time step further more into ethane (C2H6) by hydrogen subtraction when reacting with ethyl radicals. During the final time step hexadecane reacted with hydrogen radicals formed during various preceding reactions to form hydrogen and large C16 radicals. At 10 µs, the radicals would break down into ethylene (C2H4) and methyl radicals. Ethylene would further break down into acetylene (C2H2) by hydrogen subtraction Equation B.10. The radicals would also disintegrate to form olefins and furthermore radicals as in Equation B.11. At this stage we have only gone through the break up regime of the hexadecane molecule over the polytropic analysis, however as further outcomes occur due to the breakup of the rest of the species present in the initial model fuel further analysis will be made.

C3H7 radical→ CH3 + C2H4

C4H9 radical → C2H5 +C2H4

C2H4 + M → C2H2 +H2 +M

Equation B.10

C16 Radical→C4 radical + dodecene

Equation B.11

In summary, the paraffins broke down to form smaller chained paraffins and olefins, and various radicals. Larger radicals were formed back to paraffins and olefins by hydrogen subtraction and larger radical break up. So far the presence of these compounds has not found any direct link to the formation of BIN class compounds.

Analysis of the mono-aromatics found that ethyl-benzene broke down to form benzyl C7H7 and methyl radicals; and butynyl radicals. Further on, reactions between Benzene and ethyl radicals led to the formation of ethyl-benzene. Towards the end of the time steps the ethyl-benzene via hydrogen subtraction produced benzothiophene C8H9 by hydrogen subtraction, a heterocyclic compound with one benzene ring and one cyclo-pentene ring. At higher residence time the reverse process took place and ethyl benzene was formed. Reactions between benzene and ethyl radicals, and 2 butynyl radicals lead to the formation of ethyl benzene at higher residence times. The rate of consumption was preceded by its formation and thus between the last two time steps, ethyl-benzene mole fraction increased. Of the aromatic compounds, benzene underwent the largest amount of change in terms of breaking down into various other species. The reaction leading to formation of BINs is the formation of the phenyl group C6H5 and methane via the hydrogen subtraction reaction of benzene and methyl radicals. Phenyl reacts with benzyl radicals (C7H7) formed by the breakup of ethyl benzene to form benzyl benzene (C13H12). Benzene reacts with methyl radicals formed during hexadecane break up to form toluene. It also broke down to form C4H5 and acetylene which at higher residence time saw the reverse process dominate and more benzene being produced. The phenyl radical later reacts with acenaphthylene (A2R5) to form BIN1 particles. Furthermore reactions in di-aromatic naphthalene with methyl radicals form 1- and 2-naphthylacetylene which is another precursor onto formation of BIN particles. It reacts with biphenyl, acenaphthylene, pyrene, phenanthrene already present in the model diesel to form

these particles. Methyl-naphthalene is another precursor to forming naphthylacetylene. Phenyl is also another soot precursor as it leads to the formation of larger BIN classes by reactions with smaller BIN classes. Reactions between phenyl and biphenyl have also lead to the formation of BIN compounds. Naphthylacetylene species start forming at 5 μs and continue till the end of analysis by the reaction:

$$C10H8+CH3 \rightarrow \text{Naphthylacetylene} + CH4$$

Equation B.12 The formation of BIN precursor naphthylacetylene from naphthalene

Naphthylacetylene also reacts with aromatics present to form larger PAHs i.e. fluoranthene (C16H10), benzo[k]fluoranthene (C20H12), benzo[a]fluorene (C17H12) and perylene (C20H12). An increase in benzene production over its consumption was observed at higher residence times. Reactions between benzene and naphthylacetylene form fluoranthene and phenylnapthalene (C16H12).

The production of BIN1 radicals started at lower residence time (5 μs) due to reactions between acenaphthylene and biphenyl with phenyl radicals; acenaphthylene, phenantherene, pyrene with naphthylacetylene.

The other precursor C6H5 is formed from reactions between benzene and methyl radicals as seen in Equation B.13

$$C6H6+CH3 \leftrightarrow C6H5+CH4$$

$$C6H6+C2H5 \leftrightarrow C6H5+C2H6$$

$$C7H7+C6H6 \leftrightarrow C7H8+C6H5$$

$$C12H10+CH3 \leftrightarrow C7H8+C6H5$$

Equation B.13 The formation of C6H5 from benzene and naphthalene

C6H5 reactions have led to the formation of fluoranthene, benzyl benzene (C13H12), styrene (C8H8) and phenyl naphthalene (C16H12) and other smaller PAH.

The decomposition of aromatics has also shown production of smaller alkane hydrocarbons. This may however be different if other constituents of aromatics were present and the presence of other paraffins and olefins in the reaction file. One downfall of the combined kinetic mechanism reaction file is that it does not include a lot of large paraffins and olefins which are present in diesel fuels and thus the pathways to their formation is unavailable. However from whatever species present, breakdown in aromatics has shown formation of small paraffins.

A2R5(Acenanaphthalene)+C6H5→ 7.50E-01BIN1+ 1.50H2+H

A2R5+ Naphthylacetylene → 9.17E-01BIN1+ 1.50H2+H

C12H10+C6H5→ 7.50E-01BIN1+ 2.50H2+H

C12H10+ Naphthylacetylene → 9.17E-01BIN1+ 2.50H2+H

A3+ Naphthylacetylene →BIN1+2H2+H

PYRENE+ Naphthylacetylene → 1.08BIN1+ 1.50H2+H

Equation B.14 Formation of BINs by reaction between PAH and naphthylacetylene and phenyl

Increase in BIN classes has been caused by reactions by lower BIN classes with naphthylacetylene, phenyl or methyl naphthalene. Reactions of PAH species with the lower BIN radicals has also led to the formation of the lower BIN radicals and BIN radicals of the next class via hydrogen subtraction from the PAH and PAH break down.

BIN1+H→BIN1J+H2

BIN1→BIN1J+H

Equation B.15 Formation of BINJ radicals from BIN

C6H5+BIN1→ 7.50E-01BIN1+ 2.50E-01BIN2+ 5.00E-01H2

Naphthylacetylene +BIN1→ 5.83E-01BIN1+ 4.17E-01BIN2+ 5.00E-0H2 +H

C6H6+BIN1J→ 7.50E-01BIN1+ 2.50E-01BIN2+ 5.00E-01H

C10H8+BIN1J→ 5.83E-01BIN1+ 4.17E-01BIN2+ 5.00E-01H

A2CH3-1+BIN1J→ 5.42E-01BIN1+ 4.58E-01BIN2+ 1.25H2

A2R5+BIN1J→ 5.00E-01BIN1+ 5.00E-01BIN2+H

C12H10+BIN1J→ 5.00E-01BIN1+ 5.00E-01BIN2+H2+H

A3+BIN1J→ 4.17E-01BIN1+ 5.83E-01BIN2+ 5.00E-01H2+H

A3L+BIN1J→ 4.17E-01BIN1+ 5.83E-01BIN2+ 5.00E-01H2+H

PYRENE+BIN1J→ 8.33E-01BIN2+H

A4+BIN1J→ 8.75E-01BIN2+ 5.00E-01H2+H

Equation B.16 Formation of higher BIN classes from BIN and BINJ radicals

The presence of tri(+) aromatics in the diesel fuel was not crucial to the formation of BIN particles as reactions between mono- and di- aromatics present in the fuels with each other or the phenyl and naphthylacetylene have led to the formation of large PAHs and thus BINs. In the reactions seen in Equation B.16 and Equation B.14, most of them are reactions of mono- and di- aromatics with precursors. The formation of very large BINs i.e. BIN6 was formed by reactions of BIN5 with phenyl and naphthylacetylene and napthylvinyl, the later to have been formed by reactions between methyl radicals and naphthylacetylene.

A search was carried out to find the link for the formation of aromatics from paraffins, to find out whether paraffins itself would lead to the formation of BINs through aromatics. Researchers have shown large reductions in soot formations during combustion of purely paraffins fuels such as GTL however soot formations still exist and thus however low their propensity to form soot, there must still be a link from paraffins to aromatics and thus soot

formation. Researcher at Sasol in conjunction with DaimlerChrysler have shown a reduction of up to 35% soot formation during combustion of GTL as compared to conventional diesel fuels [219]. Wu et. al [220] found a reduction in soot and particulate matter of up to 27.6 % of GTL combustion when compared to diesel fuel combustion. Results obtained from experimental investigations by Soltic et.al [221] show a reduction of soot mass by approximately 45 % obtained prior to exhaust gas treatment.

It was found that the link to formation of C6H6 from hexadecane occurred at higher residence times when the decomposition of hexadecane had led to formation of acetylene as previously mentioned. During the middle residence times large radicals formed from decomposition of hexadecane resulted in forming olefins (C16-C6) of which the formation of dodecene has been previously shown. Reactions between the olefins and methyl radicals lead to the formation of butadiene (C4H6), methane and radicals. Butadiene further reacts with methyl radicals at high residence times to form C4H5 isomers (CH//CHCH//CH2) and methane. The isomers would then react with acetylene to form benzene and hydrogen radical as seen in Equation B.17.

$$\text{DODECENE } (C_{12}H_{24}) + CH_3 \rightarrow CH_4 + \text{BUTADIENE} + \text{C8 RADICAL}$$

$$\text{BUTADIENE} + CH_3 \rightarrow C_4H_5 + CH_4$$

$$C_4H_5 + C_2H_2 \rightarrow C_6H_6 + H$$

Equation B.17

Once the benzene was formed it would react with methyl radicals to form C6H5 and methane. The C6H5 formed would open doors to various other aromatics and BINS formation at higher residence times.

$$C_6H_5 + C_6H_6 \rightarrow C_{12}H_{10} + H$$

$$C_6H_5 + C_2H_4 \rightarrow C_8H_8 + H$$

$$C_6H_5 + CH_3 \rightarrow C_7H_8$$

Equation B.18

The formation of acetylene was the key for the link for the formation of aromatics from paraffins. Another route was the formation of the vinyl radical by the reaction of C_2H_4 and C_2H_5 radicals earlier formed. The vinyl radical would break up into acetylene at higher residence time. Reaction between the vinyl radical and methyl radicals would also produce C_3H_6 which would then react with C_2H_5 to form allyl radicals. Reactions between vinyl radicals and C_4H_5 isomers would lead to the formation of benzene. Reaction between vinyl radicals (C_2H_3) would also lead in the formation of butadiene. The allyl radical could react with benzene to form the BIN precursor C_6H_5.

$$\text{Butadiene} + \text{Vinyl radical} \rightarrow C_4H_5 + C_2H_4$$

Equation B.19

C_2H_3 would be formed at higher residence times by reactions between C_2H_4 and methyl or C_2H_5 radicals. Ethynyl (C_2H) radicals were formed between reactions of acetylene and C_2H_5 radicals. Ethynyl radicals would then react with C_2H_4 radicals to form C_4H_4 and hydrogen radicals. The C_4H_4 would react with C_2H_3 formed to produce benzene. These reactions are seen in Equation B.18. This has just been a summary however they may be a lot of other possible ways to form aromatics from hexadecane.

$$C_2H_4+CH_3 \rightarrow C_2H_3+CH_4$$

$$C_2H_4+C_2H_5 \rightarrow C_2H_3+C_2H_6$$

$$C_2H_4+\text{Ethynyl radical} \rightarrow C_4H_4+H$$

$$C_4H_4+C_2H_3 \rightarrow C_6H_6+H$$

$$C_4H_4+C_2H_2 \rightarrow C_6H_6$$

$$C_4H_4+\text{Vinyl radical} \rightarrow C_6H_6+H$$

Equation B.20

In summary of the above analysis of the pyrolysis of a model diesel fuel, it can be concluded that the presence of aromatics in the fuel leads to formation of particles (BINs). The paraffins were found to breakdown into lower chained compounds and olefins and would lead into the formation of aromatic compounds at higher residence times. The kinetic mechanism employed does not include a lot of large chained paraffins and olefins and thus the breakdown into smaller chained alkanes is not clearly distinguishable. Aromatics have broken down and reacted to form smaller chained paraffins, however as earlier mentioned due to there not being a large number and variety of paraffins present in the kinetic model employed the breakdown into other paraffins is not clearly identified. The presence of aromatics presence has led to the formation of naphthylacetylene and phenyl groups which have been found as key to the formation of BIN classes. The presence and formation of these species are essential in forming larger BIN classes. Furthermore only a few out of the thousands of species present in diesel fuels has been included in this analysis. Diesel fuels vary in composition from their origin and refining and thus changes to the composition will lead to changes in the species being formed as part of the analysis. The analysis here has been carried out to obtain the bigger picture of the routes to particle formation when a diesel fuel undergoes a pyrolysis like process which has been modelled as a polytropic process. The analysis has shown the routes

to the formation of BIN (Soot) precursors which lead to the formation and growth of BIN particles.

The intention of the work here was to use a qualitative mechanism to determine the amount of soot formed from a polytropic model of a small bubble collapse and relate to the GC x GC measurements and optical absorptivity in order to check whether the indication of aromatic components leading to soot formation was viable. No validated models were available for the decomposition of diesel fuel to soot formation and thus the data available from two separate models was combined to be able to perform an indicative study of the cause of soot formation.

The work here is to check the plausibility of hydrocarbon species being subjected to pressure and temperature conditions occurring during bubble collapse, leading to soot formation. The modelling shows this and the particle counter results previously discussed support these results.

Appendix C

C.1 Nozzle Manufacturing Consistency- Calibration Charts

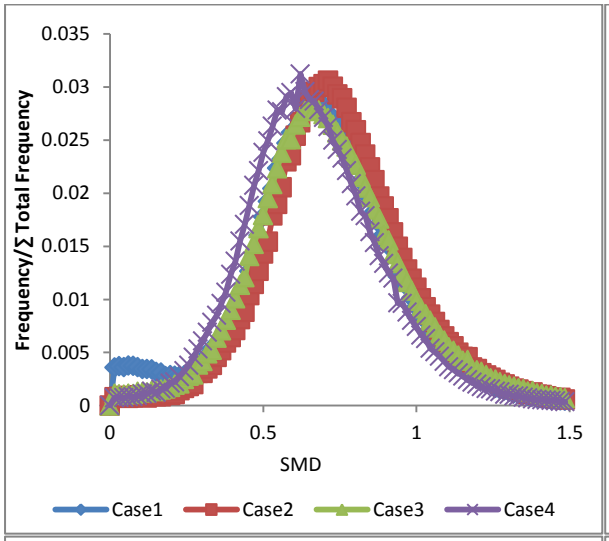

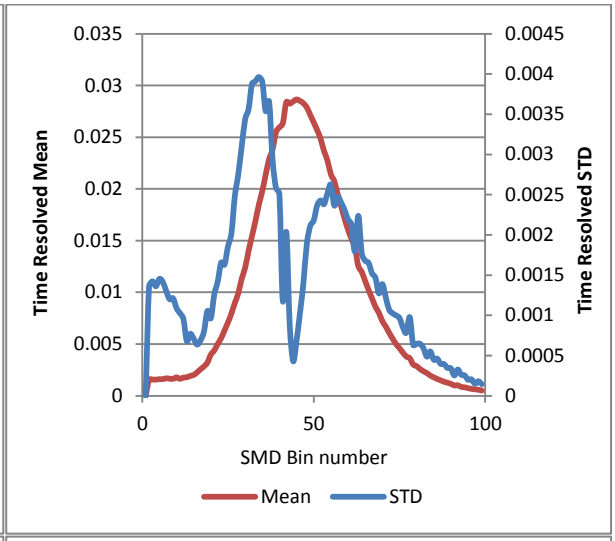

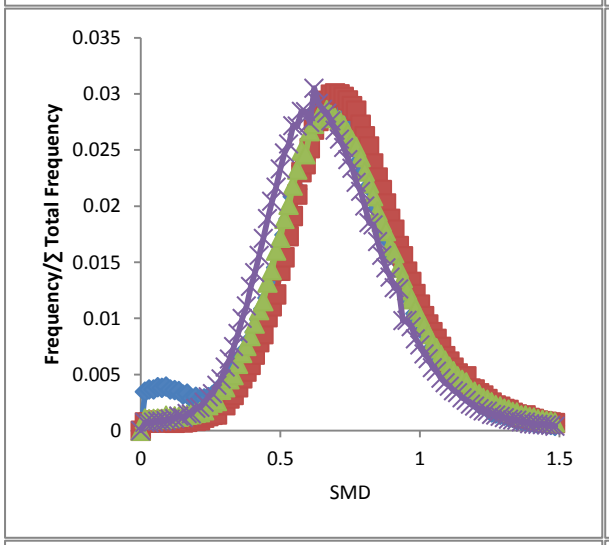

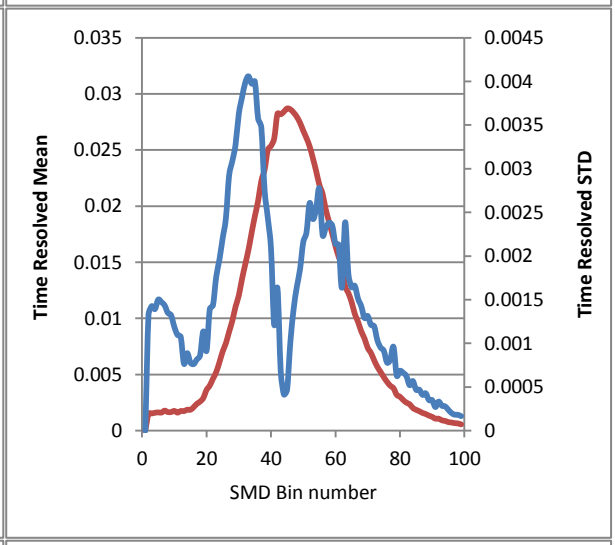

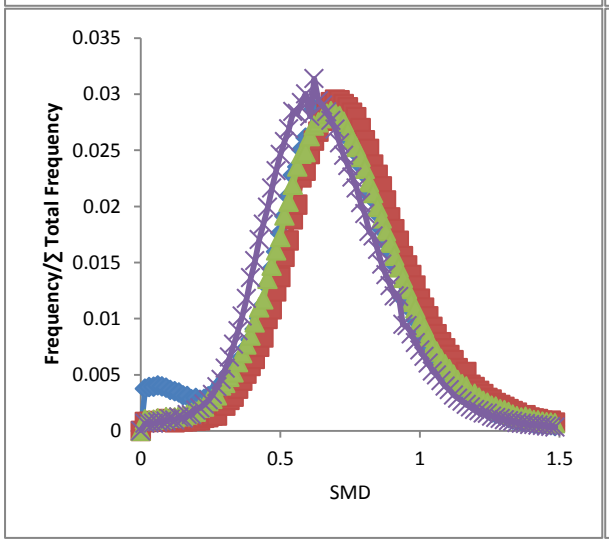

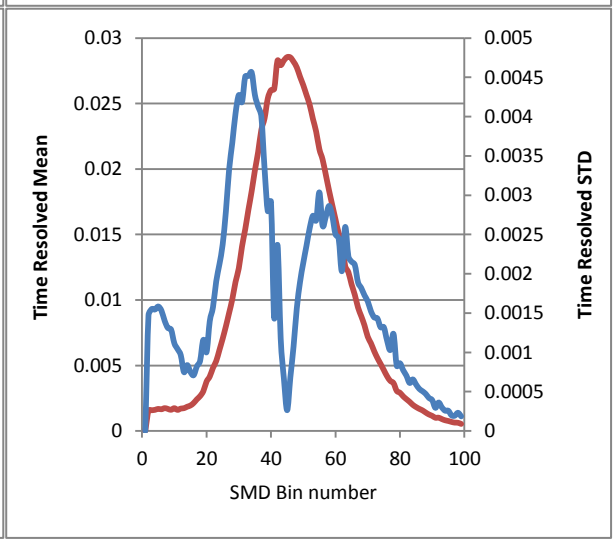

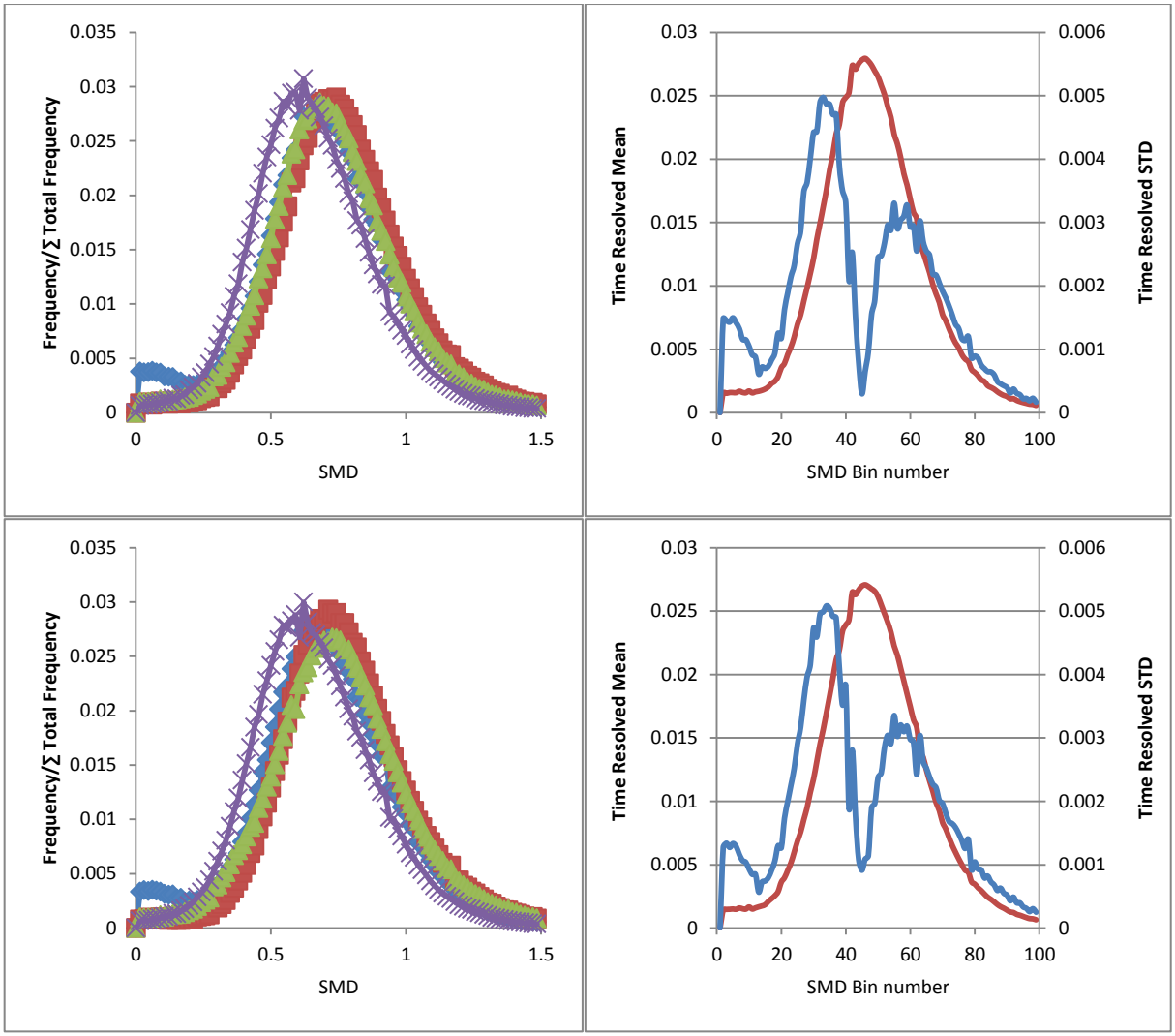

Figure C.1 Sum of BIN frequency relative SMD distributions obtained at the start of injection between 2.1 - 2.4 ms (top to bottom) for cases 1 – 4 and their corresponding mean and standard deviation

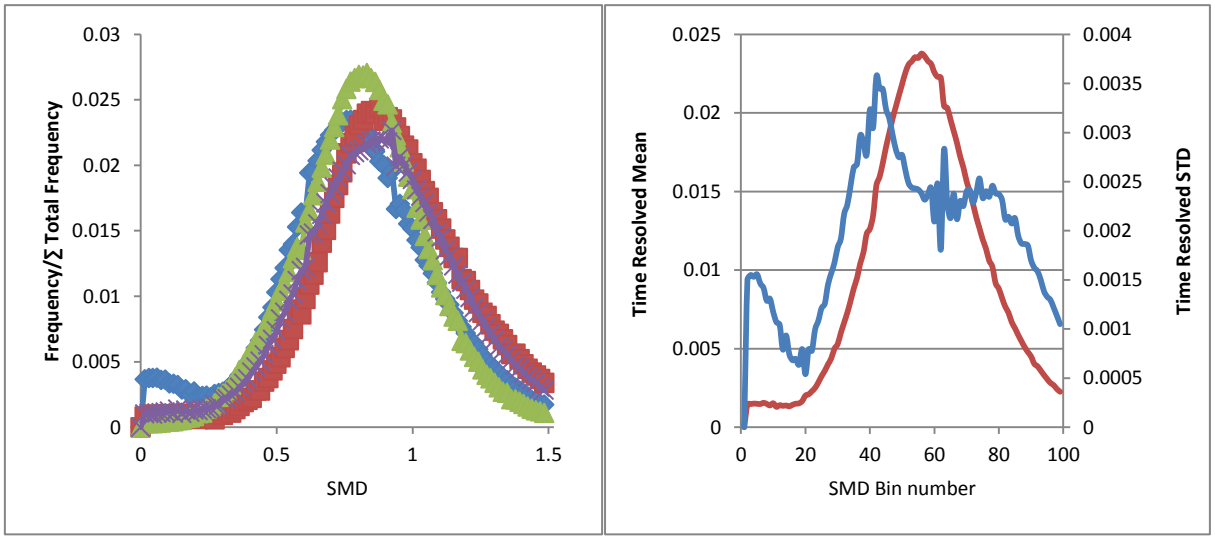

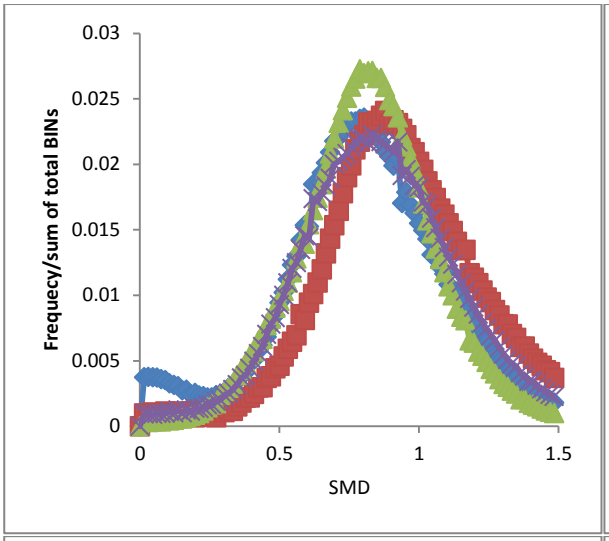
Frequecy/sum of total BINs
0.03
0.025
0.02
0.015
0.01
0.005
0
0
0.5
1
1.5
SMD

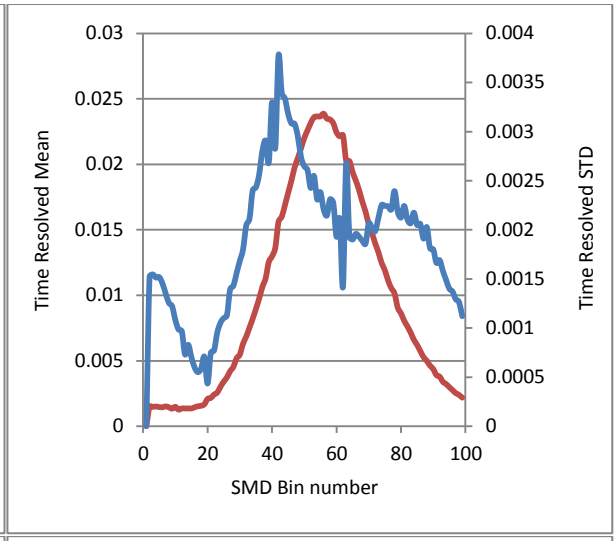
Time Resolved Mean
Time Resolved STD
0.03
0.025
0.02
0.015
0.01
0.005
0
0.004
0.0035
0.003
0.0025
0.002
0.0015
0.001
0.0005
0
0
20
40
60
80
100
SMD Bin number

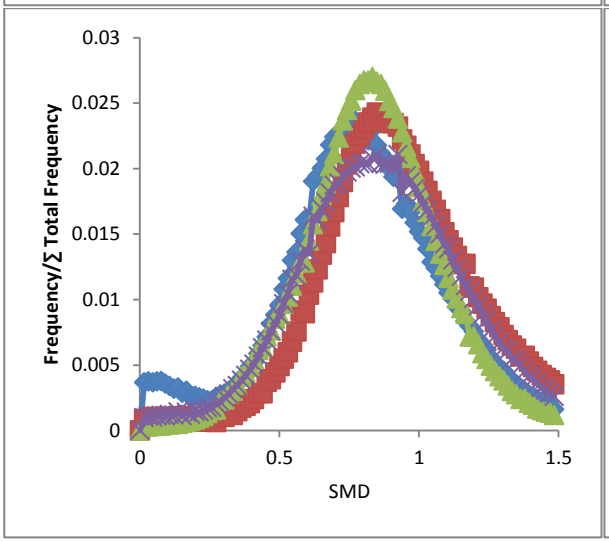
Frequency/∑ Total Frequency
0.03
0.025
0.02
0.015
0.01
0.005
0
0
0.5
1
1.5
SMD

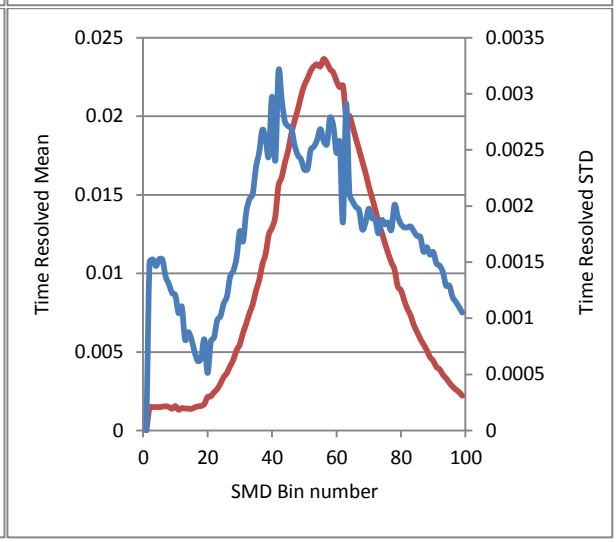
Time Resolved Mean
Time Resolved STD
0.025
0.02
0.015
0.01
0.005
0
0.0035
0.003
0.0025
0.002
0.0015
0.001
0.0005
0
0
20
40
60
80
100
SMD Bin number

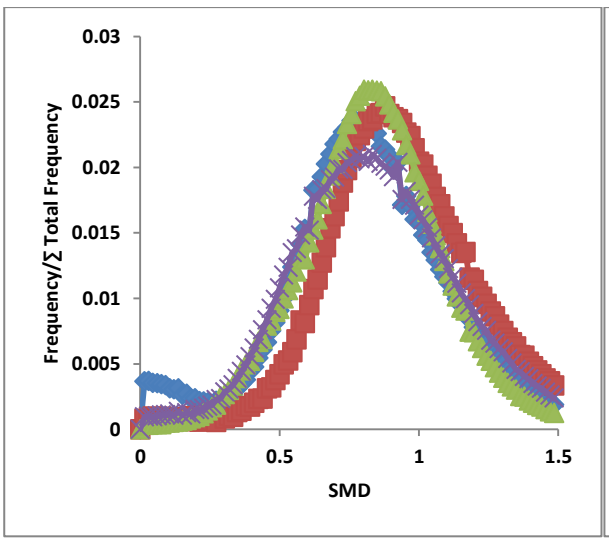
Frequency/∑ Total Frequency
0.03
0.025
0.02
0.015
0.01
0.005
0
0
0.5
1
1.5
SMD

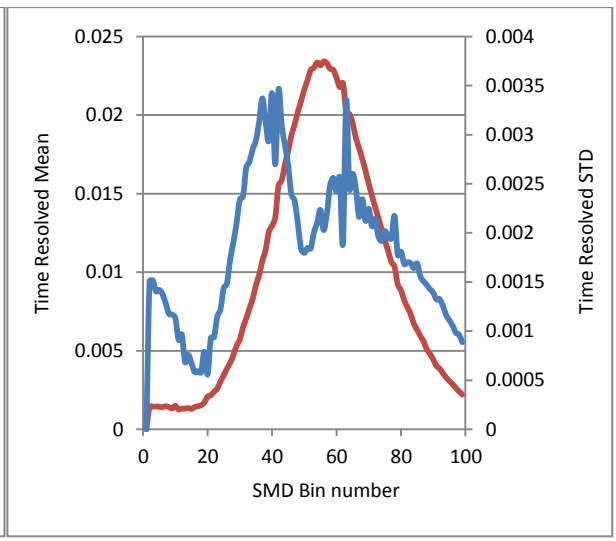
Time Resolved Mean
Time Resolved STD
0.025
0.02
0.015
0.01
0.005
0
0.004
0.0035
0.003
0.0025
0.002
0.0015
0.001
0.0005
0
0
20
40
60
80
100
SMD Bin number

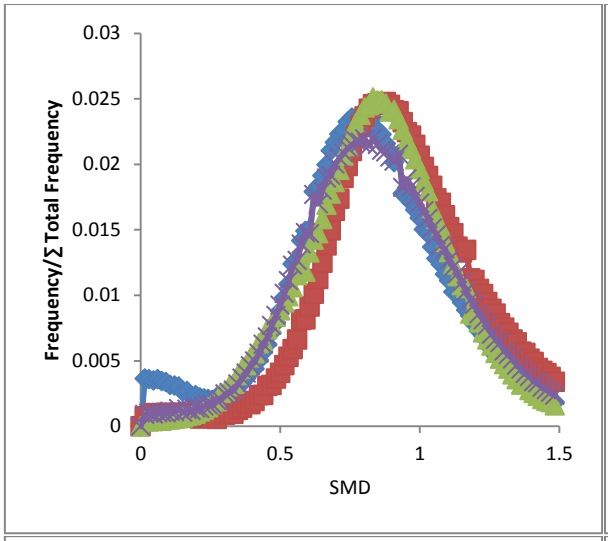
Frequency/∑ Total Frequency
0.03
0.025
0.02
0.015
0.01
0.005
0
0
0.5
1
1.5
SMD

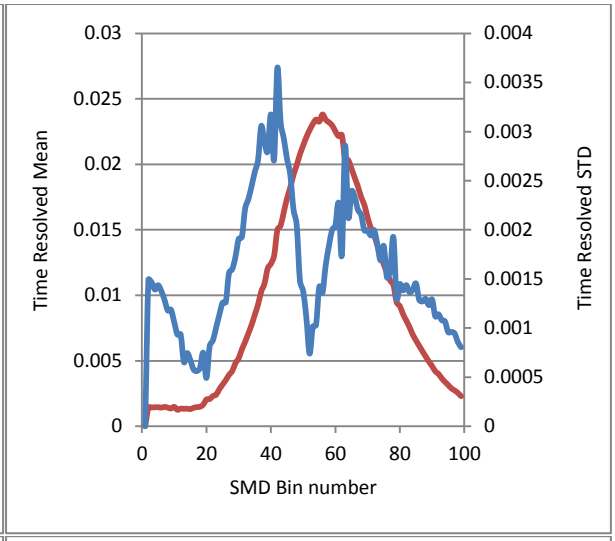
Time Resolved Mean
Time Resolved STD
0.03
0.025
0.02
0.015
0.01
0.005
0
0.004
0.0035
0.003
0.0025
0.002
0.0015
0.001
0.0005
0
0
20
40
60
80
100
SMD Bin number

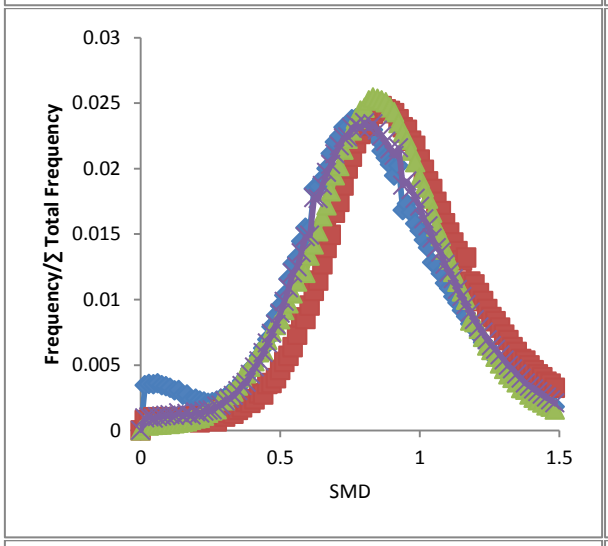
Frequency/∑ Total Frequency
0.03
0.025
0.02
0.015
0.01
0.005
0
0
0.5
1
1.5
SMD

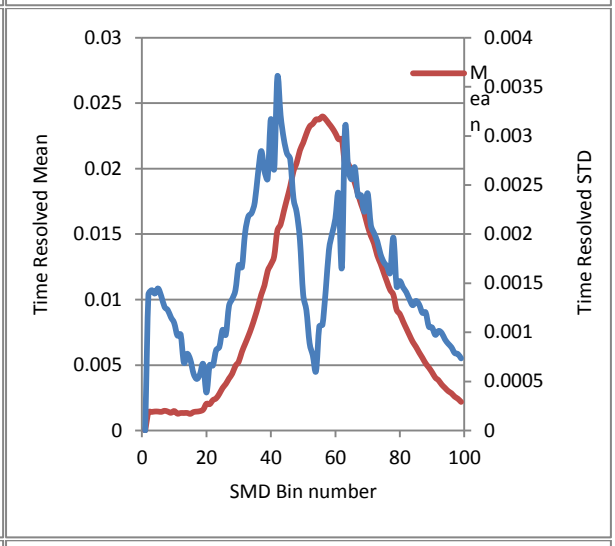
Time Resolved Mean
Time Resolved STD
Mean
0.03
0.025
0.02
0.015
0.01
0.005
0
0.004
0.0035
0.003
0.0025
0.002
0.0015
0.001
0.0005
0
0
20
40
60
80
100
SMD Bin number

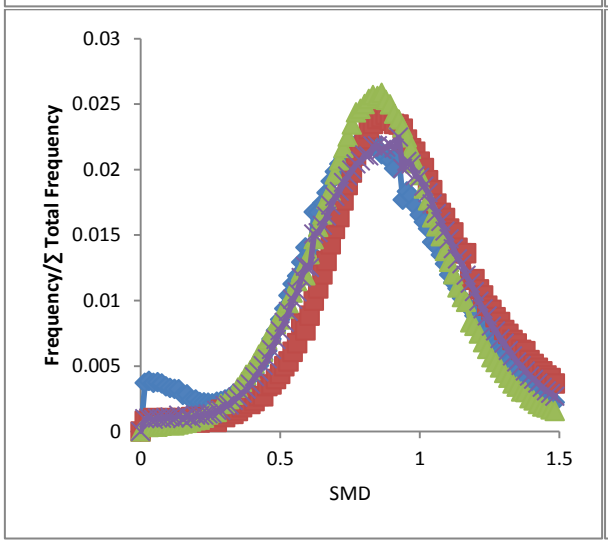
Frequency/∑ Total Frequency
0.03
0.025
0.02
0.015
0.01
0.005
0
0
0.5
1
1.5
SMD

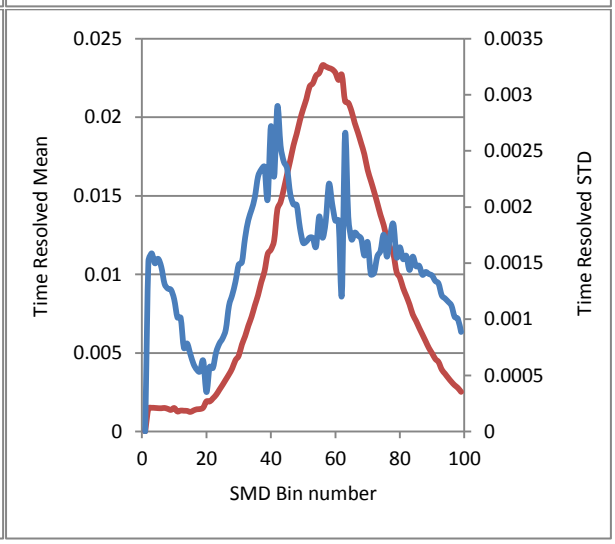
Time Resolved Mean
Time Resolved STD
0.025
0.02
0.015
0.01
0.005
0
0.0035
0.003
0.0025
0.002
0.0015
0.001
0.0005
0
0
20
40
60
80
100
SMD Bin number

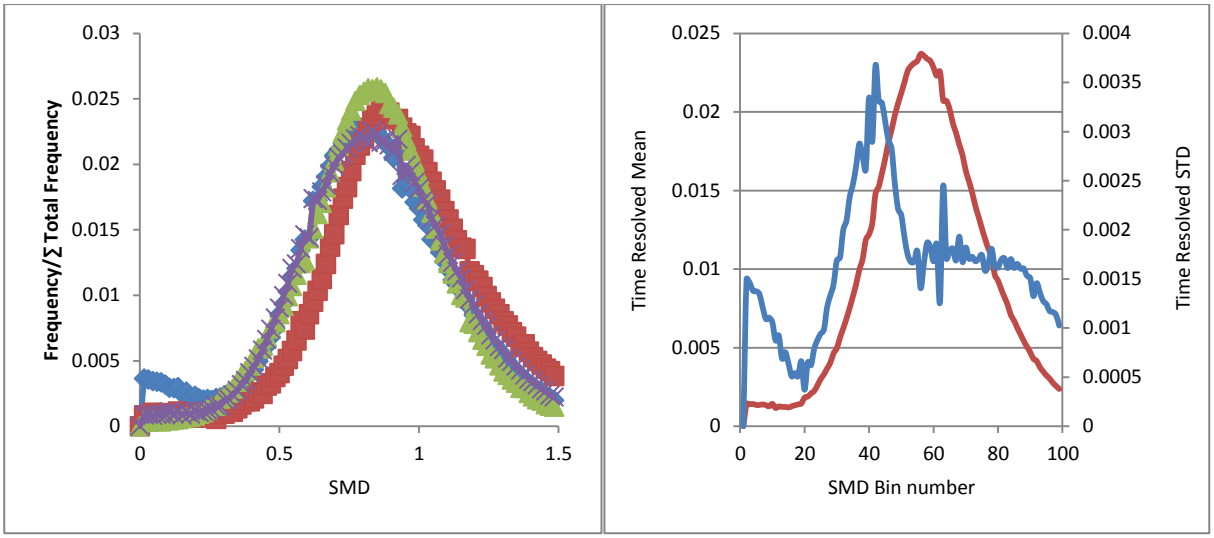

Figure C.2 Sum of BIN frequency relative SMD distributions obtained at the peak needle lift between 3.9 – 4.5 ms (top to bottom) for cases 1 – 4 and their corresponding mean and standard deviation

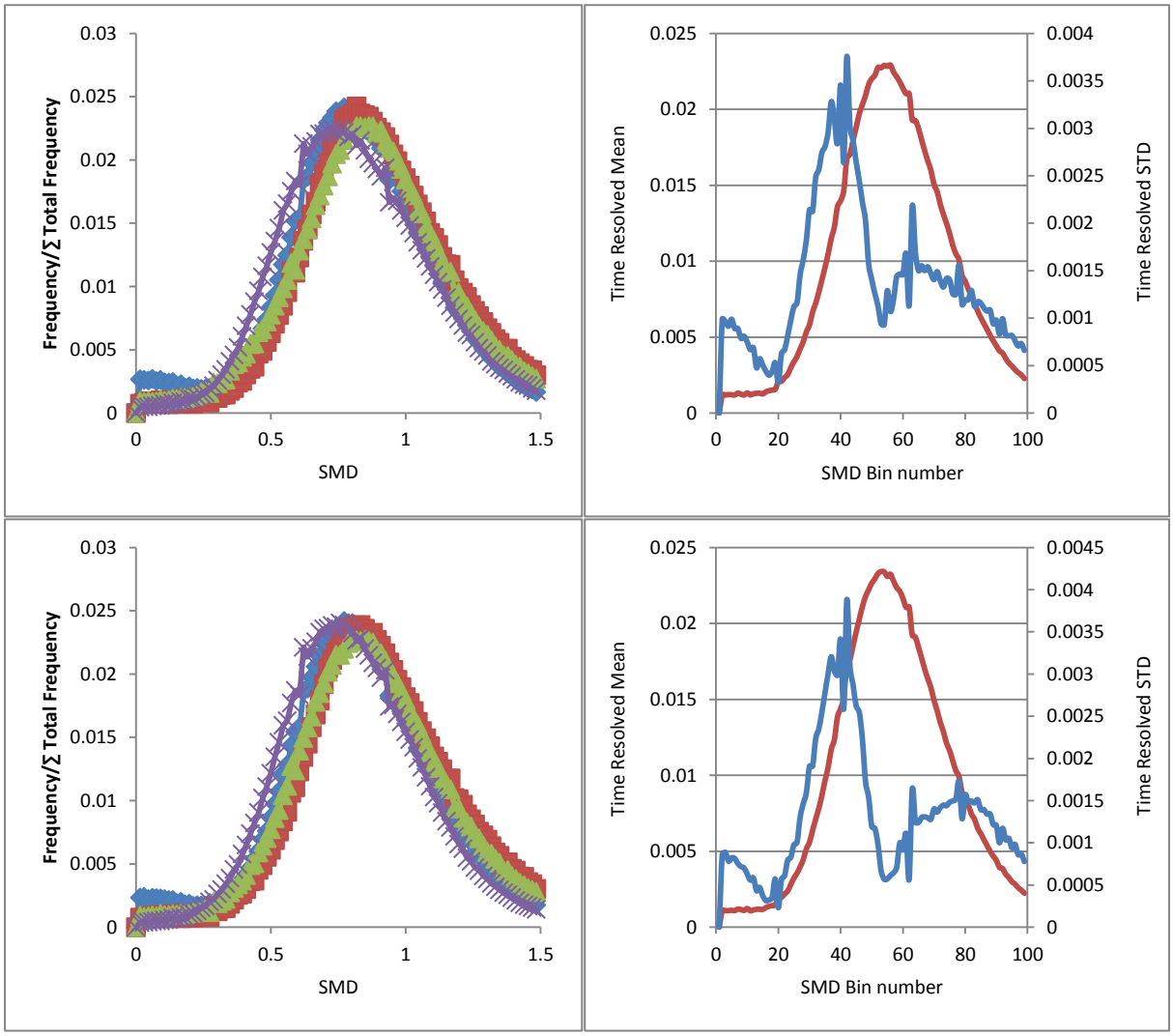

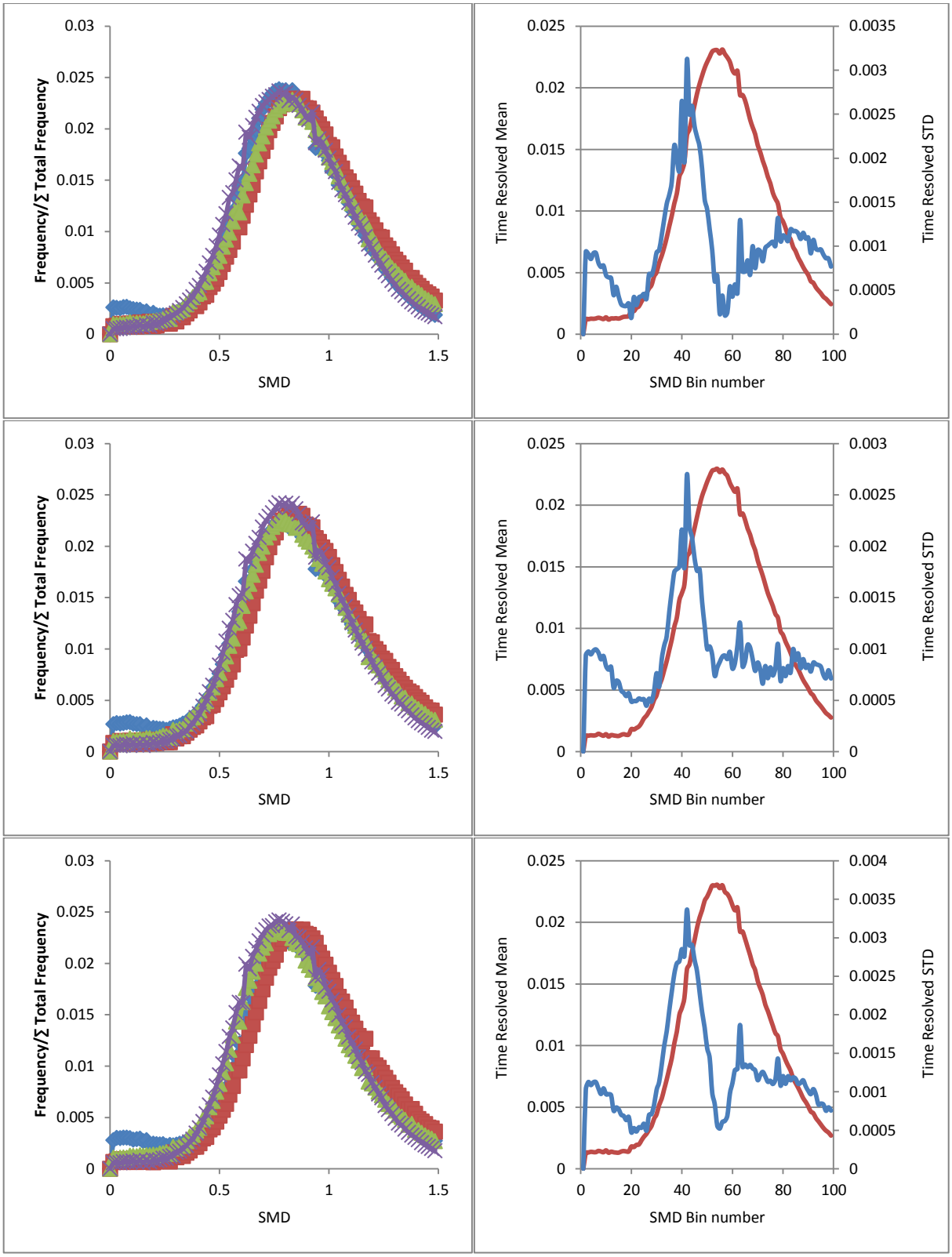

Figure C.3 Sum of BIN frequency relative SMD distributions obtained at the peak needle lift between 5.1 – 5.5 ms (top to bottom) for cases 1 – 4 and their corresponding mean and standard deviation